

JOURNAL OF THE Electrochemical Society

VOL. 117 NO. 11

NOVEMBER 1970



ELECTROCHEMICAL SCIENCE

Pages 1339-1383

SOLID STATE SCIENCE

Pages 1384-1442

ELECTROCHEMICAL TECHNOLOGY

Pages 1443-1462

REVIEWS AND NEWS

Pages 381C-414C

Call For Papers-Washington, D.C. Meeting — 415C

**Chlor-Alkali Producers
can count
on the**

**PROVEN
PERFORMANCE
OF GLC
GRAPHITE
ANODES**

**under
"Upset Conditions"**

GRAPHITE PRODUCTS DIVISION

**GREAT
LAKES
CARBON
CORPORATION**

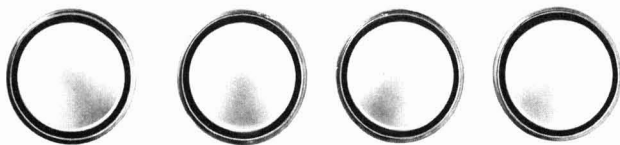
299 Park Avenue • New York, N.Y. 10017

Offices and Agents Coast-to-Coast and Around the World

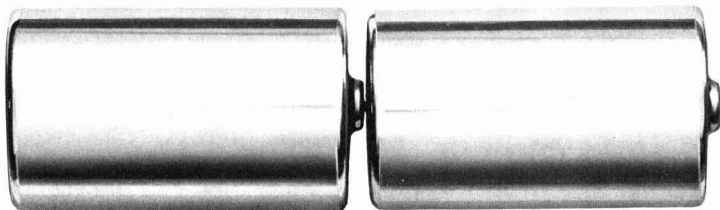


Great Lakes Carbon Corporation is one of the world's largest manufacturers of graphite for electrothermic and electrochemical processes—and for aerospace, nuclear, metallurgical and other industrial uses.

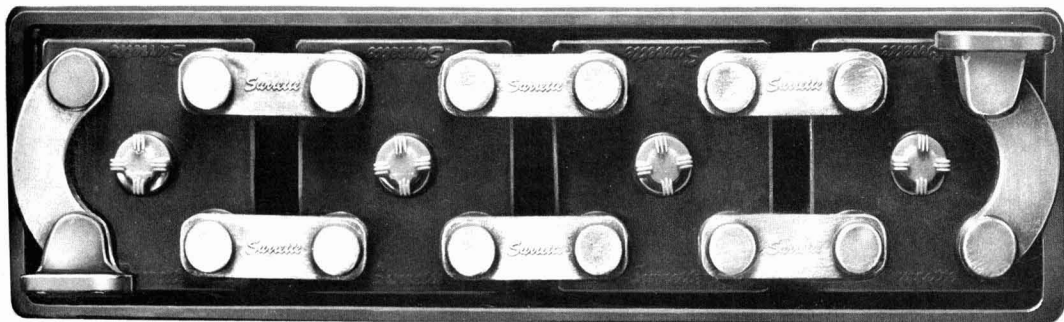
IMPROVE



BATTERY



PERFORMANCE



Battery performance gets a boost when you use Webril® nonwoven fabrics for separators and absorbers. For a number of very good reasons.

If primary and secondary battery systems are to perform much more reliably, they must inhibit dendrite growth and passage. Permit free ionic passage. Remain unaffected by acid or alkali. Loss of active plate material must be minimized. And electrolyte contact with plates must be assured. Webril nonwoven fabrics can do all this.

They have been performance-tested for over millions of hours in mercury-zinc, zinc-air, lead-acid, cuprous chloride, and nickel-cadmium systems. The unusually broad line of fine Webril products gives you greater design flexibility . . . even in fuel cells. You can choose from polypropylene, Dynel*, nylon, highly purified cotton, modified cellulose, and other fibers.

Find out more today. Write to Mr. P.N. Dangel, Electrical Specialties Department.



The Kendall Company
Fiber Products Division Walpole, Mass. 02081

*Union Carbide Corp. trademark for its modacrylic fiber.

EDITOR

Norman Hackerman

DIVISIONAL EDITORS

BATTERY

R. J. Brodd
Elton J. Cairns
L. W. NiedrachIsaac Trachtenberg
J. L. Weininger

CORROSION

Richard C. Carlston
Z. A. Foroulis
Harry C. Gatos
Jerome KrugerKen Nobe
J. Paul Pemsler
Earl S. Snavely, Jr.

DIELECTRICS AND INSULATION

T. W. Dakin
Donald M. SmythNewton Schwartz
Lawrence Young

ELECTRODEPOSITION

E. B. Saubestre

Seymour Senderoff

ELECTRONICS

Ephraim Banks
George R. Cronin
Simon Larach
Ernest Paskell
Bertram Schwartz
P. WangCharles M. Chapman
H. F. Ivey
I. Arnold Lesk
Jerome Prener
Alan J. Strauss
J. M. Woodall

ELECTRO-ORGANIC

Manuel M. Baizer

Stanley Wawzonek

ELECTROTHERMICS AND METALLURGY

J. M. Blocher, Jr.
W. E. KuhnJoan Berkowitz-Mattuck
J. H. Westbrook

INDUSTRIAL ELECTROLYTIC

P. A. Danna

Scott Lynn

THEORETICAL ELECTROCHEMISTRY

Allen J. Bard
M. W. Breiter
A. J. de BethuneR. M. Hurd
Royce J. Murray
C. W. Tobias

EDITORIAL STAFF

Cecil V. King, *Advisory Editor*
Angel Leshikar, *Assistant to the Editor*
Julius Klerer, *Book Review Editor*

PUBLICATION STAFF

Ruth G. Sterns, *Publication Editor*
Natalie M. Aust, *Associate Publication Editor*
Hanneliese Haitzinger, *Publication Assistant*

PUBLICATION COMMITTEE

Newton Schwartz, *Chairman*
Elton Cairns
Frederick Fowkes
Norman Hackerman
Earl S. Snavely, Jr.
Fred Strieter
Dennis R. Turner
Ernest B. Yeager

ADVERTISING OFFICE

30 East 42 St.
New York, N. Y. 10017

NOVEMBER 1970

ELECTROCHEMICAL SCIENCE

TECHNICAL PAPERS

W. O. Butler
C. J. Venuto
D. V. Wisler
... 1339

Electron Microscope Study of Positive Lead-Acid Electrodes during Formation

D. Elliot
D. L. Zellmer
H. A. Laitinen
... 1343

Electrochemical Properties of Polycrystalline Tin Oxide

J. A. Davis
B. E. Wilde
... 1348

Electrochemical Measurements on Austenitic Stainless Steels in Boiling Magnesium Chloride

S. Wawzonek
A. R. Zigman
G. R. Hansen
... 1351

Preparation of 2,3,4,5-Tetraphenyl-1,6-hexanedioic Acid

R. Hand
R. F. Nelson
... 1353

The Electrochemical Oxidation of N, N-dimethylaniline

D. L. Muck
E. R. Wilson
... 1358

Preparation of N-Alkylacetamides by the Anodic Oxidation of Carboxylic Acid Salts

A. M. Bond
G. A. Heath
R. L. Martin
... 1362

Polarography in Acetone of Tris (Dithioacetylacetonato)-Complexes of Iron(III), Ruthenium(III), Osmium(III), and Rhodium(III)

R. A. Bonewitz
G. M. Schmid
... 1367

Oxygen Adsorption on Gold and the Ce(III)/Ce(IV) Reaction

A. J. Appleby
... 1373

Oxygen Reduction and Corrosion Kinetics on Phase-Oxide-Free Palladium and Silver Electrodes as a Function of Temperature in 85% Orthophosphoric Acid

J. I. Masters
... 1378

The Ultraviolet Photovoltaic Effect in Evaporated Silver Bromide Conduction Cells

SOLID STATE SCIENCE

TECHNICAL PAPERS

- N. S. Choudhury**
J. W. Patterson
... 1384
- Steady-State Chemical Potential Profiles in Solid Electrolytes
- W. Lehmann**
... 1389
- Alkaline Earth Sulfide Phosphors Activated Copper, Silver, and Gold
- G. A. Antypas**
... 1393
- Liquid-Phase Epitaxy of $\text{In}_x\text{Ga}_{1-x}\text{As}$
- J. Bloem**
... 1397
- Silicon Epitaxy from Mixtures of SiH_4 and HCL
- C. M. Drum**
C. A. Clark
... 1401
- Anisotropy of Macrostep Motion and Pattern Edge-Displacements during Growth of Epitaxial Silicon on Silicon Near {100}
- M. L. Barry**
... 1405
- Doped Oxides as Diffusion Sources II. Phosphorus into Silicon
- J. E. Foster**
J. M. Swartz
... 1410
- Electrical Characteristics of the Silicon Nitride-Gallium Arsenide Interface
- H. A. Allen**
... 1417
- The Orientation Dependence of Epitaxial $\text{InAs}_x\text{P}_{(1-x)}$ on GaAs
- A. J. Strauss**
J. Steininger
... 1420
- Phase Diagram of the CdTe-CdSe Pseudobinary System
- J. R. Carruthers**
M. Grasso
... 1426
- Phase Equilibria Relations in the Ternary System $\text{BaO-SrO-Nb}_2\text{O}_5$
- A. D. Dalvi**
W. W. Smeltzer
... 1431
- Thermodynamics of the Iron-Nickel-Oxygen System at 1000°C

TECHNICAL NOTES

- R. W. Bartlett**
M. Barlow
... 1436
- Surface Polarity and Etching of Beta-Silicon Carbide

DIVISION OFFICERS

Battery Division

Paul C. Milner, Chairman
Alvin J. Salikind, Vice-Chairman
Howard R. Karas, Secretary-Treasurer
General Battery Corporation
P. O. Box 1262
Reading, Pa. 19603

Corrosion Division

M. J. Pryor, Chairman
Z. Andrew Forouls, Vice-Chairman
J. Paul Pemsler, Secretary-Treasurer
Ledgemont Laboratory
Kennecott Copper Corp.
128 Spring St.
Lexington, Mass. 02173

Dielectrics and Insulation Division

Donald M. Smyth, Chairman
Dieter Gerstenberg, Vice-Chairman
Lyon Mandelcorn, Treasurer
L. V. Gregor, Secretary
IBM—East Fishkill Facility
Hopewell Junction, N. Y. 12533

Electrodeposition Division

Seward E. Beacom, Chairman
Edward B. Saubestre, Vice-Chairman
Rolf Weil, Secretary-Treasurer
Dept. of Metallurgy
Stevens Institute of Technology
Hoboken, N. J. 07030

Electronics Division

Roger Newman, Chairman
Harry Sello, Vice-Chairman (Semiconductors)
Frank Pailila, Vice-Chairman (Luminescence)
E. M. Peil, Vice-Chairman (General Electronics)
Bertram Schwartz, Secretary-Treasurer
Bell Telephone Laboratories, Inc.
Murray Hill, N. J. 07974

Electro-Organic Division

Thomas B. Reddy, Chairman
Allen J. Bard, Vice-Chairman
Robert E. Visco, Secretary-Treasurer
Engineering Research Center
Western Electric Co., Inc.
P.O. Box 900
Princeton, N. J. 08540

Electrothermics and Metallurgy Division

Stanley T. Wlodek, Chairman
Joan B. Berkowitz-Mattuck, Vice-Chairman
Walter W. Smeltzer, Vice-Chairman
Rolf Haberecht, Secretary-Treasurer
Texas Instruments, Inc.
P.O. Box 5303, Mail Station 144
Dallas, Texas 75222

Industrial Electrolytic Division

Luther Vaaler, Chairman
Nolan E. Richards, Vice-Chairman
D. N. Goens, Secretary-Treasurer
Kerr-McGee Corporation
12519 E. Washington Blvd.
Whittier, Cal. 90602

Theoretical Electrochemistry Division

Christie G. Enke, Chairman
Robert E. Medley, Vice-Chairman
Manfred W. Breiter, Secretary-Treasurer
General Electric
R & D Center
Schenectady, N. Y. 12301

SOCIETY OFFICERS

Charles W. Tobias, President
101D Gilman Hall
University of California
Berkeley, Calif. 94720

Cecil V. King, Vice-President
American Gas & Chemicals, Inc.
511 East 72 St.
New York, N. Y. 10021

Theodore D. McKinley, Vice-President
E. I. du Pont de Nemours & Co. Inc.
Pigments Department
Experimental Station
Wilmington, Del. 19898

N. Bruce Hannay, Vice-President
Bell Telephone Laboratories, Inc.
Murray Hill, N. J. 07971

Dennis R. Turner, Secretary
Bell Telephone Laboratories, Inc.
Room 1E-247
Murray Hill, N. J. 07971

R. Homer Cherry, Treasurer
2350 Huntingdon Road
Huntingdon Valley, Pa. 19006

Ernest G. Enck, Executive Secretary
The Electrochemical Society, Inc.
30 East 42 St.
New York, N. Y. 10017

Manuscripts submitted to the Journal should be sent, in triplicate, to the Editorial Office at 30 East 42 St., New York, N. Y., 10017. They should conform to the revised "Instructions to Authors" available from Society Headquarters. Manuscripts so submitted, as well as papers presented before a National technical meeting, become the property of the Society and may not be published elsewhere in whole or in part without written permission of the Society. Address such requests to the Editor.

The Electrochemical Society does not maintain a supply of reprints of papers appearing in its Journal. A photoprint copy of any particular paper may be obtained from University Microfilms, 300 North Zeeb Road, Ann Arbor, Michigan 48106.

Inquiries re positive microfilm copies of volumes should be addressed to University Microfilms, Inc., 300 N. Zeeb St., Ann Arbor, Mich. 48106.

Walter J. Johnson, Inc., 111 Fifth Ave., New York, N. Y., 10003, have reprint rights to out-of-print volumes of the Journal, and also have available for sale back volumes and single issues, with the exception of the current calendar year. Anyone interested in securing back copies should correspond direct with them.

Published monthly by The Electrochemical Society, Inc., at 215 Canal St., Manchester, N. H.; Executive Offices, Editorial Office, and Circulation Dept., and Advertising Office at 30 East 42 St., New York, N. Y., 10017, combining the JOURNAL and TRANSACTIONS OF THE ELECTROCHEMICAL SOCIETY. Statements and Opinions given in articles and papers in the JOURNAL OF THE ELECTROCHEMICAL SOCIETY are those of the contributors, and The Electrochemical Society assumes no responsibility for them.

Claims for missing numbers will not be allowed if received more than 60 days from date of mailing plus time normally required for postal delivery of JOURNAL and claim. No claims allowed because of failure to notify the Circulation Dept., The Electrochemical Society, 30 East 42 St., New York, N. Y., 10017, of a change of address, or because copy is "missing from files." Subscription to members as part of membership service; subscription to non-members \$40.00 plus \$3.00 for postage outside U.S. and Canada. Single copies \$2.50 to members, \$4.00 to nonmembers. © 1970 by The Electrochemical Society, Inc. Second Class Postage Paid at New York, New York, and Manchester, N. H. Printed in U.S.A.

SOLID STATE SCIENCE (Cont.)

R. T. Shoemaker
C. E. Anderson
G. L. Liedl
... 1438

Sputtering of Bismuth-Titanium Two-Phase Cathodes

S. H. A. Begemann
A. W. Smith
... 1440

Dielectric Properties of Surface Oxides on Aluminum

ELECTROCHEMICAL TECHNOLOGY

TECHNICAL PAPERS

R. L. Zahradnik
... 1443

Diffusional Processes in Solid Electrolyte Fuel Cell Electrodes

R. D. Cowling
H. E. Hintermann
... 1447

The Corrosion of Titanium Carbide

S. E. Craig, Jr.
R. E. Harr
J. Henry
P. Turner
... 1450

A Comparison of Various 24K Gold Electrodeposits

P. F. Grosso
R. E. Rutherford, Jr.
D. E. Sargent
... 1456

Electrophoretic Deposition of Luminescent Materials

TECHNICAL NOTES

A. M. McKissick, Jr.
A. A. Adams
R. T. Foley
... 1459

Synergistic Effects of Anions in the Corrosion of Aluminum Alloys

E. L. Hollar
F. N. Rebarchik
D. M. Mattox
... 1461

Composite Film Metallizing for Ceramics

REVIEWS AND NEWS

REVIEW

V. A. Lamb
C. E. Johnson
D. R. Valentine
... 381C

Physical and Mechanical Properties of Electrodeposited Copper
III. Deposits from Sulfate, Fluoborate, Pyrophosphate, Cyanide, and Amine Baths

NEWS

... 405C

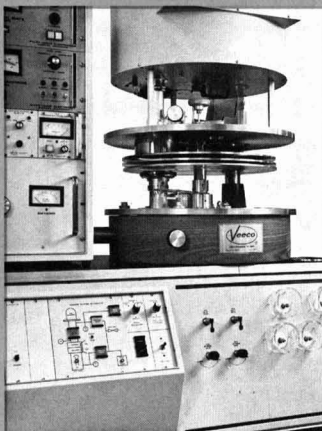
ANNOUNCING VEECO'S 30 DAY WONDER

Help yourself to improved sputtering yield with Veeco's total capability. Veeco has the sputtering system you need. And Veeco doesn't make you wait.

1 GUARANTEED DELIVERY

Veeco will deliver your system and make it operational in 30 days or less regardless of options chosen or complexity.

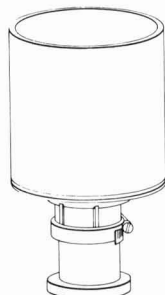
Veeco built and installed this convertible RF Sputter/E Beam system in 4 weeks



2 MODULAR DESIGN

Veeco has a complete line of interchangeable modules providing maximum versatility of sputtering capability with reliable, repeatable performance.

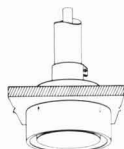
- 5 substrate holding and transfer systems
- 6 shutter configurations
- 7 RF&DC power supplies
- 5 different process control systems
- 6 RF&DC electrode assemblies (shown)



Cylindrical RF



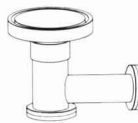
RF Sputter Up/Etch



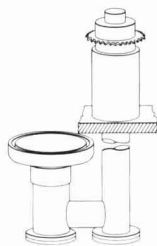
RF Sputter Down



DC



RF Right Angle



Rotary RF Bias

3 SINGLE SOURCE

Veeco offers a complete line of off-the-shelf components, modules, vacuum stations, complete systems and sputtering targets. One single, responsible source from design to delivery.

Every component in this 3 KW RF+DC Sputter/Etch/Bias System was made by Veeco



4 QUALITY WITHOUT COMPROMISE

All materials used are precision made and carefully selected. Quality control is continuous throughout assembly.

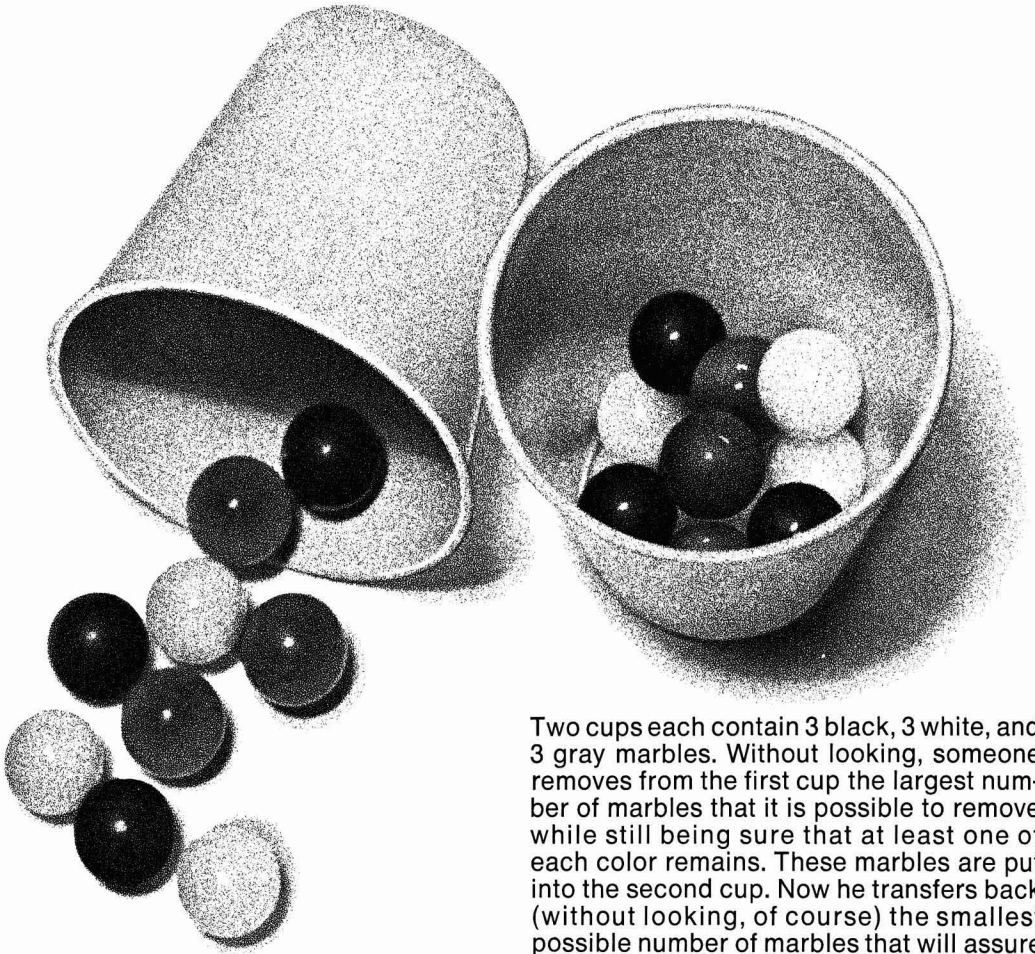
Component materials used:

1. All components 304 stainless, OFHC copper or vacuum-fired ceramic
 2. No aluminum. No cast parts.
- Vacuum joining & assembly techniques:
1. All seals baked viton
 2. All hardware vacuum relieved

So, why wait? To find the best solution to your problem, send for the new 32-page brochure describing Veeco's full sputtering capabilities.

VEECO INSTRUMENTS INC.

Terminal Drive, Plainview, N.Y. 11803
Telephone 516/681-8300



Two cups each contain 3 black, 3 white, and 3 gray marbles. Without looking, someone removes from the first cup the largest number of marbles that it is possible to remove while still being sure that at least one of each color remains. These marbles are put into the second cup. Now he transfers back (without looking, of course) the smallest possible number of marbles that will assure there being at least 2 of each color in the first cup.

How many marbles remain in the second cup?

* The solution to this puzzle is on page 412C
From the book *PUZZLE ME THIS*, Copyright © 1968 by Philip Kaplan
Reprinted by permission of Harper & Row, Publishers.



**FOR THE BEST SOLUTION TO YOUR
ANODE NEEDS, SIMPLY SPECIFY
STACKPOLE GRAPHANODES®.**

STACKPOLE CARBON COMPANY CARBON DIVISION ST. MARYS, PA. 15857





Electron Microscope Study of Positive Lead-Acid Electrodes during Formation

W. O. Butler,* C. J. Venuto,* and D. V. Wisler

ESB Incorporated, Research Center, Yardley, Pennsylvania 19067

ABSTRACT

The formation process of positive lead-acid electrodes was studied using electron microscopy, and these results were correlated with those of x-ray diffraction and chemical analysis. Both the surface and the interior reactions taking place during active material formation were examined. The study showed the conversion of PbSO_4 crystals to $\beta\text{-PbO}_2$ and the subsequent growth of $\beta\text{-PbO}_2$ crystals to fully formed crystals. In addition, the crystal habits of $3\text{PbO}\cdot\text{PbSO}_4\cdot\text{H}_2\text{O}$, PbSO_4 , and $\beta\text{-PbO}_2$ in lead-acid electrodes were characterized.

Even though a number of years have elapsed since Planté presented his first storage battery to the French Academy of Sciences in 1860, the physical and chemical reactions taking place during electrode processing are still not fully understood. The literature abounds with publications on electrical and chemical studies of the system, and in recent years the more sophisticated techniques have been used to investigate these processes. X-ray diffraction, optical and electron microscopy, and electron microprobe analysis are now being used to study not only the physiochemical reactions taking place during electrode processing but also the reactions taking place during electrode cycling.

However, the work reported here is limited to a study of the formation process, that is, the anodization of fully cured electrodes to convert the electrode's active material from a mixture of $3\text{PbO}\cdot\text{PbSO}_4\cdot\text{H}_2\text{O}$, PbO , and Pb to PbO_2 .

Simon and Jones (1) used optical microscopy to great advantage in studying the formation process. Pierson (2) combined optical microscopy with x-ray diffraction and chemical analysis in his formation studies. An electron probe was used by Chiku and Nakajima (3) to study the formation process. Fully formed active material was studied using electron microscopy by Burbank and Ritchie (4, 5). To our knowledge, only Buskirk, Boyd, and Smith (6) used electron microscopy to study the active material during the different stages of formation. However, no correlation was made between the electron microscopy data and x-ray diffraction, optical microscopy, and chemical analysis.

This paper describes a study of both the surface and interior active material, examined *in situ* on Pb grids at various stages of formation. The electron microscopy data is closely correlated with x-ray diffraction data and with previous formation studies in our laboratory using optical microscopy and chemical analysis.

Experimental

Fully cured electrodes using Pb-5.75% Sb grids were formed at the rate of 160 A-hr/lb of active material for 1, 3, 7, 9, 11, 15, and 20 hr. The formation current was selected so that at 20 hr the electrodes received a full 160 A-hr/lb and were thus considered fully formed. The forming electrolyte was 1.060 sp gr H_2SO_4 . After the desired formation time the electrodes were washed for 15 hr in distilled H_2O and then dried at 60°C in a mechanically pumped vacuum oven. Both the surface and the interior of the electrodes were examined. Single stage carbon replicas preshadowed with platinum-carbon pellets (7) were made of the surfaces of the different samples. The replicas were released using 25-50% HCl. The surface was also examined by x-ray diffraction.

The interiors of the sample electrodes were examined after scraping the surface parallel to the face of the electrode. A $1\frac{1}{2}$ in. square was cut from the sample electrode. The surface was scraped with a clean razor blade until approximately one-half of the active material was removed. Prior to replication, the scraped surface was analyzed by x-ray diffraction. The carbon replicas of the surface and interior (scraped surface) were then examined in an RCA EMU-3G electron microscope. In addition, the active material, after it was removed from the Pb grid, of all seven formed samples was examined by x-ray diffraction. To characterize fully the crystal habits of the different compounds in lead-acid electrodes, plates consisting of only PbSO_4 , $3\text{PbO}\cdot\text{PbSO}_4\cdot\text{H}_2\text{O}$, tetragonal and orthorhombic phases of PbO , and the α and β phases of PbO_2 (confirmed by x-ray diffraction) were examined by electron microscopy. The crystal habits of PbSO_4 , $3\text{PbO}\cdot\text{PbSO}_4\cdot\text{H}_2\text{O}$, and $\beta\text{-PbO}_2$ were definitely characterized. Both $\beta\text{-PbO}_2$ and PbSO_4 have an equant crystal habit. Beta- PbO_2 usually exhibits a dipyramidal crystal form while PbSO_4 exhibits a combination of crystal forms with the prismatic and domal forms being more prevalent. $3\text{PbO}\cdot\text{PbSO}_4\cdot\text{H}_2\text{O}$, as it appears in cured electrodes, is columnar in crystal habit.

* Electrochemical Society Active Member.

Key words: electrode microstructure, electron microscopy, lead acid electron microscopy, and lead acid formation.

Orthorhombic-PbO appeared as equidimensional grains and was difficult to distinguish from free Pb particles. Tetragonal-PbO has several crystal habits, one similar to orthorhombic-PbO and another tabular. Alpha-PbO₂ was particularly hard to characterize in that it is difficult to produce a pure standard and it seems to crystallize in a variety of crystal habits.

Observations

Surface examination.—A typical electron micrograph of the surface of a fully cured, unformed, positive electrode used in this study is shown in Fig. 1. The long columnar crystals are 3PbO·PbSO₄·H₂O, and the irregular grains are tetragonal or orthorhombic-PbO. X-ray diffraction indicates 3PbO·PbSO₄·H₂O and orthorhombic and tetragonal-PbO to be present on the surface. No free Pb was detected by x-ray diffraction on the surface of the cured electrode.

The surface of an electrode formed for 1 hr is shown in Fig. 2. Both the large well-developed crystals and the smaller crystals are PbSO₄. No effect of the anodization process was noted at this time. X-ray diffrac-

tion did detect a little tetragonal and orthorhombic-PbO. No 3PbO·PbSO₄·H₂O or PbO₂ was detected by x-ray diffraction.

Active material areas near grid members were converted to β -PbO₂ after 5 hr of formation. The β -PbO₂ crystals are initially rounded agglomerate crystal growths as shown in areas A of Fig. 3b. Beta-PbO₂ crystals next to the grid members, see Fig. 3a, are better formed since the formation reaction is initiated at the grid active material interface and then progresses toward the center of the active material pellets. The central portion of the active material pellets are still composed of unaltered PbSO₄ crystals as shown in Fig. 2.

After 9 hr of formation the β -PbO₂ crystals which make up the formed aggregates have become larger and their dipyrarnidal crystal form can be observed (Fig. 4). In addition, much more β -PbO₂ is present on the electrode surface.

At the end of 11 hr of formation the β -PbO₂ crystals have continued their development. At this state of formation the central portions of the pellet surface

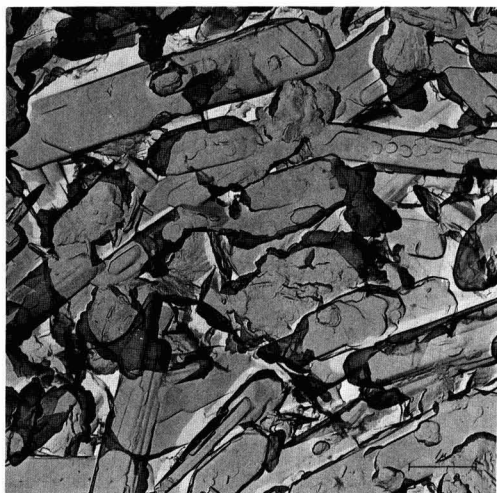


Fig. 1. Surface of a fully cured positive lead-acid electrode. Shows elongated 3PbO·PbSO₄·H₂O crystals and irregular grains of PbO.

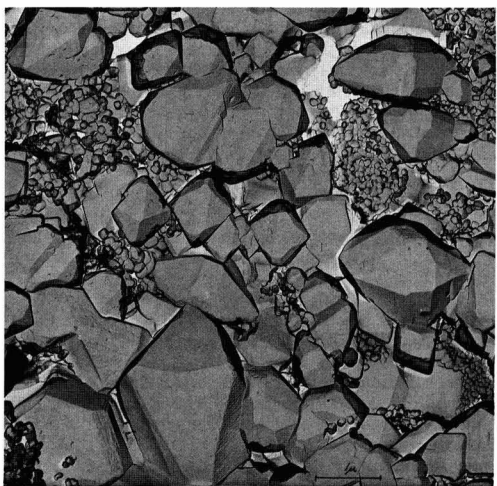


Fig. 2. Positive electrode formed for 1 hr showing electrode surface covered with large and small PbSO₄ crystals.

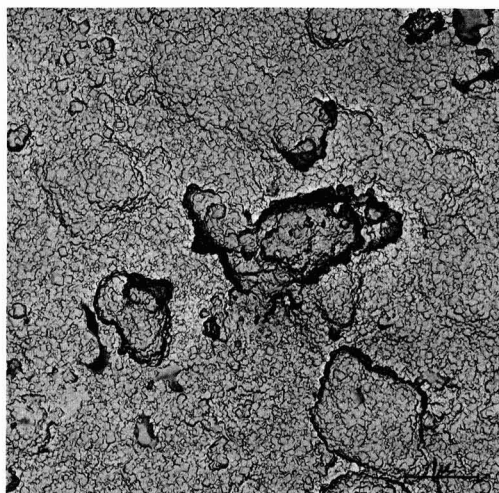


Fig. 3. Electrode surface after 5 hr of formation: (a, top) active material next to a grid member; small crystals are β -PbO₂; (b, bottom) active material further away from a grid member. Well developed crystals are PbSO₄. The initial appearance of β -PbO₂ occurs as rounded crystal agglomerates and appear in areas A of the electron micrograph.

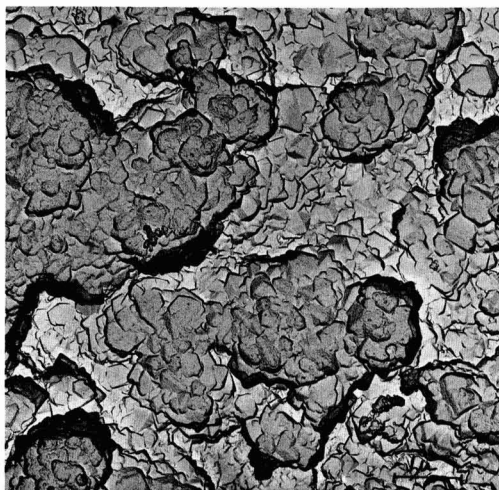


Fig. 4. Electrode surface after 9 hr of formation showing the development of the initial rounded crystal agglomerates of β - PbO_2 into larger well-defined crystal groups.

begin to form and appear similar to the areas shown in Fig. 3. These reactions continue throughout the remainder of the electrochemical formation. An electron micrograph of a fully formed surface observed in the central pellet area is shown in Fig. 5. The well-developed dipyramidal β - PbO_2 crystals are typical for a fully formed electrode. X-ray diffraction showed that the surface of the fully formed electrode consists of β - PbO_2 with trace amounts of the tetragonal and orthorhombic-PbO.

Interior examination.—The interior of the above electrodes were examined as above in order to determine if the same general sequence of formation reactions occurred in the interior as on the surface. X-ray diffraction examination of the fully cured active material indicated it is composed of mainly $3\text{PbO} \cdot \text{PbSO}_4 \cdot \text{H}_2\text{O}$ plus minor amounts of Pb and orthorhombic and tetragonal PbO.

The interior active material after 1 hr of formation (Fig. 6) is still essentially the same as for a fully cured electrode (unformed). It consists of $3\text{PbO} \cdot \text{PbSO}_4 \cdot \text{H}_2\text{O}$, tetragonal and orthorhombic-PbO, PbSO_4 , and Pb.

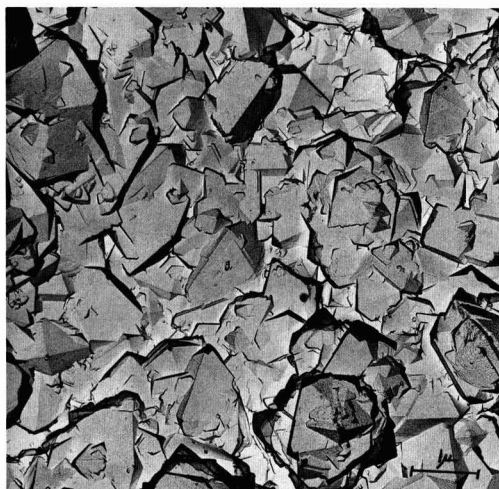


Fig. 5. Surface of a fully formed (20 hr) positive electrode. Shows well developed β - PbO_2 dipyramidal crystals.



Fig. 6. Interior active material of a 1-hr formed electrode. Compounds present are $3\text{PbO} \cdot \text{PbSO}_4 \cdot \text{H}_2\text{O}$, PbSO_4 , orthorhombic and tetragonal-PbO, and free Pb.

After 5 hr of formation, only a small amount of $3\text{PbO} \cdot \text{PbSO}_4 \cdot \text{H}_2\text{O}$ remains (Fig. 7). The interior is primarily composed of PbSO_4 , β - PbO_2 , and tetragonal-PbO. A small amount of α - PbO_2 was also detected by x-ray diffraction.

The interior of an 11 hr formed electrode no longer contains any $3\text{PbO} \cdot \text{PbSO}_4 \cdot \text{H}_2\text{O}$ (Fig. 8). It is primarily composed of β - PbO_2 , tetragonal-PbO, α - PbO_2 , and PbSO_4 . Figure 8 shows agglomerates of β - PbO_2 forming at the expense of large PbSO_4 crystals.

The reaction sequences are very similar to those observed on the electrode surfaces for the remainder of the formation time. X-ray diffraction shows that the fully formed interior active material is composed of α - and β - PbO_2 plus some tetragonal-PbO. Chemical analysis indicates the total (surface and interior) fully formed active material contains 81% PbO_2 , 17% PbO, with the remaining 2% being Pb and PbSO_4 .

An electron micrograph of a typical fully formed interior is shown in Fig. 9. The overgrowths on the

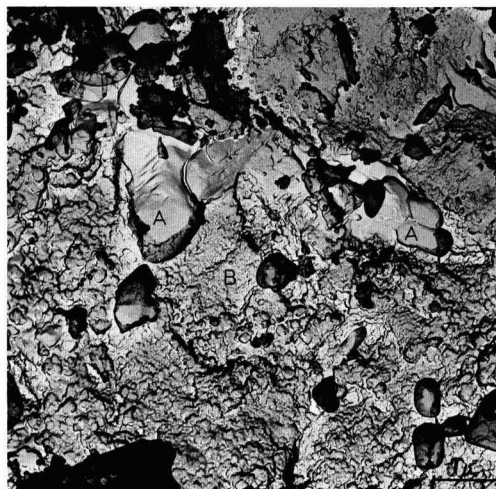


Fig. 7. Electrode interior after 5 hr of formation. Large PbSO_4 crystals (A), agglomerate crystalline mass of β - PbO_2 (B), and a small amount of tetragonal-PbO which is indistinguishable are shown.



Fig. 8. Interior of positive electrode after 11 hr of formation showing large PbSO_4 crystals being converted to crystalline aggregates of $\beta\text{-PbO}_2$.

faces of the $\beta\text{-PbO}_2$ crystals in Fig. 9 were observed on crystals both on the surface and in the interior of the fully formed electrode. Once the $\beta\text{-PbO}_2$ crystals reach a definite size, growth of an individual crystal slows considerably or even ceases, and any further formation occurs as new crystals developing on the faces (presumably where imperfections are present) of the fully matured crystals. This phenomenon was naturally more prevalent in active material nearer grid members.

The sequence of reactions observed in the interior of the electrodes is very similar to those observed on the electrode surfaces. The main differences are (i) the presence of more PbSO_4 on the surface, especially during the initial formation period, and (ii) no $\alpha\text{-PbO}_2$ was detected on the surfaces of the different formed electrodes. Crystals believed to be $\alpha\text{-PbO}_2$ were observed in the active material interior near the grid members as shown in Fig. 10. However, these

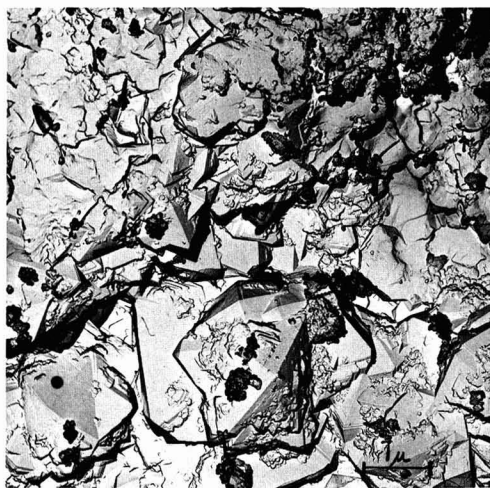


Fig. 9. Interior of a fully formed (20 hr) positive electrode showing well-developed $\beta\text{-PbO}_2$ dipyrnidal crystals.



Fig. 10. Interior of active material after 15 hr of formation showing undeveloped crystalline masses (A) and large well-developed crystals believed to be $\alpha\text{-PbO}_2$ (B). Active material area is very near a grid member. These and similar areas were observed in both 15- and 20-hr formed electrodes.

crystals could not be definitely characterized as $\alpha\text{-PbO}_2$ with a standard as was done with the other lead compounds.

Concluding Remarks

This study established that the initial reactions taking place during formation are essentially chemical. These chemical reactions consist mainly of converting $3\text{PbO} \cdot \text{PbSO}_4 \cdot \text{H}_2\text{O}$ and orthorhombic-PbO to PbSO_4 . Tetragonal-PbO is not as easily converted to PbSO_4 . Second, the resulting PbSO_4 and PbO are then electrochemically converted to PbO_2 . The interior and surface reactions are essentially the same. The one major difference is the absence of $\alpha\text{-PbO}_2$ forming on the electrode's surface. Also, $\alpha\text{-PbO}_2$ preferentially forms in the interior near the grid members and assumes a variety of crystal habits.

The crystal habits of $3\text{PbO} \cdot \text{PbSO}_4 \cdot \text{H}_2\text{O}$, PbSO_4 , and $\beta\text{-PbO}_2$ in positive lead-acid electrodes were definitely established, and electron micrographs were obtained showing the conversion of PbSO_4 crystals to PbO_2 crystals and the subsequential growth of $\beta\text{-PbO}_2$ crystals to their full size as found in a fully formed electrode.

Manuscript submitted May 19, 1970; revised manuscript received ca. July 22, 1970.

Any discussion of this paper will appear in a Discussion Section to be published in the June 1971 JOURNAL.

REFERENCES

1. A. C. Simon and E. L. Jones, *This Journal*, **109**, 760 (1962).
2. J. R. Pierson, *Electrochem. Technol.*, **5**, 323 (1967).
3. T. Chiku and K. Nakajima, *This Journal*, **116**, 1407 (1969).
4. J. Burbank, *ibid.*, **113**, 10 (1966).
5. J. Burbank and E. J. Ritchie, *ibid.*, **116**, 125 (1969).
6. J. E. Buskirk, P. D. Boyd, and V. V. Smith, Paper 19 presented at the Houston Meeting of the Society, Oct. 9-13, 1960.
7. D. E. Bradley, "Techniques for Electron Microscopy," H. Kay, Editor, p. 109, F. A. Davis Co., Philadelphia (1965).

Electrochemical Properties of Polycrystalline Tin Oxide

D. Elliott, D. L. Zellmer,¹ and H. A. Laitinen*

Department of Chemistry, University of Illinois, Urbana, Illinois 61801

ABSTRACT

Some electrochemical properties of polycrystalline tin oxide in the form of thin films have been examined. For a variety of antimony-doped specimens the carrier concentration has been determined from the space charge capacity and compared with donor concentrations. Disparities between the two values have been found, and explanations have been sought in terms of structural defects as well as chloride impurity and nonstoichiometry. Analyses for the last two have been made. The kinetics of several reactions at highly doped specimens (5.9×10^{20} carriers/cc) indicate that the space charge region is completely transparent to electrons due to tunneling. With a series of samples of diminishing carrier concentration the increasing limitation of the tunneling process is demonstrated until it becomes the principal current controlling factor at about 3×10^{19} carriers/cc.

Polycrystalline tin dioxide, deposited as a thin conducting layer on glass or quartz, has recently come into some use as an electrode material with unique properties. Among these are transparency, resistance to oxidation, and the absence of adsorption by organic surfactants.² Extensive use of the first property, for example, has been made by Kuwana and co-workers (1), and also by others (2). The present investigation is part of a series aimed at characterizing the electrode surface (3, 4). The latter reference contains a fairly comprehensive list of references dealing with the electronic properties of tin oxide. A recent paper by others on the electrode properties has also appeared (5).

Tin oxide is a semiconducting material of large band-gap (3.7 eV). Its intrinsic resistivity is very high but may be decreased enormously by the introduction of appropriate doping agents. Minimum values down to about 2.5×10^{-4} ohm cm are reached with a few per cent antimony. Further increase in the antimony concentration causes the resistance to get larger again, probably caused by increasing lattice disorder (6, 7).

Experimental

Two types of electrode have been used in the study. The first was a commercially available tin oxide coated glass (here designated IRR).³ This was analyzed⁴ to contain 2.5 m/o (mole per cent) Sb. Also included under this heading are some special samples made by the same manufacturer to the author's specifications and containing varying percentages of antimony (Table I). The second type was prepared in the laboratory by hydrolysis of an atomized solution of acidified SnCl_4 containing various percentages of SbCl_3 on a hot substrate which was variously Pyrex, quartz, or polished platinum. In both cases the thickness ranged up to about $1 \mu\text{m}$. The mounting technique has been described (3). Electrical contact was made via a flat silver ring of about $\frac{1}{2}$ -in. diameter which pressed against the surface concentric with the exposed working area of $5/32$ -in. diameter (0.1236 cm^2). This ensured that for tin oxide layers on nonconducting bases the series resistance was as low as possible to facilitate capacitance measurements up to 20 kHz. Such a contact also minimizes capacitance dispersion due to the distributed resistance of the thin film (Appendix). Capacitance measurements were made with base elec-

Table I. Carrier concentrations

Spray	Sb content, m/o Analysis*	Carrier conc./cm ³	Donor conc. equiv. to carriers, m/o	Resistivity, ohm cm
8**	13	$2.9_7 \times 10^{21}$ †	10.7	1.32×10^{-2}
3**	5.4	$1.3_0 \times 10^{21}$	5.0	1.62×10^{-3}
0.8**	1.7	$4.8_3 \times 10^{20}$	1.74	1.23×10^{-3}
0.3**	0.6	$3.4_9 \times 10^{20}$	1.26	9.7×10^{-4}
0.1**	0.2	$2.6_5 \times 10^{20}$	0.95	2.09×10^{-4}
Sample IRR	2.5	$5.9_3 \times 10^{20}$	2.13	9.2×10^{-4}

* By emission spectroscopy.

** Special samples made by Corning.

† At 10 kHz corrected for "transmission sheet" dispersion.

trolyte only under conditions of cyclic linear potential scan at a rate of 0.5 V/min. Using a phase sensitive detector, Fig. 1, and with a Pt counterelectrode of about 24 cm^2 area, the reciprocal capacitance was recorded directly. No change in capacitance or background current was produced by deaeration of the electrolyte or shielding from daylight. With electroactive species present linear sweep voltammograms at the stationary electrode were recorded using a conventional three-electrode system. Thickness of the conducting layer was determined from the variation of the interference maxima and minima as a function of wavelength for a reflected light beam at 45° inci-

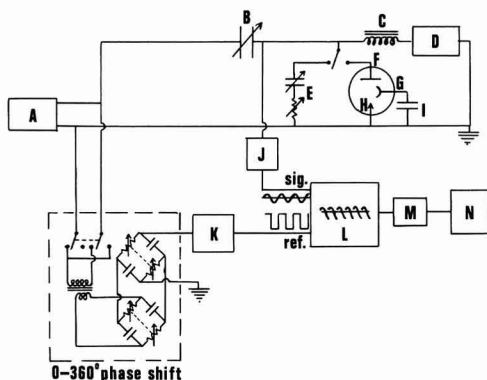


Fig. 1. Diagram of circuit for the automatic recording of capacitance and resistance: A, signal generator; B, capacitor, variable 50-1000 pf; C, choke, 300H; D, linear sweep voltage source; E, standard resistance and capacitance decade boxes; F, tin oxide electrode; G, counterelectrode; H, saturated calomel electrode (SCE); I, 250 μF capacitor; J, amplifier; K, square wave generator; L, phase sensitive detector; M, filter; N, recorder.

* Electrochemical Society Active Member.

¹ Present address: Fresno State College, Department of Chemistry, Fresno, California 93721.

² The measured capacity is unaffected for example by the addition of 0.01% Triton X-100.

³ "Infra-Red Reflecting" from Corning Glass Works, Corning, New York.

⁴ By emission spectroscopy.

Key words: semiconductor, thin film electrode, transparent electrode, differential capacitance measurement.

dence. Conductivity was determined by a four-point probe method. Reproducible results for the capacity and linear sweep base current were found only after specimens had been polished. Polishing was effected with 0.3 and 0.05 μm alumina abrasives and also with a polishing compound made of powdered tin oxide.⁵ The electrodes were then boiled in water or cleaned in steam before use, and allowed to dry in air or heated in an air oven.

Results

Variation of capacity with various parameters.—Measurements made in the first minutes after contact with the electrolyte are about 5% lower than the values finally reached after several hours when equilibrium is attained. This may be associated with the slow adsorption of ions causing a shift in the flat band potential. A positive shift is indicated suggesting that a slow chemisorption of H^+ ions to the oxide ions of the lattice is the dominant factor. This is in accordance with the observation that the surface after contact with acid electrolyte is completely wetted whereas the initially prepared surface after polishing and boiling in water is strongly hydrophobic. Measurements of the contact angle in fact show large changes during the first hour of contact. This phenomenon together with an account of the adsorption of halide ions is discussed in ref. (4). The measurements of capacitance were made after several hours contact, and data were taken from the recorded graph after two or three cycles of the scanning voltage. Only a small difference ($\sim 1\%$) is noted in the capacitance values for the cathodic and anodic sweeps; likewise the difference between the first and successive cycles is less than 1% suggesting that the value recorded was at equilibrium. The background current varies between specimens but is generally between 0.1 and 0.05 μA for the area used (0.124 cm^2) in 1M acid. Such values are observed within the cathodic and anodic limits set by the decomposition of the electrolyte. The potential of H^+ reduction is near the reversible value especially after prolonged contact with the electrolyte. Oxidation, however, occurs with a large overvoltage which depends on the doping level; e.g., for IRR this takes place at about +2V vs. SCE in 1M H_2SO_4 .

In the absence of surface states the capacity of a semiconductor-electrolyte system may be subdivided into three series capacitances due to the semiconductor space charge, the compact double layer, and the diffuse double layer. The last two would be expected to be large in 1M electrolyte especially at the positive potentials used (up to +2.0V vs. SCE) so that the measured capacitance should closely approximate to the space charge value. The experimental justification for this is based on the application of the Mott-Schottky relationship (8, 9) valid for high carrier concentrations.

$$\frac{1}{C^2} = \frac{2}{qK\epsilon C_D} \left(V - \frac{RT}{F} \right)$$

- where C = space charge capacitance
 q = electronic charge
 K = dielectric constant (mean value 12.7)
 ϵ = permittivity of vacuum
 C_D = carrier concentration
 V = potential with respect to the flat band potential V_B (zero charge potential)

It is implicit in the use of this relationship that the surface potential should remain constant while the potential of the bulk of the semiconductor is varied, thus approximating to the one sided step junction concept (9). Because of the adsorption of ions the surface potential differs from the bulk value even in

concentrated electrolytes. For this difference to remain constant the net adsorbed charge must increase negatively as the electrode is positively changed. If these charges are not matched, the $1/C^2$ graph can be curved or have a slope other than that determined solely by the carrier concentration. Electrode roughness can also cause curvature of the characteristic since the effective area decreases as the depletion layer extends into the bulk of the electrode with increasing applied voltage. These considerations are particularly relevant for highly doped specimens where the depletion layer (9) is only a few tens of angstroms thick, e.g., for IRR containing 5.9×10^{20} carriers/ cm^3 the thickness is 16.9Å at 1.0V vs. SCE).

Effect of donor concentration and frequency.—Satisfactory linear graphs of $1/C^2$ vs. applied potential have been obtained for samples containing up to 13% antimony; an example is shown in Fig. 2.

Table I shows a comparison of computed carrier concentrations based on capacitance measurements (at 20 kHz except where noted) with the antimony concentrations of a series of samples coated on glass.

At low concentrations the carrier values are higher than those due to the antimony alone probably because of other carrier mechanisms, e.g., oxygen deficiency and residual chloride. The two values agree at about 1.7% Sb which is not far from the value where the conductivity is a maximum. Samples containing more than this percentage are noticeably blue colored (the 13% sample is almost opaque). This behavior, together with the sharp increase in resistance, has been interpreted as being due to increasing lattice disorder (6, 7) causing scattering of the carriers. Such disorder could also involve appreciable segregation of the antimony in its stable oxidized form (Sb_2O_5) which would not then donate carriers. This accounts for the fall off in apparent carrier concentration with percentage of antimony. In addition, the finite value of the solution-side capacitance would cause the measured value to be lower than the true space charge capacitance causing the carrier concentration to appear lower.

These results are for polished samples in 2N H_2SO_4 . Other strong acids give similar results. The effect of polishing is to reduce the measured capacity, possibly by reducing the surface area, and to eliminate surface states of the type described previously (3). Such surface states show up in the impedance characteristic as peaks in the capacity and resistance, particularly at

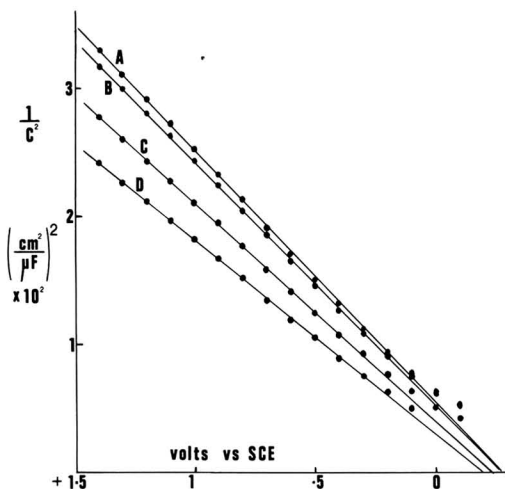


Fig. 2. $1/C^2$ vs. voltage, tin-oxide electrode, IRR in 2M HCl: A, 20 kHz; B, 10 kHz; C, 1 kHz; D, 50 Hz.

⁵ All products of Beuhler, Ltd., Evanston, Illinois.

low frequencies. Surface states can also be produced by adsorbed impurities from the electrolyte. For example, some samples of KCl electrolyte at pH 2 gave a particularly marked enhancement in capacitance at $-0.4V$ which persisted up to 20 kHz indicating very fast states. Peaks in the linear sweep voltammograms were also present. The behavior was finally traced by spectroscopic analysis of the KCl as being due to molybdenum impurity. In a separate experiment with "pure" NaCl at pH 2 as little as $2 \times 10^{-6}M$ molybdate produced a fourfold increase in capacitance. This surface property could not be removed even with boiling HCl. Surface states of some sort are probably responsible for the frequency dispersion observed even for polished specimens. Under the most favorable conditions, high doping and strong acid electrolytes, the capacity tends to a constant value with frequency at about 20 kHz whereas the value at 50 Hz is about 15% higher. The series resistance also tends to a constant value at 10–20 kHz being much higher at lower frequencies. Such dispersion is not predicted for a purely space-charge capacitance under depletion conditions although it would occur under so-called "inversion" conditions (8) where the minority carriers (holes) become predominant in the space charge region. This might occur if the applied potential with respect to the flat band value approaches the band gap (3.7V); however, it is not relevant in the present instance.

Frequency dispersion increases as the doping level diminishes. In such cases, as the potential increases positively, marked frequency dispersion is still present at 20 kHz and the $1/C^2$ values are not linear with voltage. The slope increases as the potential increases positively. This is not to be explained by the ionization of deep donors with increasing voltage which would cause a decrease in slope (8). For such samples the slope of the first part of the graph is used where the dispersion is small. Extrapolation of this part of the graph also provides an intercept, (V_B), in the region of those for the highly doped samples, and this would not be expected to change much with doping level. The less highly doped specimens have a higher resistance tending to cause "transmission sheet dispersion" (Appendix). Some samples were made by putting the test layer on top of a more highly doped layer, but because of the possibility of contamination a series of samples was made by deposition on a polished platinum disk at approximately 700°–800°C. The layer does not adhere so tenaciously as it does to glass or quartz and may be scratched off. However, it is quite coherent enough to withstand polishing and can be examined electrochemically provided the potential excursion on the cathodic side stops short of the hydrogen evolution region ($\sim 0V$). Extension into this range causes the layer to be lifted off in patches possibly due to the evolution of gas underneath.

Table II shows the variation of carrier concentration with the spray concentration of donor. These results are for 1N H_2SO_4 at 20 kHz. The variation of apparent donor concentration with spray concentration bears a similar relationship to the variation of the analyzed antimony concentration in the case of the glass samples (Table I). Thus for the glass samples, the ratio Sb (analyzed)/Sb (spray) is about 2 over the range while the ratio Donor equiv./Sb (spray) for the platinum varies between 3 and 5. Direct determination of

Table III. Variation of properties of IRR

pH	–0.2	1.95	4.2	6.9	9	12
Carrier conc (10 kHz)	5.84	5.81	5.21	5.24	5.09	5.09×10^{19}
V_B (vs. SCE)	–0.25	–0.45	–0.61	–0.95	–1.42	–1.52

antimony has not yet been accomplished due to difficulty in removing the film in a form suitable for emission spectrographic analysis. Because of the above it is believed that the actual values approach the donor equivalents much more closely than in the case of the samples on glass. The much higher temperatures operative during the preparation on platinum (800°) compared with that for glass ($\sim 600^\circ$) should favor lower chloride retention, less oxygen deficiency, and less lattice disorder. Further studies are under way to test these conclusions. The greater concentration in the layer compared to the spray is qualitatively the same as indicated in one of the patents dealing with the material (7). With no doping, the carrier concentration drops to about 3×10^{19} which, being far above the intrinsic level, may be due to residual chloride or to oxide vacancies. Possible oxide deficiency (nonstoichiometry) was looked for in samples of IRR. The technique, which has been described (4), was to dissolve⁶ the layer in a molten bead of LiCl/KCl eutectic at 450° in a stream of dry HCl causing the Sn(IV) component to volatilize and leaving the Sn(II) behind. The latter was determined by anodic stripping from a stationary mercury drop. The Sn(II) was found to vary between 0.02 and 0.3 m/o SnO for a series of samples of IRR. Analysis for chloride was conducted on specimens prepared by hydrolysis on an electrically heated gold wire and was determined by spark source mass spectrometry to be in the region of 0.1 to 0.2%.

Effect of pH.—The variation of the properties of IRR in 2M Cl^- with pH is shown in Table III.

Frequency dispersion increases with increase in pH, and the apparent carrier concentration at 10 kHz decreases. Surface states due to adsorbed impurities could be responsible; slight peaks in the capacity curves are observed. Displacement of adsorbed chloride with hydroxyl could also affect the variation of net adsorbed anions with applied potential thus causing changes in the $1/C^2$ slope as discussed above. These factors make the extrapolation of high pH values very uncertain. At low pH values the trend is not far from 60 mV/pH unit which is the value observed for ZnO (11) and generally expected for oxide electrodes (12, 13).

Reaction kinetics at the tin oxide electrode.—**Reaction at highly doped specimens (IRR).**—The techniques of chronopotentiometry and linear sweep voltammetry were used to examine the kinetics of a number of reactions.

Studies of the bromine-bromide couple showed highly irreversible behavior at the IRR electrodes, whereas this couple is reversible on platinum electrodes. Chronopotentiometric and linear sweep tests for adsorption or other complications indicated simple diffusion controlled irreversible charge transfer kinetics (4).

The kinetics of several other couples were studied to determine if the slow charge transfer rates could be attributed to depletion effects taking place at potentials far removed from the flat-band potential of tin oxide. Rate constants were measured using chronopotentiometry (14) or linear sweep voltammetry (15, 16); the results are given in Table IV.

Comparing these seven systems, there seems to be no correlation between the equilibrium potentials of

⁶ The material is impervious to most normal reagents such as strong acids or oxidizing agents. It can, however, be brought into solution by electrolytic reduction or with acid chromous chloride solution.

Table II. Variation of carrier concentration

Spray Sb, m/o	Carrier conc./cm ³	Donor conc. equiv. to carriers, m/o
2.5	3.47×10^{21}	12.5
1.0	1.19×10^{21}	4.3
0.25	2.53×10^{20}	0.91
0.08	7.02×10^{19}	0.25
0	3.2×10^{19}	0.11

Table IV. Comparison of charge transfer rate constants for tin oxide and platinum electrodes

Substance	Medium		E_{formal} vs. SCE	E_p	$E_{p/2}$	$E_{p,\text{return}}$	αn_a	Estimated k_{ch} , cm/sec
*10 mM Ce^{4+}	1M H_2SO_4	/Pt	1.20	0.905	1.805	1.330	0.26	1.4×10^{-4}
		/SnO ₂	1.20	0.460	0.756	—	0.16	2.2×10^{-5}
*12.5 mM Cu^{3+} ($\rightarrow \text{Cu}^+$)	1M HCl	/Pt	0.205	0.174	0.255	0.291	—	1.4×10^{-3}
		/SnO ₂	0.205	0.008	0.141	0.410	0.36	1.8×10^{-4}
*10 mM HBr	1M HClO_4	/Pt	0.92	0.946	0.903	0.887	—	reversible
		/SnO ₂	0.92	2.276	2.084	0.319	1-0.25	1.2×10^{-8}
*9.56 mM Fe^{3+}	1M H_2SO_4	/Pt	0.435	0.363	0.460	0.600	—	4×10^{-4}
		/SnO ₂	0.435	0.063	0.174	1.290	0.43	6.3×10^{-6}
*10.7 mM $\text{Fe}(\text{o-phen})_3^{3+}$	1M H_2SO_4	/Pt	0.870	0.900	0.840	0.840	—	reversible
		/SnO ₂	0.870	0.917	0.825	0.825	—	reversible
** $\text{K}_3\text{Fe}(\text{CN})_6$	1M KCl in pH 4.5 buf.	/Pt	0.289	—	—	—	—	reversible
		/SnO ₂	0.289	—	—	—	—	reversible
**1.24 mM bromine	2M HBr	/Pt	0.689	—	—	—	—	reversible
		/SnO ₂	0.689	—	—	—	0.44	6.6×10^{-6}

* Linear sweep voltammetry.

** Chronopotentiometry.

the couples and their reversibility on tin oxide. Iron (II) o-phenanthroline is very nearly reversible at +0.87V vs. SCE, whereas HBr at 0.92V is highly irreversible on tin oxide. The reversibility of ferricyanide at 0.289V has been demonstrated at concentrations as high as 0.2M and current densities up to 6.61 mA/cm² (4). On the other hand, Fe(III) at 0.435V and chlorocomplexes of Cu(II)/Cu(I) at 0.205V show 10 to 100 times faster rates on platinum than on tin oxide.

Since semiconductor depletion effects do not account for the irreversibility of some couples on the highly doped IRR tin oxide, the explanation for the slow charge transfer kinetics observed may lie in interferences caused by the oxide nature of the surface. It may be significant that the couples which are reversible on tin oxide have bulky ligands which may prevent a surface interference effect.

Variation of reaction rate with doping level.—The specimens prepared on platinum and described in Table II were used with two redox couples, the $\text{Fe}(\text{CN})_6^{4-}/\text{Fe}(\text{CN})_6^{3-}$ and the $\text{Fe}(\text{o-phen})_3^{3+}/\text{Fe}(\text{o-phen})_3^{2+}$ systems where o-phen represents 1, 10, o-phenanthroline. Both were chosen for their substantial reversibility on highly doped specimens. Linear sweep voltammograms are shown in Fig. 3 and 4. In

the case of $\text{Fe}(\text{CN})_6^{3-}/\text{Fe}(\text{CN})_6^{4-}$ a transition to apparently irreversible behavior is observed as the donor concentration is lowered. The effect is more marked for the second redox system which has a reversible potential of 0.87V. The initially symmetric drop in rate constant is due to the diminishing density of states of the semiconductor according to the theory of Dogonadze and Chizmadzev (17, 18). At lower carrier concentrations asymmetry in the current characteristic is introduced because of limitation of the tunneling process through the depletion layer. For the lowest carrier concentration the anodic peak is suppressed completely and dependence on sweep rate is eliminated though there is a small difference in the current as the potential scan is reversed. This represents the condition when tunneling becomes current limiting. The corresponding potential diagram is shown in Fig. 5 where for simplification the variation of potential in the double layer is left out. E_0 is the reversible potential of the couple which is considered to be a sufficiently large source of electrons that concentration polarization does not occur. The tunneling probability into the bulk of the semiconductor is governed by the shape of the energy barrier which in principle should follow the quadratic relationship (9).

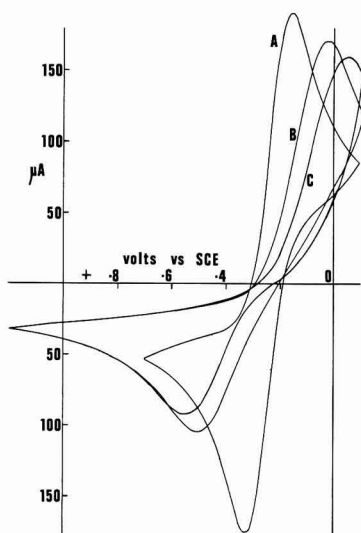


Fig. 3. Linear sweep voltammograms with tin oxide on platinum 1N Na_2SO_4 , 0.1N H_2SO_4 , 10 mM $\text{K}_3\text{Fe}(\text{CN})_6$, 10 mM $\text{K}_4\text{Fe}(\text{CN})_6$. Area = 0.124 cm²; sweep rate = 2 V/min. A, 2.52×10^{20} carriers/cm³; B, 7.02×10^{19} carriers/cm³; C, 3.2×10^{19} carriers/cm³.

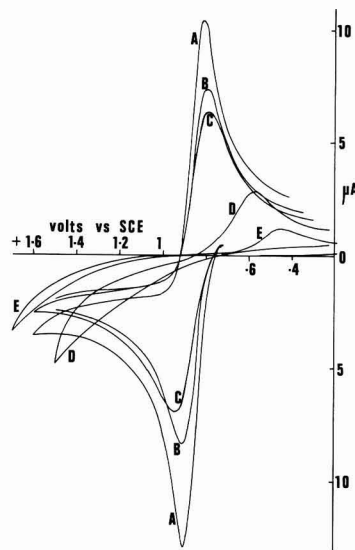


Fig. 4. Linear sweep voltammograms with tin oxide on platinum 1N Na_2SO_4 , 1 mM Fe^{3+} , 1 mM Fe^{2+} , 33 mM 1, 10 o-phenanthroline; pH 2.5; area = 0.124 cm² sweep rate = 2 V/min. A, 3.47×10^{21} carriers/cm³; B, 1.19×10^{21} carriers/cm³; C, 2.52×10^{20} carriers/cm³; D, 7.02×10^{19} carriers/cm³; E, 3.2×10^{19} carriers/cm³.

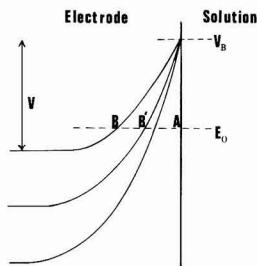


Fig. 5. Potential energy diagram at tin-oxide solution interface

$$\phi = x \sqrt{\frac{2qC_D V}{K_\epsilon}} - \frac{qC_D x^2}{2K_\epsilon} \quad [1]$$

where ϕ = potential in the space charge region and x = distance from the surface. The validity of the band model at such high fields as are necessary to promote tunneling is, however, suspect so that it is reasonable for ease of treatment to consider a linear barrier. As V becomes increasingly greater than $E_0 - V_B$ the linear approximation becomes more satisfactory because tunneling occurs across the gap AB or AB' (Fig. 5). In this region also, only the current in the direction $A \rightarrow B, B'$ need be considered. Under these conditions the anodic current is given by (19, 20)

$$i = I \exp \left[- \frac{4\pi(8m^*)^{1/2}}{3h} \cdot (q[E_0 - V_B])^{1/2} l \right] \quad [2]$$

where m^* is the effective mass, h = Planck's constant, $(E_0 - V_B)$ is the value (in volts) by which the potential barrier height exceeds the total energy of electrons incident on the barrier, l is the gap AB , and I is a factor depending on the rate and energy of electron collision at the barrier. Assuming I to be constant for a given reagent concentration, and expanding l (from Eq. [1]) in the form

$$l = \sqrt{\frac{K_\epsilon}{2qC_D V}} (E_0 - V_B) \left[1 + \frac{1}{4} \frac{E_0 - V_B}{V} \dots \right]$$

one obtains

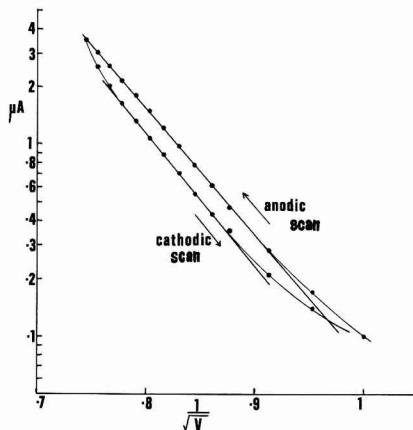
$$\begin{aligned} \text{Log } i = \text{Log } I - \frac{1}{2.303} \frac{4\pi}{3h} \left(\frac{8m^* K_\epsilon}{2C_D} \right)^{1/2} \\ (E_0 - V_B)^{3/2} \frac{1}{\sqrt{V}} \left[1 + \frac{1}{4} \frac{E_0 - V_B}{V} \dots \right] \end{aligned}$$

The second order term is to some extent compensated for by the fact that the actual barrier slope is curved rather than flat causing the current to be larger than indicated in Eq. [2]. Consequently, by eliminating the second order term and putting $C_D = 3.2 \times 10^{19}$ carriers/cm³ and $V_B = -0.1V$ (for $1N \text{ SO}_4^{2-}$) one obtains

$$\text{Log } i = \text{Log } I - 9.23 \left(\frac{m^*}{m} \right)^{1/2} \cdot \frac{1}{\sqrt{V}}$$

Figure 6 shows a graph of $\text{Log } i$ vs. $1/\sqrt{V}$ which gives a mean slope of 6.73 thus indicating a mass ratio of approximately 0.54. A range of values for this ratio for the bulk semiconductor has been given varying between 0.15 (6, 21) to 0.3 (10). It is not clear whether such bulk values are relevant to the present situation so that considering the drastic approximations applied, the experimental results can be considered reasonable.

For undoped specimens with approximately 3×10^{19} carrier/cm³ it is concluded that tunneling probability is the principal current limiting factor. The carrier concentration and conductivity can be further reduced by prolonged heating, e.g., at 800° for 12 hr and also by

Fig. 6. $\text{Log}_{10} i$ vs. $1/\sqrt{V}$. Area = 0.124 cm²; sweep rate = 2V/min; 3.2×10^{19} carrier/cm³.

the addition of indium (5). Under these conditions it is expected that two other current generating mechanisms would become dominant. These are the space charge generation current which is proportional to the depletion layer thickness and the diffusion current which is independent of this thickness (9, 22). These currents depend on the characteristics of the semiconductor material, e.g., number of defects, electron-hole pair generation, diffusion lifetime of carriers, etc., and are strongly influenced by temperature and illumination. These currents can become significant only when tunneling becomes negligible which happens as the carrier density drops still further below the lowest value encountered in the present study. It is suggested that the more highly resistive specimens investigated in reference (5) are operating in the nontunneling region since the currents reach limiting values as the voltage increases.

Acknowledgment

This research was supported by the National Science Foundation under grants GP 7773 and GP 12831. Mass spectrometric analysis by Mr. W. C. Philips of the University of Illinois and by Dr. A. E. Cameron of Oak Ridge National Laboratory, and neutron activation analysis by Dr. W. D. Shults and Mr. J. F. Emery of Oak Ridge National Laboratory are gratefully acknowledged.

Manuscript submitted May 4, 1970; revised manuscript received July 10, 1970.

Any discussion of this paper will appear in a Discussion Section to be published in the June 1971 JOURNAL.

APPENDIX

The finite resistance of the thin layer causes the potential to vary over the area that is exposed to the electrolyte. The equivalent circuit for the electrode only is a finite, two-dimensional, transmission line or transmission "sheet" with distributed resistance and capacitance. If the exposed area is circular and contact is made via a concentric ring, the distribution of potential follows a solution of the equation

$$\frac{\partial^2 v}{\partial r^2} + \frac{1}{r} \frac{\partial v}{\partial r} - \rho C \frac{\partial v}{\partial t} = 0$$

where v = voltage at distance r from the center
 ρ = resistivity per square
 C = capacitance per unit area

The solution of an equivalent problem (in heat conduction) with periodic boundary conditions, has been given (23). The result here is to cause frequency dis-

person in the measured impedance. The measured capacity, C^* , can be expressed in the form

$$\frac{1}{C^*} = \frac{1}{C} \left[1 + \frac{\rho^2 \omega^2 C^2 a^4}{26.3} - \frac{\rho^4 \omega^4 C^4 a^8}{210.32 \cdot 5} + \dots \right]$$

where ω is the angular frequency and a is the radius of the area exposed to the solution. The correction is negligible at 20 kHz for samples of optimum conductivity (~ 10 ohms per square) but increases rapidly with decreasing conductivity.

REFERENCES

1. J. W. Strojek and T. Kuwana, *J. Electroanal. Chem.*, **16**, 471 (1968).
2. W. Cooper, *Nature*, **194**, 569 (1962).
3. H. A. Laitinen, C. A. Vincent, and T. M. Bednarski, *This Journal*, **115**, 1024 (1968).
4. D. L. Zellmer, Ph.D. Thesis, University of Illinois, 1969.
5. O. G. Deryagina and E. N. Paleolog, *Elektrokhim.*, **5**, 315 (1969).
6. T. Arai, *J. Phys. Soc. Japan*, **15**, 916 (1960).
7. J. M. Moche, U.S. Pat. 2,564,707, Aug. 21, 1951.
8. V. A. Myamlin and Yu V. Pleskov, "Electrochemistry of Semiconductors," (translated from Russian) Plenum Press, New York (1967).
9. A. S. Grove, "Physics and Technology of Semiconductor Devices," John Wiley & Sons, Inc., New York (1967).
10. H. J. Van Daal, *Solid State Comm.*, **6**, 5 (1968).
11. F. Lohmann, *Ber. Bunsengesell. Berlin*, **70**, 87 (1966).
12. S. M. Ahmed and D. Maksimov, *J. Coll. Interface Sci.*, **29**, 97 (1969).
13. D. J. G. Ives and G. J. Janz, "Reference Electrodes, Theory and Practice," Academic Press, New York (1961).
14. M. Passnovic, *J. Electroanal. Chem.*, **14**, 447 (1967).
15. R. S. Nicholson and I. Shain, *Anal. Chem.*, **36**, 706 (1964).
16. R. S. Nicholson, *ibid.*, **37**, 1351 (1965).
17. R. R. Dogonadze and Yu A. Chizmadzev, *Dokl. Akad. Nauk. USSR*, **145**, 849 (1962).
18. M. V. Vojnovic and D. B. Sepa, *J. Chem. Phys.*, **51**, 5344 (1969).
19. N. H. Frank and L. A. Young, *Phys. Rev.*, **38**, 80 (1931).
20. A. G. Chynoweth, W. L. Feldman, C. A. Lee, R. A. Logan, G. L. Pearson, and P. Aigrain, *ibid.*, **118**, 425 (1960).
21. K. Ishiguro, T. Sasaki, T. Arai, and I. Imai, *J. Phys. Soc. Japan*, **13**, 296 (1958); I. Imai, *ibid.*, **15**, 937 (1960).
22. M. Green, in "Modern Aspects of Electrochemistry," No. 2, p. 343. J. O'M. Bockris, Editor, Academic Press Inc., New York (1959).
23. H. S. Carslaw and J. C. Jaeger, "Conduction of Heat in Solids," O. U. P., 1959.

Electrochemical Measurements on Austenitic Stainless Steels in Boiling Magnesium Chloride

J. A. Davis and B. E. Wilde*

Applied Research Laboratory, U. S. Steel Corporation, Monroeville, Pennsylvania 15146

ABSTRACT

Electrochemical polarization measurements have been made on AISI Type 304 and USS 18-18-2 stainless steels in magnesium chloride boiling at 150°C. Little difference in the cathodic Tafel constant was noted; the observed values being equal to that expected from a charge transfer rate-determining step. Steady-state corrosion currents increased in the order Type 304 > USS 18-18-2 for the unstressed and the stressed condition. Analysis of corrosion potential vs. time and cyclic polarization data indicates the presence of a film on the corroding surface, which affects the corrosion kinetics. The presence of two mixed potentials during cyclic polarization does not support the noble metal enrichment concept of crack propagation, but rather, the film rupture model.

The mechanism of stress corrosion cracking (SCC) in austenitic stainless steels exposed to chloride-containing media has been the subject of many publications (1-6) and has recently received an excellent review (7). It appears that two major theories have been proposed for crack propagation, both involving plastic deformation at the crack tip and the subsequent influence on the anodic dissolution kinetics.

The mechanochemical model proposed by Hoar and Hines (8) outlines the concept of stress- (or strain-) assisted anodic dissolution of the film-free metal at the tip of the crack.

The film rupture model suggested by Champion (9) and Logan (10) invokes the repetitive rupture of a passive film at the crack tip due to plastic deformation, allowing localized anodic dissolution to take place. This latter model has been criticized because it is not considered likely for passive films to form on austenitic stainless steels in magnesium chloride solutions (8, 11). To overcome this criticism, the concept of noble metal enrichment has been proposed by Latanision and Staehle (12), who suggest the forma-

tion of a nickel-rich film at the crack tip which is subsequently ruptured periodically by dislocation movement resulting from plastic flow.

The present work was conducted on both a resistant and a susceptible austenitic stainless steel to see if the different cracking behavior could be explained in terms of electrochemical parameters, and also to see if information could be gained to support either of the above mechanistic theories.

Materials and Experimental Work

The composition of the alloys studied are shown in Table I, and some pertinent mechanical properties determined at 150°C appear in Table II. Tests were conducted on wires having a diameter of 0.102 cm. The

Table I. Chemical composition of test materials

Material	C	Mn	P	Weight per cent S	Si	Cu	Ni	Cr	Mo
Type 304 stainless steel	0.042	1.23	0.028	0.013	0.39	0.21	9.07	18.4	0.16
USS 18-18-2 stainless steel	0.061	1.5	0.007	0.009	1.90	0.03	18.0	18.4	0.01

* Electrochemical Society Active Member.

Key words: electrochemical polarization, stress corrosion, scanning microscopy, anodic dissolution kinetics, film rupture.

Table II. Mechanical properties of the test materials at 150°C

	0.2% Offset yield strength ksi	Ultimate tensile strength ksi
Type 304 stainless steel	33	67
USS 18-18-2 stainless steel	33	73

wires were heat-treated at 1000°C in argon for 15 min and water-quenched. The annealed wires were abraded through 600-grit silicon carbide paper, degreased in a detergent in an ultrasonic cleaner, washed and dried in hot air. The corrodent was aqueous magnesium chloride boiling at 150°C prepared from reagent grade chemical and distilled water (6.3 megohm cm, at 25°C).

Potentiostatic and potentiodynamic polarization measurements were conducted by using the apparatus and procedure described elsewhere (13, 14). All potentials were measured against a saturated calomel electrode at 25°C, connected to the corrodent through a ground-glass stopper filled with solid MgCl_2 . No attempt was made to correct for junction, thermal diffusion, or IR potentials.

The wires were mounted in a glass cell similar to that described elsewhere (11), such that stress was applied by uniaxial dead weight loading. The steady-state corrosion current, I_{corr} , was determined by extrapolating the linear activation controlled region of the polarization curve to steady-state corrosion potential, E_{corr} .

Reaction films formed on the alloys after 200 hr ($3\mu\text{ Al}_2\text{O}_3$ polished unstressed coupons 2.54 cm by 2.54 cm by 0.127 cm) in boiling MgCl_2 were stripped by treating the specimens with 10% iodine/methanol solution similar to that described previously (15).

Results and Discussion

A summary of the electrochemical parameters of the alloys determined potentiostatically in boiling MgCl_2 is given in Table III. All unstressed polarization measurements were made after the specimens had reached a steady-state E_{corr} . In the case of the stressed experiments, the stress was applied to the wire at steady-state E_{corr} , and the runs were commenced after 5 min of application of stress on Type 304 stainless steel and 1 hr on 18-18-2 stainless steel. The polarization parameters for the test alloys were very similar in the unstressed state. No reliable anodic data could be obtained due to the interference of pronounced pitting at potentials only 25 mV noble to E_{corr} .

With the application of stress (90% of the 150°C yield strength), a marked increase in I_{corr} was observed on Type 304 stainless steel while I_{corr} increased only slightly on 18-18-2 stainless steel. The application of stress also shifted E_{corr} of both steels in the active direction. While E_{corr} on 18-18-2 stainless steel returned to the unstressed E_{corr} in 30 to 40 min, the E_{corr}

on Type 304 stainless steel only shifted to slightly more noble values with time.

Potentiostatic anodic polarization on stressed Type 304 specimens produced early cracking or failure due to pitting through the wire in approximately 5 to 15 min. On the basis of the data shown in Table III, it is not apparent why the silicon steel is superior to Type 304 stainless steel. It is possible, however, that the effect of stress on the E_{corr} reflects the tendency of surface films to rupture (in a manner similar to the scratching experiment), and in this light the films formed on USS 18-18-2 stainless steel may be more resistant to fracture.

The unstressed potential vs. time behavior of the two steels was recorded and is shown in Fig. 1. The character of the transient was similar to that reported by Hoar and Hines (16) for Type 304 stainless steel. They suggest that the shift in the noble direction was due to the formation of a protective film. Other workers (12), however, have described this type of transient to be the result of noble component enrichment on the corroding surface. When an unstressed specimen of Type 304 stainless steel was equilibrated to steady-state E_{corr} and scratched with a diamond stylus, the E_{corr} immediately decreased from $-0.360\text{ V}_{\text{SCE}}$ to $-0.415\text{ V}_{\text{SCE}}$. This behavior was taken as confirmation that the establishment of the noble E_{corr} was the result of a surface reaction between the metal and the corrodent. Unfortunately, both of the above hypotheses for the shape of the transient could be invoked to explain the scratching experiment.

The time required for the potential to reach steady state (less than 5 mV shift in 15 min), was markedly different for the two test materials. Type 304 stainless steel achieved steady state after 2 to 10 min, compared with 50 to 100 min for USS 18-18-2. The shape of the potential-time transient observed in these experiments was reminiscent of that observed by other workers when studying the active to passive transition of stainless steels in aerated acidic media (17, 18). The similarity in these transients suggested that an analogous passivation process was occurring in boiling MgCl_2 but not necessarily by the same species as with steels in dilute acid.

The polarization behavior of the two materials under potentiodynamic conditions is of interest. Typical cyclic polarization curves are shown in Fig. 2, where an unstressed specimen of USS 18-18-2 stainless steel was polarized from the steady-state corrosion potential to -0.800 V at a rate of 15 volts per hour in boiling MgCl_2 . At -0.800 V the sweep was reversed and continued to -0.200 V , after which it was reversed again to -0.800 V . It is clear from Fig. 2 that two steady-state mixed potentials exist at points A and B, similar to those reported on other materials in dilute acid (19, 20). The results for Type 304 stainless steel (Fig. 3) were practically the same.

Table III. Summary of potentiostatic electrochemical parameters in boiling MgCl_2

Material	Condition	β_c , V	β_a , V	E_{corr} , V_{SCE}	I_{corr} , $\mu\text{A}/\text{cm}^2$
Type 304 stainless steel	Unstressed	-0.162	0.069	-0.360**	260
USS 18-18-2	Unstressed	-0.170	0.062	-0.312**	210
Type 304 stainless steel	Stressed to 90% of yield	-0.100	N.D.*	-0.420†	900
USS 18-18-2	Stressed to 90% of yield	-0.175	N.D.	-0.312†	310

* N.D. = not determined.

** Steady-state value (see Fig. 1).

† Value attained within 5 min after applying the load to Type 304 stainless steel specimen. In the case of USS 18-18-2 stainless steel, the load was applied after 1 hr at the unstressed steady-state E_{corr} .

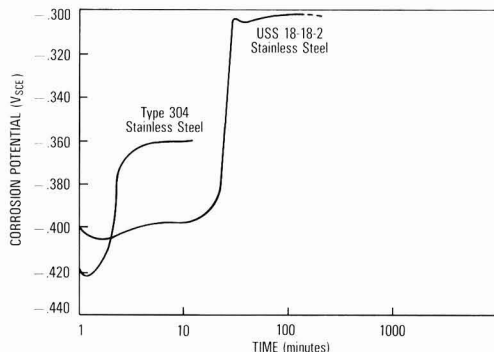


Fig. 1. Potential-time transients in boiling magnesium chloride

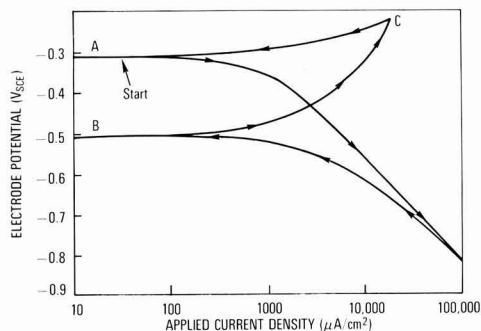


Fig. 2. Cyclic polarization curve for unstressed USS 18-18-2 stainless steel in boiling MgCl_2 . (Sweep speed 15 V/hr.)

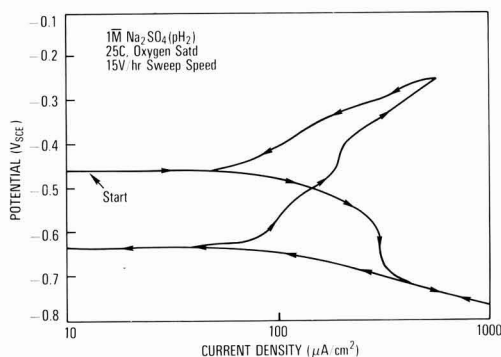


Fig. 3. Cyclic polarization curve for unstressed AISI Type 304 stainless steel in acidified Na_2SO_4 . (Sweep speed 15 V/hr.)

To explain this behavior we suggest that E_{corr} at point A in Fig. 2 is the result of a reaction film covered surface after the specimen has come to steady state (see Fig. 1). When polarized in the active direction, hydrogen-ion reduction occurs and normal Tafel behavior is obtained down to -0.800V , during which process the film on the surface is reduced. Reversal of the sweep results initially in hydrogen-ion reduction at the same rate as with the active-going sweep. However, since the surface is now film-free, a new mixed potential is developed at B. Electrochemical oxidation of this surface results in anodic dissolution along BC and is not significantly affected by pitting because of the rather rapid sweep rate. Polarization in the cathodic direction from C results in the dissolution curve AC, which is similar to that obtained by anodic polarization of a steady-state surface from A.

If the above interpretation is correct, it should be possible to duplicate the cyclic response (Fig. 2) with a steel in an unambiguous state of stable passivity. In an attempt to demonstrate this behavior, a Type 304 stainless steel electrode was exposed to an oxygen-saturated solution of $1\text{M Na}_2\text{SO}_4$ (where the pH was adjusted to 2.0 with H_2SO_4). Cyclic polarization of this electrode produced a similar type of curve to that in Fig. 2, as shown in Fig. 3. An active mixed potential was observed because the kinetics for the re-passivation of the surface following cathodic reduction are slower than the speed of the sweep. These data lend strong support to the theory of film formation and passivation-type electrode kinetic behavior of austenitic alloys in boiling MgCl_2 .

Although the theory of noble metal enrichment could account for the phenomenon observed in both the unstressed potential-time behavior and the scratch experiment, it cannot in our opinion be reconciled with

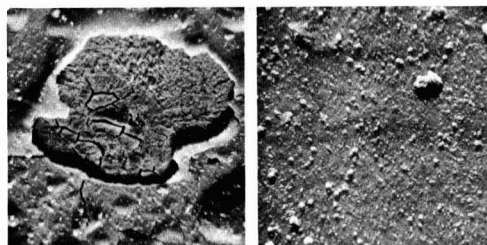


Fig. 4. Scanning electron micrographs of austenitic stainless steels exposed for 200 hr unstressed to boiling magnesium chloride (150°C) X 1000. (Left) AISI Type 304 stainless steel. (Right) USS 18-18-2 stainless steel.

the presence of a new mixed potential following cathodic reduction.

Attempts to strip films off corroded surfaces were successful. Films of variable thickness were lifted from both steels after 200 hr exposure to boiling MgCl_2 . Bulk electron diffraction studies produced an unidentified pattern, with diffuse Debye rings. It is worthy of note, however, that the patterns from both Type 304 and USS-18-18-2 stainless steel appeared to be identical. Small inclusions were observed in the films which gave diffraction patterns of a chromium nitride structure, which is isomorphous with NiO .

Emission spectrographic analysis of film residues indicated that the composition was the same for both steels, with magnesium as a major component. Scanning electron micrographs were obtained on corroded surfaces (after 3 hr at steady-state E_{corr} , as in Fig. 1) of two alloys and are shown in Fig. 4. A wide variation in surface structure was observed at $2000\times$. The Type 304 stainless steel sample evidenced pronounced spalling of the surface film while USS 18-18-2 stainless steel showed a rather featureless nonporous film.

Conclusions

The following conclusions can be drawn from the data presented:

1. The values of the cathodic Tafel constant for Types 304 and USS 18-18-2 stainless steel in boiling MgCl_2 are equal to that which would be expected for a charge transfer controlled discharge process.
2. No systematic relationship between electrochemical polarization parameters (stressed or unstressed) and the stress corrosion cracking behavior of the above two materials was observed.
3. Analysis of potential-time data and cyclic polarization curves has indicated the presence of a stable film on the metal surface, which can be reduced by cathodic hydrogen evolution.
4. The presence of two mixed potentials on a cyclic polarization plot cannot be rationalized on the basis of noble metal enrichment, but it can be explained by a passive type of behavior entirely analogous to that observed on Type 304 stainless steel in sodium sulfate solutions at room temperature.

Manuscript submitted Jan. 12, 1970; revised manuscript received ca. June 25, 1970. This was Paper 63A presented at the Detroit Meeting, October 5-9, 1969.

Any discussion of this paper will appear in a Discussion Section to be published in the June 1971 JOURNAL.

REFERENCES

1. H. L. Logan, *J. Res. Nat. Bur. Std.*, **48**, 99 (1952).
2. T. P. Hoar and J. G. Hines, *J. Iron Steel Inst.*, (London) **177**, 248 (1954).
3. C. Edeleanu, *ibid.*, **173**, 140 (1953).
4. R. B. Mears, R. H. Brown, and E. H. Dix, "Symposium on Stress Corrosion Cracking of Metals," p. 323, ASTM-AIME (1945).
5. J. C. Hodge and J. L. Miller, *Trans. Am. Soc., Metals*, **28**, 25 (1940).

6. W. D. Robertson, in "Stress Corrosion Cracking and Embrittlement," W. D. Robertson, Editor, p. 32, Wiley, New York (1956).
7. E. N. Pugh, J. A. S. Green, and A. J. Sedriks, RIAS Technical Report 69-3, (March 1969).
8. T. P. Hoar and J. G. Hines, in "Stress Corrosion Cracking and Embrittlement," W. D. Robertson, Editor, p. 107, Wiley, New York (1956).
9. F. A. Champion, "International Symposium on Stresses in Metals and Alloys," p. 468, Institute of Metals, London (1948).
10. H. L. Logan, *J. Res. Nat. Bur. Std.*, **48**, 99 (1952).
11. S. Barnartt and D. Van Rooyen, *This Journal*, **108**, 222 (1961).
12. R. M. Latanision and R. W. Staehle, "Stress Corrosion Cracking of Iron-Nickel-Chromium Alloys," in "Proceedings of Conference on Fundamental Aspects of Stress Corrosion Cracking," R. W. Staehle, A. J. Forty, and D. Van Rooyen, Editors, NACE, Houston, Texas (1969).
13. B. E. Wilde and J. S. Armijo, *Corrosion*, **23**, 208 (1967).
14. W. D. Henry and B. E. Wilde, *ibid.*, **25**, 515 (1969).
15. J. S. Armijo and B. E. Wilde, *Corrosion Sci.*, **8**, 649 (1968).
16. T. P. Hoar and J. G. Hines, *J. Iron Steel Inst.*, (London), **182**, 124 (1956).
17. C. Edeleanu, *Metallurgia*, **50**, 113 (1954).
18. B. E. Wilde and N. D. Green, *Corrosion*, **25**, 300 (1969).
19. B. E. Wilde and F. G. Hodge, *Electrochim. Acta.*, **14**, 619 (1969).
20. C. Wagner and W. Traud, *Z. Elektrochem.*, **44**, 391 (1938).

Preparation of 2,3,4,5-Tetraphenyl-1,6-Hexanedioic Acid

S. Wawzonek,* A. R. Zigman, and G. R. Hansen

Department of Chemistry, University of Iowa, Iowa City, Iowa 52240

ABSTRACT

2,3,4,5-Tetraphenyl-1,6-hexanedioic acid has been prepared electrochemically by the reductive dimerization of α -phenylcinnamic acid and α -phenylcinnamionitrile. The latter gave a mixture of 1-amino-2,3,4,5-tetraphenyl-5-cyano-1-cyclopentene and 2,3,4,5-tetraphenyl-1,6-hexanedinitrile. Both the cyclopentene derivative and the dinitrile were converted chemically to the desired acid. Chemical methods based on condensation reactions of benzil were not successful for the preparation of this acid.

2,3,4,5-Tetraphenyl-1,6-hexanedioic acid (V) was required as a starting material for the preparation of 5,11-diphenyl-6,12-diketochrysene. This paper describes electrochemical and chemical studies of the preparation of this acid.

Experimental¹

2,3,4,5-Tetraphenyl-1,6-hexanedioic acid (V).—The electrochemical reductive dimerization of α -phenylcinnamic acid (22.4g) in dimethylformamide (190 ml) containing 28% sulfuric acid (72 ml) was carried out at a mercury cathode using the directions given for cinnamic acid (I). The resulting solution was poured into water, and the oily layer was separated and taken up in benzene. Extraction with sodium hydroxide followed by acidification of the alkaline solution gave an oil which solidified. Treatment with benzene and chloroform gave 5.2g of a white solid melting at 275°–290°C. Two crystallizations from ethanol gave the desired acid (0.7g); mp 306°–308°C. The IR spectrum showed absorptions at 3.5–3.8 (OH) and 5.84, 6.04 μ (COOH).

Anal. Calcd. for $\text{C}_{30}\text{H}_{26}\text{O}_4$: C, 79.91; H, 5.81; Found: 79.67; H, 5.81.

Electrolytic reduction of α -phenylcinnamionitrile.—A solution of α -phenylcinnamionitrile (20.5g) in dimethylformamide (300 ml) containing 150 ml of a 57% solution of tetraethylammonium *p*-toluenesulfonate in water was reduced at a mercury cathode (68 cm²). The platinum anode was placed in a porous cup in a similar solution without the nitrile. The solution during the electrolysis was kept neutral by the addition of acetic acid. After the passage of a current of 1A for 3 hr the white solid (13.8g) formed was filtered and could be separated into two compounds with hot

benzene. The soluble fraction (75%) was the cyanoamine (I) and the insoluble part was 2,3,4,5-diphenyl-1,6-hexanedinitrile (25%). Addition of water to the filtrate gave an additional 2.2g of the cyanoamine (I). This compound, 2,3,4,5-tetraphenyl-5-cyano-1-amino-1-cyclopentene (I), melted at 219°–225°C after one recrystallization from a mixture of benzene and ethanol; IR: 3.03 (NH₂), 4.54 (CN) and 6.15 μ (C = C); NMR (CD_3CN) 87.5 (s C_6H_5); 7–7.48 (m $3\text{C}_6\text{H}_5$), 5.04 (d 1 H J = 10 Hz), 4.02 (s 2 H) and 3.54 (d 1 H J = 10 Hz). In the presence of D_2O the broad singlet at 4.02 disappeared.

Anal. Calcd. for $\text{C}_{30}\text{H}_{24}\text{N}_2$: C, 87.37; H, 5.86; N, 6.79. Found: C, 87.70; H, 5.83; N, 6.57.

2,3,4,5-Tetraphenyl-1,6-hexanedinitrile after recrystallization from a large volume of benzene melted with sublimation at 348°–355°C. TGA indicated that the sublimation started at 240°C; IR 4.53 μ (CN); mass spectral analysis gave a peak at 412.

Anal. Calcd. for $\text{C}_{30}\text{H}_{24}\text{N}_2$: C, 87.37; H, 5.86; N, 6.79. Found: C, 87.75; H, 5.85; N, 6.66.

2,3,4,5-Tetraphenyl-2-cyanocyclopentanone (II).—A solution of the cyanoamine (I) (1.2g) in dioxane (50 ml) was refluxed with 6N hydrochloric acid (15 ml) for 1 hr and poured into water. The cyanoketone (1.1g) melted at 178°–180°C after two crystallizations from ethanol. On solidification this compound would occasionally remelt at 190°–192°C. The IR and NMR spectra, however, were the same as those for the 178°–181°C compound; IR: 4.45 (CN) and 5.74 μ (CO); NMR (CDCl_3): 87.04–7.25 (m $4\text{C}_6\text{H}_5$); 3.92–4.21 (m 3 H).

Anal. Calcd. for $\text{C}_{30}\text{H}_{23}\text{NO}$: C, 87.14; H, 5.61; N, 3.39. Found: C, 87.30; H, 5.73; N, 3.28.

2,3,4,5-Tetraphenyl-5-cyanopentanoic acid (III).—The cyanoketone (II) (1g) was refluxed with potassium hydroxide (1g) in methanol (40 ml) for 15 hr. The resulting solution when poured into water and acidified gave a solid (1.0g) which was recrystallized

* Electrochemical Society Active Member.

Key words: hydromerization; 1-amino-2,3,4,5-tetraphenyl-5-cyano-1-cyclopentene; 2,3,4,5-tetraphenyl-1,6-hexanedinitrile.

¹ Melting points are not corrected. Infrared spectra were determined as nujol mulls on a Perkin-Elmer Infracord. NMR spectra were determined on a Varian A60 Spectrometer.

from benzene; yield, 0.35g; mp 235°–237°C. A second recrystallization from benzene gave a sample melting at 236°–237°C; IR: 3.5–3.9 (OH), 4.43 (CN) and 5.8 μ (COOH). The more soluble fraction obtained in this reaction was not investigated further.

Anal. Calcd. for $C_{30}H_{25}O_3N$: C, 83.53; H, 5.80; N, 3.25. Found: C, 83.34; H, 5.94; N, 3.31.

2,3,4,5-Tetraphenyladipamic acid (IV).—The nitrile acid (III) (0.4g) was refluxed with 10 ml of 50% sulfuric acid in acetic acid (28 ml) for 28 hr and the resulting solution was poured into water. The solid (0.32g) obtained, when recrystallized from a large volume of benzene, melted at 292°–293°C; IR: 2.8–3.0 (NH_2), 3.5–9 (OH); 5.83 (COOH) and 6.01 μ ($CONH_2$).

Anal. Calcd. for $C_{30}H_{27}O_3N$: C, 80.18; H, 6.01; N, 3.12. Found: C, 79.97; H, 6.14; N, 3.19.

2,3,4,5-Tetraphenyl-1,6-hexanedioic acid (V).—The amide acid (0.5g) in 10 ml of acetic acid containing 1 ml of concentrated hydrochloric acid was treated at 100°C with excess 20% sodium nitrite solution. The white solid (0.4g) on recrystallization from ethanol and water melted at 304°–307°C and gave an identical ir spectrum to that of the acid obtained by the dimerization of α -phenylcinnamic acid.

Hydrolysis of 2,3,4,5-tetraphenyl-1,6-hexanedinitrile.—The dinitrile (2.75g) was refluxed with 25 ml of 50% sulfuric acid in acetic acid (250 ml) until all the solid material had dissolved. This process required 11 days. The resulting solution was poured into water, and the white solid (3.0g) was filtered. Extractions with alkali gave a mixture of acids containing nitrogen. Deamination of a portion (0.8g) in acetic acid (10 ml) containing concentrated hydrochloric acid (1 ml) at 100° with 2 ml of 20% sodium nitrite gave 0.42g of an isomeric 2,3,4,5-tetraphenylhexanedioic acid. Recrystallization from benzene gave a sample melting at 291°–295°C. A mixture with the acid prepared from the cyanoketone method melted at 265°–280°C. IR: 3.5–4 (OH) and 5.88 μ (COOH).

Anal. Calcd. for $C_{30}H_{26}O_4$: C, 79.91; H, 5.81. Found: C, 79.70; H, 5.94.

Cyclization of 2,3,4,5-tetraphenyl-1,6-hexanedinitrile.—The dinitrile (0.65g) was refluxed in benzene (150 ml) and absolute ethanol (50 ml) with sodium methoxide (0.3g) for 22 hr. Removal of the solvent gave a solid which was treated with water, filtered, and dried. The resulting solid was treated with cold benzene, and the insoluble starting material was separated; yield, 0.38g. The filtrate was treated with ethanol and on concentration gave a white crystalline solid (0.21g) melting at 239°–242°C; IR: 2.9 (NH_2), 4.45 (CN) and 6.10 μ (C = C); NMR ($CDCl_3$) δ 6.6–7.6 (m 4 C_6H_5), 4.63 (d 1H J = 8 Hz), 3.95 (d 1H J = 8 Hz) and 3.8 (broad s 2H). In the presence of D_2O the broad singlet at 3.8 disappeared. The NMR spectrum in CD_3CN in which the compound is much less soluble gave a similar coupling constant for the two doublets. A mixture with isomer I melted at 199°–220°C.

Anal. Calcd. for $C_{30}H_{24}N_2$: C, 87.37; H, 5.86; N, 6.79. Found: C, 86.99; H, 5.59; N, 6.45.

Reaction of benzil with benzyl cyanide.—A solution of benzil (15.7g) and benzyl cyanide (17.5g) in ethanol (250 ml) was treated at reflux with a solution of potassium hydroxide (3g) in ethanol (15 ml). The solution became purple and was refluxed for 30 min. Removal of the solvent was followed by acidification and extraction with ether. The ether layer after treatment with dilute alkali and acid gave an orange oil (28g). Addition of alcohol gave crystals of α -phenylcinnamionitrile (4.0g); mp 85°–88°C. Identification was made by comparison with an authentic sample (2).

Reaction of benzil with ethyl α -bromophenylacetate.—A stirred refluxing mixture of zinc dust (6.8g) in dry benzene (100 ml) was treated with a solution

of benzil (11.56g) and ethyl α -bromophenylacetate (25.0g) in benzene (100 ml). After approximately 40 ml of this solution was added, reaction occurred, and the addition was completed dropwise with further heating. The resulting solution was refluxed an additional 12 hr, cooled, and treated with ice-cold 10% sulfuric acid. The benzene layer gave 16g of the mono-adduct. Recrystallization from ethanol gave a sample melting at 121°–124°C; IR: 2.87 (OH), 5.80 ($COOC_2H_5$) and 5.91 μ (CO).

Anal. Calcd. for $C_{24}H_{22}O_4$: C, 77.00; H, 5.92. Found: C, 76.51; H, 5.78.

Results

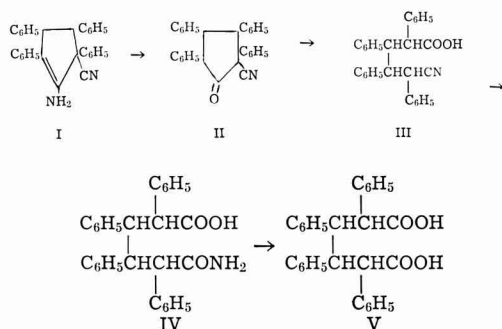
2,3,4,5-Tetraphenyl-1,6-hexanedioic acid (V) was prepared directly by the electrochemical reductive dimerization of α -phenylcinnamic acid using the procedure for dimerizing cinnamic acid (1). The amount of benzene soluble by-products formed was larger than that obtained with cinnamic acid. In view of the complexity reported for these products (1), the by-products were not studied further.

The low yield of acid obtained suggested a study of the electrochemical hydrodimerization of α -phenylcinnamionitrile as a source of this acid. This reduction actually behaved differently than expected and gave a mixture of 1-amino-2,3,4,5-tetraphenyl-5-cyano-1-cyclopentene (I) and 2,3,4,5-tetraphenyl-1,6-hexanedinitrile. The structure of the former was based on IR and NMR spectra and its chemical behavior.

The NMR spectrum showed two doublets centered at δ 3.54 and 5.04 ppm for the 3- and 4-hydrogens and a broad singlet at δ 4.02 integrating for two hydrogens which disappeared in the presence of deuterium oxide. This spectrum favors the designation of I exclusively as the enamine form. The presence of the imine isomer would be expected to shift the hydrogen absorptions to the same region shown by the ketone II.

The large splitting constant of 10 Hz indicates that the 3- and 4-hydrogens are cis and that the configuration is *meso* for this portion of the compound.

Hydrolysis with acid gave the ketonitrile (II) which could be cleaved with alkali to the cyano acid (III). This acid (III) when hydrolyzed with sulfuric acid gave the amide acid (IV) which was resistant to further hydrolysis with acid or alkali. Deamination with nitrous acid gave the same acid (V) as is obtained by the dimerization of α -phenylcinnamic acid.

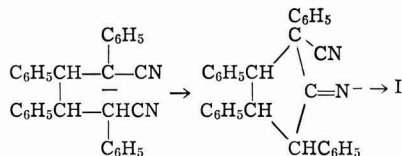


A similar cyclization has been observed in the electrochemical reductive dimerization of benzalacetophenone in dimethylformamide in the presence of carbon dioxide (3) and ethyl cinnamate in aqueous dimethylformamide (4).

The structure of 2,3,4,5-tetraphenyl-1,6-hexanedinitrile was based on its ir spectrum, mass spectral data, and chemical conversion to an isomeric 2,3,4,5-tetraphenylhexandioic acid (V) and an isomeric 1-amino-2,3,4,5-tetraphenyl-5-cyano-1-cyclopentene (I). The last compound gave an nmr spectrum which showed two

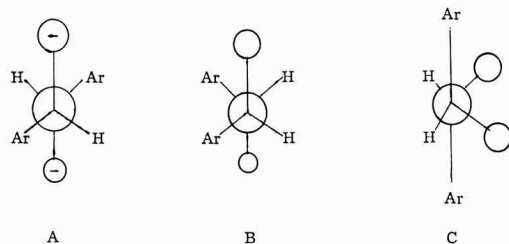
doublets centered at $\delta 4.63$ and 3.95 ppm for the 3 and 4-hydrogens and a broad singlet at $\delta 3.8$ for the two hydrogens of the amino group. A coupling constant of 8 Hz indicates that the 3- and 4-hydrogens are *trans* and that the configuration is *dl* for this portion of the molecule. Such an assignment is based on the Karplus rule (5).

The cyclopentene derivative I no doubt is formed from the anion of the expected hydrodimer (VI) by a Ziegler condensation even though the electrolyte was kept at the neutral point with acetic acid during the electrolysis.



This anomaly may be caused by the tetraethylammonium ions adsorbed on the electrode surface. Such an environment would be more anhydrous than that of the bulk of the solution and less susceptible to the addition of acid.

The higher ratio of *meso/dl* suggests that in the dimerization of the anion radical directly at the surface of the electrode, steric factors and repulsion of the negative charges would favor form A and would lead to the formation of the *meso* isomer which cyclizes to the cyclopentane derivative I.



The second method of forming the dimer is by dimerization of the radical formed by protonation of the anion radical. Such a dimerization would be governed only by the steric effects of the groups involved and could give forms B and C. This type of addition would be expected to predominate in the bulk of the solution and to give the *dl*-isomer of the dinitrile.

Similar factors may be involved in the high ratio of *meso/dl* pinacols observed in the reduction of benzaldehyde in the presence of tetraalkylammonium and iodide ions (6).

Chemical methods leading to the synthesis of 2,3,4,5-tetraphenyl-1,6-hexanedioic acid (V) based on the condensation reactions of benzil were not successful. The Reformatsky reaction with ethyl α -bromophenylacetate gave only the monoadduct, ethyl 2,3-diphenyl-3-benzoyl-3-hydroxypropionate.

The alkaline condensation of phenylacetoneitrile with benzil gave α -phenylcinnamoneitrile.

Manuscript submitted Feb. 26, 1970; revised manuscript received ca. July 13, 1970. This was Paper 136 presented at the New York Meeting of the Society, May 4-9, 1969.

Any discussion of this paper will appear in a Discussion Section to be published in the June 1971 JOURNAL.

REFERENCES

1. C. L. Wilson and K. B. Wilson, *Trans. Electrochem. Soc.*, **84**, 153 (1943).
2. S. Wawzonek and E. M. Smolin, *Org. Syntheses, Coll.*, **3**, 715 (1955).
3. S. Wawzonek and A. Gundersen, *This Journal*, **111**, 324 (1964).
4. J. P. Petrovich, M. M. Baizer, and M. R. Ort, *ibid.*, **116**, 749 (1969).
5. M. Karplus, *J. Am. Chem. Soc.*, **85**, 2870 (1963).
6. V. J. Puglisi, G. L. Clapper, and D. H. Evans, *Anal. Chem.*, **41**, 279 (1969).

The Electrochemical Oxidation of N,N-Dimethylaniline

Rodney Hand and R. F. Nelson*

Department of Chemistry, Sacramento State College, Sacramento, California 95819

ABSTRACT

The electrochemical oxidation of N,N-dimethylaniline (DMA) has been investigated in nonaqueous media in some detail. The products formed were found to depend on DMA concentration and the time of electrolysis. At low concentrations (10^{-3} M), the main product formed is N,N,N',N'-tetramethylbenzidine. At intermediate concentrations (10^{-2} M) the major product is 4,4'-methylenebis (N,N-dimethylaniline), and at higher concentrations, especially at longer electrolysis times, the dye crystal violet and its leuco form were produced in large amounts. The mechanism to form these products depends on the lability of the methyl groups on the amine nitrogen; when other N,N-dialkylanilines were electrolyzed under similar conditions, only the corresponding tetraalkylbenzidines could be isolated.

The oxidation of N,N-dimethylaniline (DMA), by both chemical and electrochemical means, has commanded a good deal of attention for a number of years. The amine exhibits a multitude of reactions, as evidenced by the large number of products generated under varying conditions. The products formed seems

to depend upon a bewildering series of variables: the solvent medium, the oxidizing agent, temperature, and concentration of reactants, for example, (1-9) and references therein. In addition, electrochemical oxidation under proper conditions can lead to substitution in either the aromatic ring (10-12) or on the N-methyl groups (13, 14). Thus, upon oxidation one can expect the cation radical to decompose by one or more of several pathways.

* Electrochemical Society Active Member.

Key words: organic electrochemistry, mechanism, coulometry, cyclic voltammetry.

As part of a study involving the anodic oxidation pathways of aromatic amines, the electrochemistry of DMA was investigated in some detail. Previous work in both aqueous and nonaqueous media had shown *N,N,N',N'*-tetramethylbenzidine (TMB) to be the primary electrolysis product. However, upon inspection of cyclic voltammograms in acetonitrile, it was apparent that indeed TMB was being formed by oxidation of DMA at platinum, but the amount formed was not at all equivalent to the quantity of DMA present, *i.e.*, it appeared that other unidentified products were forming. Various electrochemical and spectroscopic techniques were employed and it was found that other products were formed, the identities and amounts of which depended markedly upon solution conditions. In addition, several other *N,N*-dialkylanilines were studied electrochemically and their behavior correlated with that of DMA.

Experimental Procedures

The electrochemical and spectroscopic instrumentation and techniques were as previously described (15). The NMR spectra were recorded in CDCl_3 using a Perkin-Elmer R-20 spectrometer.

The *N,N*-dimethylaniline was obtained commercially and purified according to a standard procedure (16). *N,N*-Diethylaniline, *N,N*-di-*n*-butylaniline, *N,N*-di-sec-butylaniline, and *N,N*-di-*n*-decylaniline were all obtained commercially and were not further purified. The tetramethylbenzidine and tetraethylbenzidine were prepared by methylation and ethylation, respectively, of benzidine using trialkyl phosphates and were purified by column chromatography and recrystallization. *N,N,N',N'*-Tetramethyl-2,2'-diaminobiphenyl (*o*-oTMB) and *N,N,N',N'*-tetramethyl-2,4'-diaminobiphenyl (*o*-pTMB) were prepared by catalytic hydrogenation of the dinitro compounds (17). The diamino compounds were then methylated and purified by chromatography and recrystallization. 4,4'-Methylenebis(*N,N*-dimethylaniline) (MBDMA) and 4,4'-methylidynetris (*N,N*-dimethylaniline) (LCV) were obtained commercially and purified by recrystallization. *N*-p-Dimethylaminobenzyl-*N*-methylaniline was prepared by a benzoyl peroxide oxidation of DMA (1).

The purification of acetonitrile and the preparation and purification of tetraethylammonium perchlorate (TEAP) have also been previously described (15). Benzonitrile was obtained commercially and used with no further purification.

Constant potential mass electrolyses were carried out using a Wenking 61RH potentiostat. A two-compartment cell with a fine frit was used for electrolyses. A platinum gauze electrode was used as the working electrode, and an SCE was used as the reference electrode. All oxidation potentials were set about 100 mV anodic of the primary oxidation waves of the dialkylanilines as determined from cyclic voltammograms. The electrolyses were carried to virtual completion, *i.e.*, to a point where the current was less than 1% of the value at initiation of the electrolysis. In addition, after exhaustive oxidation the solutions were electrolyzed at -0.6V in order to convert any species in the oxidized state to the neutral form and to reduce protons generated by the various coupling reactions involved. It was found that if these protons were not electrolyzed before product isolation appreciable amounts of starting material and electrolysis products were lost during work-up.

Constant current mass electrolyses were carried out using the Wenking potentiostat modified according to procedures set forth in the operation manual (18). The constant current electrolyses were stopped after proceeding for calculated time intervals corresponding to one-half, one, one and one-half, and two electron *n*-values for DMA.

Products were isolated by evaporation of the solvent from the electrolysis mixture and extraction with dichloromethane. The TEAP taken up was precipitated

out by the addition of ether. The supernatant was taken to dryness and chromatographed on Woelm neutral alumina with benzene, then dichloromethane and, if necessary, ethanol; the products were then recrystallized from benzene-ethanol. Thin layer chromatography experiments were carried out on "Bakerflex" aluminum oxide grade 1B T.L.C. paper using mixtures of benzene and petroleum ether as solvents (the per cent composition was not critical). The chromatograms were developed with iodine.

Results and Discussion

When the possible products that could form by oxidation of DMA were considered, the most likely prospects seemed to be the isomeric benzidines, TMB, *o*-pTMB, and *o*-oTMB. This was based on intuition as well as tritium tracer experiments run on DMA suggesting some sort of *ortho*-coupling (6) taking place. Consequently, the electrochemical properties of the previously mentioned benzidines were studied, and their cyclic voltammograms matched up with the DMA system, as shown in Fig. 1. One can see that a fertile imagination could find any of the benzidines in the DMA cyclic upon careful inspection. Consequently, recourse was taken to other means of identification of products. Attempts were made to detect the benzidines using *in situ* electrolysis in a Cary 14 uv-visible spectrometer, but the TMB band was so broad and intense that it swamped out any *o*-pTMB or *o*-oTMB (both of which had weak bands in this region) that might be present. Results with thin-layer chromatography were somewhat more successful. Using benzene-petroleum ether as a solvent medium, solutions from electrolysis of 10^{-3}M DMA were spotted along with authentic samples of the three isomeric benzidines.

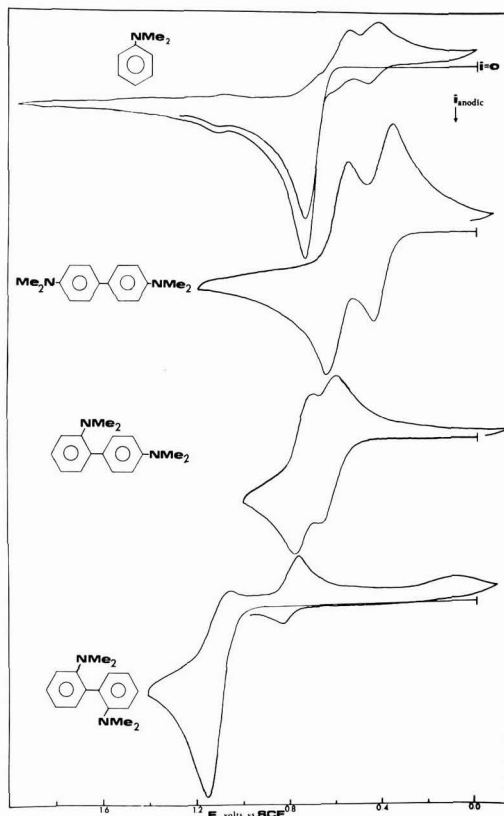


Fig. 1. Cyclic voltammograms of DMA and the isomeric benzidines in acetonitrile/0.1M TEAP.

TMB was definitely identified and another spot from the electrolysis solution matched up with either the *o*-pTMB or the *o*-oTMB. Since there is considerably less steric hindrance to *ortho-para*-coupling, it is believed that the other product formed in dilute solution is *o*-pTMB, in minor amounts.

Thus, in the region of milliformal concentration, the reaction mechanism seems to be relatively uncomplicated; DMA is oxidized to the cation radical; these then couple in one or more of several ring coupling fashions. As would be anticipated, the least sterically hindered pathway, *para-para*-coupling, predominates. One problem was finally solved after considerable consternation: on cyclic voltammograms it seemed that much less than quantitative amounts of TMB were forming from the oxidation of DMA. In addition, the electrochemical data gave an *n*-value of about one as opposed to the two electrons that would be expected for this classical ECE system (TMB is more easily oxidized than DMA). This is due to the fact that appreciable amounts of the DMA are protonated by protons released in the coupling reaction to form TMB. Since DMA is a moderately strong base, the degree of protonation, estimated at 40-50% when compared with aliphatic amines (19), is appreciable. This factor must be considered when one is working on the electrochemistry of organic bases in nonaqueous media.

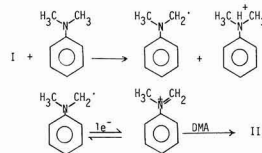
As the concentration of DMA is increased from 10^{-3} to 10^{-1} M, the composition of the electrolysis products obtained changes markedly. At intermediate concentrations (10^{-3} to 10^{-2} M), relatively little TMB is obtained, and instead, another product resulted in fairly high yields (30-40%). This product eluded identification for some time until heed was paid to work that cited the formation of MBDMA from DMA via various chemical oxidation pathways (1,2); small amounts had also been isolated from electrochemical oxidations in aqueous media (4). Once the product was acknowledged, identification was straightforward. Normally, cyclic voltammograms are not a reliable matching-up tool for suspected electrolysis products, but in this case the cyclic of the electrolysis product was found to be very similar to that of an authentic sample of MBDMA, as shown in Fig. 2. The electrolysis product was verified by melting point, its IR spectrum and its NMR spectrum, in each case compared with an authentic sample of MBDMA.

Since the MBDMA contains a methylene group inserted between two DMA segments, the question of the origin of the methylene group seemed pertinent. In the normal electrolysis situations, a methylene group

could conceivably be abstracted from either the solvent (CH_3CN) or the ethyl groups of the supporting electrolyte, TEAP. Accordingly, a mass electrolysis of a 10^{-2} M solution of DMA in benzonitrile using 0.1M sodium perchlorate as supporting electrolyte was conducted. In this system, the only source of methyl groups would be from the DMA. Similar results were obtained compared to the acetonitrile/TEAP experiments (however, product yields were much lower due to problems in work-up from benzonitrile), so it seems safe to conclude that the electrochemical oxidation pathway involves abstraction of a methyl group from the dimethylamino portion of DMA to form the MBDMA. In addition, chemical oxidations of DMA to MBDMA have been carried out in solvents such as benzene and carbon tetrachloride using benzoyl peroxide as oxidant (1, 20).

The most plausible mechanism for formation of MBDMA from DMA has been proposed as the reaction pathway followed in the benzoyl peroxide oxidation and gamma radiolysis of DMA (21, 22). This involves initial formation of a DMA cation radical, not an unreasonable assumption. It should be pointed out that no direct evidence for the existence of DMA cation radical was found in the present work or in any previous studies. However, based on other studies on aromatic amines in general and substituted DMA's in particular, it seems safe to assume that the DMA cation radical is the first intermediate formed (I). This radical can then attack a parent DMA molecule, the *para*-ring position of the cation attacking one of the methyl groups of the parent to form a substituted benzyl amine, N-p-dimethylaminobenzyl-N-methylaniline (II). This species is then protonated to form (III). This then breaks up to give (IV) and N-methylaniline. A molecule of DMA then reacts with (IV) to form MBDMA. Attack of (I) on MBDMA could then lead to a molecule of leuco crystal violet, LCV. Since LCV is more easily oxidized than DMA, formation of crystal violet dye from LCV ensues. In addition to all this, there is a parallel reaction pathway, the one classically cited, whereby TMB is formed by coupling of two DMA radicals. The over-all reaction pathway is shown in Fig. 3. Due to the coupling reactions occurring in these systems, protons are generated in substantial amounts; protonation of DMA and the various products certainly occurs, but this has not been shown for the sake of clarity.

Several alternative paths to this general mechanism are possible and should be mentioned, although they are difficult or impossible to verify. Reaction [3] in Fig. 3 may go by the pathway shown below¹ rather than by attack of (I) on the methyl group of a parent DMA molecule. The over-all result is identical in both cases, i.e., formation of (II), but this alternative mechanism is certainly a possibility.



These mechanistic steps are consistent with the fact that MBDMA and crystal violet are formed only at intermediate and high DMA concentrations, where parent DMA molecules are available to act as bases toward DMA cation radicals. Deprotonation of the cation radical (I) has also been suggested from the results of chemical oxidation studies (23). This work is particularly pertinent since the oxidizing agents employed, chloranil and copper(II), are one-electron types and hence might furnish data more applicable to reactions of the DMA cation radical. In fact, the product distribution obtained in this study was markedly similar to that from the present electrochemical work.

¹ This alternative mechanism was suggested by a referee.

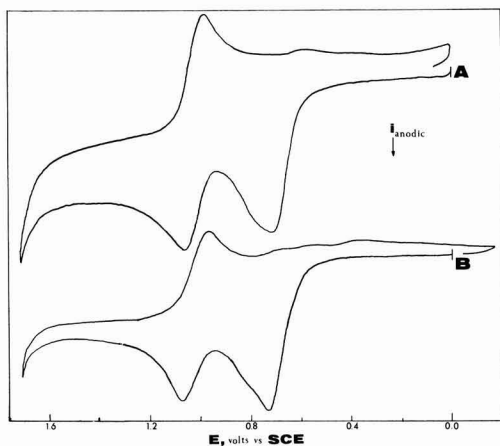


Fig. 2. Curve A, cyclic voltammogram of the product isolated from an electrolysis of 10^{-2} M DMA in acetonitrile/0.1M TEAP; curve B, cyclic voltammogram of an authentic sample of MBDMA in acetonitrile/0.1M TEAP.

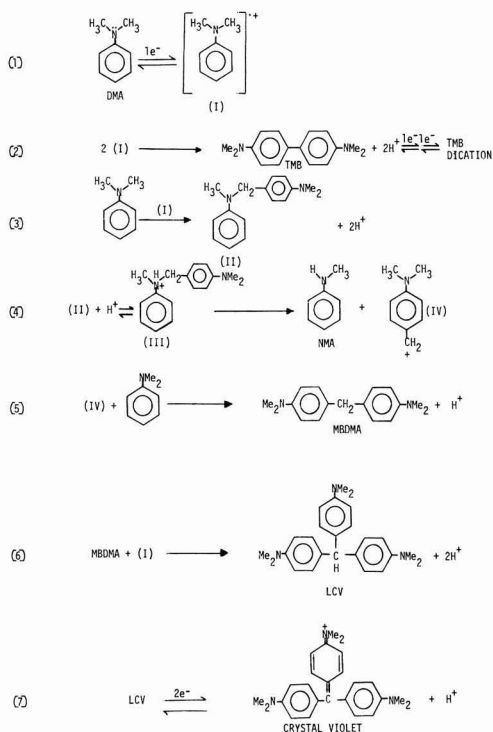


Fig. 3. Proposed reaction pathways for the anodic oxidation of N,N-dimethylaniline in acetonitrile.

Reaction [6] in Fig. 3 is also somewhat less than certain. It would seem just as likely that the formation of leuco crystal violet might occur via reaction between oxidized MBDMA and parent DMA, rather than by the opposite radical-parent route; this is so because the oxidation potentials of DMA and MBDMA are almost identical. Thus, it was not possible to carry out studies where one would be electrolyzed in the presence of the other to induce formation of leuco crystal violet. Again, the pathways are different, but the end product is identical; verification of the correct pathway must await more sensitive studies in order to differentiate.

Repeated attempts were made to isolate the substituted benzyl amine intermediate by terminating electrolyses well short of the calculated end point and attempting recovery by chemical means. These attempts were singularly unsuccessful probably due to the fact that this intermediate is quite unstable; the application of even moderate heat induces its conversion to MBDMA in the presence of any excess DMA.

It was felt that detection of N-methylaniline (NMA) in the electrolysis mixtures was essential to verifying the proposed mechanism, but this task was hampered by the fact that NMA is oxidized at about the same potentials as DMA, leading to unknown products. However, visible absorption spectra of electrolysis solutions of DMA and NMA show a common peak at about 550 $m\mu$ that cannot be ascribed to any of the DMA oxidation products previously mentioned. Likewise, a common spot is obtained on thin-layer chromatograms of the two solutions. Further work now under way on the oxidation of NMA may clarify this aspect of the work.

At higher DMA concentrations (10^{-1}M and higher), less MBDMA is found; as shown in the reaction scheme the next highest analog, leuco crystal violet, is formed in small amounts and a goodly portion of the yield is in the form of the dye crystal violet. This is an in-

tensely colored dye and its presence was confirmed by comparison of the visible absorption spectra of a DMA electrolysis solution and an authentic sample of the dye; the match-up is striking. The gradual formation of the dye can be seen in the visible absorption spectra shown in Fig. 4. These spectra were recorded after various times of electrolysis of a 0.2M solution of DMA in acetonitrile. Note that even at this concentration it appears that TMB is formed initially. However, as the electrolysis proceeds the concentration of crystal violet increases and the TMB fades away in comparison. At the end of the electrolysis the only species giving rise to an absorption band in the visible region of the spectrum is the crystal violet dye. It is felt that parallel reaction pathways are operative to produce TMB and the other electrolysis products; fairly extensive studies on the electrochemical oxidation of TMB alone and in the presence of DMA, though complicated, have not shown evidence for formation of MBDMA or crystal violet (24). At first, the concept of crystal violet being formed from the oxidation of DMA is implausible at best, but again recourse to the literature shows that it is not unheard of. In fact, chemical oxidation of DMA by chloranil and copper(II) leads to appreciable yields of crystal violet (23,25) (see above).

In order to verify that all the products cited are formed concurrently, a constant current electrolysis of a 1M DMA solution in MeCN was run and terminated well before completion ($n = 0.5$). The major products formed were MBDMA and LCV; small amounts of TMB and crystal violet were also detected. It would seem, then, that the formation of the various products depends markedly on DMA concentration. This is certainly true, but another variable was also found to be important, namely current density (or electrolysis duration). At low current densities (or long electrolysis times), more of the crystal violet and its leuco form were produced from DMA. This was confirmed with a series of constant current electrolyses at varying current densities, and it was found that solutions containing intermediate concentrations of DMA (10^{-2} to 10^{-1}M) yielded progressively larger amounts of the

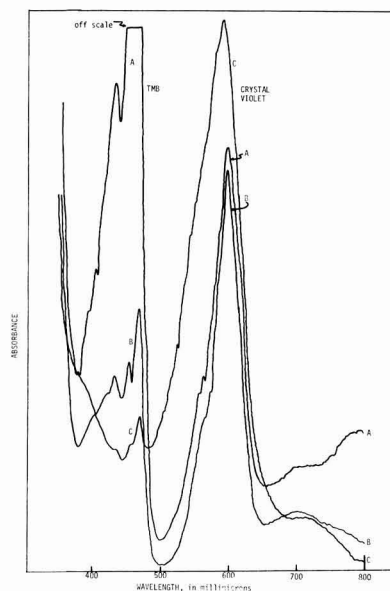


Fig. 4. Visible absorption spectra recorded during electrolysis of a DMA solution (0.2M) in acetonitrile/0.1M TEAP. Concentrations are not comparable (samples were diluted to various extents) from one curve to the next. Curve A, early in the electrolysis; curve B, middle electrolysis; curve C, late in the electrolysis.

dye with decreasing current density. This is reasonable in view of the deprotonation mechanism mentioned above. At low current densities, the ratio of parent DMA to cation radical is greater and deprotonation is more likely to occur.

Several other N,N-dialkylanilines were briefly investigated to determine whether the bulk and abstractability of the alkyl group would have an effect on the course of the electrochemical oxidation pathway. The electrochemical properties of DMA and these other N,N-dialkylanilines are shown in Table I. Over-all, the properties do not vary a great deal with the nature of the alkyl group; most of the variation can be ascribed to differences in diffusion coefficients. Electrochemical data for N,N-dimethyl-p-anisidine, a model one-electron, reversible system, are included for purposes of comparison. The n -value data obtained at varying concentrations confirm the relatively uncomplicated behavior at low concentrations, i.e., formation of benzidines, and the complex nature of the electrode process at higher concentrations, especially for DMA. At low concentrations, one would anticipate a ratio of reverse to forward current of 0.5 if only benzidine formation were taking place, analogous to the triphenylamine-tetraphenylbenzidine system (26). This is generally observed for all the dialkylanilines at low concentrations and for all but DMA at intermediate and higher concentrations. The very low value for DMA at 10^{-4} M is due to the fact that the major product formed by multiple electrochemical and chemical steps, crystal violet, is not re-reduced after the initial oxidation.

When exhaustive electrolyses were carried out on 10^{-1} M solutions of the ethyl and *n*-butyl derivatives, only the *para-para*-benzidines corresponding to the dialkylanilines were isolated, with some difficulty and in only moderate yields of 40-50%. The fact that the ethyl and *n*-butyl analogs of MBDMA and crystal violet were not detected is further evidence to confirm the origin of the central carbon of MBDMA and crystal violet as coming from DMA itself and not the solvent or supporting electrolyte. No other products could be isolated and identified in these systems, although the rather low yield of benzidines indicates further complications. This may be due, in fact, to follow-up reactions involving the benzidine dications. These systems, previously thought to consist only of reversible electron transfer steps, have been found to contain chemical complications as yet undefined (24).

From the foregoing data, it would seem that the products formed in the anodic oxidations of N,N-dialkylanilines depend on a number of factors, namely, concentration, length of electrolysis (or current density), and the nature of the alkyl groups attached to the amine nitrogen. The concentration dependence

most likely stems from the relative concentrations of parent amine and radical cation near the electrode surface, the area in which the homogeneous chemical reactions take place. At low bulk concentrations of parent amine, the ratio of radical to parent near the electrode surface is high, hence radical-radical coupling occurs to form the benzidines. At higher bulk concentrations there is more parent amine near the electrode surface, and so the rather complicated series of homogeneous chemical reactions leading ultimately to crystal violet dye ensues. However, even at high DMA concentrations benzidine formation still occurs as a parallel reaction pathway.

It was not unexpected that the anodic oxidation pathways of the other N,N-dialkylanilines, as opposed to DMA, would be less complicated. In the former species, the alpha-carbon of the dialkylamino groups is much less susceptible to attack by incoming radicals; therefore, it is not surprising that benzidine formation predominates even at higher concentrations.

Acknowledgments

Grateful acknowledgment is made to NSF Grants GP-8941 and GY-4189 for financial support of this work. Special thanks are also due to Dr. R. N. Adams and Dr. D. E. Smith for their support and encouragement.


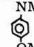
Manuscript submitted March 30, 1970; revised manuscript received ca. June 19, 1970.

Any discussion of this paper will appear in a Discussion Section to be published in the June 1971 JOURNAL.

REFERENCES

1. J. M. Fayadh, D. W. Jessop, and G. A. Swan, *Proc. Chem. Soc.*, 236 (1964).
2. D. M. Graham and R. B. Mesrobian, *Can. J. Chem.*, **41**, 2938 (1963).
3. Fr. Fichter and E. Rothenberger, *Helv. Chim. Acta*, **5**, 166 (1922).
4. W. Lob, *Z. Elektrochem.*, **7**, 579 (1901).
5. Z. Galus and R. N. Adams, *J. Am. Chem. Soc.*, **84**, 2061 (1962).
6. Z. Galus, R. M. White, F. S. Rowland, and R. N. Adams, *idem.*, 2065.
7. T. Mizoguchi and R. N. Adams, *idem.*, 2058.
8. J. E. Dubois, P. C. Lacaze, and A. Arana, *Compt. rend.*, **260**, 3383 (1965).
9. V. Dvorak, I. Nemecek, and J. Zyka, *Microchem. J.*, **12**, 99 (1967).
10. Fr. Fichter and P. Schonmann, *Helv. Chim. Acta*, **19**, 1411 (1936).
11. E. L. Helwig, U.S. Pat. 1,816,848 (1931); *Chem. Abstr.*, **25**, 5355 (1931).
12. N. N. Mel'nikov and E. M. Cherkasova, *J. Gen. Chem. USSR Eng. Transl.*, **16**, 1025 (1946).
13. N. L. Weinberg and E. A. Brown, *J. Org. Chem.*, **31**, 4058 (1966).
14. N. L. Weinberg and T. B. Reddy, *J. Am. Chem. Soc.*, **90**, 91 (1968).
15. J. F. Ambrose and R. F. Nelson, *This Journal*, **115**, 1159 (1968).
16. A. I. Vogel, "A Textbook of Practical Organic Chemistry," 3rd Ed., p. 573, Wiley & Sons, New York (1956).
17. S. D. Ross, G. J. Kahan, and W. A. Leach, *J. Am. Chem. Soc.*, **74**, 4122 (1952).
18. "Wenking Potentiostat 61RH Operating Instructions," 1968.
19. P. J. Smith and C. K. Mann, *J. Org. Chem.*, **34**, 1821 (1969).
20. R. B. Roy and G. A. Swan, *Chem. Commun.*, 427 (1966).
21. J. M. Fayadh and G. A. Swan, *J. Chem. Soc. (C)*, 1775 (1969).
22. G. A. Swan, *idem.*, 2015.
23. J. R. L. Smith, R. O. C. Norman, and W. M. Walker, *J. Chem. Soc. (B)*, 1968, 269.
24. R. Hand, Unpublished data.
25. J. W. Eastman, G. Engelsma, and M. Calvin, *J. Am. Chem. Soc.*, **84**, 1339 (1962).
26. E. T. Seo, R. F. Nelson, J. M. Fritsch, L. S. Marcoux, D. W. Leedy, and R. N. Adams, *ibid.*, **88**, 3498 (1966).

Table I. Electrochemical properties of N,N-dialkylanilines

NR ₂ 	$E_{p/2}^a$	$i_{p/2}/i_{1/2}^b$	$i_{1/2}/i_{1/2}^c$	n -values ^d	$i_{rev}/i_{for. f}$
R = CH ₃	0.72	35.0	57.0	1.1, 1.0, 1.2	0.50, 0.34, 0.05
C ₂ H ₅	0.70	34.0	54.0	1.1, 1.1, 1.4	0.50, 0.47, 0.37
<i>n</i> -C ₄ H ₉	0.69	32.5	49.6	1.2, 1.2, 1.4	0.48, 0.40, 0.35
sec-C ₄ H ₉	0.70	33.5	51.0	1.1, 1.2	0.54, 0.48
<i>n</i> -C ₁₀ H ₂₁	0.69	29.0	43.0	1.0, 1.1	0.47, 0.42
NMe ₂ 	0.52	36.0	58.0	1.0, 1.0	1.0, 0.98
OMe ^e					

^a Half-peak potentials measured at a scan rate of 21.0 V/min; in volts vs. SCE. There is a marked anodic shift with increasing scan rate.

^b Peak current data; values stated are averages from several different scan rates ranging from 3.0 to 60.0 V/min.

^c Chronoamperometry data; values stated are average values taken from current-time curves from 0.5 to 8.0 sec.

^d Values stated are for concentrations of 10^{-6} , 10^{-3} and 10^{-1} M, respectively.

^e One-electron model compound; data are presented for purposes of comparison.

^f Ratio of reverse to forward integrated currents taken from coulometric n -value determinations shown. The oxidation potential was set at +0.90V; re-reduction was effected at 0.00V; thus proton reduction is not included in i_{rev} .

Preparation of N-Alkylacetamides by the Anodic Oxidation of Carboxylic Acid Salts

D. L. Muck* and E. R. Wilson

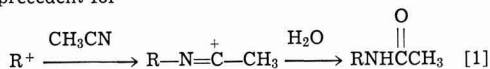
The Procter & Gamble Company, Miami Valley Laboratories, Cincinnati, Ohio 45239

ABSTRACT

The possibility of preparing N-alkylacetamides by the electrolytic oxidation of carboxylate ions at a carbon anode in the presence of acetonitrile has been investigated. A yield of substituted acetamide of about 50% was obtained with potassium valerate, but it gradually dropped to zero in favor of the Kolbe coupled product in going from potassium octanoate to potassium laurate. An explanation of this effect involving specific orientation of the adsorbed long chain carboxylates on the electrode surface is included. Products derived from intermediate carbonium ions were found, and a mechanism for their formation is proposed.

After a period of time when little work was done on the Kolbe electrolysis, the last few years have seen a definite surge of interest in the reaction. Most of this recent work has been directed toward the elucidation of the mode of electron transfer taking place at the electrode surface, but one very important feature which may have definite synthetic implications is the relatively recent discovery that carbonium ions are sometimes formed in the reaction (1-14). The important variables affecting carbonium ion formation are apparently the nature of the anode material and the structure of the carboxylate salt employed. In the case of an oxidation run under normal Kolbe conditions where platinum anodes are employed, carbonium ions are apparently formed only when the radical initially generated in the reaction has an electron impact ionization potential (I.P.) of less than 8 eV (3). However, Koehl (6) has shown that the use of a carbon anode promotes carbonium ion formation even with carboxylates derived from simple straight chain fatty acids, where the I.P. may be 8-10 eV. We have been very interested in this development, since it ideally presents a way to functionalize the alkyl chains derived from fatty acids.

In addition to the more common nucleophiles known to react with carbonium ions, acetonitrile has been shown to give nitrilium salts (7, 15) which can then react with water to give N-substituted acetamides. A precedent for



the trapping of anodically generated carbonium ions with acetonitrile had previously been set by Ebersson (7), so we also used acetonitrile and employed carbon anodes to promote carbonium ion formation. During the period of our work, the results of a similar study were published by Kornprobst and co-workers (12). In this case, however, the oxidations were carried out at platinum anodes, so that products derived from carbonium ions were isolated in yields of more than 20% only when branched chain carboxylates were employed (where the I.P. of the alkyl radical was less than 8 eV). In our work we have found that butyl cations react with acetonitrile and water to give two unexpected products, an N-acylvalerylamine and an N-butylvalerylamine in addition to the desired acetamide and other by-products. This work confirms and complements the results of Kornprobst and co-workers. We have also uncovered an intriguing phenomenon involving a gross variation in reaction products: longer chain

fatty acid carboxylates give decreasing amounts of carbonium ions as the chain length increases, thereby yielding larger quantities of normal Kolbe coupled products. Explanations for this variation are discussed.

Experimental

Materials.—The acetonitrile employed was Matheson, Coleman, and Bell spectral grade. The carboxylic acids, the isomeric heptyl alcohols, and docosane used were all obtained commercially and were used without further purification.

Apparatus.—A d-c power supply capable of producing 5A current and potentials of up to 220V was employed. The electrolysis cell consisted of a resin pot with 3 ground glass joints in the lid through which the electrode leads and a cooling coil were sealed. The system was flushed with He before each reaction. The gases evolved during the reaction were passed through the tube of Drierite, a tared tube of Ascarite, and finally through a trap cooled in liq N₂. The electrodes were carbon rods 1 in. in diam and 2 in. long (*A* = 7.0 in.²; 45.7 cm²). Infrared spectra were obtained with a Perkin-Elmer Infracord spectrophotometer, while the NMR spectra were obtained on Varian T-60 and HA-100 spectrometers. Gas chromatographic separations were made on an F&M Model 700 equipped with a 6 ft x 0.25 in. column packed with 10% Apiezon L on 60-80 mesh Chromosorb W, acid washed and dimethyldichlorosilane treated. Mass spectra were obtained with an Atlas CH-4 instrument.

General electrolysis procedure.—A description of the oxidation of potassium valerate is given as being typical. Potassium valerate (140.0g, 0.10 mole) was dissolved in 22 cc of water and diluted with 200 cc of acetonitrile. A d-c voltage of about 20V was applied until a current of 2.0A flowed. The applied voltage was then held constant and the electrolysis was continued for a period equal to three times the half-life of the reaction (the half-life of each reaction was taken as the time required for the current to drop to 50% of its original value). The reaction solution was then removed from the cell, the cell was rinsed with a little water, and the rinse was combined with the bulk solution. The resulting solution was analyzed for octane and butyl alcohol by GLC, and then refluxed under a condenser connected to a liq N₂ trap to collect any remaining volatile hydrocarbons. The solvents were then removed from the reaction solution on a rotary evaporator, about 75 cc of water were added, and this solution was extracted with ether. The ether extracts were combined, dried over MgSO₄, and concentrated on a rotary evaporator to give about 5g of organic products. The aqueous layer was acidified with 6N

* Electrochemical Society Active Member.

Key words: Kolbe electrolysis, n-alkylacetamides, carbon anodes, carbonium ions.

HCl, extracted continuously overnight with ether, and the resulting ether layer was dried over MgSO_4 before evaporation on a rotary evaporator to give 0.5-3g of unreacted valeric acid. The volatile hydrocarbons collected in both liq N_2 traps were warmed to dry ice-acetone temperature before being weighed, and were then analyzed by NMR and mass spectrometry. They were found to be essentially the same mixture of butenes and methyl cyclopropane as previously reported. The liquid organic products were isolated and purified by preparative scale GLC. The identities of the products were established by comparison of GLC retention times, IR spectra and NMR spectra with those obtained on samples prepared by independent methods.

Preparation of N-alkylacetamides.—Samples of the various N-alkylacetamides needed for comparison purposes were prepared by adding an ether solution of acetyl chloride drop-wise to an equimolar quantity of the appropriate amine in ether at room temperature. The resulting ether solution was filtered and the solvent removed from the filtrate on a rotary evaporator. The crude acetamides were then purified by preparative scale GLC.

N-(sec-butyl)-N-acetylvalerylamine.—To 4.8g (0.03 mole) of N-(sec-butyl)valerylamine which was prepared by reacting valeryl chloride with sec-butyl amine were added 100 ml of ether and 4.8g (0.06 mole) of pyridine. A solution of 2.4g (0.03 mole) of acetyl chloride in 20 ml of ether was added drop-wise, and the resulting solution was refluxed for 2 hr. More acetyl chloride (1.2g; 0.015 mole) was then added and the mixture was refluxed for 2 hr more. About 5 ml of ethanol were added, and the resulting solution was washed twice with dil HCl, 3 times with satd. NaHCO_3 , and finally once with water before drying over anhyd MgSO_4 . The solvents were removed with a rotary evaporator to give 1.0g (17%) of a clear oil with no N-H infrared absorption. Purification by preparative scale GLC gave a colorless liquid.

Anal Calc for $\text{C}_{11}\text{H}_{21}\text{NO}_2$: C, 66.33; H, 10.55; N, 7.04.
Found: C, 66.50; H, 10.85; N, 7.32.

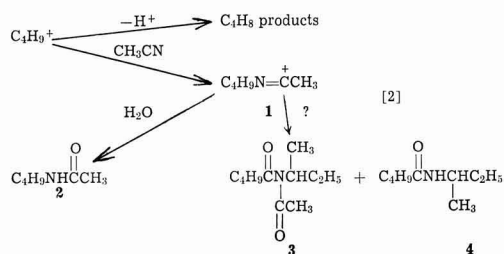
Stability of N-(sec-butyl)-N-acetylvalerylamine to reaction conditions.—The conditions for the electrolysis of potassium valerate as described above were repeated, except that 15% water in acetonitrile was used as the solvent, and 2.0g of N-(sec-butyl)-N-acetylvalerylamine were added. The electrolytic oxidation of the valerate was then carried out as before, and the products were isolated. Octane (0.1g; 0.0009 mole) and N-sec-butyl acetamide (1.8g; 0.016 mole) were obtained along with 4.8g of the above substituted valeryl amide. Subtracting out the amount of this latter material that was added to the initial reaction solution (2.0g), a yield of 2.8g (0.014 mole) was obtained, which is very close to the average of 2.4g obtained in three normal reactions.

Electrolysis of potassium octanoate in water.—Octanoic acid (14.4g; 0.10 mole) and 5.6g (0.10 mole) of potassium hydroxide were dissolved in 200 ml of water and electrolyzed according to the general procedure described before. The aqueous solution obtained was then extracted three times with ether, and the combined extracts were dried over anhydrous magnesium sulfate. The solvent was then removed on a rotary evaporator to give 0.8g of heptyl alcohols. This mixture was analyzed on capillary column GLC using known samples of the various isomeric heptyl alcohols as standards. The following amounts of each were found: 1-heptanol, 18.5%; 2-heptanol, 43.8%; 3-heptanol, 37.7%.

Results

Since long-chain compounds are often difficult to work with, potassium valerate was employed initially

as the starting material. In every case, contrary to normal Kolbe reaction conditions, the valeric acid was completely neutralized, since it has previously been shown that high carboxylate concentrations favor carbonium ion formation (14). For anodes, we initially attempted to use the types of carbon used before by Koehl (6), but the acetonitrile dissolved the organic binders they contained and eroded the electrodes badly. A shift was then made to regular amorphous hard carbon rods, the apparent density of which varied in the range of 1.42-1.53 g/ml, and these anodes seemed to serve very well. A cylindrical perforated copper cathode was used, and the initial reactions were run in a 10% water in acetonitrile solvent mixture. We did obtain the desired acetamide 2 in a 26% yield, but we also isolated the unexpected products 3 and 4 as well as isomeric butenes and methyl cyclopropane arising from loss of a proton from the intermediate butyl cation.



In an effort to maximize the yield of the desired acetamide 2, a study of the variation of products with an increase in the amount of water employed was made. Concentrations of water below 10% were not used because the starting material was not completely soluble. At least four runs were made for each set of conditions, and the average values of these are shown in Table I. The yields for each run were generally within 5% of the average value, but they sometimes varied as much as 15% from the average.

Since it was conceivable that products 2 or 4 could have resulted from a degradation of 3, a sample of 3 prepared by an independent synthesis was added to a normal electrolytic reaction to check its stability to reaction conditions. The amount of 3 obtained from this reaction was greater than normal by essentially the amount added to the reaction, and the quantities of other products isolated were within their normal ranges. Therefore, 3 is stable to the reaction conditions and could not be a source of 2 or 4.

In order to investigate the possible variations in the product distribution with changes in the type of carbon used for the anode, normal graphite as well as pyrolytic graphite anodes were also used. The characteristics of

Table I. Product distribution as a function of the water concentration

Yields are based on mole per cent of the organic products.

Per cent water	10	15	20	25	30	35	40
	26	50	50	40	26	31	26
	35	23	15	12	2	0	0
	8	8	11	8	6	3	0
C_4H_8 Products	21	13	23	39	23	44	26
C_4H_{10}	10	6	1	1	0	0	0
$\text{C}_4\text{H}_8\text{OH}$	0	0	0	0	43	22	48

these materials are shown in Table II, and the data on the product trends observed in a 15% water in acetonitrile solvent mixture are listed in Table III. The yields obtained on a platinum anode are included in Table III for the sake of comparison.

From Table I, one can see that the best yields of N-sec-butyl acetamide were obtained in 15-20% water in acetonitrile solvent mixtures. Therefore, the potassium salts of octanoic and lauric acids were electrolyzed under these conditions to verify that similar results could be obtained with longer chain fatty acids. Surprisingly however, the results differed with these salts. As the length of the carbon chain attached to the carboxy group increased, the amount of normal Kolbe coupled product increased markedly to the point at which only docosane, $C_{22}H_{46}$, was formed in the oxidation of potassium laurate. A summary of the data obtained from the oxidation of these salts is shown in Table IV.

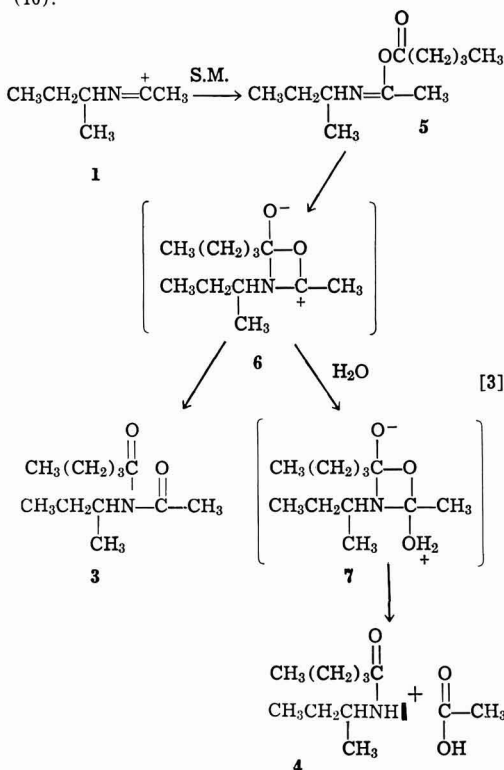
Kornprobst and co-workers (12) observed a number of alkyl group rearrangements in their work. With potassium valerate we found the same isomerization of the C_4H_9 chain to give sec-butyl derivatives. In order to study the alkyl rearrangements in longer chain salts, we analyzed the alcohols obtained from the oxidation of potassium octanoate in a 50% water in acetonitrile solvent mixture by capillary column gas chromatographic comparison with known samples of the isomeric heptyl alcohols. The results showed 18.5% 1-heptanol, 43.8% 2-heptanol, and 37.7% 3-heptanol with no 4-heptanol found.

Discussion

Oxidation of valeric acid.—The products obtained from the oxidation of potassium valerate were generally those expected. It has previously been established that side reactions of the butyl cation give iso-

meric butenes as well as some methylcyclopropane (6). The fact that butyl alcohol was observed in these reactions is not unusual because its formation from a carbonium ion generated in the presence of water would certainly be predicted, but it does seem unreasonable that the amount of water would have to be greater than 25% for this reaction to take place. One can justify the result by assuming that adsorption of carboxylate ions and/or acetonitrile on the anode surface prevents the water from reaching the reactive carbonium ion generated on that surface.¹

While the above products were generally expected, the formation of the N-acyl amide **3** and the valeryl amide **4** was somewhat unusual. In order to explain the formation of these products, the following is presented as a reasonable mechanism which is consistent with the observed results. The basic concept was substantiated by the report of Kornprobst and co-workers (12), who also explained the formation of the N-acyl amide **3** by rearrangement of **5**. The rearrangement of **5** to the products **3** and **4** is postulated in our mechanisms as proceeding via a 4-membered ring transition state which may or may not be a concerted process. The hypothetical intermediate **6** is shown to illustrate the rearrangement more clearly. A similar rearrangement involving a 1,3-acyl migration from carbon to nitrogen has been reported by Curtin and Richman (16).



The trends in the variation of these products as the concentration of water changes are generally consistent.

¹ A referee has suggested that the anode potential in these reactions may be high enough that water is being oxidized, thereby depleting its concentration at the electrode surface. This could explain the high concentration of water required to form alcohol from the butyl cation. We cannot rule out this possibility but tend to discount it for the following reasons. Numerous electrochemical studies in the past have demonstrated that the electrolysis of water ceases in the Kolbe electrolysis when the potential becomes anodic enough to oxidize carboxylate ions. In addition, one would not expect the current to decrease in value with time as it does in these reactions if water were being electrolyzed because the amount of water is so great that its concentration would remain essentially constant during the time span involved.

Table II. Carbon used for anodes

Form of carbon	Manufacturer	Type	Apparent density (g/ml)
Unmachined amorphous carbon	Great Lakes Carbon	BC	1.42-1.53
Graphite	Poco Graphite	AXZ	1.50-1.60
Graphite	Poco Graphite	AXZ-5Q	1.80-1.88
Pyrolytic graphite	General Electric	EC	2.20-2.23

Table III. Product distribution as a function of the anode

Yields are based on mole per cent of the organic products.

	Amorphous carbon	Pyrolytic graphite	AXZ graphite	AXF-5Q graphite	Platinum
$CH_3C(=O)NHCH(CH_3)CH_2CH_2CH_3$	50	29	49	46	19
$CH_3(CH_2)_2C(=O)NHCH(CH_3)CH_2CH_2CH_3$	23	3	10	18	0
$CH_3(CH_2)_3C(=O)NHCH(CH_3)CH_2CH_2CH_3$	8	12	10	8	6
C_4H_9 Products	13	56	31	28	42
C_4H_9	6	0	0	0	33
C_4H_9OH	0	0	0	0	0

Table IV. Kolbe product distribution as a function of chain length

Yields are based on amount of starting acid used up.

Acid	Product	Yield
$C_6H_5CO_2H$	C_6H_5	10
$C_{11}H_{21}CO_2H$	$C_{11}H_{21}$	58
$C_{11}H_{21}CO_2H$	$C_{22}H_{42}$	69

ent with the scheme above. The yield of N-(sec-butyl)acetamide, 2, increases sharply as the per cent of water changes from 10 to 15%, indicating that the concentration of water is such that it can effectively compete with the starting material for reaction with the nitrilium cation. The large molar excess of water required for this to happen may be the result of the carboxylate anion adsorbing on the positively polarized anode. The yield of substituted acetamide then begins to decrease with increasing water concentration due to increased side reactions of the butyl cation, initially to form olefins and later to react directly with the water to form alcohol. The drop in the amount of the N-acyl amide 3 formed with an increase in the amount of water present would be predicted. The over-all yield of N-(sec-butyl) valeril amide formed was never high and, therefore, the small changes observed are not significant. The Kolbe product in this case is octane, and while about 10% was formed in the 10% water in acetonitrile solvent system, generally negligible quantities were observed in the solutions with greater amounts of water present.

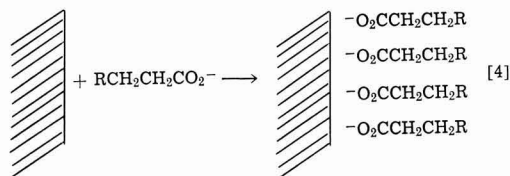
Although the data obtained in the above studies involving varying water concentrations were reproducible only to about $\pm 15\%$, there seems to be no obvious explanation. Each experiment was conducted with a new carbon anode, and while a third electrode for maintaining a controlled potential at the electrode surface was not employed, each reaction was initiated at a potential necessary to generate an initial current of 2A. The applied potential was then held constant throughout the reaction and the current allowed to decrease as the starting material was depleted. An attempt was made to use a third electrode for monitoring the potential near the surface of a rotating carbon rod, but the potentials observed were so high (3.5-5V vs SCE) that it was apparent that uncompensated IR drop was making the measurement meaningless. A factor which might have caused the inconsistency in the yields of products would be variation in the extent of reaction of the starting material. Most of the reactions were continued for a period of time equivalent to three half-lives of the reaction (as measured by the current drop). However, varying amounts of unreacted valeric acid were recovered from these reactions. When a series of oxidations was run to a degree of completeness where essentially equal amounts of valeric acid remained, a similar trend in product distribution was obtained. Since an accurate measure of the net potential at the electrode surface was not attainable, the nonreproducibility in yields observed may simply be due to a variation in the potential obtained at the surface of the anode. It has been suggested (13) that the potentials required for the oxidation of carboxylate ions and for the oxidation of alkyl radicals are significantly different to allow two distinct waves. Assuming that the oxidation of an alkyl radical to a carbonium ion takes place at a more anodic potential than the oxidation of a carboxylate ion, it is possible that some of the reactions described herein might have been carried out at potentials slightly more cathodic than that required for efficient oxidation of the alkyl radicals to carbonium ions. This would lead to differing rates of formation of carbonium ions, and thereby varying yields of products from these ions.

The results obtained from the electrolysis of potassium valerate at a number of different anodes (Table III) indicate that similar processes are taking place at amorphous carbon and normal graphite anodes. This agrees with the work of Koehl reported earlier (6). However, of the other carbons studied, pyrolytic graphite behaved atypically. This is not unreasonable since the surface structure of pyrolytic graphite is essentially voidless due to the layered platelet structure it possesses.

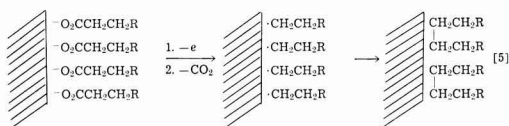
When platinum anodes were employed, much larger quantities of the normal Kolbe dimer were obtained, as would be expected. However, the amount of products derived from the butyl cation are higher than would be predicted. The N-(sec-butyl)acetamide formed in a 19% yield represents carbonium ion which has reacted with acetonitrile, while the 42% yield of C_4H_8 products indicates the amount of carbonium ion which lost a proton. Since the electron impact ionization potential of the n-butyl radical is higher (8.64 eV) than the 8 eV limit suggested as being the maximum value for promoting carbonium ion formation, this combined yield of 61% of ion is unreasonably high.

Oxidation of octanoic and lauric acids.—The observation that the yield of Kolbe coupled products increased with increasing chain length in the fatty acids studied was not anticipated. The yield of dimer obtained under normal Kolbe reaction conditions is generally constant as the chain length increases, except for propionic and butyric acids which give unusually low yields (17).

In considering an explanation of the phenomenon observed in this work, the most logical proposal to make is that attractive forces between the long chain alkyl radicals are keeping them from reaching the electrode surface where they would undergo further oxidation. A reasonable scheme based on this premise can be proposed if two assumptions are made. First, assume that as the carboxylate anions approach the electrode surface they will assume an orientation dependent on the chain length of the molecule involved. Short chain carboxylates (possibly up through C_6) will be adsorbed on the surface in a more or less random fashion. However, as the alkyl chains become longer, they will tend to adsorb in an orientation perpendicular to the electrode surface, with a subsequent stacking or layering effect becoming pronounced as more and more ions are adsorbed. This stacking effect



would be predicted to be enhanced by the Van der Waals attraction of the hydrophobic alkyl chains for each other, since they would constantly be searching for a more organic environment than the polar solvent surrounding them. Now also assume that the radicals generated in this reaction are separated from the electrode surface at the instant of formation by the width of the leaving CO_2 molecule (about 6Å), as has been previously postulated by Eberson (3, 10). The over-all net effect predicted then would be that the radicals would be generated in layers perpendicular to the electrode surface, and about 6Å away from the surface. Whether or not the intermolecular attractions these radicals experience would be enough noticeably to slow their migration through such a short distance is debatable, but it is certain that the stacked orientation described would be predicted to increase significantly the probability of radical coupling.



Since both the processes of radical-radical coupling and migration through a few angstroms of solution would be expected to be very fast, it would not take much of an effect to noticeably favor one or the other

of these processes. The simple slowing of the rate of migration of long chain alkyl radicals due to the increase in molecular weight might even be enough of a factor to cause the observed change in reaction.

The assumption made above that the radicals formed in the Kolbe reaction are separated from the electrode surface by the width of a molecule of carbon dioxide deserves further discussion. Eberson made this proposal after obtaining evidence that the radicals generated under similar conditions did not react stereospecifically as one would predict for reaction of an adsorbed radical. It now appears that the "long chain effect" observed in this work supports Eberson's postulation. If the radicals were generated in an adsorbed state and were never really "free," the only obvious way one could explain the observed increase in coupling with increasing chain length would be by assuming that there existed enough difference in the ionization potentials of the alkyl radicals to cause preferential oxidation of those with shorter chain lengths. However, this argument is unreasonable since the ionization potentials that have been measured for alkyl radicals decrease with increasing chain length, which would indicate that the long chain radicals would be more easily oxidized to carbonium ions.

Acknowledgments

The authors are deeply grateful to Drs. D. W. Leedy, J. P. Haberman, W. F. Erman, and L. Benjamin for helpful discussions, to Mr. L. H. Sickman, Jr., for his technical assistance, and to Mrs. R. Schlensker and Mrs. L. Walsh for secretarial help in preparing the manuscript.

Manuscript submitted April 10, 1970; revised manuscript received ca. July 14, 1970. This was Paper 129 presented at the New York Meeting of the Society, May 4-9, 1969.

Any discussion of this paper will appear in a Discussion Section to be published in the June 1971 JOURNAL.

REFERENCES

1. H. J. Dauben and M. A. Muhs, Private communication in C. Walling, "Free Radicals in Solution," p. 581, John Wiley & Sons, New York (1957).
2. E. J. Corey, N. L. Bauld, R. T. LaLonde, J. Casanova, Jr., and E. T. Kaiser, *J. Am. Chem. Soc.*, **82**, 2645 (1960).
3. L. Eberson, *Acta. Chem. Scand.*, **17**, 1196 (1963).
4. J. A. Waters, *J. Org. Chem.*, **29**, 428 (1964).
5. W. A. Bonner and F. D. Mango, *ibid.*, **29**, 430 (1964).
6. W. J. Koehl, Jr., *J. Am. Chem. Soc.*, **86**, 4686 (1964).
7. L. Eberson and K. Nyberg, *Acta. Chem. Scand.*, **18**, 1567 (1964).
8. J. S. Dehn, "Anodic Oxidations of Medium Ring Cycloalkanecarboxylic Acids," Thesis, Louisiana State Univ., 1966.
9. B. E. Conway and A. K. Uijh, *Electrochim. Acta*, **12**, 102 (1967).
10. L. Eberson, *ibid.*, **12**, 1473 (1967).
11. L. Rand and C. S. Rao, *J. Org. Chem.*, **33**, 2704 (1968).
12. J. M. Kornprobst, A. Laurent, and E. Laurent-Dieuzide, *Bull. Soc. Chim. France*, **1968**, 3657.
13. P. H. Reichenbacher, M. D. Morris, and P. S. Skell, *J. Am. Chem. Soc.*, **90**, 3432 (1968).
14. L. Eberson, in "Chemistry of Carboxylic Acids and Esters," S. Patai, Editor, Chap. 6, John Wiley & Sons, London (1969).
15. (a) J. J. Ritter and P. P. Minieri, *J. Am. Chem. Soc.*, **70**, 4045 (1948).
(b) H. Meerwin, P. Laasch, R. Mersch, and J. Spille, *Ber.*, **89**, 209 (1956).
(c) L. L. Miller and A. K. Hoffmann, *J. Am. Chem. Soc.*, **89**, 593 (1967).
16. D. Y. Curtin and J. E. Richman, *Tetrahedron Letters*, 3081 (1969).
17. B. C. L. Weedon, in "Advances in Organic Chemistry," R. A. Raphael, E. C. Taylor, and H. Wynberg, Editors, Vol. 1, p. 5, Interscience, New York (1960).

Polarography in Acetone of Tris(Dithioacetylacetonato)-Complexes of Iron(III), Ruthenium(III), Osmium(III), and Rhodium(III)

A. M. Bond, G. A. Heath, and R. L. Martin

Department of Inorganic Chemistry, University of Melbourne, Parkville, 3052, Australia

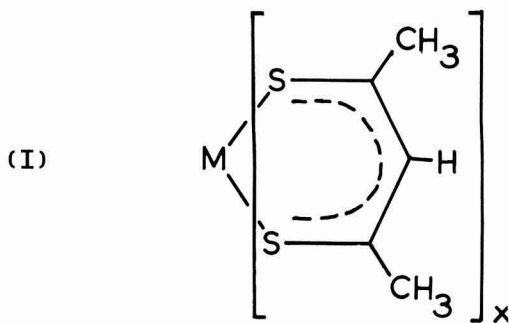
ABSTRACT

Polarographic studies have been carried out in acetone on the dithio(acetylacetonato)-complexes $[M(\text{SacSac})_3]$ ($\text{SacSac}^- = \text{CH}_3\text{CS}\cdot\text{CH}\cdot\text{CS}\cdot\text{CH}_3^-$) where $M = \text{Fe(III)}$, Ru(III) , Os(III) , (all d^5 , low-spin) and Rh(III) (d^6 , low-spin). The iron and osmium complexes are reversibly reduced at the DME, whereas the ruthenium complex undergoes a quasi-reversible reduction. For the d^5 systems the electrode reaction is believed to be $[M^{III}(\text{SacSac})_3] + e^- \rightleftharpoons [M^{II}(\text{SacSac})_3]^-$. However reduction of $[\text{Rh}(\text{SacSac})_3]$ is highly irreversible and may involve adsorption or compound formation at the mercury surface. Millicoulometric studies indicate the electrode reaction is $\text{Rh(III)} + 2e^- \rightarrow \text{Rh(I)}$. The half-wave potentials (Fe , -0.21 ; Ru , $+0.04$; Os , -0.05 ; Rh , 1.05V vs. Ag/AgCl) accord with the known chemistry and spectroscopic properties of the complexes. The development of polarographic techniques for use in acetone is described in detail.

Recently, considerable attention has been directed to transition metal derivatives of the sulfur-containing ligand dithioacetylacetone (1-17). Complexes of all the group VIII transition metals have been character-

Key words: polarography, tris(dithioacetylacetonato)-complexes, acetone.

ized although the parent ligand has not yet been isolated in the monomeric state. X-ray structural investigations confirm that the coordinated dithioacetylacetonato anion is planar and attached to the metal by both sulfur atoms as in (I). Table I summarizes the compounds $[M(\text{SacSac})_3]$ (I) presently known.



Studies by various workers have employed the techniques of infrared, electronic, e.s.r., p.m.r., and mass spectroscopy. Magnetic susceptibility and magnetic anisotropy measurements have also been performed. However, until recently no electrochemical studies had been reported.

The polarographic method is capable of furnishing considerable thermodynamic and structural information on such compounds. It is also an effective means of identifying new species which are related to the known compounds by oxidation or reduction. In this way further synthetic and chemical investigations may be suggested.

Examination of Table I reveals that the complexes $[\text{Co}(\text{SacSac})_3]$ and $[\text{Co}(\text{SacSac})_2]$ provide the only instance where dithioacetylacetonate derivatives have been characterized for two oxidation states of the one transition metal.

The reduction of $[\text{Fe}(\text{SacSac})_3]$ with sodium dithionite was reported to yield "auto-oxidizable" $[\text{Fe}(\text{SacSac})_2]$, but no further characterization was described (3). Attempts to repeat this work have been unsuccessful (18). A more recent report of $[\text{Fe}(\text{SacSac})_2]$ (12), based on a sulfur analysis only, has been questioned (14) and, in our hands, the published method reliably yields $[\text{Fe}(\text{SacSac})_3]$ with the expected analytical and physical properties (15). In these circumstances, we thought it worthwhile to make a detailed polarographic investigation of the redox behavior of $[\text{Fe}(\text{SacSac})_3]$.

The compounds $[\text{Fe}(\text{SacSac})_3]$, $[\text{Ru}(\text{SacSac})_3]$, and $[\text{Os}(\text{SacSac})_3]$ were thus chosen as a representative group for the initial polarographic studies of dithioacetylacetonate complexes. Each of these low-spin d^5 chelates was found to undergo a ready one-electron reduction which might be regarded as completing the metal d_e subshell. A convenient comparison was provided by the polarographic behavior of the low-spin d^6 complex $[\text{Rh}(\text{SacSac})_3]$, in which the metal d_e subshell is fully occupied. These results, which have been briefly reported elsewhere (15), are now discussed in detail.

Recently, polarographic data for the analogous cobalt(II) and nickel(II) complexes were described in a note by Ouchi *et al.* (19). However, neither the compounds, the solvent system, nor the reference electrode are common to the studies described herein.

The dithioacetylacetonate complexes are insoluble in water. Acetone was chosen as a suitable solvent since

preliminary investigations showed that a stable Ag/AgCl reference electrode could be maintained in this solvent. Furthermore, acetone was known not to interact chemically with the compounds and was commercially available in sufficient purity. Polarographic techniques, suitable for use in acetone, have been developed and are described here. These techniques include conventional and rapid polarography with a dropping mercury electrode (DME), inverse polarography with a hanging drop mercury electrode (HDME), and the millicoulometric determination of n values with a DME.

So far as the present authors are aware, acetone has been used only occasionally as an electrolytic solvent (20), and rarely for polarography (21). One of the problems confronting its use is the need for a suitable reference electrode system. Aqueous calomel electrodes have been used (20), but are undesirable in otherwise nonaqueous media, particularly if junction potentials are to be minimized. A satisfactory $\text{Hg}/\text{Hg}_2\text{Cl}_2$, LiCl (acetone) system has been reported (22), but the $\text{Ag}/\text{AgCl}/\text{LiCl}$ (acetone) electrodes described here commend themselves for stability and ease of construction.

Acetone is a versatile solvent for both organic and complex inorganic compounds; the development of this simple reference system may encourage its much wider use as a polarographic medium.

Experimental

Polarography.—Conventional d-c polarographic studies were carried out in B.D.H. Analar grade acetone with tetraethyl-ammonium perchlorate (0.1 mole/liter) as the supporting electrolyte. A Metrohm Polarecord, E 261, was used in conjunction with a Metrohm IR compensator, E 446, and a three-electrode system. The two reference electrodes were identical Metrohm Ag/AgCl EA 425 electrodes filled with a solution of LiCl in acetone (0.1 mole/liter). The glass capillary dropping mercury electrode (DME) had the following characteristics in acetone/0.1M Et_4NClO_4 (at open circuit and a mercury column height of 40 cm): flow rate of mercury, $m = 3.25 \text{ mg sec}^{-1}$; drop time, $t = 2.70 \text{ sec}$; $m^{2/3}t^{1/6} = 2.58$. In the rapid polarographic method, the short controlled drop times were achieved with a Metrohm Polarographie Stand, E 354. Hanging mercury drops used in this work were 0.52 mm in diameter with a surface area of $1.38 \pm 0.04 \text{ mm}^2$ and were produced by a Metrohm BM 5-03 hanging drop mercury electrode (HDME).

Preliminary experiments showed that acetone/0.1M LiClO_4 gave a polarographically useful potential range of $+0.8$ to -1.6 V at the DME *vs.* Ag/AgCl , whereas for acetone/0.1M Et_4NClO_4 the useful range was $+0.8$ to at least -2.0 V . The latter supporting electrolyte was preferred because of the wider potential range. The reference electrodes were fitted with geometrically identical salt bridges containing acetone/0.1M Et_4NClO_4 to minimize LiCl leakage into the test solution. Potentials measured relative to a Ag/AgCl (acetone) reference electrode are qualitatively similar to those measured relative to Ag/AgCl (water). In acetone, LiClO_4 and $\text{Co}(\text{ClO}_4)_2$ reduction and Hg oxidation all occur at potentials about 0.4V more positive than the corresponding processes in water.

The very high resistance of acetone, even with a carrier electrolyte, makes compensation of the large ohmic potential (IR drop) essential. The three-electrode system provides a convenient means for achieving this. For optimum compensation, the measuring reference electrode should be positioned in the field shadow of the mercury electrode and the working reference electrode, *i.e.*, the three electrodes must be in one plane. Identical Ag/AgCl electrodes were thus employed and were symmetrically disposed in the test solution in relation to the mercury electrode. With only one reference electrode in circuit (*i.e.*, no IR com-

Table I. Dithioacetylacetonate complexes

$[\text{M}(\text{SacSac})_x]$	Spin state, S	Structure (by x-ray)	References
$[\text{Ni}(\text{SacSac})_2]$	0	Planar ^{2,17}	(1), (2), (4), (9), (12), (19)
$[\text{Pd}(\text{SacSac})_2]$	0	—	(1), (12)
$[\text{Pt}(\text{SacSac})_2]$	0	—	(1), (12)
$[\text{Co}(\text{SacSac})_2]$	$\frac{1}{2}$	Planar ^{2,9}	(1), (2), (9), (12), (13), (16), (19)
$[\text{Co}(\text{SacSac})_3]$	0	—	(10), (11)
$[\text{Rh}(\text{SacSac})_3]$	0	Octahedral ¹⁷	(10), (11)
$[\text{Ir}(\text{SacSac})_3]$	0	—	(10), (11)
$[\text{Fe}(\text{SacSac})_3]$	$\frac{1}{2}$	Octahedral ¹⁴	(3), (14), (15)
$[\text{Ru}(\text{SacSac})_3]$	$\frac{1}{2}$	—	(15)
$[\text{Os}(\text{SacSac})_3]$	$\frac{1}{2}$	—	(15)

pensation), the ohmic potential drop rendered any polarographic wave unobservable (cf. Fig. 4).

The reliability of the three-electrode system and the stability of the nonaqueous reference electrodes were checked throughout this work by frequent recording of the polarogram of $[\text{Rh}(\text{SacSac})_3]$ in acetone solution (among other tests). As reported below, this system has a well-defined wave with $E_{1/2} = -1.05\text{V vs. Ag/AgCl}$. Over three months duration, the reproducibility of this value was better than $\pm 10\text{ mV}$. Transposition of the functions of the two Ag/AgCl electrodes was regularly confirmed not to alter the polarogram in any respect.

Test solutions were degassed with argon which was previously passed through two acetone-filled wash bottles and a spray-trap. Twenty minutes was sufficient for effective deoxygenation. All solutions were thermostated in a water-jacketed cell at $20.0^\circ \pm 0.1^\circ\text{C}$, unless otherwise stated.

Millicoulometry.—The number of electrons involved in the reduction of $[\text{Rh}(\text{SacSac})_3]$ was determined by coulometric studies involving controlled-potential reduction at the DME. The decrease in concentration due to reduction was conveniently measured by the change in the polarographic diffusion current. The coulometric determination of n values with the DME employed a considerably smaller volume of solution than that used in conventional polarography. The small volume limits the time necessary for the reduction of the compound at controlled potential to cause a significant decrease in concentration. The polarographic cell was modified as in Fig. 1 and enabled volumes between 0.5 and 3 ml to be used. For $[\text{Rh}(\text{SacSac})_3]$, electrolysis times were between 30 min and 1 hr.

Each test solution was prepared by dissolving the compound in degassed acetone/0.1M Et_4NClO_4 in a 5-ml standard flask fitted with a rubber seal. By means of a micrometer syringe an accurately known volume was transferred directly to the inner coulometry cell, the whole apparatus having been previously flushed with argon. Throughout the electrolysis, the whole vessel was thermostated at 0°C to minimize evaporation, and acetone-saturated argon was gently bubbled through the acetone in the outer "moat". Blank runs, where no electrolysis occurred, showed that the concentration of the test solution did not alter measurably over 90 min.

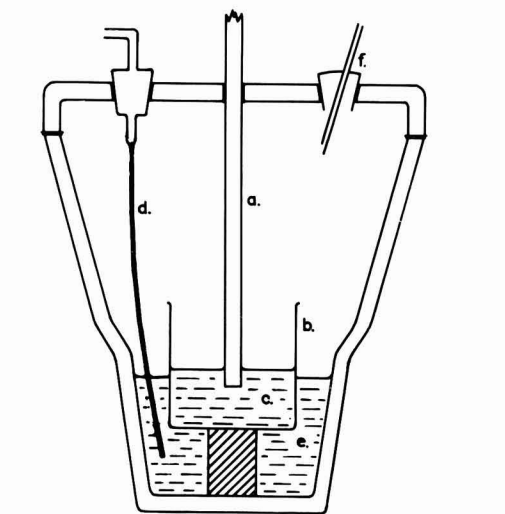


Fig. 1. Millicoulometry apparatus: a, three-electrode planar array, viewed side-on; b, inner cell; c, test solution; d, argon inlet; e, acetone moat; f, rubber seal, with argon outlet.

Materials.—Tetraethyl-ammonium perchlorate was prepared by admixture of aqueous solutions of Et_4NI and NaClO_4 . The precipitated product was recrystallized three times from 95% alcohol and dried under vacuum. The pure compound was stored over silica gel until use. Solutions in dilute nitric acid gave no precipitate with silver nitrate.

The dithioacetylacetonato chelates $[\text{Fe}(\text{SacSac})_3]$ (14, 15), $[\text{Ru}(\text{SacSac})_3]$ (15), $[\text{Os}(\text{SacSac})_3]$ (15), and $[\text{Rh}(\text{SacSac})_3]$ (10) were prepared and purified as described elsewhere. The concentration of each compound in solution was checked spectrophotometrically by reference to the known optical spectrum (15).

Results and Discussion

$[\text{Fe}(\text{SacSac})_3]$, $[\text{Ru}(\text{SacSac})_3]$, $[\text{Os}(\text{SacSac})_3]$.—These complexes form a useful group for comparison since the first, second, and third row transition metals are all represented, and in each case the central metal atom formally has oxidation state III and d electron configuration d^5 . The complexes each exhibit one extremely well-defined polarographic reduction wave at a potential near zero volt vs. Ag/AgCl. Figure 2 shows a typical $[\text{Os}(\text{SacSac})_3]$ polarogram. Polarograms of the other complexes have a similar appearance.

For each complex, graphical plots of diffusion current, i_d , vs. concentration are linear, and pass through the origin. Plots of i_d vs. the square root of the mercury column height, h , are linear. The waves are therefore diffusion controlled.

Plots of $E_{d.c.}$ vs. $\log i/(i_d - i)$ are linear for $[\text{Fe}(\text{SacSac})_3]$ and $[\text{Os}(\text{SacSac})_3]$. In each case the slope of this plot is $60 \pm 2\text{ mV}$, indicating that the electrode reaction is a reversible one-electron step. For $[\text{Ru}(\text{SacSac})_3]$, the log plot (Fig. 3) is slightly curved and the electrode reaction is quasi-reversible. The limiting slope, determined from potentials at the foot of the wave, is 62 mV in accord with a quasi-reversible one-electron reduction (23).

For the iron and osmium systems, the $(E_{1/4} - E_{3/4})$ values are independent of DME drop-time and equal to $58 \pm 2\text{ mV}$, providing further evidence for the reversible nature of the electrode reactions. In the case of $[\text{Ru}(\text{SacSac})_3]$, $(E_{1/4} - E_{3/4})$ values increase slightly with decreasing drop-time (Table II). The latter feature is consistent with the electrode possessing a high but not complete degree of reversibility, and confirms the quasi-reversible assignment.

The $E_{1/2}$ values for each complex (Fe, -0.21 ; Ru, $+0.04$; Os, $-0.05\text{V vs. Ag/AgCl}$ /0.1M LiCl) are independent of drop-time; typical results for $[\text{Ru}(\text{SacSac})_3]$ are included in Table II.

In general, reversible half-wave potentials $E_{1/2}^r$, rather than measured $E_{1/2}$ values, have real thermodynamic significance as they are closely related to E^0 values. For the reversible iron and osmium electrode reactions, $E_{1/2}^r = E_{1/2}$. For the quasi-reversible $[\text{Ru}(\text{SacSac})_3]$ electrode process, $E_{1/2}^r$ may be calcu-

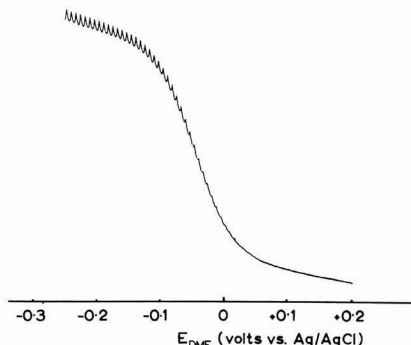
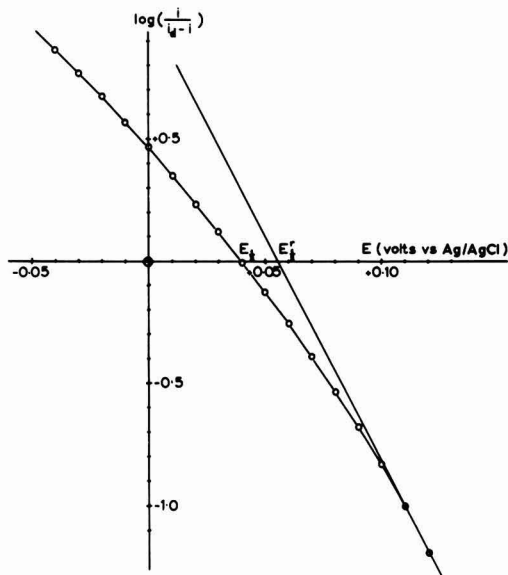
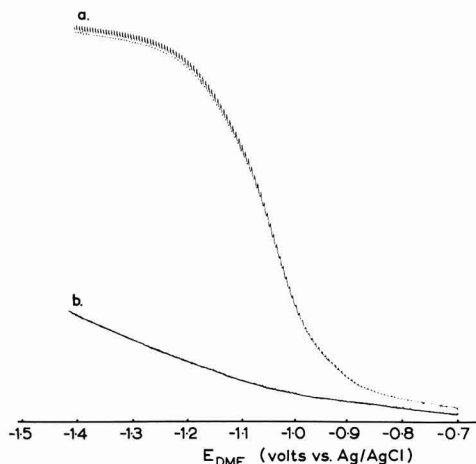


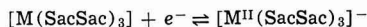
Fig. 2. $[\text{Os}(\text{SacSac})_3]$ polarogram (in acetone/0.1M Et_4NClO_4)

Fig. 3. Logarithmic analysis of $[\text{Ru}(\text{SacSac})_3]$ polarogramFig. 4. $[\text{Rh}(\text{SacSac})_3]$ polarogram (in acetone/0.1M Et_4NClO_4): a, IR compensated, 3-electrode system; b, uncompensated, 2-electrode system.

lated (23) from the limiting slope of the logarithmic analysis shown in Fig. 4 and is found to be $+0.055\text{V}$ vs. Ag/AgCl . Comparison of the $E_{1/2}$ values shows that the standard free energy required for reduction of the complexes decreases in the order $\text{Fe} > \text{Os} > \text{Ru}$.

When a reversible electrode process is observed, it is implied that the charge transfer kinetics are rapid compared to the time scale of the polarographic experiment. It generally follows that the oxidized and re-

duced forms have the same molecular structure and differ only in their electronic populations. Therefore, in the present systems, the suggested electrode reaction is



The reduced form, $[\text{M}^{\text{II}}(\text{SacSac})_3]^-$ should have essentially the same six-coordinate structure as the original $[\text{M}(\text{SacSac})_3]$ species. If the reduction did involve gross structural change, such as the loss of a bidentate ligand, then this step would be unlikely to occur rapidly in terms of the polarographic time scale and a nonreversible electrode process should result. The kinetic inertness of low spin d^5 and d^6 systems is well known. That rapid, reversible, and complete ligand dissociation does not occur is indeed clear from the absence of subsequent polarographic steps which would be anticipated for the free divalent metal ions. The slight departure of the $\text{Ru}^{\text{III}} \rightarrow \text{Ru}^{\text{II}}$ wave from reversibility might result from a minor structural modification during the reduction; however, it is not clear why $[\text{Ru}(\text{SacSac})_3]$ should behave differently from its congeners.

Several interesting features of the polarography of these complexes are apparent. First, all three compounds are reduced around 0V vs. Ag/AgCl , i.e., reduction of the complexed metal ion to the divalent oxidation state is relatively easy. However no further reduction occurs in the useful potential range. The ready one-electron reduction corresponds to completion of the stabilized metal d_e subshell so that the reduced species $[\text{M}^{\text{II}}(\text{SacSac})_3]^-$ would be isoelectronic with the neutral $\text{Co}(\text{III})$, $\text{Rh}(\text{III})$, and $\text{Ir}(\text{III})$ complexes. Further reduction would require electrons to be placed in the much higher energy d_f level.

Second, these compounds are typified by rather low-frequency ligand-to-metal electronic charge transfer transitions as well as ready one-electron reduction waves (15). Both these properties are no doubt associated with the vacancy in the metal d_e subshell. The readier reduction of $[\text{Ru}(\text{SacSac})_3]$ than either its first or third row congener, while unexpected in itself, correlates nicely with the observation that $[\text{Ru}(\text{SacSac})_3]$ has the lowest frequency ligand-to-metal charge transfer absorption.

Finally, crystalline derivatives of the postulated $[\text{M}^{\text{II}}(\text{SacSac})_3]^-$ complex anions are now being sought. The polarography suggests that the trivalent complexes should react readily with moderately strong reducing agents. Sodium dithionite has been reported to reduce $[\text{Fe}(\text{SacSac})_3]$ to a species having no e.s.r. signal (3), however the suggested product, neutral $[\text{Fe}^{\text{II}}(\text{SacSac})_2]$, is now questioned. It is, of course, possible that chemical reduction takes a different route from the polarographic electrode process, or that the complex anions are only stable during the life-time of the polarographic experiment.

$[\text{Rh}(\text{SacSac})_3]$.—This complex shows one well-defined reduction wave at the DME with $E_{1/2} = -1.05\text{V}$ vs. Ag/AgCl (Fig. 4).

The graph of i_d vs. concentration is linear, and the dependence of i_d on h is almost linear (Fig. 5). The electrode process therefore possesses a high degree of diffusion control. Table III shows that, as the drop-time increases, $E_{1/2}$ remains constant but $(E_{1/4} - E_{3/4})$ values increase markedly. Plots of $E_{d,e}$ vs. $\log i_d - i$ also vary greatly with drop-time. Such behavior indicates that the electrode reaction is highly irreversible.

In this case the number of electrons involved in the reduction, n , cannot be evaluated by the logarithmic analysis of the polarographic wave.

The current-voltage curve obtained with an HDME in unstirred solution (Fig. 6) was almost identical to the conventional d-c polarogram. A potential at half-wave height, $E_{p/2}$, of -1.00V vs. Ag/AgCl and a $(E_{p/4} - E_{3p/4})$ value of 80 mV were observed using a potential scan rate of 1 V/min . Such current-voltage curves were only obtained as the first scan on a new

Table II. Variation of $E_{1/2}$ and $(E_{1/4} - E_{3/4})$ with drop-time for $[\text{Ru}(\text{SacSac})_3]$

Drop-time, t, sec	$E_{1/2}$, V vs. Ag/AgCl	$(E_{1/4} - E_{3/4})$, mV
4.21	+0.040	72
3.67	+0.044	74
3.10	+0.042	76
2.70	+0.040	78
2.15	+0.038	80
1.62	+0.042	80

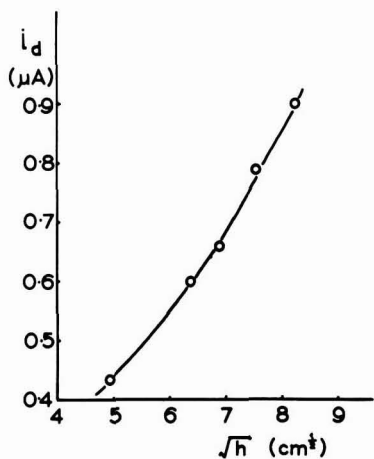


Fig. 5. Dependence of i_d on \sqrt{h} for $[\text{Rh}(\text{SacSac})_3]$ (concentration = $6.5 \times 10^{-5} \text{ M}$).

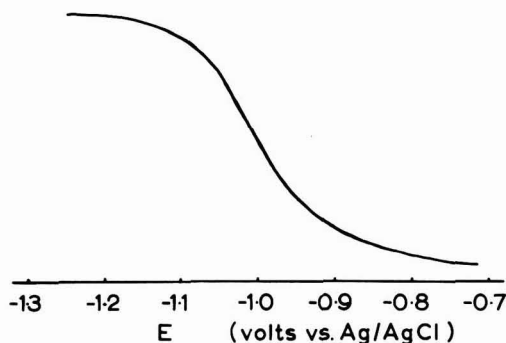


Fig. 6. $[\text{Rh}(\text{SacSac})_3]$ current-voltage curve at the HDME (in acetone/0.1M Et_4NClO_4).

mercury drop. Repeated scans using the same drop produced diminishing currents until no reduction was observable. When a fixed potential more negative than that required for reduction was maintained, the cathodic current decayed to zero within a few minutes. After such electrolysis at $-1.45 \text{ V vs. Ag/AgCl}$, inverse scanning in the positive direction revealed no anodic wave. The mercury drop was not affected by mere immersion, but became obviously tarnished during electrolysis.

Apparently, at sufficiently negative potentials, a reduced species or decomposition product becomes adsorbed on the HDME. The adsorbed substance eventually covers the entire surface of the drop preventing further reduction. Since inverse scans do not strip this species from the drop it must be tightly bound. Pos-

sibly mercury compound formation rather than adsorption occurs at the drop surface.

The interaction of $[\text{Rh}(\text{SacSac})_3]$ with the HDME indicated that coulometric evaluation of n would require a continually renewing mercury surface. A millielectrode method at the DME was resorted to in the apparatus described above. A controlled potential of $-1.45 \text{ V vs. Ag/AgCl}$ was employed, and the charge consumed by the electrode process was calculated by graphical integration of the current-time curves. Four independent determinations gave n values of 2.27, 2.09, 2.18, and 2.05.

The suggested electrode process is therefore $\text{Rh(III)} + 2e^- \rightarrow \text{Rh(I)}$. The electrode reaction is undoubtedly more complicated for $[\text{Rh}(\text{SacSac})_3]$ than for the previous complexes. It shows substantial diffusion control, irreversibility, and evidence for compound formation or adsorption at the mercury surface. A feasible product of the two-electron reduction of $[\text{Rh}(\text{SacSac})_3]$ would be $[\text{Rh}(\text{SacSac})_2]^-$, isoelectronic with the well-characterized planar d^8 complex, $[\text{Pd}(\text{SacSac})_2]$. However, the reduction product is not identified by these electrochemical studies.

It seems that, for $[\text{Rh}(\text{SacSac})_3]$, the completely filled metal d_{π} subshell is associated with two properties; the highly negative $E_{1/2}$ value and the absence of low energy ligand-to-metal charge transfer. In comparison, one-electron reduction of the d^5 systems, $[\text{Fe}(\text{SacSac})_3]$, etc., occurs relatively easily to give complex anions isoelectronic with $[\text{Rh}(\text{SacSac})_3]$; not surprisingly, no further reduction is observed.

Reduction of $[\text{Rh}(\text{SacSac})_3]$ has been attempted using zinc amalgam, sodium borohydride, and other strong chemical reductants without success. This is understandable in view of the polarographic data.

In conclusion, it appears that the polarographic results for the present complexes are consistent with their known chemical and spectroscopic properties. The existence of new stable entities has been indicated. Polarographic studies on other dithioacetylacetonato derivatives have been equally informative, and will be reported shortly.

Manuscript submitted May 25, 1970; revised manuscript received July 8, 1970.

Any discussion of this paper will appear in a Discussion Section to be published in the June 1971 JOURNAL.

REFERENCES

1. R. L. Martin and I. M. Stewart, *Nature*, **210**, 522 (1966).
2. R. Beckett and B. F. Hoskins, *Chem. Commun.*, **909**, 1967.
3. K. Knauer, P. Hemmerich, and J. D. W. van Voorst, *Angew. Chem. Int. Edn.*, **6**, 262 (1967).
4. A. Ouchi, M. Hyodo, and Y. Takahashi, *Bull. Chem. Soc. Japan*, **40**, 2819 (1967).
5. G. A. Heath, R. L. Martin, and I. M. Stewart, *Chem. Commun.*, **1969**, 55.
6. G. A. Heath, R. L. Martin, and I. M. Stewart, *Aust. J. Chem.*, **22**, 83 (1969).
7. G. A. Heath, R. L. Martin, and I. M. Stewart, *Inorg. Nucl. Chem. Letters*, **5**, 169 (1969).
8. M. Nakatani, Y. Takahashi, and A. Ouchi, *J. Inorg. Nucl. Chem.*, **31**, 3330 (1969) and references cited therein.
9. C. G. Barraclough, R. L. Martin, and I. M. Stewart, *Aust. J. Chem.*, **22**, 891 (1969).
10. G. A. Heath and R. L. Martin, *Chem. Commun.*, **1969**, 951.
11. G. A. Heath and R. L. Martin, *Proc. XIIth I.C.C.C.*, pp. 116, 117, 1969.
12. O. Siiman and J. Fresco, *Inorg. Chem.*, **8**, 1846 (1969).
13. R. J. Fitzgerald and G. R. Brubaker, *ibid.*, **8**, 2265 (1969).
14. R. Beckett, G. A. Heath, B. F. Hoskins, B. P. Kelly, R. L. Martin, I. A. G. Roos, and P. L. Weickhardt, *Inorg. Nucl. Chem. Lett.*, **6**, 257 (1970).
15. G. A. Heath and R. L. Martin, *Aust. J. Chem.*, **23**, 1721 (1970).

Table III. Variation of $E_{1/2}$ and $(E_{1/4} - E_{3/4})$ with drop-time for $[\text{Rh}(\text{SacSac})_3]$

Drop-time, t , sec	$E_{1/2}$, V vs. Ag/AgCl	$(E_{1/4} - E_{3/4})$, mV
3.41	-1.048	72
2.03	-1.050	84
1.68	-1.052	88
1.38	-1.056	96
1.13	-1.052	104
0.32 ^a	-1.050	120

^a Drop-time of 0.32 sec by rapid polarographic method.

16. A. K. Gregson, R. L. Martin and S. Mitra, *Chem. Phys. Letters*, **5**, 310 (1970).
17. R. Beckett and B. F. Hoskins, To be published.
18. D. H. Gerlach and R. H. Holm, *Inorg. Chem.*, **8**, 2292 (1969).
19. A. Furuhashi, S. Kawai, Y. Hayakawa, and A. Ouchi, *Bull. Chem., Soc. Japan*, **43**, 553 (1970).
20. C. K. Mann, "Electroanalytical Chemistry," A. J. Bard, Editor, Vol. 3, pp. 124, 125, Marcel Dekker, New York (1969).
21. J. F. Coetzee and W. S. Siao, *Inorg. Chem.*, **2**, 14 (1963).
22. P. Arthur and H. Lyons, *Anal. Chem.*, **24**, 1424 (1952).
23. J. Heyrovsky and J. Kuta, "Principles of Polarography," Academic Press, New York (1966).

Oxygen Adsorption on Gold and the Ce(III)/Ce(IV) Reaction

R. A. Bonewitz*¹ and G. M. Schmid*

Department of Chemistry, University of Florida, Gainesville, Florida 32601

ABSTRACT

In 1N HClO₄ and in 2N H₂SO₄, "oxygen" uptake on Au electrodes begins at 1.25V vs. NHE. Using a roughness factor of 1.4, monolayer coverage (600 $\mu\text{Coul}/\text{cm}^2$) is reached at 1.45V; a second monolayer is completed at 1.75V. Oxygen, once adsorbed, is removed at approximately 1.3V. Thus, the kinetic parameters of the Ce(III)/Ce(IV) reaction in 1N HClO₄ and in 2N H₂SO₄ can be obtained at oxygen coverages $\theta = 1.5$ -2.0 and $\theta = 0.7$ -2.0, respectively. Apparent exchange current densities, i_0^a , were obtained from low overvoltage data (≤ 10 mV). The charge transfer coefficient, $\alpha = 0.65 \pm 0.06$, was determined from the slope of plots of $\log i_0^a$ vs. equilibrium potential. It is independent of oxygen coverage in the range indicated. The apparent rate constant, k_o^a , was calculated from i_0^a and α to be $k_o^a \approx 3 \times 10^{-4}$ cm/sec in the range $1 \leq \theta \leq 2$ ($1.5 \leq \theta \leq 2.0$ in HClO₄). Extrapolation of the data to $\theta = 0$ yields $k_o^a \approx 12 \times 10^{-4}$ cm/sec. This change in k_o^a can be interpreted as a change in the potential across the inner double layer which appears as a change in ϕ_2 , $\Delta\phi_2 = 7.9$ mV. It appears that up to $\theta = 1$, oxygen adsorbs uniformly and is an excellent electronic conductor which simply serves as an extension of the electrode surface. The constancy of k_o^a at $1 \leq \theta \leq 2$ indicates no changes in the over-all structure of the interface in this region.

The influence of noble metal surface "oxides" on redox reactions has been known for some time. Davis (1) noted an increase in the standard rate constant of the vanadium(IV)-vanadium(V) reaction on platinum electrodes in the presence of surface oxides followed by a decrease in the rate constant as the oxygen coverage increased. A similar effect was shown for the oxidation of oxalic acid and the reduction of iron(III). Baker and MacNevin (2) found that heavy platinum oxides decreased the electrolysis currents for iron(II) and arsenic(III) by approximately an order of magnitude. Greef and Aulich (3) have shown that the reduction of cerium(IV) is inhibited more by platinum oxides in perchloric than in sulfuric acid.

Anson (4,5) has explained the increased reversibility of the iron(II)-iron(III) reaction and the iodate and vanadium(V) reduction by an increase in electrode surface area due to platinization upon oxide reduction. Müller, on the other hand, pointed out that the platinum oxides themselves can have a twofold effect. At low oxide coverage they exhibit a catalytic effect on the reduction of such molecules as hydrogen peroxide (6,7), thiosulfate (8,9), iodate (8), hypochlorite (10), nitrous acid and hydroxylamine (8). Here the oxide effects a catalytic heterogeneous dissociative adsorption breaking or weakening the X-O or X-OH bond (X represents the main portion of the molecule) allowing reduction to proceed more readily at more anodic potentials than might ordinarily be found. As the oxide coverage increases, however, the electrochemical charge transfer is inhibited and the reduction current decreases. On the other hand, reduction of such species as cobalt(III) (8,11) and oxygen (6,7) is inhibited only. Thus the presence of surface oxides

may have a variety of effects on the reaction of an electroactive species.

Except for the work of Davis (1) no attempts have been made to determine quantitatively the influence of oxides on the standard rate constant of an electrochemical reaction. The present work was undertaken in view of the theoretical interest attached to the effect of adsorbed layers on reaction kinetics. The system cerium(III)-cerium(IV)-gold was chosen because the cerium(III)-cerium(IV) reaction is a relatively simple one and because gold is inert in acidic solution. In addition, oxygen shows considerable hysteresis in its adsorption on gold (12,13) and the kinetics of a redox reaction can be studied for a variety of oxygen coverages for any given equilibrium potential of the particular electrochemical reaction.

Experimental Procedure

The all-Pyrex cell was of standard design with the reference electrode compartment separated from the main cell by two ground glass stopcocks to prevent chloride contamination of the test solution. It initially contained a cylindrical platinum gauze polarizing electrode (Engelhard Industries) of approximately 100 cm² apparent area. Use of this electrode apparently caused platinum plating at the test electrode. The gauze was therefore plated with gold from a cyanide bath prepared according to Rosebury (14). In measurements where rapid stirring was important the gauze was removed and replaced by a gold foil electrode. The reference electrode was a saturated calomel electrode. All potentials are reported with respect to the normal hydrogen electrode.

The test electrode was a gold disk 0.071 cm² in apparent (geometric) area. It was made by pressure sealing a gold rod (Engelhard Industries, Fine Gold) into a Teflon mount according to Breiter (15). The

* Electrochemical Society Active Member.

¹ Present address: Alcoa Research Laboratories, New Kensington, Pennsylvania.

Key words: oxygen coverage, gold, kinetics of redox reaction.

test electrode was prepared by grinding with No. 1 to No. 4/0 emery paper and then polishing the surface with 600 grit alumina (Buehler). Excess alumina was removed by polishing the electrode on a clean cloth using copious amounts of water. The electrode was cleaned with warm chromosulfuric cleaning solution and rinsed thoroughly with triply distilled water before being placed in the cell. Before use all test electrodes were electrochemically "aged" by holding the potential alternately at 1.65 and -0.25 V for 10 min each. The cycle was repeated three times to bring the electrode to a reproducible state.

All solutions were prepared from water first distilled from alkaline permanganate and then twice more in a Heraeus quartz still. The supporting electrolyte was 1N perchloric or 2N sulfuric acid prepared from Baker reagent grade 70% perchloric or concentrated sulfuric acid. Ultrahigh-purity perchloric acid (E. Merck Suprapur), acid-washed charcoal, and acid treated with H_2O_2 according to Visscher and Devanathan (16) did not affect the results and were therefore not used.

Cerium sulfate solutions were prepared from G. F. Smith reagent grade cerous and ceric sulfate without further purification. The 0.1N stock solutions were standardized with ferrous ammonium sulfate using Ferroin as an indicator (17). Cerous solutions were first oxidized with ammonium persulfate. When ceric sulfate solutions were first oxidized and then standardized, their normality was increased by 7.5%, indicating the presence of cerous ions. Test solutions were prepared volumetrically from the standardized stock solutions taking the amount of cerous ion in the ceric sulfate into account. Solutions were made with either the cerous or ceric concentration constant at 0.01N, varying the other between 0.01 and 0.0008N.

Solutions were prepared, also, using cerous sulfate which had previously been recrystallized three times from triply distilled water. These solutions were electrolyzed between gold electrodes to obtain the correct ceric concentrations for the desired equilibrium potential. In all cases the cerous concentration was 0.01N. The concentrations were checked by the Brucine method (18).

Cerium perchlorate solutions were prepared using G. F. Smith reagent grade cerous perchlorate salt and ceric perchlorate solution. Because perchlorates interfere with the oxidation of cerous to ceric ion with ammonium persulfate (17), silver(II) oxide was used as the oxidant (19). When the ceric perchlorate solutions were first oxidized and then standardized, the normality increased by 3.5%, again indicating the presence of cerous ion. Because of the high equilibrium potentials, E_e , in perchlorate solutions (see below) and the danger of irreversible oxidation of the gold at potentials above 1.75V, only test solutions containing 0.01N cerous and from 0.001 to 0.0001N ceric ion were used.

The solutions were purged of oxygen with a constant stream of helium (99.99% pure). This gas was purified by passing it through a 12 cm column of Linde 5A molecular sieve pellets held at -78°C . All gas lines were made of Pyrex glass and 5/16-in. Teflon tubing connected with Teflon Swageloks.

The charge necessary to remove adsorbed oxygen was determined by constant current cathodic stripping. The potential from which stripping was initiated was set with a Wenking 61TRS potentiostat allowing the potentiostat to buck the current from a Hewlett Packard 881A power supply. After waiting 10 min for the oxygen coverage to come to steady state, the potentiostat was removed from the circuit with a Western Electric mercury wetted relay (total switching time 1 msec), and the potential time curve was observed on a Tektronix 549 storage oscilloscope. The constant current from the power supply was measured with a Keithley 602 electrometer. The current density was usually 1.27 mA/cm² referred to the geometric

area. Going in the anodic direction the electrode was first held at potentials less than 0.5V where the surface was free of adsorbed oxygen. The potential was then set to a value in the range of 1.25 to 1.75V. After 10 min at this potential, the constant cathodic current was applied and the charge due to adsorbed oxygen was obtained from the potential-time curve. Going in the cathodic direction the potential was raised from a value less than 0.5V to between 1.40 and 1.75V. The potential was held there for 10 min and was then lowered to the desired value ≥ 1.25 V for another 10 min. The electrode was then stripped, and the charge obtained as before.

In order to determine the influence of cerium in solution on the charge due to the adsorbed oxygen on gold, a linear cathodic potential sweep of 50 mV/sec was applied, and the current was recorded as a function of time with a Beckman Electroscan 30. The area under the reduction peak represents the charge necessary for removal of the adsorbed oxygen.

The apparent exchange current, i_0^a , for the cerium(III)-cerium(IV) reaction was obtained at various equilibrium potentials between 1.35 and 1.50V and electrode coverages with adsorbed oxygen between $\theta = 0.7$ and 2. First, the electrode was set for 10 min at the anodic potential giving the desired electrode coverage with a Wenking 61TRS potentiostat. The potential was then lowered to about 15 mV above E_e as estimated from the Nernst equation, and the current was measured at 5 mV intervals over a range of 30 mV through E_e . These potentials could be set to within 0.1 mV using a Keithley 660 guarded differential voltmeter. The current was determined by placing a standard resistor ($\pm 0.1\%$) across the recorder output of the potentiostat and measuring the potential drop across it with a Keithley 602 electrometer. The apparent exchange current was then calculated from the slope of the potential-current curve taking into account the proper correction for mass transfer.

Results and Discussion

Cathodic stripping.—In preliminary work in 1N perchloric acid on etched disk electrodes, two types of stripping curves were found, one with arrests at 1.25V and at 0.75V, and one with only one arrest at 1.25V (20). Several aspects of the electrodes with an arrest of 0.75V were observed: (A) the total charge on the electrode surface was the same whether one or two arrests were present; (B) the length of the second arrest was not dependent on the stirring rate, indicating that it was not due to bulk solution impurity; and (C) electrodes with an arrest at 0.75V showed higher H_2 evolution currents (order of magnitude) at -0.25 V than did freshly prepared electrodes. The arrest at 0.75V appeared only on electrodes that were not repolished over a period of several weeks; then if they were polished, the arrest disappeared.

Because the tendency of platinum to dissolve under mild anodic conditions has been recently recognized (21-24), contamination of the test electrode with platinum from the auxiliary electrode seemed possible. Therefore, an electrode with only one potential arrest (at 1.25V) was cathodized in a 2% solution of platinum chloride in 2N HCl for 10 sec at 10^{-5} A/cm². After potentiostating for 10 min at 1.65V and at -0.25 V each several times, the arrest at 0.75V became apparent. Simultaneously, the H_2 evolution current increased from 10 to 200 mA/cm² at -0.25 V. This is in agreement with Breiter (25), who demonstrated that as gold is made richer in platinum the activity of the electrode towards the Volmer reaction increases. Thus it appears that the arrest at 0.75V found in this laboratory (13, 20) and by other workers (26) is due to platinum deposition on the test electrode. After the auxiliary electrode was goldplated, the arrest at 0.75V was never detected and H_2 evolution currents always stayed below 10 mA/cm² at -0.25 V. The adsorbed

oxygen is removed during cathodic stripping with 1.27 mA/cm² during a single arrest at 1.25V.

Charge-potential curves for a freshly mounted and polished gold electrode (never used in the presence of platinum) are shown in Fig. 1. The charge due to oxygen adsorption differed from electrode to electrode by $\pm 20\%$. Any one electrode could be reproduced to $\pm 5\%$. Each point shown was done in triplicate in 1N perchloric and in 2N sulfuric acid. There were no differences in the two media, and the results were computed together.

The charge values found here agree well with the results of other work. For example, at 1.65V they are within 10% of the data shown by Laitinen and Chao (12), Vetter and Berndt (27), and Schmid and O'Brien (13), and within 25% of those of Brummer and Makrides (26). The values of Will and Knorr (28) are some 35% higher. The hysteresis between the charge found on electrodes cathodically pretreated and those which were anodically pretreated has previously been noted by Schmid (13) and by Laitinen and Chao (12). A break at 1.45V in the curve coming from cathodic potentials is apparent in Fig. 1 at 600 $\mu\text{C}/\text{cm}^2$. Hickling (29) has calculated the charge equivalent of a monolayer of divalent oxygen adsorbed on gold and found it to be about 450 $\mu\text{C}/\text{cm}^2$. Brummer and Makrides (26) considered the break at 1.45V to be the point at which a monolayer of divalent oxygen atoms are adsorbed on the surface. Adopting this interpretation leads to the conclusion that the electrodes used here had a roughness factor of about 1.4, a reasonable value for mechanically polished electrodes. Brummer and Makrides (26) found only 400 $\mu\text{C}/\text{cm}^2$ for monolayer coverage. However, they were using electropolished electrodes which might be expected to have a roughness factor very close to 1.0.

Various values have been given for the potential at which oxygen adsorption on gold goes to zero. The cathodic stripping data presented here show that this potential is 1.25V, i.e., adsorption at this point is less than about 25 $\mu\text{C}/\text{cm}^2$, the smallest charge that could be clearly measured in the present work. Brummer and Makrides (26) concluded that the surface was essentially free of oxygen below 1.3V and Huq (30) found it free below 1.2V. Laitinen and Chao (12) find oxygen adsorption at potentials as low as 0.65V. However, if one linearly extrapolates the major portion of their charge curves to zero charge, one finds a value of 1.25V. This is also the actual potential of the arrest

in their stripping curves. The electrodes used by Laitinen and Chao were heated to 300°C. It has been noted by Clark, Dickinson, and Mair (31) that the potential arrest on annealed electrodes is followed by a region of slope much less steep than one usually associates with double layer charging. They suggest that this is due to impurities in the gold accumulated on the surface during heating. Apparently, Laitinen and Chao mistook this for oxygen adsorption. Thus, it appears that significant oxygen adsorption is absent at potentials below 1.20 to 1.30V.

The cerium(III)-cerium(IV) reaction.—The cerium redox couple shows different apparent standard potentials in solutions containing various electrolytes. Thus, in 2N sulfuric acid a formal potential of 1.44V is found (32). Here, cerium(IV) is complexed to $\text{Ce}(\text{SO}_4)^{++}$, $\text{Ce}(\text{SO}_4)_2$, and $\text{Ce}(\text{SO}_4)_3^=$, with stability constants of 3500, 200, and 20, respectively (32, 33). Therefore, virtually all the cerium(IV) is in the form of $\text{Ce}(\text{SO}_4)_3^=$ and the activity of the free cerium(IV) ion is considerably less than its formal concentration. Also, about half of the total cerium(III) in solution undergoes complexation to $\text{Ce}(\text{SO}_4)^+$ (32, 34). On the other hand, in 1N perchloric acid the formal potential is about 1.70V (32). This higher value is due to the fact that neither cerium(IV) nor cerium(III) forms complexes with the perchlorate ion. Instead cerium(IV) hydrolyzes to $\text{Ce}(\text{OH})^{+3}$ which dimerizes to CeOce^{+6} , the stability constant being 5.2 and 6.5, respectively (32, 35). Cerium(III) apparently does not undergo any reaction in perchloric acid (32). This difference in the formal potentials between a sulfuric acid and a perchloric acid solution makes reaction kinetic studies possible in various regions of oxygen coverage and was used to advantage in this study.

Effect of cerium ion on electrode coverage.—Results from potential sweep measurements showed an 11% reduction in the charge associated with the oxygen reduction peak in cerium-containing solutions as compared to blank acid solutions. This is within the error limits of the experimental procedure used in view of a 5% reproducibility in the charge on the electrode (stripping curve measurements), a 5% reproducibility in peak area measurements, and a 5% reproducibility of the Electroscan. It appears, then, that the oxygen coverage of the gold electrode is determined only by the potential pretreatment of the electrode and is independent of the cerium concentration in solution. Greef and Aulich (3) obtained an identical result on platinum. They concluded also that cerium had essentially no effect on oxygen adsorbed on their electrodes.

The apparent exchange current.—The polarization resistance, R_p , was obtained as the slope of the potential-current curves at zero overvoltage. It is thought to be composed of a charge transfer resistance, R_t , and a diffusion resistance, R_d , according to

$$R_p = R_t + R_d$$

$$= \frac{RT}{nF} \left(\frac{1}{i_o^a} \right) + \frac{RT}{nF} \sum_j \left| \frac{\nu_j}{i_{d,j}} \right|$$

where ν_j and $i_{d,j}$ are the stoichiometric factor and diffusion limiting current of species j . From this the apparent exchange current, i_o^a , was found as a function of oxygen coverage of the electrode by appropriate selection of the initial anodic potential of the electrode. As can be seen in Fig. 1, the coverage initially set at potentials $>1.30\text{V}$ is retained down to 1.30V and, therefore, for a given E_e in the range from 1.75 to 1.40V various initial coverages could be chosen. All values for i_o^a were averaged from three separate determinations.

The results of these experiments are shown in Fig. 2-4. All values are given in terms of the true area by using the roughness factor of 1.4 previously obtained. The reproducibility of i_o^a in all sulfate solutions was

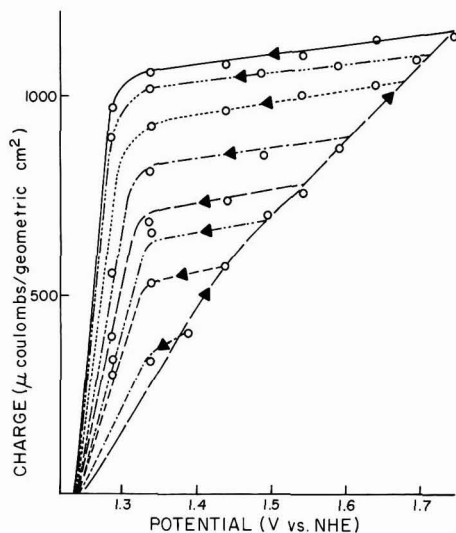


Fig. 1. Charge vs. potential for oxygen adsorption, Au in 1N HClO_4 and in 2N H_2SO_4 .

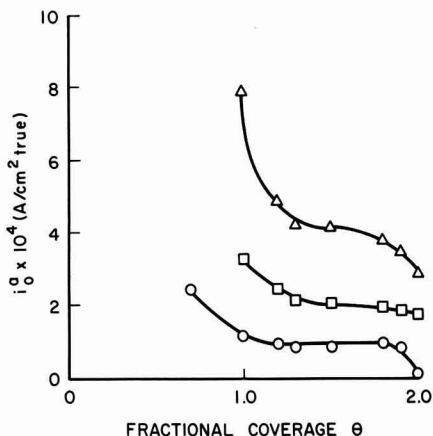


Fig. 2. Apparent exchange current, i_o^a , vs. coverage, Au in 2N H_2SO_4 with 0.01N Ce(III) and Δ : 1×10^{-2} , \square : 5×10^{-3} , and \circ : 1×10^{-3} N Ce(IV) sulfate (recrystallized).

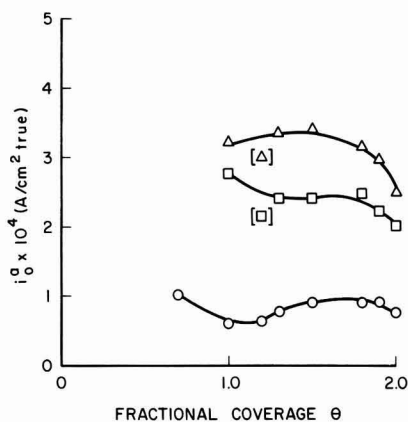


Fig. 3. Apparent exchange current, i_o^a , vs. coverage, Au in 2N H_2SO_4 with 0.01N Ce(III) and Δ : 1×10^{-2} , \square : 5×10^{-3} , and \circ : 1×10^{-3} N Ce(IV) sulfate.

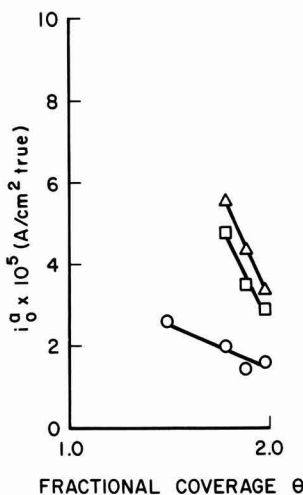


Fig. 4. Apparent exchange current, i_o^a , vs. coverage, Au in 1N HClO_4 with 0.01N Ce(III) and Δ : 1×10^{-3} , \square : 3×10^{-4} , and \circ : 1×10^{-4} N Ce(IV) perchlorate.

better than $\pm 6\%$. Agreement between recrystallized and unrecrystallized salts was good. A slight depression which appears in the i_o^a for unrecrystallized salts (Fig. 3) at $\theta = 1.2$ is not significant and is probably due to the adsorption of impurities. The i_o^a with cerium(IV) = 0.01N is smaller by a factor of 0.8 in unrecrystallized salts as compared with the recrystallized ones. This is possibly due to the greater amounts of impurities introduced in unrecrystallized solutions. In perchlorate solutions, due to the large E_e potentials, the i_o^a could be obtained only for coverages of $\theta = 1.5$ to 2.0. The relative standard deviation there was less than $\pm 5\%$.

The charge transfer coefficient.—The anodic charge transfer coefficient, α , was obtained using the expressions (36)

$$(\partial \log i_o^a / \partial E_e)_{c_r} = \alpha F / 2.3RT$$

and

$$(\partial \log i_o^a / \partial E_e)_{c_o} = -(1 - \alpha) F / 2.3RT$$

where c_o and c_r are the concentrations of the oxidized and the reduced species, respectively. Thus, α is obtained from the slope of plots of $\log(i_o^a)$ vs. E_e , keeping either c_r or c_o and the coverage with adsorbed oxygen constant. One such plot is shown in Fig. 5 for $\theta = 1.3$, the coverage set at 1.55V. The slope was determined by a least squares analysis (37), assuming E_e to be known precisely. At a 70% confidence level $\alpha = 0.65 \pm 0.06$ for all values of θ between 0.7 and 2 in both sulfuric and perchloric acid.

Values of α for the cerium(III)-cerium(IV) reaction have been reported by other authors. Galus and Adams (38) determined α to be 0.79 and 0.72 on platinum and carbon paste electrodes, respectively. Vetter (39) determined α to be 0.75 on platinum. The charge transfer coefficient found here is somewhat less but not significantly so. This indicates that the mechanism of the cerium reaction is essentially independent of the electrode material.

The constancy of α with oxygen coverage found here is in agreement with the results obtained on other systems. Davis (1) found no change in α with the extent of oxygen coverage of a platinum electrode for either the vanadium(IV)-vanadium(V) or arsenic(III)-arsenic(V) couples. This same phenomenon has also been found with adsorption of organic species. Aramata and Delahay (40) found that α for the zinc(II) discharge on a zinc amalgam electrode was not affected by coverage with *n*-amyl alcohol. Biegler

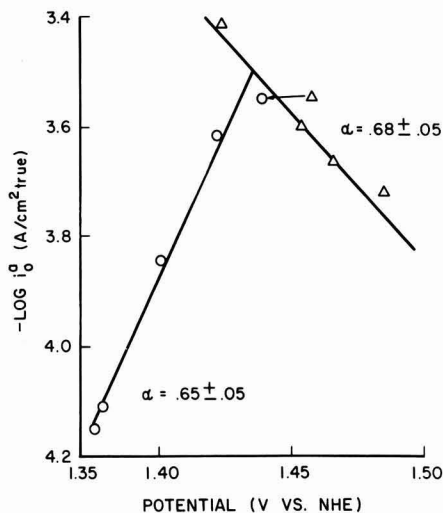


Fig. 5. Plot of $\log i_o^a$ vs. equilibrium potential, Au in 2N H_2SO_4 with Ce(III)/Ce(IV) sulfate, oxygen coverage $\theta = 1.3$.

and Laitinen (41) concluded that for the discharge of cadmium(II), α possibly decreased slightly on mercury, but this conclusion is not at all certain. On the other hand, Müller (10) found that for hypochlorite reduction on platinum α decreases with coverage.

The standard rate constant.—From the data for i_o^a and α , the standard rate constant, k_o^a , was calculated using the equation (36)

$$i_o^a = nFk_o^a c_r^{(1-\alpha)} c_o^\alpha$$

with $\alpha = 0.65$. The concentrations c_r and c_o were taken as their bulk values since the diffusion-limiting currents (not shown) are the same in both sulfuric and perchloric acid and approximately of the magnitude expected from the analytical concentration of cerium(III) and cerium(IV) in solution. Thus, even though the equilibrium potential is dependent on the activity of free cerium, all the cerium is available when needed for reaction. This means that there is no limiting chemical reaction step and kinetic parameters may be calculated on the basis of bulk concentrations.

Values of k_o^a vs. oxygen coverage are given in Fig. 6. Each point on this curve was averaged from five values in sulfates and four values in recrystallized sulfates and perchlorates corresponding to the different cerium(III)-cerium(IV) ratios obtained for each coverage. The relative standard deviation was $\pm 7\%$ in unrecrystallized sulfates and $\pm 17\%$ in recrystallized sulfates and perchlorates.

It is seen that in sulfates k_o^a is approximately constant at 4×10^{-4} cm/sec above $\theta = 1.0$, i.e., above monolayer coverage with oxygen. This can be compared to $k_o^a = 3.7 \times 10^{-4}$ cm/sec (38) and 4.8×10^{-4} cm/sec (39) found on platinum and $k_o^a = 3.8 \times 10^{-4}$ cm/sec (38) on carbon paste electrodes. The similarity between k_o^a found on different electrode surfaces indicates that the energy of activation is essentially independent of the electrode surface for the cerium(III)-cerium(IV) reaction. In perchlorates k_o^a appears to decrease from $\theta = 1.5$ to 2.0. However, this is still within experimental error and may not be significant. Further, the point at 1.5 is based on limited data so that speculation seems tentative.

The presence of adsorbed oxygen can have several effects on an electrochemical reaction. (i) It can cause a change in $\Delta\phi_c$, the potential drop across the compact double layer, and since the electrode potential is kept constant, this will result in a change in ϕ_2 , the potential drop across the diffuse double layer. This changes the electric field and would directly affect k_o^a but not α . (ii) Alternatively, the presence of adsorbed oxygen

could result in a change in the position of the effective plane at which the reaction occurs, leaving the electric field unchanged. This would lead to a change in the fraction of $\Delta\phi_c$ effective on the activation energy and would thus change α . (iii) It could cause a change in both $\Delta\phi_c$ and the effective plane of the reaction. This would cause a change in both α and k_o^a . Finally, (iv) a change in the reaction mechanism may lead to a change in α and k_o^a .

The results presented here indicate that α is independent of coverage, and possibilities ii, iii, and iv can therefore be discarded. This means, as a first order approximation, that there is no change in the reaction mechanism and that the plane of the reaction is not affected by the adsorbed oxygen, at least not with respect to the potential across the compact double layer. Because k_o^a does decrease, however, there must be a change in $\Delta\phi_c$ with a concomitant change in ϕ_2 .

This change in ϕ_2 can be estimated from the following consideration. Assuming that there is an apparent standard rate constant for oxygen covered surfaces, k_o^a , and one for bare surfaces, k_o^t , then the latter can be obtained to a first order approximation by linear extrapolation to $\theta = 0$ of the plot in Fig. 6. Thus, $k_o^t \approx 12 \times 10^{-4}$ cm/sec. Then, writing

$$k_o^a = k_o^t \exp [-(z_r + \alpha) F/RT \phi_2] \quad (36)$$

and

$$k_o^t = k_o^t \exp [-(z_r + \alpha) F/RT \phi_2']$$

where k_o^t is the true standard rate constant and z_r is the charge of the reduced species, one obtains $\Delta\phi_2 = \phi_2 - \phi_2' = 7.9$ mV as the difference in $\Delta\phi_c$ between a bare surface and an oxygen-covered surface at any given potential E .

This small change in $\Delta\phi_c$ indicates that the adsorbed oxygen is a good electronic conductor which contributes only little to the potential drop in the compact double layer. The adsorbed oxygen then acts simply as an extension of the electrode surface, and the double layer forms outside the adsorbed oxygen atoms as usual. Thus, the over-all potential drop effective on the electrochemical reaction is the same as before, less a small potential drop of a few millivolts in the adsorbed oxygen layers.

The gradual decrease in k_o^a up to $\theta = 1.1$ indicates a uniform adsorption of oxygen over the gold surface. This occurs possibly by a continuous transition with increasing potential from adsorbed water to adsorbed oxygen, with little difference in the electron

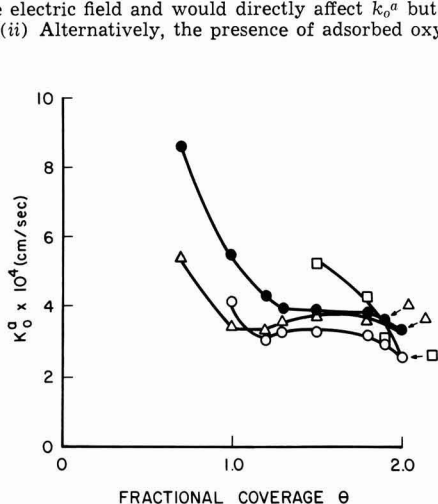
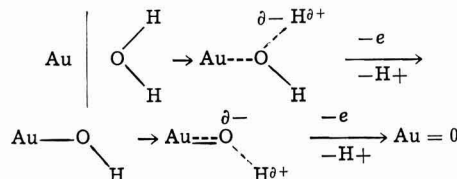


Fig. 6. Standard rate constant for the Ce(III)/Ce(IV) reaction on Au as a function of coverage with oxygen. ●: Recrystallized sulfates, Ce(III) = 0.01N, ○: sulfates, Ce(III) = 0.01N, △: sulfates, Ce(IV) = 0.01N, □: perchlorates, Ce(III) = 0.01N.



exchange through adsorbed water, adsorbed hydroxyl radical and/or adsorbed oxygen.

The constancy of k_o^a at higher coverages where $\theta > 1$ indicates that once a monolayer is formed further adsorption has little effect on the reaction rate. This argues that there is little change in the over-all structure of the interface in this range.

Conclusion

The adsorption of oxygen on gold electrodes in 1N perchloric acid and in 2N sulfuric acid was measured as a function of potential and potential-prehistory using constant current cathodic stripping. Coming from potentials < 1.20 V, oxygen uptake begins at 1.25V. A slight inflection in the charge-potential curve at 600 $\mu\text{Coulombs/cm}^2$ (1.45V) is thought to indicate monolayer coverage and corresponds to an electrode roughness factor of 1.4. A coverage of $\theta = 2$ is reached at 1.75V. Coming from potentials ≥ 1.35 V the cover-

age with adsorbed oxygen is essentially independent of potential down to 1.35V. The electrode is free of adsorbed oxygen at $\leq 1.20V$. Potential arrests found in cathodic stripping curves below 1.20V are probably due to platinum deposition on the gold electrode, either from solution or from the interior of the electrode.

The kinetic parameters of the Ce(III)/Ce(IV) reaction on gold in 1N perchloric acid and in 2N sulfuric acid were obtained at coverages $\theta = 1.5$ -2.0 and $\theta = 0.7$ -2.0, respectively. Apparent exchange current densities, i_0^a , were calculated from potentiostatic low overvoltage data. The anodic charge transfer coefficient, α , was determined, at constant coverage, from the slope of plots of $\log i_0^a$ vs. the equilibrium potential at constant Ce(III) or Ce(IV) concentration. At the 70% confidence level $\alpha = 0.65 \pm 0.06$. Apparent standard rate constants, k_0^a , were calculated from i_0^a and α to $k_0^a \approx 4 \times 10^{-4}$ cm/sec, independent of coverage $1 \leq \theta \leq 2$. Extrapolation of the data to $\theta = 0$ yields $k_0^a \approx 12 \times 10^{-4}$ cm/sec.

The slight change in k_0^a in going from $\theta = 0$ to $\theta = 1$ (at constant potential) is considered to be due to a change in the potential drop across the inner double layer caused by the adsorbed oxygen accompanied by a corresponding change in the potential across the diffuse double layer, ϕ_2 . The latter can be calculated to 7.9 mV. Once monolayer coverage has been reached, further adsorption to $\theta = 2$ does not change the potential drop across the double layer.

It seems that the adsorbed oxygen on gold in acidic solution, as far as the Ce(III)/Ce(IV) reaction is concerned, is an excellent electronic conductor, contributes only little to the potential drop across the inner double layer, and simply serves as an extension of the electrode surface. There is little discernible change at $1 \leq \theta \leq 2$ and this suggests no change in the over-all structure of the interface in this region.

Acknowledgment

The authors would like to take this opportunity to thank the National Science Foundation for financial support of this work under Grant No. NSF-GP-7742. One of the authors is indebted to The Electrochemical Society for the Colin Garfield Fink Fellowship, 1968.

Manuscript submitted Feb. 18, 1970; revised manuscript received July 15, 1970.

Any discussion of this paper will appear in a Discussion Section to be published in the June 1971 JOURNAL.

REFERENCES

1. D. G. Davis, Jr., *Talanta*, **3**, 335 (1960).
2. B. B. Baker and W. M. MacNevin, *J. Am. Chem. Soc.*, **75**, 1476 (1953).
3. R. Greef and H. Aulich, *J. Electroanal. Chem.*, **18**, 295 (1968).
4. F. C. Anson, *Anal. Chem.*, **33**, 934 (1961).
5. F. C. Anson and D. M. King, *ibid.*, **34**, 362 (1962).
6. L. Müller and L. N. Nekrassow, *J. Electroanal. Chem.*, **9**, 282 (1965).
7. L. Müller and L. N. Nekrassow, *Dokl. Akad. Nauk. SSSR*, **157**, 416 (1964).
8. L. Müller, *J. Electroanal. Chem.*, **16**, 531 (1968).
9. L. Müller, *ibid.*, **13**, 275 (1966).
10. L. Müller, *Elektrochim. Acta*, **4**, 199 (1968).
11. L. Müller, *Electrochim. Acta*, **12**, 557 (1967).
12. H. A. Laitinen and M. S. Chao, *This Journal*, **108**, 726 (1961).
13. G. M. Schmid and R. N. O'Brien, *ibid.*, **111**, 832 (1964).
14. R. Rosebury, "Handbook of Electron Tube and Vacuum Technique," Addison-Wesley, Reading, Mass. (1965).
15. M. W. Breiter and K. H. Hoffmann, *Z. Elektrochem.*, **64**, 462 (1960).
16. W. W. Visscher and M. A. V. Devanathan, *J. Electroanal. Chem.*, **8**, 127 (1964).
17. I. M. Kolthoff, P. J. Elving, and E. B. Sandell, "Treatise on Analytical Chemistry," Part II, Vol. 8, pp. 71-77, Interscience, New York (1963).
18. E. B. Sandell, "Colorimetric Determination of Traces of Metals," pp. 357-562, Interscience, New York (1944).
19. J. J. Lingane and D. G. Davis, *Anal. Chim. Acta*, **15**, 201 (1956).
20. R. A. Bonewitz, *This Journal*, **116**, 78C (1969).
21. S. B. Brummer, *ibid.*, **112**, 633 (1965).
22. A. N. Chemedanov, Ya. M. Kolotyrkin, M. A. Demrovske, and T. V. Krudryavina, *Dokl. Akad. Nauk. SSSR*, **171**, 1384 (1966).
23. S. D. James, *This Journal*, **114**, 1113 (1967).
24. P. Malachuk, R. Jasinski, and B. Burrows, *ibid.*, **111**, 1122 (1964).
25. M. W. Breiter, *J. Electroanal. Chem.*, **11**, 157 (1966).
26. S. B. Brummer and A. C. Makrides, *This Journal*, **111**, 1122 (1964).
27. K. J. Vetter and D. Berndt, *Z. Elektrochem.*, **58**, 378 (1958).
28. F. G. Will and C. A. Knorr, *ibid.*, **64**, 270 (1960).
29. A. Hickling, *Trans. Faraday Soc.*, **42**, 518 (1946).
30. A. K. M. Shamsul Huq, *Sci. Tech. Aerospace Rept.*, **3**, 1036 (1965). N.A.S.A. Accession No. N 65-16949, rept. no. AD414800 (1963).
31. D. Clark, T. Dickenson, and W. N. Mair, *Trans. Faraday Soc.*, **55**, 1937 (1959).
32. E. Wadsworth, F. R. Duke, and C. A. Goetz, *Anal. Chem.*, **29**, 1824 (1957).
33. T. J. Hardwick and E. Robertson, *Can. J. Chem.*, **29**, 828 (1951).
34. T. W. Newton and G. M. Arcand, *J. Am. Chem. Soc.*, **75**, 2449 (1953).
35. T. J. Hardwick and E. Robertson, *Can. J. Chem.*, **29**, 818 (1951).
36. P. Delahay, "Double Layer and Electrode Kinetics," Interscience, New York (1965).
37. H. A. Laitinen, "Chemical Analysis," pp. 537-594, McGraw-Hill Book Co., Inc., New York (1960).
38. Z. Galus and R. N. Adams, *J. Phys. Chem.*, **67**, 866 (1963).
39. K. J. Vetter, *Z. Physik. Chem. (Leipzig)*, **196**, 360 (1951).
40. A. Aramata and P. Delahay, *J. Phys. Chem.*, **68**, 880 (1964).
41. T. Biegler and H. A. Laitinen, *This Journal*, **113**, 852 (1966).

Correction

In the paper "Oxygen Reduction on Oxide-Free Platinum in 85% Orthophosphoric Acid: Temperature

and Impurity Dependence" by A. J. Appleby which appeared on pp. 328-335 in the March 1970 JOURNAL, Vol. 117, No. 3, on p. 333, Eq. [1] should read

$$i_{\text{forward}} = F \frac{kT}{h} (\theta^*) [H^+] \left(\exp - \frac{[\Delta G^\ddagger + (1 - \beta)(\Delta G_D - \Delta G_R)]}{RT} \right) \cdot \exp - \left(\frac{(1 - \beta)FV}{RT} \right) \quad [1]$$

Oxygen Reduction and Corrosion Kinetics on Phase-Oxide-Free Palladium and Silver Electrodes as a Function of Temperature in 85% Orthophosphoric Acid

A. J. Appleby*

Institute of Gas Technology, Chicago, Illinois 60616

ABSTRACT

Oxygen reduction on oxide-free palladium and silver surfaces has been studied as a function of temperature in purified 85% orthophosphoric acid. In each case, oxygen reduction is first order, and available evidence suggests that on both metals the reaction

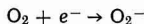


is the rate-determining step. Experimental activation energies, extrapolated to the reversible oxygen electrode potential, are 22.4 ± 2.0 kcal on palladium and about 26 kcal on silver. Activity of the palladium electrode is only slightly (< 1 decade) less than on platinum under the same conditions, whereas silver is even less active than gold. On palladium, as with platinum, the extrapolated activation energy includes a heat of adsorption term corresponding to the effect of Temkin-type equilibrium adsorption of $-\text{O}$ species derived from water oxidation, which are present on the electrode under the experimental conditions. This term may be eliminated by considering activation energies extrapolated to potentials at which $-\text{O}$ adsorption is small, where an activation energy difference between silver and palladium on the order of 9.8 kcal occurs. This suggests that the intermediate (O_2H) is relatively strongly adsorbed on palladium and only weakly on silver, and accounts for the rate difference on the two metals.

Rest potentials of the metals are corrosion mixed potentials and the metal dissolution reaction is fast in both cases so anodic processes are under Nernstian control. Palladium passivates at potentials greater than 900 mV HRE. No passivation of silver was observed.

Studies on oxygen reduction on silver and palladium electrodes in acid solution have been reported relatively infrequently in the literature.

On silver, Krasil'shchikov (1,2) reported a pH-independent mechanism in neutral and acid solutions down to pH 2, and suggested that under these conditions the reaction



is rate-determining. Akopyan (3) reported the effect of temperature on the electrode reaction and Nikulin (4) showed the specific effect of single crystal faces on oxygen reduction. Bianchi *et al.* (5,6) have shown that silver electrodes give Tafel slopes for oxygen reduction of 2 RT/F in 0.5M H_2SO_4 at overvoltages even higher than those for gold (7) under similar conditions. Again, pH-dependence was shown to be small (5) at least in the neutral pH range thus confirming Krasil'shchikov's mechanism (1,2).

Palous and Buvet (8) also examined oxygen reduction on silver over a wide pH range. Their results show an H^+ dependence for the reaction in the pH range 0-2, with no pH dependence at higher pH. Hydrogen peroxide has been detected as a reaction product (1-3, 5).

In contrast with acid solution the amount of work reported on silver oxygen electrodes in alkaline solution is considerable and has been reviewed (9,10).

Oxygen reduction on palladium electrodes was reported by Sawyer *et al.* (11,12) to resemble that on platinum in acid solution. In oxygen-saturated 2N H_2SO_4 solution Hoare (13,14) reported rest potentials of palladium electrodes of about 870 mV HRE and potentiostatic Tafel plots of slope 102 mV/decade (14) for oxygen reduction on electrodes that had been anodized,

then reduced. Damjanovic *et al.* (15-17) indicated that Tafel behavior of oxide-free palladium and platinum in dilute HClO_4 was almost identical, although palladium electrodes were about 50 mV less active than corresponding platinum electrodes. This and other considerations, for instance, $-\text{O}$ adsorption character (18), suggest similarity of rate-determining step, which is supported by ring-disk electrode experiments using the two metals (19).

In this paper, oxygen reduction on and corrosion behavior of phase-oxide-free palladium and silver electrodes are studied in 85% orthophosphoric acid as a function of temperature.

Experimental Techniques

The present series of experiments was conducted in an all-silica cell (20) using the same galvanostatic technique as in previous work (21). Temperatures were maintained to $\pm 0.2^\circ\text{C}$ by means of an oil bath or a refrigerated bath, as appropriate.

The electrodes used were palladium and silver foils of 99.99% purity, with areas of approximately 1 cm^2 . The palladium foils were welded to gold wires and were hung in the cell in Teflon sliding seals as described in previous experiments (20). The silver foils were similarly suspended in a separate series of experiments, although in this instance silver wires were used.

A gold counterelectrode was used in all experiments to avoid the possibility of contamination of working electrodes with electroactive deposits (as is the case if platinum is used). For the same reason, the electrolyte (85% orthophosphoric acid) was not given pre-electrolytic purification treatment before being used in the cell. Cleaning of the solution was done by refluxing several times with 5% hydrogen peroxide, followed by distillation of the excess water.

* Electrochemical Society Active Member.

Key words: oxygen reduction, corrosion, palladium, silver.

Oxygen or oxygen-nitrogen mixtures were supplied to the cell via presaturators from a capillary flowmeter gas mixing system and a purification train.

A dual isothermal bubbling hydrogen-85% phosphoric acid reference electrode was used, to which all potentials throughout this paper are referred (HRE potentials).

Results

Palladium electrodes.—Oxygen reduction data.—The palladium foil electrodes were degreased with organic solvents and washed with concentrated HCl, conductivity water, and the electrolyte itself before use. They were then potentiostated for a short time in oxygen-saturated electrolyte at 22.0°C at 350 mV HRE to reduce any residual oxide. After this preparation, electrodes took up rest potentials in the range 895–898 mV; these rest potentials fell by about 10 mV after 1–2 hr, thereafter remaining constant. A descending cathodic galvanostatic steady-state Tafel plot was then made on each electrode, allowing sufficient time (5–15 min) between points for a final potential to be set up at each applied current density that varied by less than 1 mV/min. This polarization study was followed by a similar ascending plot. These have been shown in Fig. 1 as "initial" Tafel plots. Results were very reproducible, and Tafel lines could be accurately retraced forward and backward.

Cathodic Tafel plots were also obtained by means of the pulsing technique used in previous work (21). Before each point was taken, the electrode was given a series of anodic and cathodic galvanostatic pulses to ensure that a surface in a reproducibly clean condition was present. Potentials were read after 2 min at each current density.

Pulses for palladium were restricted to +850–+200 mV HRE. At the high potential, some dissolution starts to occur. Below about +200 mV palladium starts to occlude large quantities of hydrogen. The plot for the palladium surface in this clean condition is shown in Fig. 1. The electrode is only slightly less active than platinum under the same conditions and has a similar Tafel slope ($\sim RT/F$).

Corrosion behavior.—Corrosion behavior was tested by means of a steady-state anodic plot (Fig. 1). A Tafel plot was obtained with the low slope of $RT/2F$ in the anodic direction. The slope led into what was apparently a diffusion current at about $i = 3.5 \times 10^{-6}$ A/cm². Corrosion currents were estimated by extrapolation of anodic and cathodic Tafel plots to their point of intersection (represented by dashed lines in Fig. 1).

The electrolyte in the cell was replaced after each series of anodic polarization studies on the electrode.

Temperature dependence.—Results were repeated at 52.0°, 76.0°, and –3.0°C. Although the freezing point of 85% orthophosphoric acid is normally quoted as being 21.1°C, it may be supercooled to a very viscous liquid at well below 0°C (22). Results obtained are shown in Fig. 2–4. In the anodic polarization experiments, no passivation was observed at 76.0°C, whereas at the other temperatures studied the onset of passivation occurred at a potential of about 900–930 mV. At –3.0°C no definite corrosion behavior was seen in the anodic plot, and anodic currents above 4.0×10^{-8}

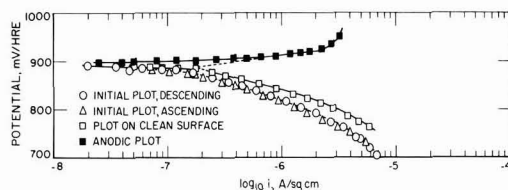


Fig. 1. Cathodic reduction of oxygen on palladium and anodic production of Pd^{++} at 22.0°C.

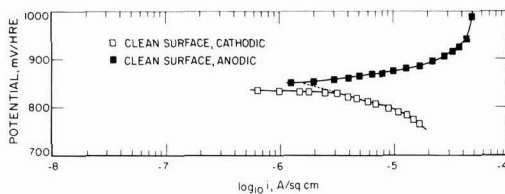


Fig. 2. Cathodic reduction of oxygen on palladium and anodic production of Pd^{++} at 52.1°C.

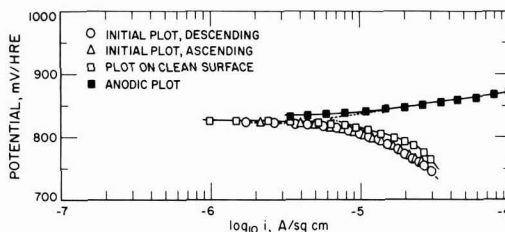


Fig. 3. Cathodic reduction of oxygen on palladium and anodic production of Pd^{++} at 76°C.

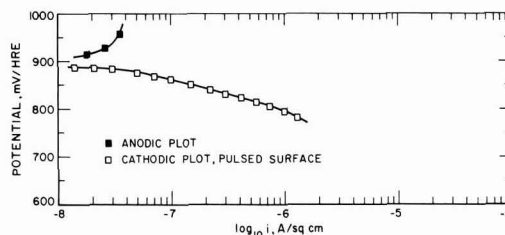


Fig. 4. Cathodic reduction of oxygen on palladium at –3.0°C

A/cm² resulted in passivation. Under these conditions, palladium exhibits a behavior like that of platinum.

Tafel slopes and $1/\alpha$ values for the oxygen reduction reaction together with values of the exchange current obtained by extrapolation of the Tafel line to the reversible potential at each temperature are given in Table I. Similarly, data for the anodic dissolution reaction are given in Table II. The corrosion current and the corrosion potential are in each case obtained from the intersection of the extrapolated anodic and cathodic Tafel plots.

Order of reaction in oxygen reduction.—A series of experiments was carried out on the same palladium foil electrode using oxygen partial pressures of 1.0, 0.26, 0.080, and 0.025 atm at 22.0°C.

The pulsing procedure mentioned previously was used before each point to ensure that a reproducible

Table I. Oxygen reduction on palladium

Temp, °C	Slope, mV/decade	$1/\alpha$	i_0 , A/cm ²
–3.0	58	1.08	3.0×10^{-15}
22.0	63	1.08	1.9×10^{-13}
52.1	68	1.06	3.5×10^{-12}
76.0	71	1.04	2.2×10^{-11}

Table II. Palladium corrosion data

Temp, °C	Anodic slope, mV/decade	$1/\alpha$	i_{corr} , A/cm ²	E_{corr} , mV/HRE
–3.0	—	—	1.7×10^{-8}	905
22.0	31	0.53	1.7×10^{-7}	868
52.1	32	0.50	1.6×10^{-6}	849
76.0	35	0.51	6.3×10^{-6}	830

surface was present. Results obtained are shown in Fig. 5, which also includes an anodic plot obtained at 0.025 atm oxygen partial pressure.

Inspection of the data indicates that oxygen reduction approximates to first order at constant potential (Fig. 9).

Activation energy for oxygen reduction on palladium.—Figure 6 shows an Arrhenius plot of extrapolated i_0 values on oxide-free palladium, corrected to 1 atm oxygen partial pressure. Activation energy at the reversible potential is 22.4 ± 2.0 kcal, close to the values previously reported on oxide-free rhodium (22.0 kcal) and platinum (22.9 kcal).

Silver electrodes.—Silver foil electrodes were degreased, welded to silver wires, and mechanically polished using graded alumina powders. They were then washed in dilute nitric acid and lightly etched in a dilute hydrogen peroxide-ammonium hydroxide solution. Preliminary experiments established that electrodes prepared in this way gave high results when cathodically polarized, with nonstirring-dependent reduction currents that were in excess of the limiting current for the oxygen reduction in the electrolyte. These high currents were apparently due to the reduction of passivating silver oxides and oxygen dissolved in the silver foil; such electrodes exhibited rest potentials 100–200 mV higher than the eventual corrosion potentials. The electrodes showed a limiting behavior after cathodic polarization for 5–8 hr at $2.0 \mu\text{A}/\text{cm}^2$, after which consistent cathodic oxygen re-

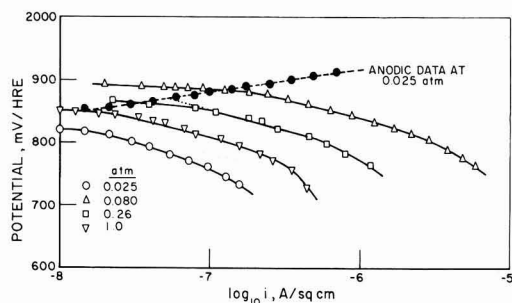


Fig. 5. Oxygen electrode on palladium at 22°C in 85% orthophosphoric acid; effect of oxygen partial pressure.

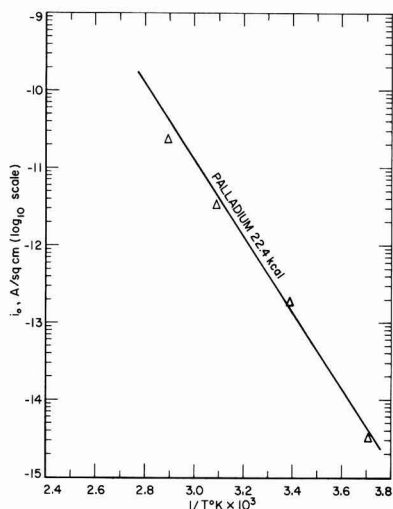


Fig. 6. Arrhenius plot for i_0 oxygen reduction on palladium in 85% orthophosphoric acid.

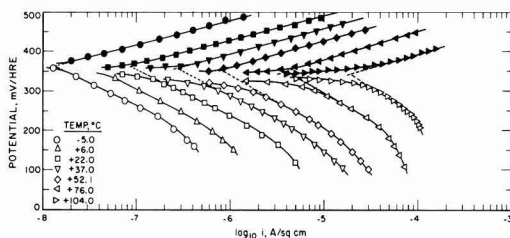


Fig. 7. Temperature dependence of cathodic reduction of oxygen and anodic production of Ag^+ on silver in 85% orthophosphoric acid.

duction Tafel plots could be obtained. Under these conditions the rest potential (corrosion potential) of the silver electrode was 360–365 mV HRE at 22°C. An alternative preparation procedure, involving heating the etched electrode in a stream of hydrogen at 330–400°C for 5–10 min followed by cooling under hydrogen, gave electrodes with the same properties as those that have been electrochemically reduced. The oxygen electrode and corrosion behavior reported here refer to electrodes that have been prepared by final treatment in hydrogen.

Oxygen reduction data.—Hydrogen-reduced electrodes took up rest potentials of 340–345 mV HRE at 104.0°C to 362–365 mV HRE at -5.0°C in the oxygen-saturated electrolyte. A galvanostatic descending Tafel plot was started immediately on immersion. As in the case of the experiments on palladium electrodes, the silver electrodes were left for sufficient time (2–5 min at each applied current density) for stabilization of the potential to within 1 mV change in 1 min. These plots could be traced forward and backward several times with little hysteresis. Potentials, once established at any given current density, were very stable and showed no tendency to decay. Preliminary pulsing of the electrode galvanostatically between 50 mV HRE and open circuit caused no changes in the Tafel plot. Silver is thus insensitive to impurity deactivation when acting as an oxygen reduction surface in acid solution. Previous work has demonstrated that gold is also essentially unaffected by impurity adsorption (23).

Tafel plots on different silver electrodes were generally within 10 mV at the same current density, the differences between individual electrodes being temperature independent. A series of Tafel plots for a typical hydrogen-reduced electrode is shown in Fig. 7; kinetic data as a function of temperature are given in Table III.

Corrosion behavior of silver electrodes.—After completion of the oxygen reduction tests on the above electrode a series of plots was carried out to show the anodic behavior of the electrode as a function of temperature. Ascending galvanostatic Tafel plots were made at each temperature, starting from the open-circuit potentials of the electrode, using a freshly prepared electrolyte for each plot. At each applied current density a stable potential was very rapidly attained (within 30 sec. at the lowest current densities

Table III. Oxygen reduction on silver

Temp, °C	Slope, mV/decade	$1/\alpha$	i_0 , $\mu\text{A}/\text{cm}^2$
-5.0	110	2.07	4.5×10^{-17}
6.0	118	2.13	5.2×10^{-16}
22.0	119	2.03	2.4×10^{-16}
37.0	131	2.13	4.6×10^{-14}
52.1	133	2.07	1.9×10^{-13}
76.0	139	2.04	2.5×10^{-12}
104.0	150	2.01	4.8×10^{-13}

* i_0 values are approximate.

Table IV. Silver corrosion data

Temp, °C	Anodic slope, mV/decade	1/ α	i_{corr} , A/cm ²	E_{corr} , mV/HRE
-5.0	62	1.17	1.35×10^{-8}	364
22.0	62	1.06	8.5×10^{-8}	363
37.0	65	1.06	2.8×10^{-7}	358
52.1	66	1.02	8.1×10^{-7}	353
76.0	71	1.04	4.2×10^{-6}	352
104.0	72	0.96	2.0×10^{-5}	344

studied, within a few seconds at 10^{-5} A/cm², and no sign of passivation was observed. Normally the electrolyte was gently stirred with oxygen at the rate of 20 ml/min, and it was noted that the potentials achieved at each current density were somewhat dependent on the rate of stirring, as was the case with palladium. Table IV gives data on the corrosion potential and corrosion current obtained by extrapolation of anodic and cathodic Tafel lines, together with anodic Tafel slopes and $1/\alpha$ values as a function of temperature.

Order of reaction for oxygen reduction.—Tafel plots were obtained on a silver electrode at oxygen partial pressures of 1.0, 0.26, 0.080, and 0.025 atm at 22.0°C. The plots obtained are shown in Fig. 8, which includes an anodic plot at the lowest oxygen partial pressure studied. The limiting current region of the plot at 0.025 atm merges with the plot for the hydrogen evolution reaction.

A $\log pO_2$ - $\log i$ plot at constant potential is given for the Tafel region of both palladium and silver electrodes in Fig. 9. In both cases the oxygen reaction order is close to unity.

Activation energy for oxygen reduction on silver.—Because of the difficulty of extrapolation over many decades of current density back to the theoretical reversible oxygen potential, activation energy for oxygen reduction has been estimated by plotting the current densities at an overpotential within the measurement range, at $\eta = 960$ mV (300 mV HRE at 22°C). Current densities have been corrected to 1 atm oxygen partial pressure.

An Arrhenius plot on this basis is shown in Fig. 10. Activation energy is 15.5 ± 0.8 kcal under these potential conditions. Tafel slopes for the oxygen electrode on silver have close to theoretical temperature dependence; the mean slope is $2.07 RT/F$. Consequently, assuming the same reaction is still rate determining at the reversible potential, we may expect that the activation energy at $\eta = 0$ to be $15.5 + \alpha \eta F$ kcal.

For $\alpha = 1/2.07$ and $\eta = 0.96$ V, $\alpha \eta F \sim 10.7$. Thus the activation energy at the reversible potential should be

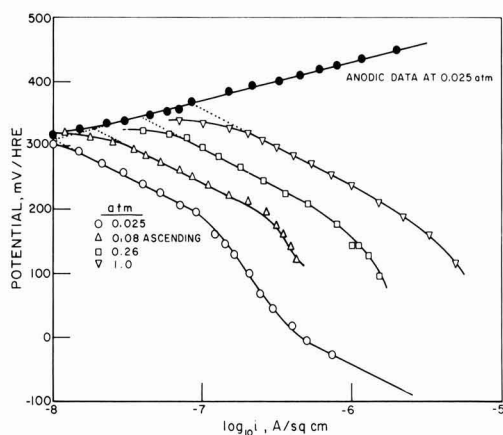


Fig. 8. Oxygen electrode on silver at 22°C in 85% orthophosphoric acid; effect of oxygen partial pressure.

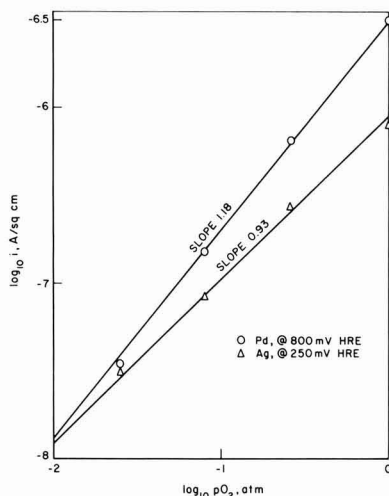


Fig. 9. Oxygen reduction reaction order at constant potential (Tafel Region) on palladium and silver electrodes.

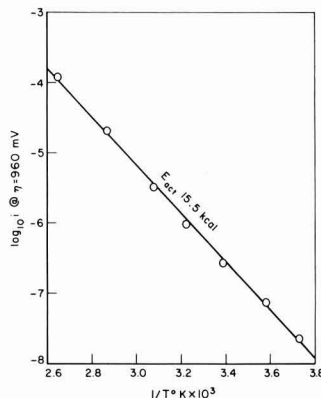


Fig. 10. Arrhenius plot of i at $\eta = 960$ mV, corrected for oxygen partial pressure, for oxygen reduction on silver in 85% orthophosphoric acid.

about 26.7 kcal on silver for the primary charge transfer step. This is somewhat greater than the value previously determined (23) on gold electrodes (23.6 kcal).

Discussion

Corrosion of palladium and silver.—Tables II and IV indicate that the anodic \log current-potential plots on palladium and silver have slopes of $RT/2F$ and RT/F , respectively.

Because of the stirring dependence of the plots and the fact that the dissolution reaction in silver has been shown by Gerischer and Tischer (24) to have an exchange current considerably in excess of the current range explored here, it is reasonable to suppose that the reactions on both metals are diffusion controlled.

In such a case we can write for the anodic process

$$E = E_0 + \frac{RT}{zF} \ln [X^{z+}]$$

where E_0 is the standard potential of the electrode, and X^{z+} is the concentration of the ion of valence z produced in the double layer by anodic dissolution.

If the reaction is under diffusion control

$$X^{z+} = \frac{\delta}{DzF} (i_a + i'_c) = k (i_a + i'_c)$$

where i_a is the imposed anodic current at potential E , and i'_c is the current due to the cathodic process (oxygen reduction) under the same conditions. In this expression D is the diffusion coefficient of X^{z+} and δ is the thickness of the Nernst diffusion layer. The other symbols have their usual meanings. Thus

$$E - E_o = \frac{RT}{zF} \ln [k(i_a + i'_c)]$$

As

$$i'_c = i_c \exp - \frac{\alpha F}{RT} (E - E_o)$$

where α is the transfer coefficient for the oxygen reduction reaction, and i_c is the rate of the oxygen reduction reaction at potential E_o , we obtain

$$i_a = \frac{1}{k} \exp \frac{zF}{RT} (E - E_o) - i_c \exp - \frac{\alpha F}{RT} (E - E_o)$$

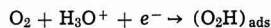
This expression has a similar form to the Butler-Volmer equation, and the right-hand term may be discarded at comparatively small values of $E - E_o$, when

$$\partial E / \partial \ln i_a = RT/zF$$

The experimental Tafel slopes are close to RT/F for silver and $RT/2F$ for palladium, indicating dissolution as Ag^+ and Pd^{++} ions or complexes with the same oxidation number. The passivation of Pd at about 900 mV appears to be due to the formation of a film of $Pd(OH)_2$ (25) or PdO . Corrosion of palladium under these conditions is a result of its lower lattice energy compared with that of platinum.

Oxygen reduction reaction.—Palladium.—Palladium has a low Tafel slope for oxygen reduction ($\sim RT/F$) and in this respect resembles platinum (21, 26) and rhodium (27). On all three oxide-free metals oxygen reduction has been determined to be first order at constant potential (21, 26, 27), implying that the stoichiometric number (ν) of the rate-determining step is unity. It has been shown previously that an RT/F Tafel slope with $\nu = 1$ is not explicable if Langmuirian adsorption of reaction intermediates is assumed. In the case of rhodium and platinum electrodes in the phase-oxide-free state, a mechanism has been proposed in which the heat of adsorption of the product of the rate-determining step ($-O_2H$) falls as the total coverage of $-O$ and $-OH$ radicals derived from water oxidation rises (26). The coverage of $-O$ and $-OH$ rises linearly with potential (26) and the experimental coverage potential data are explained in terms of an isotherm in which adsorbed molecules are considered immobile and in which interaction effects are accounted for in the second virial coefficient (Frumkin isotherm or in the coverage range $0.1 < \theta < 0.9$, the Temkin isotherm). When such an isotherm operates, it effects the heat of adsorption of all adsorbed species on the electrode (28). A similar explanation of the effect of adsorbed anions on the hydrogen evolution reaction, which assumes that the chemical potential of the activated complex in the charge-transfer reaction depends on the second virial coefficient for the adsorption of the adsorbed anion, was recently provided by Parsons (29).

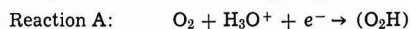
On this basis it can be shown that the observed Tafel slope and oxygen reaction order, together with the pH dependence at constant ionic strength, are consistent with theory (21, 26, 27). In view of the resemblance of linear potential-scan oxygen pseudocapacitance data on platinum (30, 31) and rhodium (32) to that on palladium (32) in acid solution, all of which may be accounted for by Temkin behavior (31), it is reasonable to suppose that the reaction



is also rate-determining on palladium. This view is supported by the similar experimental activation energies at the reversible potential on palladium, 22.4 kcal (27), and platinum, 22.9 kcal (21), for the oxygen reduction reaction.

Silver.—On silver, $-O$ and $-OH$ equilibrium coverage (from water oxidation) in the potential range where experimental measurements were made may be expected to be low because the electrode potential under these conditions was ~ 850 mV lower than the reversible potential for oxide formation (33). In alkaline solution, silver and gold electrodes show almost indistinguishable cyclic voltammetric scans (34), so on this basis a generally similar $-O$ adsorption behavior would be expected, with low coverage (Langmuir conditions) on both metals.

Experimental Tafel slopes on silver are approximately $2RT/F$, and again oxygen reduction is first order. As has been shown for gold and iridium (23), these data are consistent with a primary charge transfer under Langmuir adsorption conditions. Thus the two possible rate-determining steps on this metal are



Reaction A, involving a superoxide ion, is improbable in strongly acid solution, although it has been postulated by Krasil'shchikov (1, 2) to explain his pH-independent results for oxygen reduction on silver at pH 2. However, rotating electrode results of Palous and Buvet (8) show $(\partial \eta / \partial pH)_E > RT/F$ at pH values between 0 and 2 [see also ref. (5)]. On this basis Reaction B, shown already to be the rate-determining step on gold electrodes, appears to be the most likely rate-determining step on silver. Both metals have similar Tafel slopes ($2RT/F$) and similar activation energies at the reversible oxygen potential (23.6 kcal on gold, 26.2 kcal on silver).

The cyclic voltammetric data (34) imply similar heats of adsorption for oxygenated species on gold and silver. As this quantity, to a first approximation, is the only factor that determines activation energy differences between electrode materials, the similar experimental heats of activation on gold and silver are thus accounted for.

Conclusions

The rate-determining step in oxygen reduction on palladium and silver in strongly acid solution is a primary charge transfer, in all probability involving a proton



Although both metals have similar activation energies at the reversible potential (22.4 kcal on palladium, 26.2 kcal on silver), the figure on palladium includes a heat of adsorption term that depends on the equilibrium coverage of $-O$ and $-OH$ derived from water oxidation adsorbed on the electrode (21, 26). This coverage is linearly potential dependent—that is, adsorption follows the Temkin isotherm. For this reason it is more legitimate to compare activation energies on the two metals at potentials where $-O$ coverage is low. Under such conditions there is a marked difference in activation energy between palladium and silver. At a potential of 750 mV HRE, where both metals can be expected to show low oxygen coverage (Langmuir conditions of intermediate adsorption), the activation energy will be approximately

$$E_1 - E_2 + (\alpha_1 - \alpha_2) \eta F$$

where E and α are the respective reversible potential activation energies and transfer coefficients and η is the overpotential. Taking η to be -500 mV ($+760$ mV HRE at $25^\circ C$), with $\alpha_2 = 1.0$ (Pd), $\alpha_1 = 1/2.07$ (Ag), E silver- E palladium ~ 9.8 kcal.

Thus, the intrinsic heat of activation for oxygen reduction on phase-oxide-free palladium (in the absence of poisoning effects due to equilibrium —O and —OH coverage) is appreciably lower than on silver, which accounts for the much greater rate of the reaction on palladium electrodes. Palladium and platinum, both with d-band vacancy values of about 0.6 (18), show similar oxygen reduction rates (15), whereas gold and silver electrodes, both with filled d-bands, give rates some orders of magnitude lower. The difference in rates in acid and alkaline solution for the latter two metals is particularly striking.

Acknowledgment

The author wishes to thank the sponsors of the TARGET fuel cell program and Pratt & Whitney Aircraft Division of United Aircraft Corporation for permission to publish this work. The help of members of IGT in the preparation of this publication is also greatly appreciated.

Manuscript submitted May 25, 1970; revised manuscript received June 27, 1970.

Any discussion of this paper will appear in a Discussion Section to be published in the June 1971 JOURNAL.

REFERENCES

1. A. I. Krasil'shchikov, *Z. Fiz. Khim.*, **23**, 332 (1949).
2. A. I. Krasil'shchikov, *ibid.*, **26**, 216 (1952).
3. A. U. Akopyan, *Izv. Akad. Nauk. Arm. S.S.R., Khim. Nauki*, **11**, 141 (1958).
4. V. N. Nikulin, *Z. Fiz. Khim.*, **35**, 84 (1961).
5. G. Bianchi, *Corrosion Anti-Corrosion*, **5**, 146 (1957).
6. G. Bianchi, G. Caprioglio, F. Mazza, and T. Mussini, *Electrochim. Acta*, **4**, 232 (1961).
7. G. Bianchi, F. Mazza, and T. Mussini, *ibid.*, **11**, 1509 (1966).
8. S. Palous and R. Buvet, *Bull. Soc. Chim. France*, 1606 (1962).
9. V. S. Bagotskii, L. N. Nekrasov, and N. A. Shumilova, *Usp. Khim.*, **34**, 1697 (1965).

10. J. P. Hoare, "The Electrochemistry of Oxygen," pp. 211-238 Wiley-Interscience, New York (1968).
11. D. T. Sawyer and L. V. Interrante, *J. Electroanal. Chem.*, **2**, 310 (1961).
12. D. T. Sawyer and R. J. Day, *Electrochim. Acta*, **8**, 589 (1963).
13. J. P. Hoare, *This Journal*, **111**, 610 (1964).
14. J. P. Hoare, *ibid.*, **112**, 1129 (1965).
15. A. Damjanovic and V. Brusic, *Electrochim. Acta*, **12**, 1171 (1967).
16. A. Damjanovic and V. Brusic, *J. Electroanal. Chem.*, **15**, 29 (1967).
17. A. Damjanovic, V. Brusic, and J. O'M. Bockris, *J. Phys. Chem.*, **71**, 2741 (1967).
18. M. L. B. Rao, A. Damjanovic, and J. O'M. Bockris, *ibid.*, **67**, 2508 (1963).
19. V. V. Sobol', E. I. Khrushcheva, and V. A. Dagaeva, *Elektrokhimiya*, **1**, 1332 (1965).
20. A. J. Appleby, *J. Electroanal. Chem.*, **24**, 97 (1970).
21. A. J. Appleby, *This Journal*, **117**, 328 (1970).
22. J. R. VanWazer, "Phosphorus and Its Compounds," Vol. 1, pp. 482-483, Interscience Publishers, New York (1958).
23. A. J. Appleby, To be published.
24. H. Gerischer and R. P. Tischer, *Z. Elektrochem.*, **61**, 1159 (1957).
25. M. Pourbaix, "Atlas d'Équilibres Electrochimiques à 25°C," p. 360, Gautier-Villars, Paris (1963).
26. A. Damjanovic and V. Brusic, *Electrochim. Acta*, **12**, 615 (1967).
27. A. J. Appleby, To be published.
28. B. E. Conway and E. Gileadi, *Trans. Faraday Soc. London*, **58**, 2493 (1962).
29. R. Parsons, *J. Electroanal. Chem.*, **21**, 35 (1969).
30. F. G. Will and C. A. Knorr, *Z. Elektrochem.*, **64**, 258 (1960).
31. W. Böld and M. Breiter, *Electrochim. Acta*, **5**, 145 (1961).
32. F. G. Will and C. A. Knorr, *Z. Elektrochem.*, **64**, 270 (1960).
33. Ref. (25), p. 396.
34. J. Giner, J. M. Parry, and L. Swette, "Fuel Cell Systems II," p. 102, *Advances in Chemistry Series*, **90**, B. Baker, Editor, American Chemical Society, Washington, D. C. (1969).

The Ultraviolet Photovoltaic Effect in Evaporated Silver Bromide Conduction Cells

Joseph I. Masters

Technical Operations, Incorporated, Burlington, Massachusetts 01803

ABSTRACT

Ag/AgBr/Ag cells fabricated by a suitable masking of three overlapping evaporations exhibit a photovoltage when one semitransparent silver electrode is illuminated with 3650Å light and the AgBr electrolyte layer is much thicker than an absorption length for this radiation. Below a saturating illumination of approximately 1 mW/cm², a photocurrent proportional to the intensity of illumination flows in an external circuit. In this linear range the quantum yield is typically 40%; however, the energy conversion efficiency is only about 0.01%. In general, discoloration and gradual cell deterioration were observed as a result of photovoltaic operation. Conclusions are drawn from a comparison, using the same cell, of photoconduction and of dark conduction produced by an applied voltage. The former is characterized by a lower internal resistance.

We are concerned with the specific cell Ag/AgBr/Ag in which a current may be passed from one silver electrode to the other through an evaporated AgBr electrolyte film. The electrochemistry of solid electrolyte cells employing various types of electrodes was treated by Wagner (1,2), and several authors (3-9)

have studied mixed conduction in cells using electrolytes of compressed AgBr pellets or bulk AgBr crystals. Recently, reproducible miniature rechargeable batteries in the form of evaporated Ag/AgBr/Pt and Ag/AgI/Pt concentration cells were fabricated and studied (10).

On the other hand, photovoltaic activity from an AgBr electrolyte in contact with Ag is less well known.

Key words: Dember effect, photolysis, solid electrolyte, thin films, silver/silver bromide.

In 1929, Vanselow *et al.* (11) reported voltages in the millivolt range from the illumination of one electrode of an (Ag, AgBr)/liquid electrolyte/(AgBr, Ag) cell. Within the last decade, Eggert (12) investigated and described a photovoltaic effect caused by the illumination of an Ag/AgBr/Ag sandwich cell in which the AgBr layer was grown by brominating the surface of a bulk silver substrate rather than by the evaporation method employed here. The bromination method gave poor sample reproducibility. It was, nevertheless, possible to make observations of linearity in response, a high quantum yield, and a strong dependence on the wavelength of the illumination. By employing the evaporation method of deposition, reproducible cell samples can be fabricated more readily, allowing a convenient configuration for confirmation of earlier findings as well as a more detailed view and further study of the photovoltaic effect. The latter includes a comparison of the transient and steady photocurrent, believed characterized by both electronic and ionic diffusion, with the predominantly ionic dark current produced by application of a d-c voltage step.

Interest in the AgBr uv photovoltaic effect stems from a general interest in quantum detection, as well as from a parallel interest in evaporated AgBr as a photographic recording surface. The charge separation process associated with the effect almost certainly involves the diffusion and trapping of photolytic species, the basis of photographic sensitivity in AgBr systems. Generally speaking, successful deposition of reproducible silver halide layers by evaporation is a recent technology, and measurements of the type performed in the past using relatively thick AgBr materials have yet to be made on samples of thin evaporated AgBr films and cell structures.

Cell Fabrication

Pinhole-free Ag/AgBr/Ag overlapping sandwich cells were made by the successful evaporation procedure reported previously (10). Even in AgBr films of submicron thicknesses, continuous coatings of a contiguous domain structure are readily obtained, as shown in the Fig. 1 electron micrograph of a 0.5μ film. The sequence of evaporations for cell fabrication is shown in Fig. 2. The Ag and AgBr evaporations are best performed in separate vacuum systems to avoid bromination of the Ag electrodes by free bromine present when AgBr is evaporated. In the purification

of AgBr used in this work, the prevalent impurities are silicon, iron, lead, and copper. Normally, the concentration of silicon is held to less than 25 ppm, and the remaining impurities to less than 5 ppm. Further purification results from deposition of the AgBr by evaporation.

Ag/AgBr/Ag cells were made with an AgBr coverage of 8 mg/cm^2 , and as a check on thickness dependence, two cells were covered with 3 mg/cm^2 of AgBr. Films in this thickness range approach a density equal to the bulk density of 6.5, yielding thicknesses estimated, respectively, of 13 and $5\mu\text{m}$. The bottom Ag electrodes were deposited to an arbitrarily opaque thickness on a glass substrate. The top electrodes were deposited to give about 20% transparency at 3200Å, the approximate peak of the uv window in silver.

After fabrication, the cells' electrolyte resistance was measured with a 1000 Hz a-c bridge and their open-circuit voltage with a high-impedance vacuum-tube voltmeter. The cells with a 3 mg/cm^2 layer of AgBr had an a-c resistance in the 21-25 ohm range, and the a-c resistance of cells with an 8 mg/cm^2 layer of AgBr was in the 42-46 ohm range.¹ The non-linearity in the dependence of the measured values of electrolyte resistance with electrolyte thickness is an expected consequence of boundary effects (see following section). In general, measured values of AgBr thin film resistivity at room temperature are about 3 to 4 order of magnitude lower than bulk crystal values because the films are structure-sensitive and conduction along low resistance domain boundaries predominates.

Because of the chemical symmetry of the cells, they would be expected to have no open-circuit voltage. However, this was not the case. Cells produced by the method indicated in Fig. 2 had what appeared to be a random distribution of open-circuit voltage in the 0.0001 to 0.0005V range, with the top electrode always positive. The effect is believed to result from a difference in electrode potentials caused by a difference in the stress at the two electrodes, in turn caused by the shrinkage of the AgBr deposit in cooling to its substrate temperature. This suggests that the bottom Ag electrode remains under compression with respect to the top electrode. Support of this hypothesis is given by some related work on the deformation potential in solid-state cells (13).

In the measurements reported here, corrections for the deformation potential are made as required. However, measurements are normally under closed-circuit conditions, causing a relaxation of the open-circuit deformation potential to a much lower value.

Total Dark Conductivity

In an ionic semiconductor such as AgBr, conduction at room temperature is predominately by interstitial Ag^+ ions and silver ion vacancies, V^- . In addition, there is a small electronic contribution to the conductivity. The magnitude and type of the electronic portion of the total conduction (electrons or holes) depends on the AgBr sample's metal/nonmetal ratio. A silver excess, established by equilibration of AgBr with an Ag electrode, results in an electronic current predominately by conduction band electrons, and to detect it, the much greater ionic current must be suppressed by the use of a blocking or inert material such as carbon as the positive electrode (3). However, when a d-c voltage below the decomposition voltage is applied to an ideal Ag/AgBr/Ag cell, Ag^+ ion transport between the Ag electrodes is unblocked and ohmic, and the electronic contribution to the total conductivity is negligible. Nevertheless, in practice, the reactions that take place at the positive and negative silver electrodes are not reversible, and a significant amount of electrode resistance to Ag^+ ionic flow is encountered, generally much larger than the resistance within the thin electrolyte. This is especially noticeable if no attempt is made to fabricate graded or porous electrodes.

¹ Stated values of cell resistance, current, capacitance, etc., are for an effective cell area of 1 cm^2 .

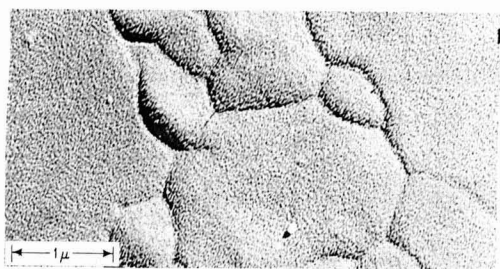


Fig. 1. Electron micrograph of a $0.5\mu\text{m}$ evaporated AgBr layer

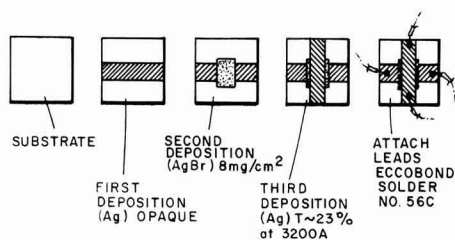


Fig. 2. Schematic of overlapping configuration

It is significant that R , the resistance to the ionic current at the electrodes, is caused by a capacitive pileup of ionic carriers unable to exchange charge with the electrodes freely. As a first order approximation, the polarization lends itself to a parallel R , C representation of the electrode interface impedance shown in the circuit analogue insert of Fig. 3. The build-up of cell voltage V to the steady state for this circuit is given by the exponential function

$$\frac{V}{V_0} = \frac{R}{R_L + R} \{1 - \exp[-(R_L + R)/R_L RC]t\} \quad [1]$$

in which V_0 is the applied voltage, R and C are constants, and where we have safely neglected the small contribution of the electrolyte resistance term $R_e \ll R$.

We may note here that the standard method of determining R_e is suggested by the circuit analogue, namely the substitution of d-c by an a-c voltage of frequency high enough (>0.1 kHz) to reduce the electrode impedance to a relatively low value of capacitive reactance. The a-c method, in which an impedance bridge is usually employed (10), yields upper bound values of R_e that may include a contribution from electrode resistance that is in effect not capacitively shunted.

From Eq. [1] the time constant of the equivalent circuit may be broken down as follows when

$$R_L \gg R, \tau \cong RC \quad [2a]$$

when

$$R \gg R_L, \tau \cong R_L C \quad [2b]$$

and for the matching condition

$$R_L \cong R, \tau = RC/2 \quad [2c]$$

In an actual cell a dependence of R and C on cell voltage, as well as differences in conduction at the two electrodes, is expected. These factors are neglected in this simple model. Nevertheless, it is a guide in the evaluation of a typical cell's dark current response to a d-c voltage step.

By using an external circuit as shown inserted in Fig. 3, typical rise and decay curves of cell voltage were recorded for applied voltage steps from 0.003 to 0.03V. The electrode capacitance C derives from a very thin double layer and for cell voltages <0.015 V, is in the order of $1000 \mu\text{F}/\text{cm}^2$. Therefore, the use of load resistances smaller than a matching load was done in accord with Eq. [2b] at a sacrifice in accuracy to avoid a sluggish transient. Note that even in this low voltage range, the curves do not asymptotically approach a true steady state. Rather the room temperature mass transfer of silver from the positive to the negative electrode appears to cause a continuous increase in the value of R , which may be accompanied by some

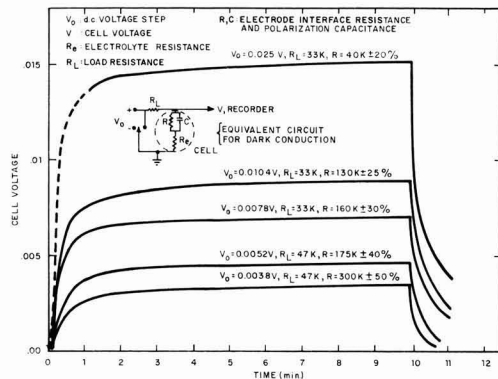


Fig. 3. Transient cell voltage, Ag/AgBr/Ag conduction cell

irreversible cell deterioration. Accordingly, cell parameters cannot generally be considered constant but depend on cell history.

To compare the dark current's slowly increasing R values with the smaller internal resistance encountered when the cell is operated as a photovoltaic element, it was necessary to assume the attainment of a quasi-steady dark current after an arbitrary 5 min time lapse, roughly the time allowed in the measurement of quasi-steady photocurrents. Thus, R is calculated from Eq. [1] for $t = \infty$, but using values of cell voltage obtained from the curves of Fig. 3, at time $t = 5$ min. The uncertainty of calculated effective internal resistance values (Fig. 4) includes variations caused by hysteresis observed as a result of reversing both the order of the measurements and the polarity of the applied voltage. We note, however, an indication of an increase in internal resistance with decreasing values of the cell voltage.

The Photovoltaic Effect

Theory.—The photovoltaic effect produces a potential difference between the electrodes of a symmetric Ag/AgBr/Ag cell. The phenomenon is observed if an asymmetry exists in the density of photolytic species as a result of the absorption of light close to a partially transparent electrode. If, for example, a 10^{-3} cm thick Ag/AgBr/Ag sandwich cell is illuminated with 4600Å light, for which the absorption coefficient is relatively low ($\alpha \cong 10^2 \text{ cm}^{-1}$), then asymmetry in the distribution of photoelectrons and photoholes would be negligible, with no possibility of a detectable electrode potential difference. In such a thin cell, asymmetry is, however, assured by illuminating with light of wavelength below 4000Å, where the absorption coefficient in AgBr rises sharply with decreasing wavelength. At the wavelength of the convenient mercury 3650Å line, α is approximately 10^4 cm^{-1} , corresponding to an absorption depth of 1μ in the AgBr electrolyte.

Clearly, the effect must depend on certain properties well established in AgBr crystals at room temperature, namely, a sufficiently small recombination rate for photoelectrons and photoholes allowing their migration to trapping sites. The trapped photoelectrons

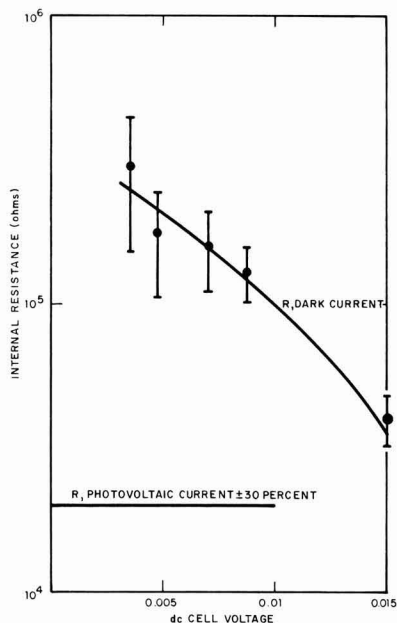


Fig. 4. Internal resistance, Ag/AgBr/Ag conduction cell dark current, photovoltaic current.

attract available interstitial Ag^+ ions, forming neutral silver atoms. A photohole can be trapped and neutralized by an existing negative silver ion vacancy V^- , or alternatively, by forcing a lattice Ag^+ ion into an interstitial site. A bound neutral bromine atom is thus formed.

Because of their much greater drift mobility (approximately 2 orders greater than the photohole mobility and with a diffusion length roughly half the thickness of a 13 μm cell), an appreciable fraction of the photoelectrons are trapped at depth in the AgBr layer, a small fraction possibly reaching the unlighted electrode. This leaves a net positive space charge near the lighted electrode due to the concentration of two relatively immobile species; the photoholes and the excess of interstitial Ag^+ ions resulting from the neutralization of trapped photoholes. In the absence of appreciable electrode charge transfer leading to an external photocurrent, this electrolyte polarization is expected to produce an induced or Dember effect photovoltage (14), measurable at the electrodes and with the lighted electrode positive. Of interest here, however, is the more complex photovoltaic effect that supports an external photocurrent of electrons from unlighted to lighted electrode and depends upon a charge transfer at both electrolyte-electrode interfaces.

The mechanism of negative charging of the unlighted electrode is postulated as follows: We assume that the aforementioned positive space charge prevents the lighted electrode from supplying Ag^+ ions to the electrolyte to make up for those that are neutralized by photoelectrons at trapping sites. Instead these ions are supplied primarily by the unlighted electrode giving this electrode a negative charge. The unlighted electrode is thus consumed by the flux of injected Ag^+ ions which numerically approaches the external photocurrent flux. A mechanism providing for the numerically equal charge transfer required at the lighted electrode is, however, less certain, as indicated by the variety of competitive reactions listed in Table I.

As a result of the photocurrent, the lighted electrode's silver mass is increased or decreased to the extent of plating or bromination as described in reactions of the type 3a or 3b (Table I). The photocurrent's quantum yield is less than unity to the extent of direct electron-hole recombination and noncontributory reactions of the type 3b. Departure from this optimum conversion would result from the arrival of some of the photoelectrons at the lighted electrode, the very unlikely arrival of the much shorter range photoholes at the unlighted electrode, or the lighted electrode acting as a donor of Ag^+ ions to replenish the electrolyte. These activities, assumed suppressed for cell thicknesses large compared to the illumination's absorption depth, cancel photovoltaic collected charges. In terms of quantum yield they are, therefore, twice as costly as recombination alone.

We must also account for a possible bromination (discoloration) of the lighted electrode. Bromination would require diffusion of normally bound neutral bromine atoms through the lattice toward a boundary. Although unlikely in a pure crystal, the outer layer of a thin AgBr film is a dislocation region which can support the diffusion of halogen atoms (15). This relates to experiments (16, 17) in the vacuum photolysis of thin silver halide films indicating that light absorbed close to the surface causes appreciable Br_2 evolution from the surface. The positive vacancy left by a diffusing neutral Br atom may be neutralized by

a neighboring Ag^+ lattice ion jumping to an interstitial site (leading to reactions 3a or 3b, Table I), or by an electron (reaction 2b). Alternatively, a V^- vacancy may trap and thus neutralize a photohole, this neutral center then diffusing to the Ag/AgBr boundary (18). Note, the diffusion of bromine atoms toward the nearby lighted electrode, followed by electrode bromination (reaction 3b), is in itself a neutral process in the sense that it fails to charge the lighted electrode positively. However, to the extent that interstitial Ag^+ ions, generated in the aforementioned production of neutral Br atoms, are in turn neutralized at photoelectron trapping sites or serve to replenish those previously so neutralized, bromination represents a loss in the collection of photolytic charges and, from a quantum yield viewpoint, is equivalent to recombination.

Response of photovoltaic cells.—The photovoltaic effect exists as an open-circuit cell voltage and does not require an external circuit. For a continuous uv illumination of the lighted electrode, the open-circuit voltage increases, but various loss phenomena cause the cell voltage to reach a quasi-steady value. Under closed-circuit conditions continuous uv illumination of the lighted electrode is partially converted, as discussed above, into a quasi-steady d-c photocurrent with the lighted electrode as the positive electrode.

The photovoltaic effect in the Ag/AgBr/Ag cell is a conversion process that alters, essentially irreversibly, the original structure. At best, the unlighted electrode is consumed and reappears as printout silver at trapping sites. This case might be approached with low current levels (low light intensity) and with small values of load resistance. On the other hand, the use of large light levels or a large load resistance appears to saturate the mechanism and to intensify the competitive processes of electrode bromination. In view of the dynamic nature of the irreversibility, defining a saturating radiant power level is difficult. For the cells tested, however, it was found that illumination exceeding $P = 1 \text{ mW/cm}^2$ of 3650Å light caused indications of saturation, and therefore measurements were made at lower levels of illumination. Here we do not make the distinction between saturation in terms of nonlinear response, or intensification of cell deterioration, hysteresis effects, electrode discoloration, etc.

A study of the transient and steady behavior of the photocurrent generated by photovoltaic cells was carried out by illuminating the covering electrode of each cell with a spatially uniform light beam from a calibrated 3650Å source; i.e., radiation in the 3650Å line from a stable mercury arc was isolated with suitable filters, and its radiant power measured with a thermopile. The intensity was varied using attenuators that were also calibrated at 3650Å. The photocurrent generated by a cell was recorded as the voltage common to both the cell and its parallel load resistor, which was varied in the $10^2 \rightarrow 10^5 \text{ ohm}$ range. Variation of the load provided data for calculating the effective internal resistance and for studying the dependence of response time on load resistance. The illumination of the cells was in the range from $P = 0.03 \text{ mW/cm}^2 \rightarrow 1.0 \text{ mW/cm}^2$, which allowed an observation of linearity and quantum yield.

Typical response curves for 13 μm thick cells under various loads are shown in Fig. 5 for cells illuminated with light at an intensity level of about 0.3 mW/cm^2 . When $R_L \ll R$, the cell behaves as a current source and the quasi-steady current is nearly independent of the load. The transient is roughly exponential, and the rise time, which is the order of 1 sec for $R_L \sim 10^2 \text{ ohms}$, increases with R_L .

The specific origin of the transient portion of the photocurrent is uncertain, because of the variation in the character of conduction throughout the electrolyte. However, some insight may be gained by satisfying charge conservation conditions. At the onset of illumi-

Table I. Lighted electrode reactions

- Charge transfer by photohole migration: $h + e \rightarrow \text{Br}^-$
- Charge transfer by electrons from external photocurrent that neutralize h and Ag^+ in electrolyte:
 - $e + h \rightarrow \text{Br}^-$ (recombination)
 - $e + \text{Ag}^+ \rightarrow \text{Ag}^0$ (print out)
- Results of Ag^+ and Br^- generated by trapped photoholes:
 - $\text{Ag}^+ + e \rightarrow \text{Ag}^0$ (charge transfer, with plating)
 - $\text{Br}^- + \text{Ag}^0 \rightarrow \text{AgBr}$ (bromination, no charge transfer)

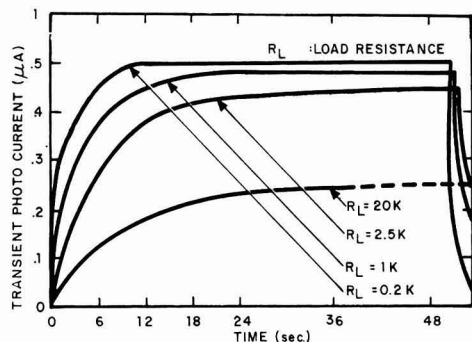


Fig. 5. Photovoltaic response of a $13 \mu\text{m}$ Ag/AgBr/Ag cell to 3650\AA , 0.3 mW/cm^2 illumination.

nation, if the proximity of photolytic charge generation causes charge transfer to one electrode² charge neutrality of the cell is satisfied, not entirely by an equal and opposite charge on the other electrode, but partially by an excess of charges of opposite sign in the electrolyte. For example, if nearby photoholes first charge the lighted electrode positively (reaction 1, Table I), cell neutrality may result from a V^- excess created by a loss of Ag^+ interstitials to electron trapping sites, and from some yet unneutralized sites, rather than by a negatively charged unlighted electrode. The transient phase of the photocurrent then appears to be due to a sluggishness in the actual negative charging of the unlighted electrode by the suggested electrode reaction $\text{Ag}^0 \rightarrow \text{Ag}^+ + e^-$. This reaction describes Ag^+ injection into the AgBr lattice that would be enhanced by the arrival at this electrode of the diffusing V^- species. The combination of low ion mobility and electrode impedance, the latter as described previously under dark conduction, are believed responsible for the sluggishness.

As in the case of dark ionic conduction (Fig. 3), a true steady photocurrent is not observed because the cells deteriorate slowly. Once the cell is illuminated, the transient response (as shown in Fig. 5) is followed by a plateau in photocurrent of several minutes duration, and then a gradual decay. For example, when a $13 \mu\text{m}$ thick evaporated cell connected to a 1 kohm load was illuminated for a prolonged period by a 3650\AA beam for which $P = 1 \text{ mW/cm}^2$, the photocurrent fell by 30% in 1 hr.

Plateau values of the photocurrent i_1, i_2, \dots , obtained by using various load resistances R_{L1}, R_{L2}, \dots , are in approximate agreement with the ratio

$$\frac{i_1}{i_2} = \frac{(R_{L2} + R)}{(R_{L1} + R)}$$

This formula applies in the case of an emf in series with an internal resistance R that is independent of the load, as in a battery. From this formula, R is defined as the effective internal resistance of an Ag/AgBr/Ag photovoltaic cell. Not only was the photovoltaic internal resistance found to be approximately independent of the load, but it was also nearly independent of P . The estimated over-all accuracy in determining the photovoltaic internal resistance is $\pm 30\%$.

When a dark cell's internal resistance is compared to the same cell's internal resistance to a photocurrent the latter is, therefore, constant over the applicable photovoltaic cell voltage range (see Fig. 4). It is also

² For a short duration after illumination ($< 0.1 \text{ sec}$) nearby photoelectrons may charge the lighted electrode negatively prior to dominant positive charging. This effect, which was not observed using the slow recording techniques of this experiment, has been reported (11, 12) in cases where positive hole migration was chemically suppressed using a halogen acceptor between electrode and electrolyte. The cell voltage resulting from such charging should endure for a time $\tau \sim R_L C_i$ where C_i is the relatively small interelectrode capacitance of the cell.

much less than the voltage-dependent internal resistance of the dark current. For either type of cell operation we recall that $R \gg R_e$, so that the origin of the difference in R lies in a comparison of electrode reactions. The unlighted electrode of an Ag/AgBr/Ag photovoltaic cell and the positive electrode of the same cell supporting dark conduction are assumed donor electrodes with similar roles, in the sense that they both supply Ag^+ ions to the electrolyte. The photovoltaic cell's lower resistance may be due in part to a larger V^- concentration at its donor electrode due to photolysis, or to dissimilarities at the acceptor electrodes of the two cell types. At the dark conduction cell's acceptor electrode plating occurs, reaction 3a, Table I; whereas the reflecting surface of the photovoltaic cell's lighted electrode, after prolonged uv exposure (cited above), shows discoloration attributed to bromination on an area strictly confined to the exposure region with no evidence of silver plating. These observations indicate that the electronic transport reactions 1 and/or 2, Table I, support the steady photocurrent whereas reaction 3b dominates over 3a and causes bromination. A technique to show the relative frequency of occurrence of reactions 1 and 2, which would give evidence of photohole diffusion length, does not seem possible in this type of experiment.

Quantum yield.—Determination of the quantum yield of the photovoltaic effect involves the use of the formula

$$Q = 3.2 \times 10^3 i / \beta P \text{ electrons/photon}$$

where i is the photocurrent in amperes for a 1 cm^2 cell, P is the intensity of the incident 3650\AA illumination in mW/cm^2 , and β is the fraction of these uv photons transmitted by the silver covering electrode (lighted) to the AgBr electrolyte. Values of the quasi-steady current i were obtained by measuring the voltage across the cell's load resistance with a precision digital voltmeter. The radiation intensity was measured with a calibrated thermopile. Unfortunately, because of the large uv absorption coefficient in AgBr, β was not measured directly. Instead the 3650\AA transmission of the partially transparent electrode film was measured at a region off the cell where it was not backed by the AgBr layer. However, as a result of equilibration with evaporated AgBr or cell aging caused by photovoltaic operation, this technique leaves some doubt as to the transmission of the part of the silver film covering the cell surface. Since such factors would tend to reduce the effective silver thickness of the covering electrode film, and hence increase β , the calculated values of Q are taken to represent, at best, an upper bound approximation of the actual quantum yield. For $P < 1 \text{ mW/cm}^2$, $13 \mu\text{m}$ thick cells, for which the measured value of $\beta = 0.017 \pm 20\%$, produced calculated values of $Q = 0.4 \pm 20\%$. This is in rough agreement with a similar determination by Eggert (12) for cells containing a $10 \mu\text{m}$ thick layer of AgBr fabricated by bromination of an Ag base. The photocurrent measurements reported here were performed on fresh cells and therefore represent a minimum of cell usage. The calculated value of Q decreases with prolonged use in proportion to the decrease in photocurrent. In the case of the thinner $5 \mu\text{m}$ cells the quantum yield was considerably less, namely, $Q = 0.1$ to 0.15 , presumably a result of the aforementioned competitive phenomena arising from the proximity of the unlighted electrode.

The efficiency of converting radiant power into useful electrical power is

$$\eta = i^2 R_L 10^3 / P \approx Q^2 \beta F R_L / 10^4$$

where $F = \beta P$ is the radiant power in mW/cm^2 delivered to the electrolyte, and the condition $R_L = R$ is implied for optimizing η . For the configuration of the cells tested, in which β is the order of 0.01 and hence the saturation value of $F \approx 10^{-2} \text{ mW/cm}^2$, the conver-

sion efficiency is very small, namely, $\eta \cong 0.0001$. It would appear that η should increase if β and P are increased. For instance, the efficiency of solar cells does not become large ($\eta = 0.1$) until the power input approaches the solar constant ($P = 100 \text{ mW/cm}^2$). However, more than likely any increase in the value of F above the aforementioned estimated saturation limit will bring down the value of Q , and no increase in η will be realized. Relevant to this argument are some measurements by Eggert (12). Although his data are widely scattered, there is evidence of a decrease in Q as β is increased above the value of $\beta \cong 0.01$ employed in this investigation.

Manuscript submitted Dec. 3, 1969; revised manuscript received July 17, 1970.

Any discussion of this paper will appear in a Discussion Section to be published in the June 1971 JOURNAL.

REFERENCES

1. C. Wagner, Proceedings of 7th Meeting of International Committee of Electrochemical Thermodynamics and Kinetics, Butterworth Publications, Ltd., London (1957).
2. J. Wagner and C. Wagner, *J. Chem. Phys.*, **26**, 1597 (1956).
3. B. Ilshner, *ibid.*, **28**, 1109 (1958).
4. R. J. Friauf, *J. Phys. Chem.*, **66**, 2380 (1962).
5. R. J. Friauf, *J. Chem. Phys.*, **22**, 1329 (1954).
6. J. N. Mrgudich, "Solid Electrolyte Batteries," in "Encyclopedia of Electrochemistry," p. 84, C. A. Hampel, Editor, Reinhold Publishing Co., New York (1964).
7. D. O. Raleigh, "Progress in Solid State Chemistry," Vol. 3, pp. 102-107, Pergamon Press, New York (1966).
8. G. Luckey and W. West, *J. Chem. Phys.*, **24**, 879 (1956).
9. R. C. Hanson and F. C. Brown, *J. Appl. Phys.*, **31**, 210 (1960).
10. P. Vouros and J. Masters, *This Journal*, **6**, 880 (1969).
11. W. Vanselow, S. E. Sheppard, and V. C. Hall, *J. Phys. Chem.*, **33**, 331, 1403 (1929).
12. J. Eggert, *Angew. Chem.*, **73**, 417 (1961).
13. Unpublished memorandum: J. H. Mrgudich, U.S. Army Electronics Command, Fort Monmouth, New Jersey.
14. Y. T. Tan and F. Trautweiler, *J. Appl. Phys.*, **40**, 66 (1969).
15. J. I. Masters, *Nature*, **223**, 611 (1969).
16. G. Luckey, *J. Phys. Chem.*, **57**, 791 (1953).
17. F. A. Kroger, "The Chemistry of Imperfect Crystals," pp. 951-952, John Wiley & Sons, Inc., New York (1964).
18. N. Mott and R. Gurney, "Electronic Processes in Ionic Crystals," 2nd ed., p. 231, Oxford Press, London (1950).

Correction

In the paper "Theory of the Separation in Displacement Electrophoresis" by G. Brouwer and G. A. Postema which appeared on pp. 874-878 in the July 1970 JOURNAL, Vol. 117, No. 7, on p. 876, Eq. [17]-[19] should read

$$\beta_{lk} = E_l/E_k \quad [17]$$

it results in

$$\sum_{K=G}^Q \frac{\alpha_K C_{KK}}{\mu_G/\mu_K - \beta_{lk}} = 0 \quad [18]$$

for

$$1 < \beta_{lk} < \mu_G/\mu_H \quad [19]$$



Steady-State Chemical Potential Profiles in Solid Electrolytes

N. S. Choudhury and J. W. Patterson

Department of Metallurgy and Engineering Research Institute, Iowa State University, Ames, Iowa 50010

ABSTRACT

Steady-state chemical potential profiles in a solid electrolyte under open-circuit and ion-blocking conditions, may be obtained by balancing the steady-state flux at points inside the electrolyte. Steady-state oxygen chemical potential profiles inside a scaling layer of thoria and inside yttria-doped thoria specimens under open-circuit and ion-blocking (d-c polarization) conditions are illustrated in special cases.

Wagner (1) has shown that the oxidation of metals may be treated quantitatively in cases where the tarnishing is rate limited by steady-state transport through the tarnishing layer. Many other problems may be considered which also conform to this type of irreversible thermodynamic steady-state treatment. A partial listing might include specific diffusion problems and thermal conduction problems as well as problems involving charge conduction through mixed conductors with various blocking electrodes. The important feature common to all such problems is that quantitative expressions for local internal transport fluxes may be integrated over the length of the transport medium. By this integration device, the steady-state flux may be written in terms of the boundary values of the driving force potential, i.e., the limits of integration. To arrive at explicit relationships, however, one must know how the transport parameter (thermal conductivity, for example) depends on the magnitude of the potential (temperature or thermal energy, for example). Here we are concerned with the problem of deducing steady-state profiles for certain of these potentials inside transport media for which the required conductivity dependences are known functions.

In particular we are concerned with deducing the steady-state chemical potential profiles (μ_{X_2} or equivalently $\log P_{X_2}$ vs. x) inside M_aX_b mixed conductors subjected to selected boundary conditions and/or boundary values for $\log P_{X_2}$. Applying the analysis to solid electrolytes allows interesting prediction regarding the emf generated by double electrolyte tablets placed in series in galvanic cell measurements (2-4). The same analysis may also be used to calculate the steady-state $\log P_{X_2}$ vs. x profile that prevails in a homogeneous solid electrolyte being employed in a typical solid electrolyte galvanic cell experiment. Actually the profile determination in solid electrolytes is a special case of the profile determination problem for general mixed conductors. This more general problem is solved below and then used to discuss the $\log P_{X_2}$ profile types that may occur in ionic and electronic conducting scaling layers. In addition to these open-

circuit type problems, the method may be used to calculate the steady-state $\log P_{X_2}$ profiles induced in mixed conductor specimens subjected to applied emf's under selected ion-blocking conditions. In particular, $\log P_{X_2}$ vs. distance profiles corresponding to the Hebb-Wagner (5-7) d-c polarization technique are calculated and discussed below.

General Determination of Steady-State Profiles

Before proceeding to specific cases, we outline the general features of the method by considering a somewhat generalized transport medium. We consider the medium to be capable of supporting a flux transport I_η (where η may be mass, charge, heat, etc.). This flux results locally from a gradient in some variable V (where V may be a chemical potential, electrostatic potential, temperature, etc.). The local flux equation may be written as

$$I_\eta/A = J_\eta(x) = -\sigma_\eta(x) \nabla V \quad [1]$$

where $J_\eta = I_\eta/A$ is the η flux or the amount of η transported per unit time and cross sectional area due to the local gradient ∇V of the potential V . Equation [1] is typical of conductive-type transport processes such as Fick's law of diffusion, Fourier's law of heat conduction, or Ohm's law of charge conduction. In such processes ∇V acts as the driving force for the transport process and the proportionality parameter σ_η is called the conductivity parameter for η and very often is found to be a function of V . Although more general geometries may be readily considered, we limit consideration to the case of linear conduction geometry for simplicity. In this case ∇V in Eq. [1] may be replaced by dV/dx so that the equation may be rearranged and integrated to give

$$\int_0^L \frac{I}{A} \eta dx = \int_{V(0)=V'}^{V(L)=V''} \sigma_\eta(V) dV \quad [2]$$

Because we are considering the steady-state case, I_η is independent of x and because of the linear geometry, A is independent of x . Equation [2] may be recast as

$$J_\eta L = \Delta \quad [3]$$

where I_η/A has been replaced by J_η

Key words: chemical potential, solid electrolytes, mixed conductors, d-c polarization, scaling, electronic conductivity, hole conductivity, ionic conductivity, ionic transference number, open circuit emf.

$$\Delta = \int_{V(O)=V'}^{V(L)=V''} \sigma_{\eta}(V) dV \quad [4]$$

and L is the total specimen thickness measured in the direction of transport. Note that Δ may be evaluated explicitly in terms of the end point values $V(L) = V''$ and $V(O) = V'$ if the functional dependence of $\sigma_{\eta}(V)$ on V is known.

Applying these elementary results to the series composite medium depicted in Fig. 1 yields for medium L

$$x^i J_{\eta}' = \Delta' \quad [5]$$

where

$$\Delta' = \int_{V(O)=V'}^{V(x^i)=V^i} \sigma_{\eta}'(V) dV \quad [6]$$

and yields for medium R

$$(L - x^i) J_{\eta}'' = \Delta'' \quad [7]$$

where

$$\Delta'' = \int_{V(x^i)=V^i}^{V(L)=V''} \sigma_{\eta}''(V) dV \quad [8]$$

The primes and double primes denote quantities in the left and right hand medium, respectively. To be consistent with these steady-state expressions, however, we must also invoke the additional steady-state relation

$$I_{\eta}' = I_{\eta}'' \quad [9]$$

For the linear transport geometry being considered, this result is equivalent to

$$J_{\eta}' = J_{\eta}'' \quad [10]$$

which, together with expressions [5] and [7], yields

$$\frac{x^i}{L} = \frac{\Delta'}{\Delta' + \Delta''} \quad [11]$$

where Δ' and Δ'' may be evaluated from the integrals in Eq. [6] and [8], respectively. Wagner used an alternative, equivalent approach to calculate the silver chemical potential at the interface between contacting Ag_2S and AgI specimens (8).

In cases where the left and right side portions of the transport medium are the same material, Eq. [11] gives a formula for deducing the V vs. x profile. This is done by merely picking values of V intermediate between V' and V'' , evaluating the Δ' and Δ'' integrals from Eq. [6] and [8], and then calculating the x/L values to which these selected V values correspond. For example, in the analysis of oxide solid electrolyte galvanic cell applications or of oxidation processes,

V' and V'' may be taken to be the end point $\log P_{\text{O}_2}$ values $\log P_{\text{O}_2}'$ and $\log P_{\text{O}_2}''$, respectively. The Δ' and Δ'' expressions are then generated by the appropriate integration of Wagner's general expression (1) for the net flux of mobile ions through any compact M_aX_b scaling layer as discussed in more detail below.

In the cases where the composite medium is actually two different materials, the $\log P_{\text{X}_2}$ profiles inside each medium may be calculated individually according to the procedure outlined above with both contacting surfaces sharing the same μ_{X_2} value, i.e., the interfacial value, $\log P_{\text{X}_2}^i$. It is apparent from Eq. [6], [8], and [11] that when the conductivity parameters of both media are V independent, the V vs. x profiles reduce to two straight line segments connected at the point V^i, x^i . Much more interesting and less obvious profiles result when the conductivities exhibit a more or less complicated functional dependence on the driving force variable V .

Application to Mixed Conductors under Open-Circuit Conditions

Consider the case of a general mixed conductor specimen pressed between two reversible electrodes that establish the nonmetal chemical potential μ_{X_2} at the left and right hand faces of the specimen. According to Wagner's scaling rate theory (1), J_{η} for this case may be taken to be the electronic current J_e and the driving force variable is the electrochemical potential for electrons η_e . Under various assumptions involving local equilibria among various electronic, ionic, and atomic components and assumptions involving virtual stoichiometry constraints on the M_aX_b compound, Wagner's theory allows $\nabla \eta_e$ to be written in terms of $\nabla \mu_{\text{X}_2}$ so that the location-independent steady-state electronic current density $J_e = I_e/A$ may be written in terms of the alternative driving force variable μ_{X_2} as follows

$$J_e = [1/(2z_X F)] t_{\text{ion}} t_e \sigma d\mu_{\text{X}_2}/dx \quad [12]$$

where z_X is the anion's valence, F is Faraday's constant, σ is the total electrical conductivity, and t_{ion} and t_e are the ionic and electronic transference numbers, respectively. Rearranging Eq. [12] and integrating from $x = 0$ to x^i and from x^i to L (i.e., over two mixed conductors in series contact at x^i) yields

$$\Delta' = [1/(2z_X F)] \int_{\mu_{\text{X}_2}'}^{\mu_{\text{X}_2}^i} t_{\text{ion}}' t_e' \sigma' d\mu_{\text{X}_2} \quad [13]$$

$$\Delta'' = [1/(2z_X F)] \int_{\mu_{\text{X}_2}^i}^{\mu_{\text{X}_2}''} t_{\text{ion}}'' t_e'' \sigma'' d\mu_{\text{X}_2} \quad [14]$$

These may be used in Eq. [11] to generate μ_{X_2} vs. x profiles in cases where the functional dependences of t_{ion}' , t_e' , σ' and t_{ion}'' , t_e'' , and σ'' on μ_{X_2} are known. For example, one may use Eq. [11], [13], and [14] to calculate the μ_{X_2} profile prevailing inside a scaling layer growing on an oxidizing metal. This is done by letting x^i be any arbitrary location inside the scale. In such cases, however, it is more conventional to use $\log P_{\text{X}_2}$ instead of μ_{X_2} as the variable V . Then, for the scaling layer example, $P_{\text{X}_2}^i$ is the P_{X_2} value established by equilibrium coexistence between the metal and the M_aX_b scale material and may be calculated from tabulated data for the standard free energy of formation ΔG° of the M_aX_b compound. $P_{\text{X}_2}^i$, the ambient P_{X_2} of the "X-iding" atmosphere, must be determined from the specified ambient conditions. In this example the interface at x^i separates two regions of the same material, hence the functional forms of t_{ion} , t_e , and σ are the same whether double or single primed. Figure 2 shows the results of such a $\log P_{\text{O}_2}$ vs. x/L profile inside a scaling layer of ThO_2 forming on thorium metal in O_2 gas at 1 atm pressure and at 1000°C . The necessary transport parameters (P_\oplus , P_\ominus , n and σ as discussed in detail below) were deduced from reported conductivity measurements on ThO_2 (9, 10) and also

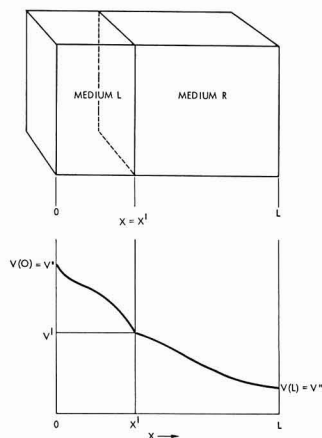


Fig. 1. Schematic steady-state potential distance profile inside two transport media in series contact.

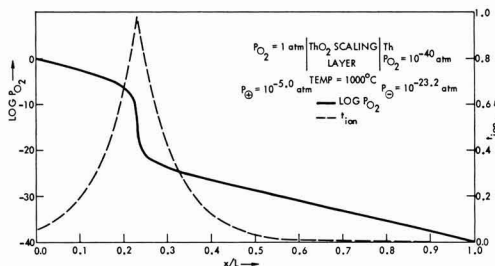


Fig. 2. Log P_{O_2} vs. x/L profile inside a ThO_2 scaling layer forming on Th metal at 1000°C in 1 atm P_{O_2} .

from as yet unpublished measurements on ThO_2 made in our laboratory.

To further illustrate the application of these ideas, let us specialize considerations to the class of mixed conductors known as solid electrolytes. For these materials, $t_{ion} \equiv \sigma_{ion}$ is known to be invariant over wide ranges of $\log P_{X_2}$ and may therefore be moved outside the integrals of Δ' and Δ'' in these ranges. Considering the entire medium between $x = 0$ and L to be comprised of the same solid electrolyte material, Eq. [11] reduces to

$$\frac{x/L}{L} = \frac{\log \left| \frac{P_{X_2}'}{P_{X_2}''} \right| - \int_{\log P_{X_2}'}^{\log P_{X_2}''} t_{ion} d \log P_{X_2}}{\log \left| \frac{P_{X_2}'}{P_{X_2}''} \right| - \int_{\log P_{X_2}'}^{\log P_{X_2}''} t_{ion} d \log P_{X_2}} \quad [15]$$

where we have changed the variable of integration from μ_{X_2} to $\log P_{X_2}$ through the relationship

$$\mu_{X_2} = \mu_{X_2}^0 + 2.303RT \log P_{X_2} \quad [16]$$

According to an analysis by Schmalzried (11, 12) the integrals appearing in Eq. [15] may be evaluated by employing the formula

$$\int_{\log P_{X_2}(a)}^{\log P_{X_2}(b)} t_{ion} d \log P_{X_2} = [2.303n/\sqrt{w}]$$

$$\log \left| \frac{2(P_{X_2}/P_{\oplus})^{1/n} + 1 - \sqrt{w}}{2(P_{X_2}/P_{\oplus})^{1/n} + 1 + \sqrt{w}} \right| \quad \begin{matrix} P_{X_2}(b) \\ P_{X_2}(a) \end{matrix} \quad [17]$$

where

$$w = 1 - 4 \left(\frac{P_{\ominus}}{P_{\oplus}} \right)^{1/n} \quad [18]$$

In Eq. [17] and [18], P_{\oplus} is the P_{X_2} where $\sigma_{\oplus} = \sigma_{ion}$. P_{\ominus} is the P_{X_2} where $\sigma_{\ominus} = \sigma_{ion}$, and \ominus and \oplus denote excess electron and positive hole carriers, respectively. The empirical parameter n characterizes Schmalzried's presumed dependence of the electronic conductivities σ_{\oplus} and σ_{\ominus} on $P_{X_2}^{-1/n}$ and $P_{X_2}^{+1/n}$, respectively. Thus the parameters P_{\oplus} , P_{\ominus} , and n must be known from independent experiments if quantitative results are to be obtained. A computer program with these parameters and P_{X_2}' and P_{X_2}'' as input is used to generate x/L values according to Eq. [15], [17], and [18] for an array of P_{X_2}' values between P_{X_2}' and P_{X_2}'' . The resulting tabulation of x/L vs. P_{X_2}' values is then plotted to provide the desired profiles. All the profiles for open-circuit conditions, i.e., Fig. 2-5 were generated in this fashion.

Figures 3-5 show the results of such an application for the oxide solid electrolyte YDT ($Th_{0.85}Y_{0.15}O_{1.925}$)

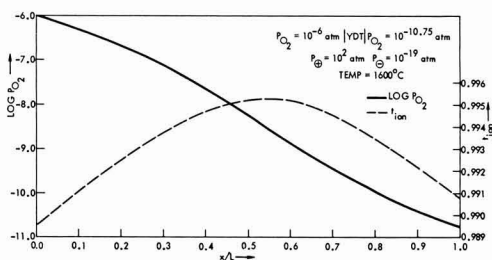


Fig. 3. Log P_{O_2} vs. x/L profile inside a yttria-doped thoria electrolyte for reversible electrode P_{O_2} values within the electrolytic domain at 1600°C.

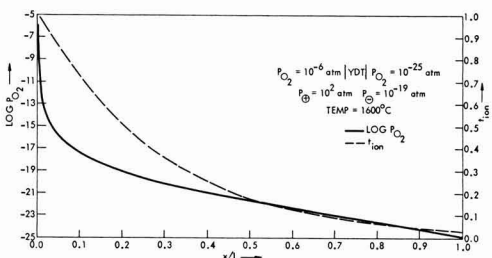


Fig. 4. Log P_{O_2} vs. x/L profile inside a yttria-doped thoria electrolyte for reversible electrode P_{O_2} values spanning the mixed conduction region between the electrolytic and excess electron conduction domains at 1600°C.

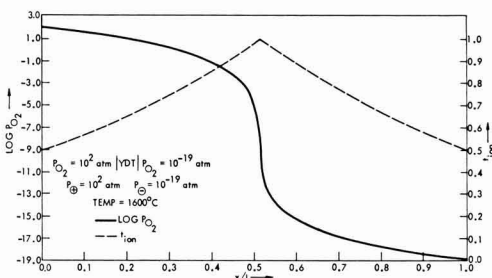


Fig. 5. Log P_{O_2} vs. x/L profile inside a yttria-doped thoria electrolyte for reversible electrode P_{O_2} values located at P_{\oplus} and P_{\ominus} , respectively, at 1600°C.

at 1600°C. The values of P_{\oplus} , P_{\ominus} , and n at 1600°C were determined from an assessment of conductivity and galvanic cell data involving the electrolyte YDT. The values of P_{O_2}' and P_{O_2}'' were chosen so that three interesting cases could be demonstrated. Figure 3 shows the $\log P_{O_2}$ vs. x/L profile for the case where P_{O_2}' and P_{O_2}'' both lie within the electrolytic conduction domain¹ for YDT. The P_{O_2}' and P_{O_2}'' values for Fig. 4 span a mixed conduction region from the electrolytic domain down into the domain where excess electron conduction becomes predominant. Similarly the P_{O_2}' and P_{O_2}'' values for Fig. 5 were chosen well outside the domain where ionic conduction predominates. Thus in this case $P_{O_2}' = P_{\oplus}$ and $P_{O_2}'' = P_{\ominus}$ so that the entire electrolytic domain is spanned. In addition to giving the $\log P_{O_2}$ vs. x/L profile, each figure also shows the t_{ion} vs. x/L profile. The t_{ion} values were determined

¹ That is, the $\log P_{O_2}$, $1/T$ domain where $t_{ion} > 0.99$ according to a recent paper (13) which also elucidates the details of electron hole and excess electron conduction domain on $\log P_{X_2}$, $1/T$ diagrams.

for these log P_{O_2} profiles by evaluating

$$t_{ion} = [1 + P_{\oplus}^{-1/n} P_{O_2}^{1/n} + P_{\ominus}^{-1/n} P_{O_2}^{-1/n}]^{-1} \quad [19]$$

Note that the log P_{X_2} profiles show a steep gradient at the region where t_{ion} is a maximum, the region having predominantly ionic conduction. Wagner long ago (1)

$$\frac{x}{L} = \frac{[P_{\oplus}^{-1/n} P_{X_2}^{1/n}(O) \{\exp(-2z_X F E(x/L)/nRT) - 1\} + P_{\ominus}^{-1/n} P_{X_2}^{-1/n} \{1 - \exp(2z_X F E(x/L)/nRT)\}]}{[P_{\oplus}^{-1/n} P_{X_2}^{1/n}(O) \{\exp(-2z_X F E(L)/nRT) - 1\} + P_{\ominus}^{-1/n} P_{X_2}^{-1/n} \{1 - \exp(2z_X F E(L)/nRT)\}]} \quad [24]$$

alluded to this feature of such chemical potential profiles inside mixed conductors but reported no quantitative calculations.

This procedure may be readily adapted to the determination of log P_{X_2} values that prevail at the contacting interface between two different X (or M) ion conductors in series. In cases where two different oxide solid electrolytes are used in series for galvanic cell emf measurements, it is important that the log P_{O_2} value prevailing at their contacting interface lie within the electrolytic domain for both electrolytes at all times. Otherwise the measured emf's will depart from the thermodynamic values by unknown amounts. However, by applying the above methods one may readily calculate the log P_{O_2} values to be sure they do fall within the electrolytic domains. No example profiles for this type problem are offered in the present context, however, because others (4,8) have already solved this class of problems by an alternate method.

Application to Mixed Conductors Subjected to Applied EMF's and Ion Blocking Conditions

Now let us consider the case of a mixed conductor between a reversible electrode and an ion-blocking electrode which are both capable of transporting electrons with negligible impedance. Let an emf E be applied across the mixed conductor, as in d-c polarization experiments (14-17). The situation is schematically illustrated in Fig. 6.

For ion-blocking conditions, Wagner (6,7) has derived a general expression for the steady-state current due to electrons and holes in ionic crystals. Wagner's result is related to the quantity of Eq. 3 by the relation

$$\Delta = J_e L = - [1 (2z_X F)] \int_{\mu_{X_2}(O)}^{\mu_{X_2}(L)} \sigma_e d\mu_{X_2} \quad [20]$$

where

$$\mu_{X_2}(L) = \mu_{X_2}(O) - 2z_X F E(L) \quad [21]$$

and where $\sigma_e = \sigma_{\oplus} + \sigma_{\ominus}$ is the sum of the electron hole \oplus and excess electron \ominus conductivities inside the specimen.

For most ionic compounds capable of predominant ionic conduction we may assume the following transport parameter dependences

$$\sigma_{\oplus} = \sigma_{ion} P_{\oplus}^{-1/n} P_{X_2}^{1/n} \quad [22]$$

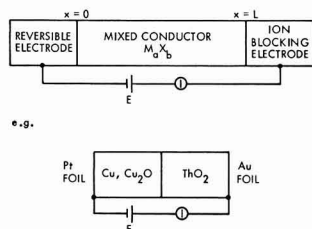


Fig. 6. Schematic cell arrangements for Hebb-Wagner d-c polarization experiments.

$$\sigma_{\ominus} = \sigma_{ion} P_{\ominus}^{-1/n} P_{X_2}^{-1/n} \quad [23]$$

σ_{ion} is P_{X_2} independent where as before $\sigma_{\oplus} = \sigma_{ion}$ at $P_{X_2} = P_{\oplus}$ and $\sigma_{\ominus} = \sigma_{ion}$ at $P_{X_2} = P_{\ominus}$. Equations [11], [20], [21], [22], and [23] may be combined to yield

Equation [24] combined with Eq. [21] gives the log P_{X_2} profile within the mixed conductor under ion-blocking conditions.

Figures 7 and 8 show log P_{O_2} profiles induced in YDT under ion-blocking conditions at 1600°C. Figure 7 shows such a profile for both electrodes having P_{O_2} values inside the electrolytic domain. The P_{O_2} value at the reversible electrode is established by the presence of oxygen gas at 10^{-6} atm, whereas the effective P_{O_2} at the blocking electrode is established at $10^{-10.75}$ atm as a result of the imposed emf $E = -0.442V$. Figure 8 shows the effect of increasing the magnitude of the applied voltage. In this case the reversible electrode is presumed to be established at P_{\oplus} so that the applied emf of $E = -1.951V$ renders the effective P_{O_2} at the blocking electrode to be $P_{\ominus} = 10^{-19}$ atm at 1600°C.

Interestingly, an emf vs. x/L profile for Ag_2S has been obtained by Hebb (5). Unfortunately, his data cannot be correlated with Eq. [24] because no effort was made to establish the silver chemical potential with a reversible electrode in Hebb's experiment.

A comparison of Fig. 7 and 8 shows that, under blocking conditions at least, a significant region of an oxide conductor can be made substantially n-type by merely controlling the magnitude of the applied voltage. Theoretically reversing the voltage (under

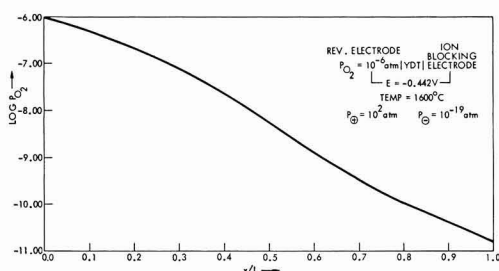


Fig. 7. Log P_{O_2} vs. x/L profile inside a yttria-doped thoria electrolyte with the reversible electrode P_{O_2} at 10^{-6} atm and the ion-blocking electrode at 0.442V negative polarity, $T = 1600^\circ C$.

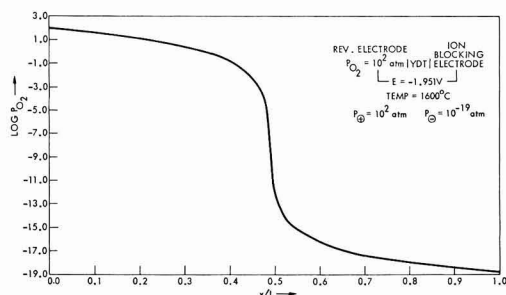


Fig. 8. Log P_{O_2} vs. x/L profile inside a yttria-doped thoria electrolyte with the reversible electrode at P_{\oplus} and the ion-blocking electrode at a sufficient negative emf to induce an effective P_{O_2} equal to P_{\ominus} at 1600°C.

blocking conditions) should induce a p-type region. This property could be important in catalysis engineering where the electronic nature of the catalyzing substrate is often vital, although the above calculations assume that there is no source of oxygen (the mobile species) other than at the reversible electrode. These calculations do suggest that some degree of control over the n- or p-type nature of an oxide lateral surfaces may be possible even if a limited amount of oxygen exchange between the oxide and the ambient is permitted.

APPENDIX

The Conductance of a Solid Electrolyte When Subjected to a Difference in the Nonmetal Chemical Potential at the Ends under Open-Circuit Condition

With reference to Fig. A-1, let us assume the mixed conductor of length L and uniform cross section A , subjected to nonmetal chemical potential $\mu_{X_2}(1)$ and $\mu_{X_2}(2)$ at its two ends.

The conductance is then given by

$$1/G = [1/A] \int_0^L [1/\sigma(l)] dl \quad [25]$$

where G = total conductance and $\sigma(l)$ = the total conductivity at location l .

We can write Eq. [25] as

$$1/G = [1/A] \int_0^L [t_{ion}/\sigma_{ion}(l)] dl \quad [26]$$

In the case of solid electrolyte σ_{ion} is a constant and is independent of l . Therefore

$$1/G = 1/(A\sigma_{ion}) \int_0^L t_{ion}(l) dl \quad [27]$$

Since a plot of t_{ion} vs. x/L can be obtained, as discussed earlier, graphical integration of Eq. [27] is possible, yielding the value of G .

Experimental determination of the quantity G under open-circuit condition becomes difficult if an a-c bridge or any other instrument is connected across the ends of the specimen, because the open-circuit condition is violated. However, the cell assembly illustrated in Fig. A-2 allows determination of the conductance.

The total conductance G' of the double cell can be determined with an a-c bridge without violating the open-circuit condition, because the nonmetal chemical potentials at the two ends are identical. The total conductance G' is then given by

$$1/G' = [1/(A\sigma_{ion})] \left\{ \int_0^{L_1} t_{ion}(l) dl + \int_0^{L_2} t_{ion}(l) dl \right\} \quad [28]$$

The quantities on the right can be determined as explained earlier and thus an experimental check may be obtained.

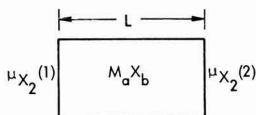


Fig. A-1. A mixed conductor $M_a X_b$ of length L and uniform cross section A , subjected to nonmetal chemical potential $\mu_{X_2}(1)$ and $\mu_{X_2}(2)$ at its two ends.

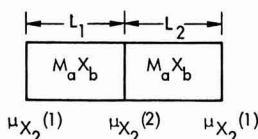


Fig. A-2. A symmetric double cell with solid electrolyte $M_a X_b$ to determine the conductance when the solid electrolyte is subjected to a difference in the nonmetal chemical potential at its two ends.

LIST OF SYMBOLS

A	cross-sectional area
E	electrical potential difference
$E(L)$	electrical potential difference from O to L
$E(x/L)$	electrical potential difference from O to x
F	Faraday's constant
G	total electrical conductance
I_η	current of species η
J_e	electronic current density
J_η	flux of species η
l	distance coordinate inside the specimen
L	total length of the specimen
n	empirical parameter characterizing presumed dependence of electronic conductivity
P_{X_2}	partial pressure of nonmetal gaseous dimer (X_2 gas)
P^\oplus	P_{X_2} at which $\sigma^\oplus = \sigma_{ion}$
P^\ominus	P_{X_2} at which $\sigma^\ominus = \sigma_{ion}$
R	gas constant
t_e	electronic transference number
t_{ion}	ionic transference number
T	temperature, $^\circ K$
V	generalized potential
V'	potential at location O
V''	potential at location L
VI	potential at location x^I
x	distance coordinate inside the specimen
z_X	valence of anion
η_e	electrochemical potential for electrons
μ_{X_2}	chemical potential/mole of nonmetal gaseous dimer (X_2 gas)
$\mu_{X_2}^\ominus$	chemical potential for one mole of X_2 gas in the standard state
σ	total electrical conductivity
σ_e	total electronic conductivity
σ_{ion}	ionic conductivity
σ_η	conductivity parameter for species η
σ^\oplus	hole conductivity
σ^\ominus	excess electronic conductivity

Acknowledgment

Research was sponsored by the Aerospace Research Laboratories, Office of Aerospace Research, United States Air Force, Contract F33615-68-C-1034.

Manuscript received May 4, 1970.

Any discussion of this paper will appear in the Discussion Section to be published in the June 1971 JOURNAL.

REFERENCES

1. C. Wagner, *Z. Phys. Chem.*, **21**, 25 (1933).
2. C. B. Alcock and B. C. H. Steele, in "Science of Ceramics," Vol. 2, p. 397, G. H. Stewart Editor, Academic Press, London (1965).
3. T. L. Markin and M. H. Rand, in "Thermodynamics I," p. 145, International Atomic Energy Agency Symposium (1966).
4. D. A. Shores and R. A. Rapp, Private communication.
5. M. Hebb, *J. Chem. Phys.*, **20**, 185 (1952).
6. C. Wagner, *Z. Elektrochem.*, **60**, 4 (1956); **63**, 1027 (1959).
7. C. Wagner, in "International Committee of Electrochem. Thermodynamics and Kinetics Proc. 7th Meeting London 1955," Butterworth Scientific Publications, London (1957).
8. C. Wagner, *Z. Elektrochem.*, **40**, 365 (1934).
9. M. F. Lasker and R. A. Rapp, *Z. Physik. Chem. N.F.*, **49**, 198 (1968).
10. J. E. Bauerle, *J. Chem. Phys.*, **45**, 4162 (1966).
11. H. Schmalzried, *Z. Elektrochem.*, **66**, 572 (1962).
12. H. Schmalzried, *Z. Physik. Chem. N.F.*, **38**, 87 (1963).
13. J. W. Patterson, in "The Physics of Electronic Ceramics," L. L. Hench and D. B. Dove, Editors, Marcel Dekker Inc., New York (1970).
14. J. B. Wagner and C. Wagner, *J. Chem. Phys.*, **26**, 1597 (1957).
15. B. Ischner, *ibid.*, **28**, 1109 (1958).
16. D. O. Raleigh, *J. Phys. Chem. Solids*, **26**, 329 (1965).
17. J. W. Patterson, E. C. Bogen, and R. A. Rapp, *This Journal*, **114**, 752 (1967).

Alkaline Earth Sulfide Phosphors Activated by Copper, Silver, and Gold

Willi Lehmann*

Westinghouse Research Laboratories, Pittsburgh, Pennsylvania 15235

ABSTRACT

Emission spectra of cathodoluminescence of Cu, Ag, and Au in MgS, CaS, SrS, and BaS, at room temperature and near 80°K, are presented. The spectra depend very much on the coactivators used including the alkalies and the halides. The observations indicate the luminescence to be caused by centers containing both activator and coactivator.

Copper, silver, and gold are well known to be most effective activators in ZnS-type phosphors. They are probably incorporated as acceptors and, for charge compensation, require the simultaneous incorporation of a donor impurity, *e.g.*, a halide (except F) or a trivalent metal (*e.g.*, Al) as coactivator. Earlier workers have noted already, that the situation is quite different in alkaline earth sulfides where not Cl, Br, or I but F is the preferred halide and where even alkalies are effective coactivators (1, 2).

Investigations on alkaline earth sulfide phosphors activated by copper, silver, or gold are surprisingly rare, and the few publications are not always in agreement with each other. Lenard (1) reported three different emission bands, at 420, 512, and 600 nm, respectively, in CaS:Cu, but in view of the uncertain compositions of the materials of his days, the results may be questioned. More recently, and apparently working with better materials, Sorge (2) reports a single emission band in CaS:Cu,F, at 430 nm with 0.1% Cu and at 480 nm with 1% Cu. Gradual replacement of CaS by SrS and BaS shifts the copper emission to lower energies. Other reports on CaS:Cu include those by Avinor *et al.* (3) (one emission band at 460 nm) and by Wachtel (4) (two bands, at 435 and 500 nm). Reports on silver or gold activated alkaline earth sulfides do not seem to exist. Our investigations were made to clarify the reported contradictions on CaS:Cu and, more generally, to improve our knowledge of the entire alkaline earth sulfide phosphor system.

The compounds MgS, CaS, SrS, and BaS all crystallize in the cubic NaCl lattice. Some properties of interest are summarized in Table I. The optical absorption "edge" actually is the spectral position where, in a compound as pure as we could make, the optical absorption coefficient goes through the value of about 100 cm^{-1} . These points were determined by simple powder reflection measurement at room temperature; they are not necessarily identical to the true band gaps of the compounds which may be (and apparently are) obscured by various native defects, exciton absorptions, *etc.*, and which may be slightly higher than the "edges" mentioned in Table I. The cationic radii are those reported by Pauling (5), and the next-neighbor distances are simply the sums of cationic

and anionic radii (with 1.84 Å for S^{--}). The interstitial radius is the maximum radius of a solid sphere which could be placed interstitially in the lattice without deformation of the latter.

Preparation

Alkaline earth sulfides of luminescence grade purity do not seem to be commercially available. We prepared CaS, SrS, and BaS by a method described by Sorge (2) and Wachtel (4). The purest available nitrates are dissolved in water and, for several hours, kept boiling in the presence of magnesium metal ribbon. Heavy metal impurities either deposit on the magnesium or are trapped in small amounts of hydroxide which, afterwards, is filtered out. The sulfates are then precipitated with H_2SO_4 , briefly washed in water to remove excess acid, dried, and converted to the sulfides by firing in an atmosphere of H_2 and H_2S (4). The results are white, nonluminescent powders containing no spectroscopically detectable traces of Fe, Mn, Cu, *etc.* The major remaining impurity is silicon (usually about 100 ppm), probably from the quartz containers. Oxygen, due to unavoidable contact with atmospheric air, probably is also present but cannot be detected spectroscopically. We believe silicon to have no effect on the luminescence properties of the sulfides, and a possible effect of oxygen is minimized by the strongly sulfurizing atmosphere of the final firing step and by protection of the phosphors from air by an inert atmosphere (*e.g.*, argon) during storage. Only MgS cannot be prepared in this way (MgSO_4 is soluble in water). It was made by firing MgCO_3 (luminescence grade purity) in argon loaded with CS_2 (6). The conversion is quantitative but the resulting MgS has, at best, only the purity of the used MgCO_3 .

Desired impurities were added to the prefired pure sulfides before the final firing step. It is considered to be an important point in these investigations that, whenever possible, only one activator element (here Cu, Ag, or Au) and one co-activator element were tested in any one of the samples, and that all other impurities were kept out as well as possible. Copper and silver were added as sulfides, gold as fine metal powder. Alkali metals, whose sulfides are too inconvenient to handle, were added as sulfates or carbonates. Halides were added as alkaline earth halides (*e.g.*, CaF_2 in case of CaS phosphors) or as ammonium halides, the latter react quickly with the host sulfides with liberation of small amounts of NH_3 and H_2S . The presence of traces of ammonium in this case, or of carbon in case of added carbonates, are not harmful since it was especially ascertained that both have no visible effect on the luminescence of the final phosphor. The presence of oxygen from decomposing sulfate or carbonate is somewhat more serious, but we believe to have reduced the influence to a negligibly low level by means of the sulfurizing atmo-

* Electrochemical Society Active Member.

Key words: magnesium sulfide, calcium sulfide, strontium sulfide, barium sulfide, alkaline earths, phosphors, luminescence, spectra, copper, silver, gold.

Table I. Some properties of alkaline earth sulfides

		MgS	CaS	SrS	BaS
Optical abs. edge	(eV)	~5.4	4.8	4.4	3.8
Cation radius	(Å)	0.65	0.99	1.13	1.35
Next-neighbor distance	(Å)	2.49	2.63	2.97	3.19
Interstitial radius	(Å)	0.32	0.61	0.73	0.93

sphere during firing. All samples were fired in small amounts (a few grams) either in open quartz boats in flowing H_2S , or in capped quartz tubes containing, besides the phosphor, some free sulfur, and surrounded by argon¹ for one to two hours, MgS and CaS at 1200°C , SrS at 1000°C , and BaS at 800°C . Strontium sulfide and especially barium sulfide tend to form polysulfides if prepared in sulfurizing atmosphere. They were converted back to single sulfides by a brief refiring, at 700°C , in pure H_2 .

Measurements

The emission spectra of luminescence were measured on thin powder layers excited in a demountable cathode-ray tube by 10 kV electrons at approximately $1 \mu\text{A}/\text{cm}^2$ current density, either at room temperature or cooled to near 80°K . The luminescence was observed through a quartz window, with a quartz prism monochromator (Beckman DU) and a photomultiplier (1P28) in quartz glass. Spot tests showed the mode of excitation (electron beam or short wave ultraviolet) to have little or no effect on the spectra. All spectra presented here are corrected for monochromator transmission and photomultiplier response by means of a standard incandescence lamp supplied by the National Bureau of Standards, and given in terms of quantum intensity per unit energy interval as function of the quantum energy. The limit of spectral resolution is about 0.02 eV , or better, fairly independent of the spectral position. All spectra are normalized to equal peak height ($= 100$ units) irrespective of the emission intensities actually observed.

Experimental Results

The influence of the added copper concentration on the emission spectra of a series of $\text{CaS}:\text{Cu},\text{Na}$ (3%) phosphors is demonstrated in Fig. 1. The emission intensity increases with the copper concentration up to about 0.1% Cu and then decreases again. At low copper concentrations, the spectrum consists of two structureless bands about 0.28 to 0.30 eV apart. These

¹ The latter method is described by Wachtel (4).

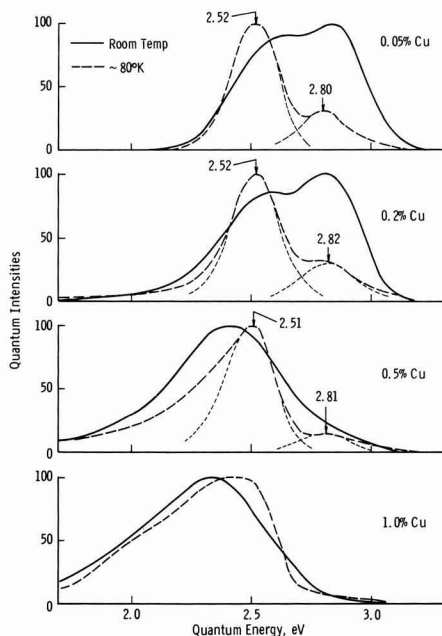


Fig. 1. Emission spectra of $\text{CaS}:\text{Cu},\text{Na}$ (3% added) phosphors of varied copper concentrations.

two bands disappear at high copper concentrations (about 0.5% and more) and, instead, a very broad and irregularly shaped band with the peak at about 2.3 to 2.4 appears. We observe similar dependence on the activator concentration also within other alkaline earth sulfides activated by copper, silver, or gold. The spectra observed at low concentrations apparently are due to isolated luminescence centers and the broad bands, observed at high concentration, to interaction between adjacent centers. The following results are limited to materials with low activator concentrations, i.e., about 0.1 mole % or less.

Various co-activators have an influence (reproducible) on the peak positions and the widths of the two emission bands of $\text{CaS}:\text{Cu}$ and (less quantitatively reproducible) on their intensity ratio. Some representative spectra are shown in Fig. 2. The following observations may especially be mentioned:

(a) Even $\text{CaS}:\text{Cu}$ containing only copper (no intentionally added coactivator) is well luminescent in two separate emission bands.

(b) The observed peak positions, as function of the added coactivator, scatter over a range clearly exceeding the unavoidable uncertainties in phosphor reproducibility (about $\pm 0.02 \text{ eV}$) and accuracy of measurements.

(c) The two emission bands resemble, in width and separation, very much the two emission bands observed in $\text{ZnS}:\text{Cu}$ phosphors.

(d) The emission of $\text{CaS}:\text{Cu}$ with Cl (similar also Br) as coactivator is weak. Its emission spectrum resembles the broad band observed, with other coactivators, only at high copper concentrations.

The influence of the coactivator on the emission spectrum is not limited to $\text{CaS}:\text{Cu}$ but almost universally observable within all alkaline earth sulfides activated by Cu, Ag, or Au. It is very pronounced in some cases (e.g., in $\text{SrS}:\text{Au}$, Fig. 3), weaker but still clearly visible in others (e.g., in $\text{BaS}:\text{Cu}$, Fig. 4) but nearly always present. This is demonstrated also in Fig. 5 and 6 showing the peak positions of the

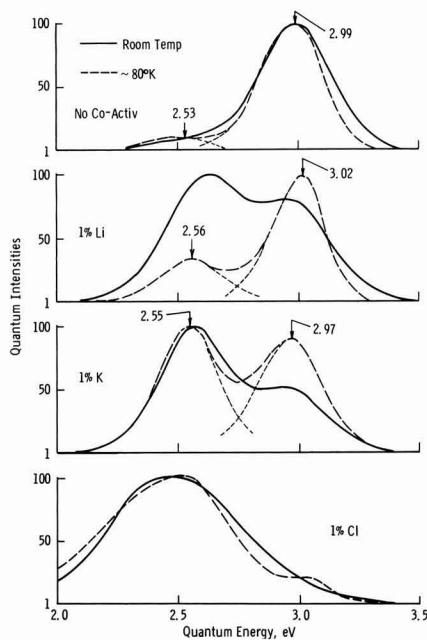


Fig. 2. Emission spectra of $\text{CaS}:\text{Cu}$ (0.1%) with different coactivators (1% added).

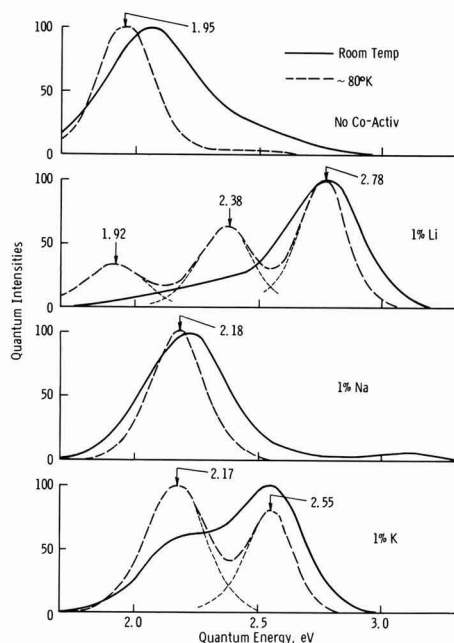


Fig. 3. Emission spectra of $\text{SrS:Au}(0.1\%)$ with different coactivators (1% added).

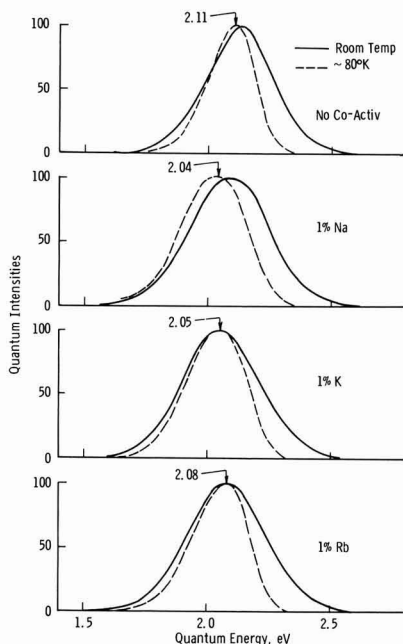


Fig. 4. Emission spectra of $\text{BaS:Cu}(0.1\%)$ with different coactivators (1% added).

emission bands of alkaline earth sulfides activated by Cu and by Au as function of the used co-activator. The length of each horizontal bar indicates approximately the accuracy of the determination of the peak positions. It is clear that the scatter due to variation of the coactivator by far exceeds the limit of accuracy in many cases. It may especially be stressed here that these variations are not accidental due to poor re-

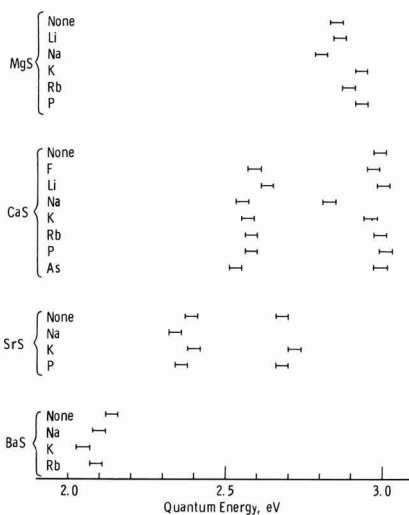


Fig. 5. Peak positions of alkaline earth sulfide phosphors all made with 0.1% of copper and 1% of various coactivators, measured at room temperature.

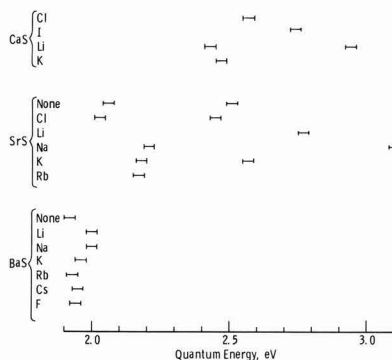


Fig. 6. Same as Fig. 5 but Cu replaced by Au (MgS:Au is non-luminescent).

producibility of the materials; they are well reproducible.

In view of these complications it is not surprising that no simple "shift" of an emission spectrum to lower energies is observed if, with any activator-coactivator pair, the host crystal is varied from MgS to CaS to SrS to BaS . Some spectra demonstrating this are shown in Fig. 7-9. The closest resemblance to a simple spectral shift exists for copper (Fig. 7), but deviations appear here also. Any regular behavior is missing in cases of silver (Fig. 8) and gold (Fig. 9).

The following general remarks may be made to the efficiencies of copper, silver, and gold in alkaline earth sulfide phosphors:

Copper-activated alkaline earth sulfides normally are efficient phosphors, quantum efficiencies of photoluminescence of about 50% or more, and energy efficiencies of cathodoluminescence of 10 to 15%, can routinely be obtained. Exceptions are only materials containing Cl, Br, or I which perform very poorly.

Silver is an inefficient activator in any one of the alkaline earth sulfides and with any coactivator, efficiencies of photo- and of cathodo-luminescence rarely come to about 10% and 1%, respectively. Silver does enter the lattices, however, and produces emission spectra clearly different from those caused by copper or gold.

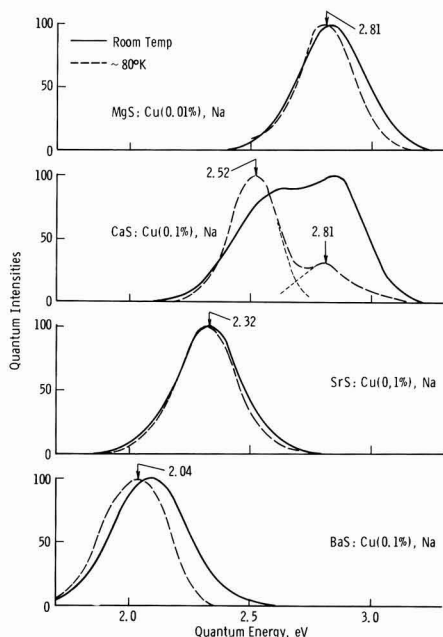


Fig. 7. Emission spectra of MgS, CaS, SrS, and BaS activated by copper and sodium (1% added).

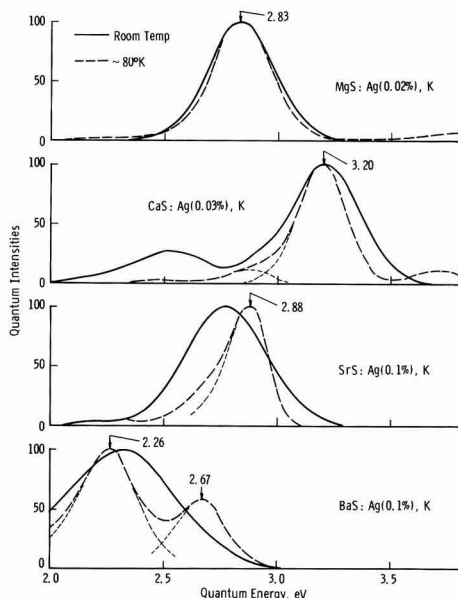


Fig. 8. Emission spectra of MgS, CaS, SrS, and BaS activated by silver and potassium (1% added).

Gold-activated alkaline earth sulfides containing Cl, Br, or I as coactivator are about as efficient in photo- and in cathodo-luminescence as Cu-activated materials containing halides. The alkalis perform somewhat poorer in combination with gold. Gold is completely ineffective in MgS, however. All attempts to make luminescent MgS: Au phosphors, without or with added coactivators (tested: F, Cl, Br, I, Li, Na, K, Rb, P) failed; the materials invariably were dead. It

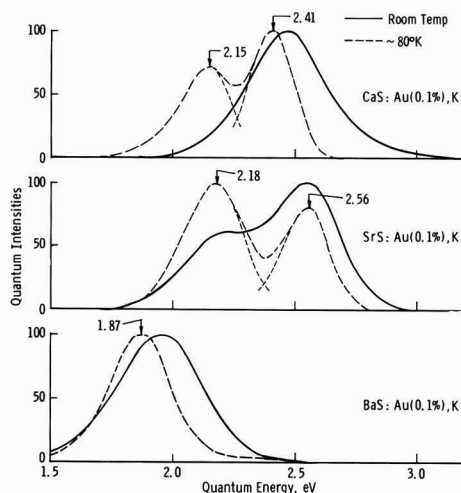


Fig. 9. Emission spectra of CaS, SrS, and BaS activated by gold and potassium (1% added). MgS: Au is nonluminescent.

may be that gold is too big (ionic radius = 1.37\AA) to replace the small Mg^{2+} ion (0.65\AA) in the lattice of MgS.

Discussion

The Schön-Klasens model of luminescence in ZnS-type phosphors assumes the emission to be due to an electron transition from the lower edge of the conduction band, or from a level very close to that edge, into a previously emptied level (caused by Cu^+ , etc.) not too far above the valence band edge. This model certainly does not apply to alkaline earth sulfide phosphors because:

- It would require independence of the emission spectra on the used coactivator.
- It would require the emission spectra simply to shift to lower energies, parallel to the change of the width of the band gap, as the host crystal is varied from MgS to CaS to SrS to BaS.

Both predictions are in strong disagreement with the observations. The emission spectra do very definitely depend on the coactivator, and there is no spectral shift over a range corresponding to the change in band gap (compare Fig. 5-7 with data in Table I). The observations can only be understood on the basis of a Prener-Williams type of recombination (7, 8) in which both, activator and coactivator, are directly involved. Shionoya *et al.* (9) recently presented strong evidence that this type of recombination is responsible for all the main emission bands of copper and silver in ZnS-type phosphors.

No attempt shall be made here to present a model to explain quantitatively the observed variations in alkaline earth sulfide phosphors activated by copper, silver, or gold.

Acknowledgment

The writer is indebted to H.F. Dorman for much careful preparation work.

Manuscript submitted March 2, 1970; revised manuscript received June 3, 1970.

Any discussion of this paper will appear in a Discussion Section to be published in the June 1971 JOURNAL.

REFERENCES

- P. Lenard, F. Schmidt, and R. Tomaschek, "Handb. d. Exp. Phys.," Vol. 23 (1928).
- O. Sorge, "Untersuchungen über die Erdalkalisulfidphosphore," Thesis, Techn. Univ. Berlin (1959).

3. M. Avinor, A. Carmi, and Z. Weinberger, *J. Chem. Phys.*, **35**, 1978 (1961).
4. A. Wachtel, *This Journal*, **107**, 199 (1960).
5. C. H. Ballhausen, "Introduction to Ligand Field Theory," McGraw-Hill (1962).
6. E. Tiede and F. Richter, *Ber. Deutsch. Chem. Ges.*, **55**, 69 (1922).
7. J. S. Prener and F. E. Williams, *This Journal*, **103**, 342 (1956).
8. E. F. Apple and F. E. Williams, *ibid.*, **106**, 224 (1959).
9. S. Shionoya *et al.*, *Proc. Intern. Conf. Lumin., Budapest*, pp. 962 and 1164 (1966), and *J. Phys. Chem. Solids*, **29**, 1827, 1843 (1968).

Liquid-Phase Epitaxy of $\text{In}_x\text{Ga}_{1-x}\text{As}$

G. A. Antypas*

Central Research Laboratories, Varian Associates, Palo Alto, California 94303

ABSTRACT

$\text{In}_x\text{Ga}_{1-x}\text{As}$ layers grown by liquid-phase epitaxy were obtained in the range of $0.0 < x < 0.23$, when grown on the (111 Ga) plane of GaAs. Attempts to grow alloys on the (110), (111 As), (100), and (112 As) planes resulted in polycrystalline layers. The alloy composition was determined by x-ray fluorescence and the band gap by infrared transmission. The ternary-phase diagram was calculated using Darken's quadratic formalism to describe the ternary liquid and assuming the solid solution in equilibrium with the liquid to be regular. It was found that the experimental results were in good agreement with the calculated phase diagrams. A number of liquidus isotherms were calculated in the temperature range of 700°–1200°C. Gallium arsenide isoconcentration curves are shown for 0.95, 0.90, 0.80, 0.50, and 0.30 GaAs mole fraction.

Early experimental investigation of the solid solutions of III-V compounds indicated that systems having a column V common element do not form continuous solid solutions, while systems having a common III element do. This observation was based on the report by Koster and Thoma (1) on GaSb-InSb, AlSb-InSb, and GaSb-AlSb, and the work of Folberth (2) on the InAs-InP and GaAs-GaP systems. Goryunova and Fedorova (3), however, reported that complete solid solutions were obtained in the InSb-GaSb system, and an almost complete solid solution was obtained for the InAs-GaAs system when the alloys were annealed at relatively high temperatures for extended periods of time. Since then, the InAs-GaAs system has received wide attention primarily due to its wide direct band gap range. Woolley and Smith (4) have obtained a series of alloy compositions by annealing compressed powders at 900°C. X-ray diffraction studies on these samples indicate that Vegard's law was obeyed. Abrahams *et al.* (5) studied the electrical, thermal, and optical properties of InGaAs alloys prepared either by gradient freezing or zone leveling techniques. Van Hook and Lenker (6), using the techniques described by Shafer and Weiser (7), obtained InGaAs alloys across the whole composition range. All of the mentioned techniques yielded polycrystalline material; furthermore, the mixed crystals were annealed or grown at temperatures close to the melting point of InAs (942°C).

Liquid-phase epitaxy as reported by Nelson (8) has been used previously in growing high-quality epitaxial layers with low native defect density (9). This technique was used by Antypas and James (10) in growing GaAs, Sb_{1-x}As_x epitaxial layers on GaAs substrates in the range $1.00 > x > 0.75$. Olsen *et al.* (11) reported the growth of InGaAs epitaxial layers on GaAs substrates in the temperature range of 750°–600°C. The author, however, was unable to obtain any more information on the growth characteristics and/or properties of the grown layers. Recently, Stringfellow and Greene (12) reported that Ewing grew InGaAs epitaxial layers across the alloy series on (111 As) InAs substrates by liquid-phase epitaxy. Their results were in excellent agreement with their calculated ternary-phase diagram based on the quasi-chemical theory.

The present investigation was oriented toward developing InGaAs epitaxial layers, preferably on GaAs substrates, to be used as high-efficiency, long-wavelength threshold semitransparent photoemitters. Similar investigations in our laboratory have led to the development of high-efficiency 1.06 μ photoemitters based on GaAs_xSb_{1-x} epitaxial layers.

Experimental Procedure

The epitaxial layers were grown using the horizontal technique initially described by Nelson (8). The In-Ga melts are prepared in a carbon boat, over which palladium-purified hydrogen is flowing, inside a quartz tube. A preweighed InAs crystal which is the source of As is also placed in the boat. The melts are heated to the starting growth temperature (sgt) for approximately 3 hr. After the equilibrium amount of InAs is dissolved, any further dissolution will result in the growth of a ternary layer of InGaAs on the seed, which will be in equilibrium with the melt. This would prevent any further dissolution of the substrate.¹

Following saturation, the undissolved InAs is removed and reweighed, thus determining the composition of the melt. The saturation experiments are repeated for longer periods of time, and at 750°C (which is the temperature of interest in our investigation) weight losses between experiments of less than 1% were observed. This could be accounted for by both temperature fluctuations of the furnace and As evaporation. In any event, the loss of As as a source of error in determining the liquidus composition can be neglected at low temperatures.

Prior to growth, the substrate was placed at one end of the boat and a dendrite of GaAs was introduced in the melt so that it would prevent any etch-back from the substrate due to temperature fluctuations in the furnace or due to the loss of As from the melt. The furnace was then tilted about 10° from the horizontal position so that the melt would roll over the substrate, at which point a programmed cooling cycle was initiated. At the end of the growth cycle, the furnace was

¹ We attempted to identify this thin epitaxial layer on experiments performed on the GaAsSb system by monitoring the photoluminescence spectra of GaAs seeds that were used in saturating GaSb melts. In all cases, only GaAs band gap radiation was observed. Apparently the layers present cannot be detected by this technique.

* Electrochemical Society Active Member.

Key words: III-V alloy semiconductors, InGaAs ternary phase diagram.

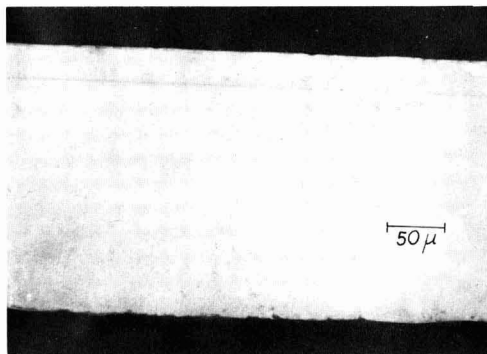


Fig. 1. Cross section on cleaved (110) plane showing an $\text{In}_{0.03}\text{Ga}_{0.97}\text{As}$ epitaxial layer grown on (100) oriented GaAs substrate.

tipped back to the horizontal position and the melt was removed from the substrate with the aid of a quartz hoe.

Experimental Results

During early experiments, it was observed that the distribution coefficient of GaAs when grown from In-Ga-As solutions is greater than unity. Similar behavior has been observed for GaAlAs when grown from Ga-Al-As melts (13). Thus, epitaxial layers of InGaAs will have to be grown from In-rich melts. Figure 1 shows an epitaxial layer (sample No. 4-5-B) of InGaAs grown on (100) Cr-doped GaAs substrates. The sample was cleaved and etched in a $\text{H}_2\text{O}:\text{H}_2\text{O}_2:\text{HF}$ (10:1:1) delineation etch for 10 sec. Details of melt composition, solid composition, and growth temperatures are given in Table I.

A representative epitaxial layer grown on (100) GaAs substrates from melts having higher In concentration than those from which sample No. 4-5-B was prepared is shown in Fig. 2. The layers were polycrystalline in nature, with a very rough surface which is the result of a great number of In-Ga inclusions. Further experimentation showed that it was impossible to grow high-quality InGaAs epitaxial layers having InAs concentrations greater than 5% on (100) GaAs substrates.

Growth of InGaAs layers on (110), (111 As), and (112 As) GaAs faces exhibited similar characteristics to those grown on (100) faces. However, when growing on the (111 Ga) plane, the layers have mirror-smooth surfaces and planar interfaces. Figure 3 represents an epitaxial layer of InGaAs (1.17 eV band gap) grown from In-rich melts, the details of which are shown in Table I. The (111 Ga) GaAs substrates were chemically polished in dilute NaOCl solutions. Epitaxial layers grown on the (112 Ga) plane of GaAs were of lower quality and did not have the mirror-smooth surface exhibited by the layers grown on the (111 Ga) plane.

The band gap of the epitaxial layers grown on GaAs substrates was determined by infrared transmission corrected for sample thickness. The absorption edge

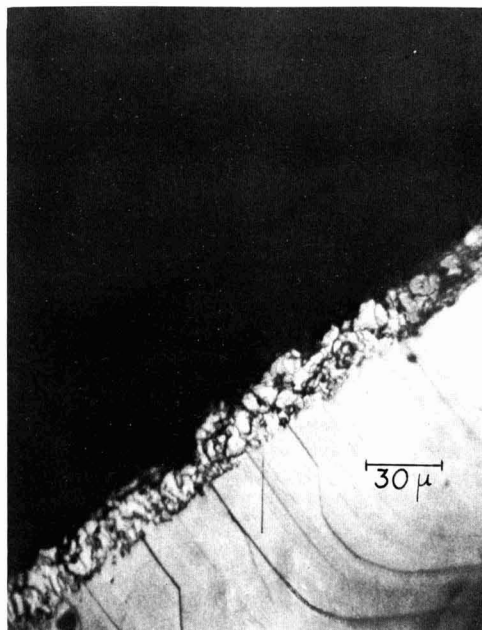


Fig. 2. Cross section of polycrystalline InGaAs epitaxial layer grown on the (100) plane of GaAs substrates. Similar layers have been obtained when InGaAs epitaxial layers are grown on the (110), (111 As), and (112 As) planes of GaAs from melts resulting in $x_{\text{InAs}} > 0.05$.

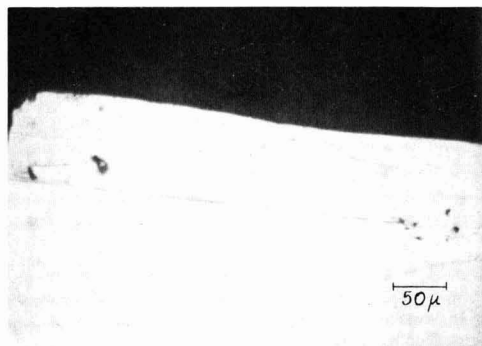


Fig. 3. Cross section of representative InGaAs epitaxial layers grown on the (111 Ga) plane of GaAs. Similar layers were obtained in the composition range of $0.77 < x_{\text{GaAs}} < 1.0$.

was very sharp, and the band gap was taken as the 10% transmission point. Figure 4 shows the band gap variation as a function of alloy composition. The band gap of InGaAs alloys reported by a number of investigators is also shown.

Epitaxial layers of InGaAs grown on (111 As) InAs substrates had mirror-smooth surfaces only when grown at temperatures around 650°C. At higher temperatures ($\sim 750^\circ\text{C}$), it was observed that on a number of occasions the layer substrate interface was completely obliterated and, in general, the layers appeared rougher than those grown at lower temperatures.

Phase Diagram Calculation

Phase diagram calculations for ternary III-V compounds have been reported by Stringfellow and Greene

Table I. Results and summary of the growth conditions of the InGaAs epitaxial layers

Sample No.	Melt composition in a/o			Growth temp (°C)	Band gap (eV)	x_{GaAs}	Substrate orientation
	In	Ga	As				
4-5-B	55.5	40.5	4.0	740-690	1.35	0.97	(100)
9-15-A	61.5	33.5	5.0	740-700	1.30	0.94	(111 Ga)
9-16-A	67.0	27.5	5.5	740-700	1.26	0.93	(111 Ga)
9-17-A	71.0	21.5	7.5	750-720	1.22	0.91	(111 Ga)
8-28-A	74.0	18.0	8.0	730-700	1.17	0.89	(111 Ga)
9-29-C	81.0	8.5	10.5	740-690	0.98	0.77	(111 Ga)

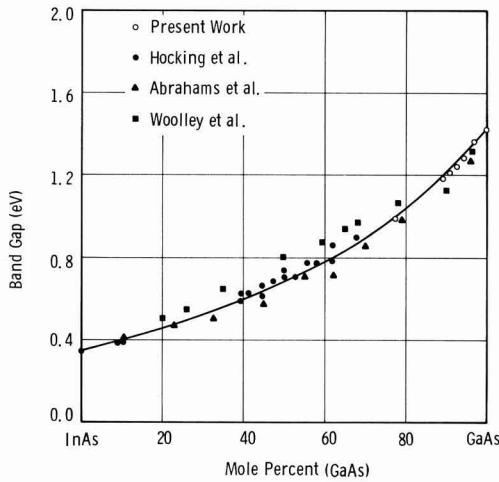


Fig. 4. Dependence of the band gap on the composition of InGaAs alloys prepared by a variety of techniques.

(12) who used the quasi-chemical approach to describe both the solid and liquid solutions, and by Ilegems and Pearson (13) who calculated the ternary-phase diagrams of $\text{Ga}_x\text{Al}_{1-x}\text{As}$ using the regular solution theory to describe the ternary liquid and ideal solution for the pseudobinary solid. Antypas and James (10) recently calculated the ternary-phase diagrams of $\text{GaAs}_{1-x}\text{Sb}_x$ using Darken's (14) quadratic formalism to describe the liquid and assuming the pseudobinary solid to be described by a regular solution. They found it to be in good agreement with experiment. Antypas (15) has also calculated the ternary-phase diagram of GaAsP based on the same theory and found it to be in excellent agreement with available experimental data.

In computing the conditions for equilibrium between a ternary liquid solution A, B, C , ($\text{In}, \text{Ga}, \text{As}$) and a pseudobinary solid solution $AC-BC$ (InAs-GaAs), Stringfellow and Greene (12) derived the following equations:

$$\begin{aligned} \ln \gamma_{AC}x &= \ln 4N_A N_C + \ln (\gamma_A \gamma_C / \gamma_A^{STC} \gamma_C^{STC}) \\ &\quad + \Delta S_{AC}^F (T_{AC}^F - T) / RT \\ \ln \gamma_{BC}(1-x) &= \ln 4N_B N_C + \ln (\gamma_B \gamma_C / \gamma_B^{STC} \gamma_C^{STC}) \\ &\quad + \Delta S_{BC}^F (T_{BC}^F - T) / RT \end{aligned} \quad [1]$$

where γ_{AC} and γ_{BC} are the activity coefficients of AC and BC in the solid solution, x is the mole fraction of AC , N_i and γ_i ($i = A, B, C$) are the atom fraction and activity coefficient of i in the liquid solution, respectively, γ_i^{STC} is the activity coefficient of N_i at the stoichiometric composition, ΔS_{AC}^F is the entropy of fusion of AC , T_{AC}^F is the temperature of fusion of AC , R is the universal gas constant, and T is the temperature in $^\circ\text{K}$.

Under the restriction

$$N_A + N_B + N_C = 1 \quad [2]$$

Eq. [1] can be solved numerically on a computer to yield two sets of curves, one describing the liquidus isotherms and the other describing the solidus iso-concentration curves of the system.

In previous investigations, the activity coefficients were determined by the quasi-chemical equilibrium (12) approach and by considering the ternary liquid as a strictly regular solution (13). In the present communication, however, the determination of the activity coefficient in the liquid phase is based on Darken's (16) quadratic representation, which for a binary liquid is

$$\ln \gamma_A = \alpha_{AC} N_C^2$$

$$\ln (\gamma_C / \gamma_C^0) = \alpha_{AC} (-2N_C + N_C^2) \quad [3]$$

where A is the solvent and C is the solute, γ_C^0 is the activity coefficient of C at infinite dilution, and α_{AC} is the interaction parameter of the system. Equation [2] reduces to that describing a regular solution if $\ln \gamma_C^0 = \alpha_{AC}$. This formalism has been satisfactorily applied by Darken (16) and Turkdogan and Darken (17) to a number of liquid metallic solutions for concentration of up to 60%. This formalism is consistent with the Gibbs-Duhem equation and satisfies Raoult's and Henry's laws as the limiting cases. The activity coefficients for a ternary liquid based on Darken's quadratic formalism are given by

$$\begin{aligned} \ln \gamma_A &= \alpha_{AB} N_B^2 + \alpha_{AC} N_C^2 + (\alpha_{AB} + \alpha_{AC} - \alpha_{BC}) N_B N_C \\ \ln (\gamma_B / \gamma_B^0) &= -2\alpha_{AB} N_B + (\alpha_{BC} - \alpha_{AB} - \alpha_{AC}) N_C \\ &\quad + \alpha_{AB} N_B^2 + \alpha_{AC} N_C^2 + (\alpha_{AB} + \alpha_{AC} - \alpha_{BC}) N_B N_C \\ \ln (\gamma_C / \gamma_C^0) &= -2\alpha_{AC} N_C + (\alpha_{BC} - \alpha_{AB} - \alpha_{AC}) N_B \\ &\quad + \alpha_{AB} N_B^2 + \alpha_{AC} N_C^2 + (\alpha_{AB} + \alpha_{AC} - \alpha_{BC}) N_B N_C \end{aligned} \quad [4]$$

where component A is the solvent and components B and C are the solutes, γ_B^0 is the activity coefficient of component B at infinite dilution, and α_{i-j} are the interaction energies of the various binary systems. The above formalism is also consistent with the Gibbs-Duhem equation, and furthermore it reduced to the binary quadratic formalism as one of the solutes in the ternary approaches infinite dilution.

The solid solution in equilibrium with the ternary liquid was assumed to be regular, i.e. $\Delta F_{ss} = \alpha_{AC-BC}x(1-x)$, where α_{AC-BC} is the interaction energy and x is the mole fraction of one of the components in the solid. The activity coefficients are thus given by

$$\begin{aligned} \ln \gamma_{AC} &= \alpha_{AC-BC}(1-x)^2 \\ \ln \gamma_{BC} &= \alpha_{AC-BC}x^2 \end{aligned} \quad [5]$$

Substituting Eq. [4] and [5] in Eq. [1], the ternary-phase diagram can be calculated numerically to yield the liquidus and solid distribution curves.

The parameters necessary in calculating the ternary-phase diagram are the temperatures T^F and entropies ΔS^F of fusion of the III-V compounds and the interaction parameters α_{AB} , α_{AC} , α_{BC} , and α_{AC-BC} . T^F and ΔS^F for InAs and GaAs can be obtained directly from the literature and are shown in Table II. Vieland (18) has used regular solution theory to calculate the liquidus of III-V compounds. The interaction parameter obtained from such a treatment is

$$\alpha = \frac{\Delta S^F (T - T^F) [1 + R/\Delta S^F] \ln 1/4x(1-x)}{2(x-0.5)^2} \quad [6]$$

where x is the column V element in solution. For a regular solution, α should be independent of temperature and composition. Thurmond (19), however, demonstrated that for GaAs α is a linear function of temperature given by

$$\alpha_{\text{GaAs}} = 9960 - 11.15T \quad [7]$$

(When the interaction parameter, α , is divided by RT so that it will be thermodynamically consistent with Darken's formulation, it takes the form of

$$\omega = \frac{L}{RT} - \frac{\delta}{R} \quad [8]$$

Table II. Parameters used in calculating the ternary-phase diagram

	InAs	GaAs	In-Ge	InAs-GaAs
α (cal/mole)	$-9.160 T + 4300$	$-3.7 T$	1000	2000
ΔS^F (eu)	14.52 [Ref. (24)]	16.64 [Ref. (24)]	—	—
T^F ($^\circ\text{C}$)	942	1238	—	—

which is of the form derived by Turkdogan and Darken (17), where \mathcal{L} and δ have the units of enthalpy and entropy, respectively.)

In calculating α_{GaAs} , Thurmond assumed a $\Delta S_{\text{GaAs}}^{\text{F}}$ value of 14.0 eu. Arthur (20) pointed out that, when a recently measured value for $\Delta S_{\text{GaAs}}^{\text{F}}$ of 16.64 eu is used, then

$$\alpha_{\text{GaAs}} = 5160 - 9.16T$$

Arthur has also calculated the activity coefficient of As from As vapor pressure measurements, and using a regular solution treatment found that the interaction parameter is accurately given by

$$\alpha_{\text{GaAs}} = -3.7T$$

A similar analysis performed on the InAs system based on the solubility data of Hall (21) and Liu and Peretti (22) resulted in an interaction parameter given by

$$\alpha_{\text{InAs}} = -9.160T + 4300$$

The interaction parameter for the In-Ga system was calculated to be 1000 cal/mole by fitting the liquidus curve to a regular solution model and comparing it to available experimental data (23). Similarly, the interaction parameter of the InAs-GaAs system was determined by fitting the solidus curve to published data of the InAs-GaAs pseudobinary. Calculations performed are in good agreement with experiment when $\alpha_{\text{InAs-GaAs}} = 2000$ cal/mole. In the ternary phase diagram calculations, the activity coefficient of Ga at infinite dilution, $\ln \gamma_{\text{Ga}}^0$, was varied between 0 and -1.8. The best fit to the experimental liquidus, and solidus, data for the 750° and 700°C isotherms were obtained when $\ln \gamma_{\text{Ga}}^0 = -0.8$.

Figure 5 shows the calculated phase diagram where the solid lines represent the liquidus isotherms, while the dotted lines are the GaAs isoconcentration curves. A number of experimental points are also shown. The composition of the pseudobinary solid was determined by x-ray fluorescence. The pseudobinary diagram obtained from Fig. 5 is shown in Fig. 6. It is seen that the calculated phase diagram is in good agreement with available experimental data. For Fig. 7, we replotted a portion of the ternary-phase diagram in cartesian coordinates. It shows the calculated solidus isotherms for 700° and 800°C along with experimental results.

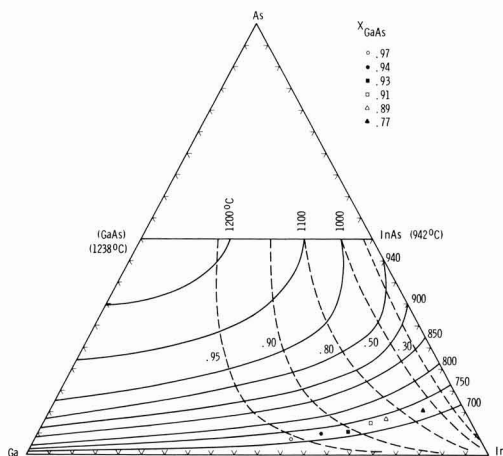


Fig. 5. In-Ga-As ternary-phase diagram. Solid lines represent the liquidus isotherms, while dotted lines represent GaAs isoconcentration curves. Details of the experimental points shown are given in Table I.

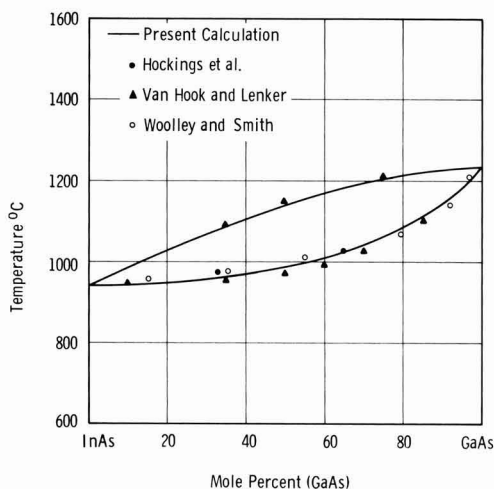


Fig. 6. InAs-GaAs pseudobinary phase diagram

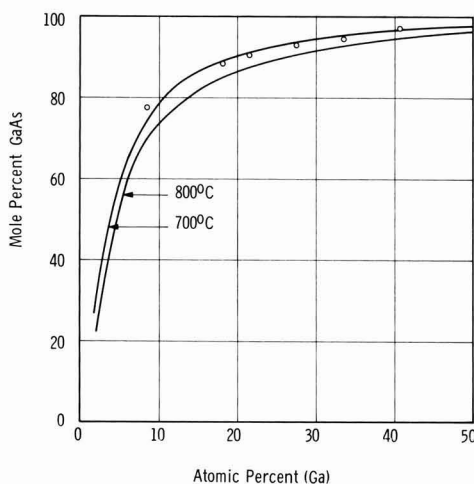


Fig. 7. The 700° and 800°C calculated GaAs solidus isotherms. Details of experimental points are given in Table I.

Conclusions

InGaAs layers have been grown on GaAs substrates. It has been observed that, when growing from In-rich melts, epitaxy of $\text{In}_x\text{Ga}_{1-x}\text{As}$ layers on GaAs with $x > 0.05$ can be obtained only when growing on the (111 Ga) face. The In-Ga-As ternary-phase diagram was calculated using Darken's quadratic formalism to describe the ternary liquid while treating the solid as a regular solution; it was found to be in good agreement with experiment. The calculated pseudobinary phase diagram was in excellent agreement with available experimental data. The composition of the mixed crystals was determined by x-ray fluorescence techniques, and the band gap by infrared transmission, corrected for sample thickness. The variation of the band gap was plotted as a function of composition along with the data obtained by a number of investigations for InGaAs alloys prepared by a variety of techniques. Stringfellow and Greene (12) reported that Ewing obtained alloys of InGaAs grown on InAs substrates across the alloy series, from a starting growth temperature of as high as 780°C. Our experi-

ence is that high-quality epitaxial layers on InAs substrates could be grown only at lower temperatures.

Acknowledgments

The author wishes to thank L. Garbini who performed the x-ray fluorescence analysis of the samples, and S. Reita for his technical assistance.

Manuscript submitted Jan. 20, 1970; revised manuscript received ca. July 2, 1970.

Any discussion of this paper will appear in a Discussion Section to be published in the June 1971 JOURNAL.

REFERENCES

1. W. Koster and B. Thoma, *Z. Metallk.*, **46**, 291 (1955).
2. O. G. Folberth, *Z. Naturforsch.*, **10a**, 502 (1955).
3. N. A. Goryunova and N. N. Fedorova, *Zh. Tekhn. Fiz.*, **25**, 1339 (1955).
4. J. C. Woolley and B. A. Smith, *Proc. Phys. Soc.*, **72**, 214 (1958).
5. M. S. Abrahams, R. Braunstein, and F. D. Rosi, *J. Phys. Chem. Solids*, **10**, 204 (1959).
6. H. J. Van Hook and E. S. Lenker, *Trans. Met. Soc. AIME*, **227**, 220 (1963).
7. M. Shafer and K. Weiser, *J. Phys. Chem.*, **61**, 1424 (1957).
8. H. Nelson, *RCA Rev.*, **24**, 603 (1963).
9. E. W. Williams and D. M. Blacknall, *Trans. Met. Soc. AIME*, **239**, 387 (1967).
10. G. A. Antypas and L. W. James, *J. Appl. Phys.*, **41**, 2165 (1970).
11. H. Olsen, H. Robbins, and R. K. Willardson, *Abs. No. 103, Extended Abstract, Electrochem. Soc. Meeting, Dallas, May 7-12, 1967*.
12. G. B. Stringfellow and P. E. Greene, *J. Phys. Chem. Solids*, **30**, 1779 (1969).
13. M. Ilegems and G. L. Pearson, "Proceedings 1968 Symposium on GaAs," p. 3, Institute of Physics and Physical Society, London (1969).
14. L. S. Darken, *Trans. Met. Soc. AIME*, **239**, 90 (1967).
15. G. A. Antypas, *This Journal*, **117**, 700 (1970).
16. L. S. Darken, *Trans. Met. Soc. AIME*, **239**, 80 (1967).
17. E. T. Turkdogan and L. S. Darken, *ibid.*, **242**, 1997 (1968).
18. L. J. Viehland, *Acta Met.*, **11**, 137 (1963).
19. C. D. Thurmond, *J. Phys. Chem. Solids*, **26**, 798 (1965).
20. J. R. Arthur, *ibid.*, **28**, 2257 (1967).
21. R. N. Hall, *This Journal*, **110**, 385 (1963).
22. T. S. Liu and E. A. Peretti, *Trans. ASME*, **45**, 677 (1953).
23. G. J. Macur, R. K. Edwards, and P. G. Wahlbeck, *J. Phys. Chem.*, **72**, 1047 (1968).
24. B. D. Lichter and P. Sommelet, *Trans. Met. Soc. AIME*, **245**, 1021 (1969).

Silicon Epitaxy from Mixtures of SiH₄ and HCl

J. Bloem*

Semiconductor Development Laboratory, N. V. Philips Gloeilampenfabrieken, Nijmegen, Holland

ABSTRACT

An investigation of the epitaxial growth of silicon from SiCl₄ in H₂ and from mixtures of SiH₄ and HCl in H₂ indicates that the gas phase reactions are slow and that equilibrium between solid and gas occurs at the interface. Kinetic data point to a diffusion controlled reaction rate, and it is shown that thermodiffusion in the stagnant gas layer on the silicon surface retards the growth rate of silicon and enhances the etching reaction.

In the epitaxial growth of silicon several studies of the thermodynamics and kinetics of the system have been published. Surveys are given in ref. (1) and (2).

At temperatures over 1100°C the reaction is considered to be diffusion controlled, with chemical equilibrium occurring at the solid-gas interface.

Recently Eversteyn *et al.* (2) introduced the concept of a stagnant gas layer of constant thickness over the substrates in a horizontal reactor. In the stagnant layer a steep temperature gradient (~1000°/cm) is present (2), and it is interesting to examine whether gas phase reactions occur in this boundary layer and whether the diffusion of species from and to the growing interface will be influenced by the presence of the temperature gradient.

In this investigation epitaxy from SiCl₄ in H₂ and from mixtures of SiH₄ and HCl in H₂ is studied because, if chemical equilibrium is attained in the gas phase, SiCl₄ in H₂ would be expected to give the same growth rate and the same temperature dependence of growth rate, as a mixture of SiH₄ + 4HCl in H₂.

The calculations of Eversteyn *et al.* (2) on the growth rate have been extended to include the effect of thermodiffusion (3). The results of the extended calculation are applied here to the growth rate of Si from SiH₄ and to the etch rate of Si by HCl. The former reaction is governed by the diffusion of SiH₄ toward the reacting surface, the latter by the diffusion of the reaction products of the etching reaction, mainly SiCl₂ (1, 4) away from the interface.

Growth and Etch Rates

In a diffusion controlled reaction involving a stagnant layer of constant thickness, δ cm, the growth rate of silicon can be calculated from the material balance at the interface.

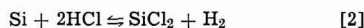
The flux of material toward the interface in moles/cm² sec, for a given position on the susceptor, is given by (5)

$$J_x = -D_1 n \left[\frac{d \frac{n_1}{n}}{dy} \right] \quad [1]$$

where D_1 is the diffusion coefficient of the rate-determining species in cm²/sec, n is the total gas density (moles/cm³), n_1 is the concentration of the diffusing species (moles/cm³), and y is the direction perpendicular to the growing interface.

In the Appendix the growth rate of silicon is calculated for the case where the diffusion of SiH₄ toward the surface is the rate-controlling step.

At temperatures around 1150°C HCl etching of silicon proceeds via the reaction.



For $p_{\text{H}_2} = 1$

$$K_{\text{SiCl}_2} = \frac{p_{\text{SiCl}_2}}{(p_{\text{HCl}})^2} \quad [3]$$

The value of K_{SiCl_2} at 1500°K is nearly unity (1, 4), which implies that with $p_{\text{HCl}} = 10^{-2}$ the maximum value of p_{SiCl_2} will be about 10^{-4} atm. For a diffusion

* Electrochemical Society Active Member.
Key words: silicon, epitaxy, vapor growth.

limited reaction the silicon etch rate will be slow, because the diffusion of SiCl_2 away from the surface constitutes the rate-controlling step in the steady-state condition, assuming that the diffusion coefficients of HCl and SiCl_2 in hydrogen do not differ markedly. The HCl partial pressure at the silicon interface will be nearly equal to the HCl partial pressure in the main gas ($\sim 10^{-2}$ atm).

Because the growth rate depends on diffusion toward the interface and the etch rate depends on diffusion away from the interface, the ratio of growth and etch rates may give information regarding second order effects in the transport processes, i.e., thermiodiffusion.

For a binary gas mixture in a temperature gradient a concentration gradient is produced, given by (3, 5, 6)

$$\frac{d \frac{n_1}{n}}{dy} = K_T \frac{d \ln T}{dy} \quad [4]$$

where n_1 is the concentration of the heavier molecule in the gas (moles/cm³), K_T is the thermiodiffusion ratio, and T is the temperature with a gradient in the y -direction ($^{\circ}\text{K}$).

The thermiodiffusion ratio can also be expressed as

$$K_T = \alpha \frac{n_1}{n} \cdot \frac{n_2}{n} \quad [5]$$

where α is the thermiodiffusion factor, and n_2 is the concentration of the second component in the binary gas mixture.

Equations [4], [5], and [1] can be combined to give the expected growth and etch rates including the thermiodiffusion effect. In the Appendix it is shown that the ratio of growth rate (G) and etch rate (E), neglecting thermiodiffusion, is given by (13)

$$\frac{G}{E} = \frac{D_{\text{SiH}_4} \cdot p_{\text{SiH}_4}}{D_{\text{SiCl}_2} \cdot p_{\text{SiCl}_2}} = \frac{D_{\text{SiH}_4} \cdot p_{\text{SiH}_4}}{D_{\text{SiCl}_2} \cdot K_{\text{SiCl}_2} \cdot (p_{\text{HCl}})^2}$$

Including thermiodiffusion for the simplified case that α_1 and α_2 are equal the expression [20] in the Appendix becomes

$$\frac{G}{E} = \frac{D_{\text{SiH}_4} \cdot p_{\text{SiH}_4}}{D_{\text{SiCl}_2} \cdot K_{\text{SiCl}_2} \cdot (p_{\text{HCl}})^2} \cdot \frac{T_g^{\alpha_1}}{T_s^{\alpha_2}}$$

where D_{SiH_4} and D_{SiCl_2} are the diffusion coefficients in H_2 of SiH_4 and SiCl_2 , respectively (cm^2/sec), p_{SiH_4} is the partial pressure of SiH_4 in the main gas (atm), p_{SiCl_2} is the equilibrium pressure of SiCl_2 at the silicon surface (atm), T_g and T_s are the temperatures of the main gas and the substrate in $^{\circ}\text{K}$, and α_1 and α_2 are the thermiodiffusion factors of SiH_4 and SiCl_2 , respectively.

The greater the values of α and the smaller the ratio T_g/T_s the greater will be the difference between growth and etch rates arising from the diffusion of SiH_4 toward the interface being hampered and the diffusion of SiCl_2 away from the interface being promoted. The value of α depends on the relative molecular diameters and relative masses of solute and solvent. For heavy molecules in a light gas, relatively high values of α can be expected, up to a value of about 3 for an extreme case (6, 7).

Taking reasonable values for the molecular diameters gives the following results

$$\alpha_{\text{SiH}_4-\text{H}_2} = 1.0; \alpha_{\text{SiCl}_2-\text{H}_2} = 1.5; \alpha_{\text{SiCl}_4-\text{H}_2} = 1.7$$

Not much is known about the temperature dependence of α , but a slight increase with temperature is to be expected (5).

Apart from thermiodiffusion there are other factors that can cause growth and etch rates to differ from the values calculated. Two important ones are the temperature dependence of the diffusion coefficients and the value of the chemical equilibrium constant, K_{SiCl_2} . For the diffusion coefficients, the value of the expo-

nent, m , in the expression for the temperature dependence $D = D_0(T/T_0)^m$, theoretically may vary from 1.5 to 2.0 (8); a smaller value of m being expected for SiH_4 than for SiCl_2 . Analysis of the literature (9, 10) indicates a value of 1.0 ± 2.5 for the equilibrium constant K_{SiCl_2} at 1500°K . Moreover SiH_2Cl_2 and possibly SiHCl_3 also occur in concentrations that increase the etch rate, and an effective value of K_{SiCl_2} of 2.5 therefore is not unreasonable.

The experimental approach involves: (a) estimating the magnitude of the thermiodiffusion effect for SiH_4 , (b) selecting the temperature dependence of D_{SiH_4} to fit the experimental growth rate of silicon, (c) using the data of (a) and (b) to estimate reasonable values of α and m for SiCl_2 , (d) obtaining an estimate of the magnitude of K_{SiCl_2} from the closeness of the fit between experimental and calculated rates, and from the ratio of growth and etch rates.

Experimental

The conventional horizontal RF heated epitaxial reactor employed an 80 cm long quartz tube with rectangular cross section ($10 \times 2.5 \text{ cm}^2$), in which a SiC coated graphite susceptor was placed ($10 \times 24 \times 1.25 \text{ cm}^3$). The total hydrogen gas stream was kept at 75 l/min giving a stagnant layer thickness over the heated susceptor of about 0.30 cm at a mean gas temperature of 750°K (2).

The exhaust gas left the system via a water-cooled heat exchanger; the gas pressure in the system being 1 atm. Flow rates of SiH_4 , SiCl_4 , and HCl were controlled by calibrated flow meters. Ten silicon substrate slices of 38 mm diameter were placed on the susceptor in two rows. The slices were n -type, Sb -doped (0.007 ohm cm) with an orientation 3° from the (111) orientation in the direction of the nearest (110) (11). After slicing, the silicon substrates were lapped, etched and polished to a surface finish good enough to allow epitaxial growth, free of stacking faults without HCl etching prior to growth. By giving the susceptor a tilt of $1^{\circ}30'$ against the direction of gas flow the growth and etch rates over the length of the susceptor were kept constant to within $\pm 5\%$ excluding the first 4 cm of the susceptor. Prior to epitaxial growth the silicon slices were heated in H_2 at 1250°C for 15 min. Growth rates were obtained from measurements of epitaxial layer thickness by the infrared interference technique. A linear plot of layer thickness vs. growth time was found. In the thickness determination the ASTM correction for the phase shift at the interface between epitaxial layer and substrate was used (12). The temperature of the substrates were measured with an optical pyrometer, and the values were corrected for the emissivity of silicon and absorption of the quartz wall (13).

Results and Discussion

In Fig. 1 the growth rates from $\text{SiH}_4 + 4\text{HCl}$ in H_2 , SiCl_4 in H_2 , and SiHCl_3 in H_2 are given as a function of temperature. In the literature conflicting data are presented on the temperature dependence of the growth rate, but the results given here agree with those of Shepherd (1), Charig (14), and Oldham *et al.* (15). It will be noted that, in order to reach a growth rate of $1 \mu/\text{min}$, concentrations of about 0.1% for SiH_4 (10^{-3} mole $\text{SiH}_4/\text{mole H}_2$), 0.2% for SiHCl_3 , and 0.5% for SiCl_4 were required. In the high-temperature region the temperature dependence of the growth rates was small and the influence of concentration was great, as expected for a diffusion controlled reaction rate (Fig. 1, curves for SiCl_4 0.1% and 0.5%). At lower temperatures the temperature dependence was much greater, with surface reactions controlling the rate and the concentration dependence being much smaller.

The difference between the behavior of $\text{SiH}_4 + 4\text{HCl}$ and SiCl_4 indicates that equilibrium in the gas phase is not established, the differences in growth rate at the higher temperatures being of the order to be expected from the differences in diffusion coefficients of the re-

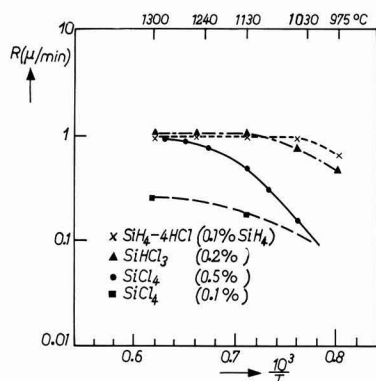


Fig. 1. Temperature dependence of the growth rate of epitaxial silicon layers from SiCl_4 , SiHCl_3 , and a mixture of $\text{SiH}_4 + 4\text{HCl}$ in H_2 . The concentrations indicated refer to mole percentages of the silicon compound in the gas phase.

acting silicon compounds. Gas phase reactions are expected to be nearly absent. This, however, does not exclude the possibility of equilibrium being reached at the solid-gas interface at the higher temperatures.

The temperature dependences of the reaction rates in the low-temperature region indicate that here the reaction rate was controlled by the rate at which surface reactions proceed, and not by mass transfer over the stagnant gas layer. The higher the chlorine content of the species the higher the temperature at which mass transfer became the dominant factor. For silicon growth from SiH_4 and for etching of silicon by HCl the temperature dependence of the reaction rates was small at temperatures from 1100° to 1300°C (16). This indicates that for both processes surface reactions are fast, and it can be assumed that in this range of temperatures equilibrium between solid and gas was reached. This means that for SiH_4 the surface concentration was practically zero and that for SiCl_2 , the main reaction product in etching, a concentration as given by [3] was reached.

Figure 2 shows the growth rate of silicon at 1150°C from mixtures of SiH_4 and HCl , the HCl concentration varies up to an HCl/SiH_4 ratio greater than 15 where etching of the substrates occurs. Growth rates from mixtures with an HCl/SiH_4 ratio of 3 and 4, corresponding to the stoichiometry of SiHCl_3 and SiCl_4 , respectively, are only 5-10% smaller than those for SiH_4 . The growth rate decreases proportionally to $(p_{\text{HCl}})^2$ and can be described by¹

$$G = 0.95 \times 10^3 p_{\text{SiH}_4} - 4.27 \times 10^3 (p_{\text{HCl}})^2 \mu/\text{min} \quad [6]$$

If gas phase reactions are absent, then SiH_4 and HCl are diffusing independently through the stagnant layer, transport of SiH_4 giving silicon growth, transport of HCl leading to the etching of silicon. The net result is the growth rate given in Eq. [6] and shown in Fig. 2. The etch rate of silicon deduced from [6] should have the same value as etching with HCl in H_2 without the presence of SiH_4 . In Fig. 3 the etch rate given by [6] is plotted as a function of the partial pressure of HCl , together with the etch rates for pure HCl in H_2 found by Spakovskis (17) in a comparable reactor.¹

The fit between the two curves is good; for low HCl concentrations the etch rate is proportional to $(p_{\text{HCl}})^2$, and for HCl partial pressures greater than 0.1 the etch

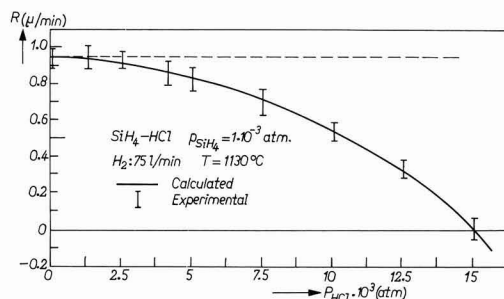


Fig. 2. Growth rate of silicon from mixtures of SiH_4 and HCl , the partial pressure of SiH_4 is kept constant at 1.10^{-3} (atm).

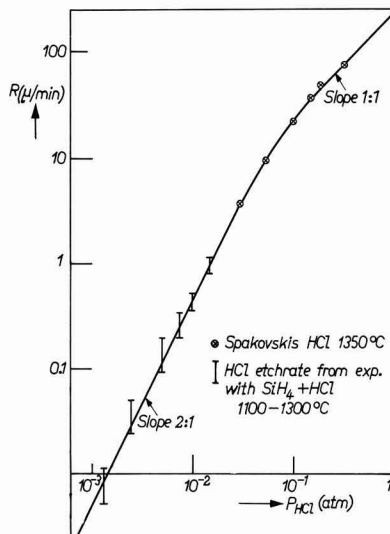


Fig. 3. Etch rate of silicon in $\text{HCl} + \text{H}_2$ as a function of the partial pressure of HCl . The low concentration values are from the present work, the high concentration values from Spakovskis (17). The curve gives a best fit of the experimental data to lines of slope 2:1 or 1:1 (see text).

rate is proportional to p_{HCl} . Here the assumption $p_{\text{H}_2} = 1$ in [3] is no longer valid, and the transport of HCl toward the interface is beginning to be rate controlling.

With Eq. [6], [11], and [12] it is possible to compare the experimental and the calculated results.

Introducing room temperature diffusion coefficients of SiH_4 and SiCl_2 of 0.60 cm^2/sec and 0.26 cm^2/sec , respectively (1), together with $\delta = 0.3$ cm, $T_s = 1500^\circ\text{K}$; $T_g = 750^\circ\text{K}$, $T_0 = 273^\circ\text{K}$, $R = 82$ cal/atm degree, and $K_{\text{SiCl}_2} = 1$ the calculated values of growth and etch rates are found to be

$$G = 2.57 \times 10^3 p_{\text{SiH}_4} \quad (\text{experimental value } G = 0.95 \times 10^3 p_{\text{SiH}_4}) \quad [7]$$

$$E = 1.10 \times 10^3 (p_{\text{HCl}})^2 \quad (\text{experimental value } E = 4.2 \times 10^3 p_{\text{SiH}_4}) \quad [8]$$

The calculated growth rate is nearly a factor of three higher than the experimental one, and the calculated etch rate is more than a factor of 3 lower than that found experimentally.

The silicon growth rate including thermodiffusion effects corresponding to the estimated value $\alpha_{\text{SiH}_4} = 1$ gives, according to the calculation in the Appendix [18].

¹ Another set of experiments in a comparable reactor gave

$$G = 0.7 \times 10^3 p_{\text{SiH}_4} - 3 \times 10^3 (p_{\text{HCl}})^2 \mu/\text{min}$$

From these results it can be seen that small differences in reactor geometry, temperature distribution, gas flow pattern, and boundary layer thickness cause differences in the absolute values of the growth and etch rates; the ratio between the values remaining about the same.

$$J = \frac{D_{\text{SiH}_4} \cdot p_{\text{SiH}_4}}{\delta R T_o^2} \cdot T_g \quad [9]$$

This gives a decrease in growth rate by a factor 1.43 compared with [11]. In the expression for D_{SiH_4} the temperature dependence is taken to be $D = D_o(T/T_o)^2$. Experimental and calculated results are brought into agreement if the exponent is taken to be 1.6 instead of 2.0. For SiH_4 , $\alpha_{\text{SiH}_4} = 1.0$ and $m = 1.6$ are selected, and for SiCl_2 $\alpha = 1.5$ and $m = 2$ are thought to be realistic values.

Introducing these quantities in the etch rate formula [17] gives an increase in etch rate by a factor of 1.64. To bring the experimental and calculated results into agreement an effective value of $K_{\text{SiCl}_2} = 2.4$ has to be taken, which is well within the possible limits.

In view of the accuracies involved it can be said that a reasonable fit is obtained and that the model used has been shown to yield a qualitative and semi-quantitative description of the epitaxial process.

Conclusion

Silicon growth rates from mixtures of SiH_4 and HCl can be interpreted in terms of a mutually independent growth of silicon from SiH_4 and an etching of silicon by HCl . Comparison of growth rates from mixtures of SiCl_4 in H_2 and $\text{SiH}_4 + 4\text{HCl}$ in H_2 indicates that gas phase reactions are slow, and that equilibrium between solid silicon and the gas phase is established.

Growth and etch rates calculated on the basis of a diffusion controlled model differ somewhat from the experimental results, the growth rates being lower and the etch rates being higher than those calculated from the model. Three possibilities to explain the differences are discussed: (i) thermiodiffusion in the steep temperature gradient over the silicon substrates; (ii) uncertainty in the temperature dependence of the diffusion coefficients giving rise to differences in the calculated growth rate by up to a factor of two; and (iii) uncertainty in the chemical equilibrium constant K_{SiCl_2} which gives the SiCl_2 concentration during HCl etching of silicon; K_{SiCl_2} at $1500^\circ\text{K} = 1.0 \pm 2.5$.

It is shown that the growth and etch rates may be explained by taking account of these three factors.

APPENDIX

The mass transfer of silicon in the diffusion controlled model is given by

$$J = \frac{G \cdot \rho}{6.10^5 M} = -D \cdot n \left[\frac{d \frac{n_1}{n}}{dy} \right] \quad [10]$$

G is the growth rate in μ/min , ρ is the density of Si in g/cm^3 , and M is the molecular weight of Si. It will be assumed that the temperature dependence of the diffusion coefficients is given by $D = D_o(T/T_o)^2$, $T_o = 273^\circ\text{K}$. For an ideal gas the total gas density $n = p/RT$ moles/ cm^3 , and in the open tube reactor $p = 1$ atm, and thus $n = (RT)^{-1}$ and $n_1/n = p_1$ (atm).

Furthermore, in the stagnant layer over the susceptor a linear temperature gradient gives

$$T = T_s - \frac{\Delta T}{\delta} \cdot y$$

where T_s is the surface temperature of silicon, T_g is the temperature of the main gas, $\Delta T = T_s - T_g$, δ is the thickness of the stagnant layer (cm), and y is the distance from the surface (cm). For $p_{\text{SiH}_4} = 0$ at the solid-gas interface the growth rate is found to be

$$G = \frac{7.2 \times 10^6 \cdot D_{\text{SiH}_4} \cdot p_{\text{SiH}_4}}{\delta R T_o^2} \cdot \frac{\Delta T}{\ln(T_g/T_s)} \quad [11]$$

The etch rate of Si by HCl , assumed to depend on the transport of SiCl_2 away from the substrate, gives

$$E = \frac{7.2 \times 10^6 \cdot D_{\text{SiCl}_2} \cdot p_{\text{SiCl}_2}}{\delta R T_o^2} \cdot \frac{\Delta T}{\ln(T_s/T_g)} \quad [12]$$

From [11] and [12] the ratio of growth and etch rates is found to be

$$\frac{G}{E} = \frac{D_{\text{SiH}_4} \cdot p_{\text{SiH}_4}}{D_{\text{SiCl}_2} \cdot p_{\text{SiCl}_2}} \quad [13]$$

Thermiodiffusion gives an additional concentration gradient in the temperature gradient over the substrates

$$\frac{d \frac{n_1}{n}}{dy} = K_T \frac{d \ln T}{dy}$$

With $K_T = \alpha n_1/n \cdot n_2/n$, $n_2 \approx n$ and 1 atm total pressure, $n_1/n = p_1$ (atm), this gives for the extra concentration gradient

$$K_T \frac{d \ln T}{dy} = \frac{\alpha p_1}{T} \frac{dT}{dy} \quad [14]$$

Equation [14] can be combined with [10] to include the effect of thermiodiffusion in the calculation of growth and etch rates.

$$J = -D n \left(\frac{d p_1}{dy} + \frac{\alpha p_1}{T} \frac{dT}{dy} \right) \quad [15]$$

with

$$D = D_o (T/T_o)^2 \text{ and } n = (RT)^{-1}$$

$$J = -\frac{D_o}{R T_o^2} (T d p_1 + \alpha p_1 d T) / dy$$

in the model

$$T = T_s - \frac{\Delta T}{\delta} \cdot y$$

then

$$J = -\frac{D_o}{R T_o^2} \left\{ \left(T_s - \frac{\Delta T}{\delta} \cdot y \right) \frac{dp}{dy} - \alpha p_1 \frac{\Delta T}{\delta} \right\} - \frac{J R T_o^2}{D_o} + \alpha p_1 \frac{\Delta T}{\delta} = \left(T_s - \frac{\Delta T}{\delta} \cdot y \right) \frac{dp}{dy}$$

integration gives

$$\int \frac{dt_1}{-\frac{J R T_o^2}{D_o} + \alpha p_1 \frac{\Delta T}{\delta}} = \int \frac{dy}{T_s - \frac{\Delta T}{\delta} \cdot y}$$

and

$$\ln \left(-\frac{J R T_o^2}{D_o} + \alpha p_1 \frac{\Delta T}{\delta} \cdot p_1 \right) = \ln \left(T_s - \frac{\Delta T}{\delta} \cdot y \right)^\alpha + c$$

for Si growth: at $y = 0$, $p_1 = 0$, $T = T_s$

$$\text{at } y = \delta, p_1 = p_{\text{SiH}_4}, T = T_g$$

$$J = \frac{D_{\text{SiH}_4} p_{\text{SiH}_4} \cdot \Delta T}{\delta R T_o^2} \cdot \frac{\alpha_1 T_g^{\alpha_1}}{T_s^{\alpha_1} - T_g^{\alpha_1}} \quad [16]$$

for Si etching: at $y = 0$, $p_1 = p_{\text{SiCl}_2}$, $T = T_s$

$$\text{at } y = \delta, p_1 = 0, T = T_g$$

$$J = \frac{D_{\text{SiCl}_2} \cdot p_{\text{SiCl}_2} \cdot \Delta T}{\delta R T_o^2} \cdot \frac{\alpha_2 T_s^{\alpha_2}}{T_s^{\alpha_2} - T_g^{\alpha_2}} \quad [17]$$

For $\alpha > 0$ the growth rate decreases and the etch rate increases. For SiH_4 the value of α is expected to be $\alpha_{\text{SiH}_4} = 1.0$ giving

$$J = \frac{D_{\text{SiH}_4} \cdot p_{\text{SiH}_4}}{\delta R T_o^2} \cdot T_g \quad [18]$$

For etching $\alpha = 1$ gives

$$J = \frac{D_{\text{SiCl}_2} \cdot p_{\text{SiCl}_2}}{\delta R T_o^2} \cdot T_s \quad [19]$$

For α values greater than 1 and $T_s \gg T_g$, Eq. [19] approximates to

$$J = \frac{D_{\text{SiCl}_2} \cdot p_{\text{SiCl}_2}}{\delta R T_o^2} \cdot \Delta T \cdot \alpha_2$$

directly proportional to the values of α and the temperature gradient over the slices.

The ratio of growth and etch rates, including thermally diffusion, from [16] and [17] is found to be

$$\frac{G}{E} = \frac{D_{\text{SiH}_4} \cdot p_{\text{SiH}_4}}{D_{\text{SiCl}_2} \cdot p_{\text{SiCl}_2}} \cdot \frac{\alpha_1}{\alpha_2} \cdot \frac{T_6^{\alpha_1} (T_5^{\alpha_2} - T_6^{\alpha_2})}{T_5^{\alpha_2} (T_5^{\alpha_1} - T_6^{\alpha_1})} \quad [20]$$

Manuscript submitted Jan. 5, 1970; revised manuscript received May 5, 1970.

Any discussion of this paper will appear in a Discussion Section to be published in the June 1971 JOURNAL.

REFERENCES

1. W. H. Shepherd, *This Journal*, **112**, 988 (1965).
2. F. C. Eversteyn, P. J. W. Severin, C. H. J. v.d. Brekel, and H. I. Peek, *ibid.*, **117**, 925 (1970).
3. S. Chapman and T. G. Cowling, "The Mathematical Theory of Nonuniform Gases," Cambridge University Press, London (1952).
4. R. F. Lever, *IBM J.*, **1964**, 460.
5. J. O. Hirschfelder, C. F. Curtiss, and R. B. Bird, "Molecular Theory of Gases and Liquids, J. Wiley & Sons, Inc., New York (1954).
6. K. E. Grew and T. L. Ibbs, "Thermomigration in Gases," Cambridge University Press, London (1952).
7. S. Chapman, *Proc. Roy. Soc.*, **A177**, 38 (1940).
8. Ref. (5) section 14.4.
9. H. Schäfer and J. Nickl, *Z. anorg. u. allgem. Chem.*, **274**, 250 (1953).
10. E. Wolf, *ibid.*, **313**, 228 (1961).
11. K. E. Bean and P. S. Gleim, *Proc. IEEE*, **57**, 1469 (1969); S. K. Tung, *This Journal*, **112**, 437 (1965).
12. ASTM F 95-68T.
13. F. G. Allen, *J. Appl. Phys.*, **28**, 1510 (1957).
14. J. M. Charig and B. A. Joyce, *This Journal*, **109**, 957 (1962).
15. W. G. Oldham and R. Holmstrom, *ibid.*, **114**, 381 (1967).
16. G. A. Lang and T. Stavish, *RCA Rev.*, **24**, 488 (1963).
17. V. Spakovskis, Private communication.

Anisotropy of Macrostep Motion and Pattern Edge-Displacements during Growth of Epitaxial Silicon on Silicon Near {100}

C. M. Drum and C. A. Clark

Bell Telephone Laboratories, Incorporated, Allentown, Pennsylvania 18103

ABSTRACT

For growth of epitaxial silicon by the SiCl_4/H_2 process onto silicon surfaces oriented from 0° to 9° off {100}, data are reported on the lateral motion of fabricated macrosteps ($\sim 500\text{\AA}$ high) and on the resultant displacement of shallow surface depressions bounded by the steps. The displacements ranged from less than a tenth of the layer thickness to greater than twice the layer thickness, depending on the surface orientation. The depressions mark the sites of localized n^+ diffused regions which become buried layers after epitaxy in the fabrication of integrated circuits. Step-broadening was found to be anomalously large for exact {100} surfaces for growth at 1215°C , whereas all orientations from 0° to 9° off {100} had similar step-broadening at 1240°C . At 1240°C , the displacement of the center of the depression relative to the center of the buried layer was a minimum for exact {100} surfaces. Both advancing and receding step-motion was found, and the symmetry of the step-motion was consistent with the crystal symmetry as previously reported for surfaces near {111}. A design graph is developed relating the necessary tolerance of substrate orientation near {100} to the desired epitaxial thickness and allowable alignment errors of masks during the fabrication of integrated circuits. For example, with an allowable $1\text{ }\mu\text{m}$ displacement and with $\leq 15\text{ }\mu\text{m}$ epitaxial thickness, the surface should be {100} within 10 min of arc, whereas up to 30 min off {100} is adequate for $\leq 2\text{ }\mu\text{m}$ displacement with a $7\text{ }\mu\text{m}$ epitaxial layer.

During the fabrication of p-n junction isolated integrated circuits with buried layers of n^+ material, epitaxial silicon is grown onto substrates whose surfaces contain an array of steps about 500\AA high. These macrosteps mark the positions of the buried layers, whose function is to reduce the collector series resistance (1, 2). During epitaxy, the steps may be displaced laterally, which can lead to errors in the alignment of subsequent masking operations. The reason for this is that growth at steps can be anisotropic whereas volume diffusion (the buried layer) is isotropic. It was previously reported that the exact substrate orientation near {111} has a considerable influence on the displacement of the steps (3, 4). Here we present new data on this effect for substrates oriented up to 9° off {100}. One purpose of this work was to establish tolerances on the substrate orientation for the control of the displacement.

Key words: epitaxial silicon, buried layers, step motion, integrated circuits.

The motion of steps during crystal growth has previously been studied for a variety of systems, with the usual point of view being that lateral motion of steps can be a basic part of the growth mechanism. Theoretical treatment is given by Burton *et al.* (5) and by Schwoebel and Shipsey (6). The present case is somewhat different in that we are dealing with fabricated steps of height equal to several hundred monolayers. There is evidence that spreading of monolayer steps does occur during the growth of epitaxial silicon near {111}, both for the cases of epitaxy by sublimation-condensation (7) and by chemical reaction (8, 9). For {100} epitaxial silicon, similar observations have not been reported. It is generally believed that the ideal {100} surface is rather rough structurally, hence should be expected to grow without the necessity of step-motion. However, the present work shows that the macrosteps can move considerably, and the relationship between the motions of macrosteps and the monolayer steps is yet to be established.

Experimental

The fabrication of the steps during integrated circuit processing was described previously (4). Briefly, windows are opened in an oxide on a p-type substrate using standard photolithographic techniques. Then n^+ regions are formed by diffusion, and a subsequent thermal oxidation causes growth of about 1000 Å of SiO_2 at the site of the diffusion. Removal of all the SiO_2 with HF leaves the silicon surface with an array of depressions bounded by steps which mark the sites of the n^+ regions. Then an epitaxial layer is grown, with thickness usually greater than a micron. The array of steps on the epitaxial surface will correctly identify the buried n^+ regions if the displacements of the steps during growth are taken into account. Epitaxial growth was by the $\text{SiCl}_4 + \text{H}_2$ process, with 1 m/o (mole per cent) of SiCl_4 . Temperatures were near 1200°C (after correcting for emissivity) as indicated in the data. Surface orientations were measured with Laue x-ray photographs and with x-ray goniometry (10).

Definitions

Characterization of the step-motion involves many geometrical variables such as surface orientation, step-orientation, sense of the step, and also growth temperature. Cross-sectional drawings for the case of n-type and p-type epitaxial layers are shown in Fig. 1, along with a drawing of the steps and buried layers as observed by interference contrast of angle-lapped sections. The coordinate system is chosen to be symmetrical, with origin at the center of the buried layer and with positive directions outward from the center. The displacements of the steps relative to the border of the stain are denoted X_R and X_L for the right- and left-hand steps, respectively; the detailed crystallographic meaning of these designations for the purposes of this paper is given by Fig. 2. For a deep (9 μm) diffused layer, X_R and X_L will each measure $\sim 9 \mu\text{m}$ prior to epitaxial growth. The most important quantity is the magnitude of the displacement of the center of the depression relative to the buried layer, given by

$$X_C = |(X_R - X_L)/2| \quad [1]$$

For a rectangular depression X_C can be measured for two independent directions in the plane of the surface. Perfectly symmetrical pattern-edge motion would give $X_C = 0$ in each case. For good results on registry of the next mask, X_C should be smaller than 2.5 μm . The over-all measurement error can be nearly 1 μm , however, since X_C for a slice prior to epitaxy was measured to be 0.7 μm . This is due to the fact that there is a finite width to the surface step and some uncertainty about the exact position of the edge of the stain. So a value of $X_C \leq 1 \mu\text{m}$ after epitaxy is about as low

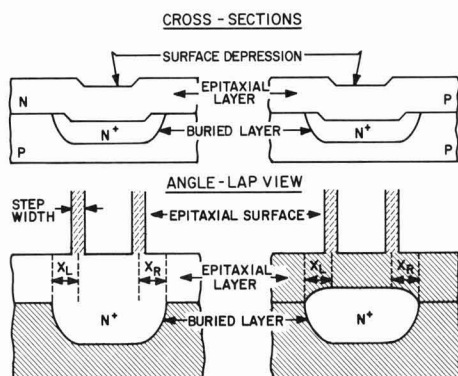


Fig. 1. Drawings of cross-section view and angle-lap view of n-type and p-type epitaxial layers with n^+ buried layers. The sense of X_R and of X_L is negative as shown.

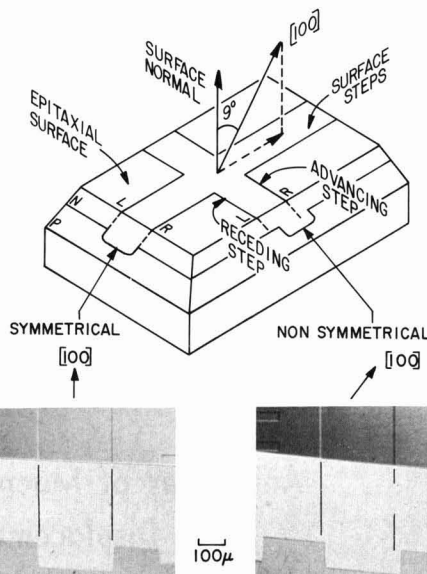


Fig. 2. Drawing of double-angle-lapped epitaxial layer, to illustrate orientation relationships used in this study.

as one can expect to measure. The sensitivity of the measurement (200X photograph, comparator) is about 0.5 μm .

The relationship of the steps to the crystal symmetry is important. We define the symmetrical case as that in which a mirror plane of symmetry in the lattice is normal to the surface and is also parallel to the macrosteps. This is illustrated by Fig. 3. Whatever crystal face is exposed by the left step, the same face will be exposed by the right step by symmetry. This is not true for the nonsymmetrical case illustrated in Fig. 3.

Results

One set of data on X_R , X_L , and X_C is plotted vs. substrate orientations from 0° to 9° off (100) toward

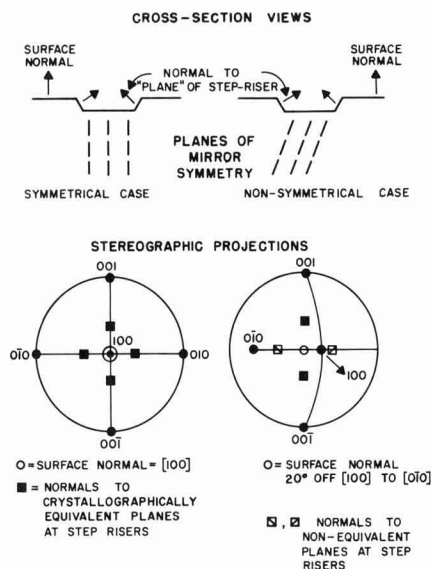


Fig. 3. Cross-section views and stereographic projections of the symmetrical case and the nonsymmetrical case.

a nearest {110}, in Fig. 4. For each surface with a pattern of rectangular depressions, data on the displacement were recorded for four edges of the depressions. We have deliberately oriented the surface and pattern so that one pair of these edges would always be the "symmetrical case" as in Fig. 3. For exact {100} surfaces, the other pair of edges would then also be the symmetrical case; the geometry is illustrated in Fig. 3 by a stereographic projection for surfaces $1^\circ \rightarrow 9^\circ$ off {100}, and the other pair of edges would be the nonsymmetrical case. The distinctions of symmetrical and nonsymmetrical are indicated in the data of Fig. 4. Four situations were studied, growth at 1215° and 1240°C , with and without HCl etching (1% HCl in H_2 , 2 min at 1250°C). Complete data from one set are given in Fig. 4. Data from the other sets show essentially the same features. In each case there was a marked effect of crystal symmetry. Even at 9° of {100}, X_C is very small for the symmetrical part but large for the nonsymmetrical part as illustrated in Fig. 2. Both portions of the patterns were symmetrical on the exact {100} and exhibited very small X_C . It should be noted that the positive displacements of Fig. 4 correspond to receding step-motion, illustrated in Fig. 2.

Further data were recorded for slices 0° , 0.5° , and 1° off {100}, as shown in Fig. 5. Each point is the average of several measurements. In spite of the scatter, the trend of larger X_C with larger misorientation is evident.

Data on the observed step widths are given in Fig. 6. The lower temperature (1215°C) leads to a broadening of steps only on the 0° to 0.5° off {100} surfaces, whereas all orientations had similar step-widths after growth at 1240°C . Larger step-broadening is undesirable since it is associated with imprecise definition of the boundary of the surface depression. This effect is illustrated in Fig. 7.

Further information of interest is obtained by plotting X_C vs. epitaxial thickness; this is shown in Fig. 8. Taking X_C to be ideally zero at zero epitaxial thickness, the data show that the displacement of the center is greater with increasing film thickness, but it is still less than $2\text{ }\mu\text{m}$ at $15\text{ }\mu\text{m}$ thickness for exact {100} surfaces.

A design graph (Fig. 9) can be constructed, to select orientation tolerances when desired values of X_C and epitaxial thickness are known. This information can be

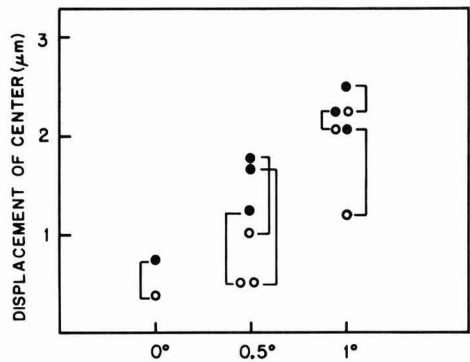


Fig. 5. Displacement data for surfaces 0° , 0.5° , 1° off {100}. Brackets indicate data from the same slice.

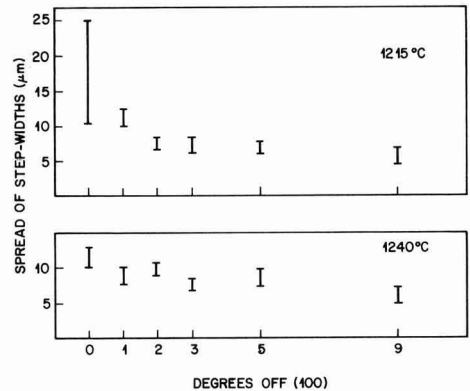


Fig. 6. Data on spread of step widths vs. angular orientation from {100}, in direction indicated in Fig. 2.

important when large quantities of material are being considered. Data with the greatest displacement have been used to construct Fig. 9, to give the greatest design safety.

To use the graph, one chooses the epitaxial thickness t and center displacement X_C . Let $t = 15\text{ }\mu\text{m}$, $X_C = 2.5\text{ }\mu\text{m}$. Find the point on the $t = 15\text{ }\mu\text{m}$ line with $X_C = 2.5\text{ }\mu\text{m}$, and note that the corresponding angle is 10 min off {100}. This means that surfaces $(100) \pm 10\text{ min}$ would be required. For another example, let $t = 7\text{ }\mu\text{m}$. For $X_C = 2.5\text{ }\mu\text{m}$, then the maximum allowed angular misorientation is 35 min . So $(100) \pm 35\text{ min}$ would be adequate. To make this graph reasonably complete, interpolated lines for 9, 11, 13 μm thickness are drawn. Actual data are used for 7 and 15 μm thicknesses. It may be argued that a limitation of these design data is that only one type of misorientation from {100} was studied. However, the region of interest is clearly from 0° to 1° off {100}, and in this region the distinction between the various ways of misorienting a surface off {100} is difficult to determine in practice.

From the previous data, it is predicted that pattern displacement would be very small for thin epitaxial layers. This has been confirmed by the data in Table I for p-type epitaxial layers on p-type substrate with n^+ buried layers.

Discussion

The data show that lateral motion of macrosteps can range from a negligibly small value up to several times the epitaxial layer thickness, depending on the orientations of the surface and of the steps. Also, the

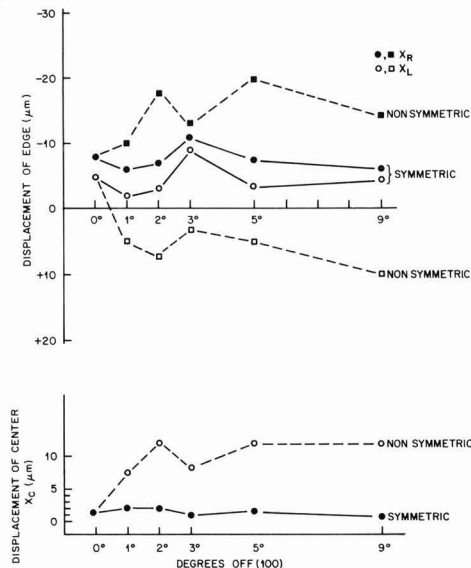


Fig. 4. Data for displacements on HCl etched, 1240°C , $14\text{ }\mu\text{m}$ n-type epitaxial layer. The direction of the misorientation is indicated in Fig. 2.

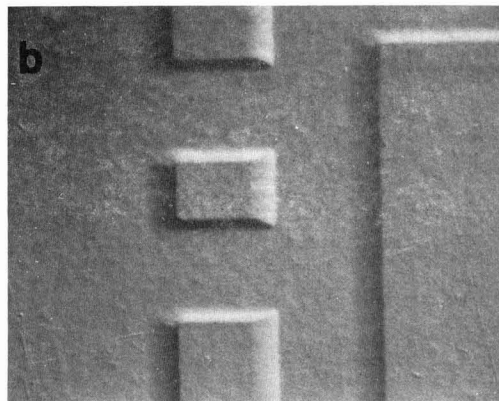
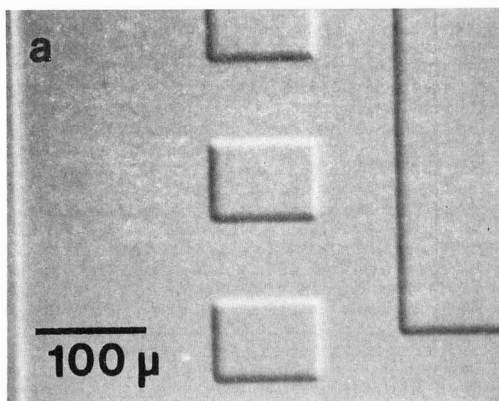


Fig. 7. Interference contrast photographs of $[100]$ surfaces after epitaxy showing: *a*, sharp steps, growth at 1240°C ; *b*, wide steps, growth at 1215°C .

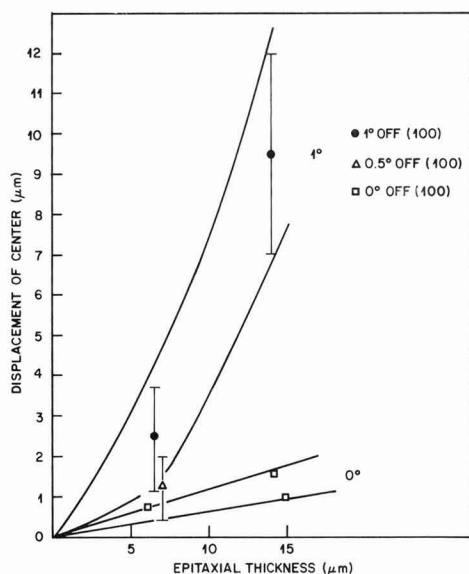


Fig. 8. Center displacement X_C vs. epitaxial thickness, growth at 1240°C .

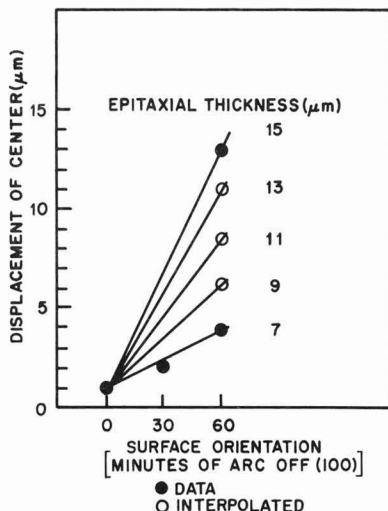


Fig. 9. Design graph for tolerance on surface orientation near $\{100\}$.

symmetry of the step-motion follows the symmetry of the lattice. In addition to the advance of steps across a surface, receding step-motion was also observed while at the same time vertical growth occurred on either side of the receding step. Each of the above results for $\{100\}$ was also found previously for substrates near $\{111\}$, but with the opposite effect that greater displacements occurred nearer $\{111\}$ whereas greater displacements occur farther from $\{100\}$ according to the present data.

The results provide information on the orientation tolerances, as given in Fig. 9. Furthermore, the results raise some more fundamental questions about the growth mechanism. One can ask how these steps would move as a function of step-height. Very small steps should approach the behavior of monolayer steps which may be fundamental to growth. Very large steps ($25\ \mu\text{m}$) have been studied by Runyan *et al.* (11), and the relationships between behavior of these various steps should be clarified. Very small steps can be fabricated by the present technique by reducing the oxide thickness, and 30\AA steps can be observed optically with interference contrast (12), so it should be possible to obtain data on the behavior of steps covering a wide range of heights.

Information on the behavior of the steps during epitaxy by other techniques such as molecular beam (13), evaporation, and silane decomposition should be useful. The receding motion of steps is apparently an unexpected etching effect which may be associated with the inevitable HCl by-product in the SiCl_4/H_2 system. Other growth systems should be helpful in clarifying this phenomenon.

To interpret the macrostep motion, it is tempting to start with a macroscopic model which assumed that an appreciable facet exists at the step-riser as drawn in Fig. 3, and that the end result depends primarily on the growth rates of the various exposed crystallo-

Table I

Epitaxial thickness (μm)	Orientation	X_C (for two directions) (μm)
4.1	181° off $\{111\}$ *	$<1, <1$
5.0	23° off $\{100\}$	$<1, <1$
3.2	19° off $\{100\}$	$<1, <1$
5.6	158° off $\{111\}$ *	1, 1.5
2.9	180° off $\{111\}$ *	$<1, <1$

* Toward a nearest $\{110\}$.

graphic planes. This model is unsatisfactory, since it does not explain (a) why the displacement is generally greater for larger misorientation from {100}, (b) why the lower temperatures cause step-broadening at {100}, or (c) why some receding step-motion occurs. This model might be more plausible if the data on growth rate vs. orientation showed a definite minimum at {100}, but this was not the case with the present study. Bean and Gleim (14) on the other hand do report a lower growth rate for {100} as opposed to 1.5° off {100}; as pointed out by Runyan (15) data from various experimenters seldom seem to agree on the numerical values of the growth rate.

An alternate model of greater complexity would involve a consideration of the atomic structure at the steps; the rate at which atoms could be attached to the various structures would then determine the resultant displacement. Edge effects, e.g., at the bottom of a step, would probably be important in this model, whereas the simpler macroscopic model would ignore what happens at such an edge. Either model is sufficient to explain the symmetry effect, since in each model the growth rate depends on the crystal structure. This implies that atoms are readily supplied to all possible growth centers by transport mechanisms, which may include surface diffusion as suggested by the work of Runyan et al. (11).

Manuscript submitted Feb. 2, 1970; revised manuscript received ca. July 9, 1970.

Any discussion of this paper will appear in a Discussion Section to be published in the June 1971 JOURNAL.

REFERENCES

1. K. E. Bean and W. R. Runyan, U.S. Pat. 3,379,584 (1968).
2. B. T. Murphy, V. J. Glinski, P. A. Gary, and R. A. Pedersen, *Proc. IEEE*, **57**, 1523 (1969).
3. D. W. Boss and V. Y. Doo, Ex. Abs. 186, Electronics Div., Vol. 15, No. 2, p. 59, Electrochem. Soc. Meeting, Philadelphia, Oct. 9-14, 1966.
4. C. M. Drum and C. A. Clark, *This Journal*, **115**, 664 (1968).
5. W. K. Burton, N. Cabrera, and F. C. Frank, *Phil. Trans. Roy. Soc. (London)*, **A243**, 299 (1950).
6. R. L. Schwoebel and F. J. Shipsey, *J. Appl. Phys.*, **37**, 3682 (1966).
7. H. C. Abbink, R. M. Broudy, and G. P. McCarthy, *ibid.*, **39**, 4673 (1968).
8. A. G. Revesz and R. J. Evans, *Trans. Met. Soc. AIME*, **230**, 581 (1964).
9. B. A. Joyce, J. H. Neave, and B. E. Watts, *Surface Science*, **15**, 1 (1969).
10. E. A. Wood, "Crystal Orientation Manual," Columbia Univ. Press, New York (1963).
11. W. R. Runyan, E. G. Alexander, and S. E. Craig, Jr., *This Journal*, **114**, 1155 (1967).
12. R. H. Dudley, *J. Appl. Phys.*, **35**, 1360 (1964).
13. B. A. Joyce and R. R. Bradley, *Phil. Mag.*, **14**, 289 (1966).
14. K. E. Bean and P. S. Gleim, *Proc. IEEE*, **57**, 1469 (1969).
15. W. R. Runyan in "Semiconductor Silicon," p. 169, R. R. Haberecht and E. L. Kern, Editors, Electrochem. Soc., New York (1969).

Doped Oxides as Diffusion Sources

II. Phosphorus into Silicon

M. L. Barry*

Research and Development Laboratory,
Fairchild Camera and Instrument Corporation, Palo Alto, California 94304

ABSTRACT

The diffusion of phosphorus from a deposited doped oxide into silicon has been found to be consistent with a previously derived model describing doped oxides as diffusion sources. Diffusion coefficients of phosphorus in both silicon and silicon dioxide have been measured in terms of this model over surface concentrations varying from 6×10^{17} to 2×10^{20} atoms/cm³ at diffusion temperatures of 1000°, 1100°, and 1200°C.

The use of doped oxides which have been deposited at low temperatures as diffusion sources adds considerable flexibility to the processing of semiconductor devices. Perhaps the greatest advantage over standard gas-phase doping techniques is independent control of the surface concentration over several orders of magnitude. Other advantages include better process control, adaptability to low defect processing, and the ability to control the final oxide thickness independently of the diffusion conditions. In addition, it is possible to make certain device configurations, such as self-aligned-gate metal-oxide-semiconductor transistors, or complementary MOS integrated circuits, which are very difficult with standard technology.

In an earlier paper (1), a model describing the diffusion of a dopant into a semiconductor from a doped oxide was presented and shown to describe reasonably well the case of boron diffusing into silicon. The purpose of this paper is to extend this model to the case of phosphorus diffusing into silicon and to report mea-

sured values of the constants of the diffusion. Interpreting these constants in terms of atomistic descriptions of the diffusion mechanism is not within the scope of the present paper.

Diffusion from deposited doped oxides has been reported fairly extensively (2-13), including several descriptions of the diffusion of phosphorus into silicon. However, values of the appropriate diffusion coefficients have not been reported in these papers over the range of temperature and concentration covered in the present work. The literature treating the diffusion process itself of phosphorus into silicon is very extensive and cannot be reviewed here.

Theory

The general one-dimensional case for diffusion of a dopant from a uniformly doped oxide of thickness $x_0 - x_B$ and initial concentration C_0 into a silicon substrate is shown in Fig. 1. Inclusion of an undoped oxide of thickness x_B , which acts as a barrier to diffusion, allows the measurement of the diffusion parameters of the dopant in the oxide; in actual device

* Electrochemical Society Active Member.

Key words: solid-state diffusion, semiconductor processing.

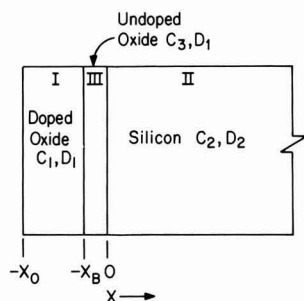


Fig. 1. Diffusion from a deposited doped oxide through a barrier oxide into a semiconductor substrate.

fabrication, this barrier oxide is normally reduced to a minimum. The diffusion equations in each region can be written

$$\frac{\partial C_i(x, t)}{\partial t} = D_i \frac{\partial^2 C_i(x, t)}{\partial x^2} \quad [1]$$

where the subscript i takes the value 1, 2, or 3 depending on the region. This formulation implicitly assumes that no field-aided diffusion terms are operating on ionized dopants and that ion-vacancy interactions can be ignored. The conditions under which these assumptions appear valid and the corrections to be made when they are not are discussed in a later section. The solution of Eq. [1] with the appropriate boundary conditions has been described in some detail in earlier work (1); suffice to say that when the thickness of the doped oxide is much greater than the diffusion length of the dopant in the oxide, the solution for the concentration in the silicon reduces to a simple form

$$C_2(x, t) = \frac{C_0 \sqrt{D_1/D_2}}{(1+k)} \operatorname{erfc} \left[\frac{x_B + mkx}{2\sqrt{D_1 t}} \right] \quad [2]$$

where t is the diffusion time; m is the segregation coefficient, or the ratio of the concentration of dopant in the silicon to the concentration in the oxide at the silicon-oxide interface; and

$$k = \frac{1}{m} \sqrt{D_1/D_2} \quad [3]$$

Determination of D_2 .—For the case of no undoped barrier oxide ($x_B = 0$), Eq. [2] reduces to the simple case of diffusion from a semi-infinite source into a semi-infinite sink, or a complementary error-function diffusion with an equivalent surface concentration C_s

$$C_s = \frac{C_0 \sqrt{D_1/D_2}}{(1+k)} \quad [4]$$

Thus, the surface concentration for this simple case is independent of time and depends on the initial concentration of dopant in the oxide, the square root of the ratio of the diffusion coefficients, and the segregation coefficient. Integration of Eq. [2] also leads to a simple expression for the sheet conductivity when $x_B = 0$ and the substrate resistivity is reasonably high (greater than 1 ohm-cm for this work)

$$I/V = 8.15 \times 10^{-23} \bar{\mu} C_s \sqrt{D_2 t} \quad [5]$$

where I/V is the inverse of the V/I commonly measured with a 4-point probe, $\bar{\mu}$ is the effective mean mobility of carriers, and the constant includes the electron charge, the spreading-current factor for the 4-point probe, and $2/\sqrt{\pi}$, a constant of the integration. It can also be shown for the case of no barrier oxide that the junction depth can be written

$$x_j = 2\sqrt{D_2 t} \operatorname{argerfc} \left[\frac{C_b}{C_s} \right] \quad [6]$$

where C_b is the bulk concentration of the substrate.

From Eq. [5] and [6], the junction depth and sheet conductivity should be linear functions of the square root of the diffusion time, and the slopes of the corresponding straight lines are measures of the diffusivity of the dopant in silicon

$$\sqrt{D_2} = \frac{1.23 \times 10^{22}}{\bar{\mu} C_s} \frac{d(I/V)}{d(\sqrt{t})} \quad [7]$$

$$\sqrt{D_2} = \frac{\frac{d(x_j)}{d(\sqrt{t})}}{2 \operatorname{argerfc} \left[\frac{C_b}{C_s} \right]} \quad [8]$$

If the surface concentration is greater than about 1×10^{19} atoms/cm³, it is possible to measure C_s by a plasma-frequency method; it is then possible to determine two independent values of D_2 from sheet conductivity and junction depth data. For low values of C_s , Eq. [7] and [8] can be combined, and self-consistent values of D_2 and C_s can be calculated.

Determination of D_1 .—Inclusion of an undoped barrier oxide as shown in Fig. 1 allows the measurement of D_1 , the diffusivity of the dopant in the oxide. If the subscript B refers to a wafer with a thin, undoped oxide of thickness x_B , and the subscript N refers to a wafer with no such barrier oxide, then Eq. [2] can be manipulated to show for a given C_0

$$\sqrt{D_1} = \frac{x_B}{2\sqrt{t} \operatorname{argerfc} \left[\frac{\bar{\mu}_N(I/V)_B}{\bar{\mu}_B(I/V)_N \sqrt{\pi}} \right]} \quad [9]$$

$$\sqrt{D_1} = \frac{x_B}{2\sqrt{t} \operatorname{argerfc} \left[\frac{(C_s)_B}{(C_s)_N} \right]} \quad [10]$$

$$\sqrt{D_1} = \frac{x_B \sqrt{D_2}}{(x_j)_N - (x_j)_B} \quad [11]$$

Thus, by measuring the differences in sheet conductivities, junction depths, and surface concentrations between wafers diffused with and without a barrier oxide, it is possible to determine D_1 by three independent measurements.

Determination of m .—In theory, the segregation coefficient can be determined from different variants of Eq. [2] once D_1 and D_2 are known and C_0 , the concentration of the dopant in the oxide, is measured (1). Numerically, however, m is calculated as the reciprocal of a small difference between two large experimentally determined numbers, and for the case of phosphorus the resulting uncertainties are large enough to render its calculation meaningless. This will be enlarged upon in a later section.

Experimental

The substrates used in this study were (111) silicon wafers, sliced from Czochralski-grown crystals, lapped on both sides, and mechanically and chemically polished on one side. The phosphorus doped oxides were deposited by oxidation of silane and phosphine at a substrate temperature of 400°C, and the diffusions were performed in dry nitrogen ambients at within $\pm 2^\circ\text{C}$ of the nominal diffusion temperature. The thickness of the doped oxide normally was 0.6μ . The

phosphorus concentration in the films was determined by a spectrophotometric analysis using films deposited simultaneously with those used for diffusion (14). The sheet conductivity was measured with a 4-point probe, and junction depths were measured using the Nomarsky interference technique after grooving and staining. The mean mobilities were calculated as a function of surface concentration by numerical integration of Irvin's conductivity mobility data (15) assuming complete ionization. The junctions were delineated by staining with a nitric-hydrofluoric acid solution (0.1:50:50 by volume of 70% HNO_3 :49% HF : H_2O). The surface concentration was determined from the minimum in the infrared reflection spectrum (plasma-frequency), using the curves of Gardner *et al.* (16) and corrected for shallow junctions by the method of Abe and Nishi (17). Ellipsometric methods were used to measure the thickness of the barrier oxides.

Results

Values of the diffusivity of phosphorus in silicon as determined by this technique are shown in Fig. 2 for surface concentrations ranging from 6×10^{17} to 2×10^{20} atoms/cm³ and temperatures from 1000° to 1200°C. For surface concentrations of 1×10^{19} atoms/cm³ and above, where C_s generally could be measured independently, the values of $\sqrt{D_2}$ measured by the sheet conductivity method are shown as closed points, while the values measured from the junction depth method are open points. For lower values of C_s , the calculated self-consistent values of $\sqrt{D_2}$ and C_s are shown as partially closed points. These data indicate that the diffusivity of phosphorus in silicon is relatively independent of C_s up to values of about 1×10^{19} atoms/cm³ and that it then increases with increasing concentration.

The reliability of these values of $\sqrt{D_2}$ has been estimated by geometrically combining the standard deviations or uncertainties of each of the factors entering into the calculations. The estimated accuracy of $\sqrt{D_2}$ as measured by the sheet conductivity method includes a 20% uncertainty in the measurement of C_s , a 10% uncertainty in the mean mobility, and a 1% relative standard deviation in the slope of the $I/V - \sqrt{t}$ curve (from a least-squares fit assuming no uncertainty in the diffusion time). These combine to yield a total uncertainty of about 25%; however, at high surface concentrations (over 1×10^{20}) the uncertainty in C_s reduced to about 10%, and the total uncertainty drops to about 15%. In a similar fashion, the $\sqrt{D_2}$ as measured by the junction depth method has an estimated uncertainty of less than 10%, primarily because it is relatively insensitive to values of C_s . As Fig. 2 shows, there is generally excellent agreement between values determined by the two tech-

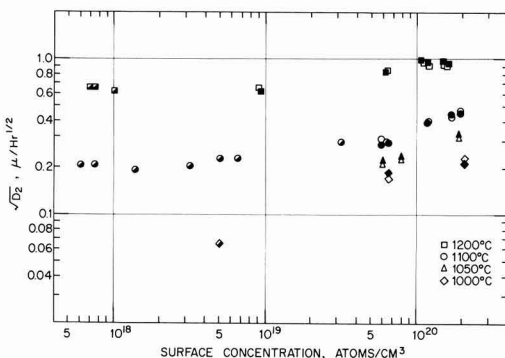


Fig. 2. Diffusion coefficients of phosphorus in silicon at various temperatures and surface concentrations.

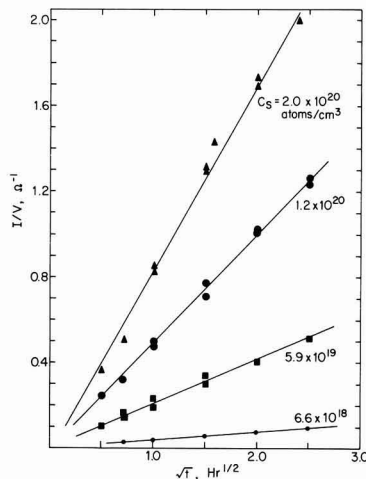


Fig. 3. Sheet conductivities resulting from diffusion of phosphorus into silicon at 1100°C from deposited oxides with different initial phosphorus concentrations.

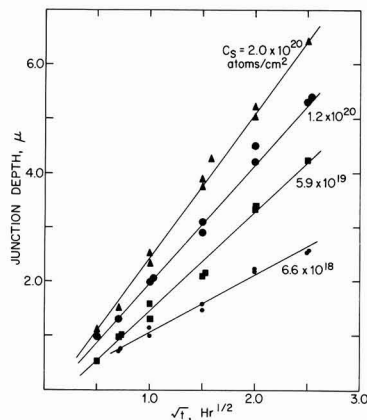


Fig. 4. Junction depths resulting from diffusion of phosphorus into silicon at 1100°C from deposited oxides with different initial phosphorus concentrations.

niques, and agreement between duplicate measurements also is good.

In the case of boron diffusing from a doped oxide at high surface concentrations ($C_s > 1 \times 10^{20}$ atoms/cm³), the sheet conductivity was found to be anomalously high at short diffusion times (1). This behavior appears to be absent in the case of phosphorus, as indicated by Fig. 3 and 4. The sheet conductivity, as shown in Fig. 3, is a linear function of \sqrt{t} at surface concentrations as high as 2×10^{20} ,¹ and it extrapolates properly back through the origin or to a very small intercept on the positive time axis. The junction depth is also linear in \sqrt{t} over all concentration ranges utilized. In addition, the surface concentration remains independent of the diffusion time in all these studies, as predicted by Eq. [4]. The surface concentrations of phosphorus in the silicon for various initial concentrations of phosphorus in the oxide are shown in Fig. 5.

¹ The upper limit of C_s in these experiments is controlled by a phase change of the doped oxide. At high phosphorus concentrations, the oxide appears to liquefy at the diffusion temperature, increasing $\sqrt{D_1}$ to a high value and thereby increasing C_s , as indicated by Eq. [4]. This phase change corresponds quite well to the phase diagram for $\text{SiO}_2\text{-P}_2\text{O}_5$ proposed by Tien and Hummel (18).

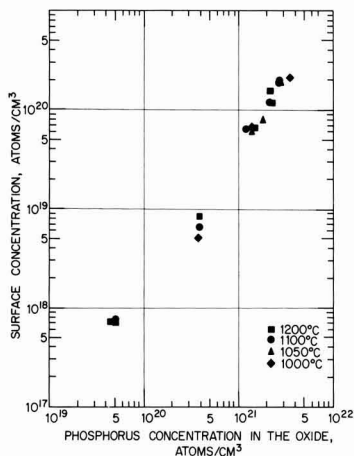


Fig. 5. Surface concentrations of phosphorus in silicon resulting from various concentrations of phosphorus in the deposited oxide.

Concentration profiles for diffusions from two different concentrations of doped oxide are shown in Fig. 6. These profiles were determined by measuring the sheet conductivity gradient normal to the wafer surface using the anodic oxidation technique of Tanenbaum (19). The deviation of the high surface concentration profile from the expected erfc relation is discussed in a later section.

The measurement of D_1 , the diffusivity of phosphorus in the oxide, is slightly more complicated than in the case of boron. Glasses containing more than about 2×10^{21} phosphorus atoms/cm³ dissolve the undoped barrier oxide at a finite rate at the diffusion temperatures, and this tends to obscure the diffusion process in the oxide. This case can be treated as diffusion from a moving boundary (20), but the experimental results do not justify the effort. This dissolution does not affect the measurement of $\sqrt{D_2}$, of course, wherein no barrier oxide is used. As a matter of fact, the dissolution of the very thin naturally occurring oxide on the silicon surface insures that the sheet conductivity and junction depth curves for high surface concentrations will pass through the origin rather than be shifted along the positive time axis, as may be the case for boron.

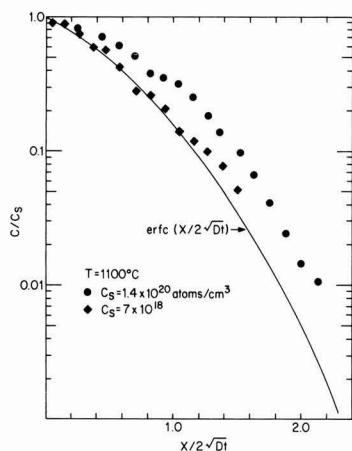


Fig. 6. Concentration profiles of phosphorus diffusing into silicon from deposited oxides.

For phosphorus concentrations below about 2×10^{21} atoms/cm³ in the oxide, the dissolution of the barrier oxide is negligible, and the diffusion coefficient can be measured. Figure 7 shows values of $\sqrt{D_1}$ at temperatures from 1050° to 1200°C. Because of the required low concentrations, determination of D_1 by differences in C_s (Eq. [10]) is not possible, but there is good agreement between the other two techniques. Of these, the method using differences in junction depths (Eq. [11]) appears most reliable. The sheet conductivity technique (Eq. [9]) involves estimating the effective mean mobility, and electron mobilities change quite rapidly with surface concentration in the region where these measurements are made. In addition, for much of the data the surface concentrations are too low to be measured directly; in these cases calculation of C_s , μ_s , and D_1 must be done by a reiterative procedure. On the other hand, measurement of D_1 by the junction depth method can involve taking small differences between two large numbers. Estimated uncertainties in these measurements vary from 10% at 1100°C to about 25% at 1200°C, and must be combined with the uncertainties in $\sqrt{D_2}$, since this quantity enters directly into the calculation of D_1 . As a result, values of $\sqrt{D_1}$ may be good only within $\pm 30\%$. Typical data for this technique are shown in Fig. 8.

As mentioned earlier, values of the segregation coefficient, m , are not reported here. The equations for

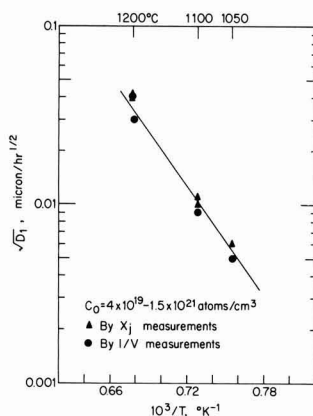


Fig. 7. Diffusion coefficients of phosphorus in SiO₂

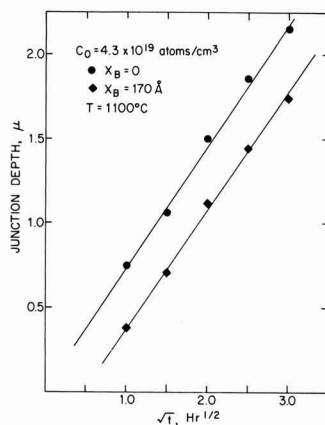


Fig. 8. Measurement of the diffusivity of phosphorus in oxide by the difference in junction depths after diffusion through a barrier oxide.

calculating m all have the form

$$m = \frac{1}{\frac{C_o}{C_s} - \sqrt{D_2/D_1}} \quad [12]$$

Since values of m are expected to be greater than unity (21), the denominator of Eq. [12] will be less than one. Since the ratios of C_o to C_s and $\sqrt{D_2}$ to $\sqrt{D_1}$ are typically in the range twenty to fifty, with sizable uncertainties, small differences between these ratios cannot be considered significant.

Discussion of Results

At high surface concentrations the diffusivity of phosphorus in silicon is not strictly independent of concentration, as has been assumed in this simple model. As can be seen from Fig. 2, there is a one-and-a-half- to threefold increase in $\sqrt{D_2}$ as the surface concentration varies from below 1×10^{19} to 2×10^{20} atoms/cm³, depending on the diffusion temperature. Effects that have been advanced to account for such an increase are the action of the self-induced field on the ionized impurities (22, 23) and an increase in the equilibrium lattice vacancy concentration (24-26). The first effect should result in a factor of 2 increase in D_2 as the dopant concentration becomes large compared to the intrinsic carrier concentration at the diffusion temperature. The vacancy mechanism should result in D_2 being nearly proportional to the dopant concentration at values well above the intrinsic carrier concentration.

Profiles for the low surface concentration diffusions agree within the accuracy of the profiling technique with the predicted complementary error function, as shown in Fig. 6. However, a higher surface concentration diffusion shows some deviation from the expected profile (the kinks in either curve are not significant experimentally). The non-normalized data for this second diffusion are plotted in Fig. 9 together with curves representing the expected behavior mentioned above, as interpolated from the curves of Hu and Schmidt (25). Curve A is the concentration profile predicted for this surface concentration if only field-aided diffusion terms are taken into account, while curve B shows the additional effect of the equilibrium vacancy terms. In both cases, the value of the intrinsic $\sqrt{D_2}$ has been

taken as $0.20 \mu/\text{hr}^{1/2}$, the apparent value of the low- C_s asymptote at 1100°C as shown in Fig. 2. As can be seen from Fig. 9, agreement of the data with either of these curves is worse than with the simple error function curve of Fig. 6. The curve that seems to fit the data best is that for field-aided diffusion using $0.40 \mu/\text{hr}^{1/2}$, the value of $\sqrt{D_2}$ which was actually measured for this diffusion assuming a simple erfc relation.

The proper interpretation of the high surface concentration data is not obvious, and as mentioned in the introduction, it is beyond the scope of this paper to discuss mechanisms of diffusion in silicon. The deviations of the concentration profiles from the expected values are not large, but are significant. On the other hand, there is excellent agreement between the values of $\sqrt{D_2}$ measured independently from both sheet conductivity and junction depth data, and this should not be the case for large deviations from the erfc relation. The conclusion drawn is that the low surface concentration values of D_2 are valid intrinsic diffusivities of phosphorus in silicon, while the values at high surface concentrations are effective diffusivities (averaged over some range of concentration) which adequately describe the diffusion characteristics.

A comparison is made in Fig. 10 of some of these data with that reported by other investigators. The values of the diffusivity presented here for high surface concentrations are lower in general than those reported by Mackintosh (27), but higher than those of Fuller and Ditzemberger (28). The apparent activation energy is lower for the high surface concentration diffusion than for the low surface concentration (2.6 eV compared to 3.7 eV), as predicted by the vacancy mechanism, but the difference is larger than that suggested by Hu and Schmidt (25).

Conclusions

Diffusion of phosphorus from a deposited doped oxide source is an attractive technique for fabricating both emitter and base junctions in silicon transistors because of the independent control of surface concentration over a wide range. The diffusion appears describable by a simple model, although there are small discrepancies in the concentration profiles at surface concentrations near 1×10^{20} atoms/cm³. Measurement of diffusivities of phosphorus in heavily doped oxides is complicated by the dissolution of the undoped barrier oxide used in this technique. However, values of the diffusivity of phosphorus in lightly doped oxides are measurable.

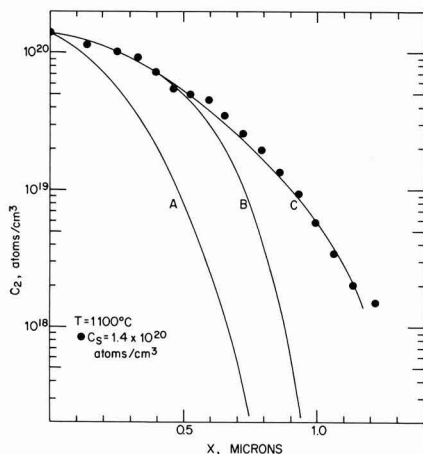


Fig. 9. Comparison of the concentration profile of phosphorus from a high surface concentration diffusion with profiles predicted for: curve A, field-aided diffusion only; curve B, field-aided plus equilibrium-vacancy diffusion; curve C, best fit by field-aided diffusion with $\sqrt{D_2} = 0.40 \mu/\text{hr}^{1/2}$.

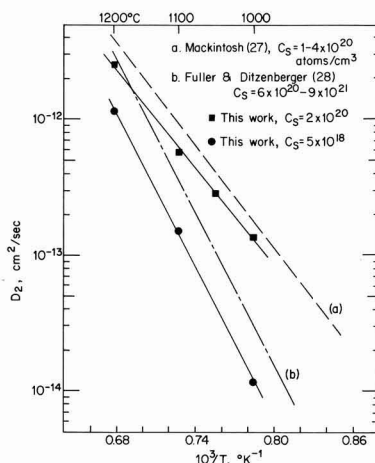


Fig. 10. Effect of temperature on the diffusion coefficient of phosphorus in silicon.

Acknowledgment

The author is indebted to Mrs. J. Bien for her assistance in the experimental part of this work, to R. Ceynowa for development of suitable techniques of chemical analysis, and to W. H. Shepherd for many technical discussions and much administrative support.

Manuscript received April 2, 1970.

Any discussion of this paper will appear in a Discussion Section to be published in the June 1971 JOURNAL.

REFERENCES

1. M. L. Barry and P. Olofsen, *This Journal*, **116**, 854 (1969).
2. P. F. Schmidt and A. E. Owen, *ibid.*, **111**, 682 (1964).
3. J. Scott and J. Omstead, *RCA Rev.*, **26**, 357 (1965).
4. P. F. Schmidt, T. W. O'Keefe, J. Oroshnik, and A. E. Owen, *This Journal*, **112**, 800 (1965).
5. W. von Meunch, *Solid-State Electron.*, **9**, 619 (1966).
6. D. L. Tolliver and D. L. Elgon, Paper 183 presented at the Philadelphia Meeting of the Society, Oct. 9-14, 1966.
7. T. L. Chu and G. A. Gruber, *Electrochem. Technol.*, **5**, 44 (1967).
8. D. B. Lee, *Solid-State Electron.*, **10**, 623 (1967).
9. A. E. Owen and P. F. Schmidt, *This Journal*, **115**, 548 (1968).
10. B. M. Mees, Paper 93 presented at the Boston Meeting of the Society, May 5-9, 1968.
11. K. Nagano, S. Iwauchi, and T. Tanaka, *Japan. J. Appl. Phys.*, **7**, 1361 (1968).
12. T. Abe, K. Sato, M. Konaka, and A. Miyazaki, Paper 184 presented at the Detroit Meeting of the Society, Oct. 5-9, 1969.
13. F. L. Gittler, Paper 182 presented at the Detroit Meeting of the Society, Oct. 5-9, 1969.
14. AASGP Committee Rept., *J. Am. Water Works Assoc.*, **50**, 1563 (1958), as modified by B. Yurash and R. Ceynowa, Fairchild Research and Development Laboratory.
15. J. C. Irvin, *Bell System Tech. J.*, **41**, 387 (1962).
16. E. E. Gardner, W. Kappallo, and C. R. Gordon, *Appl. Phys. Letters*, **9**, 432 (1966).
17. T. Abe and Y. Nishi, *Japan. J. Appl. Phys.*, **7**, 397 (1968).
18. T.-Y. Tien and F. A. Hummel, *J. Am. Ceram. Soc.*, **45**, 422 (1962).
19. E. Tannenbaum, *Solid-State Electron.*, **2**, 123 (1961).
20. C. T. Sah, H. Sello, and D. A. Tremere, *J. Phys. Chem. Solids*, **11**, 288 (1959).
21. A. S. Grove, O. Leistiko, and C. T. Sah, *J. Appl. Phys.*, **35**, 2695, (1964).
22. F. M. Smits, *Proc. IRE*, **46**, 1049 (1958).
23. S. Zaromb, *IBM J. Res. Develop.*, **1**, 57 (1957).
24. M. F. Millea, *J. Phys. Chem. Solids*, **27**, 315 (1966).
25. S. M. Hu and S. Schmidt, *J. Appl. Phys.*, **39**, 4272 (1968).
26. S. M. Hu, *Phys. Rev.*, **180**, 773 (1969).
27. I. M. Mackintosh, *This Journal*, **109**, 392 (1962).
28. C. S. Fuller and J. A. Ditzenger, *J. Appl. Phys.*, **27**, 544 (1956).

Electrical Characteristics of the Silicon Nitride-Gallium Arsenide Interface

J. E. Foster and J. M. Swartz

*The National Cash Register Company, Dayton, Ohio 45409
and The Ohio State University, Columbus, Ohio 43210, respectively*

ABSTRACT

The results of an investigation of the electrical characteristics of the silicon nitride-gallium arsenide interface as determined by capacitance-voltage (C-V) curves is presented and discussed. The Si_3N_4 was pyrolytically deposited from SiH_4 and NH_3 in the range 650°-750°C on n- and p-type, <111>, GaAs. A hysteresis of the C-V curve is noted; the amount of curve shift is shown to be heavily process dependent. Times involved in curve shift both with and without applied bias are given. Surface state density for the best sample is in the 10^{12} range.

In the rapid advance of the semiconductor industry over the last two decades, silicon has emerged as the most important material. Silicon can be purified to a very high degree by relatively simple methods so that high-purity material is readily available at low cost. In the 1960's, the III-V compounds have attracted increased attention. Of these materials, gallium-arsenide (GaAs) is the most serious competitor to silicon. The major advantages of GaAs over silicon as a transistor material are: (a) greater energy gap allowing operation at higher temperatures, (b) high electron mobility giving theoretically higher frequency response, and (c) a direct band gap providing much shorter recombination time. The materials technology of GaAs is, however, much more difficult than silicon. Because of the volatility of arsenic from the compound, refinement is much more difficult than for the elemental semiconductors. Only recently have such new technologies as liquid encapsulation (1) been developed. It is to be expected that, as research and de-

velopment continue on this important material, high-purity, economical substrates will be achieved.

In order to maximize drain current, transconductance, and operating frequency of an insulated gate field effect transistor (IGFET), it is desirable to have the largest possible value of effective channel conductance ($\bar{\mu}$) and also to use a gate insulator having a high dielectric constant (2). The value of $\bar{\mu}$ depends on the mobility, μ , of the substrate— $\bar{\mu}$ being typically one half that of μ . It has been widely recognized, therefore, that GaAs with its high electron mobility is potentially a better substrate material for FET's than silicon.

There has recently been a great deal of attention (3-35) focused on amorphous silicon nitride (Si_3N_4) as a passivating and masking film partly or fully replacing silicon dioxide. Silicon nitride is much more impervious to diffusants of all kinds than silicon dioxide. In addition, the use of silicon nitride as an insulator in a metal-nitride-semiconductor (MNS) FET increases the

transconductance and drain current compared to SiO_2 by 50% because of its higher dielectric constant.

A GaAs FET utilizing silicon nitride as the gate insulator would have considerable advantage over the silicon MOS-FET. Before such a GaAs metal-nitride-semiconductor (MNS) FET can be realized, however, a great deal of investigation into the Si_3N_4 -GaAs interface must be made. This paper gives the results of an investigation of the Si_3N_4 -GaAs interface with particular attention to those properties which would affect the achievability of a GaAs MNS-FET. The Si_3N_4 films were pyrolytically deposited from SiH_4 (silane) and NH_3 . Major emphasis was placed on p-material since an n-channel enhancement-mode device would be desired to utilize the high electron mobility of GaAs.

A hysteresis effect in the Si_3N_4 -Si system has been reported (18). This effect is also present in the Si_3N_4 -GaAs system as is shown.

The metal-insulator-semiconductor (MIS) capacitor was used as the principal device for this investigation. The theory of MIS capacitors has been presented by many authors (36-37) and hundreds of articles have been written on the metal-insulator-semiconductor system. An extensive bibliography has been given by Schlegel (38, 39).

Deposition and Measurement Techniques

Si_3N_4 deposition.—The vapor deposition of Si_3N_4 has been accomplished by the ammonolysis of both silicon tetrachloride and silane (7). The reaction between silane (SiH_4) and ammonia (NH_3) has been favored recently. Films deposited using SiH_4 and NH_3 are reported to be amorphous at deposition temperatures below 900°C (9) with deposition possible down to 650°C (11). The vapor pressure of As over GaAs is given for four-atom and two-atom molecules of arsenic vapor in the range $950^\circ\text{--}1200^\circ\text{K}$ by Drowart and Goldfinger (40). Using their results as a guide, it was anticipated that amorphous films of Si_3N_4 could be deposited at the low end of the SiH_4 - NH_3 temperature range (e.g., $650^\circ\text{--}750^\circ\text{C}$) without appreciable loss of arsenic from the GaAs surface.

Semiconductor-grade nitrogen used as a carrier gas was purchased from the Mineweld Company. The SiH_4 diluted with nitrogen (96% N_2 , 4% SiH_4) and the ultrahigh-purity (99.999%) NH_3 was purchased from Matheson.

A schematic of the deposition apparatus used is shown in Fig. 1. All tubing was Teflon; flow meters were stainless steel. A two-way valve allowed the NH_3 and SiH_4 to be turned from exhaust to the quartz reaction tube to start deposition. N_2 was allowed to flow to exhaust as well as through the quartz tube at all times when depositions were not being made. In this manner, the system did not have to be pumped down or otherwise purged.

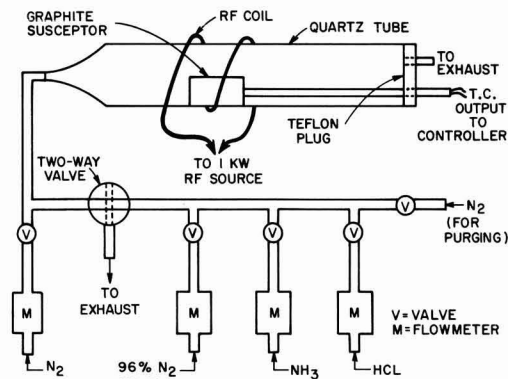


Fig. 1. Schematic representation of deposition apparatus

The quartz reaction tube was 30 mm ID. The susceptor was formed from a graphite cylinder 1 in. in diameter and $\frac{1}{2}$ in. long. The cylinder was cut in half (lengthwise) to form a 1 in. x $\frac{1}{2}$ in. horizontal surface upon which the sample was laid. A hollow quartz tube served as a handle for the graphite susceptor.

A thermocouple rod passed down the hollow quartz handle into the graphite susceptor. The leads from the thermocouple connected to a Research Inc., Thermac 6000 Temperature Controller. The controller output, by means of an interfacing circuit, controlled the d-c plate voltage of 1 kW, 475 kHz Ther-Monic induction heating unit.

Sample preparation.—The GaAs wafers used in this investigation were purchased from Bell and Howell Research Laboratories. Both n- and p-type wafers were 0.020 in. thick and $\langle 111 \rangle$ oriented. The n-type material was tellurium doped and showed an electron mobility of $6600 \text{ cm}^2/\text{V-sec}$ and a carrier concentration of $3.84 \cdot 10^{16} \text{ cm}^{-3}$ as determined by Hall measurements. Carrier concentration of the zinc-doped p-material was $1.4 \times 10^{17} \text{ cm}^{-3}$.

The wafers were hand lapped on an iron plate using 9μ aluminum oxide in an oil slurry to obtain a dull, smooth surface, then mounted on a polishing block and polished on a wheel covered with a polishing cloth (Buehler Ltd., No. 40-7618). A $\frac{1}{2}\%$ solution of bromine in methanol was dripped onto the cloth to effect the chemical polishing. This method of polishing GaAs was first reported by Sullivan and Kolb (41). The wafers were polished to a mirror finish, scribed by a diamond scribe, and broken into chips approximately $\frac{1}{4}$ in. square.

Final preparation included ultrasonic cleaning in trichloroethylene and acetone, rinsing in methanol, then rinsing in deionized water having a resistivity greater than 15 meg and etching for 20 sec in an etch consisting of HCl , H_2O_2 , and H_2O in volume ratio 3:1:1. The chips were again rinsed in the deionized water, blown dry with high-purity N_2 , and put on the graphite susceptor in the quartz tube of the rf furnace. N_2 flowed through the tube until the deposition temperature was reached, at which time the SiH_4 and NH_3 gases were switched to the tube to begin the deposition. The color changes were clearly visible as the Si_3N_4 deposited. Nearly all samples tested had film thickness in the 850-1050 Å range (dark blue to blue).

After deposition of the Si_3N_4 , aluminum dots were evaporated onto the chip through a metal mask. The dots were nominally 10 and 20 mils in diameter. The aluminum was approximately $10,000 \text{ Å}$ thick.

Since C-V measurements were to be made on the MNS (metal-nitride-semiconductor) capacitors, a contact resistance at the substrate (i.e., the back contact) of less than 100 ohms was adequate. Indium was applied to the back of n-type chips with a soldering iron. This gave a contact resistance of less than 10^{-3} ohm-cm^2 . An alloy of 30% Ag-70% Ga was used on the back surface of p-type chips. This alloy could be applied to the chips with a soldering iron, and gave a contact resistance of 20-50 ohms.

C-V measuring techniques.—The chips were placed on the stage of a micromanipulator for making the C-V tests. The stage was gold plated and provided the electrical contact to the substrate. A 0.010 in. beryllium-copper wire probe made contact to the aluminum dot field plate.

Leads from the probe station were connected to the appropriate test instrument. Most measurements were made with a Boonton Electronics Model 75C Capacitance Bridge which has a frequency range of 5-500 kHz. Measurements at higher frequencies were made on a modified Boonton Type 250A RX Meter which has a frequency range from 0.5 to 250 MHz.

Experimental Results

An overview.—Table I gives the results of a preliminary test on several n-type samples at different

Table I. Etch rate, dielectric constant, and maximum field strength of Si_3N_4

Flow rate of NH_3 (cc/min)	Vol ratio NH_3 to SiH_4	Etch rate (Å/min)	ϵ_r	Max field strength (V/cm)
18	5:1	300-350	7.9	5×10^6
30	25:1	800-1000	6.3	9×10^6
60	62.5:1	800-1000	6.2	1.1×10^7
290	80:1	800-1000	6.1	2.9×10^7
290	121:1	800-1000	6.15	2.8×10^7

NH_3 to SiH_4 ratios. Deposition temperature was 725°C with an N_2 carrier flow of $5 \text{ ft}^3/\text{hr}$. The etch test was made in 49% HF acid at room temperature. The relative dielectric constant given in the table is the average of 3 to 5 samples.

Thickness was measured by interference fringes and by means of a Bausch and Lomb Spectrophotometer (Model 505). Only a slight difference is seen in the etch rate, dielectric constant, and maximum field strength for films deposited with NH_3 to SiH_4 ratios of 25 to 1 or greater. The relative dielectric constant appears to decrease somewhat and the field strength increases as the NH_3 : SiH_4 ratio increases—both effects saturating at high ratios. The film deposited at 5:1, however, shows a distinct difference in all three parameters. Other workers (6, 7, 10, 31) have reported Si_3N_4 films deposited at $900^\circ\text{--}1100^\circ\text{C}$ on silicon to have etch rates of 150-300 Å/min in 49% HF. Their results also show higher etch rates for lower deposition temperatures. The etch rates of 800-1000 Å/min given here for a deposition temperature of 725°C are in good agreement with their findings. The relatively low etch rate of 300-350 Å/min for the 5:1 film suggests that this film contains excess silicon. This agrees also with the conclusion of Bean *et al.* (9) that a 5:1 ratio is silicon rich. It is interesting to note that Saxena and Thal (26) reported etch rates of 350 Å/min with films deposited at 400°C from NH_3 and SiH_4 in a glow discharge. The ratio of NH_3 to SiH_4 was not reported, however. The higher dielectric constant and lower field strength for the 5:1 film here also would seem to support the conclusion that the film is silicon rich.

The C-V curves obtained on p-substrates showed two prominent characteristics, presence of fast surface states and a field-induced hysteresis. The presence of fast surface states is indicated by the curves of Fig. 2. For this sample, a test frequency of 1.5 MHz was required to "freeze out" the fast states, frequencies above 1.5 meg yielding the same curve. Zaininger (42) has outlined a method of determining the effective density of surface states which can respond to frequencies up to that of the test signal. The intent here is to point out that the energy distribution and frequency response of these fast states is affected by the NH_3 : SiH_4 ratio. The NH_3 to SiH_4 ratio for the sample of Fig. 2 was 25:1; at higher NH_3 to SiH_4 ratios, the frequency

response of the fastest states decreased until at a ratio of 55:1 the surface states for good samples could not follow a 500 kHz signal (Fig. 3). A comparison of Fig. 2 and 3 shows, moreover, a difference in the energy position of those states which could respond to 100 kHz but not 500 kHz. In Fig. 2, the greatest difference between the 100 and 500 kHz curves is in the inversion region. In Fig. 3, however, the greatest difference between the 100 and 500 kHz curves lies in the accumulation and depletion regions. This indicates that, whereas the fastest states lie near or above midgap (the inversion position of the Fermi level) for the sample of Fig. 2, they lie in the lower half of the band gap (the depletion and accumulation position of the Fermi level) for the sample of Fig. 3. A frequency of 500 kHz was sufficiently high to freeze out all fast states for nearly all films deposited at NH_3 to SiH_4 ratios of 55:1 or greater. The curves of Fig. 3 are shifted toward more negative voltages than the curves of Fig. 2. This shift was found to be generally true as the NH_3 to SiH_4 ratio was increased.

Depositions on n-type substrates were made only at 700°C with NH_3 : SiH_4 ratios ranging from 25 to 121 to 1. These samples also show a very large effect of fast surface states. Figure 4 shows a sample for which a frequency of 1.5 meg was required to "freeze out" the fast states. The flat band voltage is $+20\text{V}$. As in the case of p-type samples, depositions made at high NH_3 to SiH_4 ratios (62.5 and above) gave surface states that could not respond at 500 kHz. Figure 5 shows C-V curves for six representative samples taken at 1.5 MHz. There is considerable difference in samples deposited at the same NH_3 to SiH_4 ratio as for examples N30 and N33. N-type samples showed much poorer repeatability than p-type samples. Flat band voltages for most samples were greater than 22V —cor-

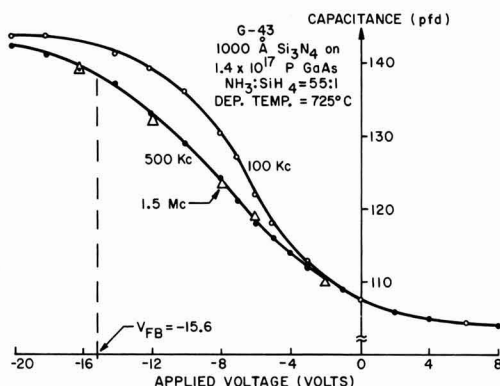


Fig. 3. C-V curves showing fast states in depletion region.

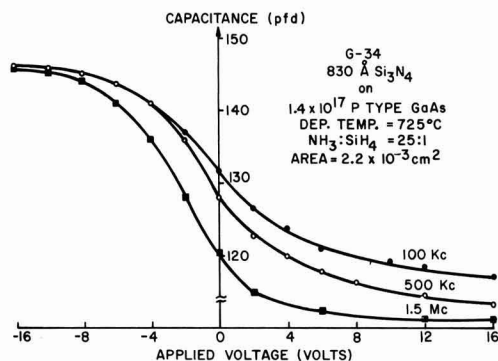


Fig. 2. C-V plot showing fast states

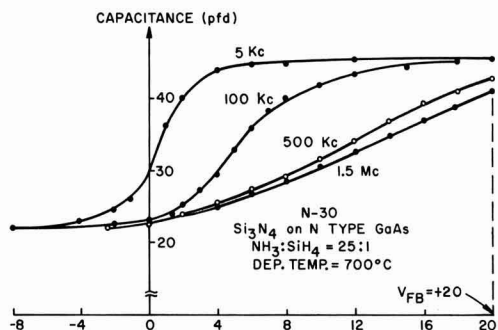


Fig. 4. C-V curves for n-sample showing effect of fast surface states.

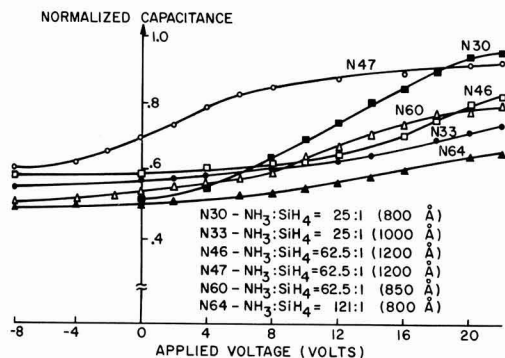


Fig. 5. Normalized C-V curves for samples on n-substrates

responding to field strengths greater than $2-3 \times 10^6$ V/cm.

The Fermi level for the p-substrates lies very close to the valence band (within 0.1 eV) so that at flat band most of the energy gap lies above the Fermi level. For the n-substrates, the Fermi level is about 0.125 eV below the conduction band, so that most of the energy gap is below the Fermi level at flat band. For n- and p-type samples processed in the same manner, the ionic contamination should be similar. Any significant difference in flat band voltage beyond that due to ϕ_{MS} (difference in metal, semiconductor work functions) should, therefore, reflect the nature of the surface states. The C-V curves for n-substrates are shifted to the right giving positive flat band voltages in contrast to negative flat band voltages for p-type samples. This strongly suggests that the surface states are negative when below the Fermi level, thus accounting for the difference between the curves on p- and n-substrates. The positive charge causing the shift of C-V curves on p-substrates must, then, be accounted for by traps that are positive when empty.

The hysteresis effect.—Figure 6 shows a C-V plot made on an x-y plotter. The voltage sweep was 5 V/sec so that both curves were swept out in about 15 sec. The curve swept from left to right lies some 8V to the left of the return sweep. This field-induced hysteresis has been reported in the case of Si_3N_4 deposited on Si (17, 18) and is also present for the Si_3N_4 -GaAs system.

The displacement of the two curves indicates either a transfer of charge across the Si_3N_4 -GaAs interface, or a movement of charge within the Si_3N_4 . The direction of the curve shifting is, however, in the wrong direction to be explained by movement of charge within the Si_3N_4 . It must be concluded that charge moves across the semiconductor-insulator interface and is trapped. The direction of the curve shifting as well as the recovery times involved can be explained, at least in a qualitative way, by such a trapping model. Herman and Warfield (43) have treated the effects of traps in the MOS structure. Ross and Wallmark (44) have dealt with trapping in the metal- Si_3N_4 , SiO_2 -silicon

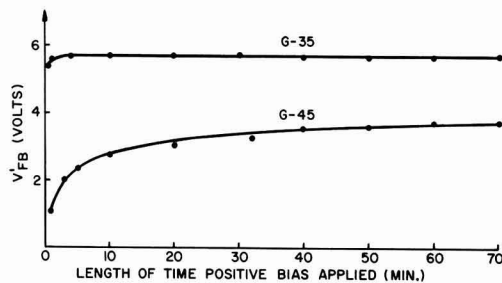


Fig. 7. Shift of flat band voltage by positive bias

system. The difficulty in obtaining a quantitative model lies in the fact that no method has yet been devised to determine both the spatial and energy distribution of the traps.

Figure 7 shows the "trap filling" response for two p-type samples having Si_3N_4 thicknesses of 850 Å. A 20V bias was applied and the capacitance at flat band, which had previously been determined, was used as an indication of curve shift. The application of the bias was interrupted at each test point for about 10 sec in order to determine how much the flat band voltage (i.e., the voltage required to yield flat band capacitance) had shifted. Whereas sample G-35 reached equilibrium in about 2 min with a shift of 5.7V, G-45 reached a shift of only 3.7V after an hour. G-35 was deposited at a $\text{NH}_3:\text{SiH}_4$ ratio of 49:1 at 725°C, whereas G-45 was deposited at a 62:1 ratio at 700°C. It can be concluded that, whereas G-35 has a relatively high density of traps near the interface (i.e., within the tunneling distance) and/or the traps have a large electron capture cross section so that equilibrium is soon reached, G-45 has a lower density of states near the interface so that when equilibrium is finally reached the shift in flat band voltage is less.

The filling of traps involves electrons crossing the semiconductor-nitride interface and being captured by traps, which accounts for the right-most curve of Fig. 6. As the bias voltage sweeps out to +20V traps fill, so that the return path is displaced to the right indicating a net increase of negative charge at the interface.

The complementary part of the cycle is completed as the bias swings negative. The bias is then in a direction to raise the energy levels of the traps causing trapped electrons to tunnel back to the semiconductors. As the bias is swept negative to -20V, traps empty as electrons tunnel back to the semiconductor. The subsequent sweep from left to right is displaced to the left, indicating a net gain of positive charge.

In addition to the emptying of those traps which at flat band lie above the Fermi level, it is possible that some traps which are below the flat band Fermi level also empty as they are raised in energy by the negative bias. When the negative bias is released, these latter traps must fill before equilibrium is again achieved.

Establishing an equilibrium condition.—The discussion above has pointed out the nature of the hysteresis cycle—filling of traps with positive bias, emptying of traps with negative bias. Before quantitative measurements could be made on the samples, however, it was necessary to establish an equilibrium or reference condition. In particular, the "zero bias, equilibrium capacitance" (ZBEC) would be the value of capacitance at zero bias when the sample is in complete thermal equilibrium. Any procedure outlined for returning the sample to the ZBEC¹ should be repeatable. Such a procedure can be drawn up only after examination of the relaxation times involved in returning the sample to equilibrium.

¹ The term ZBEC will be used interchangeably to denote "zero bias equilibrium capacitance" and "zero bias equilibrium condition." The meaning should be clear from context.

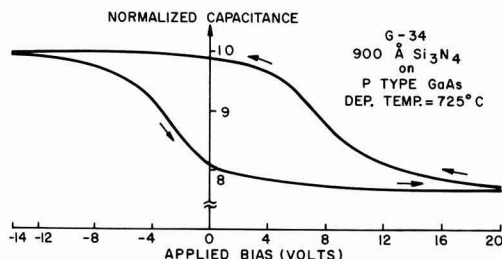


Fig. 6. C-V curves showing hysteresis

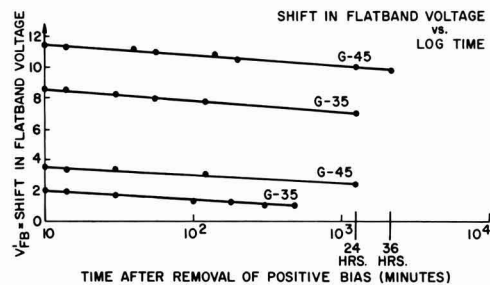


Fig. 8. Relaxation after filling of traps by positive bias

Figure 8 shows relaxation curves for two p-samples after removal of positive bias. The two curves for each sample result from a difference in the initial shift before relaxation. V'_{FB} represents the change in flat band voltage from its value prior to application of the positive bias.

It is apparent from the straight line plots of Fig. 8 that

$$\Delta V'_{FB} = -A \log t$$

with A in the range 0.5-0.7 for t in minutes. All samples tested showed similar relaxation curves. There was no apparent correlation between the $\text{NH}_3:\text{SiH}_4$ ratio and the value of A . The relaxation of filled traps is very slow. For an initial shift of 6V in flat band voltage, and using a value of 0.6 for A , 10^{10} min would be required for relaxation back to equilibrium. This is nearly 20,000 years.

In contrast to the extremely long time required for the traps to empty with no applied bias, they could be emptied in a short time by the application of a negative bias. A typical plot of this resetting of V'_{FB} as a function of time is shown in Fig. 9. Notice that V'_{FB} does not return to zero but goes to negative values. In terms of the C-V plot of Fig. 10, the following sequence has occurred:

1. Starting at "equilibrium" curve A, a positive bias is applied which shifts the curve to the position marked B as traps fill.

2. A negative bias is applied which moves the curve from B to C, overshooting the equilibrium position A.

In going from position B to C, not only have the traps that were filled by application of the positive bias been emptied, but also some traps which are filled in the equilibrium condition have been emptied. It is to be expected that these latter traps would fill exponentially, the dominant process being described by

$$\frac{dn_t}{dt} = A n (N_t - n_t)$$

where n_t is the density of filled traps, N_t is the total density of filled traps at equilibrium, n is the density of conduction band electrons, and A is a capture con-

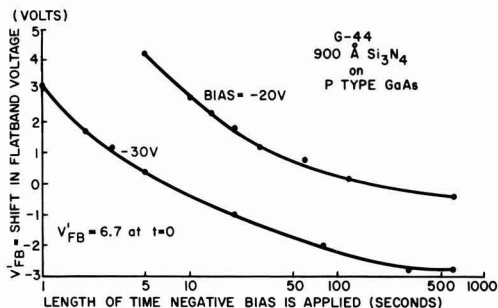


Fig. 9. Re-emptying of traps by application of negative bias

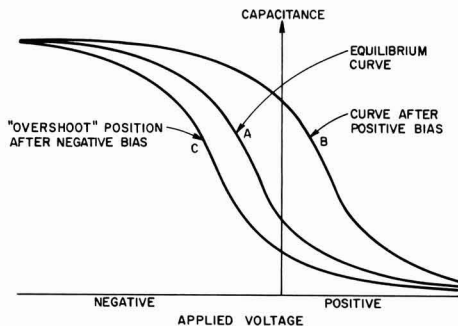


Fig. 10. Shift of C-V curve shift with positive and negative bias.

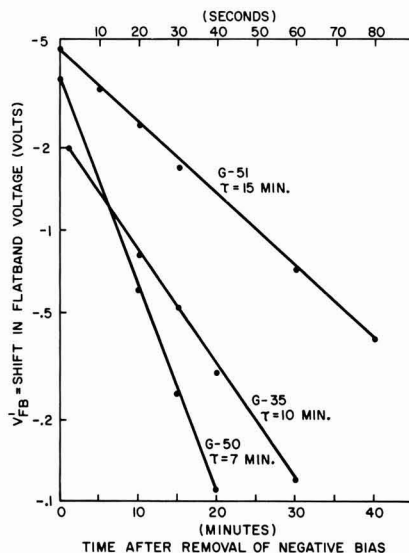


Fig. 11. Filling of traps after removal of negative bias

stant. Figure 11 shows this recovery for three samples. The shift in flat band voltage is given by

$$V'_{FB} = V_0 e^{-t/\tau}$$

Typical values for τ are 5-15 min for the samples in the dark.

At this point a procedure for establishing a ZBEC can be given:

1. Apply a negative bias for 5 min. A bias of -30V for Si_3N_4 films in the 850-1000Å range is adequate. All traps above the flat band Fermi level will empty, as will some traps below the flat band Fermi level.

2. Remove all bias for 45 min to allow traps below the Fermi level to fill.

Effects of $\text{NH}_3:\text{SiH}_4$ ratio on hysteresis.—A detailed investigation was made to determine how the hysteresis varies as the $\text{NH}_3:\text{SiH}_4$ ratio is changed. Over a hundred samples were investigated. The zero bias equilibrium capacitance (ZBEC) was carefully established for each sample as outlined above. Using this capacitance as a reference, a positive bias was first applied to the sample and the voltage (V_0') required to again achieve the reference capacitance was noted. This cycle was repeated for a given positive bias until no further voltage shift was obtained. In this manner, the amount of shift in the C-V curve for a given bias was found. The flat band capacitance could have been

used as the reference point, but the ZBEC was more convenient since it could be found directly by measurement.

Figure 12 shows the shift in C-V plot, as determined by monitoring the voltage (V_o') required to obtain the ZBEC, as a function of bias for seven representative p-type samples. Film thickness for all samples was $900\text{\AA} \pm 10\%$. The samples can be divided into two groups, those deposited at $\text{NH}_3:\text{SiH}_4$ ratios above or below about 50:1. Samples deposited at ratios below 50:1 show a relatively large amount of shift at low bias with the rate of shift reducing at higher bias. Samples deposited at ratios above 60:1 show the reverse effect, i.e., lower shift at low bias and a great deal of shift as the bias voltage was increased. A ratio of about 55:1 gave a nearly linear plot—intermediate to the two groups.

The above grouping was independent of deposition temperature over the temperature range $700^\circ\text{--}725^\circ\text{C}$. It was found, however, that depositions at 725°C at ratios above 60:1 did not give good C-V plots. Little or no change in capacitance vs. bias was found, although the films had good physical appearance and good field strength ($> 10^7$ V/cm). Judging from the thickness of the films, the capacitances were always low. This indicated that the samples were so heavily inverted that it was impossible to achieve accumulation. Reducing the temperature to 700°C gave good curves at high ratios.

Looking at Fig. 12 in greater detail, it is clear that processing has a very pronounced effect on the density of traps as a function of distance from the insulator-semiconductor interface. Samples G-25, G-26, G-34, and G-35 exhibit 2-3 times as much shift as the other samples at a bias of 10V. Since the bias at each value was repeatedly applied until no more shift was obtained, it must be concluded that G-25, G-26, G-34, and G-35 have a much greater density of traps within the tunneling distance than do the other samples. This is also in agreement with the discussion relating to Fig. 7 above where it was concluded that G-35 had a much higher density of traps near the interface than G-45. At higher bias ($> 25\text{V}$), samples G-26, G-34,

and G-35 show a decreasing amount of shift—indicating a decreasing density of traps.

Samples G-45, G-49, and G-50 show an increasing amount of shift with increasing bias. At high bias, the slopes of these curves approach unity. These samples appear to have a high density of traps at greater distance from the interface.

Depositions were made on p-substrates from 650° to 725°C at $\text{NH}_3:\text{SiH}_4$ ratios ranging from 25:1 to 300:1. Best results were obtained at a $\text{NH}_3:\text{SiH}_4$ ratio of about 60:1 at 700°C . These samples show low hysteresis at fields below $2\text{--}3 \times 10^6$ V/cm. Higher $\text{NH}_3:\text{SiH}_4$ ratios (up to at least 121:1) give about the same amount of hysteresis at low fields, but the C-V curves for these samples are increasingly shifted toward negative voltages. Figure 13 shows the improvement in hysteresis at low fields ($< 3 \times 10^6$) for one of the best p-type samples (G-45) processed at 700°C at a $\text{NH}_3:\text{SiH}_4$ ratio 62:1 over the best sample (G-35) obtained at 725°C . Both curves were made at 100 kHz on an x-y plotter.

Although the C-V curves for n-type samples are quite different from those for p-type samples, the hysteresis effect is very similar. As for p-samples, the C-V curves for n-samples show the effect of trap filling and emptying. Application of positive bias results in a shift of the C-V curve toward more positive voltages. The relaxation (trap emptying) with no bias applied was again found to be logarithmic with time. A relaxation rate of 0.5-0.6 V/decade in excellent agreement with that of p-type samples was found. Again the traps could be emptied by the application of negative bias—a field of $2\text{--}3 \times 10^6$ V/cm for 2-5 min being sufficient.

Figure 14 shows the shift in ZBEC for several n-samples. As in the case of p-type samples, the shapes of the curves are quite dependent on the NH_3 to SiH_4 ratio. Samples deposited at low ratio show greatest shift at low fields, while samples having higher NH_3 to SiH_4 ratios (62.5:1 or greater) show the opposite effect. These results are in good agreement with those for p-type samples.

Density of surface states.—Because of the hysteresis effect in these samples, the concept of surface state density does not have its usual meaning. In the normal situation (e.g., grown silicon dioxide on silicon) surface state density is a function of surface potential but is not dependent on the past history of the sample. The situation here is different, however, since the shape of the C-V curve is a function of the direction in which the voltage is varied. Figure 15 shows two curves for the p-type sample (G-45) exhibiting the least amount of hysteresis at low fields. Curve A was taken by varying the voltage in the negative and positive direction starting each time from zero volts in the equilibrium condition. This was the standard procedure used in taking C-V curves as discussed above. Curve B was taken by first adjusting the bias to +25V and then taking data as the voltage was decreased back through zero to negative voltages. The dotted curve in Fig. 15 is Curve B shifted next to Curve A. Curve B is somewhat steeper than Curve A.

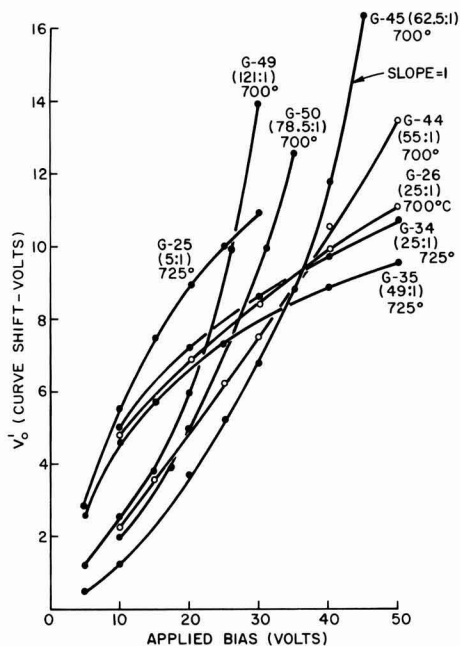


Fig. 12. Effect of NH_3 to SiH_4 ratio on amount of curve shift

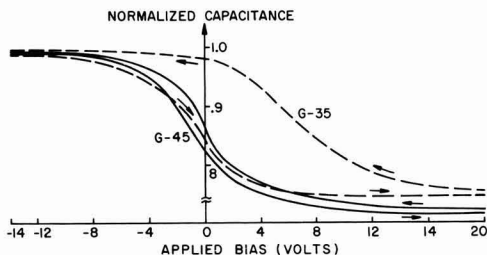


Fig. 13. C-V curves showing hysteresis improvement

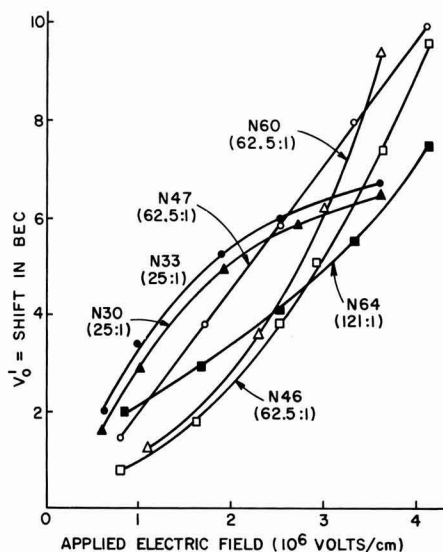


Fig. 14. Curve shift for n-type samples with positive applied voltage.

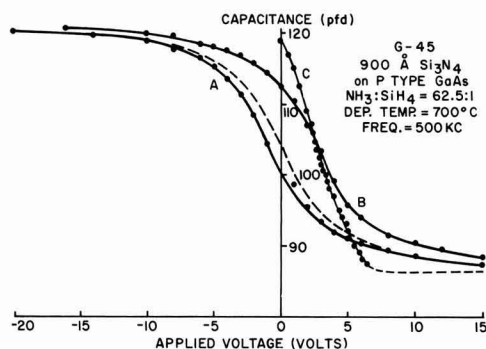


Fig. 15. C-V curves for best p-type sample

This is due to the fact that the traps were first filled before taking Curve B. Since the traps empty very slowly until negative voltages are reached, this curve gives the minimum effect of hysteresis as far as determining surface state density. The fact that the curve is shifted to the right of the equilibrium Curve A does not affect surface state density measurements. Such a shift is analogous to that produced by a non-zero ϕ_{MS} (metal-semiconductor work function difference) and has no effect on determination of surface state density.

Curve C in Fig. 15 is the calculated theoretical C-V curve (45) for values of surface potential, ψ_s , ranging from 0 to +1.1V. This corresponds to the Fermi level going from 0.1V above the valence band ($\psi_s = 0$) to 0.2V below the conduction band ($\psi_s = 1.1$). The surface state density was calculated from Curves B and C and is shown in Fig. 16. N_{SS} is the effective density of surface states per square centimeter per unit voltage. N_{SS} is in the 10^{12} - 10^{13} range—being highest for low values of ψ_s . Values of ψ_s between 0 and 0.1V correspond to negative values of the applied voltage. The emptying of traps in this region could account for the large increase in N_{SS} . The lowest value of N_{SS} is 1×10^{12} for ψ_s of 0.4-0.5V.

Summary

The predominant characteristic of the Si_3N_4 -GaAs interface is the presence of hysteresis due to the filling

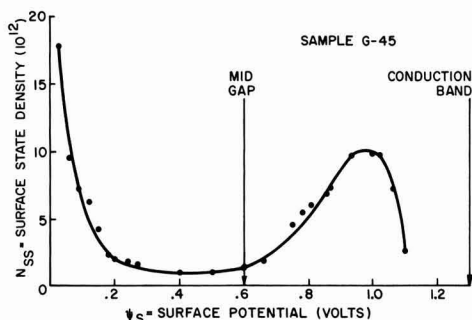


Fig. 16. Surface state density for best p-sample

and emptying of traps in the Si_3N_4 near the interface. The spatial distribution of these traps from the interface is strongly dependent on the $\text{NH}_3:\text{SiH}_4$ ratio. The amount of this hysteresis was minimized to less than 2V for fields below 1.7×10^6 V/cm for the best p-type sample. Best results were obtained at a deposition temperature of 700°C and a $\text{NH}_3:\text{SiH}_4$ ratio of 62.5:1.

The relaxation (emptying) of filled traps with no applied bias is extremely slow and logarithmic in time. Recovery times as long as 20,000 years are indicated. The refilling of traps to equilibrium after removal of a negative bias is exponential in time with time constants of a few minutes in the dark. Surface states at the interface appear to be negative when below the Fermi level and account for the opposite polarity of flat band voltage for n- and p-samples.

A method was found for obtaining repeatable C-V measurements. This involved the establishing of a zero bias equilibrium condition—ZBEC. This condition could be achieved in a few minutes by relaxation after the application of a negative bias.

Surface state density for the best p-sample was in the 10^{12} - 10^{13} range. Repeatability on p-type samples was good—apparently being primarily determined by repeatability of the processing. Repeatability for n-type samples was relatively poor for reasons not yet determined.

Some further reduction in the amount of hysteresis is needed before stable gates can be fabricated from GaAs- Si_3N_4 FET's.

Manuscript submitted Feb. 4, 1970; revised manuscript received ca. June 22, 1970.

Any discussion of this paper will appear in a Discussion Section to be published in the June 1971 JOURNAL.

REFERENCES

- H. T. Minden, *Solid State Technol.*, 25 (April 1969).
- A. S. Grove, "Physics and Technology of Semiconductor Devices," pp. 323-326, John Wiley & Sons, Inc. (1967).
- V. Y. Doo, *Electron Devices*, ED-13, 561 (1966).
- V. Y. Doo, D. R. Nichols, and G. A. Silvey, "Vapor Detection of Silicon Nitride," Paper presented at Electrochem. Soc. Meeting, Buffalo, N. Y., Oct. 10-14, 1965.
- J. V. Dalton, "Sodium Drift and Diffusion in Silicon Nitride Films," Paper presented at Electrochem. Soc. Meeting, Cleveland, Ohio, May 1-6, 1966.
- W. van Gelder and V. E. Hauser, *This Journal*, 114, 869 (1967).
- T. L. Chu, C. H. Lee, and G. A. Gruber, *ibid.*, 114, 717 (1967).
- V. Y. Doo, D. R. Nichols, and G. A. Silvey, *ibid.*, 113, 1279 (1966).
- K. E. Bean, P. S. Gleim, and R. L. Yeakly, *ibid.*, 114, 733 (1967).
- D. M. Brown, W. E. Engeler, M. Garfinkel, and F. K. Heumann, *ibid.*, 114, 730 (1967).
- Sugano et al., *Japan. J. Appl. Physics*, 7, 122 (1968).
- S. M. Sze, *J. Appl. Phys.*, 38, 2951 (1967).
- S. Yoshioka and S. Takayanagi, *This Journal*, 114, 962 (1967).

14. T. L. Chu, J. R. Szeldon, and C. H. Lee, *This Journal*, **115**, 318 (1968).
15. M. J. Grieco, Paper 148 presented at Electrochem. Soc. Meeting, Philadelphia, Oct. 9-14, 1966.
16. H. Sterling and R. Swann, *Solid State Electron.*, **8**, 653 (1967).
17. S. M. Hu, *This Journal*, **113**, 693 (1966).
18. T. L. Chu, J. Szeldon, and C. H. Lee, *Solid State Electron.*, **10**, 897 (1969).
19. N. C. Tombs *et al.*, *Proc. IEEE*, **54**, 87 (1966).
20. S. M. Hu and L. V. Gregor, *This Journal*, **114**, 826 (1967).
21. R. S. Levitt and W. K. Zucker, *ibid.*, **114**, 1192 (1967).
22. E. J. Kendall, *Brit. J. Appl. Phys., Ser. 2*, **1**, 1409 (1950).
23. V. Y. Doo, D. R. Kerr, and D. R. Nichols, *This Journal*, **115**, 61 (1968).
24. F. K. Heumann, D. Brown, and E. Mets, *ibid.*, **115**, 99 (1968).
25. N. C. Tombs and F. A. Sewell, *ibid.*, **115**, 101 (1968).
26. A. N. Saxena and O. N. Tkal, *ibid.*, **115**, 227 (1968).
27. J. R. Yeargan and H. L. Taylor, *ibid.*, **115**, 273 (1968).
28. P. F. Schmidt and D. R. Wonsidler, *ibid.*, **114**, 603 (1967).
29. R. C. G. Swann, R. R. Mehta, and T. P. Cauge, *ibid.*, **114**, 713 (1967).
30. B. E. Deal and P. J. Fleming, *ibid.*, **115**, 300 (1968).
31. D. M. Brown *et al.*, *ibid.*, **115**, 311 (1968).
32. M. J. Griers, F. L. Worthing, and B. Schwartz, *ibid.*, **115**, 525 (1968).
33. M. V. Coleman and D. J. Thomas, *Phys. Stat. Solidi*, **25**, 241 (1968).
34. E. J. M. Kendall, *Can. J. Phys.*, **46**, 2509 (1968).
35. D. J. D. Thomas, *Phys. Stat. Solidi*, **20**, 131 (1967).
36. A. S. Grove, B. E. Deal, E. H. Snow, and C. T. Sah, *Solid State Electron.*, **8**, 145 (1965).
37. K. H. Zaininger and G. Warfield, *IEEE Trans. Electron Devices*, **ED-12**, 179 (1965).
38. E. S. Schlegel, *ibid.*, **ED-14**, 728 (1967).
39. E. S. Schlegel, *ibid.*, **ED-15**, 951 (1968).
40. J. Drowart and P. Goldfinger, *J. Chem. Phys.*, **55**, 721 (1958).
41. M. V. Sullivan and G. A. Kolb, *This Journal*, **110**, 585 (1963).
42. K. H. Zaininger and G. Warfield, *IEEE Trans. Electron Devices*, **ED-12**, 179 (1965).
43. F. P. Heiman and G. Warfield, *ibid.*, **ED-12**, 167 (1965).
44. E. C. Ross and J. T. Wallmark, *RCA Rev.*, **30**, 366 (1969).
45. K. H. Zaininger, "Surface-State Density from High Frequency Capacitance Measurements," *RCA Product Engr.*, pp. 50-52 (1968).

The Orientation Dependence of Epitaxial InAs_xP_(1-x) on GaAs

H. A. Allen*

Texas Instruments Incorporated, Dallas, Texas 75222

ABSTRACT

The orientation dependence of the deposition of InAs_xP_{1-x} epitaxial layers on GaAs using an AsH₃, PH₃, indium, and HCl vapor-deposition system was studied. The total flow rate and the ratio of Group III to total Group V components were held constant while deposits were made simultaneously on (100), (110), (111)A, and (111)B substrates. Similar deposits were made under the same conditions on spherical, single-crystal GaAs substrates. Growth on these spheres exhibited facets that correspond to slow growth and high-perfection orientations. The sphere surface morphologies were similar to the planar substrates over much of the composition range.

Many of the properties of the InAs_xP_(1-x) alloy system have been known for some time. It has only been more recently that this material has been grown epitaxially by chemical-vapor deposition on InAs (1), GaAs, and GaP (2) substrates. The perfection of hetero-epitaxial layers is, generally, strongly dependent on the substrate orientation and in binary alloy systems, the preferred orientation can also be a function of alloy composition. In order to determine which is the preferred growth orientation for a given alloy, a systematic investigation under controlled growth conditions is necessary. The goal of this investigation is to define the preferred growth planes of the InAs_xP_(1-x) alloy system on GaAs as a function of alloy composition.

Materials Preparation

An open-tube deposition system constructed of fused quartz was used in these studies (2) (Fig. 1). Purified hydrogen and high-purity AsH₃ and PH₃ each in hydrogen gas are mixed in a mixing chamber prior to introduction to the reactor. Anhydrous HCl gas (purchased from the Matheson Company) which has also been mixed with purified hydrogen, is passed

through the heated indium reservoir and transports the volatile InCl to the deposition zone (1, 2). In these experiments 4% AsH₃ and 4% PH₃ each in hydrogen obtained from the Matheson Company, were sources. Elemental indium was six-nines pure and was purchased from Cominco American Incorporated. The composition of the deposited alloys was controlled by the relative flow rates of the AsH₃ and PH₃ gases and was reproducible to a standard deviation of 1% in alloy composition. The flow rates could be varied continuously from 0 to about 250 cc/min for AsH₃ and

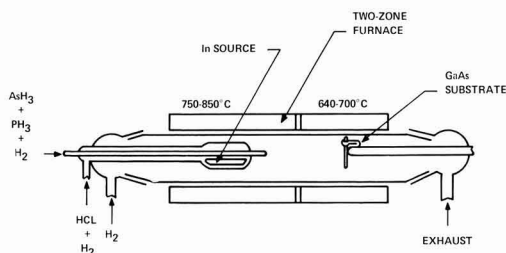


Fig. 1. Horizontal vapor growth system

* Electrochemical Society Active Member.
Key words: III-V semiconductor alloys, infrared materials, chemical vapor deposition.

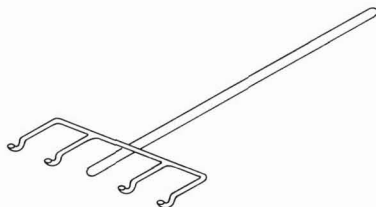


Fig. 2. Four-slice seed holder

PH_3 in hydrogen. The total flow rate was held constant at 300 cc/min. The Group III to Group V ratio was held constant at 5:4 with an anhydrous HCl flow of 14 cc/min and a total Group V flow of 11.3 cc/min.¹ The flow rates of AsH_3 and PH_3 relative to the alloy composition were determined in earlier studies (1, 2).

A two-zone resistance furnace provided temperature control of the indium reservoir and the GaAs substrates. The indium zone was controlled at 800°C and the substrate temperature was controlled at a temperature between 640° and 700°C; the seed temperature was increased from 640°C for InP to 700°C for InAs (2). The temperature gradient in the system was gradual within the indium reservoir and the seed being separated by 3-4 in. In most runs the seed or seeds were held normal to the direction of gaseous flow by quartz pins through a hole in the slice (Fig. 2). All temperatures were maintained at $\pm 2^\circ\text{C}$ throughout a given run.

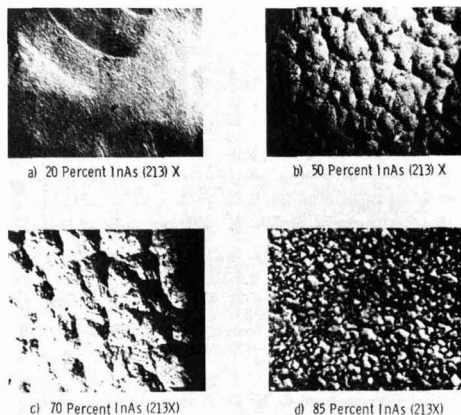
The GaAs substrates used in this investigation were from Czochralski-grown crystals that had been sawed in the (100), (110), (111)A, and (111)B planes and polished to about 20 mils in thickness. These substrates were sawed to within $\pm 0.5^\circ$ of the given direction as evidenced by x-ray diffractometer readings of the slices. The substrates were chemically polished with 8:1:1 ($\text{H}_2\text{SO}_4:\text{H}_2\text{O}_2:\text{H}_2\text{O}$) immediately prior to use. The GaAs spheres were mechanically ground from cubes which had been sawed from Czochralski-grown crystals. The spheres were between 0.063 and 0.125 cm in diameter. Immediately prior to use, the spheres were polished with the non-preferential 40HCL:4H₂O₂:1H₂O etch (3). The deposition times were 20 min for all substrates and 2-3 hr for the sphere deposits. Layer thicknesses varied between 8 and 20 μm and were determined by cleave or angle lap-and-stain techniques (2).

Large Area Deposits

The regular substrate deposits are referred to as large area as compared to the hypothetical point locations of each orientation on a sphere.

The (100), (110), (111)A, and (111)B substrates were suspended normal to the gas flow in the same run by use of a four-hooked fused silica seed holder (Fig. 2). Thus, in each run a nearly constant set of growth conditions was maintained. Very shiny deposits with smooth substrate-epitaxy interface could be grown reproducibly on the (111)A substrates from compositions consisting of pure InP up to about 80% InAs. The alloy deposits above 80% were generally polycrystalline in nature with the frequency of the poly layers increasing with the InAs concentration in alloy. Figure 3 is photomicrographs of representative (111)A deposits.

The (111)B deposits were erratic throughout the composition range and were generally polycrystalline in nature. The (110) deposits were similar in trend to the (111)A, but the frequency of poly layers was much higher above 75% and below 25% InAs. The deposits on (100) substrates, below 75% InAs, were practically all poly. The highest perfection InAs layers

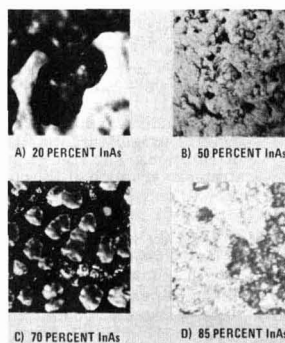
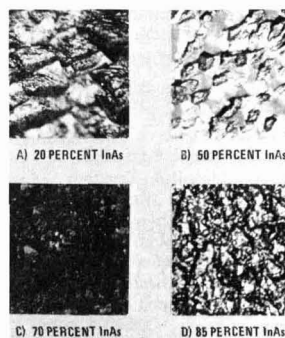
Fig. 3. Undoped $(\text{InAs})_x(\text{InP})_{1-x}(\text{III})\text{A}$ surfaces

were grown on this orientation. Representative photomicrographs of the (111)B, (110), and (100) surfaces are shown respectively in Fig. 4-6.

The compositions of the above samples were obtained by electron microprobe analysis and checked by x-ray diffraction techniques (4). The crystallinity was determined by x-ray diffraction and Laue back-reflection techniques (5). Single crystals had well-defined Laue patterns as well as diffractometer peaks sharp enough to enable composition analysis to $\pm 2\%$. Table I gives the results of these measurements.

Sphere Deposits

Deposition on a sphere, ideally, makes it possible to have all orientations present at the same time. The

Fig. 4. $(\text{InAs})_x(\text{InP})_{1-x}(\text{III})\text{B}$ surfaces. 213 XFig. 5. $(\text{InAs})_x(\text{InP})_{1-x}(\text{110})$ surfaces. 213 X

¹ Assuming a 1:1 ratio of indium transported to HCl introduced.

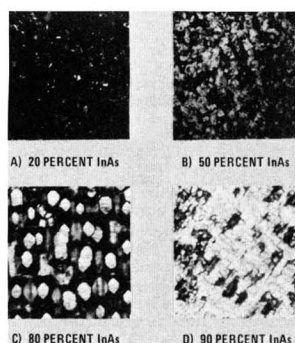
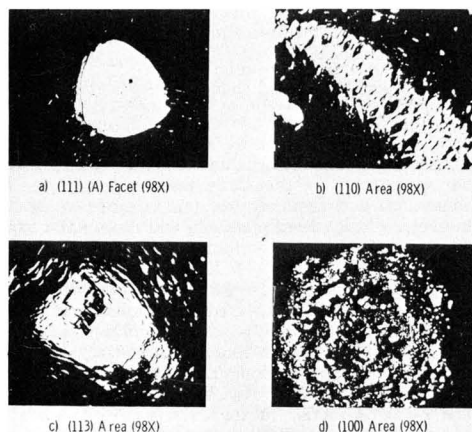
Fig. 6. $(\text{InAs})_x(\text{InP})_{1-x}$ (100) surfaces. $213\times$ 

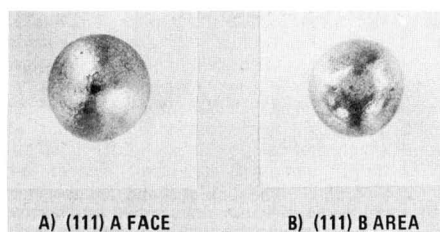
Fig. 7. InP sphere facets

faster growing planes will "grow out" leaving only the slower growing orientations as facets. In general, these facets represent optimum growth directions for high-perfection crystal growth. This proved to be the case with the epitaxial growth of InP on a GaAs sphere. The only true facet was a (111)A, with the (110) and (113) directions exhibiting shiny, shingled flats. The (100) and (111)B area could be located and were dull in appearance. The (111)A facet was distinguished by its surface similarity with control slices included in the run. Figure 7 is the facets observed on the InP deposited sphere.

Table I. Mole per cent InAs

Orientation	Run numbers								
	18	19	12	21	23	24	25	26	27
(111)A	0	17	25	50	77	80	79	89	93
(110)	0	17	24	52	66	83	82	87	95
(111)B	0	18	24	49	78	85	79	85	
(100)	0	22	30	55	80	87	85	84	94

Note: — denotes single crystallinity.

Fig. 8. $(\text{InAs})_{0.50}(\text{InP})_{0.50}$ on GaAs sphere

Unfortunately, the InP deposited GaAs sphere was the only one which lent itself to such a straightforward explanation. Five more spheres were deposited with various compositions of the alloy between an InAs composition of 20 and 90 m/o (mole per cent). In all cases the only discernible facet was a (111)A with the (111)B direction identifiable by a triangular banded area 180° from each (111)A facet as shown in the (111)A and (111)B polar photographs in Fig. 8. No other identifiable facets were seen on these spheres.

Discussion

The composite of the large area and sphere deposits indicate that the (111)A direction of GaAs is the best plane for high-perfection epitaxial $\text{InAs}_{1-x}\text{P}_x$ alloy layers in the 0-80% InAs range. There is a pronounced orientation shift in large-area 85-100% InAs alloys to the (100) as the preferred growth. The above results were observed as the general rule through many depositions; it was occasionally possible to grow a high-perfection layer on an orientation which had previously given all poly deposits. Though no extensive experiments were conducted, the general trends stated in the test were seen on selected deposits with temperature conditions varied widely ($\pm 75^\circ\text{C}$), on the seed and feed and with change in the Group III to Group V ratio between 0.5 and 3.0.

The fact that there were no identifiable facets on the alloy sphere deposits other than (111)A and in particular no (100) facets for alloy layers of greater than 85% InAs, is not well understood. It should be stressed that although one expects agreement, large-area and sphere deposits are very different. As was mentioned earlier, with a sphere each orientation is only a point on the sphere's surface and therefore, only slow-growing orientations tend to increase this point to a real geometrical area as growth occurs. Thus, it is possible that a preferred growth direction could be fast growing and not produce a facet on a sphere. Obviously, this would not be a problem with large-area deposit.

Manuscript submitted April 1, 1970; revised manuscript received ca. June 22, 1970.

Any discussion of this paper will be published in a Discussion Section to be published in the June 1971 JOURNAL.

REFERENCES

1. J. J. Tietjen, H. P. Maruska, and R. B. Clough, *This Journal*, **116**, 492 (1969).
2. H. A. Allen and E. W. Mehal, *This Journal*, **117**, 1081 (1970).
3. D. W. Shaw, *Proc. 1968 Sym. on GaAs* (London Inst. of Phys. and Phys. Soc.), Paper 8.
4. J. K. Howard and R. P. Dobrott, *This Journal*, **113**, 567 (1966).
5. H. F. Buckley, "Crystal Growth," John Wiley & Sons, Inc., New York (1951).

Phase Diagram of the CdTe-CdSe Pseudobinary System

Alan J. Strauss* and Jacques Steininger

Lincoln Laboratory, Massachusetts Institute of Technology, Lexington, Massachusetts 02173

ABSTRACT

The liquidus and solidus curves of the CdTe-CdSe pseudobinary system have been determined by thermal analysis of cooling and heating curves, respectively, for homogenized liquid and solid alloy samples. The phase diagram has a eutectic point at $1091 \pm 1^\circ\text{C}$ near 20 m/o (mole per cent) CdSe. Above the eutectic composition both liquidus and solidus temperatures increase monotonically and sublinearly with increasing CdSe content. In this region the experimental values of the liquidus-solidus gap do not exceed 11 m/o and are in excellent agreement with the ideal thermodynamic liquidus-solidus relationship. The phase diagram below the solidus has been investigated by x-ray diffraction measurements on alloy powders annealed between 770° and 1050°C and quenched. It consists of two broad single-phase regions, one of alloys with the zinc blende structure of CdTe and the other of alloys with the wurtzite structure of CdSe, separated by a two-phase region only about 3 m/o wide, whose boundaries shift toward increasing CdSe content with decreasing temperature. For compositions between 30 and 45 m/o CdSe, either structure could be obtained at room temperature, depending on annealing temperature and rate of cooling. In addition, a polytype of unknown structure, which appears to be a metastable intermediate in the wurtzite-to-zinc blende transformation, was observed in two melt-grown furnace-cooled ingots containing 45-50 m/o CdSe.

The II-VI compounds CdTe and CdSe have the cubic zinc blende and hexagonal wurtzite structures, respectively, when prepared by solidification of stoichiometric melts or nonstoichiometric Cd-Te or Cd-Se solutions. [Other methods of preparation can be used to obtain CdTe with wurtzite structure (1) or CdSe with zinc blende structure (2).] The phase diagram of the CdTe-CdSe system has not been determined previously but x-ray diffraction studies (3, 4) on a limited number of samples prepared by solidifying stoichiometric melts indicate that pseudobinary solid solutions are formed over the entire composition range. According to these studies, undoped alloys containing less than about 40 m/o CdSe have the zinc blende structure, those containing at least 70 m/o CdSe have the wurtzite structure, and those with intermediate compositions may have either structure.

In this investigation, the liquidus and solidus curves in the CdTe-CdSe pseudobinary system have been determined by thermal analysis measurements on homogenized liquid and solid alloy samples. The cubic-hexagonal transition in the solid phase has been studied by x-ray diffraction analysis of annealed and quenched alloy powders. The x-ray data show that the cubic and hexagonal phase fields are separated by a two-phase region about 3 m/o wide, whose boundaries shift toward increasing CdSe content with decreasing temperature. Therefore, within a certain composition range, alloys can be obtained with either cubic or hexagonal structure, as reported earlier (3, 4), depending on the annealing temperature and rate of cooling. In addition to these two phases, a previously unreported polytype of unknown structure can also be formed as shown by x-ray diffraction data for two melt-grown, furnace-cooled ingots containing 45-50 m/o CdSe.

Experimental Procedure

Alloys for thermal analysis and x-ray diffraction studies were prepared from CdTe and CdSe. The CdTe was synthesized by fusion of the elements (nominal purity 99.9999%) in forepump-evacuated and sealed fused silica ampoules coated with pyrolytic graphite. To prepare CdSe, the elements (same nominal purity) were combined in an open-tube fused silica reactor

(5) heated to 1050° - 1100°C under helium gas at 1 atm. The composition of the CdSe was then adjusted by sublimation in a dynamic vacuum in order to remove the excess of unreacted elements and reduce the vapor pressure during subsequent high temperature annealing.

To prepare each alloy for x-ray analysis, a 10g mixture of the two powdered compounds was sealed in a fused silica ampoule containing helium gas (pressure of about 400 Torr at room temperature), annealed at 950°C for 21 days or longer, and quenched by dropping the ampoule into water. Annealing was continued until x-ray diffraction measurements gave no evidence of inhomogeneity, and the measured lattice parameters were consistent with the nominal compositions.

Samples for thermal analysis were either alloy powders annealed in the manner described or unannealed mixtures of CdTe and CdSe powders. A sample weighing about 10g was sealed in an evacuated fused silica ampoule and placed in a DTA apparatus described previously (6), together with a similar ampoule containing about 8g of silicon used as a reference. The sample and reference temperatures were measured with Pt-Pt, 13% Rh thermocouples inserted into re-entrant wells in the ampoules. Calibration with a gold sample (melting point 1063.0°C) gave melting and freezing arrests of $1063.0^\circ\text{C} \pm 0.1^\circ\text{C}$ and showed that no correction of the sample temperature readings was necessary. Solidus temperatures were obtained from thermal arrests observed either during initial heating of the annealed powder samples or during heating of both types of samples after they had been melted, frozen, and then homogenized by annealing in the DTA apparatus for 16 hr at about 20°C below the solidus temperature. The two types of experiments gave solidus temperatures which agreed to within a fraction of a degree. The liquidus temperatures were obtained from the thermal arrests observed when the samples were cooled after homogenization in the DTA apparatus for 16 hr at about 50°C above the liquidus temperature. Liquidus temperatures reproducible to $\pm 1^\circ\text{C}$ were obtained from repeated runs on the same sample. Rates of 1° - $2^\circ\text{C}/\text{min}$ were used for both heating and cooling. Supercooling was observed during most of the cooling runs but was limited to only a few degrees (Table I). When supercooling occurred, the liquidus arrest temperature was taken to be the

* Electrochemical Society Active Member.

Key words: phase diagram, cadmium telluride, cadmium selenide, alloys, polytypes, crystal growth.

Table I. Thermal analysis data

Composition CdTe	CdSe	Cooling curves			Heating curves		
		Super- cooling, °C	Liquidus arrest, °C	Repro- ducibility, °C	Solidus arrest	Repro- ducibility	
1.000	0	0	1091.8	±0.2	1091.8	±0.2	
0.900	0.100	0	1092.9	±0.1	1089.6	±0.1	
0.800	0.200	3.3	1092.3	±0.4	1091.3	—	
0.700	0.300	5.0	1100.0	0	1097.0	—	
0.675	0.325	7.0	1101.0	±0.3	1098.5	0	
0.650	0.350	2.0	1108.3	±0.4	—	—	
0.625	0.375	6.6	1106.8	±0.2	1099.8	±0.2	
0.600	0.400	0.9	1107.2	±0.2	1101.5	—	
0.550	0.450	3.7	1118.4	±1.0	—	—	
0.500	0.500	0.1	1125.8	±0.2	1110.5	—	
0.450	0.550	0.3	1136.7	±1.0	—	—	
0.400	0.600	4.0	1147.3	±1.0	1125.0	—	
0.300	0.700	0.2	1169.5	±1.0	1143.5	—	
0.200	0.800	2.3	1196.0	±0.5	—	—	
0.100	0.900	0.3	1222.0	±0.5	1200.5	—	
0	1.00	0	1252.3	±0.2	1252.3	—	

maximum in the recalescence curve. Otherwise, both liquidus and solidus arrest temperatures were obtained from the intersection of the practically straight lines below and above the break in the sample temperature curve. Because of the large thermal effects in this system, differential temperature recording was used only as a confirmation of the arrests observed on the sample temperature curve. The over-all accuracy is estimated to vary from within $\pm 1^\circ\text{C}$ near the terminal compounds to within a few degrees in the middle of the composition range.

To investigate the cubic-hexagonal transition below the solidus, pairs of homogenized alloy powders with the same composition, in the range 30–50 m/o CdSe, were preannealed so that one was initially cubic and the other initially hexagonal. Portions of the samples weighing 1–2g were then sealed in separate fused silica ampoules containing helium gas, annealed at temperatures between 770° and 1050°C , quenched by dropping the ampoules into water, and ground to minus 325 mesh. The phases present were determined from x-ray diffractometer patterns obtained with $\text{Cu K}\alpha$ radiation. Annealing was repeated if necessary until both samples were either single-phase cubic, single-phase hexagonal, or two-phase. The total annealing times ranged from 16 hr at 1050°C to 30 days at 800°C . A sample was taken to be single-phase cubic if the noncoincident (111) hexagonal line in the vicinity of $2\theta = 23^\circ$ was not detected, and single-phase hexagonal if the noncoincident (400) cubic line in the vicinity of $2\theta = 58^\circ$ was not detected. [Use of these criteria gives a considerably lower detection limit for the hexagonal phase than for the cubic phase, since the (111) hexagonal line is 5–10 times more intense than the (400) cubic line.]

X-ray diffraction patterns were also obtained with a Debye-Scherrer camera for all the alloys following initial homogenization and for a number of samples after subsequent annealing. These patterns were used to calculate the cubic or hexagonal lattice parameters to an accuracy of $\pm 0.001\text{\AA}$ by a least-squares extrapolation method (7).

In addition to the alloys prepared by annealing mixtures of powdered CdTe and CdSe, a number of polycrystalline alloy ingots each weighing 150g were obtained by the Bridgman method of crystal growth. Stoichiometric melts containing up to 60 m/o CdSe, which were prepared from the elements in evacuated and sealed fused silica ampoules coated with pyrolytic graphite, were frozen directionally by lowering the ampoules at the rate of about 1 mm/hr out of a vertical resistance-heated furnace. One ingot, containing 35 m/o CdSe, was quenched by pulling the ampoule out of the furnace with part of the material still molten. The others were allowed to cool in the furnace after the power had been turned off. Portions of the ingots were analyzed with an electron microprobe (8) to determine their alloy composition, and a number of these and other portions were ground for x-ray dif-

fraction analysis with the diffractometer and/or Debye-Scherrer camera.

Results

The phase diagram determined for the CdTe-CdSe system is shown in Fig. 1. The compositions plotted are the nominal compositions calculated from the weights of CdTe and CdSe used to prepare the alloys. The thermal analysis data are listed in Table I, which gives the liquidus and solidus arrest temperatures, the amount of supercooling observed during the liquidus determinations, and the reproducibility when repeated runs were made. Melting and freezing arrests of $1091.8^\circ \pm 0.2^\circ\text{C}$ were obtained for CdTe, in good agreement with the literature values of $1090^\circ \pm 2^\circ\text{C}$ [Ref. (9)], $1092^\circ \pm 3^\circ\text{C}$ [Ref. (10)], and $1091^\circ \pm 2^\circ\text{C}$ [Ref. (11)]. The liquidus and solidus temperatures for 10 and 20 m/o CdSe do not differ significantly from each other or from the melting point of CdTe and suggest the presence of a eutectic point at $1091^\circ \pm 1^\circ\text{C}$ and near 20 m/o CdSe. (The separation between liquidus and solidus curves in this region is not shown in Fig. 1 because of the small scale of the diagram.) Above 20 m/o CdSe, both liquidus and solidus temperatures increase monotonically and sublinearly with increasing CdSe content. The liquidus-solidus gap in this region remains rather narrow, never exceeding 11 m/o. Melting and freezing arrests of $1252.5^\circ \pm 0.5^\circ\text{C}$ were obtained for CdSe, in fair to good agreement with previously reported values of $1239^\circ \pm 3^\circ\text{C}$ [Ref. (12)], $1250^\circ \pm 2^\circ\text{C}$ [Ref. (11)], $1258^\circ \pm 3^\circ\text{C}$ [Ref. (13)], $1259^\circ \pm 4^\circ\text{C}$ [Ref. (14)], and $1264^\circ \pm 10^\circ\text{C}$ [Ref. (15)].

The results of the x-ray diffractometer measurements on annealed and quenched powders are represented by circles in Fig. 1—closed circles for single-phase cubic samples, open circles for single-phase hexagonal samples, and half-closed circles for two-phase samples. (There was no evidence for ordering of the Te and Se atoms in either the cubic or hexagonal structure.) Over the limited composition range where the relationship between structure and temperature has been studied in detail, the cubic and hexagonal phase fields are separated by a two-phase region only about 3 m/o wide. The boundaries of this region are well represented by parallel straight lines, along which the temperature decreases with increasing CdSe content. According to these lines, the two-phase field extends from 26 to 29 m/o CdSe at 1000°C and from 46.5 to 49.5 m/o CdSe at 800°C . The composition range investigated was not extended to lower CdSe content because of the difficulty anticipated in retaining the hexagonal phase by quenching as the hexagonal-cubic transformation temperature increased. The range was not ex-

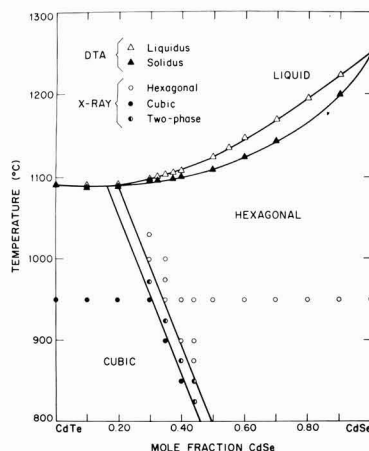


Fig. 1. Phase diagram of the CdTe-CdSe pseudobinary system

tended to higher CdSe content because the time required to attain equilibrium in the solid phase became inconveniently long as the transformation temperature decreased. (Some two-phase samples may have been incorrectly identified as single-phase because the quantity of the minor phase was too small to be detected by the x-ray diffraction method used. Errors of this kind would tend to make the width of the two-phase region shown in Fig. 1 somewhat less than the actual width.)

As shown in Fig. 1, when extrapolated linearly the lower and upper boundaries of the two-phase field intersect the solidus curve at 17 and 20 m/o CdSe, respectively, consistent with a eutectic point near 20 m/o CdSe. Linear extrapolation to lower temperatures gives an hexagonal-cubic transformation temperature around 250°C for pure CdSe, although such an extended extrapolation is obviously of limited significance. Partial transformation from cubic to hexagonal CdSe after annealing for 10 hr at 130°C has been reported (2).

The cubic (a_0) and hexagonal (a_0 , c_0) lattice parameters measured for annealed single-phase alloy powders are listed in Table II, together with the values calculated from them for the unit cell volume (V) and for the c/a ratio of the hexagonal alloys. (Where duplicate results are given for the same composition, they were obtained for independent samples, not for aliquots of the same sample.) The c/a ratios range from 1.631 to 1.638, compared with the theoretical value of 1.633 for the wurtzite structure. For CdTe, the measured a_0 is 6.481 Å, compared with literature values of 6.480–6.483 Å [Ref. (3, 16–18)]. [The value of 6.423 Å given by Litwin (4) is obviously incorrect.] For CdSe, $a_0 = 4.301$ Å and $c_0 = 7.016$ Å, compared with literature values of a_0 from 4.297 to 4.309 Å, and values of c_0 from 7.007 to 7.034 Å [Ref. (3, 4, 14, 19)]. Most of the lattice parameters reported previously (3, 4) for the alloys with cubic structure agree fairly well with the present ones, but there is greater disagreement among the parameters for the hexagonal alloys.

The values of a_0 for cubic samples, a_0 and c_0 for hexagonal samples, and V for all samples are plotted against nominal alloy composition (expressed in mole fraction CdSe, x) in Fig. 2, 3, and 4, respectively. The three lattice parameters vary linearly with composition, according to the following expressions which correspond to the straight lines in Fig. 2 and 3: a_0 (cubic) (Å) = 6.481–0.411 x ; a_0 (hexagonal) (Å) = 4.580–0.279 x ; c_0 (Å) = 7.502–0.486 x . Except at the extremes of the composition range, the values of V fall slightly below the straight line joining the unit cell volumes of CdTe and CdSe. For the region ($0.3 \leq x \leq 0.45$) in which both cubic and hexagonal samples have been obtained, the values of V are generally somewhat lower for cubic samples than for hexagonal.

For the CdTe_{1-x}Se_x ingots which were prepared by directional freezing of stoichiometric melts, the results of electron microprobe analysis of small sections close

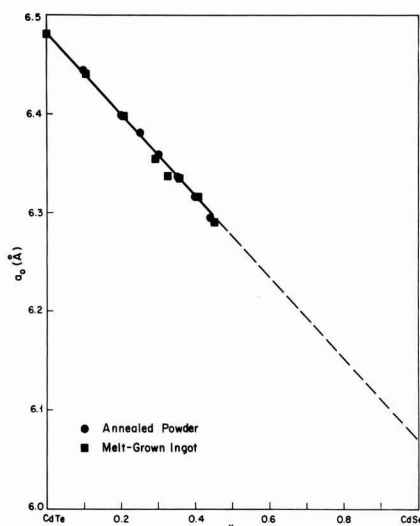


Fig. 2. Lattice parameter a_0 as a function of mole fraction CdSe in CdTe_{1-x}Se_x alloys with cubic structure.

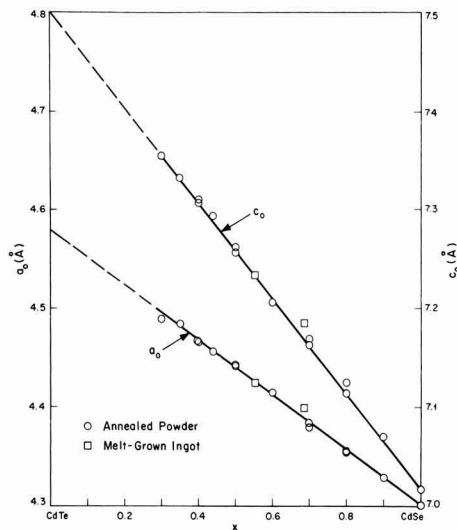


Fig. 3. Lattice parameters a_0 and c_0 as a function of mole fraction CdSe in CdTe_{1-x}Se_x alloys with hexagonal structure. The ordinate scale for a_0 is at the left side of the figure and the scale for c_0 is at the right side.

Table II. Lattice parameters of CdTe_{1-x}Se_x alloys

x	Cubic a_0 (Å)	V (Å ³)	a_0 (Å)	Hexagonal c_0 (Å)	c_0/a_0	V (Å ³)
0	6.481	68.06				
0.1	6.444	66.90				
0.2	6.398	65.47				
0.25	6.381	64.95				
0.3	6.359	64.28	4.489	7.355	1.638	64.18
0.35	6.336	63.59	4.484	7.333	1.635	63.84
0.4	6.316	62.99	4.465	7.310	1.637	63.10
			4.466	7.308	1.636	63.12
0.44	6.295	62.36	4.456	7.293	1.637	62.70
0.5			4.442	7.257	1.634	62.00
			4.441	7.262	1.635	62.02
0.6			4.414	7.206	1.633	60.79
0.7			4.380	7.169	1.637	59.55
			4.383	7.163	1.634	59.59
0.8			4.355	7.114	1.634	58.42
			4.354	7.125	1.636	58.49
0.9			4.328	7.070	1.634	57.34
1.0			4.301	7.016	1.631	56.20

to the tip are qualitatively consistent with the liquidus-solidus relationships shown in Fig. 1. If solidification of an alloy occurs under equilibrium conditions, the first-to-freeze composition is the solidus composition corresponding to the liquidus composition given by the nominal ingot composition. For CdTe_{1-x}Se_x ingots with nominal x up to 0.3, within the error of the microprobe (estimated to be $\pm 3\%$) the measured compositions are the same as the nominal ingot compositions, presumably because the gap between liquidus and solidus compositions is quite small in this region. For 3 ingots with nominal $x = 0.4$, 0.4, and 0.5, the measured compositions were $x = 0.41$, 0.45, and 0.55, respectively, compared with the solidus compositions of $x = 0.50$, 0.50, and 0.61 given by the phase diagram. The measured compositions are all less than the corresponding

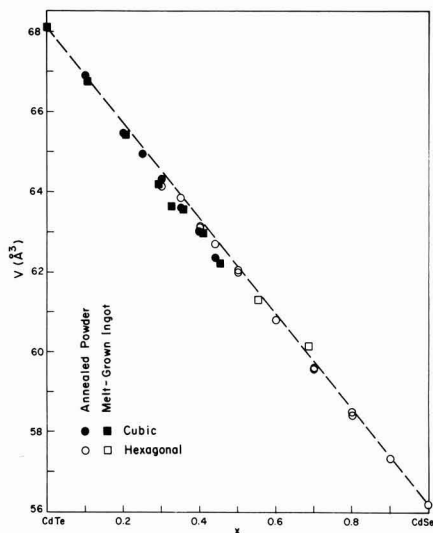


Fig. 4. Unit cell volume (V) as a function of mole fraction CdSe in $\text{CdTe}_{1-x}\text{Se}_x$ alloys.

solidus compositions; these discrepancies are in the direction expected if the rate of solidification was too high for equilibrium to be established between the liquid and solid or if the samples analyzed were too far removed from the first-to-freeze region.

Although the x-ray diffractometer measurements made on the alloy ingots were not extensive, the data are sufficient to show that the phases present depend on ingot composition, the location of the sample in the ingot, and the method of cooling. Thus all samples from ingots with $x \leq 0.2$ are cubic, and all those from an ingot with $x = 0.6$ are hexagonal. (The compositions quoted in this discussion are nominal, and the ingots were furnace cooled unless otherwise specified.) The first-to-freeze portions of ingots with $x = 0.3, 0.4$, and 0.45 are either entirely cubic or contain a small amount of the hexagonal phase in addition to the cubic. A sample frozen later in one of the ingots with $x = 0.4$ contains a larger proportion of the hexagonal phase but is still primarily cubic. In contrast, samples from an ingot with x of only 0.35 , which had been air quenched by removing the growth ampoule from the hot furnace, are entirely hexagonal.

For two ingots with $x = 0.45$ and 0.5 , the first-to-freeze portions are single-phase cubic and hexagonal, respectively. However, a number of other samples from these ingots give diffractometer patterns which cannot be attributed to these two phases. Part of one such pattern is shown in Fig. 5, together with the same angle range ($20^\circ \leq 2\theta \leq 28^\circ$) from patterns for single-phase cubic and hexagonal samples of about the same composition. The unusual features of the new patterns are: (a) the appearance of new although poorly defined lines at 25.4° and 42.9° ; (b) an increase in the relative intensity of the line at 24.6° , which cannot be attributed to the cubic phase because the characteristic cubic line at 58.8° is either weak or absent; and (c) a marked decrease in the relative intensities of the lines at 26.3° , 44.4° , and 76.5° which appear in the wurtzite pattern. We attribute these features to the presence of a polytype, like those observed for ZnS and SiC, whose structure is intermediate between the zinc blende structure (with entirely cubic close packing) and the wurtzite structure (with entirely hexagonal close packing). In the ingot with $x = 0.5$, the region containing the polytype is in the interior, completely surrounded by a thin outer shell of the wurtzite phase.

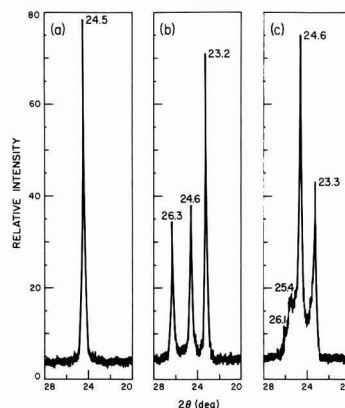


Fig. 5. X-ray diffraction patterns over the angle range $20^\circ \leq 2\theta \leq 28^\circ$ for $\text{CdTe}_{1-x}\text{Se}_x$ alloys with $x \sim 0.5$: (a) cubic, (b) hexagonal, (c) polytype.

The two regions are easily distinguished by visual observation of a lapped cross section.

In addition to the diffractometer patterns for ingot samples, Debye-Scherrer patterns were also obtained for a number of such samples which were powdered after they had been analyzed with the electron microprobe. The lattice parameters and unit cell volumes measured for single-phase cubic and hexagonal samples, which are plotted in Fig. 2-4 as a function of the measured composition, are the same within experimental error (including the error of the microprobe analysis) as those for annealed alloy powders.

Discussion

The qualitative features of the CdTe-CdSe phase diagram (Fig. 1) reflect the fact that the crystal structures of CdTe and CdSe are different but very closely related. Because of their difference in structure, the compounds cannot form a complete series of solid solutions along the solidus curve. Therefore the CdTe-CdSe diagram has the eutectic form, rather than the simple lens form of the II-VI pseudobinary CdTe-ZnTe [Ref. (6)] and HgTe-HgSe [Ref. (20)] diagrams. In each of the latter systems, involving two binary compounds with zinc blende structure which exhibit complete mutual solid solubility, both liquidus and solidus temperatures increase monotonically and sublinearly with increasing ZnTe or HgSe content across the entire diagram. Thus the liquidus and solidus curves in these systems resemble those for the hexagonal branch of the CdTe-CdSe diagram (i.e., the region between about 20 m/o CdSe, the eutectic composition, and pure CdSe). Over this entire region CdTe_{1-x}Se_x alloys with wurtzite structure are stable along the solidus curve, according to a linear extrapolation of the hexagonal phase boundary from lower temperatures.

Liquidus-solidus relationship.—For a binary alloy system of completely miscible components A and B , by expressing the equality of the partial free energies of mixing in the liquid and solid phases, it has been shown (21) that the liquidus and solidus compositions in equilibrium at temperature T are related by

$$RT \left(\ln \frac{X_A^s}{X_B^s} - \ln \frac{X_A^l}{X_B^l} \right) = \Delta H_A \left(1 - \frac{T}{T_A} \right) - \Delta H_B \left(1 - \frac{T}{T_B} \right) - D \quad [1]$$

with

$$D = \frac{\partial \Delta G_{e,m}^s}{\partial X_A^s} - \frac{\partial \Delta G_{e,m}^l}{\partial X_A^l}$$

where X_i^l and X_i^s are the mole fractions of component i in the liquid and solid phases, respectively, T_i and ΔH_i are the temperature and enthalpy of fusion of the pure component, and $\Delta G_{e,m}^s$ and $\Delta G_{e,m}^l$ are the excess molar free energies of mixing in the respective phases. Equation [1] is a general thermodynamic expression which is applicable to any system. If both liquid and solid solutions are ideal, the excess free energies of mixing are zero and $D = 0$. The ideal form of Eq. [1] with $D = 0$ has also been found to fit the experimental data for a large number of binary and pseudobinary alloy systems (metallic, semiconducting, and ionic) in which the liquidus and solidus temperatures vary monotonically with composition (21). Although in general the liquid and solid phases in these systems are not ideal solutions, the ideal liquidus-solidus expression is applicable because the deviations from ideality in the two phases are comparable, and therefore, the difference between the partial excess free energies of mixing is small enough to be neglected. (An excellent fit to Eq. [1] with $D = 0$ is obtained for the CdTe-ZnTe system but not for the HgTe-HgSe system. We believe that the deviations between experiment and calculation in the latter case are probably due to errors in the experimental determination of the solidus curve.)

The ideal form of Eq. [1] can be used to calculate one of the boundaries of the two-phase field when the other boundary and the enthalpies of fusion of the pure components are known. In the present study this expression has been used to calculate the solidus curve for the CdTe-CdSe system from the experimental liquidus data and the enthalpies of fusion of CdTe and CdSe determined by Kulwicki (11) (12.0 and 10.5 kcal/mole, respectively). As shown in Fig. 6, the calculated curve is in excellent agreement with the experimental solidus data for the hexagonal branch of the diagram. (The root mean square of the difference between calculated and experimental temperatures for 8 data points is 2.4°C.) The agreement indicates that over this composition range the deviations from ideality are comparable for the liquid and solid phases, as in systems where the liquidus and solidus temperatures vary monotonically over the whole range of composition. The agreement between calculation and experiment for the hexagonal branch also implies that the zinc blende and metastable wurtzite structures of CdTe do not differ greatly in free energy, since the temperature and enthalpy of fusion used in the calculations were measured for CdTe with zinc blende structure.

It should be noted that calculation of the solidus curve from our initially limited liquidus data facilitated the selection of temperatures close to the solidus for annealing the frozen alloy samples. Because homogenization was accelerated by the increased rates of diffusion, the heating curves for such samples an-

nealed for only 16 hr at these high temperatures gave thermal arrests almost as sharp as those obtained with powder samples annealed at 950°C for 3 weeks or more.

Sub-solidus phases.—The zinc blende and wurtzite structures have the same primary coordination, with each cation surrounded by four nearest-neighbor anions in tetrahedral configuration, and *vice versa*. This close structural relationship, together with the chemical similarity between Te and Se, explains the broad range of mutual solid solubility exhibited by CdTe and CdSe. Within the temperature region where the boundaries of the cubic and hexagonal phases have been determined, the miscibility gap at a fixed temperature is only about 3 m/o, and its position shifts sufficiently with temperature to permit formation of solid solutions over the whole range of compositions.

According to the phase diagram of Fig. 1, for any composition up to 17 m/o CdSe the zinc blende structure is stable at all temperatures below the solidus curve. For any other composition, this structure is stable only up to a transition temperature which decreases quite rapidly with increasing CdSe content. Above this temperature there is an interval of about 15°C in which no solid solution of this composition is stable, and at still higher temperatures the wurtzite structure is stable. The same sequence of low-temperature zinc blende, intermediate two-phase, and high-temperature wurtzite regions has recently been observed by Shalimova *et al.* (19) for fixed compositions near 40 m/o CdSe in the pseudobinary system formed by CdSe and ZnSe, which like CdTe has the zinc blende structure. According to their results for annealing temperatures between 800° and 1200°C, the phase diagram below the solidus in this system is similar to that of the CdTe-CdSe system, since it too consists of cubic and hexagonal phase fields separated by a narrow two-phase region whose boundaries shift toward increasing CdSe content with decreasing temperature.

For ZnS, the prototype compound for both structures, the zinc blende structure is the low-temperature form and the wurtzite structure the high-temperature form, just as in the two alloy systems. The fact that in all three cases there is a temperature at which the two phases have the same free energy is another result of their close structural relationship. In each case, at constant composition the free energy of the zinc blende phase increases more rapidly with increasing temperature than that of the wurtzite phase. [For the alloys, the temperature of equal free energy lies in the region where neither structure is stable with respect to the formation of a mixture of two phases with different compositions. Shalimova *et al.* (19) claim that the zinc blende and wurtzite structures are both stable for any composition and temperature within the two-phase region of the CdSe-ZnSe system. This is thermodynamically impossible.]

Although the zinc blende and wurtzite structures have the same primary coordination, transformations from one to the other require the breaking of nearest-neighbor bonds (22). Such reconstructive transformations involve an appreciable activation energy, and their rates therefore depend approximately exponentially on temperature. It is this strong temperature dependence which makes it possible to establish equilibrium phase relations for elevated temperatures by means of phase determinations at room temperature on samples which have been annealed and quenched. The use of this method requires the transformation rates to be high enough at the annealing temperature for equilibrium to be achieved in a convenient time and low enough at any phase boundary for the high-temperature phase to be retained by quenching. In our investigation of the CdTe-CdSe system, these conditions were apparently satisfied for small powder samples with compositions between 30 and 44 m/o CdSe, corresponding to transition temperatures between about 950° and 800°C at the upper boundary of the cubic phase field. Within this range single-phase sam-

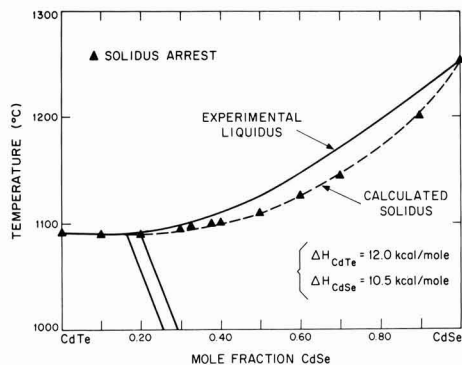


Fig. 6. Comparison of calculated solidus curve with experimental solidus data for CdTe-CdSe system.

ples of a given composition were prepared with both wurtzite and zinc blende structures by annealing above or below the transition temperature, respectively. No attempt was made to prepare hexagonal samples containing less than 30 m/o CdSe, because of the difficulty anticipated in cooling rapidly enough to prevent conversion to the cubic phase at temperatures of 1000°C and above. Cubic samples containing more than 44 m/o CdSe were not prepared because it would have taken too long to transform them from the hexagonal phase at temperatures below 800°C.

In the two earlier investigations (3, 4) of the structure of CdTe-CdSe alloys, the samples studied were prepared by solidification from the melt. Those containing up to 30 m/o CdSe were entirely cubic. Stuckes and Farrell (3) found that samples containing 40 and 50 m/o CdSe were cubic with only a trace of the hexagonal phase, and Litwin (4) observed both phases for compositions of 36, 50, and 60 m/o CdSe. Only samples containing at least 70 m/o CdSe were entirely hexagonal. According to the phase diagram of Fig. 1, however, alloys containing more than about 20 m/o CdSe crystallize from the melt in the hexagonal structure. Therefore the presence of the cubic phase in samples containing 30-60 m/o CdSe must have resulted from the partial or complete transformation of the hexagonal phase during cooling, after the temperature had fallen below the hexagonal-to-cubic transition temperature. The cubic phase was not formed for compositions exceeding 60 m/o CdSe because of the decrease in the transition temperature with increasing CdSe content and the decrease in transformation rate with decreasing temperature. In this range, the cubic phase becomes stable at such low temperatures (less than about 700°C) that the transformation rate was never high enough for appreciable transformation to occur at the cooling rates used. Since cooling rates were not discussed in either paper, it can be assumed that they were neither extremely fast nor extremely slow, and that times of the order of hours were probably required to cool to room temperature. This indicates that the rates of the hexagonal-to-cubic transformation were much faster for solid samples than for the powdered samples annealed in our investigation at fixed temperatures, which required many days for complete transformation to the cubic phase even at 800°C.

Increased transformation rates in solid samples were also observed for ingots prepared in our investigation by directional solidification of stoichiometric melts. The hexagonal phase was retained without transformation in a 35 m/o CdSe ingot which was air quenched to room temperature from above the transition temperature, while transformation occurred in furnace-cooled ingots containing up to 45 m/o CdSe. In one such furnace-cooled ingot containing 30 m/o CdSe, cubic single-crystal regions up to about 1 cm on a side were identified by sandblasting, which reveals the grain boundaries in these alloys. Thus under suitable experimental conditions the transformation to the cubic phase can occur without introducing polycrystallinity. This is another consequence of the close relationship between the zinc blende and wurtzite structures.

This relationship is also reflected by the rather close agreement in unit cell volume measured at room temperature (Fig. 4) between alloys with the zinc blende and wurtzite structures. The volume difference for a given composition does not exceed 0.6% in the range ($0.3 \leq x \leq 0.45$) where both structures have been obtained. However, the significance of the comparison is limited because the wurtzite structure is metastable at room temperature in the overlapping range and also for compositions considerably richer in CdSe—quite possibly for CdSe itself. A valid comparison would require x-ray diffraction measurements at temperatures high enough for each structure to be

stable over a wide composition range. Such high-temperature measurements would also be necessary to satisfactorily test the conformity of the CdTe-CdSe alloys to Vegard's law. According to the room temperature volume data, the alloys with zinc blende structure deviate by as much as 0.8% from the straight line shown in Fig. 4, while the wurtzite alloys generally exhibit smaller deviations.

As a final result of the zinc blende-wurtzite relationship, we note the formation of a polytype in two furnace-cooled ingots with nominal compositions of 45 and 50 m/o CdSe. A large number of polytypes with structures intermediate between zinc blende and wurtzite are known for ZnS and SiC, but to our knowledge none has been reported for a ternary alloy. No attempt has been made to identify the polytype by single-crystal x-ray diffraction analysis, but calculations of the powder diffraction patterns for the 4H, 6H, 8H, 12H, and 15R polytypes of $\text{CdTe}_{0.5}\text{Se}_{0.5}$ indicate that it is probably not one of these.

Apparently the polytype was formed as an intermediate stage in the hexagonal-to-cubic transformation because the rate of cooling was too slow to permit retention of the hexagonal phase but too fast to permit complete transformation to the cubic phase. (The first-to-freeze tip of the ingot containing 45 m/o CdSe was cubic, apparently because it reached the transition temperature and transformed before the furnace was shut off. In the ingot containing 50 m/o CdSe, a thin outer shell remained hexagonal because it cooled rapidly enough to prevent transformation, but the center was converted to the polytype because it cooled more slowly.) Our experiments do not give any evidence that the polytype is a thermodynamically stable phase rather than a metastable intermediate, since it was not observed in any of the powdered samples which were quenched after annealing. Polytype formation as an intermediate step in the cubic-to-hexagonal transformation of thin films of ZnS has recently been reported (23).

Acknowledgments

This work was sponsored by the Department of the Air Force.

The authors wish to acknowledge the assistance of R. E. England and Mrs. M. C. Plonko in the phase diagram determination, R. L. MacLean in crystal growth, Mary C. Finn in electron microprobe analysis, and E. L. Mastromattei and Mrs. M. J. Button in the x-ray measurements. They are also indebted to J. M. Longo and R. F. Brebrick for discussions of the crystallographic and thermodynamic properties of the alloys.

Manuscript submitted March 31, 1970; revised manuscript received ca. July 8, 1970.

Any discussion of this paper will appear in a Discussion Section to be published in the June 1971 JOURNAL.

REFERENCES

1. M. Weinstein, G. A. Wolff, and B. N. Das, *Appl. Phys. Letters*, **6**, 73 (1965).
2. A. S. Pashinkin and R. A. Sapozhnikov, *Soviet Phys.—Cryst.*, **7**, 501 (1962).
3. A. D. Stuckes and G. Farrell, *J. Phys. Chem. Solids*, **25**, 477 (1964).
4. J. Litwin, *Phys. Stat. Sol.*, **5**, 551 (1964).
5. T. B. Reed and W. J. LaFleur, *Solid State Research Report*, Lincoln Lab., M.I.T. (1968: 1), p. 19.
6. J. Steininger, A. J. Strauss, and R. F. Brebrick, *This Journal*, **117**, 1305 (1970).
7. J. B. Nelson and D. P. Riley, *Proc. Phys. Soc.*, **57**, 160 (1945).
8. M. C. Finn, *Anal. Chem.*, **42**, 1084 (1970).
9. D. de Nobel, *Philips Res. Rept.*, **14**, 361 (1959).
10. M. R. Lorenz, *J. Phys. Chem. Solids*, **23**, 939 (1962).
11. B. M. Kulwicki, Ph.D. Dissertation, Univ. of Michigan (1963).
12. A. Reisman, M. Berkenblit, and M. Witzten, *J. Phys. Chem.*, **66**, 2210 (1962).
13. D. R. Mason and D. F. O'Kane, *Proc. Intern. Conf. Semicond. Phys., Prague*, 1960, p. 1026 (1961).

14. W. R. Cook, *J. Am. Ceram. Soc.*, **51**, 518 (1968).
15. L. A. Sysoev, E. K. Raikin, and V. R. Gur'ev, *Inorg. Mater.*, **3**, 341 (1967).
16. P. W. Davis and T. S. Shilliday, *Phys. Rev.*, **118**, 1020 (1960).
17. J. C. Woolley and B. Ray, *J. Phys. Chem. Solids*, **13**, 151 (1960).
18. G. A. Slack and S. Galginitis, *Phys. Rev.*, **133**, A253 (1964).
19. K. V. Shalimova, A. F. Botnev, V. A. Dmitriyev, M. Z. Kognovitskaya, and V. V. Starostin, *Sov. Phys. Cryst.*, **14**, 531 (1970).
20. T. C. Harman "Physics and Chemistry of II-VI Compounds," M. Aven and J. S. Prener, Editors, p. 786, John Wiley & Sons, Inc., New York (1967).
21. J. Steininger, *J. Appl. Phys.*, **41**, 2713 (1970).
22. A. R. Verma and P. Krishna, "Polymorphism and Polytypism in Crystals," p. 50, John Wiley & Sons, Inc., New York (1966).
23. K. N. Rai, O. N. Srivastava, and P. Krishna, *Bull. Am. Phys. Soc.*, **14**, 1187 (1969).

Phase Equilibria Relations in the Ternary System BaO-SrO-Nb₂O₅

J. R. Carruthers and M. Grasso

Bell Telephone Laboratories, Incorporated, Murray Hill, New Jersey 07974

ABSTRACT

Phase equilibria in the binary system SrO-Nb₂O₅ and the Nb₂O₅-rich region of the ternary system BaO-SrO-Nb₂O₅ were investigated by DTA, x-ray diffraction, strip heater, and Curie temperature measurement techniques. The ternary-phase fields of three tetragonal-tungsten-bronze type structures have been located. Only one of these structures is a ternary compound; it is located along the SrNb₂O₆-BaNb₂O₆ binary join, extending from 20 to 80 m/o BaNb₂O₆, and melts congruently near 50% BaNb₂O₆. The ternary solubility extends from about 4% excess (Ba + Sr) to about 1% excess Nb₂O₅. This phase possesses observable orthorhombic distortion in the BaNb₂O₆-rich region of the solid solution. The implications of the phase diagram for the crystal growth of these compounds are briefly discussed.

The existence of a ferroelectric compound Ba_xSr_(1-x)Nb₂O₆ (BSN) was independently reported in 1960 by Francombe (1) and Ismailzade (2). The structure was found to be closely related to the tetragonal tungsten bronze structure. The existence regions were found to be $0.30 \leq x \leq 0.80$ by Francombe and $0.35 \leq x \leq 0.75$ by Ismailzade. No indication of the extent of solid solution in the ternary region was given. Both workers reported that the tetragonal structure was distorted to orthorhombic over a part of the range; however, Francombe found the orthorhombic structure for $x < 0.45$, while Ismailzade found the values $x > 0.40$ corresponded to this structure. Both workers also reported that the Curie temperatures varied from 50°C at the high SrNb₂O₆ end of the solution to 200°-300°C at the high BaNb₂O₆ end. Ismailzade reported that the paraelectric phase was tetragonal over the entire solid solution range.

The first large BSN single crystals were grown in this system by Ballman and Brown (3) over a range of melt compositions $0.25 \leq x \leq 0.75$. Chemical analysis indicated that the solid compositions were quite similar to those of the melt. Also the Curie temperature was found to vary in a similar manner to that found for the ceramic specimens. These crystals have been used by Jamieson, Abrahams, and Bernstein (4) for structure determination as well as Glass (5, 6) for investigations of the electrical properties with special reference to the pyroelectric detection of infrared radiation. These crystals have also been shown to have interesting electro-optic properties (7).

The crystal structure was determined by Jamieson *et al.* (4) for the composition $x = 0.27$ (grown from a melt with $x = 0.25$). In agreement with Ismailzade, the structure was found to be tetragonal tungsten bronze and to belong to the space group P4bm. This

structure consists of a framework of NbO₆ octahedra sharing corners so that there are three different types of interstitial sites, two of which may be occupied by Ba or Sr ions. There are five formula units per unit cell so that the five Ba/Sr ions can be distributed on six possible interstitial sites (two A1 sites with distorted tetragonal symmetry and four A2 sites with distorted trigonal symmetry). In addition, it was found, for $x = 0.27$, that only Sr ions were found in the two A1 sites with an occupancy factor of 82.2% and Sr and Ba ions in the four A2 sites with occupancy factors 50.3 and 34.4%, respectively. As Glass (6) points out, if the A1 site continues to be occupied only by Sr ions as the Sr/Ba ratio changes, then the entropy of distribution of the ions becomes a minimum when $x = 0.67$. At this composition, only Sr ions occupy the A1 sites and Ba ions occupy the A2 sites (for the same occupancy factors).

The electrical properties of BSN were investigated by Glass (6) over the solid-solution range and from 10°-500°K. His dielectric constant and electrical conductivity measurements showed a behavior at the Curie temperature which correlated with the degree of randomness in the Ba/Sr distribution. Glass also measured the field and frequency dependence of the dielectric properties and the specific heat and pyroelectric coefficients of BSN.

There have been no phase equilibria studies of the ternary BaO-SrO-Nb₂O₅ system or of the SrO-Nb₂O₅ system. The BaO-Nb₂O₅ system was reported by Roth and Waring (8). The ternary oxide system SrO-NbO₂-Nb₂O₅ has been reported by Ridgley and Ward (9). These studies showed that the compounds SrNb₂O₆ (SN) and BaNb₂O₆ (BN) existed and possessed a complex and an orthorhombic crystal structure, respectively. In addition, the compounds 3BaO.5Nb₂O₅ (B₃N₅) and BaO.3Nb₂O₅ (BN₃) were observed with distorted tungsten-bronze-type structures. The structures of both SN and BN have been

observed to be quite sensitive to the valence state of the Nb. Partial reduction of the Nb causes SN to become cubic perovskite with characteristics of the tungsten bronzes (8) while in the case of BN, less direct evidence suggests that a hexagonal phase is stabilized which is apparently an intermediary structure between orthorhombic BN and the tungsten-bronze type structures.

The present investigation was undertaken to complete the ternary BaO-SrO-Nb₂O₅ phase diagram around the tungsten-bronze structures in this system. We wished to establish the crystal-growth equilibria and existence regions for these compounds.

Experimental Procedure

Specimen preparation.—Specimens were prepared from dried Ba(NO₃)₂ and Sr(NO₃)₂ (Fisher reagent grade) and Nb₂O₅ (CIBA optical grade). Specimens were multiply ground, pelletized, and sintered in air at temperatures 50°C below solidus temperatures. The ternary region along the binary join SN-BN possessed some strange reactivity problems to be discussed later which required the use of a strip heater to obtain completely reacted samples.

Measurements.—DTA measurements were made on a DuPont 1600 Thermoanalyzer. X-ray diffraction measurements were performed on a Nonius-Guinier focusing camera using monochromatic CuK α radiation. Curie temperature (T_c) measurements were made on small ceramic pellets (~2 mm on a side) using a General Radio 1673A capacitance bridge at 1 kHz with platinum electrodes. Firm electrode pressure was essential for these measurements. Silver paste electrodes, although used on most specimen surfaces, were found not to be necessary. The Curie temperature was reported as the position of the capacitance maximum, although Glass (6) has shown that this does not exactly coincide with the actual Curie temperature. Nevertheless we are only interested in relative changes in the position of the peak with composition.

Experimental Results

SrO-Nb₂O₅ system.—The DTA and x-ray results are shown in Fig. 1. In addition to SN, three new compounds were observed, S₅N₂, S₂N, and S₂N₅. The d-

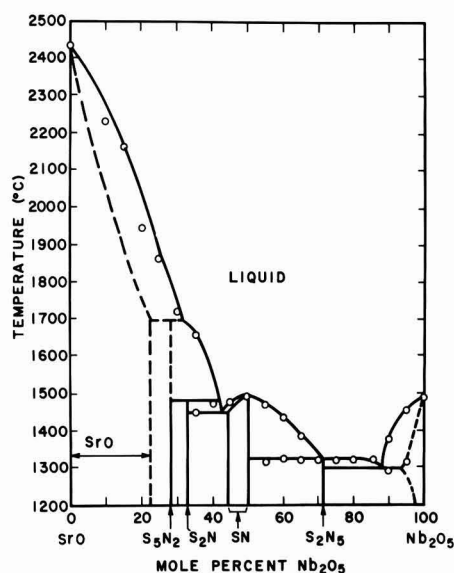


Fig. 1. Phase equilibrium diagram for the system SrO-Nb₂O₅

Table I. d-Spacings of compounds in the SrO-Nb₂O₅ system

SrO		(SrO) ₅ (Nb ₂ O ₅) ₂		(SrO) ₂ (Nb ₂ O ₅) ₃		SrNb ₂ O ₆	
d (Å)	I	d (Å)	I	d (Å)	I	d (Å)	I
4.80	1	3.00	10	18	<1	5.50	<1
4.15	1	2.83	10	5.3	<1	5.02	3
2.92	10	2.05	8	4.4	<1	4.50	1
2.06	5	1.77	3	3.92	1	4.20	1
1.66	5	1.655	5	3.89	1	3.95	4
1.455	3	1.625	4	3.53	2	3.88	4
1.310	2	1.495	3	3.35	3	3.45	3
		1.405	3	3.22	3	3.40	<1
		1.320	3	3.05	10	3.15	4
		1.275	3	2.94	5	3.05	10
				2.88	3	3.00	2
				2.85	5	2.91	2
				2.77	7	2.84	2
				2.16	3	2.80	5
				2.12	1	2.78	2
				2.06	3	2.75	1
				1.97	5	2.59	1
				1.94	2	2.46	1
				1.82	1	2.38	1
				1.805	<1	2.37	1
				1.730	1	2.33	1
				1.735	1	2.34	3
				1.710	1	2.22	3
				1.690	1	2.13	1
				1.670	1	2.08	3
				1.620	4	2.04	1
				1.615	4		

spacings for the compounds SrO, S₅N₂, S₂N, and SN are shown in Table I. SrO has a simple cubic structure while S₅N₂ has a hexagonal structure which resembles its counterpart B₅N₂ in the BaO-Nb₂O₅ system (8). The structures of S₂N and SN are seen to be complex and will not be considered further. The structure of S₂N₅ is of the tungsten-bronze type and is identical to that of BN₃. This compound will be discussed later in more detail.

Liquidus temperatures in excess of 1500°C in Fig. 1 were determined by means of an optical pyrometer using SN as a calibration and an iridium strip as the heating source. This method minimized SrO volatilization for these compositions and also insured completion of the reaction. Sintering temperatures of 1400° were insufficient to achieve solid-state reaction over this composition range (0-30% Nb₂O₅).

SrNb₂O₆-BaNb₂O₆ pseudobinary system.—The DTA and x-ray results for the SN-BN binary join are shown in Fig. 2. The structure of (BSN)₁ is of the tetragonal tungsten bronze type and will be discussed later. At room temperature, compositions greater than $x = 0.55$ (where x = mole fraction BaNb₂O₆) showed orthorhombic splittings in agreement with the work of Ismailzade (2).

It is of some interest here to mention the reactivity problem encountered in this system. Attempts to

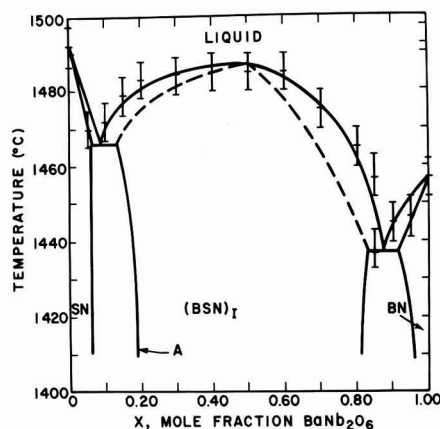


Fig. 2. Pseudobinary phase equilibrium diagram for the system SrNb₂O₆-BaNb₂O₆.

produce a single-phase BSN by sintering at 1000°C failed completely, even with ten regrindings and using a reducing ambient of 15% H₂-85% N₂ for 6 hr. As the sintering temperature was progressively raised by 100°C increments to 1400°C, the single-phase field opened up starting with the BN-rich end. The solvus line, A, in Fig. 2 moved to the left and was located at 35% BN after sintering at 1400°C. The final location of solvus line A at 20% BN was determined by melting these specimens on a platinum strip heater, slowly freezing under a microscope, and looking for second-phase SN lines with the Nonius-Guinier camera.

The liquidus shown in Fig. 2 is flat within experimental error over the composition range 20-60% BN. The location of the liquidus maximum and associated congruently melting composition was determined with the aid of T_c measurements described later. The solidus lines (shown as dashed lines) were located approximately using the composition shifts reported by Ballman and Brown (3) as guidelines and also the end-points of the eutectic arrest lines (which are observable by DTA).

BaO-SrO-Nb₂O₅ ternary system.—The compositions investigated in the ternary oxide region are shown in Table II together with the x-ray and DTA results. The room temperature existence regions are reproduced in Fig. 3 where the compounds (BSN)_I, (BSN)_{II}, (BSN)_{III}, and (BSN)_{IV} have been identified. Data points have been omitted for clarity. These compounds all have tetragonal-tungsten-bronze type structures and the d-spacings are given in Table III. Compound I and its orthorhombic modification, II, is the compound shown in the binary join (Fig. 2) and was the subject of the introduction of this paper. Compound III corresponds to the ternary solid solution of B₃N₅, while compound IV corresponds to the ternary solid-solution range of the isomorphous S₂N₅-BN₃ series. Both III and IV show orthorhombic splittings as can be seen in Table III.

The high-temperature phase equilibria for these ternary compounds may be seen from the isopleth taken at 25% BaO shown in Fig. 4. The DTA data points are shown as well as the solid-solution extent of the three bronze structures in this particular section. The solidus curves for (BSN)_I are seen to be quite steep, especially in comparison to their behavior in the binary join of Fig. 2. This indicates that growth from melts with compositions off the binary SN-BN join will readily give rise to the usual types of com-

Table II. Experimental data for compositions in the ternary system BaO-SrO-Nb₂O₅

Sample designation	Composition			Phases present	Temperature arrests, °C
	BaO	SrO	Nb ₂ O ₅		
BSN 160	0.05	0.20	0.75	(BSN) _{IV} + Nb ₂ O ₅	1323
163	0.10	0.15	0.75	(BSN) _{IV} + Nb ₂ O ₅	1323
167	0.15	0.10	0.75	(BSN) _{IV} + Nb ₂ O ₅	1316
153	0.20	0.05	0.75	(BSN) _{IV}	1323
150	0.25	—	0.75	(BSN) _{IV}	1323
149	0.25	0.025	0.725	(BSN) _{IV}	1308, 1312
159	0.05	0.25	0.70	(BSN) _{IV} + SN	1320
162	0.10	0.20	0.70	(BSN) _{IV} + SN	1316
166	0.15	0.15	0.70	(BSN) _{IV} + SN	1312
152	0.20	0.10	0.70	(BSN) _{IV}	1312
148	0.25	0.05	0.70	(BSN) _{III} + (BSN) _{IV}	1312
147	0.25	0.075	0.675	(BSN) _{III}	1312
158	0.05	0.30	0.65	SN + (BSN) _{IV}	1320
161	0.10	0.25	0.65	SN + (BSN) _{IV}	1323
165	0.15	0.20	0.65	SN + (BSN) _{III} + (BSN) _{IV}	(1312), 1319
151	0.20	0.15	0.65	(BSN) _{III}	1312, 1335
146	0.25	0.10	0.65	(BSN) _{III}	1312, 1330
154	0.30	0.05	0.65	(BSN) _{III}	1305
145	0.25	0.125	0.625	(BSN) _{III} + (BSN) _{III}	1292, 1312, 1384
157	0.05	0.35	0.60	SN + (BSN) _{IV}	1312, 1402
100A	0.10	0.30	0.60	SN + (BSN) _{III} + (BSN) _{IV}	1312, 1395
164	0.15	0.25	0.60	SN + (BSN) _{III} + (BSN) _{IV}	1312, 1392
101	0.20	0.20	0.60	(BSN) _{III} + (BSN) _{III}	1312, 1411
144	0.25	0.15	0.60	(BSN) _{III}	1315, 1411
102	0.30	0.10	0.60	(BSN) _{III}	1307, 1391
136	0.175	0.25	0.575	(BSN) _I + (BSN) _{III}	1312, 1442
137	0.20	0.225	0.575	(BSN) _I + (BSN) _{III}	1312, 1448
132	0.25	0.175	0.575	(BSN) _I + (BSN) _{III}	1312, 1430
139	0.30	0.125	0.575	(BSN) _I + (BSN) _{III}	1298, 1425
140	0.325	0.10	0.575	(BSN) _I + (BSN) _{III}	1303, 1427
141	0.35	0.075	0.575	(BSN) _I + (BSN) _{III}	1296, 1407
156	0.05	0.40	0.55	SN + (BSN) _{III} + (BSN) _{IV}	1312, 1442
111	0.10	0.35	0.55	SN + (BSN) _{III}	1308, 1439
132	0.15	0.30	0.55	(BSN) _I + (BSN) _{III}	1321, 1456
133	0.20	0.25	0.55	(BSN) _I + (BSN) _{III}	1312, 1456
134	0.25	0.20	0.55	(BSN) _I + (BSN) _{III}	1312, 1456
135	0.30	0.15	0.55	(BSN) _I + (BSN) _{III}	1312, 1456
103	0.35	0.10	0.55	(BSN) _I + (BSN) _{III}	1294, 1447
142	0.375	0.075	0.55	(BSN) _{II} + (BSN) _{III}	(1303), 1429
125	0.10	0.38	0.52	(BSN) _I	1460
126	0.15	0.33	0.52	(BSN) _I + (BSN) _{III}	1300, 1463
127	0.20	0.28	0.52	(BSN) _I + (BSN) _{III}	1312, 1481
128	0.25	0.23	0.52	(BSN) _I + (BSN) _{III}	(1384), 1474
129	0.30	0.18	0.52	(BSN) _{II}	(1429), 1470
130	0.35	0.13	0.52	(BSN) _{II}	(1429), 1465
131	0.38	0.10	0.52	(BSN) _{II}	1472
143	0.40	0.08	0.52	(BSN) _{II} + BN	1447
112	0.10	0.42	0.48	SN + (BSN) _I	1447, 1456
113	0.15	0.37	0.48	(BSN) _I	1420, 1468
114	0.20	0.32	0.48	(BSN) _I	1438, 1472
115	0.25	0.27	0.48	(BSN) _I	1429, 1465
116	0.30	0.22	0.48	(BSN) _I	1471
117	0.35	0.17	0.48	(BSN) _{II}	1420, 1465
118	0.40	0.12	0.48	(BSN) _{II}	1456
110	0.10	0.45	0.45	SN + S ₂ N + (BSN) _I	1461
119	0.15	0.40	0.45	SN + (BSN) _I	1442
120	0.20	0.35	0.45	SN + (BSN) _I	1438
121	0.25	0.30	0.45	SN + (BSN) _I	1429
122	0.30	0.25	0.45	SN + (BSN) _I	1420, 1452
123	0.35	0.20	0.45	SN + (BSN) _I	1414, 1456
124	0.40	0.15	0.45	BN + (BSN) _I	1361, 1434
104	0.45	0.10	0.45	BN + (BSN) _I	1335, 1384, 1429
109	0.10	0.50	0.40	(BSN) _I + S ₂ N	1344, 1466
108	0.20	0.40	0.40	(BSN) _I + S ₂ N	1420, 1510
155	0.25	0.35	0.40	(BSN) _I + S ₂ N	1420, 1470
107	0.30	0.30	0.40	(BSN) _I + S ₂ N	1413, 1420, 1438
106	0.40	0.20	0.40	(BSN) _I + B ₃ N ₅	1384, 1411
105	0.50	0.10	0.40	(BSN) _I + B ₃ N ₅	1384, 1406

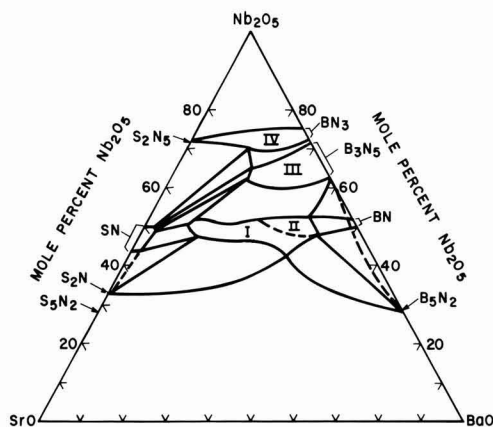


Fig. 3. Ternary phase relationships in the room-temperature isotherm of the system BaO-SrO-Nb₂O₅. Phases I, II, III, IV have tetragonal-tungsten-bronze type structures and the d-spacings shown in Table III.

positional variations in the grown crystals. Compounds (BSN)_{III} and (BSN)_{IV} both melt peritectically in agreement with the behavior observed by Roth Waring (8) in the end members, B₃N₅ and BN₃, respectively.

Curie temperature measurements.—The results of the capacitance measurements are shown in Fig. 5 where (a) shows the behavior across the pseudo-binary join (48 and 50% Nb₂O₅ isopleths) and (b) shows the behavior along the 25% BaO isopleth. Also shown in Fig. 5(a) are the Curie temperatures for

Table III. X-ray diffraction data for ternary BSN tungsten-bronze type structures

(BSN) _I [BSN-40]		(BSN) _{II} [BSN-80]		(BSN) _{III} [BSN-146]		(BSN) _{IV} [BSN-149]	
d(Å)	I	d(Å)	I	d(Å)	I	d(Å)	I
3.95	7	5.60	2	8.80	2	8.80	2
				6.30	2	6.25	2
				4.40	1	4.40	1
		3.95	4	3.99	8	3.97	8
				3.93	6	3.92	6
				3.87	1		
3.45	7	3.47	7	3.62	2		
				3.53	2		
				3.45	7	3.43	7
				3.33	4	3.33	4
				3.22	8	3.21	8
				3.10	1	3.15	1
3.00	9	3.02	10	3.08	1	3.10	1
				3.00	10	3.00	10
				2.94	6	2.93	6
				2.93	3	2.92	6
				2.91	2		
				2.90	1		
2.78	10	2.80	8	2.85	1	2.85	1
				2.78	8	2.78	8
				2.77	5	2.77	5
				2.70	1	2.70	1
				2.67	1	2.67	1
				2.60	4	2.60	4
2.59	4	2.60	4	2.62	2		
				2.60	4		
				2.51	1		
				2.44	2	2.43	3
				2.40	1		
				2.30	1	2.30	1
2.30	1	2.31	1	2.27	1	2.26	1
				2.25	1		
				2.13	3	2.13	3
				2.12	3		
				2.06	1	2.06	1
				1.98	6	1.975	6
1.955	5	1.982	6	1.95	3	1.955	3
				1.870	1		
				1.842	3	1.840	3
				1.840	3		
				1.822	2		
				1.750	6	1.750	7
1.860	1	1.850	3	1.730	3	1.735	3
				1.710	2	1.710	2
				1.670	2	1.670	1
				1.645	5	1.645	5
				1.635	2	1.635	2
				1.601	3	1.601	1
1.685	2	1.715	2	1.599	5	1.599	3

Note: d-spacings of tetragonal bronzes in barium strontium niobate (orthorhombic splittings denoted by braces).

crystals grown from the melt compositions (shown on the abscissa) as reported by Glass (6). Ceramic specimen results are given in terms of solid composition.

The results of Fig. 5(a) will be discussed first. The relationship between the Curie temperature of crystals and ceramics has been used in the binary lithium niobate (10) and lithium tantalate (11) sys-

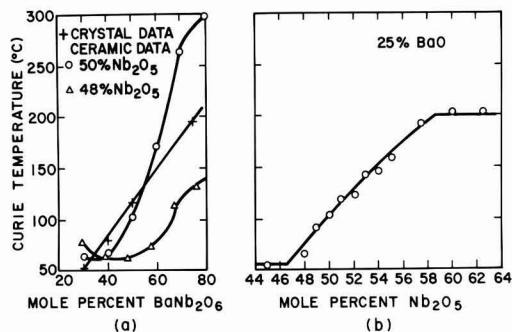


Fig. 5. Curie temperatures as a function of composition (a) along the binary join SrNb_2O_6 - BaNb_2O_6 and (b) along the 25% BaO isopleth (ceramic specimens).

tems to locate the congruently melting composition and establish liquidus-solidus tie lines. It is not strictly possible to use this procedure in ternary systems because the ternary tie lines move on three dimensional surfaces. Nevertheless the technique can be useful in pseudobinary regions such as the SN-BN join. A comparison of the slopes of the solidus curves of Fig. 2 and 4 suggests that melt compositions on the binary join freeze along the binary join. In fact the low values of T_c measured in the 48.0% Nb_2O_5 isopleth support this conclusion. These two observations do not agree with the composition shifts reported by Ballman and Brown (3) on the basis of chemical analysis. The error in the ceramic T_c measurements is quite large in the region 20-50% BN because of the very broad dielectric peaks in this region. This agrees with the results of Glass (6) on crystals in this composition range. We estimate the uncertainty in T_c as $\pm 8^\circ\text{C}$ at 50% BN. Thus the location of the congruently melting composition is $54 \pm 4\%$ BN in the 50% Nb_2O_5 isopleth.

The variation of T_c with Nb_2O_5 concentration is shown for ceramic specimens in Fig. 5(b) along the 25% BaO isopleth. The composition range, 46-52% Nb_2O_5 , represents the solid-solution range of $(\text{BSN})_I$ traversed by this isopleth at room temperature. The composition range 52-60% Nb_2O_5 represents the two-phase region $(\text{BSN})_I + (\text{BSN})_{III}$, and the change in T_c corresponds to the change in composition of $(\text{BSN})_I$ along this direction in the two-phase region. An internal check on the consistency of this data is provided by noting that the composition corresponding to the constant value of $T_c = 200^\circ\text{C}$ from Fig. 5(b) on the binary section [Fig. 5(a)] is 63% BN. If this point is joined by a straight line to pure Nb_2O_5 on Fig. 3, the line can be seen to pass through the coordinates (60% Nb_2O_5 , 25% BaO) at the solid-solution boundary of $(\text{BSN})_{III}$ as would be expected.

The dielectric properties of $(\text{BSN})_{III}$ and $(\text{BSN})_{IV}$ were not studied because the phase diagram indicates that these compounds melt incongruently and cannot be easily prepared as large single crystals. We did observe a capacitance peak at 287°C for specimen No. 150 (compound BN_3). However we observed no capacitance peak for $(\text{BSN})_{III}$ specimens up to 400°C .

Some mention should be made of the early Curie temperature work of Francombe (1) where regions of constant T_c were observed in ceramic specimens across the binary join [phase $(\text{BSN})_I$ and $(\text{BSN})_{II}$]. Our observations in Fig. 5(a) show that T_c varies smoothly. However, very small variations in the $(\text{BaO} + \text{SrO})/\text{Nb}_2\text{O}_5$ ratio cause large shifts in T_c , and it may be conceivable that Francombe's specimens possessed a variable ratio due to insufficient reaction and consequently scatter in the transition temperature. It is also possible that the disorder of Ba/Sr ions on the A1 and A2 sites may influence T_c in a fashion

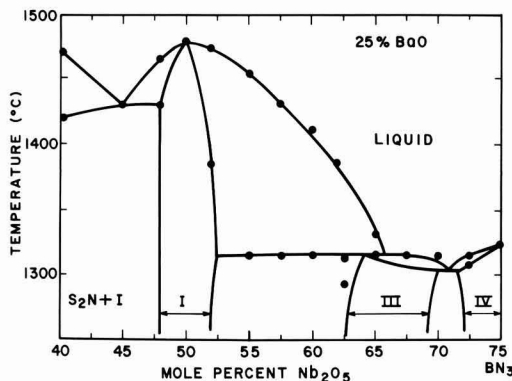


Fig. 4. High-temperature portion of 25% BaO isopleth shown as a function of Nb_2O_5 concentration.

similar to that reported by Burns and O'Kane (12) for barium sodium niobate. We observed no shift by fast air cooling from 1000°C. Since our specimens were all furnace cooled to 1000°C, it remained possible that the degree of cation ordering could be influenced by the cooling rate through the range 1300°-1000°C. Although Franccombe did not report his preparation technique in detail, it is probable that his specimens were removed from the furnace at 1300°C and air cooled to room temperature in view of the short (1 hr) sintering times used. A check on several of our (BSN)_I specimens with x near 0.5 showed that air cooling from the furnace at 1200°C did in fact decrease T_c by 20°-40°C. We were thus satisfied that the T_c measurements shown in Fig. 5 were made on specimens properly equilibrated with respect to both temperature and composition.

The crystal growth of ferroelectric compounds of controlled or uniform composition and properties requires a knowledge of the high-temperature phase equilibria for the particular system. Recent investigations have been undertaken for lithium niobate (13-15), barium sodium niobate (16-18), strontium potassium niobate (19), and potassium lithium niobate (20). These are all systems which exhibit a wide solid-solution range and a congruently melting composition which is substantially different from the "stoichiometric" composition. In practical crystal growth, we wish to operate as closely to a congruently melting composition as possible in order to avoid the problems associated with the redistribution of an excess component at the growing interface. However the desired properties, such as phase matching temperatures above room temperature, may be obtainable only at noncongruently melting compositions. Consequently, a system such as barium sodium niobate, where the congruently melting composition has desirable properties, is of more practical interest. In the present system, we can therefore eliminate compounds (BSN)_{III} and (BSN)_{IV} as being potential crystal growth candidates, since neither melts congruently at any point in the ternary solid-solution range. However the compound BSN [representing (BSN)_I and (BSN)_{II}], which has been grown as large single crystals by Ballman and Brown (3), can be seen from Fig. 2 to melt congruently near 50% BN. Furthermore, the liquidus and solidus curves are very close together for this compound across the pseudo-binary SN-BN section. This behavior is reminiscent of the SN-rich region of strontium potassium niobate (19) and the BN-rich region of barium sodium niobate (17, 18). Thus it is possible to prepare large crystals of reasonable optical perfection at compositions other than the congruent composition in this compound. This fact allowed Glass (5, 6) to use crystal compositions in the SN-rich region where there are large pyroelectric effects.

Summary

This investigation of the phase equilibria in the BaO-SrO-Nb₂O₅ system shows the existence of three

tetragonal-tungsten-bronze type structures as well as the ternary phase fields. Only one of these structures is a ternary compound; it has the formula Ba_xSr_(1-x)Nb₂O₆ and has been estimated to melt congruently near BaO:SrO:Nb₂O₅ = 0.27:0.23:0.50. This phase possesses a large existence region along the binary SrNb₂O₆-BaNb₂O₆ join and some adjacent ternary solubility. This structure possesses observable orthorhombic distortion in the BaNb₂O₆-rich region.

Acknowledgments

We wish to thank A. A. Ballman and A. M. Glass for many discussions and for providing us with single crystals. We also thank R. A. Laudise for discussions and suggestions.

Manuscript submitted April 22, 1970; revised manuscript received ca. June 22, 1970. This was Recent News Paper 352 presented at the Los Angeles Meeting of the Society, May 10-15, 1970.

Any discussion of this paper will appear in a Discussion Section to be published in the June 1971 JOURNAL.

REFERENCES

1. M. H. Franccombe, *Acta Cryst.*, **13**, 131 (1960).
2. I. G. Ismailzade, *Kristallografiya*, **5**, 268 (1960).
3. A. A. Ballman and H. Brown, *J. Cryst. Growth*, **1**, 311 (1966).
4. P. B. Jamieson, S. C. Abrahams, and J. L. Bernstein, *J. Chem. Phys.*, **48**, 5048 (1968).
5. A. M. Glass, *Appl. Phys. Letters*, **13**, 147 (1968).
6. A. M. Glass, *J. Appl. Phys.*, **40**, 4699 (1969).
7. P. V. Lenzo, E. G. Spencer, and A. A. Ballman, *Appl. Phys. Letters*, **11**, 23 (1967).
8. R. S. Roth and J. L. Waring, *J. Res. NBS*, **65A**, 337 (1961).
9. D. Ridgley and R. Ward, *J. Am. Chem. Soc.*, **77**, 6132 (1955).
10. J. R. Carruthers, G. E. Peterson, P. M. Bridenbaugh, and M. Grasso, To be submitted to *J. Appl. Phys.*
11. R. L. Barns and J. R. Carruthers, Submitted to *J. Appl. Cryst.*
12. G. Burns and D. F. O'Kane, *Phys. Letters*, **28a**, 776 (1969).
13. P. Lerner, C. Legras, and J. P. Dumas, *J. Cryst. Growth*, **3**, 4, 231 (1968).
14. G. E. Peterson and J. R. Carruthers, *J. Solid State Chem.*, **1**, 98 (1969).
15. J. R. Carruthers, G. E. Peterson, M. Grasso, and P. M. Bridenbaugh, Submitted to *J. Appl. Phys.*
16. B. A. Scott, E. A. Giess, and D. F. O'Kane, *Mat. Res. Bull.*, **4**, 107 (1969).
17. J. R. Carruthers and M. Grasso, *ibid.*, **4**, 413 (1969).
18. E. A. Giess, B. A. Scott, B. L. Olson, G. Burns, and D. F. O'Kane, *J. Am. Ceram. Soc.*, **53**, 14 (1970).
19. B. A. Scott, E. A. Giess, D. F. O'Kane, and G. Burns, *ibid.*, **53**, 106 (1970).
20. B. A. Scott, E. A. Giess, B. L. Olson, G. Burns, A. W. Smith, and D. F. O'Kane, *Mat. Res. Bull.*, **5**, 47 (1970).

Thermodynamics of the Iron-Nickel-Oxygen System at 1000°C

A. D. Dalvi** and W. W. Smeltzer*

Department of Metallurgy and Materials Science, McMaster University, Hamilton, Ontario, Canada

ABSTRACT

The isothermal section of the Fe-Ni-O system at 1000°C has been defined by determining the compositions and structures of the equilibrated solid phases. Wustite can coexist with Fe-Ni alloys containing up to 79.6 a/o (atomic per cent) Ni. The three-phase field wustite-spinel-alloy consists of wustite containing 0.51 a/o Ni, spinel containing 0.6 a/o Ni, and an alloy containing 79.6 a/o Ni. The three-phase field, spinel-nickel oxide-alloy, consists of nickel ferrite, nickel oxide containing 6.5 a/o Fe, and an alloy containing 99.5 a/o Ni. Tie lines in the spinel-alloy field were investigated in detail. Wustite-nickel oxide solid solutions exhibited nonideal behavior.

The properties of the Fe-Ni-O system at high temperatures where the iron-nickel alloys occur in the form of austenitic solid solution have not been intensively investigated. Brabers and Birchenall (1) determined the equilibrium compositions of wustite, spinel oxide, and alloys containing up to 60 w/o (weight per cent) Ni at 1050°C. The latest available results obtained for temperatures in the range 700°-1100°C are those reported by Viktorovich and Lisovskii (2) and Viktorovich *et al.* (3) for compositions within the wustite-alloy phase field including the limiting compositions of wustite and alloy coexisting with spinel. Values for the dissociation pressures of wustite containing nickel in solid solution have been reported for the temperature of 1000°C by Oriani (4) and Roeder and Smeltzer (5). Accordingly, the purpose of this work has been to obtain more complete knowledge of this ternary system at 1000°C by investigating the nickel-rich region of the phase diagram.

Experimental

Specimens were prepared by two methods. Mixtures of powders containing iron and nickel (99.99 w/o pure) in given proportions and one or more of the C.P. reagent grade oxides (99.6 w/o pure)—nickel oxide, hematite, and nickel ferrite—were compressed into tablets, 12.5 mm diameter and 2 mm thick, at a pressure of 6.5 tons/cm² by means of a hydraulic press. In the second method, alloy plates, 2 x 1 x 0.05 cm of various compositions ranging from 40 to 95% Ni were oxidized to desirable degrees in oxygen at 1000°C. The tablets and oxidized alloy specimens were sealed in quartz tubes containing argon [99.99 v/o (volume per cent) pure]. All encapsulated specimens were equilibrated at 1000° ± 2.5°C and then cooled to room temperature within 5 min by means of an air quench. Tablets were equilibrated for 30 days, while the oxidized alloy plates were equilibrated for periods up to 75 days. The phases in the quenched specimens were identified by x-ray techniques using a diffractometer equipped with a copper tube and nickel filter.

Specimens were mounted in epoxy cold setting resin, polished on silicon carbide papers 200 through 600 grit with kerosene as lubricant, then polished on a wax lap impregnated with 30μ alumina. This procedure resulted in best retention of oxide grains and in obtaining a flat surface. The final polishing was done on 6 and 1μ diamond wheels with napless cloths and kerosene as lubricant. It was necessary to etch the specimens for identification of phases by optical microscopy. A 5% concentrated hydrochloric acid solution in ethyl alcohol was used to preferentially etch wustite in structures

containing wustite, spinel, and alloy. A 50% concentrated hydrochloric acid solution in water, which preferentially etched spinel, was used as etchant for structures containing nickel ferrite, nickel oxide, and alloy.

Chemical analyses were carried out by means of a CAMECA electron-probe microanalyzer operating at 15 kev with an x-ray beam take-off angle of 18°. This instrument was calibrated according to the method described by Friskney and Haworth (6, 7). Essentially the method consisted of successively applying atomic number (8), absorption (9, 10), and fluorescence (11, 12) corrections to an assumed set of compositions for a solid phase and calculating the intensity ratio for each metal to that for the pure metal. This procedure yielded iron and nickel calibration curves for each solid. In all cases, the fluorescence correction was significant. The atomic number correction was significant only for the oxides due to the presence of oxygen. Standards used to check the calibration curves for the alloys were alloys of several known compositions. The calibration procedure for the wustite phase could be verified only for pure wustite. For spinel oxide, the calibration procedure was verified for magnetite and nickel ferrite. The homogeneity of each phase in a specimen was determined by subjecting different areas to point counts. In addition, x-ray and electron back-scatter pictures were used for phase identification and to determine qualitatively the metal compositions in the coexisting phases.

Results

The photomicrographs in Fig. 1 and 2 illustrate typical oxide-alloy structures of equilibrated specimens. The structures obtained from both compacts and oxidized alloy plates exhibited an essential feature in that the different phases, which were bonded to one another, were sufficiently large for accurate analyses by the electron microprobe. At the acceleration voltage of 15 kev used for these analyses, the diameter of the x-ray production zone was only about 2μ and hence the minimum size of the particle for accurate analysis was about 5μ. The minimum size of particles analyzed in this investigation was 15μ. Identification of the phases present in a specimen by x-ray diffraction and microscopic observation showed complete agreement.

Information given by the electron probe micrographs was very useful. For example, the micrographs shown in Fig. 3 were obtained from a specimen consisting of spinel containing 1.4 w/o Ni and 71 w/o iron, and an alloy containing 84 w/o Ni. In the electron back-scatter image, the alloy was black and the spinel completely white. Also, the x-ray intensities clearly defined the amounts of iron and nickel in the different phases.

The compositions for the coexisting oxide and alloy phases are recorded in Table I. The mass concentra-

** Electrochemical Society Student Associate Member.

* Electrochemical Society Active Member.

Key words: thermodynamics, Fe-Ni-O system, Gibbs-Duhem relations, phase composition of wustite, nickel, ferrite, spinel, nickel oxide, iron-nickel alloys.



Fig. 1. Equilibrium two-phase fields wustite-alloy and the spinel-alloy. In both micrographs, the dark phases are the oxide phases and the bright phase is the alloy phase: (a) upper micrograph—wustite + alloy etched in 5% HCl in ethyl alcohol, 250X; (b) lower micrograph—spinel + alloy etched in 50% HCl in water, 320X.

tions obtained experimentally were converted to atomic concentrations which are also given in Table I. Wustite coexisted with alloys containing up to 79.6 a/o Ni, the maximum nickel solubility in wustite being 0.51 a/o. It was found that spinel coexisted with alloys containing from 79.6 to 99.5 a/o Ni. The spinel in equilibrium with wustite and alloy contained 0.6 a/o Ni, while the compositions of the spinel in equilibrium with nickel oxide and alloy corresponded to stoichiometric nickel ferrite. The maximum iron solubility in nickel oxide was 6.5 a/o.

Discussion

The isothermal section of the phase diagram at 1000°C constructed from the compositional determi-

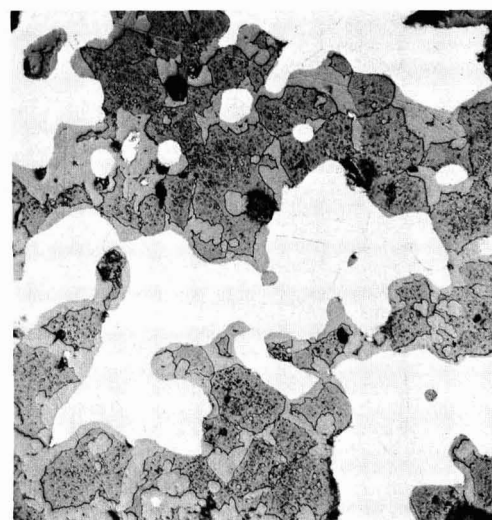
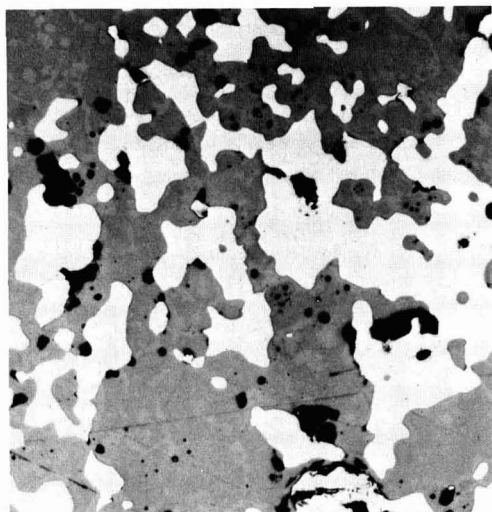


Fig. 2. Equilibrium three-phase field wustite-spinel-alloy. (a) Upper micrograph—microstructure before etching, 200X. (b) Lower micrograph—specimen surface after etching in 5% HCl in ethyl alcohol, 400X; bright phase—alloy, dark matrix phase—wustite, gray precipitates—spinel.

nations is illustrated in Fig. 4. The oxygen solubilities in the alloys have been magnified for clarity and are in fact negligibly small and unknown. The diagram is symmetric about the spinel-alloy field which is bounded by three-phase fields containing wustite-spinel-alloy and nickel oxide-spinel-alloy. These fields are bounded in turn by two-phase fields containing wustite and alloy on the iron-rich side and nickel oxide and alloy on the nickel-rich side of the diagram. Wustite, which exhibits only a small nickel solubility, is stable over a wide range of alloy composition; on the other hand, nickel oxide exhibits a relatively large iron solubility but its stability is confined to a very narrow range of alloy composition. The tie lines in the wustite-alloy and spinel-alloy fields are not proportionately spaced. They fan out from oxide in the iron-rich region and from the alloy in the nickel-rich region of the diagram.



Fig. 3. Electron probe images of sample in the two-phase field spinel + alloy, 1000X. (a) Upper micrograph—electron backscatter image. The spinel phase appears as bright and the alloy phase appears as dark. (b) Middle micrograph—Fe- K_{α} x-ray image showing distribution of iron in the two phases. (c) Lower micrograph—Ni- K_{α} x-ray image showing nickel distribution.

A terminal nickel solubility of 0.51 a/o in wustite agrees with a reported value (2) and it lies between two determinations where the nickel contents were reported virtually absent (1) and 1.3 a/o (5). The iron concentration as well as the total metal concentration in wustite decreased with increasing nickel content of the alloy. At the terminal composition, the total amount of metal was 46.7 a/o. Since this value is equal to the iron concentration in wustite upon its equilibration with magnetite, it would appear that there is

an isomorphous substitution of nickel for iron in the wustite lattice. The nickel composition of 0.6 a/o for spinel S_1 , shows wide divergence from an earlier determination of 5 a/o (1). Magnetite exhibits an inverse spinel structure with ferrous ions occupying octahedral sites and ferric ions occupying both octahedral and tetrahedral sites between oxygen ions (13). Apparently, nickel replaces iron in the divalent sites in the spinel up to the terminal composition corresponding to nickel ferrite (14, 15).

The values reported for the dissociation pressures and nickel contents of wustite are sufficient for thermodynamic evaluation of the solution behavior of nickel in wustite. Values reported for the dissociation pressures of wustite containing nickel in solid solution are compared to that for pure wustite in Fig. 5. The Gibbs-Duhem relationship may be applied to the alloy and oxide phases because these pressures determine oxygen activities

$$N_{O^A} d \ln a_{O^A} + N_{Ni^A} d \ln a_{Ni^A} + N_{Fe^A} d \ln a_{Fe^A} = 0 \quad [1]$$

$$N_{O^W} d \ln a_{O^W} + N_{Ni^W} d \ln a_{Ni^W} + N_{Fe^W} d \ln a_{Fe^W} = 0 \quad [2]$$

where N is a mole fraction and a is an activity in the alloy (A) and wustite (W) phases. At equilibrium, Eq. [1] and [2] yield the variation of oxygen activity with respect to nickel activity, for

$$\frac{d \ln a_O}{d \ln a_{Ni}} = - \frac{N_{Ni^A} - N_{Ni^W} N_{Fe^A}/N_{Fe^W}}{N_{O^A} - N_{O^W} N_{Fe^A}/N_{Fe^W}} \quad [3]$$

Since the oxygen solubility in the metal is extremely small, 0.0003-0.015 w/o (16, 17), we may neglect the term N_{O^A} in integrating Eq. [3]. Therefore

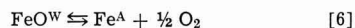
$$\ln P_{O_2}/P_{O_2}^0 = 2 \int_{O}^{N_{Ni^A}} \left\{ \frac{N_{Ni^A} - N_{Ni^W} N_{Fe^A}/N_{Fe^W}}{N_{O^W} N_{Fe^A}/N_{Fe^W}} \right\} d \ln (\gamma_{Ni^A} N_{Ni^A}) \quad [4]$$

where $P_{O_2}^0$ is the dissociation pressure of pure wustite. This equation was integrated numerically by means of a computer since values are available for the mole fractions of iron, nickel, and oxygen in wustite as well as the activity coefficients of nickel in the alloy (2, 4, 18, 19).

Equation [3] may be simply integrated to the following expression if it is additionally assumed that the small concentration of nickel in wustite approximates to zero and that the mole fractions of iron and oxygen are equal as for stoichiometric wustite

$$\log P_{O_2}/P_{O_2}^0 = 2 \log (1/1 - N_{Ni^A}) \quad [5]$$

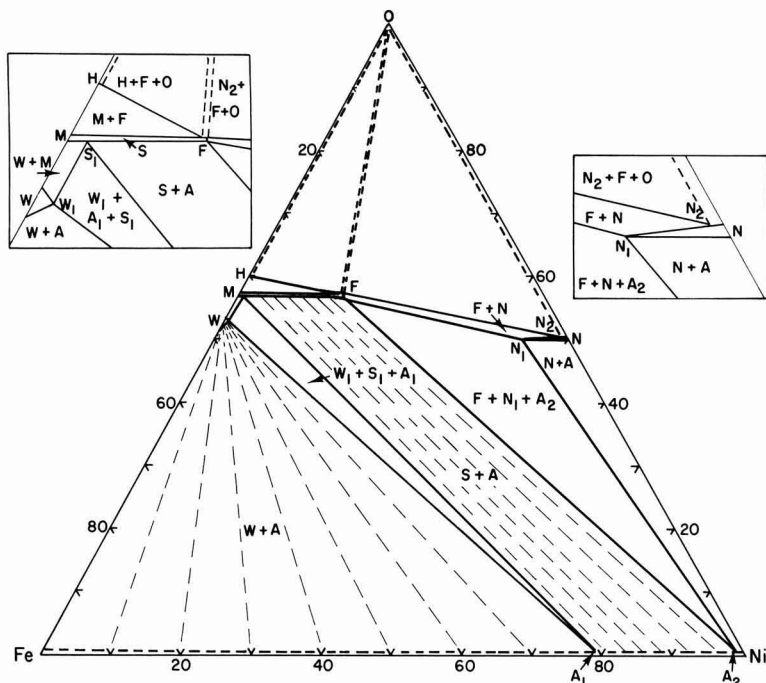
This expression is also obtained by comparing the dissociation pressures of pure wustite with that of wustite equilibrated with the alloy



under the approximations of unit activity for wustite and ideal solution behavior of iron in the alloy.

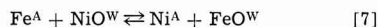
Comparison of the values for the dissociation pressures calculated by means of Eq. [4] and [5] to those determined experimentally are shown in Fig. 5. Although there are large uncertainties in the evaluations of the alloy compositions in the case where dissociation pressures were determined for wustite-alloy compacts (5), both equations serve as a first approximation to the experimental results. The better fit, however, is obtained by Eq. [4] where account has been given to the degree of nickel solubility in wustite and to the activity coefficients for the alloy components. Equation [4] gives the invariant oxygen partial pressures in the wustite-spinel-alloy phase field as 3.26×10^{-14} atm, a value considerably larger than the dissociation pressure of pure wustite, $P_{O_2}^0 = 1.32 \times 10^{-15}$ atm. Since

Fig. 4. Iron-nickel-oxygen phase diagram at 1000°C (a/o). W_1 — $Ni_{0.01}Fe_{0.87}O$ (wustite); S_1 — $Ni_{0.04}Fe_{2.96}O_4$ (spinel). A_1 —79.6 a/o Ni, 20.4 a/o Fe (alloy). F — $NiFe_2O_4$ (ferrite); N_1 — $Fe_{0.13}Ni_{0.87}O$ (nickel oxide). A_2 —99.5 a/o Ni, 0.5 a/o Fe (alloy). N_2 — $Fe_xNi_{1-x}O$ where $x \approx 0.0005$ (nickel oxide). Phase notations: W—wustite, $Ni_xFe_{1-(x+y)}O$; M—magnetite, Fe_3O_4 ; H—hematite, Fe_2O_3 ; N—nickel oxide, $Fe_xNi_{1-x}O$. The dashed line across the bottom of the diagram represents oxygen solubilities in the alloy magnified for clarity. Dashed lines in the vicinity of the oxygen corner represent undetermined boundaries of phase fields involving oxygen. The insets on either side represent corresponding phase regions on an expanded scale.



the dissociation pressure of wustite containing the maximum nickel content is less than that for wustite-magnetite equilibrium, 1.62×10^{-13} atm, it can be inferred, as was found, that the limiting nickel content of wustite, 0.51 a/o, should be less than the corresponding value for spinel, 0.60 a/o.

A useful approximation to the wustite solid solution may be made by assuming that nickel dissolves in wustite as nickel oxide. The following displacement reaction may then be considered



where

$$K = \frac{a_{Ni(A)} \cdot a_{FeO(W)}}{a_{Fe(A)} \cdot a_{NiO(W)}} = \frac{(\gamma_{Ni} \cdot N_{Ni})_A \cdot (\gamma_{FeO} \cdot N_{FeO})_W}{(\gamma_{Fe} \cdot N_{Fe})_A \cdot (\gamma_{NiO} \cdot N_{NiO})_W} \quad [8]$$

The value of K is determined to be 186 at 1000°C from

electromotive force measurements of Kiukkola and Wagner (20). Since the values of the activity coefficients for the alloy components are known, the nickel oxide content of wustite was calculated for the case of oxide ideal solid solution behavior as a function of nickel content of the alloy phase. This relationship and the experimental relationship are shown in Fig. 6. The curve through the experimental points was determined by a least-squares analysis using a computer. Division of the corresponding values obtained by these two relationships yields the activity coefficient ratio, $\gamma_{NiO}/\gamma_{FeO}$, as a function of equilibrium alloy composition. The curve representing this activity coefficient ratio is also shown in Fig. 6. It can be seen that the ratio of the activity coefficient remains constant at 3.72 for the alloy composition range of 0–40 a/o Ni and then decreases to a value of 2.33 at the limiting alloy composition for stability of wustite. Consequently, nickel oxide solubility in wustite displays a Henry law be-

Table I. Electron microprobe analysis of coexisting alloy and oxide phases at 1000°C

Sample No.	Composition of alloy						Oxide phase identification	Composition of oxide phases						
	w/o Ni	U†	w/o Fe	U†	a/o Ni	a/o Fe		w/o Ni	U†	w/o Fe	U†	a/o Ni	a/o Fe	
1	60.0	0.5	40.0	0.4	48.8	41.2	W	0.13	0.05	76.0	0.4	0.1	47.7	
2	62.9	0.5	37.1	0.4	61.8	38.2	W	0.13	0.05	75.9	0.4	0.1	47.6	
3*	81.0	0.5	19.6	0.4	79.7	20.3	W	0.84	0.05	75.4	0.4	0.50	53.3	
4*	80.5	0.5	20.1	0.4	79.1	20.9	W	0.91	0.05	71.5	0.4	0.51	42.2	
							W	0.85	0.05	75.4	0.4	0.51	53.3	
5*	81.1	0.5	19.3	0.4	80.0	20.0	S	1.08	0.05	71.4	0.4	0.51	42.1	
							W	0.85	0.05	75.4	0.4	0.51	53.3	
6	84.0	0.5	16.0	0.4	83.3	16.7	S	1.10	0.05	71.4	0.4	0.62	42.1	
7	86.3	0.5	14.0	0.4	85.3	14.6	S	1.4	0.1	71.0	0.4	0.79	42.1	
8	88.0	0.5	12.1	0.4	87.3	12.6	S	1.7	0.1	70.5	0.4	0.96	41.7	
9	88.5	0.5	12.2	0.4	87.4	12.6	S	2.3	0.2	70.1	0.4	1.29	41.4	
10	93.8	0.6	6.0	0.4	93.6	6.4	S	2.7	0.2	69.8	0.4	1.51	41.2	
11	96.0	0.6	4.5	0.4	95.4	4.8	S	5.9	0.3	66.5	0.4	3.32	39.3	
12	97.5	0.6	3.7	0.4	96.4	3.8	S	9.0	0.3	63.5	0.4	5.07	37.6	
13	98.7	0.6	1.5	0.2	98.2	1.6	S	11.7	0.3	60.8	0.4	6.60	36.1	
14	98.9	0.6	1.2	0.2	98.4	1.6	S	16.8	0.5	55.6	0.4	9.53	33.1	
15**	99.5	{	+0.3 -0.7	0.5	0.1	99.5	0.5	S	20.0	0.5	52.4	0.4	11.37	31.3
								S	25.0	0.5	47.4	0.5	14.26	28.4
								N	68.7	0.5	9.8	0.3	43.5	6.5

* Three-phase field wustite-spinel-alloy.

** Three-phase field nickel ferrite-nickel oxide-alloy.

† U corresponds to the uncertainty in the experimental determinations. Phase symbols correspond to: W—wustite; S—spinel; N—nickel oxide.

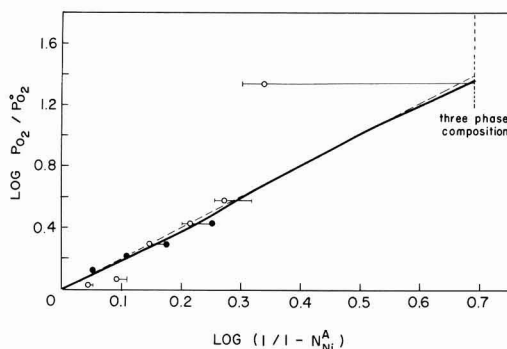


Fig. 5. Equilibrium oxygen partial pressure in the two-phase field wustite-alloy as a function of alloy composition. The solid and dashed curves were calculated according to Eq. [4] and [5], respectively. The data were obtained from Ref. (4) (●) and Ref. (5) (○).

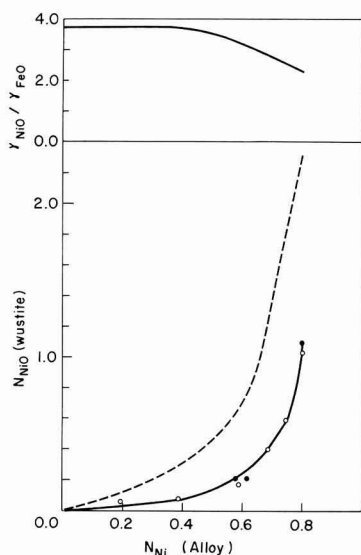
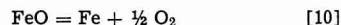
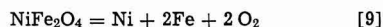


Fig. 6. Solubility of nickel oxide in wustite as a function of equilibrium alloy composition. The dashed curve was obtained with the assumption of ideality for the wustite-nickel oxide system. The data for the experimental curve were obtained from this investigation (●), and from Ref. (2) (○). The activity coefficient ratio $\gamma_{\text{NiO}}/\gamma_{\text{FeO}}$ for the wustite phase as a function of equilibrium alloy composition was obtained from the above two curves on dividing calculated values obtained on the assumption of ideality by the corresponding experimental values, Eq. [8].

havior only to a mole fraction of 0.008. A similar calculation using Eq. [8] yields $\gamma_{\text{FeO}}/\gamma_{\text{NiO}} = 4.88$ at the limiting tie line of the nickel oxide-alloy region where the alloy composition is 99.5 a/o Ni, the activity coefficients of nickel and iron in the alloy are 1.0 and 0.78, respectively, and the mole fraction of wustite in nickel oxide is 0.13. Consequently, wustite-nickel oxide solid solutions exhibit positive deviation from ideal behavior at oxygen partial pressures for equilibration with Fe-Ni alloys.

The iron contents of the nickel oxide, N_2 , and the alloy, A_2 , occurring in the spinel-nickel oxide-oxygen and in the spinel-nickel oxide-alloy regions, respectively, may be evaluated from appropriate standard free energies of formation. The following reactions may be considered



Since the standard free energies for these reactions at 1000°C are 152, 43, and 30 kcal, respectively (21, 22), we obtain for the equilibrium constants in terms of standard oxygen activities for the pure metals and oxides

$$K_9 = (a_{\text{O}}^0)^4 = a_{\text{Ni}} a_{\text{Fe}} a_{\text{O}}^4 = 7.65 \times 10^{-27} \quad [12]$$

$$K_{10} = (a_{\text{O}}^0)^{10} = a_{\text{Fe}} a_{\text{O}}/a_{\text{FeO}} = 4.14 \times 10^{-8} \quad [13]$$

$$K_{11} = (a_{\text{O}}^0)^{11} = a_{\text{Ni}} a_{\text{O}}/a_{\text{NiO}} = 7.06 \times 10^{-8} \quad [14]$$

In the three-phase region spinel-oxygen-nickel oxide, $a_{\text{O}} \approx 1$ and $a_{\text{NiO}} \approx 1$. Therefore, $a_{\text{FeO}} \approx 10^{-3}$. Accordingly, the iron content in nickel oxide, N_2 , corresponds to approximately 0.05 a/o. In the three-phase region spinel-nickel oxide-alloy, $N_{\text{NiO}} \approx 0.9$ and $a_{\text{Ni}} \approx 1$. Therefore, $a_{\text{FeO}} = 0.38$ and $a_{\text{O}} = 6.35 \times 10^{-6}$. Accordingly, the mole fraction of iron in the alloy, A_2 , $N_{\text{Fe}} = a_{\text{Fe}}/\gamma_{\text{Fe}} = 0.0047/0.78 \approx 0.006$. That is, the nickel-iron alloy existing in equilibrium with spinel and nickel oxide contains approximately 0.6 a/o iron. This calculated value is to be compared to the experimentally determined value of 0.5 a/o.

Conclusions

The phase boundaries of the two-phase fields wustite-alloy, spinel-alloy, and nickel oxide-alloy, and the three-phase fields wustite-spinel-alloy and spinel-nickel oxide-alloy were determined at 1000°C. Chemical analyses indicated that nickel solubility in wustite was governed by isomorphic replacement of iron by nickel. It was inferred that, in the spinel phase extending from magnetite to stoichiometric nickel-ferrite, ferrous ions in the octahedral interstitial sites were replaced by divalent nickel ions. The spinel phase in equilibrium with alloys extends from $\text{Ni}_{0.04}\text{Fe}_{2.96}\text{O}_4$ to NiFe_2O_4 . The wustite-spinel-alloy field consists of wustite containing 0.51 a/o Ni, spinel containing 0.60 a/o Ni, and an Fe-Ni alloy containing 79.6 a/o Ni. The spinel-nickel oxide-alloy field consists of nickel ferrite, nickel oxide containing 6.5 a/o Fe, and an alloy containing 0.5 a/o Fe. The iron content of nickel oxide in equilibrium with spinel and oxygen was calculated to be approximately 0.05 a/o. By means of the Gibbs-Duhem relationship, the dissociation pressures of wustite were related to the compositions of the alloy. Solution of nickel oxide in wustite was shown to exhibit positive deviations from ideal solid solution behavior.

Acknowledgments

This work was carried out by A. D. Dalvi in partial fulfillment of the requirements for award of the Ph.D. degree at McMaster University. He wishes to acknowledge the award of an International Nickel Company of Canada Fellowship for graduate research. The authors are indebted to Professor Carl Wagner for discussion relating to this problem. This research was carried out under auspices of the Defence Research Board and the National Research Council of Canada.

Manuscript submitted Dec. 12, 1969; revised manuscript received June 26, 1970. This was Paper 206 presented at the Detroit Meeting of the Society, Oct. 5-9, 1969.

Any discussion of this paper will appear in a Discussion Section to be published in the June 1971 JOURNAL.

REFERENCES

1. M. J. Brabers and C. E. Birchenall, *Corrosion*, **14**, 179 (1958).
2. G. S. Viktorovich and D. I. Lisovskii, *Tsvetnyye Metally*, (Eng. Transl.), **7** (11), 49 (1966).
3. G. S. Viktorovich, V. A. Gutin, and D. I. Lisovskii, *ibid.*, **7** (12), 54 (1966).

4. R. A. Oriani, *Acta Met.*, **1**, 448 (1953).
5. G. A. Roeder and W. W. Smeltzer, *This Journal*, **111**, 1074 (1964).
6. C. A. Friskney and C. W. Haworth, *Brit. J. Appl. Phys. Ser. 2*, **1**, 873 (1968).
7. C. A. Friskney and C. W. Haworth, *J. Sci. Instr.*, *Ser. 2*, **1**, 753 (1968).
8. P. Duncumb and S. J. B. Reed, *Nat. Bur. Std. (U.S.) Spec. pub. No. 298* (1968).
9. J. Philibert, X-Ray Optics and X-Ray Microanalysis, *Proc. Third Int. Symp.*, Stanford (1962).
10. P. Duncumb and P. K. Shields, "The Electron Microprobe," p. 284, T. D. McKinley, K. F. J. Heinrich, and D. B. Wittry, Editors, John Wiley (1966).
11. R. Castaing, Thesis, University of Paris (1951).
12. M. Green and V. E. Cosslett, *Proc. Phys. Soc. (London)*, **78**, 1206 (1961).
13. K. Hauffe, "Oxidation of Metals," p. 23, Plenum Press (1965).
14. S. I. Youssef, M. G. Natera, R. J. Begum, B. J. Srinivasan, N. S. Murthy, *J. Phys. Chem. Solids*, **30**, 1948 (1969).
15. A. E. Paladino, Jr., *J. Am. Ceram. Soc.*, **42**, 168 (1959).
16. M. Hansen, "Constitution of Binary Alloys," p. 1024, Mc-Graw Hill (1958).
17. J. Swisher and E. T. Turkdogan, *Trans. Met. Soc. AIME*, **239**, 626 (1967).
18. R. Hultgren, R. L. Orr, P. D. Anderson, and K. K. Kelley, "Selected Values of Thermodynamic Properties of Metals and Alloys," John Wiley (1963).
19. O. Kubaschewski and O. Von Goldbeck, *Trans. Faraday Soc.*, **45**, 959 (1949).
20. K. Kiukkola and C. Wagner, *This Journal*, **104**, 379 (1957).
21. G. G. Charette and S. J. Flengas, *ibid.*, **115**, 796 (1968).
22. J. D. Tretjakow and H. Schmalzried, *Berichte der Bunsengesellschaft*, **69**, 396 (1965).

Technical Notes



Surface Polarity and Etching of Beta-Silicon Carbide

Robert W. Bartlett* and Malcom Barlow

Stanford Research Institute, Menlo Park, California 94025

Beta-silicon carbide has the zinc blende structure and solution-grown crystals are in the form of octahedral platelets (1). Although the silicon and carbon layers alternate in the stacking sequence, the interatomic spacing in the octahedral direction, [111], is not uniform. The terminating plane for the (111) surface is ideally composed of silicon atoms, while the terminating plane for the ($\bar{1}\bar{1}\bar{1}$) surface is composed of carbon atoms.

If use is made of the anomalous phase shift, differences in x-ray diffraction intensity are detectable and the two opposite sides of noncentrosymmetric crystals can be identified (2). This method has been used by Warekois and co-workers (3,4) to identify faces of several III-V and II-VI compounds, and Brack (5) has used it to determine polarity in α -silicon carbide.

Polarity Determination

X-ray diffraction intensities from octahedral platelets of β -silicon carbide were measured on a Norelco diffractometer, using filtered $\text{CuK}\alpha$ radiation. The standard sample holder was replaced by a single-crystal goniometer to facilitate orientation and mounting of the crystals, and the x-ray beam was collimated to about 1 mm diameter. Intensities of the scattered beams were determined by a Geiger counter with chart recorder, each reflection being scanned slowly through the Bragg angle. Filters limited the intensities to the linear counting rate region of the counter.

The diffracted intensities are proportional to $|\mathbf{F}(\mathbf{hkl})|^2$. The theoretical ratios of $|\mathbf{F}(\mathbf{hkl})|^2/|\mathbf{F}(\mathbf{hkl})|^2$, calculated from the anomalous dispersion correction, are

$$\frac{|\mathbf{F}(111)|^2}{|\mathbf{F}(\bar{1}\bar{1}\bar{1})|^2} = 0.94, \quad \frac{|\mathbf{F}(222)|^2}{|\mathbf{F}(222)|^2} = 1.00, \quad \frac{|\mathbf{F}(333)|^2}{|\mathbf{F}(333)|^2} = 1.06$$

Three crystals were examined repeatedly, and the ex-

perimental ratios of intensities for the (111)/($\bar{1}\bar{1}\bar{1}$) reflections were always smaller than 1, while the experimental ratios of intensities for the (333)/(333) reflections were always larger than 1.

Etching

Etching studies were made on β -silicon carbide platelets grown from solution and on vapor-deposited β -silicon carbide grown epitaxially on platelets (6). Two etchants were used: (a) a gas mixture containing 6% chlorine and 26% oxygen in argon at 850° to 900°C and (b) a fused salt mixture of 75% NaOH and 25% Na_2O_2 at 700°C. The polarity of the crystals was determined from the ratio of x-ray diffraction intensities. Although the rate of attack was different, the same surface characteristics were observed with both etchants. Etch pits developed on the (111) face but did not develop on the ($\bar{1}\bar{1}\bar{1}$) face. Except for the etch pits, the (111) face remains smooth. These results correspond with the etching of α -silicon carbide in similar etchants (7,8) where etch pits are observed to form on the smooth face, which was identified by Brack (5) as the (0001) face terminating in silicon atoms, although pits do not usually form on the rough (0001) face. Similar results have been observed for other zinc blende and wurtzite structures among III-V and II-VI compounds (3,4).

The depth of etch pits is much less than the thickness of silicon carbide uniformly removed during etching. Uniform etch rates for the chlorine-oxygen gas etchant were obtained by measuring step heights between etched regions and the regions protected by a thermally grown oxide film. On solution-grown crystals the etch rate at 900°C was 0.3 to 0.5 $\mu\text{m}/\text{min}$. Although the etch-pitting characteristics of β -silicon carbide grown epitaxially by vapor deposition were essentially the same as those of the solution-grown platelets, there were marked differences in the uniform etching rates under identical etching conditions. The chlorine-oxygen gas-etching rate of undoped epitaxially grown

* Electrochemical Society Active Member.

Key words: silicon carbide, etching, surfaces, noncentrosymmetric crystals, semiconductors.

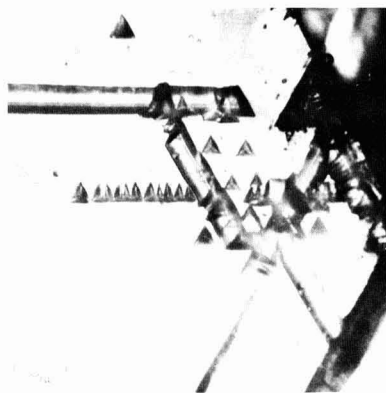


Fig. 1. Solution-grown β -SiC (111) surface etched in NaOH- Na_2O_2 .

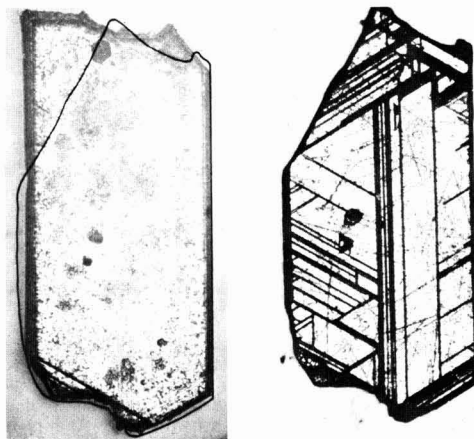


Fig. 2. Etch pit rows extending from the substrate through the epitaxial layer: (left) Etched boron-doped epitaxial layer; (right) after removal of epitaxial layer and re-etching.

crystals was less than $0.02 \mu\text{M}/\text{min}$ at 900°C . The mechanism leading to this difference in rates is not known but may be related to differences in the concentrations of specific impurities present in amounts below the detection limits of neutron activation analysis or emission spectrography.

The etch pits on solution-grown platelets have a marked tendency to cluster in rows as shown in Fig. 1. The pits are frequently sufficiently large and closely spaced to form a groove often running the entire length of the crystal. The axis of these etch pit rows is always a $\langle 110 \rangle$ direction. X-ray topographic studies (9) show that the etch pits correspond to surface-terminating partial dislocations with a $\langle 112 \rangle$ Burgers' vector that are associated with closely spaced parallel {111} stacking faults.

These dislocations continue in the vapor-deposited silicon carbide grown epitaxially on solution-grown substrates. Etch pits on the surface of the epitaxially grown layer are observed in exactly the same locations as the underlying substrate. This indicates that the stacking faults are also extending from the substrate through the epitaxy layer. This effect is demonstrated by the two micrographs of the same crystal shown in Fig. 2. Correspondence between the etch pit patterns in these micrographs is readily apparent. Both surfaces shown were given identical NaOH- Na_2O_2 etching treatments. The lefthand micrograph was taken after lapping off the epitaxial layer with 1μ diamond paste and re-etching the surface. Note that a small section of the crystal was broken during lapping. The epitaxial layer was more resistant to the NaOH- Na_2O_2 etchant than was the substrate, which is consistent with the results observed with the chlorine-oxygen gas etchant.

Etch pits that were not extensions from the substrate were also observed on (111) surfaces of epitaxially grown β -silicon carbide. These pits occur in short $\langle 110 \rangle$ oriented rows often grouped to form one or more sides of an equilateral triangle, as shown in Fig. 3. These rows are usually no longer than 25μ . The chlorine-oxygen gas etching also causes a few large craters to form in the (111) epitaxial surface, also shown in Fig. 3. Although these craters are oriented in conformance with the octahedral morphology of the smaller etch pits, they are not observed on similarly etched solution-grown substrates. On the (111) face of epitaxially grown β -silicon carbide the chlorine-oxygen gas etch rounds off twinning hillocks that were formed during vapor deposition. The nodules that result are faintly visible on the back face of the transparent crystal shown in Fig. 3.

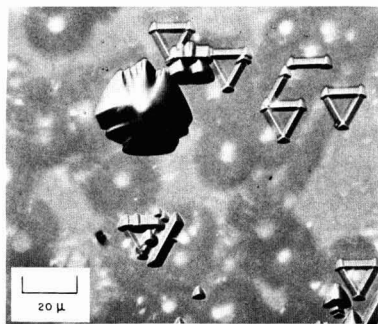


Fig. 3. Epitaxially grown β -SiC (111) surface etched in chlorine-oxygen gas mixture.

Acknowledgments

The authors wish to express their appreciation to Charlotte Meredith and David Dionne for experimental assistance. This work was sponsored by the Air Force Cambridge Research Laboratories, Office of Aeronautical Research, under Contract F19628-67-C0243.

Manuscript submitted Oct. 3, 1969; revised manuscript received ca. July 10, 1970.

Any discussion of this paper will appear in a Discussion Section to be published in the June 1971 JOURNAL.

REFERENCES

1. W. E. Nelson, F. A. Halden, and A. Rosengreen, *J. Appl. Phys.*, **37**, 333 (1966).
2. R. W. James, "Optical Principles of the Diffraction of X-Rays," Chap. IV., G. Bell & Sons Ltd., London (1958).
3. E. P. Warekois and P. H. Metzger, *J. Appl. Phys.*, **30**, 960 (1959).
4. E. P. Warekois, M. C. Levine, A. N. Mariano, and H. C. Gatos, *J. Appl. Phys.*, **33**, 690 (1962).
5. K. Brack, *J. Appl. Phys.*, **36**, 3560 (1965).
6. R. W. Bartlett and R. A. Mueller, *Mater. Res. Bull.*, **4**, S-341 (1969).
7. V. J. Jennings, *ibid.*, **4**, S-199 (1969).
8. V. J. Jennings, A. Sommer, and H. C. Chang, *This Journal*, **113**, 728 (1966).
9. R. W. Bartlett and G. W. Martin, *J. Appl. Phys.*, **39**, 2324 (1968).

Sputtering of Bismuth-Titanium Two-Phase Cathodes

R. T. Shoemaker, C. E. Anderson,*¹ and G. L. Liedl

Purdue University, Lafayette, Indiana 47907

In recent years there has been an increased interest in the development of sputtered films for electronic applications. A wide variety of elements has been investigated in the past with particular emphasis on single element films. Recently more emphasis has been placed on multiple component films produced by a number of methods such as sputtering from multiple component cathodes, reactive sputtering, or some post reaction process.

Winters, Raimondi, and Horne (1) have recently proposed a model for thin film composition by considering only the mechanisms affecting the composition at the substrate. An influence on the flux of atoms leaving the cathode has been illustrated by Anderson (2).

It is also of importance to determine the influence of the cathode morphology on the thin film structure and properties. This study is concerned with the influence of the cathode morphology on the stoichiometry of the resulting thin film. The bismuth-titanium system was selected for this study because of the large difference in the self-sputtering rates of bismuth and titanium (3).

Theory

To relate the composition of the film to the cathode, it is assumed that the number of each type of atom reaching the substrate is a function of the number of atoms of that type leaving the cathode and the probability that these atoms will reach and adhere to the substrate. Therefore, the composition of the film produced on the substrate is given by

$$y_i = N_i P_{i\alpha} / \sum_j N_j P_{j\alpha} \quad [1]$$

where N_i is the number of atoms of element i leaving the cathode per unit area per second, P_i is the probability that atom i will reach the substrate, and α_i is the sticking coefficient.

The number of atoms of element i leaving the cathode is a function of the cathode morphology, the areal coverage of each phase, the composition of each phase, and the sputtering rate of each phase. For a two-element two-phase cathode where the two phases are pure elements, the number of type i atoms leaving the cathode is

$$N_i = x_i f_i \quad [2]$$

where x_i is the atom fraction of element i in cathode and f_i is the function relating areal coverage to atom fraction and sputtering rate to sputtering parameters.

If we assume a probability function which describes the probability of each species reaching the substrate as

$$P_i = \exp [-d(K_{1i}X_i - K_{2i})] \quad [3]$$

where d is the interelectrode separation, X_i is the atomic fraction, and the constants K_{1i} and K_{2i} are dependent on the cathode morphology and atomic collisions.

Therefore, the form of Eq. [1] for the atom fraction composition of the thin film produced from a two-element two-phase cathode is

$$y_1 = \frac{\alpha_1 x_1 f_1 \exp [-d(k_{11}x_1 + k_{22})]}{\alpha_1 x_1 f_1 \exp [-d(k_{11}x_1 + k_{21})] + \alpha_2 x_2 f_2 \exp [-d(k_{22}x_2 + k_{22})]} \quad [4]$$

which can be rewritten, by assuming that $\alpha_2 f_2 / \alpha_1 f_1$ is equal to one, as

$$y_1 = \left[1 + \frac{1 - x_1}{x_1} \exp (Ax_1 + B) \right]^{-1} \quad [5]$$

The relationship of the coefficients A and B to the various parameters is dependent on several unknown factors, such as the cathode morphology, sticking coefficients, relative densities of sputtered molecules in the glow discharge, and the energy of the sputtered particles. A detailed model to describe the probability function is currently in progress.

Experimental Procedure

The cathodes were prepared by sintering 100 mesh powders of 99.9 w/o bismuth and titanium powders. Eleven disk-shaped cathodes 2½ in. in diameter and ½ in. thick were prepared with compositions varying from pure titanium to pure bismuth at 10 w/o intervals. The powders were mixed by tumbling and compressed to a pressure of 8000 psi. The green cathodes were placed in capsules which were evacuated to 2×10^{-5} Torr and were sintered at temperatures ranging from 250° to 1000°C depending on composition.

The sputtering was carried out in a conventional 4-in., oil-pumped, liquid nitrogen baffled vacuum system. Initially, the system was evacuated to 5×10^{-6} Torr. The 99.9% argon sputtering gas was then introduced through a calibrated leak valve at a constant flow rate of about 100 cc/min and the total pressure was set at 20μ by throttling the diffusion pump. The sputtering power source was a 5 kV-d-c source, and sputtering voltages varied from 2.0 kV to 4.5 kV. The sintered cathodes were presputtered for 30 min. The substrates used in this study were soft glass microscope slides.

The segregation of the elements in the thin film were analyzed with an ARL-AMX electron probe micro-analyzer, and the composition of the film was determined from the ratio of the bismuth to titanium characteristic x-ray intensities calibrated for films less than bulk thickness (4). Some of the films were stripped from the substrate and examined in transmission with the electron microscope for morphology and structure characterization. The thickness of each film was measured with a multiple beam interferometer.

Results

The sintered cathodes yielded consistent results for longer sputtering times and after presputtering. However, the sintering of the cathodes did result in some problems. It was not possible to get high density sintering because of the wide discrepancies in melting point of the two elements.

Figures 1 through 3 show the relation between the composition of the cathode and the resulting thin film for 2, 3, and 4 kV sputtering potential. These results agree favorably with the predicted form as shown by the fit of Eq. 5 in Fig. 1 through 3. An attempt to fit the data to the model of Winters, Raimondi, and Horne (1) was unsuccessful. The parameters A and B obtained by fitting Eq. [5] to the experimental data are

* Electrochemical Society Active Member.

¹ Present address: Radiation, Inc., Melbourne, Florida.

Key words: selected sputtering, sintered cathodes.

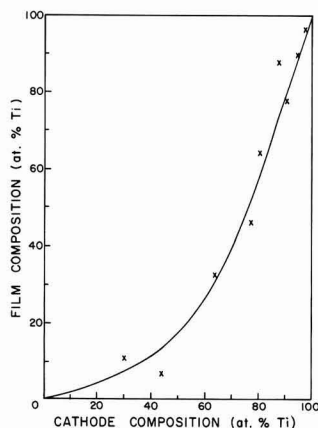


Fig. 1. Experimental and theoretical variation of titanium concentration for films sputtered at 2 kV and 20μ argon pressure from sintered bismuth-titanium cathodes.

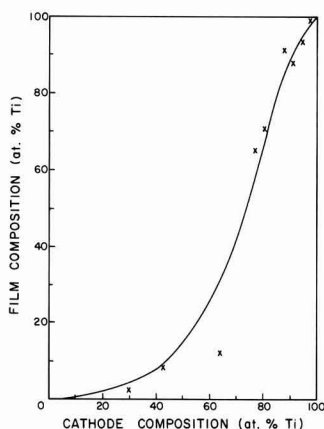


Fig. 2. Experimental and theoretical variation of titanium concentration for films sputtered at 3 kV and 20μ argon pressure from sintered bismuth-titanium cathodes.

more than the low compositions in fitting the equation. Since the probability function is empirical, no particular significance could be applied to the values found for the parameters. However, two factors are apparent. Since bismuth has a higher sputtering efficiency than titanium, bismuth composition in the film should be higher than in the cathode, especially for high bismuth cathodes. This effect contradicts the observed

Table I. Fitted parameters for equation relating titanium composition of sintered cathodes to sputtered film composition

kV	A	B
2	-1.74	2.16
3	-3.94	3.54
4	-7.42	5.24

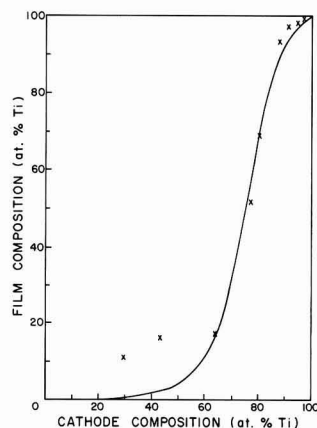


Fig. 3. Experimental and theoretical variation of titanium concentration for films sputtered at 4 kV and 20μ argon pressure from sintered bismuth-titanium cathodes.

excess titanium in the film for the high titanium cathodes. The observed S-shaped curves, especially for the higher sputtering voltages, could be the result of either a significant variation in the sticking coefficient with composition or, more likely, a net change in the flux leaving the cathode due to shape changes of the phases in the cathode.

The analysis of the electron diffraction patterns showed that the film sputtered from the 30.2 a/o titanium cathode contained at least two phases: a solid solution of titanium in bismuth and an unknown phase or phases. The films sputtered from the 87.8 a/o titanium cathode contained a solid solution of titanium in bismuth and BiTi_2 , while a very thin film sputtered from the same cathode at the same pressure and voltage contained a solid solution of bismuth in titanium and BiTi_2 . This result indicates a possible change in the sputtering rates of the two elements during the earlier stages of growth. A third film sputtered from the 96.8 a/o titanium cathode contained a solid solution of bismuth in titanium.

The results of this study verify a selective sputtering in two-phase cathodes and indicate either a composition dependence on the sticking coefficients or a morphology effect in the cathode.

Acknowledgment

The authors wish to thank the Advanced Research Projects Agency, Contract SD-102, for its support of this research.

Manuscript submitted Dec. 15, 1969; revised manuscript received ca. July 8, 1970.

Any discussion of this paper will appear in a Discussion Section to be published in the June 1971 JOURNAL.

REFERENCES

1. H. R. Winters, D. L. Raimondi, and D. E. Horne, *J. Appl. Phys.*, **40**, 2996 (1969).
2. G. S. Anderson, *ibid.*, **40**, 2884 (1969).
3. M. Kaminsky, "Atomic and Ionic Impact Phenomena on Metal Surfaces," p. 156, Academic Press, Inc., New York (1965).
4. W. E. Sweeney, R. E. Seebold, and L. S. Birks, *J. Appl. Phys.*, **31**, 1061 (1960).

Dielectric Properties of Surface Oxides on Aluminum

S. H. A. Begemann¹ and A. W. Smith

Boeing Scientific Research Laboratories, Box 3981, Seattle, Washington 98124

The impedance of barrier layer oxides on aluminum have frequently been characterized by an equivalent circuit of series-parallel resistor-capacitor combinations or by relaxation processes with a wide spread of relaxation times (1). Work on porous oxides have often used simplified models of the oxide itself while complicating the equivalent circuit with the introduction of pore resistance (2). The present work is an attempt to study the relaxation processes themselves. To make measurements as a function of temperature, a capacitor is formed by evaporating aluminum on top of the surface oxide. Measurements of capacitance and dissipation between 10 Hz and 200 kHz will be reported on both barrier layer and porous oxides between 100° and 500°K.

Experimental

A sample holder was built to allow evaporation of aluminum onto the surface of the oxide and to make measurements of the dielectric properties. This is shown in Fig. 1. The copper sample holder can be cooled with liquid nitrogen and heated electrically. Contact to the outer electrode was made by affixing a wire with a dot of colloidal silver paint at the edge of the area on which aluminum was evaporated. An NRC, Model 3114 vacuum coater was used for the evaporation and as a sample chamber. A General Radio, Type 716-C capacitance bridge was used in combination with a null detector system consisting of a Hewlett-Packard wave analyzer, Model 302A, a low noise preamplifier and filter. This allowed signal amplitudes of 20 mV to be used. The experiment has been discussed in detail elsewhere (3).

Results

Barrier layer oxides.—Aluminum specimens of 99.99% purity, were degreased and etched with 1N NaOH for 5 min and rinsed with distilled water. The anodizing was carried out in a 3% by weight ammonium tartrate solution adjusted to pH 7. An aluminum cathode was used. The voltage was raised in 10 V steps, and the current allowed to decay to a nearly constant value after each step.

The inverse capacitance/anodizing voltage ratio is close to that obtained by McMullen and Pryor for the same anodizing conditions but measured in the electrolyte solution (4). The frequency dependence of the dissipation for samples formed at several voltages, measured in ambient atmosphere, is shown in Fig. 2. The dissipation factor of these barrier layer oxides is only slightly dependent on atmospheric humidity. The dissipation decreases by at most 20% on application of vacuum and heating to 200°C. The values of the dissipation factor and its decrease with film thickness are similar to that reported by VanGeel and Scholte (5).

Figure 3 shows the temperature dependence of the dissipation factor for a 100V film measured at 1 kHz. Peaks with background subtracted out are shown at 142° and 245°K. At 50 kHz these peaks occurred at 230° and 287°K.

Porous oxides.—The formation of porous oxide layers was carried out on a commercial alloy, 2024-T3. After degreasing and alkaline cleaning, they were etched in a sulfuric acid, sodium dichromate solution. The anodizing was carried out at 36°C, the voltage reaching 40V in 10 min and held there for 30 min. The anodizing solution was a 3% by weight solution of chromic acid.

¹Present address: Laboratorium voor Technische Natuurkunde, Universiteitscomplex, Paddepoel, Groningen, The Netherlands.

Key words: dielectric properties, aluminum oxide, anodic layer, dissipation, hydration.

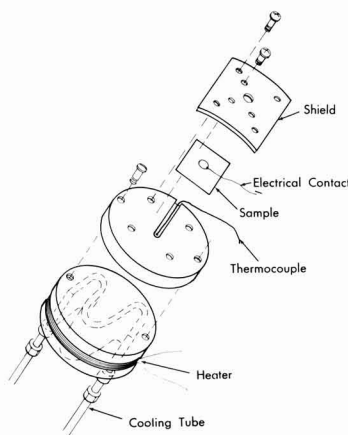


Fig. 1. Schematic drawing of sample holder

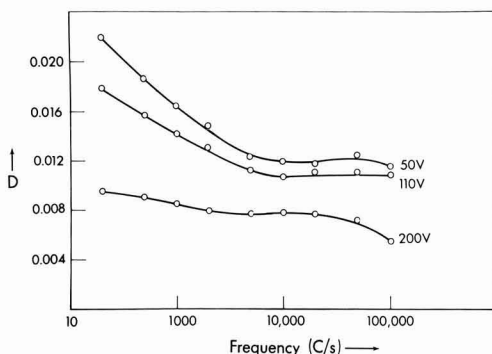


Fig. 2. Dissipation vs. frequency for barrier layer films with different anodizing voltages.

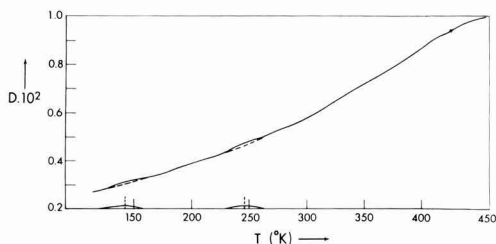


Fig. 3. Temperature vs. dissipation for a barrier layer film, anodized in a 3% ammonium tartrate solution at 100V. Measured at 1 kHz in vacuum.

Measurements made with a sodium sulfate solution counterelectrode gave results, agreeing with Dekker and Urguhart (6), that the solution penetrates the porous layer, and the measured capacity depends only on the underlying barrier layer. Results using the evaporated aluminum electrode depend on the porous layer as well, and show the sensitivity to humidity

noted by Jason and Wood (2). This was attributed by them to adsorption of water and consequential conduction down the walls of the pores.

To study the properties of the oxide layer without pore wall conduction, measurements must be made in high vacuum. Figure 4 shows typical results for the variation of dissipation with temperature below room temperature. Similar results to those of the barrier layer oxide were obtained. In one case, peaks occurred at 140° and 214°K for measurements at 1 kHz. As at 235° and 270°K for measurements at 50 kHz. As shown in Fig. 4, partial sealing of the oxide with hot water increased the background dissipation with only little increase in the dissipation peaks. Although these dissipation peaks, as well as those for the barrier layer oxides, are small, they occur consistently and the temperature shift with frequency is appropriate for processes with activation energies between 0.1 and 0.5 eV.

Peaks of a much greater magnitude were observed above room temperature with the porous oxide. Figure 5 shows the dissipation factor *vs.* temperature for several frequencies. Two peaks occur, but only one varies in position on the temperature scale with frequency. The higher temperature peak remains at about 405°K.

There is a considerable irreversible decrease in the dissipation due to the first heating cycle. The curves show no hysteresis on further heating, however. It was difficult to remove the background from the lower temperature peak to determine an activation energy, due to overlap with the second peak. The assumption was made (to be discussed later) that the second peak was a decrease in dissipation at 405°K, on a background which increased with temperature. Figure 6 is an example of this background removal.

Figure 7 is an Arrhenius plot of the log frequency *vs.* reciprocal temperature of this dissipation peak. An activation energy of 0.76 eV was obtained.

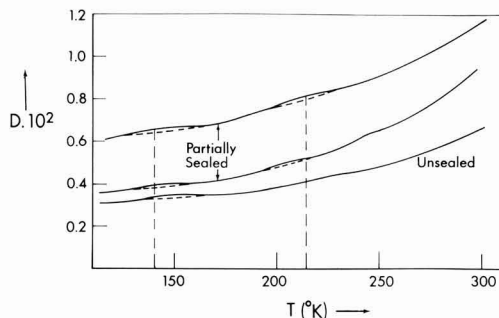


Fig. 4. Temperature *vs.* dissipation for chromic-acid anodized films with different sealing treatments. Measured at 1 kHz in vacuum.

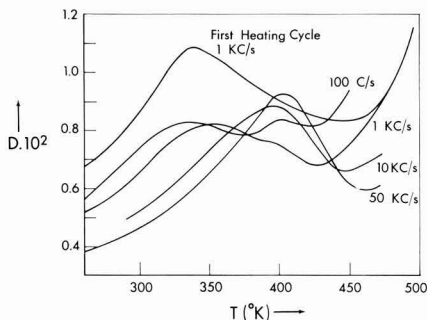


Fig. 5. Temperature *vs.* dissipation for an unsealed, chromic-acid anodized film. Measured in vacuum at different frequencies (500 Hz omitted for clarity purposes).

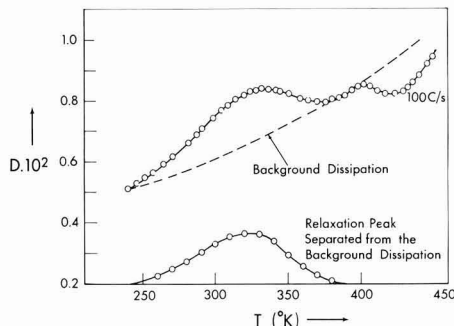


Fig. 6. Temperature *vs.* dissipation for an unsealed, chromic-acid anodized film. Measured in vacuum after the first heating cycle.

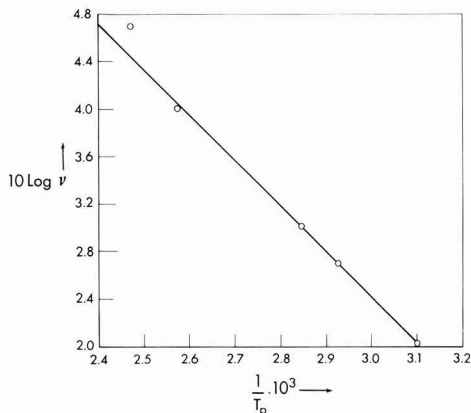


Fig. 7. Log ν *vs.* $1/T_p \cdot 10^3$ plot for anodized and partially "sealed" films. T_p = peak temperature.

Discussion

McMullen and Pryor measured the dielectric loss for a barrier layer film at low temperatures (4). Their data also show a peak at about 230°K which they do not discuss. These peaks may be the same as those found here. In addition, they find a large peak just below room temperature in ambient atmosphere which disappears under vacuum. No such peak was found in the present work. However, their apparatus has a thick porous anodic film in parallel with the barrier layer film as an insulator. At high humidities the pore walls would conduct well, and the impedance of this film may become low enough to affect their measurements.

The physical identity of the two species causing the two low temperature peaks is not apparent from the data since they are not very sensitive to humidity or heat treatment. If they are hydroxide groups, then they are stable above the 550°K outgassing used here. Boehmite is stable above this temperature (7).

The 0.76 eV dissipation peak at high temperatures for the porous oxides seems to correspond to the peak for Boehmite for which Mata-Arjona and Fripiat found an activation energy of 0.68 eV (7). Porous oxides do contain some moisture (8). The 0.76 eV relaxation peak is therefore assigned to hydroxide ions as was proposed for Boehmite (7).

It is suggested that the dissipation peak at 405°K is in fact a decrease in dissipation on a rising background curve. This can be due to an order-disorder transition (9). Such an effect was sought by Wickershen and Korpi for Boehmite in dielectric constant measurements (10). Apparently this effect shows up here in the more sensitive dissipation measurements and not in the measurements of dielectric constant.

Manuscript submitted April 16, 1970; revised manuscript received ca. July 31, 1970.

Any discussion of this paper will appear in a Discussion Section to be published in the June 1971 JOURNAL.

REFERENCES

1. L. Young, "Anodic Oxide Films," Academic Press, New York (1961).
2. A. C. Jason and J. L. Wood, *Proc. Phys. Soc.*, **B.68**, 1105 (1955).
3. S. H. A. Begemann and A. W. Smith, Boeing Scientific Research Lab. Document D1-82-0824, Feb. 1969, AD 685577.
4. J. J. McMullen and M. J. Pryor, "1st International Congress on Metallic Corrosion," p. 52, Butterworths, London (1962).
5. W. Ch. VanGeel and J. W. A. Scholte, *Philips Res. Repts.*, **6**, 54 (1951).
6. A. J. Dekker and H. M. A. Urguhart, *Can. J. Res.*, **28B**, 541 (1950).
7. A. Mata-Arjona and J. J. Fripiat, *Trans. Faraday Soc.*, **63**, 2936 (1967).
8. H. W. Phillips, "Institute of Metals Monograph and Report," Vol. 13, p. 237 (1953).
9. Frohlich, "Theory of Dielectrics," 2nd Ed., Clarendon Press, Oxford, (1958).
10. K. A. Wickersheim and G. K. Korpi, *J. Chem. Phys.*, **42**, 579 (1965).



Diffusional Processes in Solid Electrolyte Fuel Cell Electrodes

R. L. Zahradnik

Department of Chemical Engineering, Carnegie-Mellon University, Pittsburgh, Pennsylvania 15213

ABSTRACT

A mechanism is proposed to account for the polarization voltage loss encountered in the electrochemical oxidation of CO at porous, high-temperature, solid-electrolyte fuel cell anodes. The mechanism involves the transport of gaseous CO and oxygen ions to reaction sites, followed by slow electrochemical reaction. The mechanism results in an involved polarization expression, which under certain conditions simplifies to the familiar Tafel form.

High-temperature fuel cells employing either calcia or yttria stabilized zirconia electrolyte have received considerable attention as potential power generators using gaseous fuels derived from coal (1,2). At the 1000°C operating temperature of solid electrolyte fuel cells, such coal-derived gases as well as prospective fuels such as reformed hydrocarbons will contain large amounts of CO. Oxidation of CO at metallic and mixed oxide fuel cell anodes, however, is accompanied by large polarization losses (3). The presence of hydrogen reduces this loss somewhat, but it is not clear that either the high current densities which are expected from such cells or the complete combustion of CO to CO₂ can be achieved without incurring severe voltage losses. For this reason, it is important to understand in a fundamental way the irreversibilities which occur at solid-electrolyte fuel cell anodes. The purpose of this paper is to propose a possible scheme by which this polarization occurs and to derive the equations which quantitatively relate polarization voltage loss to electrode current density.

Many such analyses for liquid electrolyte fuel cell electrodes have appeared in the literature, and a complete review of the work in this area is not presented here. The pioneering work of Will should be mentioned, however, since it was the first to treat partially immersed electrodes and proposed a method for treating the electrolyte meniscus which considerably clarified the polarization phenomena (4). Will's work has been reviewed and generalized by Lightfoot, who included effects of convection as well as concentration polarization in his analysis (5).

Not all liquid electrolyte fuel cell electrodes follow the thin-meniscus model, however, and analyses of flooded porous fuel cell electrodes have been made, e.g. Brown and Rockett (6).

With a liquid electrolyte, it is possible for the gaseous species participating in the electrode reaction to reach the electrode reaction site either through a meniscus film or bulk electrolyte phase, and the reported polarization studies analyze the various ways this transport can occur. In the case of a solid electrolyte, however, such transport is impossible and alternate mechanisms must be responsible for electrode

polarization. One possibility is for the reactants (CO and oxygen ions) to counterdiffuse to a mutually acceptable location somewhere on the electrode, and there react. In an earlier paper, Zahradnik analyzed this situation for a one-dimensional electrode (7). In this paper, the analysis is extended to cover two-dimensional effects. In order to simplify the analysis, the concept of a single, rectangular pore is introduced.

A Single Rectangular Pore

Noble metals, nonnoble metals, conducting oxides, and mixtures of oxides and metals have been used at one time or other as high-temperature fuel cell anodes (3). The physical structure of all these materials has been porous, and hence it is reasonable to idealize the structure as a single pore, normal to the electrolyte surface—Fig. 1. In order to simplify the ensuing mathematics and notation, the pore is considered to be rectangular and of infinite extent in the direction normal to the paper. The distance coordinate y is introduced, directed normal to the electrolyte, with origin at the electrode-electrolyte interface and value $y = b$ at the bulk gas phase boundary. The distance coordinate x is introduced, directed parallel to the electrolyte. Its origin is at the centerline of the electrode and it has the value $x = a$ at the pore wall.

The electrode is taken to operate isothermally, and the electrochemical reaction between CO and oxygen

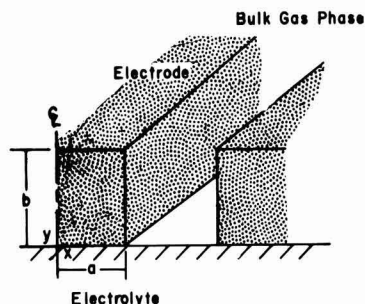
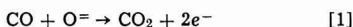


Fig. 1. Idealized pore structure

Key words: fuel cell, porous electrode, polarization (and/or) over-voltage, diffusion, limiting current, Damkohler number.

ions is assumed to occur at the walls of the pore



The rate at which this reaction proceeds per unit of pore wall area, in units of current, is symbolized by $i(y)$.

A number of kinetic expressions have been proposed for $i(y)$ but no generally accepted kinetic description is available (8, 9). At the conditions under which high-temperature solid electrolyte fuel cell anodes operate, however, it seems likely that the following, often proposed, equation is applicable (10)

$$i(y) = 2Fk_e \exp\left(-\frac{\Delta F^\circ + \alpha 2FV}{RT}\right) [\text{CO}] [\text{O}^-] \quad [2]$$

where k_e = Constant, including units of rate
 ΔF° = Standard state free energy of activation
 R = Gas law constant
 T = Temperature
 α = Fraction of generated voltage which contributes to increasing free energy of activation

Equation [2] represents only the forward rate of reaction [1]. Under most conditions of high-temperature fuel cell operation, the forward rate alone is satisfactory, although provision to include a term for the reverse reaction could be made should electrode operation be near the equilibrium condition of reaction [1].

It is assumed that the oxygen ions diffuse from the electrode-electrolyte interface under the influence only of a concentration gradient. That is, the electrode is assumed to be equipotential, so that no voltage gradient is present as an additional driving force. Under these assumptions, the oxygen ion flow is described by the following steady-state conduction equation

$$\frac{\partial^2 [\text{O}^-]}{\partial x^2} + \frac{\partial^2 [\text{O}^-]}{\partial y^2} = 0 \quad [3]$$

The nature of the oxygen ion flow need not be completely specified at this time. That is, the diffusion is assumed to be bulk diffusion, such as lattice, grain boundary, or short-circuit diffusion, but no further specification is made. In any case, Eq. [3] would have a similar form (11, 12). Also, the diffusivity of oxygen ions has been assumed to be the same in both the x - and y -direction.

The boundary conditions which apply to Eq. [3] are: at

$$x = 0, \quad \frac{\partial [\text{O}^-]}{\partial x} = 0 \quad 0 < y < b \quad [4]$$

$$y = b, \quad \frac{\partial [\text{O}^-]}{\partial y} = 0 \quad 0 < x < a \quad [5]$$

$$y = 0, \quad [\text{O}^-] = [\text{O}^-]_e \quad 0 < x < a \quad [6]$$

$$x = a, \quad -D_0 = \frac{\partial [\text{O}^-]}{\partial x} = K[\text{CO}]_b [\text{O}^-] \quad 0 < y < b \quad [7]$$

where K = A convenient kinetic parameter, representing the terms premultiplying the concentrations on the right-hand side of Eq. [2]

D_0 = Diffusivity of O^-

Equation [4] states that there is no flux across the electrode centerline; Eq. [5] similarly denies oxygen ions admission into the bulk gas phase. At the electrode-electrolyte interface, the oxygen ions have a constant concentration, $[\text{O}^-]_e$ —Eq. [6]. Equation [7] equates the diffusive flux of oxygen ions to the flux due to chemical reaction. In this equation, the concentration of CO is taken to be equal to $[\text{CO}]_b$, the bulk gas phase composition. This assumption is reasonable in

the light of the high value of diffusivity CO has at cell operating temperatures. However, if so desired, provision could be made to account for small changes in CO concentration due to changes in current level—in the manner used by Zahradnik in his one-dimensional analysis (7). This is not done here, however, since its effect is small.

Solution to Electrode Equations

The solution to the system of Eq. [2]–[7] can be expressed in terms of a Fourier series; the result is from Carslaw and Jaeger (13) (p. 168, Eq. [17])

$$[\text{O}^-] = 2K [\text{O}^-]_e [\text{CO}]_b \sum_{n=1}^{\infty} \frac{\cos \alpha_n x \cosh \alpha_n (b-y)}{[(\alpha_n^2 + D_m^2) a + D_m] \cos \alpha_n a \cosh \alpha_n b} \quad [8]$$

where α_n represents the solution to the following

$$\alpha_n a \tan \alpha_n a = D_m = \frac{K [\text{CO}]_b [\text{O}^-]_e}{D_0 = [\text{O}^-]_e} \quad [9]$$

The right-hand side of Eq. [9] is the ratio of the maximum reaction rate to a characteristic diffusion rate of O^- . Such a ratio represents an electrode Damkohler number, and is symbolized as D_m .

The total pore current per unit of length normal to the xy -plane, I , is obtained by integrating the oxygen ion flux at $x = a$ over the entire height of pore wall

$$I = \int_0^b -D_0 = \frac{\partial [\text{O}^-]}{\partial x} \bigg|_{x=a} dy$$

$$I = \int_0^b D_0 = 2K [\text{O}^-]_e [\text{CO}]_b$$

$$\sum_{n=1}^{\infty} \frac{\tan \alpha_n a \cosh \alpha_n (b-y)}{[(\alpha_n^2 + D_m^2) a + D_m] \cosh \alpha_n b} \alpha_n dy$$

This expression can be written as the ratio of I to $I_D = D_0 = [\text{O}^-]_e/a$, a characteristic oxygen ion flux

$$\frac{I}{I_D} = 2 D_m^2 \left(\frac{a}{b}\right) \sum_{n=1}^{\infty} \frac{\tanh \alpha_n b}{\alpha_n a [\alpha_n^2 a^2 + D_m^2 + D_m]} \quad [10]$$

Since it is the current-polarization relationship which is of most interest from a fuel-cell point of view, Eq. [10] can be modified slightly to indicate how these two quantities are related.

Current-Polarization Relationship

K is given explicitly by the following

$$K = 2 F k_e \exp\left(-\frac{\Delta F^\circ}{RT} - \frac{2\alpha F V}{RT}\right)$$

At this point it is convenient to utilize the fact that, on an IR free basis, electrode voltage, V , is given by the following thermodynamic relationship

$$V = E_t - \eta = -\frac{\Delta F^\circ}{2F} - \frac{RT}{2F} \ln \left\{ \frac{[\text{CO}_2]_b}{[\text{CO}]_b} [\text{O}^-]_e \right\} - \eta$$

where

η = Electrode polarization

ΔF° = Standard free energy change of reaction [1]

Hence, it is possible to relate D_m to polarization η

$$D_m = D_m^0 \exp\left(\frac{2\alpha F \eta}{RT}\right)$$

where D_m^0 denotes the value of D_m at zero polarization.

Figure 2 is a plot of $\ln(I/I_0)$ vs. $\ln D_m = \ln D_m^0 + 2\alpha F \eta / RT$, for various aspect ratios.

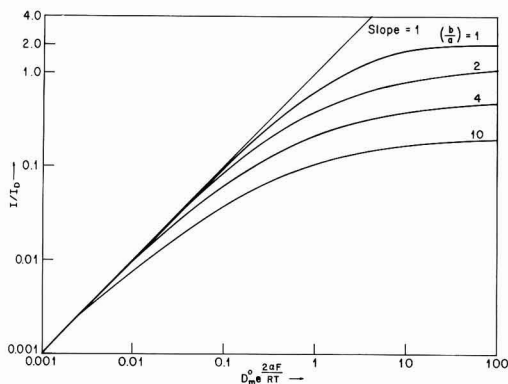


Fig. 2. Current-polarization relationship

Notice that for small values of current these two expressions are equal, suggesting that

$$\ln I/I_D = \ln D_m^0 + \frac{2\alpha F\eta}{RT} \quad (\text{small } I)$$

If $D_m^0 I_D$ is denoted as an exchange current, I_0 , this equation reduces to the familiar Tafel form

$$\eta = \frac{RT}{2\alpha F} \ln I/I_0 \quad [11]$$

Archer, Elikan, and Zahradnik have obtained polarization data for zirconia-based fuel cells equipped with sintered platinum anodes operating on CO-CO₂ mixtures (3). They report a successful fit of their data using Eq. [11]. Although a consistent value of $\alpha = 1/2$ was obtained over a range of compositions, the authors were unable to draw any firm conclusions about trends of the exchange current with composition. However, a simple dependency of (I_0) on bulk gas phase composition may be obtained

$$(I_0) \propto [\text{CO}]^{1-\alpha} [\text{CO}_2]^\alpha$$

Consider

$$[\text{CO}_2]_b = (1 - y_{\text{CO}}) C_b$$

and

$$[\text{CO}]_b = (y_{\text{CO}}) C_b$$

where C_b = Bulk gas phase concentration

y_{CO} = Mole fraction CO in bulk gas phase

Then if the value of α is taken to be $1/2$, for a constant C_b , the proportionality between (I_0) and y_{CO} is given by the following

$$(I_0) \propto [y_{\text{CO}}(1 - y_{\text{CO}})]^{1/2} \quad [12]$$

The data reported by Archer, Elikan, and Zahradnik are plotted in Fig. 3 vs. bulk gas phase percentage of CO in the CO + CO₂ mixture. The relationship suggested by Eq. [12] is also plotted in Fig. 3, with the proportionality constant adjusted to give a best fit to the data. The agreement is quite reasonable, considering the variety of conditions under which the data were obtained. Unfortunately, no data were reported in the 50% CO range.

As I increases, the current-polarization curve starts to deviate from the linear relationship. No other region is encountered where an equation of the Tafel form is a good approximation. This conclusion is different from the one based on a one-dimensional counter diffusion (7), where a second region was observed in which an equation of the Tafel form served as a good approximation to the exact equation.

In order to demonstrate that the current-polarization curve predicted by Eq. [10] does provide a good fit for

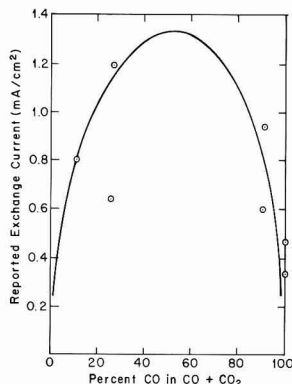


Fig. 3. Reported values of exchange current as function of per cent CO for sintered platinum electrodes (1). Curve is predicted by Eq. [12].

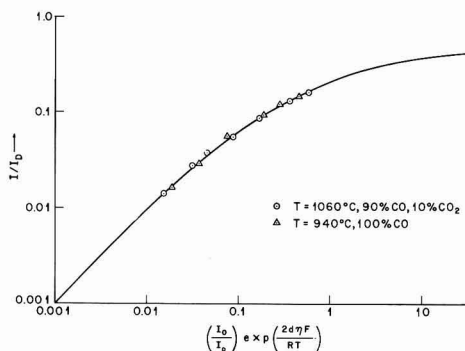


Fig. 4. Experimental data for sintered platinum electrodes (1). Curve is predicted from Eq. [10] with $(b/a) = 4$.

experimental data, some of the results reported by Archer, Elikan, and Zahradnik (3) are plotted in Fig. 4 in the format prescribed by Eq. [10]. The data were obtained at two temperatures, 940° and 1060°C, with a fuel of 100% CO and 90% CO plus 10% CO₂, respectively.

The curve derived from Eq. [10] which is used to correlate these data is for an aspect ratio $(b/a) = 4$. This ratio is felt to be reasonable for the sintered platinum electrodes used in the experiments. The sintering process causes the platinum to coalesce into individual particles whose mean diameter is about one third times the electrode thickness. If the pores are viewed as passages through a matrix of connected particles, then an aspect ratio of four to six would be expected.

The data reported in Fig. 4 were obtained with a test cell whose electrode area was 27.6 cm². From Fig. 3, it is noted that exchange current densities of about 0.3 and 0.6 mA/cm² can be expected for the 100% CO and the 90% CO fuels, respectively. This would correspond to I_0 values of 8 and 16 mA, respectively, and these were the values used to plot the data. The value of α was taken to be $1/2$.

For the 940°C, 100% CO data, the correlation was obtained with an I_D value of 1500 mA. The 1060°C, 90% CO data was correlated with an I_D value of 1700 mA. It can be seen that only the low current points are in the region of the Tafel kinetics.

The limiting current, I_L , can be obtained from Eq. [10] by letting D_m become large. The result may be expressed as

$$I_L = \left(\frac{D_0 = [O^{=}]_e}{b} \right) \lim_{D_m \rightarrow \infty} 2D_m \sum_{n=1}^{\infty} \frac{\tanh[(b/a) \alpha_n a]}{\alpha_n a [\alpha_n^2 a^2 + D_m^2 + D_m]}$$

The first bracketed term shows the limiting current to be inversely proportional to electrode thickness as expected. The exact constant of proportionality depends on the electrode aspect ratio (b/a) as seen from the second term. For (b/a) values larger than 2, this last term is relatively insensitive to (b/a) however.

The data shown in Fig. 4 correspond to limiting currents of 900 mA at 940°C and 1000 mA at 1060°C. While these values are quite low on a current density basis, it should be pointed out that the test cell did employ a thick electrode and that other cells have been operated with much thinner electrodes and consequently much higher limiting currents.

Discussion

The analysis presented here allows a number of interesting conclusions to be drawn about solid electrolyte fuel cell anodes. At low current levels, polarization is controlled by slow chemical reaction, and familiar Tafel behavior is observed. As current increases, the slope of the $\ln I$ vs. η curve decreases continuously, and no other characteristic region is noted until the limiting current is reached.

Since the object of a properly designed electrode is to support large current densities while sustaining only small polarization losses, it is clear that such an electrode should have large D_m^0 . This requirement means that the kinetics of the electrochemical reaction [1] should be fast. The data reported for platinum electrodes indicate that such is not the case for platinum. However, other materials are suitable as anodes, and one criterion in their selection should be the rate at which reaction [1] proceeds on their surface.

If an anode material of sufficient catalytic level, either natural or induced by special treatment, can be found, the fuel cell behavior would be characterized by large D_m^0 values. It is interesting to observe what happens to the current distribution in such cases. The net current at any electrode position, $I(y)$, may be obtained directly by differentiating the expression for $[O^{=}]$, and is given by the following equation

$$\frac{I(y)}{I} = 1 - \sum_{n=1}^{\infty} \frac{\sinh \alpha_n b (1-y)}{\alpha_n a [\alpha_n^2 a^2 + D_m^2 + D_m]} \quad [13]$$

For small values of D_m , this equation is nearly linear (Fig. 5). However, as D_m increases, the relationship is no longer linear, but distinctly curved, as shown in Fig. 5. At high values of D_m , the current is generated largely near the electrode-electrolyte interface and the distribution is distinctly nonuniform. Similar dis-

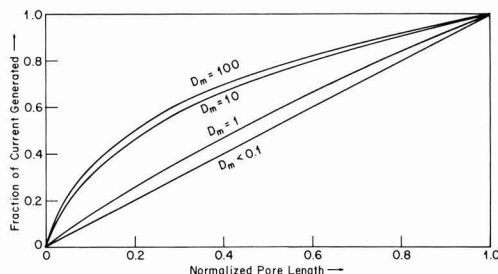


Fig. 5. Current distribution as function of electrode Damkohler number for aspect ratio = 1.

tributions are found along the meniscus of a liquid electrolyte fuel cell electrode (8). However, in the case of solid electrolyte fuel cell anodes, the high current densities that are developed in the vicinity of the electrode-electrolyte interface will produce large heat effects, due to resistance heating in the electrode, which may in turn lead to rupture of the electrode-electrolyte contact. A careful analysis will have to be made of the local heat effects produced in electrodes capable of supporting high current densities.

Manuscript submitted Dec. 5, 1969; revised manuscript received July 1, 1970.

Any discussion of this paper will appear in a Discussion Section to be published in the June 1971 JOURNAL.

REFERENCES

1. D. H. Archer, E. F. Sverdrup, and R. L. Zahradnik, *Chem. Eng. Progr.*, **60**, 64 (1964).
2. R. L. Zahradnik, L. Elikan, and D. H. Archer, pp. 343-355 in "Fuel Cell Systems," Am. Chem. Soc. (1965).
3. D. H. Archer, L. Elikan, and R. L. Zahradnik, pp. 51-75 in "Hydrocarbon Fuel Cell Technology," Academic Press, Inc., New York (1965).
4. F. G. Will, *This Journal*, **110**, 152 (1963).
5. E. N. Lightfoot, *ibid.*, **113**, 614 (1966).
6. Ralph Brown and J. A. Rockett, *ibid.*, **113**, 865 (1966).
7. R. L. Zahradnik, "Mechanism of CO Polarization at High-Temperature Solid Electrolyte Fuel Cell Anodes," *Troisiemes Journees Internationales D'Etude Des Piles a Combustible*, Bruxelles, Presses Academiques Europeennes, pp. 125-130, 1969.
8. D. N. Bennion and C. W. Tobias, *This Journal*, **113**, 593 (1966).
9. E. A. Grens, R. M. Turner, and Theodore Katan, *Advanced Energy Conversion*, **4**, 109 (1964).
10. L. G. Austin, *Proc. IEEE*, **51**, 820 (1963).
11. Karl Hauffe, "Oxidation of Metals," Plenum Press, New York (1965).
12. Per Kofstad, "High-Temperature Oxidation of Metals," John Wiley & Sons, Inc., New York (1966).
13. H. S. Carslaw and J. C. Jaeger, "Conduction of Heat in Solids," Oxford University Press (1959).

NOMENCLATURE

English

- a Electrode distance
- b Electrode thickness
- C_b Bulk gas phase molar concentration (g/cm^3)
- D_0 Diffusivity of $O^{=}$ (cm^2/sec)
- E_t Thermodynamic voltage for reaction [1]
- ΔF^\neq Activation energy for absolute rate expression for reaction [1] ($\text{kcal}/\text{g mole}$)
- ΔF^0 Standard free energy of reaction [1] ($\text{kcal}/\text{g mole}$)
- F Faraday Number (coulomb/g mole equivalent)
- $i(x)$ Local rate of reaction [1] (A/cm^2)
- I Operating electrode current
- $I(x)$ Local electrode current
- I_D Characteristic electrode current (A)
- (I_0) Exchange current
- I_L Limiting current (A)
- k Kinetic parameter with units of rate
- K Convenient kinetic parameter
- R Gas law constant ($\text{kcal}/\text{g mole}^\circ\text{K}$)
- T Electrode temperature ($^\circ\text{K}$)
- V Electrode potential (V)
- x Distance coordinate parallel to electrolyte
- y Distance coordinate normal to electrolyte
- y_{CO} Bulk gas phase CO mole fraction

Greek

- α Parameter indicating portion of anode voltage which increases activation energy of intermediate complex for reaction [1]
- α_n Solution to Eq. [9]
- η Polarization voltage loss (V)

Subscripts

- e Electrode-electrolyte interface
- b Bulk gas phase-electrolyte interface

The Corrosion of Titanium Carbide

R. D. Cowling and H. E. Hintermann*

Laboratoire Suisse de Recherches Horlogères, Neuchâtel, Switzerland

ABSTRACT

In 2N H₂SO₄, the anodic dissolution of titanium carbide begins at about 0.8V (SHE). Trivalent titanium ions could not be detected in the nitrogen-saturated solution, although this does not rule out the possibility that Ti(III) is formed in the dissolution reaction. However, at 0.8V oxidation to Ti(IV) would readily occur. The results of potentiostatic and galvanostatic experiments indicate that the subsequent passivation of the electrode, which occurs between 1.2 and 1.7V when it is polarized potentiostatically, is due to Ti(IV) oxide. At potentials above 1.7V, oxidation to Ti(VI) occurs. During the initial dissolution of the carbide, both CO and CO₂ were detected.

Although titanium carbide is an important refractory material, characterized by its extreme hardness and its relative inertness, very little attention has been given to its chemical properties. The stability of the Group IV, V, and VI transition metal carbides toward acid and alkali solutions has been examined (1), but, while a patent exists (2) for an anode incorporating titanium carbide, there appear to have been no studies on the anodic behavior of this material. It was felt that one point of interest in such a study would be to determine the nature of products arising from the bonded carbon. Thus Ervin *et al.* (3), in describing the use of titanium carbide anodes for the extraction of titanium metal in molten salt electrolysis, state that the carbide behaves during electrolysis as though it were a metal with high carbon content. From this, one might expect dissolution of titanium, leaving free carbon. On the other hand, various attempts have been made to describe the bonding in carbides (4-6), and it is more reasonable to suppose that the carbon gives rise to at least one gaseous corrosion product.

It was the aim of the present study to investigate the behavior of titanium carbide anode in sulfuric acid solution, to identify the dissolution products, and to define the limit beyond which this material cannot be regarded as inert.

Experimental

Titanium carbide was deposited onto steel disks (C, 1.4%; Cr, 1.3%) by chemical vapor deposition from a mixture of hydrogen, methane, and titanium tetrachloride vapor at high temperature (7).

The nature of the deposit was confirmed by x-ray diffraction studies. Unfortunately this method cannot be used to determine the stoichiometry of the carbide, due to the high degree of scatter in the measured lattice parameter. Chemical analyses have been performed on representative samples of carbide, in order to obtain the stoichiometry. The analysis of metallic impurities was performed by spectrographic and atomic absorption methods. Determination of oxygen and nitrogen was carried out by vacuum extraction and chemical methods, respectively, and of total carbon by oxidation to CO₂ which was subsequently determined by coulometric titration. Free carbon was determined by dissolving the sample in HF and HNO₃, filtering the free carbon on asbestos and burning it to CO₂ in a tube furnace.

Compositions vary between nearly stoichiometric (TiC_{0.98}) and about TiC_{0.9}. The variation must be due to experimental factors which may be controllable (temperature, gas composition, etc.) or not (aging of the apparatus). A systematic study of this problem has not yet been undertaken. Analysis of the impuri-

ties showed about 4% each of iron and chromium, which arise either by diffusion from the substrate or by high-temperature attack on the reactor walls by the gas stream. The level of these impurities is not high enough to affect the general characteristics of the corrosion behavior of the carbide, but uncertainties in the stoichiometry and purity made a detailed kinetic study impossible.

Anodes.—Deposits of titanium carbide 10-15 μ m thick were obtained on disks of 2 mm thickness. The carbide on one surface was planed away, and the steel then dissolved in warm hydrochloric acid, leaving flakes of titanium carbide.

Cell and instrumentation.—Experiments were performed in a simple cell at room temperature, using Reagent Grade acid solutions. A large cylindrical platinum counterelectrode was used. The basic instrument for both potentiostatic and galvanostatic experiments was a Tacussel¹ type PRT 2000 potentiostat. For potential scans this was coupled to a drive unit, type Servovit 2, and current-potential curves were obtained directly on a Sefram² XY recorder.

Results

Potentiostatic measurements.—Figure 1 shows a typical polarization curve for TiC in 2N H₂SO₄, obtained at a potential scan rate of 10 mV/min. At about 2V,³ rapid dissolution of the electrode occurs. The passivation of TiC at about 1V is a process which, at a low rate of scanning, undergoes reactivation when the potential is made progressively less positive. At a higher rate of scan, little reactivation occurs. This is shown in Fig. 2. The pH-dependence of the potential of the peak maximum was found to be -0.045 ± 0.005 mV/pH unit, the potential becoming more positive as the pH decreases. Although plots of $\log i$ vs. E during the initial stages of dissolution showed a well-defined Tafel relationship, the slopes were not sufficiently constant to enable reliable kinetic data to be extracted.

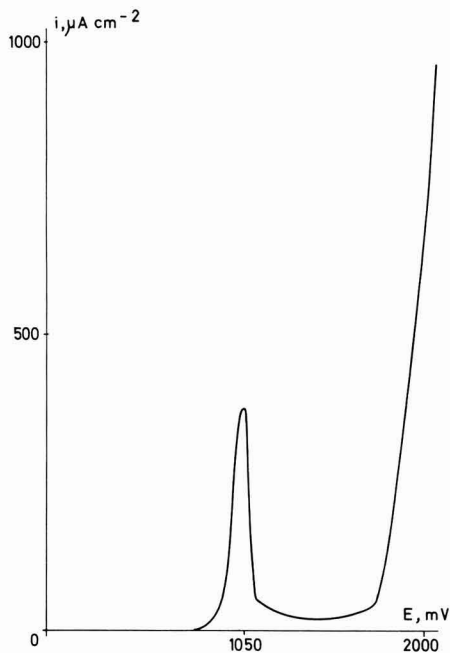
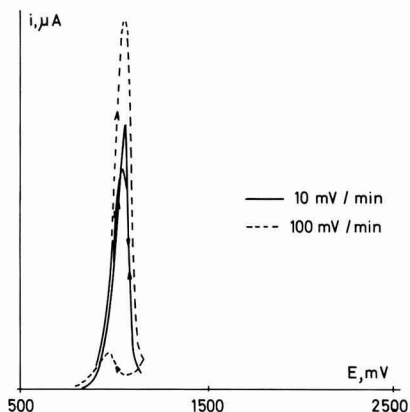
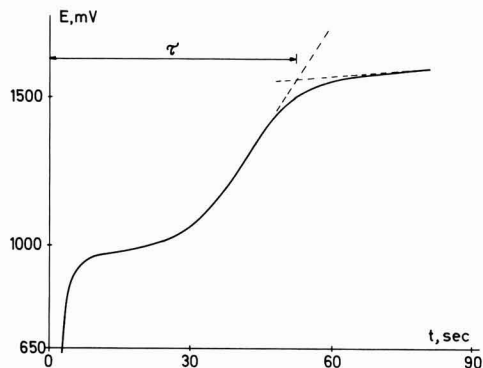
Galvanostatic measurements.—When a titanium carbide electrode was charged at constant current in the range 2×10^{-3} to 1×10^{-2} A cm⁻² in 0.1N H₂SO₄, two plateaus in the potential-time curve were found. These occurred at about the same potentials as those at which the two active regions were found during potentiostatic polarization. A typical E/t curve is shown in Fig. 3. The process giving rise to the first plateau was assumed to have finished after a time, τ , which was arbitrarily marked by the intersection of two straight lines, extrapolated from the region of rising potential and from the second plateau, in the

¹ Tacussel, 2, rue Carry, Lyon 3, France; Ryaby Associates, 38 Wall St., Passaic, N.J. 07055.

² Sefram, 74, rue de la Fédération, Paris XV, France.

³ All potentials reported in this paper are referred to the standard hydrogen electrode.

* Electrochemical Society Active Member.
Key words: anodic, dissolution, polarization.

Fig. 1. Polarization of TiC in 2N H₂SO₄, 10 mV min⁻¹Fig. 2. Polarization of TiC in 2N H₂SO₄ at different scanning ratesFig. 3. Potential-time curve for a TiC electrode charged at 5 A cm⁻² in 0.1N H₂SO₄.Table I. Transition times for galvanostatic charging of TiC in 0.1N H₂SO₄

$i \times 10^3, \text{A cm}^{-2}$	10	9	8	7	6	5	4	3
τ_1 sec	18	23	26	32	41	53	70	107
τ_2	18	23	27	33	42	53	68	104
τ_3	19	23	27	33	42	53	68	104
$t^{1/2}$	43	44	41	40	39	36	33	35

manner indicated in Fig. 3. At each current, three charging curves were obtained, each one after prior polarization to the point of hydrogen evolution, and the mean value of τ recorded. At any one current, the reproducibility in the values of τ was generally excellent. Typical results are shown in Table I.

Identification of the dissolution products.—From the titanium.—Several attempts were made to detect the presence of Ti(III) in the solution during the anodic dissolution of titanium carbide. In a standard solution of Ti(IV) in 2N H₂SO₄, containing 5 ppm of Ti and saturated with nitrogen, a platinum wire electrode was polarized cathodically to the point of vigorous hydrogen evolution. After about 5 min, the electrode was charged with a constant anodic current of 3 μ A. The E/t curve showed a plateau at 0.47V due to the oxidation of Ti(III) to Ti(IV). A titanium carbide electrode was then charged at 500 μ A in 2N H₂SO₄ saturated with nitrogen. After a sufficient time had elapsed to put a detectable amount of titanium into solution, a platinum wire electrode in the solution was charged anodically at 3 μ A, and the E/t curve recorded. No plateau corresponding to the oxidation of Ti(III) could be found. Thus, while this test was not intended to give a quantitative microanalysis of Ti(III), it indicated at least that the concentration of this ion did not build up during the dissolution to a level which was comparable to the concentration of titanium in the solution, and that therefore this titanium is almost certainly in its tetravalent oxidation state.

A similar attempt to detect the presence of Ti(III) as a result of the dissolution of TiC was made by potentiometric titration with a Ce(IV) solution. This also gave a negative result.

From the bonded carbon.—A titanium carbide electrode was charged galvanostatically at 100 μ A for 6 days, in 5 ml of 2N H₂SO₄ contained in a tube sealed with a silicon rubber bung. A platinum wire was used as the cathode. The cell voltage was recorded continuously, and was always less than 1.3V. At the end of the charging period, samples of the gas above the solution were taken by direct injection of a 1 ml syringe. This gas was analyzed with a permanent-gas chromatograph,⁴ using a silica gel, and a molecular sieve, column. The presence of both CO₂ and CO was confirmed.

Repeat experiments were performed on single crystals of titanium carbide, and in every case both gases were detected.

Discussion

The equilibrium potential-pH diagram for the system titanium-H₂O shows (8) that the most stable species at pH = 0 and at potentials in the region of 1V is the tetravalent ion TiO₂²⁺. In fact, at this pH the domain of stability of this ion extends from about zero to about 1.8V. As all attempts to detect the presence of Ti³⁺ during the anodization of titanium carbide failed, it is reasonable to suppose that the initial dissolution produces TiO₂²⁺. The actual mechanism cannot be elucidated at this stage, although further work is in progress with pure single crystals of the carbide.

It is quite possible that the dissolution actually produces Ti³⁺, but that this species is subsequently oxidized to TiO₂²⁺ at the surface of the corroding

⁴ H. Feichtinger, Schaffhausen, Switzerland.

electrode. From Pourbaix (8), the equilibrium potential for the redox couple $\text{Ti}^{3+}/\text{TiO}^{2+}$ at pH = 0 and at $\text{TiO}^{2+}/\text{Ti}^{3+} = 6$ is about 0.46V. Since the potential of the titanium carbide is above 0.8V during its dissolution, it is clear that any Ti^{3+} formed would be quickly oxidized to TiO^{2+} . Thus, while the present work cannot distinguish whether titanium carbide is oxidized directly to Ti(IV) or whether this occurs through the intermediate formation of Ti(III) , the net result is clearly an oxidation to the tetravalent state. Further experiments are planned to examine this question more fully, with the aid in particular of a rotating ring-disk electrode, and it is hoped to report these results in a further communication. It is therefore proposed here that the passivation observed between about 1.2 and 1.7V is due to a tetravalent oxide (or hydrated oxide) of titanium. The peak at about 1V in Fig. 1 can thus be attributed to the sequence

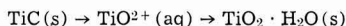


Figure 4 shows that the formation of the oxide is kinetically possible at potentials above 0.91V. At this point, the i/t curve at constant potential first shows a gradual decay, due to the depletion of active surface by the formation of solid oxide.

During the second active region, one would then expect the oxidation to produce Ti(VI) ions. The potential at which this region begins is in fact in good agreement with that indicated by Pourbaix for the process $\text{TiO}_2 \cdot \text{H}_2\text{O} \rightarrow \text{TiO}_3^{2+}$. Direct experimental evidence is given by the fact that, during the dissolution of titanium carbide at about 2V, the solution gradually becomes yellow. It shows exactly the same absorption maximum (410 nm) as the yellow solution formed by the reaction of titanium(IV) ions with hydrogen peroxide, which is due to the ion TiO_3^{2+} .

Figure 2 confirms that this oxide is relatively soluble. Reactivation on the reverse scan occurs only at slow sweep speeds; at higher scan rates, dissolution of the oxide film is not sufficiently fast to allow reactivation.

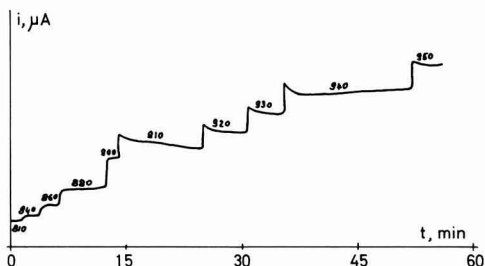
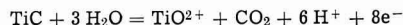


Fig. 4. Current-time curves at various potentials during the dissolution of TiC in 2N H_2SO_4 ; numbers refer to potential in millivolts.

tion. It would appear, then, that passivation is not due to anhydrous TiO_2 (rutile), which has a very low solubility, but rather to the hydrated oxide $\text{TiO}_2 \cdot \text{H}_2\text{O}$.

The gaseous corrosion products being CO_2 and CO , the initial dissolution may proceed according to the reactions



for which dE/dpH is -0.044 and -0.039V , respectively. This corresponds with the observed pH-dependence of $-0.045 \pm 0.005\text{V}$.

The potentiostatic experiments therefore indicate that the initial corrosion of TiC produces TiO^{2+} , and that at a certain potential (0.910V in 2N H_2SO_4) the formation of solid oxide ($\text{TiO}_2 \cdot \text{H}_2\text{O}$) begins. At about 1.05V, the rate of formation of oxide exceeds the rate of its dissolution, and the electrode becomes passivated. At about 1.75V, oxidation to TiO_3^{2+} occurs, and severe corrosion of the TiC follows.

This picture is confirmed by the galvanostatic experiments. The charging curve shown in Fig. 3 contains only two plateaus, of which the potential of the first clearly corresponds to the dissolution of TiC as TiO^{2+} . In general during such galvanostatic charging, where the initial corrosion product is freely soluble, the current density, i , and the time, τ , required for passivation to occur are related by: $i\tau^{1/2} = \text{constant}$. In the present case, although the transition times were very long and were rather arbitrarily determined, this relationship held reasonably well above about $6 \times 10^{-3} \text{ A cm}^{-2}$ (see Table I).

The second plateau in Fig. 3 occurs at a potential which corresponds closely to that found potentiostatically for the oxidation to Ti(VI) . The absence of an intermediate plateau is further evidence that the net reaction during the first active region is an oxidation to the tetravalent state of titanium.

Manuscript submitted April 13, 1970; revised manuscript received July 15, 1970.

Any discussion of this paper will appear in a Discussion Section to be published in the June 1971 JOURNAL.

REFERENCES

1. V. P. Kopyleva, *Zh. Prikl. Khim.*, **34**, 1936 (1961).
2. A. M. Suggs, U.S. Pat. 2,636,856 (Cl. 204-290), April 28, 1953.
3. G. Ervin, H. F. G. Ueltz, and M. E. Washburn, *This Journal*, **106**, 144 (1959).
4. S. P. Denker, *J. Phys. Chem. Solids*, **25**, 1397 (1964).
5. S. P. Denker, "Bonding Stability and Formation of Cubic Refractory Monocarbides, Mononitrides and Monoxides," Report No. CU-3553-5, U.S. Atomic Energy Contract No. AT(30-1)-3553.
6. E. Dempsey, *Phil. Mag.*, **8**, 285 (1963).
7. H. E. Hintermann and H. Gass, *Schweiz. Archiv. Angew. Wiss. Tech.*, **33**, 3 (1967).
8. M. Pourbaix, "Atlas d'Equilibres Electrochimiques à 25°C," Gauthier-Villars, Paris (1963).

A Comparison of Various 24K Gold Electrodeposits

S. E. Craig, Jr.,* R. E. Harr,* J. Henry,¹ and P. Turner²

Chemical Engineering, School of Engineering, College of Engineering Sciences,
Arizona State University, Tempe, Arizona 85281

ABSTRACT

Thick electrodeposits of 24K gold were prepared from 14 types of plating solutions in both new and replenished-used conditions. The deposits were examined by x-ray, scanning electron microscope, gravimetric, and electrical techniques. It was found that the purity, microstructure, and apparent density were functions of the plating solution type and age. The crystal lattice constants were found to be independent of both type and age.

Deposit Preparation

Fourteen types of plating solutions were selected as representative of modern commercial plating practice. They contained 8-15 g/liter gold and were operated at 3 mA/cm². The bath components are given in Table I. The used baths were taken from various production lines. They had all been "turned over" at least 10 times. The amount of use and degree of contamination could not be precisely determined for these baths. However, a partial determination is given in Table III. Before using the old baths, they were filtered, analyzed, and regenerated by adjusting the pH, density, and gold concentration to the nominal values.

Plating was accomplished in a vigorously agitated 4 liter, constant-temperature tank. The anodes were platinum-plated titanium and had approximately 5 times the area of the cathodes. During plating, small quantities of gold were periodically added to the bath to insure that the gold concentration never fell below 90% of its nominal value. The cathodes were copper plates 2.5 x 5 cm. One side of each cathode was mirror smooth while the other side had a fine mat finish. Four cathodes were used for each bath and the gold was deposited on both sides of each cathode. Immediately after deposition, the samples were cut and the copper etched away with nitric acid. The samples were ultrasonically washed in water, trichloroethylene, and methanol, dried, and stored for later examination.

The deposits were very thick (127 μ m) so that effects from the bath could be separated from effects of the copper substrate.

The properties investigated were appearance, density, purity, crystal structure, and preferred orientation. In all cases, the samples from the smooth side of the copper cathodes had the same characteristics as those from the mat side of the copper.

Visual Appearance

The visual appearances of the solution side of the deposits are tabulated in Table I. Except for deposits from baths 1, 13, and 14, the surfaces were fairly similar in appearance. They differed only in relative brightness, smoothness, and fineness of the mat. Bath 13 produced unique, smooth, uniformly brown, dull surfaces. Bath 14 produced bright, shiny, perfectly smooth surfaces. The sparkly, bright appearance of the new hot cyanide deposit is due to its large, individual grains, while the dull, orange or brown color seen in deposits 8u, 11u, and 13 is caused by many small, individual grains. Deposits from used baths tended to be duller and smoother than deposits from new baths. The addition of brighteners and hardeners caused the baths to produce a finer mat surface.

The sides of the deposit adjacent to the copper cathodes were visual replicas of the copper surface even when viewed at 30,000X.

Density

The density of each sample was determined from its weight in air and in diiodomethane. The results, corrected for buoyancy of air and further corrected

* Electrochemical Society Active Member.

¹ Present address: U.S. Army, Ft. Bliss, Texas.

² Present address, Texas Instruments, Inc., Dallas, Texas.

Key words: gold, electrodeposits, purity, crystal structure, resistivity, density.

Table I. Gold-plating deposits investigated

Bath* No.		Ref.	pH	Density * Baumé	Visual appearance	Density g/cm ³
1n	Hot cyanide, phosphate, carbonate	(1)	12	15-30	Sparkly bright, very coarse mat.	19.22
1u					Very coarse mat.	19.13
2n	Citrate, phosphate in equal amounts	(2)	5.7-6.0	15-25	Bright, coarse mat.	19.26
3n	Same as 2 plus 25 g/liter polyamino acid com- plex		5.7-6.0	15-25	Dull, smooth.	19.25
3u					Bright, fine mat.	19.27
4n	Same as 2 plus 10 g/liter metallic brightener		5.5-6.0	15-25	Dull, fine mat.	19.27
4u					Fine mat.	19.26
5n	Same as 4 plus 20 g/liter potassium chromium sulfate hardener		5.5-6.0	15-25	Dull, fine mat.	19.25
5u					Dull, smooth.	19.26
6n	Same as 5 plus 25 g/liter boric acid inhibitor		5.5-6.0	15-25	Very fine mat.	19.25
7n	Citrate plus 6 g/liter hydrazine sulfate redox agent	(3)	4.2-4.5	14-16	Fine mat.	19.26
7u					Fine mat.	19.25
8n	Phosphate plus 6 g/liter hydrazine sulfate	(4)	5.5-6	14-16	Fine mat.	19.27
8u					Dull, fine mat, orangeish stains.	19.26
9n	Ammonium citrate plus 20 g/liter potassium chromium sulfate hardener	(5)	4.5	12	Very fine mat.	19.25
9u					Dull, very fine mat.	19.27
10u	Borocitrate plus tetraethylene pentamine		5.0-6.0	20-25	Dull mat.	19.26
11u	Phosphate		6	17-18	Dull mat, orangeish stains.	19.27
12u	Phosphate		9-10	23	Dull, very fine mat.	19.27
13n	Gold sulfite with excess sulfate and sulfite	(6)	9-10	10-12	Very dull, smooth, brownish.	19.23
13u					Dull, smooth, orangeish.	19.25
14n	Same as 13 plus 15 ppm arsenic		9-10	10-12	Bright, shiny, very smooth.	19.13
14u					Bright, shiny, smooth.	19.24

* "n" and "u" signify new and used baths respectively.

Source of gold is KAu(CN)₂ for all baths, except 13 and 14. All unspecified cations are potassium. The conducting salts had concentrations of approximately 100 g/liter as required to provide the lower Baumé for new baths and the higher for used baths.

to 25°C, are shown in column 7 of Table I. Most of these densities are within 0.2% of the density of pure gold. The exceptions are deposits from baths 1, 13, and 14. The low density of deposits from bath 1 is a result of the large pores within the deposits. The lower density of the deposits from bath 13 are caused by the 5 ppm sulfur contained in this deposit and by the microscopic voids barely visible in the photomicrographs. The arsenic in bath 14 further reduces the deposit density.

Electrical Resistivity—Procedure

Strips approximately 1 mm wide and 25 mm long were cut from the deposits and tested for electrical resistivity using a standard four-contact technique. The measurements were made at room temperature, 298°K, and liquid nitrogen temperature, 77°K. The main uncertainty in any individual resistivity measurement resulted from geometric uncertainties. However, when the resistivity at room temperature is divided by the resistivity of the same sample measured at liquid nitrogen temperature, all geometric factors cancel and a ratio, R_{298}/R_{77} , is obtained which is a function of the material only. This ratio does not include the effects of voids, pores, or electrically inactive inclusions. It does include the effect of chemical purity and, to a lesser extent, grain size.

This ratio serves as a sensitive indicator of relative chemical purity. However, it yields no information as to the concentration or types of impurities present.

White and Wood (7) report R_{298}/R_{77} equals 5.0 for 99.999% pure, vacuum-annealed gold. The highest value obtained in this work was 4.91. The difference probably represents a normal amount of dissolved gases, since most of these deposits are 99.999+ % pure on a metallic basis.

Deposits from new baths without special additives (baths 1, 2, 7, 8) typically had a resistivity ratio of about 4.9, while used baths without special additives yield deposits with R_{298}/R_{77} in the range of 4.6–4.8. This reduction in purity is typical of the contamination obtained in normal industrial usage.

The high value of R_{298}/R_{77} for the deposits from bath 4 indicates an extremely low amount of codeposition of the brightener.

The addition of hardeners reduced R_{298}/R_{77} into the 4.6 range. However, as the baths were used and the special agents were depleted, the value of R_{298}/R_{77} for deposits from these baths approached the value from used baths without special additives.

Deposits from bath 13 had a lower value of R_{298}/R_{77} than expected. When these deposits were annealed to 400°C for 8 hr, the value of R_{298}/R_{77} increased to about 4.4 which still indicates a fairly high level of impurities. The exceptionally low resistivity level for deposits from bath 14 is a direct result of the 15 ppm arsenic included in the deposit.

The high value of the resistance ratio for deposits from used baths 3 and 10 indicates a very high purity of deposit. This purity can be traced to the low level of contamination of these baths and to the effectiveness of the chelating agent in preventing the deposition of contaminants.

Crystalline Structure

The crystalline structure of the deposits was examined by x-ray diffraction techniques, by Berg-Barret X-Ray Topology (8) and by Scanning Electron Microscopy (SEM). Prior to SEM examination, the sample cross sections were etched in a solution of 2.5% $(\text{NH}_4)_2\text{S}_2\text{O}_8$ and 2.5% KCN for 5–30 min at 25°C to bring out the crystal structure. Typical SEM photomicrographs are shown in Fig. 1 through 8.

Generally, the surface microstructure can be divided into four categories. The first is that produced by the alkaline cyanide baths (Fig. 1). These surfaces are composed of uniform, very large (60–120 μm) grains separated by open grain boundaries which penetrate deeply into the deposit. The second category includes most of the solutions. For this category, non-uniform grains of 5–50 μm are connected by distinct, tight-grain boundaries. Deposits from baths 4, 5, and 6, which contain a codepositing metallic brightener, show more small (1–5 μm) grains. In these first two categories, deposit surfaces made from new baths tended to contain many smooth planes, sharp angles, and straight lines identifiable with the underlying crystal structure (Fig. 2 and 4). Deposits made from used baths exhibited a less-organized structure made up of rounded surfaces and curved lines and often contained randomly distributed small (<1 μm) pits (Fig. 3 and 5). A notable exception to this is the deposit from bath 3 and to a lesser extent the deposit from bath 10, where the chelating agents have caused deposits from used baths to have the surface characteristics of new baths.

The third category of surface microstructure is exhibited by the pure sulfite bath, bath 13, Fig. 7. The grains are small and fairly uniform in size (0.2–5 μm). The grain boundaries are distinct and do not appear to

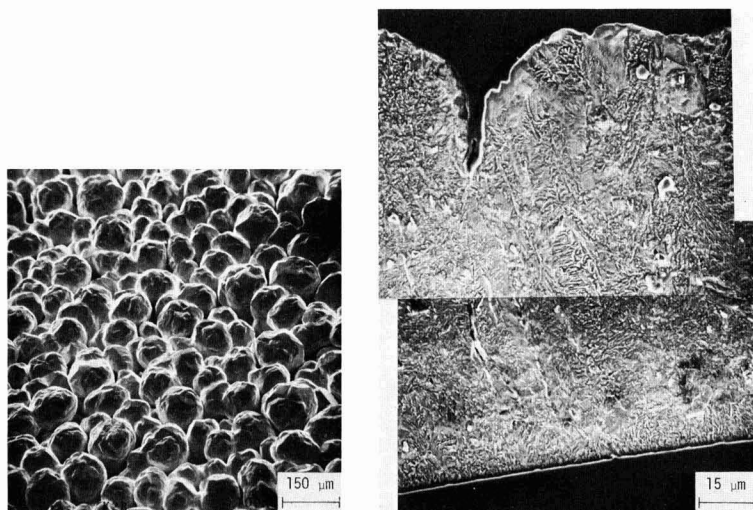
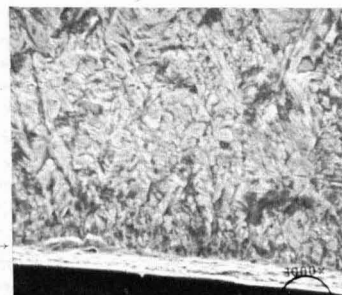
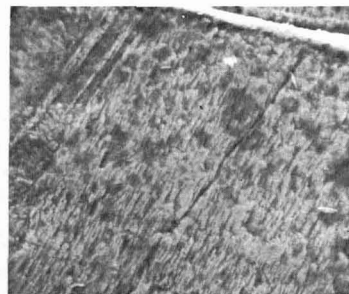
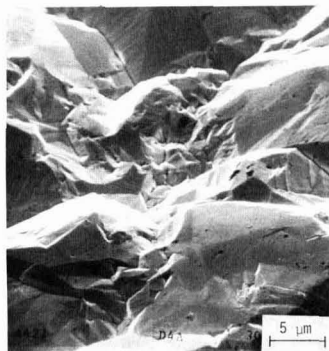


Fig. 1. SEM photomicrographs of deposit 1n from a hot cyanide solution.

Fig. 2. SEM photomicrographs of deposit 2n. The center 2/3 of the cross section is removed. The lower picture is the copper edge of the deposit, while the upper picture is the solution edge. Surfaces and sections of deposits 3u, 7n, 10u, and, to a lesser extent, 8n, were similar.



edge →

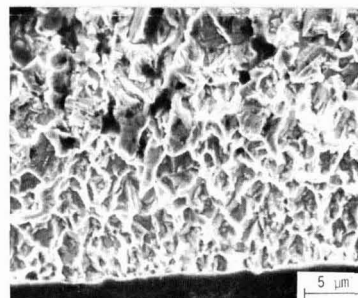
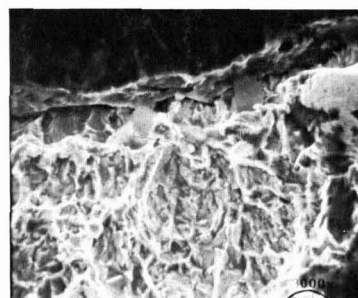
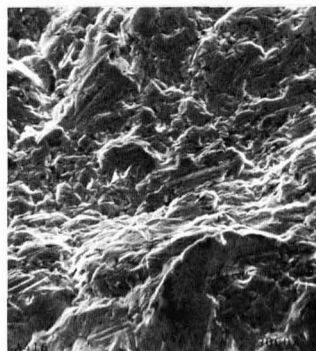


Fig. 3. SEM photomicrographs of deposit 2u.

be tightly closed. The fourth category is exhibited by bath 14. Surfaces from this bath were completely featureless even when viewed at 30,000X.

The SEM photomicrographs of cross sections may also be divided into four categories. The first is the coarse grain structure with deeply penetrating pores found in the hot cyanide bath deposits, Fig. 1. The second category includes the majority of the deposits and shows grains less than $0.5 \mu\text{m}$ in diameter on the substrate side of the deposit and crystallites $5\text{--}30 \mu\text{m}$ in diameter on the solution side of the deposits. Many of these crystallites can be followed for $20\text{--}60 \mu\text{m}$ through the deposit. Those deposits containing hardeners and brighteners, baths 4, 5, 6, and 9, fall at

the lower end of the crystallite size ranges. Deposits from used baths tend to fall in the center of the range, while deposits from new baths which do not contain metallic impurities and from used baths containing chelating agents have crystallites in the upper end of the size range. The two anomalous structures in this group are from new solution 3 which appeared almost amorphous and from new solution 9 which exhibited a distinct columnar structure (Fig. 6).

The third category consists of deposits from the non-cyanide solution, bath 13, which had extremely small grains throughout the deposit (Fig. 7).

The last category is from the non-cyanide solution containing arsenic, bath 14. Cross sections of these

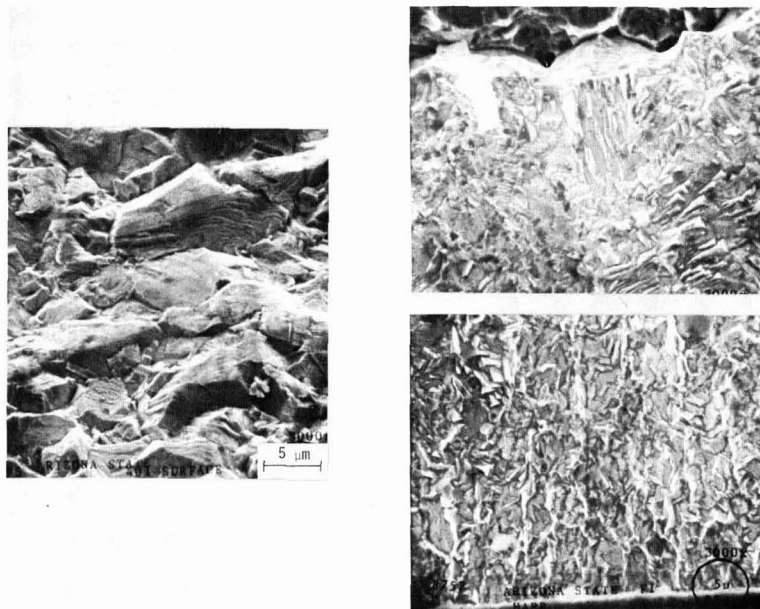


Fig. 4. SEM photomicrographs of deposit 4n. Deposits from 5n and 6n were fairly similar.

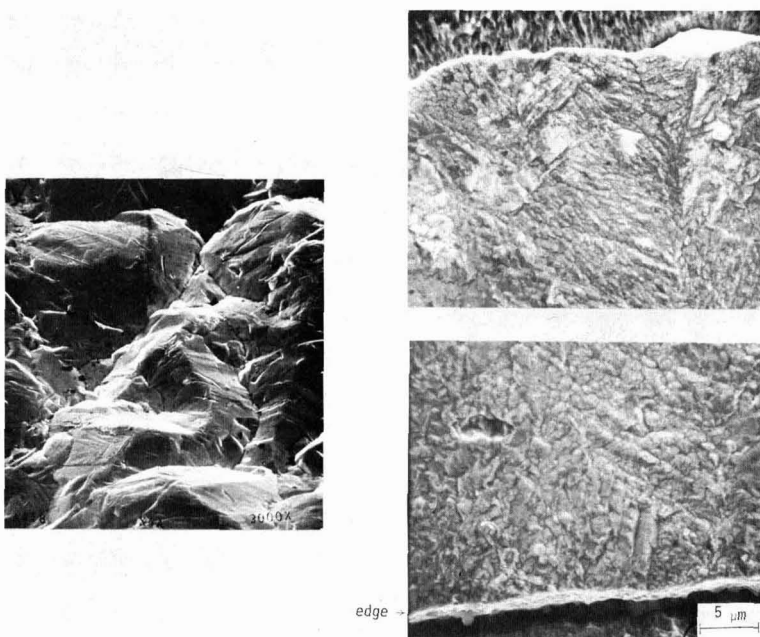


Fig. 5. SEM photomicrographs of deposit 4u.

deposits are amorphous in appearance (Fig. 8). The deposit from the new bath also shows a layered structure similar to those often found for alloy deposits (8). The deposit from a used bath shows only a random porosity.

The crystal lattice parameters were determined by x-ray back reflection. Within the limits of the equipment used, the lattice parameters were those for pure gold. Thus the density variations shown in Table I are caused by impurities, pores, inclusions, etc., but not by lattice expansion.

X-ray line broadening was used to determine the average crystal size (9). This technique is precise for crystallite sizes under $0.1 \mu\text{m}$, but for larger values

the accuracy degenerates quickly and only a lower limit can be placed on the size. The results of the line-broadening measurements are shown in columns 3 and 4 of Table II.

Berg-Barrett X-Ray Topology (10) was used to determine the maximum crystallite size. With the film used, crystals larger than $3 \mu\text{m}$ were resolved. The results are shown in parentheses in columns 3 and 4 of Table II. Where values are not reported, no individual crystals could be resolved by this technique.

The first crystals to nucleate from new baths not containing metallic impurities (baths 1, 2, 3) grew to average sizes greater than $0.1 \mu\text{m}$. However, the first crystals to grow from all other baths were much

Fig. 6. SEM photomicrographs of deposit 9n.

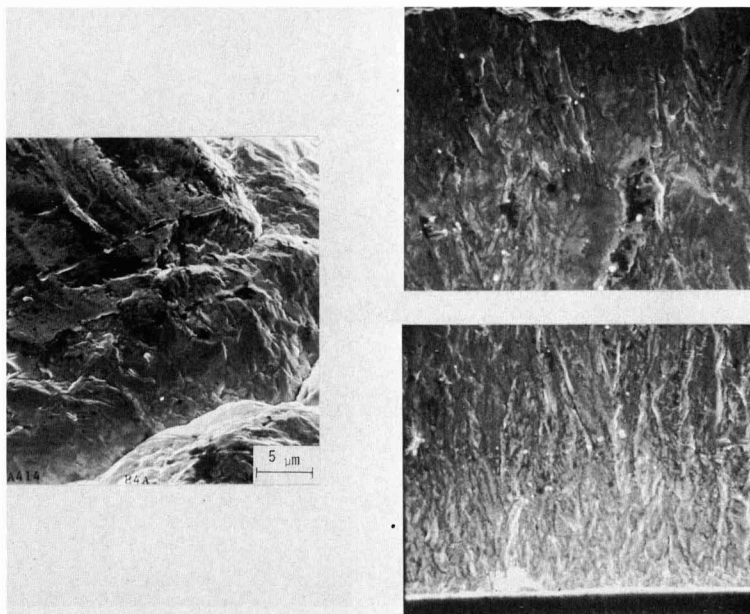
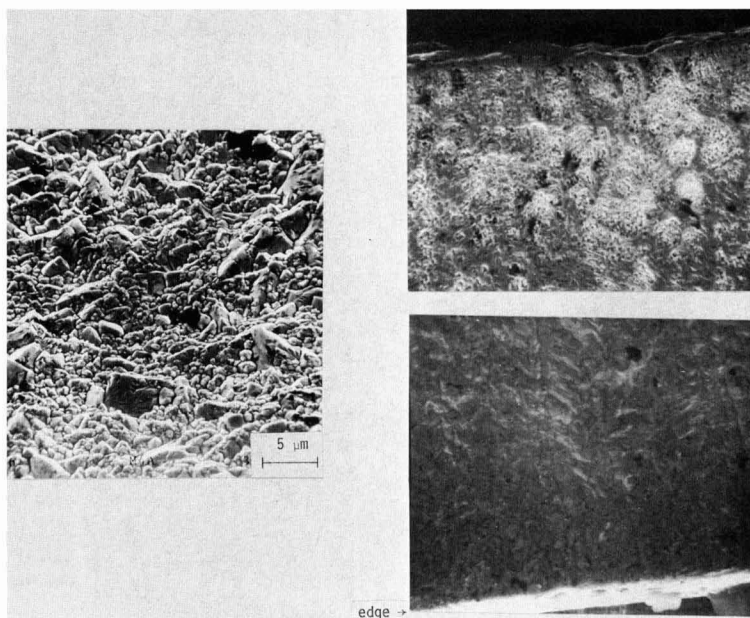


Fig. 7. SEM photomicrographs of deposit 13n. Deposit 13u was similar, but finer grained.



smaller in size (about $0.03 \mu\text{m}$). These other baths, with the exception of 7 and 8, all contained metallic impurities either because of normal contamination from use or because of addition of hardeners and brighteners. It appeared that these codepositing metallic impurities facilitated nucleation on the copper substrate so that the average crystal size was smaller. Hydrazine sulfate (baths 7 and 8) performed the same function although the mechanism by which this occurred was not clear.

The average crystallite size on the solution side of the deposit was a good indication of the ability of hardeners and brighteners to control average crystal

size. New baths 4, 5, 6, and 9, with these additives, show average solution side crystal sizes of about $0.06 \mu\text{m}$, while new baths without these addition agents produce crystals in excess of $0.1 \mu\text{m}$. As the baths were used and replenished, the effectiveness of the brighteners and hardeners in controlling crystal size was diminished. This was probably caused by a failure to replenish the baths with these additives at the same rate they were consumed. At the same time, all baths picked up impurities during use. These impurities, unless counteracted with chelating agents as in baths 3 and 10, tended to decrease the grain size. The net result was that baths with and without the

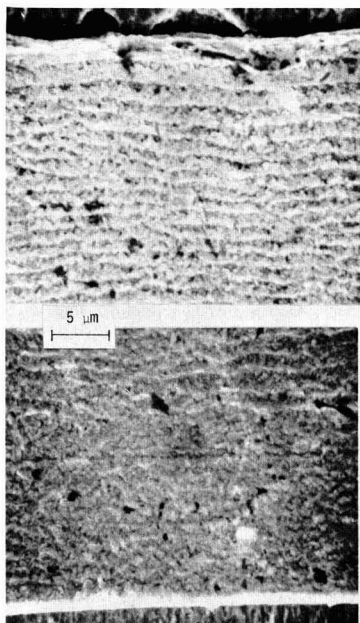


Fig. 8. SEM photomicrographs of sections of deposits 14n and 17u. Surfaces were featureless.

special additives took on the same character as they became contaminated with use.

Except for baths 1 and 14, the maximum crystallite size obtained by the deposits differed only slightly from bath to bath. Bath 14 was the only bath to produce resolvable crystals on the copper side of the deposit. The used bath 14 produced many extremely large single crystals on the solution side of the deposit. These crystals exhibited internal structure, possible parallel slip planes, and long range order

between crystals. Since these crystals were not resolved in SEM photomicrographs of either the section or the surface, we conclude that these crystals are extremely thin and oriented parallel to the surface. Crystal platelets of this type are believed to be major contributors to the smooth, shiny surfaces of these deposits.

X-ray diffraction was used to determine the preferred orientation of the deposits. For each side of each deposit, the x-ray intensities of the the first 10 diffraction peaks were measured. These peaks represent crystal orientation from (111) to (511). Intensities for redundant peaks such as (200) and (400) were combined. The intensities were then normalized and compared with NBS data for random deposits (11) and with a pure gold powder sample. The results are shown in columns 5 and 6 of Table II. A major feature of some diffraction patterns was the suppression of a particular peak intensity. This is shown in Table II by a minus sign in front of the associated orientation.

With the exception of the non-cyanide baths and acid phosphate baths, new baths without hardeners or brighteners tended to nucleate and grow (111) initially. As growth of these deposits continued, the (111) orientation was suppressed and higher order orientations, particularly the (311), became dominant. This is in keeping with the general concept that close-packed orientations are natural for heterogeneous nucleation but form the slowest growing crystal faces.

The addition of hardeners, brighteners, or normal operational contaminants usually suppressed the initial (111) nucleation so that both sides of the deposit tended to have a (311) preferred orientation or to be more nearly random. However, two baths, 6 and 9, which contained hardeners, produced deposits with strongly preferred initial (111) orientation. In addition to hardeners and brighteners, bath 6 contained boric acid as a copper conditioner. New bath 9, which contained the hardener and ammonium ion, produced a strong (111) preferred orientation throughout the deposit. The chelating agents in baths 3 and 10 were effective in controlling contaminations so that deposits from these used baths had orientations typical of deposits from new baths. The acid

Table II. Deposit characteristics

Bath No.	R_{200}/R_{111}	Crystallite size copper side	μm Solution side	Preferred orientation* Copper side	Solution* Solution side
1n	4.82	>0.1	>0.1 (20)	(111)	r, - (111)
1u	4.77	0.05	>0.1 (20)	(311), r	r, - (111)
2n	4.91	>0.1	>0.1 (12)	(111)	(311), (511)
2u	4.70	0.03	0.05 (7)	(311)	(311), (511), - (111)
3n	4.79	>0.1	0.06 (6)	(111)	(311), (422)
3u	4.92	0.03	>0.1 (7)	(111), (311)	(311), (511)
4n	4.70	0.06	0.08 (9)	(220), (311)	(220), (311)
4u	4.86	0.04	>0.1 (7)	(311), r	(311), (511)
5n	4.62	0.03	0.06 (8)	r	r
5u	4.69	0.03	>0.1 (10)	(220), (311)	(220) (311)
6n	4.72	0.03	0.06 (9)	(111)	(311)
7n	4.91	0.03	>0.1 (10)	(111), (311)	(311)
7u	4.60	0.03	0.08 (15)	(311), r	r
8n	4.87	0.03	>0.1 (15)	(311)	(220), (311)
8u	4.83	0.04	0.07 (9)	(311)	(311), (511)
9n	4.36	0.03	0.05 (11)	(111)	(111)
9u	4.65	0.03	0.05 (11)	(111)	(311)
10u	4.88	0.03	>0.1 (10)	(111)	(311), (511)
11u	4.91	0.04	>0.1 (10)	(311)	(200) (311), (511)
12u	4.82	0.06	0.06 (10)	(111)	(311)
13n	4.12	0.03	0.06 (6)	(220)	(220)
13u	4.14	0.05	>0.1 (8)	(111), r	r
14n	2.67	0.05 (8)	0.05 (3)	(200)	(200), (220)
14u	3.73	0.06 (10)	>0.1 (50)	(220)	(200)

* "r" signifies a nearly random orientation. Underlined orientations are strongly preferred orientation. Doubly underlined orientations are very strongly preferred. Orientations preceded by a minus sign are significantly diminished.

Table III. Metallic constituents in used baths

Bath No.	1u	2u	3u	4u	7u	9u	10u	14u
Gold	7.45	6.24	4.61	6.34	8.06	7.20	6.44	10.14
Silver						0.025		
Nickel	0.21	0.11	<0.01	0.019	0.017	0.01	0.052	<0.01
Copper	0.44	0.01	0.056	0.02	0.015	<0.01	N.D.	0.10
Cobalt	N.D.	0.07	N.D.	N.D.	0.07	N.D.	N.D.	N.D.
Iron	0.19	0.27	<0.01	0.044	0.026	0.008	0.054	N.D.
Lead	0.014	0.01	0.18	<0.01	<0.01	<0.01	N.D.	0.011
Zinc	N.D.	N.D.	0.50	N.D.	<0.01	0.02	N.D.	N.D.
Chromium						0.14		
Arsenic								0.40

Values are in grams per liter for baths taken from production lines.

phosphate baths (8 and 11) were unique in showing a strong tendency to (311) nucleation and growth.

The observations on preferred orientation do not correlate with the observations of crystal size, surface appearance, or grain structure, except in the case of new bath 9. The columnar structure that runs through this deposit is a direct result of the strong (111) preferred orientation for both nucleation and growth.

Conclusions

With the exceptions of the large grain porous structure of deposits from the hot cyanide bath, the very fine grain, brown deposit from bath 13, and the bright shiny deposits from bath 14, the deposits investigated were fairly similar. Special hardeners and brighteners added to new baths decreased the grain size and affected the orientation of the crystals and the surface appearance. However, as the baths were used and regenerated, the differences in deposits tended to diminish. Chelating agents were found to be effective in controlling impurity deposition from used baths.

Manuscript submitted Nov. 5, 1969; revised manuscript received July 6, 1970. This was Paper 151 pre-

sented at the Detroit Meeting of the Society, Oct. 5-9, 1969.

Any discussion of this paper will appear in a Discussion Section to be published in the June 1971 JOURNAL.

REFERENCES

1. "Metal Finishing Guidebook Directory," p. 279, Metals and Plastics Publications, Inc., Westwood, N. J. (1968).
2. B. Ostrow and F. Nobel, French Pat. 1,479,984 (1966).
3. R. Duva and D. G. Foulke, U.S. Reissue, 25,883 (1965).
4. D. G. Foulke, U.S. Pat. 3,156,634 (1964).
5. K. Schumpelt, U.S. Pat. 3,367,853 (1968).
6. P. T. Smith, U.S. Pat. 3,057,789 (1962).
7. G. K. White and S. B. Woods, *Phil. Trans. Roy. Soc. (London)*, **A251**, No. 995, 273 (1959).
8. R. Duva and D. G. Foulke, *Plating*, **55**, 10, 1056 (1968).
9. H. P. Klug and L. E. Alexander, "X-Ray Diffraction Procedures," John Wiley & Sons, Inc., New York (1954).
10. C. S. Barrett, *Trans AIME*, **161**, 15 (1945).
11. H. E. Swanson and E. Tatge, *Nat. Bur. Std. (U.S.) Circ.* **539**, I, 33 (1953).

Electrophoretic Deposition of Luminescent Materials

P. F. Grosso, R. E. Rutherford, Jr., and D. E. Sargent

Applied Physics Department, CBS Laboratories, Stamford, Connecticut 06905

ABSTRACT

Electrophoretic deposition of luminescent materials such as $2\text{CaO}\cdot\text{MgO}\cdot 2\text{SiO}_2\cdot\text{Ce}\cdot\text{Li}$ has been accomplished by the adsorption of inorganic cations of Mg^{++} , Ca^{++} , Ba^{++} , Sr^{++} , Al^{+++} , Na^+ , K^+ , Li^+ or NH_4^+ , from nitrates, chlorides, and bromides, in polar liquids such as isopropyl alcohol with a critical concentration of about 1% H_2O . An explanation of the adsorption charging and the pertinent factors which effect cataphoretic deposition for a calcium magnesium silicate-magnesium nitrate system is presented. Acetone has been found to have a beneficial depolarizing effect, while magnesium salts produce a cementing action on the deposited phosphor layer.

The electrophoretic deposition of powdered phosphors to form fluorescent screens offers several advantages over the usual gravitational sedimentation-cementation processes: (a) Curved or irregularly-shaped objects can be coated uniformly; deposition can even be accomplished in an upward direction to prevent the settling out of large phosphor aggregates onto the screen. (b) Very fine particle-size screens can be deposited quickly from suspensions that flocculate or settle very slowly (due to the similar charge on each particle); in fact, in electrophoresis, the fine particles move and are deposited more rapidly than larger particles. (c) Definite control can be exercised over the

amount and character of the final particle cementing agent; desirable cementing agents may be generated simultaneously with particle deposition by combining electrolytic with electrophoretic effects. (d) Very smooth screens of uniform and controlled thickness and density can be prepared.

In these laboratories in the past, phosphor suspensions for electrophoretic deposition have been prepared by stone-milling phosphor powders in polar organic liquids such as alcohols, acetone, etc., for substantial periods of time. Milling does indeed yield "charged" suspensions, but usually also damages the phosphor (light output and efficiency are lower than the original powder). The mechanism of this damage is not completely understood, but appears to result from severe

Key words: electrophoresis, deposition, luminescent materials, phosphors, cathode-ray screens.

physical shear, production of many particles below optimum size for efficient fluorescence, thermal damage caused by high local impact temperatures, surface chemistry such as oxidation-reduction reactions, loss or absorption of various substances (e.g. analysis shows that phosphors milled with flint stones have absorbed aluminum), etc.

During the present study, methods have been sought for "charging" phosphor suspensions without the attendant damage of stone milling. Most attention has been focused on the addition of soluble electrolytes to suspensions of various phosphors in essentially non-aqueous media, but auxiliary means such as stirring, classification by settling (elutriation), and ultrasonic dispersion have also been employed.

In the experimental work described, calcium magnesium silicate ($2\text{CaO} \cdot \text{MgO} \cdot 2\text{SiO}_2 \cdot \text{Ce} \cdot \text{Li}$) was used.

Experimental Procedure

In order to compare the efficacy of various added electrolytes and various nonaqueous liquid suspending media for promoting the cathaphoretic deposition of various phosphors the following test procedure was employed.

The electrophoretic deposition cell consisted of an unstirred vessel of 300 ml capacity, which was provided with a stainless steel frame which supported a 1 in. diameter test blank in a vertical position. The test blanks were either conductive glass or stainless steel. These blanks, one of which was used as the cathode in each experiment, were cleaned ultrasonically with acetone and were weighed before each deposition experiment. Facing the blank cathode and separated from it by a distance of $\frac{3}{8}$ – $\frac{3}{4}$ in. was a row of three $\frac{1}{4}$ in. carbon rods held in a vertical position. These rods were the anode in each experiment. Any inert material, such as platinum, can be used as an anode. A variable d-c power supply capable of providing potentials up to 500V and currents up to 250 mA was used to promote electrophoretic deposition.

In typical operation, 250 mg of the phosphor powder under test was added to 250 cc of the fluid suspending media in which the electrolyte under test had previously been dissolved. The phosphor was allowed to equilibrate with the liquid medium by stirring for 5 min, and the resulting suspension was then poured into the test cell. Sufficient potential was immediately applied to yield a current of 10 mA and the deposition was allowed to proceed at 25°C without stirring. The test cathode blank was then withdrawn, dried, and weighed. The appearance of the deposited phosphor layer was examined and noted.

Pertinent Factors

Cathaphoretic deposition is a complex phenomenon in which several variables play significant roles. First, the liquid suspending medium must be carefully chosen. It must be a suitable solvent for the added electrolytes under test, but must not yield solutions having high conductivities. It is desirable to maintain a high potential difference between the anode and the cathode, but high current flow with resultant resistance heating is not desirable. Deposition of the suspended powder rather than electrolysis of the liquid medium is desired. In addition, the liquid medium should have a low viscosity so that the charged particle can migrate at the maximum rate under the applied field. For practical reasons, it should be inexpensive, water miscible, and low in toxicity.

Previous work in these laboratories (1-3) and elsewhere (4) has shown that polar liquids such as the water soluble lower molecular weight alcohols and ketones provide good media for electrophoretic deposition. In the present study, isopropyl alcohol and acetone have been used almost exclusively, either separately or mixed together and usually with some water added. Water can be used to advantage in electrophoretic systems, but is very important to carefully control the amount added. This may be illustrated by

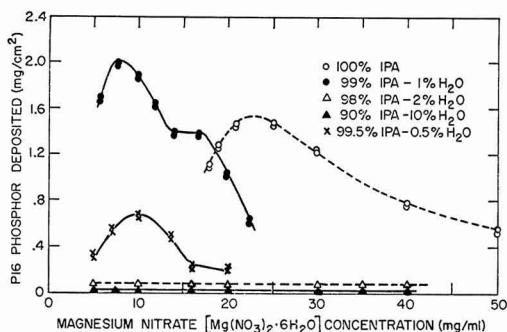
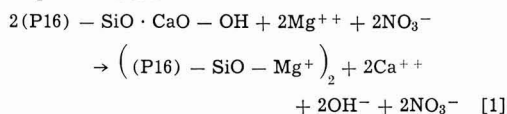


Fig. 1. Effect of magnesium nitrate and water concentrations on amount of phosphor deposited. Deposition conditions: carbon anode-stainless steel cathode; electrode spacing 5/8 in.; current 10 mA, voltage 25-100V; time 5 min; P16 phosphor concentration in suspension 1 mg/ml.

examination of $2\text{CaO} \cdot \text{MgO} \cdot 2\text{SiO}_2 \cdot \text{Ce} \cdot \text{Li}$ (P16 phosphor) deposition curves shown in Fig. 1. In the experiments represented by the curves, increasing amounts of magnesium nitrate $\text{Mg}(\text{NO}_3)_2 \cdot 6\text{H}_2\text{O}$ was added to either 100% isopropyl alcohol, 99.5% isopropyl alcohol + 0.5% water, 99% isopropyl alcohol + 1% water, 98% isopropyl alcohol + 2% water, or 90% isopropyl alcohol + 10% water. It will be noted that the highest mass deposition efficiency of phosphor (greater weight deposited during the standard 5 min time interval) occurred when about 8 mg of the magnesium nitrate was added to the 1% water system (250 mg phosphor in 250 cc 99% isopropyl alcohol + 1% water). Addition of more or less magnesium nitrate gave less deposition of phosphor. In the experiments in which water was not added, the maximum deposition occurred with approximately 22.5 mg of the nitrate. Addition of more or less than 1% water also gave less deposition of phosphor than 1% water. Use of 98% isopropyl alcohol + 2% water, 90% isopropyl alcohol + 10% water gave very poor results at all levels of added magnesium nitrate. The higher water concentrations increased the conductivity to allow electrolysis to predominate over electrophoretic deposition. Lower water concentration did not allow satisfactory ionization to take place. It is then evident that the amount of water present, as well as the amount of electrolyte added, is critical.

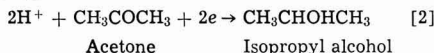
In the 1% water system, addition of the optimum amount of magnesium nitrate (8 mg) apparently gives good "charging" of the calcium magnesium silicate (P16) phosphor since the weight of deposited phosphor is high. Simultaneously, the conductivity of the system appears to increase, for without the phosphor present 20 mg of magnesium nitrate would be required to give the same conductivity. In order to explain this phenomenon, it may be suggested that the phosphor, known to have excess calcium oxide on its surface, may undergo the following type of absorption-desorption reaction:



The phosphor thus becomes "charged" and the ionic concentration (conductivity) of the suspending medium is simultaneously increased. When less than the optimum magnesium nitrate concentration is added, maximum charging is not attained, and the weight of phosphor deposition is decreased. If greater than the optimum magnesium nitrate concentration is used, the amount of phosphor deposited also decreases because either (a) the increase in conductivity causes electrolysis instead of electrophoretic deposition or

(b) the increasing electrolyte concentration may actually diminish the positive charge on the phosphor particles through the increased absorption of negative ions (5). This same type of maximum is noted in the anhydrous system but at higher electrolyte concentrations.

It was also found that acetone is an effective cathode depolarizer, *e.g.*, that when present, it largely prevents the appearance of gaseous hydrogen, presumably by acting as an acceptor of any electrolytic hydrogen generated.



When no hydrogen is evolved, very smooth, compact phosphor screens may be deposited. Experiments were conducted to determine the optimum combination of acetone, water, and alcohol.

Excellent results were obtained with 25% isopropyl alcohol + 74% acetone + 1% water (by volume) as the suspending fluid and electrolyte solvent. Below 70% acetone concentration yielded coarse phosphor screens due to gas evolution during deposition. Above 80% acetone yielded thin, nonuniform phosphor screens of low adherence.

Choice of Added Electrolyte

A large number of inorganic compounds were found to be capable of "charging" calcium magnesium silicate positively so that deposition at the cathode could be achieved. The suitability of these various additives was determined by dissolving 1 mg/ml of the inorganic compound to be investigated to either 99% isopropyl alcohol + 1% water or to 74% acetone + 25% isopropyl alcohol + 1% water (by volume), and then suspending 1 mg/ml of the phosphor in the above fluid and determining whether favorable rates of deposition and good quality screens were obtained. With promising candidate additive compounds, the concentration was varied until the maximum deposition rate and screen quality was established.

Since cataphoresis rather than electroplating was desired, principal attention was given to inorganic compounds having anions which cannot be reduced in aqueous media. Thus soluble salts of magnesium, calcium, barium, strontium, aluminum, sodium, potassium, lithium, and ammonium were evaluated. Divalent magnesium, calcium, and strontium all gave positive results. It is interesting to note that all of these cations form rather insoluble silicates and it is not surprising that they are well absorbed on and "charge" calcium magnesium silicate (probably due to reaction with exposed SiOH or SiO groups). Because of its relatively high ionic charge, low mass, low toxicity, and low solubility in combination with a variety of anions, magnesium was chosen as the preferred cation, with aluminum as a close second choice.

Insofar as the preferred anion is concerned, nitrate and chloride (and to a lesser extent, bromide) appeared to be preferable to several other anions evaluated. While the nitrates and chlorides of magnesium, aluminum, and lithium gave good deposition, the sulfates of these and other metals gave uniformly poor results. It is possible that the sulfate ion was too well removed from solution by the phosphor. When fluoride, phosphate, formate, acetate, citrate, hydroxide, *etc.*, were introduced in the form of acids and bases, the results were also not satisfactory.

P16 phosphor (2CaO·MgO·2SiO₂·Ce:Li) appears to have a "basic" surface (shown by pH of moist powder against pH paper), probably due to the presence of MgO and/or CaO or the corresponding hydroxides. It may also be "charged" by the addition of hydrochloric acid (presumably by conversion of the oxides and/or hydroxides to magnesium and calcium ions to form the oppositely charged counter layer). The addition of hydrofluoric, phosphoric, sulfuric, formic, acetic, and citric acids do not give favorable "charging." The

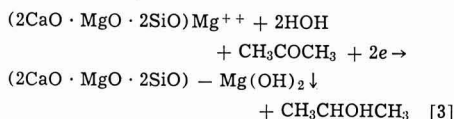
failure of hydrofluoric, phosphoric, and sulfuric acids may be explained on the basis that the anions of these acids form insoluble calcium salts (the surface is coated with an insoluble compound rather than converted to an ionized double layer), but the failure of formic, acetic and citric acids is more difficult to explain. Perhaps these acids too well "sequester" calcium and magnesium, *i.e.*, actually remove them from the surface of the phosphor, making it impossible for a double layer to form.

The behavior of nitric acid is anomalous. It should yield calcium and magnesium nitrates by reaction with the surface of the phosphor, and these nitrates are known to give favorable depositions. But when nitric acid was added to a system containing isopropyl alcohol, no deposition resulted. Perhaps it is too rapidly consumed in oxidizing the easily oxidized alcohol.

Heavier, more easily reduced cations do not give satisfactory results in general. Thus, the nitrates of lead, iron (ferric), zinc, copper, the chlorides of nickel, cobalt, manganese, palladium, and chromium sulfate either gave no deposit, very discolored deposits (probably containing the respective metals or lower valence compounds), or poorly adhering deposits. This is to be expected in view of the ease of reduction of these metallic ions at a cathode.

Added Advantage of Magnesium and Related Metallic Salts

When magnesium salts are electrolyzed, hydrogen rather than magnesium is liberated at the cathode. In the system we have been investigating, the hydrogen is apparently taken up by acetone (see above). Regardless of the fate of the hydrogen, there is an increase in hydroxyl ion concentration (or pH) in the vicinity of the cathode. This results in the formation (and deposition) of an interesting and adherent form of magnesium hydroxide which can apparently act as a cementing agent for the simultaneously cathodically deposited phosphor. The cathode reactions involved may be represented as follows



That an adherent magnesium hydroxide film is formed under the conditions employed is also indicated by the following: The addition of phenolphthalein to the system with the omission of phosphor gives a very adherent, bright red film on the cathode when current is passed. This is probably a combined film of magnesium hydroxide and the magnesium salt of the phthalein (colored, basic form). Other dyestuff compounds have also been bonded to the cathode by this process, but extensive discussion of these is beyond the scope of this paper.

Conclusions

An electrophoretic deposition process for the formation of luminescent phosphor screens has been developed which does not employ the use of stone milling to disperse and charge phosphor particles. The charging of calcium magnesium silicate phosphor particles is achieved by the adsorption of nonreducible inorganic cations of Mg⁺⁺, Ca⁺⁺, Ba⁺⁺, Sn⁺⁺, Al⁺⁺⁺, Na⁺, K⁺, Li⁺, and NH₄⁺ on the phosphor surface. The adsorbed cations cause the phosphor particles to migrate in a suitable suspending media under the influence of an electric field to the electrode of opposite charge. Salts of these cations produce a cementing action between the deposited phosphor layer and the substrate to be coated.

The resulting phosphor coating is tenacious to the substrate, uniform, dense, fine grained, and does not exhibit a decrease in luminous efficiency.

Water concentration is extremely critical with magnesium nitrate as the charging cation. Above and below 1% H_2O decreased the phosphor deposition efficiency.

Acetone has been found to be an effective depolarizing agent, thereby preventing gaseous evolution during the deposition.

Manuscript submitted December 10, 1969; revised manuscript received ca. July 22, 1970.

Any discussion of this paper will appear in a Discussion Section to be published in the June 1971 JOURNAL.

REFERENCES

1. P. Grosso, CBS Lab., "Development of Phosphor Screens for High Resolution Display Devices," Technical Documentary Report No. AL-TDR-64-

- 94, Contract No. AF 33(657)-10632, Project 4156, Air Force Avionics Lab., Wright-Patterson AFB, Ohio, May 1964.
2. P. Grosso and R. Rutherford, Jr., CBS Lab., "Cathaphoretic Screen Studies," Final Report, Contract No. DA44009 ENG 5196, Project 8F23-02-1-03, USAERDL, Fort Belvoir, Va., May 1963.
3. R. Rutherford, Jr., and K. Spiegel, CBS Labs., "Research and Investigation on Phosphor Screens for High Resolution Display Devices," Technical Documentary Report No. ASD-TDR-62-1097, Contract No. AF33(616)8509, Wright-Patterson AFB, Ohio, Nov. 1962.
4. N. F. Cerulli, "Methods of Electrophoretic Deposition of Luminescent Materials and the Product Resulting Therefrom," U.S. Pat. 2,851,408, Sept. 9, 1958.
5. S. Glasstone, "Textbook of Physical Chemistry," p. 1225, D. Van Nostrand Co. (1946).

Technical Notes



Synergistic Effects of Anions in the Corrosion of Aluminum Alloys

A. M. McKissick, Jr., A. A. Adams, and R. T. Foley*

Department of Chemistry, The American University, Washington, D. C. 20016

Aluminum and aluminum alloys are susceptible to pitting and general corrosion in chloride solutions and the fact that nitrate ion can inhibit this corrosion has been reported by several investigators. Callendar (1) measured the corrosion of Al and three Al-Cu alloys in tap water to which were added various concentrations of NaNO_3 , NaCl , and $\text{K}_2\text{Cr}_2\text{O}_7$. He reported that a critical amount of NaNO_3 , 0.008% for his tap water, was required to achieve passivation of the Al-Cu alloy and he directly related the rate of reduction of nitrate to the concentration required to achieve passivation. Blanchard and Goucher (2) in their studies of aluminum corrosion in microbial culture media containing a number of salts, including CaCl_2 and FeCl_3 , observed that a 12 mM (millimolar) concentration of KNO_3 protected aluminum alloys 2024 and 7075. At a $\text{Cl}^-/\text{NO}_3^-$ ratio of 20 there was a slight stimulation of corrosion (about 20% increase). Kassiyura and Zaretskii (3) recently reported on the anodic behavior of A-99 aluminum in 1N and 3N solutions of NaNO_3 with various chloride additions. They noted that in a specific concentration range for NaCl the region of the passive state decreased with increased chloride ion concentration. Böhm and Uhlig (4) noted that NaNO_3 additions to NaCl solutions moved the pitting potential of 99.99% Al in the noble direction and the relationship between chloride activity and inhibiting nitrate activity followed the equation

$$\log (\text{Cl}^-) = 0.65 \log (\text{NO}_3^-) - 0.73$$

From the review of the literature it may be concluded that nitrate is an inhibitor for aluminum corrosion in chloride solutions, and that the $\text{Cl}^-/\text{NO}_3^-$ ratio is important. In connection with an investigation of the chemistry of stress-corrosion cracking of high-strength aluminum alloys we have examined the effect

of a number of anions on aluminum and aluminum alloys. Certain effects that have been observed are felt to be sufficiently unusual to warrant a preliminary report. We note, particularly, certain synergistic effects that could not be predicted from a knowledge of the behavior of individual ions.

Experimental

The work reported here consists of immersion tests with three aluminum alloys. Alloy 1199-H14 was supplied by the Reynolds Metals Company and alloys 2024-T3 and 7075-T6 by the Kaiser Aluminum Company. Samples $38 \times 26 \times 0.81$ mm were cleaned in the conventional manner. The strip was immersed in NaOH solution (5 g/100 ml) at $75^\circ\text{--}80^\circ\text{C}$ for 1 min, rinsed thoroughly, dipped in NH_4OH (1:3) for 1 min at room temperature, and thoroughly rinsed in distilled water and acetone. Samples were immersed in triplicate in solutions of various salt concentrations for periods of 14 days at $22^\circ \pm 1^\circ\text{C}$. Following exposures, the corrosion product was removed with a stripping solution of 20g of chromic acid and 32.25 ml of 85% phosphoric acid/liter. The weight loss reported was the difference in weight of the sample before the test and that after the stripping. The latter was corrected with the weight loss of an uncorroded metal specimen in the stripping solution.

Results and Discussion

The weight losses for the three aluminum alloys in 0.01N NaCl solutions are given in Table I. The corrosion observed with unalloyed aluminum is of the pitting type, whereas that of the alloys progresses rapidly after the first day to a general attack over the entire surface. Also noted here is the inhibiting effect of NaNO_3 in concentrations of 0.05N and higher in solutions of 0.01N NaCl , i.e., a $\text{NO}_3^-/\text{Cl}^-$ ratio of 5. These two effects, corrosion in chloride solution and inhibi-

* Electrochemical Society Active Member.

Key words: inhibition, chloride, nitrate, aluminum alloy 7075, aluminum alloy 2024.

Table I. Weight changes of aluminum alloys after 2 week immersion in salt solutions

Alloy	Electrolyte	Weight loss (mg/cm ²) (±σ)*
1199	0.01N NaCl	0.02 ± 0.007
2024	0.01N NaCl	1.17 ± 0.21
7075	0.01N NaCl	1.44 ± 0.04
7075	0.01N NaCl/0.05N NaNO ₃	0.01 ± 0.01
2024	0.01N NaCl/0.10N NaNO ₃	0.14 ± 0.02
7075	0.01N LiCl	0.17 ± 0.003
7075	0.01N KCl	0.54 ± 0.01

* These are average values. A minimum of three replicates were run but most of these represent averages of about 12 samples run by two different investigators.

Table II. Weight changes of aluminum alloys after 2 week immersion in salt solutions of various nitrate chloride ratios

Alloy	Electrolyte	Weight loss (mg/cm ²) (±σ)
2024	0.01N NaCl/0.01N NaNO ₃	6.80 ± 0.8
7075	0.01N NaCl/0.01N NaNO ₃	10.1 ± 0.75
7075	0.01N NaCl/0.005N NaNO ₃	8.8 ± 0.48
7075	0.01N KCl/0.01N KNO ₃	0.31 ± 0.03
7075	0.01N LiCl/0.01N LiNO ₃	0.08 ± 0.001
1199	0.01N NaCl/0.009N NaNO ₃	0.07 ± 0.03
1199	0.01N NaCl/0.003N NaNO ₃	0.07 ± 0.03

tion at some critical NO₃⁻/Cl⁻ ratio have been reported previously, at least qualitatively.

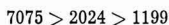
Table II lists typical results wherein the NO₃⁻/Cl⁻ ratio is reduced to one and below. Corrosion is increased by an order of magnitude in the sodium salt solutions. The effect is graphically represented in Fig. 1. The maximum effect is exhibited at a NO₃⁻/Cl⁻ ratio of about 0.7. Tables I and II also indicate that the corrosion rate is not independent of the cation, which is contrary to previously reported observations. The corrosion rate for the 7075 alloy varies, as follows



$$8.5 > 3.2 > 1.0$$

for corrosion under the stated conditions. Also, there is no synergistic effect with potassium or lithium salt solutions.

There is an alloy effect observed here and in other measurements as well. Thus in chloride solution the rates are in the following order



$$72 > 59 > 1$$

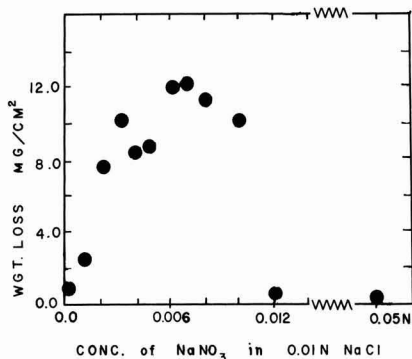


Fig. 1. Effect of NaNO₃ additions to 0.01N NaCl solutions on the corrosion of aluminum alloy 7075.

The synergistic effect was noted with both alloy types 7075 and 2024 but not with 1199. The physical appearance of the samples corroded in the nitrate-chloride solutions is different from those corroded in chloride solution, being characterized by large blisters suggesting considerable gas evolution during corrosion. After about 1 day's exposure the sample turns black, suggestive of a dealuminification type of attack. Continual exposure over a period of weeks produces a voluminous corrosion product often in the form of streamers (probably hydrated aluminum oxide). Metallographic cross section reveals considerable roughening of the sample.

At this point we are not able to offer a good explanation for these observations. The simple descriptions based on oxide films or competitive adsorption do not appear adequate. We have considered the physical properties of the salts. For example, the activity coefficients at 0.01M are given (5) as

NaCl	0.904
KCl	0.901
LiCl	0.89

These values are not significantly different. The radii of the ions (6) are in the following order

Li ⁺	0.60
Na ⁺	0.95
K ⁺	1.33

This rules out any effect dependent on a trend in size, but not an optimum size for some adsorption process.

The accelerating effect may be related to the reduction of nitrate to nitrite. Nitrite ion is not an inhibitor for aluminum but actually accelerates corrosion. Under conditions comparable to those given in Table II alloy type 7075 exhibits a weight loss in a 0.01N NaCl + 0.01N NaNO₂ of 13.3 mg/cm². This explanation, however, would not account for the cation effect.

We are looking for an explanation of these effects along two lines: The first, potentiostatic experiments to establish the effect of anion ratio on pitting inception time when the alloy is held in the passive range; the second, x-ray and metallographic studies of structural changes in the corrosion product.

Generally, it must be concluded that if these observations are borne out by future experiments we must revise our concept of "anion" effects and include cation effects as well.

Acknowledgment

The authors are pleased to acknowledge the support of the Advanced Research Projects Agency of the Department of Defense, ARPA Order No. 878, under Contract No. N 00014-68-A-0245.

Manuscript submitted May 29, 1970; revised manuscript received ca. July 21, 1970.

Any discussion of this paper will appear in a Discussion Section to be published in the June 1971 JOURNAL.

REFERENCES

1. L. H. Callendar, *Engineering*, **120**, 340 (1925).
2. G. C. Blanchard and C. R. Goucher, *Electrochem. Technol.*, **5**, 79 (1967).
3. V. P. Kassiyura and E. M. Zaretskii, *Zashchita Metallov*, **4**, 376 (1968).
4. H. Böhm and H. H. Uhlig, *This Journal*, **116**, 906 (1969).
5. W. M. Latimer, "Oxidation Potentials," p. 355, Prentice-Hall, Inc., Englewood Cliffs, N. J. (1952).
6. L. Pauling, "The Nature of the Chemical Bond," p. 346, Cornell University Press, Ithaca, N. Y. (1940).

Composite Film Metallizing for Ceramics¹

E. L. Hollar, F. N. Rebarchik, and D. M. Mattox

Sandia Laboratories, Albuquerque, New Mexico 87115

There are two primary approaches to forming a solderable/brazable surface on oxide ceramics: (a) react an oxygen active metal on the surface at high temperatures (active-metal metallizing) (1), or (b) fuse a glass-metal composite to the ceramic surface (dispersion metallizing) (2).

In the active-metal metallizing technique, the oxygen active metal reacts with the oxide surface at high temperatures to form an interfacial complex oxide system which may act as the intermediate bonding agent, as has been suggested for the glass-on-metal system (3-5). Not all of the active metal is allowed to react with the oxide, thus a brazable metal surface remains. In the dispersion-metallizing technique, the glass phase reacts with the ceramic and, by the selection of the correct coefficients of expansion, provides good bonding to the ceramic. The metal phase which is dispersed in the glass then provides the brazable surface. Both of these techniques require high temperatures to allow chemical reaction and diffusion to take place between the metallizing layer and the ceramic surface. These techniques also allow irregular penetration of the metallizing into the ceramic, particularly in the polycrystalline ceramics having a high glass content in the grain boundaries.

In some cases, design restrictions make these metallizing techniques impractical. Some of these cases are: (a) ceramics which cannot withstand high temperatures without decomposition or distortion, (b) thin ceramics where the interfacial region must be kept very thin and carefully controlled, (c) ceramic applications where the irregular penetration of the conventional metallizing imposes problems with dielectric breakdown, and (d) metallizing techniques which are incompatible with other processing.

The usual method of obtaining an adherent coating in these cases is to sputter, or vacuum evaporate, an oxygen active material on the surface and promote substrate-coating reaction by limited heating (6, 7). Without extensive heating the transitional interface region which is formed is limited in extent and the stress distribution across the interface, which is necessary to obtain a good bond (8), is not developed.

We propose that a transitional interface region, conducive to good bonding, may be formed by deposition of an oxygen-active metal in a controlled gaseous environment. In this technique, the deposition of the active metal is begun in a partial pressure of oxygen to allow partial oxidation of the deposited material and thus form a transition oxide and suboxide interfacial region. By decreasing the partial pressure of oxygen during the deposition, the composition of the interfacial region may be "graded" from the substrate material through a metal oxide-metal composite region to the pure metal. It has previously been noted that better adhesion can be obtained with oxygen active materials on glass when there is a poor vacuum (9, 10). Since

the oxygen-active metals are often difficult to braze, a more brazable surface may be formed by the co-deposition of some easily brazed material during the active metal deposition and then grading to the pure brazable metal by gradually decreasing the deposition rate of the active metal.

This investigation was primarily concerned with metallizing fused silica for a high-temperature brazing operation. Fused silica develops large internal strains when other chemical species are diffused into the surface or when recrystallization (devitrification) occurs at high temperature. These strains can crack the fused silica. Therefore, metallizing must be done at moderate temperature with controlled chemical reaction between the metallizing and the fused silica. In addition, the low thermal expansion coefficient of fused silica compared to most glasses and metals causes high stress to be developed in the interfacial region on cooling from high temperatures when conventional metallizing is used. This problem can be averted by using a thin metallizing layer and/or a ductile metal coating.

The choice of materials is dictated by the processing involved. The oxygen-active metal should be insoluble in the braze alloy so that it will not be "scavenged" from the ceramic surface during the brazing operation. In addition, it should not exhibit grain growth at the brazing temperature. The brazable metal should be relatively insoluble in the active metal to prevent excessive diffusion and should not alloy rapidly with the braze material at the brazing temperature.

To prevent scavenging, a refractory material was used in contact with the silica. Of the four refractory metals (niobium, tantalum, tungsten, and molybdenum) investigated, niobium seemed to be the most stable under brazing conditions, and the system niobium-silver with a copper-silver eutectic braze was used. The niobium and silver were deposited in a hot cathode triode sputtering system shown in Fig. 1. The relative sputtering rates were controlled by varying the bias on the sputtering cathodes. The oxygen content in the discharge was controlled using commercial argon-oxygen mixtures and pure argon with valving and a variable leak as shown. The oxygen content in the system was monitored using a differentially pumped mass spectrometer. Recorders were used to monitor the cathode current during deposition.

The sequence of steps in a typical metallizing operation was as follows. The fused quartz substrate was thoroughly cleaned by scrubbing with Alconox until water would wet the entire surface. After multiple rinses in distilled water, the fused silica was etched for 1 min in a 5 v/o (volume per cent) hydrofluoric acid solution and rinsed again. The final pre-cleaning step was air firing at 800°C for 15 min. The cleaned substrate was then placed in the sputtering chamber and the chamber evacuated to 1×10^{-5} Torr. The system was then backfilled with an Ar/5% O₂ mixture to a pressure of approximately 8×10^{-3} Torr while the chamber was continuously pumped. A hot

¹ This work is supported by the U. S. Atomic Energy Commission. Key words: ceramic metallizing, composite films, thin film metallizing, sputter deposition.

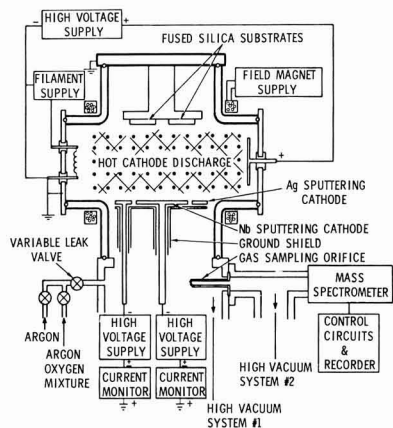


Fig. 1. Hot cathode-dual cathode sputtering apparatus showing disk niobium cathode and concentric ring-shaped silver cathode.

cathode discharge was established, and the substrate was glow-discharge cleaned (11) in the discharge plasma. The sputtering of the niobium was begun by applying a negative 2 kV bias to the niobium sputtering cathode. After a predetermined time necessary to give about 500 Å of oxide, the gas flow was switched to pure argon. As the oxygen in the system was pumped out, the film became more metallic and the deposition was continued until about 1500 Å of niobium were deposited. At this point, the negative bias on the silver sputtering cathode was gradually increased to codeposit silver with the niobium. The bias on the niobium cathode was then gradually decreased until pure silver was being deposited. The silver deposition was continued until a total thickness of about 10,000 Å

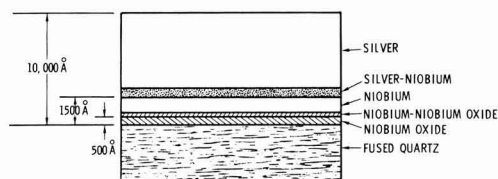


Fig. 2. Schematic of the structure of the composite film metallizing disk showing composition of regions which are graded into each other.

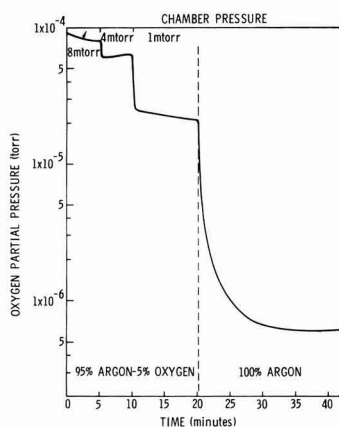


Fig. 3. Oxygen partial pressure during formation of the composite film metallizing.

Table I

Operation	Gas composition and pressure	Sputtering bias	Time (min)
1. Sputter niobium	Ar/5% O ₂ @ 8 mTorr	-2 kV	5
2. Sputter niobium	Ar/5% O ₂ @ 4 mTorr	-2 kV	5
3. Sputter niobium	Ar/5% O ₂ @ 1 mTorr	-2 kV	10
4. Sputter niobium	Pure Ar @ 1 mTorr	-2 kV	30
5. Sputter niobium & Sputter silver	Pure Ar @ 1 mTorr	-1.5 kV (niobium)	5
6. Sputter niobium & Sputter silver	Pure Ar @ 1 mTorr	-0.5 kV (silver)	10
7. Sputter niobium & Sputter silver	Pure Ar @ 1 mTorr	-1.0 kV (silver)	5
8. Sputter silver	Pure Ar @ 1 mTorr	-0.5 kV (niobium)	90

had been deposited. Figure 2 shows the resulting composition of the composite metallized surface.

The times necessary to deposit the various thicknesses of niobium and silver with a given gas composition, discharge conditions, cathode current density, and cathode bias were determined by stopping the deposition at various stages and measuring the film thicknesses with a Talysurf. Table I summarizes the sequence of steps and the times involved. Care was taken to insure that silver from the previous run was cleaned from the niobium cathode. If this is not done, silver will be deposited on the silica surface and a poor bond will be obtained.

Figure 3 shows the oxygen content of the discharge in a typical metallizing operation. Chemical and ion pumping of oxygen by the discharge substantially reduced the oxygen content of the discharge gas in the initial phase of the process. In order to have excess oxygen available during the initial niobium deposition, high gas pressure was required. The gas pressure was then reduced as the discharge electrodes were saturated and as the discharge chemical pumping decreased.

The fused silica surfaces thus metallized were then brazed with a copper-silver eutectic braze. After being subjected to the brazing operation the seals thus formed were vacuum tight, and when tested to failure the joint fractured in the fused silica.

Where a low temperature-high strength bond was desired, the aluminum-silver composite system was used. This system provided surfaces which may be soft soldered and is useful for electroding ferroelectric materials and in joining materials having large differences in coefficient of expansion such as alumina and brass.

Manuscript submitted Mar. 31, 1970; revised manuscript received June 29, 1970.

Any discussion of this paper will appear in a Discussion Section to be published in the June 1971 JOURNAL.

REFERENCES

- W. H. Kohl, "Handbook of Materials and Techniques for Vacuum Devices," p. 451, Reinhold Publishing Corp., New York (1967).
- R. N. Fulrath and E. L. Hollar, *Am. Ceram. Soc. Bull.*, **47**, 493 (1968).
- M. P. Boron and J. A. Pask, *J. Am. Ceram. Soc.*, **49**, 1 (1966).
- R. M. Pillar, T. G. Carruthers, and J. Nutting, *J. Mater. Sci.*, **2**, 28 (1967).
- T. E. Hutchinson and K. H. Olsen, *J. Appl. Phys.*, **38**, 4933 (1967).
- J. L. Vossen, *Electrochem. Technol.*, **3**, 56 (1965).
- J. M. Seeman, *Trans. Vacuum Met. Conf.* 1965, p. 269, L. M. Bianchi, American Vacuum Soc., Boston, Mass. (1966).
- D. M. Mattox, "Interface Formation and the Adhesion of Deposited Thin Films," Sandia Corp. Report, SC-R-65-852 (1965).
- P. Benjamin and C. Weaver, *Proc. Roy. Soc. (London)*, **A252**, 177 (1960).
- P. Benjamin and C. Weaver, *ibid.*, **A261**, 516 (1961).
- L. Holland, "The Properties of Glass Surfaces," p. 290, John Wiley & Sons, New York (1964).



REVIEWS AND NEWS

Physical and Mechanical Properties of Electrodeposited Copper

III. Deposits from Sulfate, Fluoborate, Pyrophosphate, Cyanide, and Amine Baths*

Vernon A. Lamb, Christian E. Johnson, and Donald R. Valentine

National Bureau of Standards, Washington, D. C. 20234

VIII. Comparisons of Deposits from All Types of Baths: Fatigue Strength, Thermal Properties, Cold Working, Structure, Composition, and General Correlations

A. Fatigue Strength

1. *Introduction, method, and apparatus.*—Fatigue strength is of interest primarily in applications in which vibration or other cyclic stressing of plated or electroformed parts may cause fracture. Several studies of the effect of plating on the fatigue strength of a basis metal have been reported, but very little information on fatigue properties of separated deposits has come to our attention [Ref. (2) for nickel, Ref. (21), p. 55, for copper].

The method that we used for measuring fatigue strength was designed by J. A. Bennett of the NBS Metallurgy Division. It is an adaptation of the Amsler "Vibrophone" test method¹⁵ to thin sheet stock (34). Specimens were milled from panel stock to the form shown in Fig. 37. They were then bent into a "U" as shown at "1" in Fig. 38. The bending procedure was as follows. A 3/4 in. diameter rod was placed transversely across the center of the flat specimen, which was supported on a deep (2-3 in.) sponge-rubber pile which acted as a female mandrel. With a small press, the rod and sheet were forced into the sponge-rubber pile. The action of the test machine is illustrated in Fig. 38. The formed specimen was attached to blocks 2 and 3 with screws through clamping plates (not shown). Block 2 was rigidly attached to the frame of the machine. Block 3 oscillated vertically, driven by the force, P . This produced lateral oscillation of the top of the specimen, as indicated by the arrows above "1." Thus, each of the four faces of the specimen was alternately stressed in tension and compression, with maximum stress at the position of minimum width.

The mean load was zero; i.e., the maximum deflections of the specimen to either side of the zero-load position were equal. Oscillation rate was 1800 cycles/min. The maximum load, P , was determined from machine adjustments; lateral displacement of the top of the specimen, illuminated with a stroboscope, was measured with a micrometer microscope. The relationships by means of which stress and strain in the specimen are determined from P and the lateral displacement of the specimen are developed in the Appendix, paragraphs X-B-1 and X-B-2.

2. *Results.*—The fatigue characteristics of several typical kinds of copper deposits are shown in Fig. 39, in which stress amplitude is plotted as a function of the number of cycles required to produce failure by cracking. The character of the curves is typical, similar to those obtained for wrought metals. The pertinent data from these curves are summarized in Table XXVI. Stress-strain parameters for three types of copper representing high and low extremes and a mid-value of

* AES Project 21 Report. Sections VIII-X published here are the third and last installment of this paper. Part 1 (Sections I-III) appears on pages 291C-318C of the September issue, and part 2 (Sections IV-VII) on pages 341C-352C of the October issue.

¹⁵ Alfred J. Amsler & Co., Schaffhouse, Switzerland; Hirschmann Corporation, Roslyn Heights, New York.

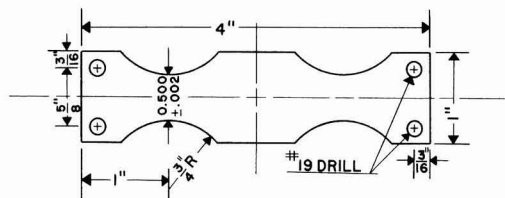


Fig. 37. Dimensions of fatigue specimens. The thickness of the specimens ranged from 0.015 to 0.02 in. (375-500 μ m).

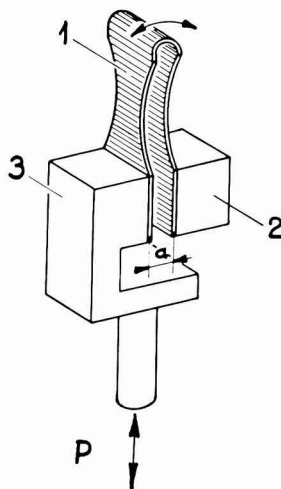


Fig. 38. Schematic representation of the specimen mounting for fatigue testing of electroformed copper. The specimen, 1, is attached to holders, 2 and 3, with screws and clamping plates (not shown). Holder, 2, is rigidly attached to the frame of the machine. Application of the pulsating force, P , causes holder, 3, to oscillate vertically, resulting in lateral oscillation of the specimen as indicated by the curved arrows. The distance "a" is 0.300 in. (7.5 mm).

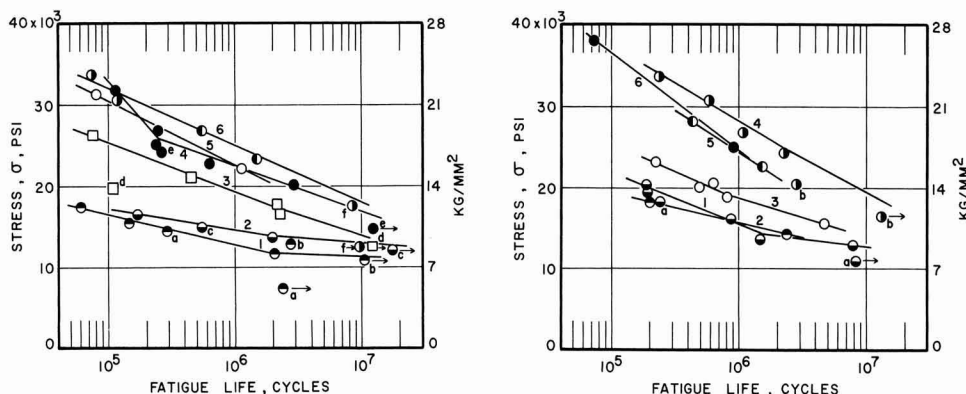


Fig. 39. Relationship between fatigue life (cycles) and stress for electroformed copper. Part A (left): (1) Cu2-H2, mild cellulosic exposure, 30°C, 2 A/dm²; (2) Cu2-H2, severe cellulosic exposure, 30°C, 2 A/dm²; (3) Cu2-H3 containing 1 mg/liter selenium, 30°C, 2 A/dm²; (4) pyrophosphate, 50°C, 2 A/dm²; (5) pyrophosphate, 50°C, 4 A/dm²; (6) Cu2-H3 containing 3.5 g/l triisopropanolamine, 50°C, 5 A/dm². Part B (right): (1) F-1, 30°C, 8 A/dm²; (2) F-2, 50°C, 20 A/dm²; (3) Cu3-H3 containing 1 g/l phenolsulfonic acid, 30°C, 2 A/dm²; (4) CN-8 containing 2 g/l KCNS, 80°C, 6 A/dm², PR, cycle 15 sec cathodic, 5 sec anodic; (5) CN-8 containing 2 g/l KCNS, 80°C, 6 A/dm², PR, cycle 30 sec cathodic, 10 sec anodic; (6) CN-8, 80°C, 6 A/dm², no addition agent, PR, cycle 15 sec cathodic, 5 sec anodic. Specimens that did not fail are indicated by a letter and an arrow. These specimens were tested further with larger loads. The point representing the re-test conditions is designated by the corresponding letter.

fatigue strength are plotted in Fig. 40.¹⁶ The curves for the non-addition agent sulfate deposits and for the pyrophosphate deposits are linear, indicating that in testing these deposits the elastic limit was not exceeded. The small deviation from linearity at the top of the stress range for the deposit from a sulfate bath containing triisopropanolamine has questionable significance.

In Table XXVI, the stress level at failure is shown for two life periods, 10⁶ and 10⁷ cycles. For 10⁶ cycles, two values of stress are shown for lines 76 and 147, designated as σ_c and σ_m . σ_c represents a "calculated" value, obtained from the basic mechanical relationships developed in Appendix B-1. σ_m represents a "measured" value, determined from direct microscope measurements of strain on statically displaced speci-

mens. The procedure is described in Appendix B-2. The magnitudes of the fatigue strength obtained by the two methods are in reasonable agreement.

The value of σ_c will first be considered in relation to the yield strength (Table XXVI). Fatigue failure would be expected to occur rapidly if the yield strength were exceeded. It is seen that several of the deposits were stressed beyond our values for yield strength, but nevertheless had fatigue lives of 10⁶ or 10⁷ cycles. This indicates that the tabulated values of yield strength, which are based on the arbitrarily selected offset of 0.05%, may be too low, or that dynamic yield strengths are higher than static yield strengths. Whatever the explanation, the results show that at the stress levels applied for lives of 10⁶ to 10⁷ cycles, plastic deformation must not have occurred.

It is of interest to intercompare the endurance ratio, i.e., the ratio of the fatigue strength to the tensile strength, for the various plated coppers and for wrought copper. The ratios vary from a low of 0.32 for a PR deposit from bath CN-8 to a high of 0.61 for a deposit from the pyrophosphate bath. Ratios for deposits from the sulfate and fluoborate baths are close

¹⁶ Explanation of stress-strain parameters in Fig. 40: From Eq. [12] of Appendix B-1, it is seen that stress is proportional to P/t^2 since a and b are constants. From Fig. 72 it can be readily shown that $\delta = t/2R$, where δ is the strain in the surface fibers of the specimen. Since R is approximately inversely proportional to the horizontal deflection of the top of the specimen, we have $R = K/D$, where K is the proportionality constant and D the deflection. Substituting this value of R in the preceding equation gives $\delta = tD/2K$. Thus, surface strain is approximately proportional to tD . See Appendix B-1 for definitions of symbols.

Table XXVI. Fatigue characteristics of electrodeposited copper

Line No., Table I	Panel No.	Bath symbol	Addition agent	Bath temp, °C	Current density, A/dm ²	Fatigue strength ^a			Yield ^{a,b} strength, psi	Tensile ^a strength, psi	Endur- ance ratio $\sigma_c/10^6$ T.S.	Inter- nal ^{a,c} stress, psi
						σ_c	σ_m No. of cycles	σ_c				
						10 ⁶	10 ⁶ psi	10 ⁷				
24	13	Cu2-H2	None	30	2	13 × 10 ³		11 × 10 ³	8 × 10 ³	25 × 10 ³	0.54	550
26	323	Cu2-H2	None	30	2	14		12	11	32	0.47	
88	77	Cu3-H3	PSA ^d	30	2	19			13	34	0.58	-420
66	172	Cu2-H3	SeO ₂	30	2	19		14	16	44	0.44	2800
76	337, 341	Cu2-H3	TIPA ^d	30	5	25	31 × 10 ³	18	43	71	0.36	7100
91	345	F-1	None	30	8	16		13	16	37	0.44	700
94	348	F-2	None	50	20	16		12	12	33	0.49	1600
139	281	CN-8	None, PR ^e	80	6	25		38	38	64	0.39	
147	294	CN-8	KCNS, PR ^e	80	6	28	33	20	57	86	0.34	5100
148	295	CN-8	KCNS, PR ^f	80	6	25			46	79	0.32	
95	318	Pyrophos- phate	None	50	2	22		17	20	38	0.61	-1600
98	314	Commercial copper ^g	Annealed	50	4	22			22	40	0.59	1700
			Half hard			15			10	31	0.46	
			Hard			23			18	38	0.51	
						24			48	54	0.44	

^a One pound per square inch (psi) = 0.000704 kilogram per square millimeter (kg/mm²).

^b 0.05% offset.

^c Negative values represent compressive stress.

^d PSA = phenolsulfonic acid; TIPA = triisopropanolamine.

^e PR cycle 15 sec cathodic, 5 sec anodic.

^f PR cycle 30 sec cathodic, 10 sec anodic.

^g Data from Ref. (35).

to 0.5, about the same as the ratios for wrought copper.

With respect to quality of deposits as measured by fatigue strength, deposits from non-addition agent sulfate and fluoborate baths are about the equal of annealed wrought copper, but poorer than cold-worked wrought copper. On the other hand, deposits from the sulfate baths containing addition agents and from the cyanide and pyrophosphate baths are equal or superior in fatigue strength to cold-worked wrought copper.

For a given type of bath, variation of operating conditions did not affect the fatigue strength significantly (Table XXVI). For example, changes in the following variables produced either no change or negligible change: degree of exposure of the sulfate bath to cellulose (lines 24, 26); bath temperature and current density (fluoborate bath, lines 91, 94 and pyrophosphate bath, lines 95, 98); and PR cycle (lines 147, 148).

Residual tensile stress adds to deformation stress to produce a higher total stress, which may be expected to hasten fatigue failure. One might, therefore, expect a relationship between fatigue strength and internal stress (Table XXVI). There are some positive correlations. For example, compare lines 26 and 88. The tensile strength is nearly the same, but the fatigue strength of the latter, with a compressive stress, is significantly higher. On the other hand, two of the highest values of fatigue strength appear in lines 76 and 147, both associated with high internal stress. At first sight this appears to be a reversal of the expected effect. However, we note that these high stress values correlate with the lowest endurance ratios. It is thus probable that, if these deposits were to retain their high strength and also had a low internal stress, the endurance ratio would be in the "normal" range of 0.5 and the fatigue strength would then be about 40,000 instead of 25,000-28,000 psi. The difference is a measure of the reduction due to the high internal stress. The correlation with internal stress fails in the case of the pyrophosphate deposits, where an apparently significant variation in internal stress does not affect the fatigue strength.

Several failed specimens were examined by J. A. Bennett to determine the character of the failure cracks, with the following results:

Panel No.	Structure type	Character of cracks
13	Large columnar, fairly fine starting grain	Cracks started on final (coarse) surface, propagated between dendrites
295	Fine uniform grain	Cracks started on both sides. Grain too fine to evaluate position of cracks with respect to grains at magnification used.
345	Like No. 13, U-bend with final surface outside	Like No. 13, cracks started on outside surface.
345	Same as above, but U-bend with final surface inside	Like No. 13, but cracks started on inside surface, in this case also the coarse surface.

The above results are what one would expect. The comparison between the two specimens from Panel No. 345 shows that the characteristics of the machine and the test procedure were such that inside and outside surfaces of the "U" were equally stressed.

B. Properties of Annealed Deposits

1. *Annealing procedures.*—Specimens were made from panel stock before annealing, i.e., operations such as machining and stripping of nickel were carried out on the as-plated stock. Annealing¹⁷ was done either in vacuum or in an argon atmosphere. Specimens were held at temperature for the times indicated in Table XXVII. They were put into and removed from a cold furnace, so the actual total annealing period was longer than the nominal period. The heat-up and cool-down periods ranged from about 15 min for 150°C to 45 min for 500°C.

Since it was not feasible to procure the extended data shown in Table XXVII for a large number of

¹⁷ Annealing was done in part by G. E. Hicho of the Metallurgy Division, NBS, and in part by the authors.

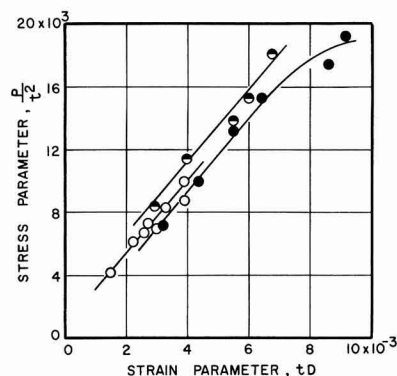


Fig. 40. Relationship between stress and strain at the surface of copper fatigue specimens from three types of baths at the point of minimum width: ○—Cu-2-H₂, 30°C, 2 A/dm²; ●—Cu-2-H₃ containing 3.5 g/l triisopropanolamine, 30°, 5 A/dm²; ●—pyrophosphate, 50°, 2 A/dm². The specimen thickness is represented by "t", the magnitude of the horizontal deflection of the top of the specimen by "D," and the applied load by "P."

copper deposits, a representative sampling was chosen, including typical soft deposits from sulfate and fluoborate baths, deposits of a hard strong type from a sulfate bath containing an addition agent, typical pyrophosphate deposits, and PR deposits from bath CN-8 containing KCNS as an addition agent. The latter was chosen because it has good properties as plated and can be produced as thick electroforms. Limited measurements were also made with thin deposits from other cyanide baths, namely CN-2, a typical low-concentration bath, CN-8 without an addition agent or PR, and CN-9, the proprietary high-efficiency bright-plating bath.

2. *Effects of annealing on mechanical properties.*—Data are summarized in Table XXVII and in Fig. 41, 42, and 43. In Fig. 41, it is seen that in general annealing caused decrease of tensile strength and increase of ductility. However, the changes are small for deposits that are initially soft and ductile, namely those from the non-addition agent sulfate bath, the fluoborate bath, and the pyrophosphate bath. The deposit from the sulfate bath containing triisopropanolamine resists change to a fairly high annealing temperature (325°-400°C), then abruptly loses strength and gains ductility. The PR cyanide deposit, on the other hand, undergoes significant changes in the same directions at the lowest annealing temperature of 150°C. The tensile strength and elongation of all of the deposits tend to the same values after annealing at 500°-550°C.

Effects of both annealing and cold rolling on modulus and hardness are illustrated in Fig. 42 and 43. In general, cold rolling has less effect on modulus than does annealing. The magnitude of the shifts due to cold rolling is within our estimated accuracy of $\pm 1 \times 10^6$ psi and the direction is random. On the other hand, annealing at 500°C causes a significant decrease of modulus in all but one case (PR deposit from bath CN-8).

The effect of annealing on hardness (Fig. 43) is similar to its effect on tensile strength. The deposits that are initially soft or fairly soft (non-addition agent sulfate, fluoborate, and pyrophosphate) undergo minor additional softening. The deposits from the triisopropanolamine sulfate bath (TIPA) and the PR CN-8 bath undergo marked reduction of hardness. The abnormally low hardness, 32 KHN, of the TIPA deposit is an "apparent" value due to an "exploded structure" of the deposit resulting from heating to 500°C. This has other related effects that are referred to subsequently.

Cold rolling in all cases causes a significant increase of hardness.

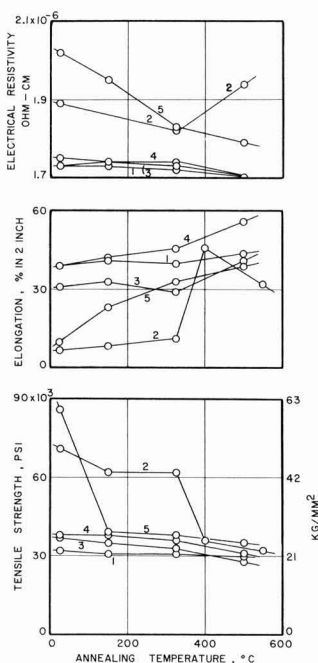


Fig. 41. Relationships between annealing temperature and tensile strength, elongation, and electrical resistivity of copper deposits from various baths: (1) Cu2-H2, 30°C, 2 A/dm²; (2) Cu2-H3 containing 3.5 g/l triisopropanolamine, 30°C, 5 A/dm²; (3) F-1, 30°C, 8 A/dm²; (4) pyrophosphate, 50°C, 2 A/dm²; (5) CN-8 containing 2 g/l KCNS, 80°C, 6 A/dm², PR, cycle 15 sec cathodic, 5 sec anodic.

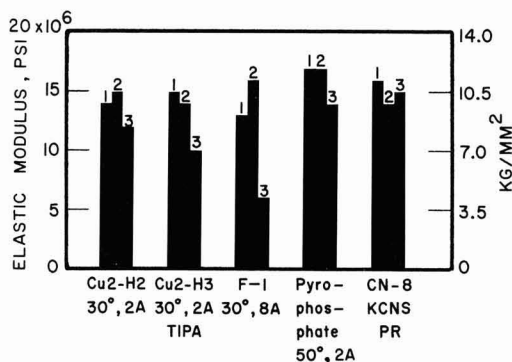


Fig. 42. Effect of cold rolling and annealing on modulus of elasticity of copper deposits from various types of baths: 1—deposits as plated; 2—deposits cold rolled, 50% reduction; 3—deposits annealed at 500°C for 15 min.

Yield strength decreases with annealing for all of the deposits, reaching the extremely low value of 3000 psi for the fluoborate deposit annealed at 500°C (Table XXVII).

3. *Effect of annealing on density.*—Since the effects of annealing on density were in general small, data were obtained only for deposits annealed at 500°C. The results are compared with as-deposited values in Table XXVII. No measurable effect was found except for the TIPA deposit. It underwent a very large decrease of density, 18%, due to "explosion" and formation of interior voids. (The effect of the same

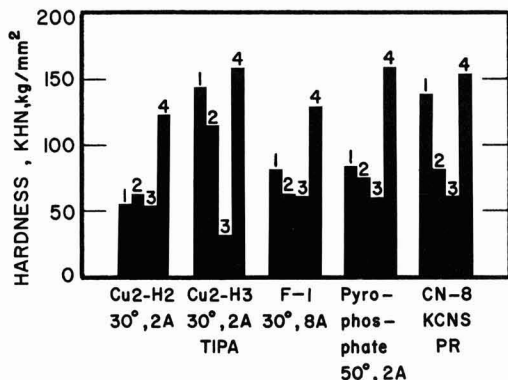


Fig. 43. Effect of annealing and cold rolling on hardness of copper deposits from various types of bath: 1—deposits as plated; 2—deposits annealed at 325°C for 15 min; 3—deposits annealed at 500°C for 15 min; 4—deposits cold rolled, 50% reduction.

phenomenon on hardness was described above in Section VIII-B-2.) The voids are shown in Fig. 45-3.

4. *Effect of annealing on electrical resistivity.*—Effect of annealing on electrical resistivity is shown in Fig. 41. As in the cases of the other properties already discussed, the deposits that are soft and have low resistivity as plated undergo little change, although their resistivity does decrease slightly. The anomalous behavior of the TIPA deposit is seen again. Its resistivity is high as plated and undergoes significant decrease after annealing at 325°C. However, after annealing at 500°C, its resistivity increases. Our interpretation is that, after heating at 325°C, the deposit still has a normal structure, with grain growth that correlates with the lower resistivity. After heating at 500°C, void formation has occurred which causes the true cross section of the deposit to be less than the nominal cross section, hence, the resistivity increases. The PR deposit from the CN-8 bath undergoes a marked regular decrease of resistivity as the annealing temperature is increased, but even after heating at 500°C its resistivity is higher than that of high-purity copper.

5. *Effect of annealing on the structure of various deposits.*—a. *A deposit from a non-addition agent sulfate bath.*—In Fig. 44 are shown the structures of specimens from panel No. 322-323 (Table XXVII, line 26), as plated, annealed at 325°C, and annealed at 500°C. At 325°C recrystallization and grain growth have involved mainly the originally fine-grained basal portion of the deposit. After annealing at 500°C, complete recrystallization has occurred, with large grains extending through the entire thickness of the deposit. The columnar character of the structure is retained.

It was seen in the preceding Sections VIII-B-2, 3, and 4, that properties of this type of deposit varied but little as a result of annealing. The change of structure is sufficient that a somewhat larger effect on properties might have been predicted.

b. *A deposit from a sulfate bath containing an addition agent.*—In Fig. 45 are shown the structures of an as-plated deposit from a sulfate bath containing 2 g/l of triisopropanolamine, the same deposit after annealing at 500°C, and a deposit from a bath containing 3.5 g/l of the addition agent after annealing at 500°C. The deposit from the bath containing the low concentration of addition agent has equiaxed grains of medium size after annealing, whereas the deposit from the bath containing the high concentration of addition agent contains many voids (black areas). This condition is discussed in detail in subsequent Section VIII-E-2. It causes the abnormally low hardness and density already described.

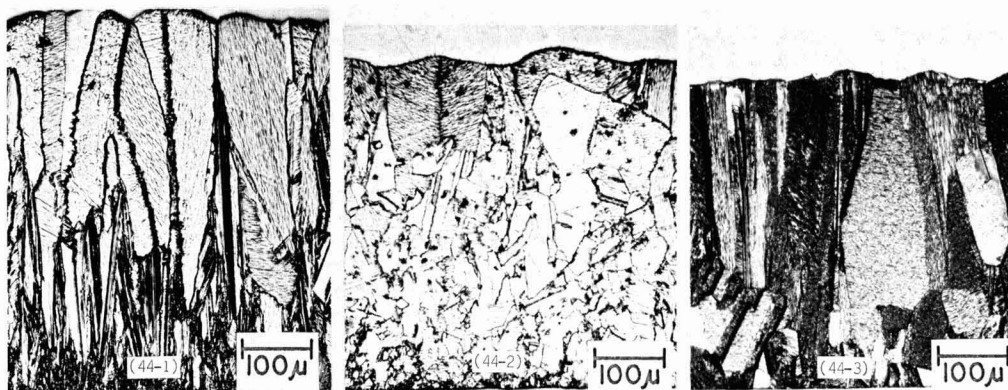


Fig. 44. Effect of annealing on structure of a copper deposit that is coarse grained as plated; from sulfate bath Cu2-H2, 30°C, 2 A/dm²: (44-1) as plated; (44-2) annealed 15 min at 325°C; (44-3) annealed 15 min at 500°C.

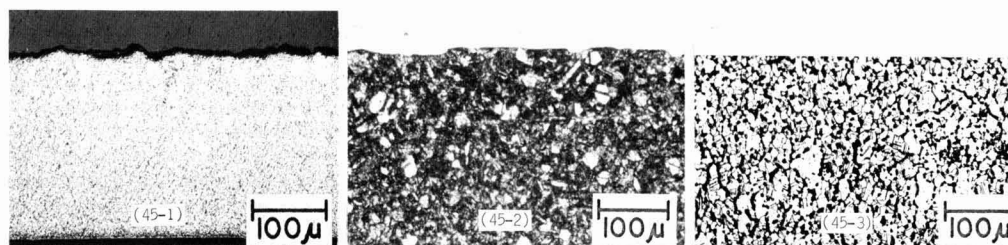


Fig. 45. Effect of annealing on structure of copper deposits that are fine grained as plated. Deposits made in a Cu2-H3 bath containing triisopropanolamine (TIPA), 30°C, 5 A/dm². Note voids caused by gas-forming impurities entrapped in the deposit from the high-TIPA bath. (45-1) 2 g/l TIPA, as-plated deposit; (45-2) 2 g/l TIPA, deposit annealed 15 min at 500°C; (45-3) 3.5 g/l TIPA, deposit annealed 15 min at 500°C.

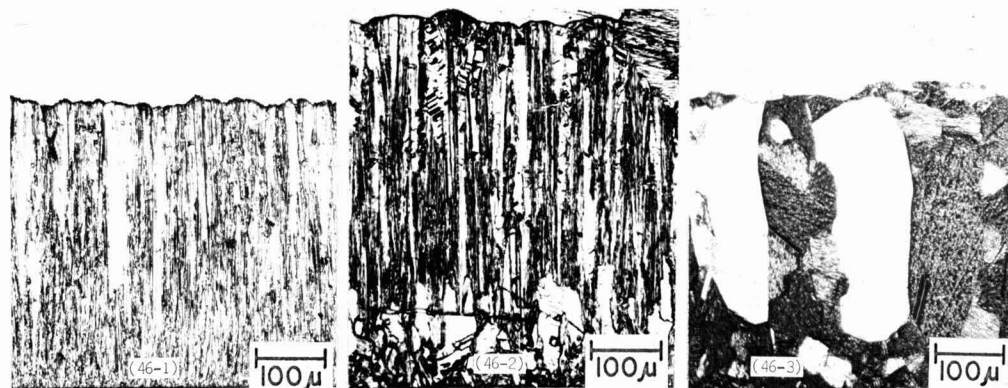


Fig. 46. Effect of annealing on structure of a copper deposit from fluoborate bath F-1, 30°C, 8 A/dm²: (46-1) as plated; (46-2) annealed 15 min at 325°C; (46-3) annealed 15 min at 500°C.

In Table XXVII we see that the hardness of the deposit shown in Fig. 45-2 is normal (footnote^a), which correlates with the absence of voids.

c. *A deposit from the fluoborate bath.*—The effect of annealing on the structure of a deposit from a fluoborate bath is shown in Fig. 46. The character of the changes is so similar to those for the non-addition agent sulfate deposit discussed above in paragraph "a" that the same remarks apply. However, there is a larger difference in grain size before and after annealing at 500°C, which correlates with a somewhat

larger effect on properties than occurred in the case of the sulfate deposit.

d. *A deposit from the pyrophosphate bath.*—The effect of annealing of a deposit from a pyrophosphate bath is shown in Fig. 47. There is scarcely any effect at 150°C (47-2) and only a small effect at 325°C (47-3). However, the specimen annealed at 500°C shows marked grain growth. The same specimen at a higher magnification (500X) is shown in Fig. 47-5. Large columnar grains with a fine substructure are seen. The magnitude of the properties and the relatively small

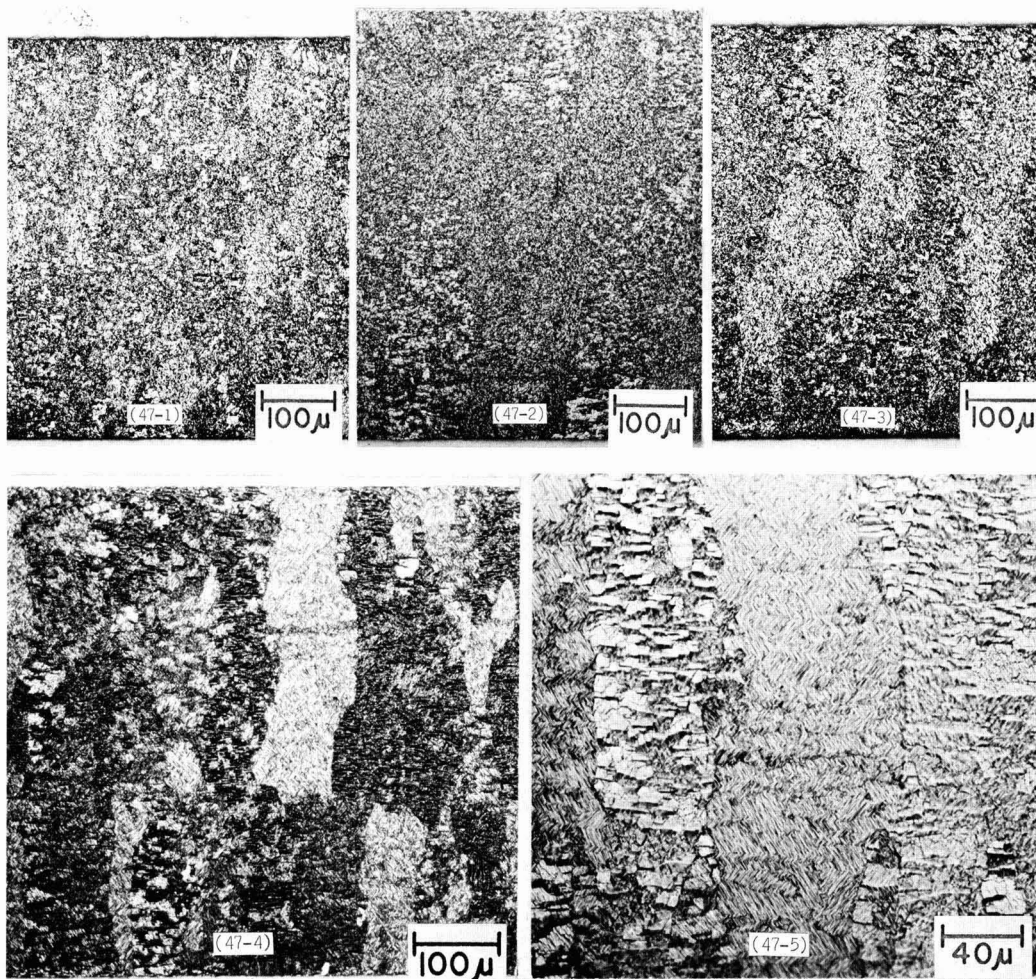


Fig. 47. Effect of annealing on structure of a copper deposit from the pyrophosphate bath, 50°C, 2 A/dm²: (47-1) as plated; (47-2) annealed 2 hr at 150°C; (47-3) annealed 15 min at 325°C; (47-4) and (47-5) annealed 15 min at 500°C.

degree of change on annealing, in comparison with the TIPA and the CN-8 deposits (Section VIII-B-2, 3, 4; Table XXVII), indicate that possibly fairly large grains as seen in Fig. 47-5 are present in the unannealed deposit and that annealing delineates the boundaries.

e. A deposit from cyanide bath CN-8, made with periodically reversed current.—The effect of annealing on the structure of a deposit made with PR in bath CN-8 is shown in Fig. 48. Annealing at 325°C (48-2) has resulted in the loss of the fibrous character of the as-plated deposit, but no distinct grains can be seen. After annealing at 500°C, fairly large equiaxed grains appear. The black spots are apparently an etch effect and do not represent voids, since the density did not change with annealing (Table XXVII, line 143). The marked changes of properties of this deposit due to annealing, seen in Table XXVII and discussed in Sections VIII-B-2, 3, and 4, correlate with the large increase of grain size.

C. Properties of Cold-Rolled Deposits

1. *Cold-rolling procedures.*—Cold rolling was done with a small hand mill. Strips of panel stock 1 in. wide, with the nickel flash removed, were rolled to 50% and 10% of their original thickness. Rolling to 10% (90%

reduction) was done primarily to determine whether the deposits were sufficiently malleable to permit such drastic reduction. All of the deposits in Table XXVII did submit to this treatment, without annealing and with no edge-cracking apparent to the naked eye. However, reductions were not carried out in one pass. About three passes were used for 50% reduction, with additional fine-adjustment passes to obtain the exact thickness desired and to straighten the strips. Specimens for measurements of properties were cut from the reduced strips.

2. *Effects of cold rolling on several properties and on structure.*—*a. Mechanical properties.*—Results are shown in Table XXVII and Fig. 49. Division of deposits into the same type-groups that occurred with annealed deposits is noted for cold working. Thus, the soft as-plated sulfate, fluoborate, and pyrophosphate deposits undergo significant strengthening and embrittlement due to cold reduction (Fig. 49). The initially strong deposits from the sulfate TIPA bath and the CN-8 bath with PR are only slightly affected.

The effects of cold reduction on yield strength are closely parallel to the effects on tensile strength. All deposits acquire a yield strength in the range of 45,000-50,000 psi after 50% reduction, essentially the

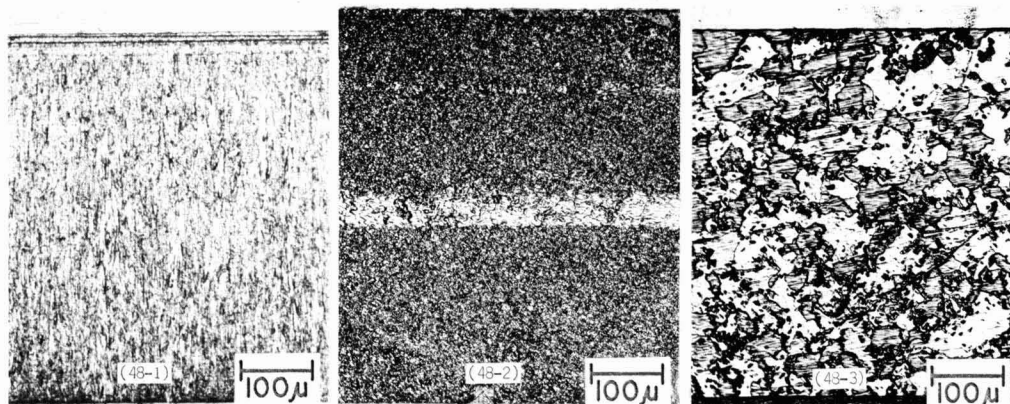


Fig. 48. Effect of annealing on structure of a copper deposit from cyanide bath CN-8 containing 2 g/l KCN, 80°C, 6 A/dm², PR, 15 sec cathodic, 5 sec anodic: (48-1) as plated; (48-2) annealed 15 min at 325°C; (48-3) annealed 15 min at 500°C.

same as that of similar wrought copper (48,000 psi).¹⁸

The effects of cold rolling on modulus and hardness were already discussed above (Section VIII-B-2, Fig. 42 and 43).

b. Density.—Only one determination of the effect of cold rolling on density was made (Table XXVII, line

¹⁸ The values in Table XXVII from the literature for cold reduced wrought copper that have no temper designation are for material that has been cold reduced 50%. Temper designation for degree of reduction is *extra hard*. The values included for half-hard materials (21% cold reduction) are for comparative purposes. For example, the material cold reduced 50% is appreciably stronger than that reduced 21%, or half hard, namely, 54,000 and 45,000 psi, respectively. Magnitudes of effects on yield strength, elongation, and hardness also depend on degree of cold reduction.

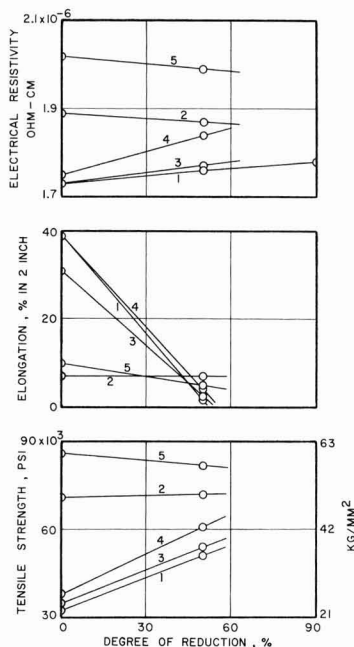


Fig. 49. Relationships between the degree of reduction by cold rolling and tensile strength, elongation, and electrical resistivity of copper deposits from various types of baths: (1) Cu₂-H₂, 30°C, 2 A/dm²; (2) Cu₂-H₃ containing 3.5 g/l triisopropanolamine, 30°C, 5 A/dm²; (3) F-1, 30°C, 8 A/dm²; (4) pyrophosphate, 50°C, 2 A/dm²; (5) CN-8 containing 2 g/l KCN, 80°C, 6 A/dm², PR, cycle 15 sec cathodic, 5 sec anodic.

26). The decrease of 0.001 g/cm³ for a soft sulfate deposit is not a significant change. Data from the literature for wrought copper (Table XXVII, last line) indicate that cold working causes a small decrease of density.

c. Electrical resistivity.—Resistivity is increased by cold rolling of the three soft-type deposits (Fig. 49). The resistivity of the soft sulfate deposit (Table XXVII, line 26) is slightly higher after 90% reduction than after 50% reduction. The hard deposits (TIPA and CN-8, PR) undergo a small decrease of resistivity with cold rolling. However, the change is of borderline significance. The small effect is what might be expected of deposits that have very fine grain and high resistivity as plated.

d. Structure.—The effects of cold rolling on structure are shown in Fig. 50-54, inclusive, for the five types of deposits appearing in Table XXVII. The soft sulfate and fluoborate deposits (Fig. 50 and 52, respectively) show elongation of grains in the direction of rolling, and irregular crumpling of columnar grains, but little reduction of grain size.

In general appearance, the effects of cold rolling on the deposit from sulfate TIPA bath, the pyrophosphate bath, and the CN-8 bath with PR are similar (Fig. 51, 53, and 54, respectively). The cold-rolled specimens in Fig. 51 and 53 show a hint of conversion from a perpendicular to a longitudinal fiber, and Fig. 54 shows a conversion from a perpendicular fiber to an equiaxed, slightly finer structure. It will be noted that the reduced specimens are not exactly half the thickness of the as-plated specimens. This is because the two were made from different but duplicate panels which were not identical in thickness.

D. Tensile Strength and Elongation of Deposits at Low and High Ambient Temperatures

1. Methods of measurement. Tensile strength and elongation were measured by the tensile pull method. Specimens were pulled with the same test machine that was used for measurements of modulus (Section III-A-1). Three temperatures were used, -78°, 150°, and 325°C. The specimens pulled at 150°C were preannealed at 150°C for 1 hr to avoid the necessity of holding them for this period at 150°C in the test machine before pulling. The specimens pulled at 325°C were held at this temperature in the test machine for 15 min before pulling. Specimens pulled at -78°C were pulled immediately with no hold at temperature. To provide the various ambient temperatures, a lightweight aluminum can was attached to the lower specimen grip and extended upward to sufficient height to enclose the specimen and the upper grip. The inside

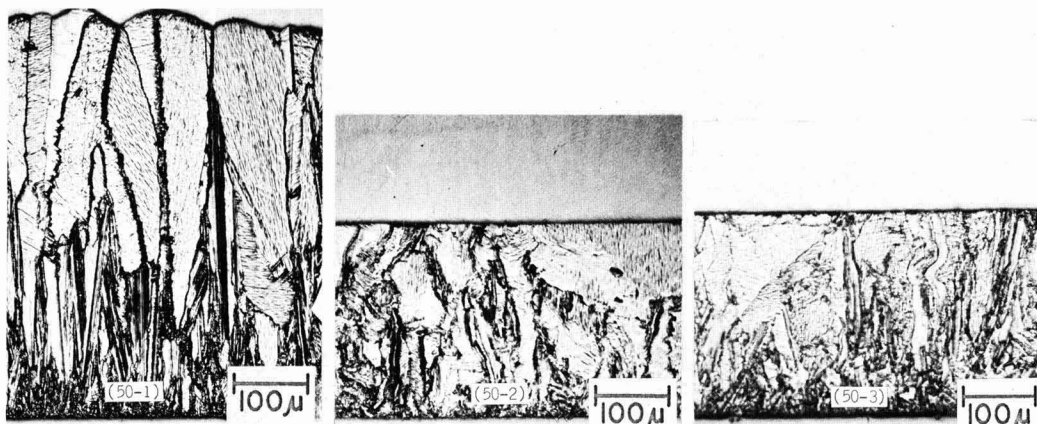


Fig. 50. Effect of cold rolling on structure of a large-grained type of deposit from copper sulfate bath $\text{Cu}_2\text{-H}_2$, 30°C , 2 A/dm^2 : (50-1) as plated; (50-2) 50% reduction, cross section parallel to direction of rolling; (50-3) 50% reduction, cross section normal to direction of rolling.

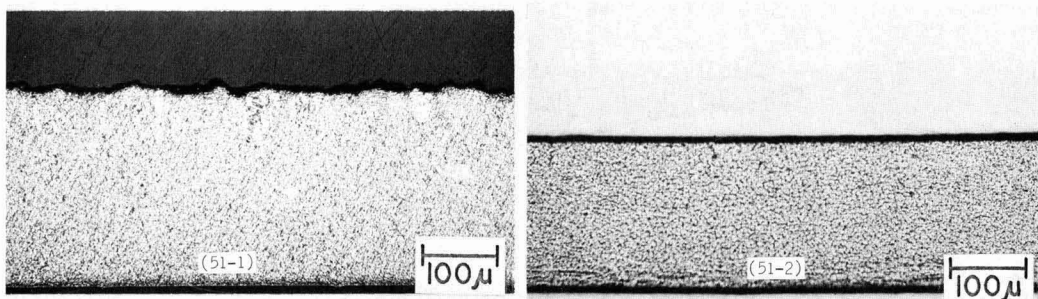


Fig. 51. Effect of cold rolling on structure of a fine-grained copper deposit from sulfate bath $\text{Cu}_2\text{-H}_3$ containing 2 g/l triisopropanolamine, 30°C , 5 A/dm^2 : (51-1) as plated; (51-2) 50% reduction, cross section parallel to direction of rolling.

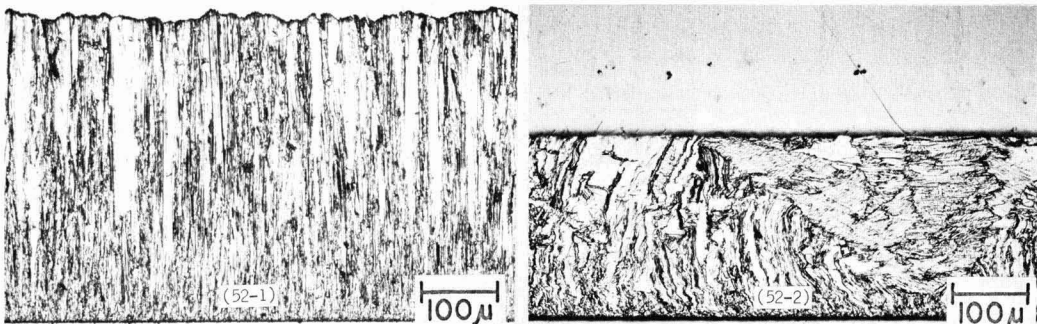


Fig. 52. Effect of cold rolling on structure of a deposit from fluoborate bath F-1 , 30°C , 8 A/dm^2 : (52-1) as plated; (52-2) 50% reduction, cross section parallel to direction of rolling.

diameter of the can was 2 in. A Nichrome winding and thermal insulation surrounded the can. Controlled current through the winding provided the elevated temperatures. Tubes with an outside diameter of $\frac{1}{4}$ in. were welded to the lower and upper ends of the can to provide inlet and exit, respectively, for argon, to provide a nonoxidizing atmosphere. A thermocouple close to the center of the tensile specimen was used to measure its temperature, which was maintained constant to $\pm 1^\circ\text{C}$. Prior determination of vertical temperature gradient within the can showed that vertical variation over the active length of the deposit was not more than 2°C . For pulling at -78°C , the can was filled with a cryogenic mixture of solid carbon dioxide and absolute alcohol.

2. *Effects of low and high ambient temperatures on tensile strength and elongation.*—The data on tensile strength and elongation at the ambient temperatures listed in Table XXVII are plotted in full in Fig. 55. Several relationships of interest may be seen. Tensile strength of all deposits increases as ambient temperature decreases from 325° to -78°C . The one exception in the case of the deposit from the CN-8 bath, between 25° and -78°C , is probably not significant, because the difference between 80,000 and 86,000 psi is within our normal accuracy range of $\pm 5\%$. The same type-grouping of deposits occurs as was seen above in Sections VIII-B and C. The soft sulfate, fluoborate, and pyrophosphate deposits remain close together in strength with parallel decreases with increase in tem-

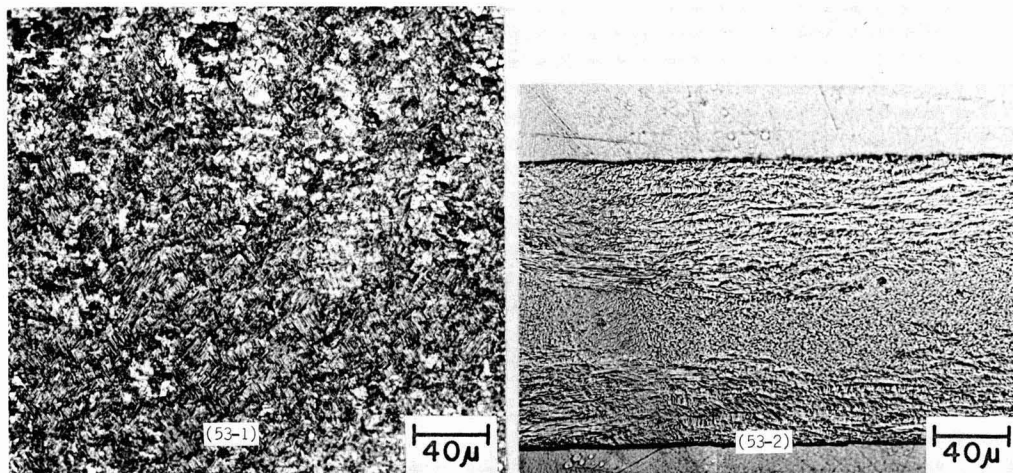


Fig. 53. Effect of cold rolling on structure of a copper deposit from a pyrophosphate bath, 50°C, 2 A/dm²: (53-1) as plated; (53-2) 50% reduction, cross section parallel to direction of rolling.

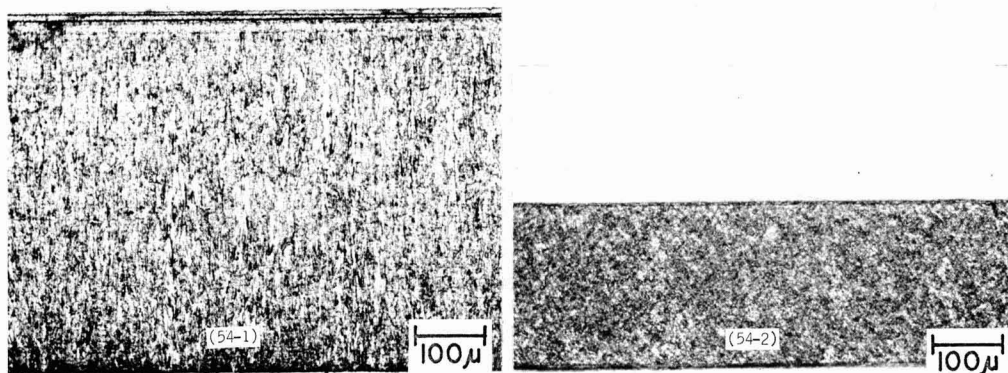


Fig. 54. Effect of cold rolling on structure of a copper deposit from cyanide bath CN-8 containing 2 g/l KCN, 80°C, 6 A/dm², PR, 15 sec cathodic, 5 sec anodic: (54-1) as plated; (54-2) 50% reduction, cross section parallel to direction of rolling.

perature. The deposits of the other group (TIPA; CN-8, PR) have higher strengths at room temperature, but lose strength more rapidly with increase of temperature; thus, deposits of both groups approach the same strength at 325°C. The CN-8 deposit, with a strength of 20,000 psi at 325°C, remains slightly stronger than the other deposits at this temperature.

The relationship between tensile strength and elongation of deposits tested at ambient elevated temperatures is opposite to that for deposits that are annealed and then tested at room temperature. In the first case, both tensile strength and elongation decrease with increase of ambient temperature. In the second case, annealing causes tensile strength to decrease, but elongation to increase, with increase of annealing temperature. The same relationships have been reported for wrought copper (35).

The type-grouping referred to above is seen again with respect to elongation. Except for two partial aberrations, ductility for both groups decreases with increase of ambient temperature. However, the soft-type deposits, which at low temperature have markedly higher ductility, decrease in ductility more rapidly with increase of temperature so that, at 325°C, all but the pyrophosphate deposit have very low and nearly equal elongation (Fig. 55).

The deviation of the elongation of the pyrophosphate deposit from the main pattern is large enough that it is

probably real and indicates that a difference in structure or a difference in rate of annealing exists that accounts for its significantly higher ductility at 325°C.

E. Thermal Expansivity

1. *Introduction and method of measurement.*—Knowledge of thermal expansivity may be needed in cases where distortion might occur due to differential expansion of coating and basis metal or of electroformed assemblies made of more than one kind of metal. Cracking due to differential thermal forces, which may occur with chromium or brittle nickel deposits, is not likely in the case of copper deposits. We know of no published data on thermal expansivity of as-plated copper (3).

Specimens were made from sheet panel stock cut into pieces $\frac{3}{4}$ in. x 6 in. These were made into 6 in.-long tubes, $\frac{1}{4}$ in. diameter, by forming over a mandrel. Several small holes were drilled adjacent to each long edge of the sheet before forming. A lacing of fine copper wire through these holes, inserted after forming, bound the edges together and prevented deformation of the tube during heating.

To measure thermal expansivity, we used an apparatus of fused quartz described by Hidnert and Souder (36). Length changes were measured with a dial gauge accurate to 0.1 mil. It was calibrated against a standard gauge block. An inert atmosphere was

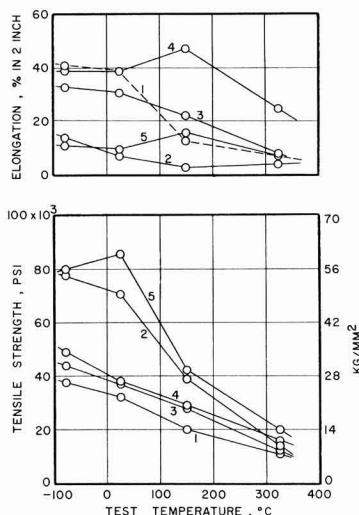


Fig. 55. Relationships between actual test temperature at which properties were measured and tensile strength and elongation of copper deposits from various types of baths: (1) Cu₂-H₂, 30°C, 2 A/dm²; (2) Cu₂-H₃ containing 3.5 g/l triisopropanolamine, 30°C, 5 A/dm²; (3) F-1, 30°C, 8 A/dm²; (4) pyrophosphate, 50°C, 2 A/dm²; (5) CN-8 containing 2 g/l KCNS, 80°C, 6 A/dm², PR, cycle 15 sec cathodic, 5 sec anodic.

maintained in the specimen container while it was heated. Calibrated thermocouples were located near each end and at the center of the specimen. End-to-end temperature variation was not more than 2°C and average temperature of a specimen over its length

was known to within less than 1°C. Measurements were made at two temperatures, 200° and 400°C. Measurements were made during both heating and cooling portions of the cycle, and several of the specimens were measured through more than one cycle.

We estimate the accuracy of our measured expansivities to be $\pm 1\%$, equivalent conservatively to an uncertainty in the coefficient of expansion of $\pm 0.2 \times 10^{-6}$ parts per unit length per °C.

As described below, the deposit from the sulfate TIPA bath underwent a large permanent expansion as a result of heating. We, therefore, decided that a limited study of the expansivity characteristics of other deposits from addition agent baths, the amine bath, etc., should be made, to determine whether permanent changes in length occur due to heating. For these limited measurements, specimens were flat strips, $\frac{1}{4}$ in. x 6 in. Their as-plated lengths were measured accurately, after which they were heated at 500°C for 15 min. After cooling to room temperature, their lengths were again measured.

2. Measured values of thermal expansivity.—The types of deposits selected for expansivity measurements are the same as were used for annealing, cold rolling, etc. Complete expansivity data for these deposits are given in Table XXVIII. Hysteresis curves are shown in Fig. 56, 57, and 58.

The expansivity of the soft deposit from the sulfate bath (Table XXVIII, line 26) is seen to be nearly identical with the values obtained by us for cold-rolled commercial sheet and with the values reported in the literature for high-purity electrolytic copper, melted, cast, and cold drawn (37). There is indication that the expansivity of this deposit is slightly higher on first heating after annealing at 500°C, but it reverts to the "normal" value on second heating.

The expansivities of the fluoborate, pyrophosphate, and CN-8 deposits are about 2% less than that of the sulfate deposit.

Table XXVIII. Coefficients of linear thermal expansion of electrodeposited copper

Line No., Table I	Panel No.	Bath symbol	Addition agent or other variable		Bath temp, °C	Current density, A/dm ²	Condition of specimen	Test cycle	Average coefficient		Permanent change in specimen length after heating in. in 6 in.
			Name	Conc. g/l					× 10 ⁻⁶ = parts per unit length per °C		
									20°-200°C	20°-400°C	
26	324	Cu2-H2	None		30	2	As plated	1st heating	17.1	17.8	
								1st cooling	16.7		—0.0001
								2nd heating	17.1	18.0	
								2nd cooling	17.0		0.0000
							Annealed at 500°C	After 500° anneal			0.001
							1 hr	1st heating	17.4	18.3	
								1st cooling	17.6		0.0000
								2nd heating	17.1	18.0	
								2nd cooling	17.0		0.0000
—	224	Cu2-H3	TIPA ^a	2 ^b	30	5	Preheated to 470°C	1st heating	17.0	18.0	
								1st cooling	17.0		0.0000
76	339	Cu2-H3	TIPA	3.5	30	5	As plated	1st heating	18.9	25.8 ^c	0.003
								1st cooling	34.9		0.02
								2nd heating	18.1	27.3 ^c	
							Annealed at 550°C	After 550° anneal			0.14
							1 hr	1st heating	18.7	19.0	
								1st cooling	17.6		0.0000
91	343	F-1	None		30	8	As plated	1st heating	16.7	17.6	
								1st cooling	16.2		0.0000
95	320	Pyrophosphate			50	2	As plated	1st heating	16.7	17.5	
								1st cooling	15.9		—0.001
								2nd heating	16.9	17.1	
								2nd cooling	16.8		—0.0003
143	293	CN-8	KCNS	2	80	6	As plated	1st heating	16.6	17.1	
			PR cycle, 15-5 seconds					1st cooling	15.0		—0.002
143	296	CN-8	KCNS	2	80	6	As plated	1st heating	16.7	16.7	
			PR cycle, 15-5 seconds					1st cooling	14.1		—0.003
		Cold-rolled sheet—half hard						1st heating	17.3 ^d	18.1 ^d	
		From P. Hidnert and H. S. Kri-der, J. Res. NBS, 39, 419 (1947).						1st cooling	17.0 ^d		—0.0001
									17.3	20°-300°C 17.7	

^a TIPA = triisopropanolamine.

^b Estimated concentration.

^c Due to the large absolute expansion it was necessary to limit the temperature in these two cases to about 325°C to avoid exceeding the limit of our gauge. This effect and the large permanent elongation is caused by formation of voids. See Fig. 45-3 and corresponding value for density, Table XXVII.

^d Values measured by authors of present research.

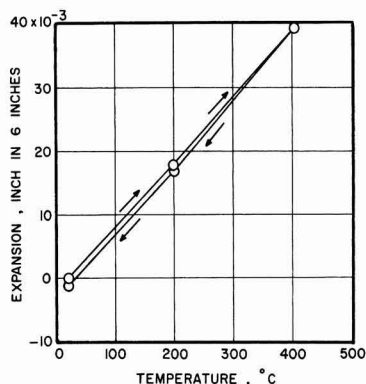


Fig. 56. Thermal expansion of a copper deposit from a pyrophosphate bath, 50°C, 2 A/dm². Curve shows first heating and cooling cycle. Hysteresis effect was much smaller on second cycle (not plotted). Specimen length, 6 in.

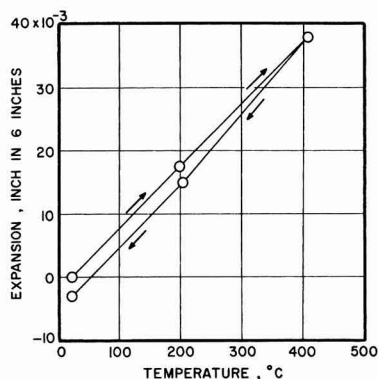


Fig. 57. Thermal expansion of a copper deposit from cyanide bath CN-8 containing 2 g/l KCN, 80°C, 6 A/dm², PR, cycle 15 sec cathodic, 5 sec anodic. Curve shows first heating and cooling cycle. Specimen length, 6 in.

The expansivities of the deposits from the sulfate TIPA bath were quite irregular. The irregular behavior of these deposits was first noted when a large permanent expansion of a specimen from panel No. 224 caused loss of data because the range of our micrometer dial gauge was exceeded. The bath from which this deposit was made contained approximately 2 g/l TIPA, whereas the bath from which panel No. 339 was made contained 3.5 g/l. It is seen that the specimen from panel No. 224 had normal expansivity after heating to 470°C, but still underwent an additional small permanent expansion. A specimen from panel No. 339 yielded very high expansivities and underwent large permanent expansion. Annealing at 550°C stabilized the specimen so that no further permanent expansion occurred, but the expansivity is about 5% higher than for the other deposits. Figure 58 shows expansion curves for two cycles for the deposit from the sulfate TIPA bath. The first cycle shows the large permanent expansion. This behavior is undoubtedly due to incorporation of addition agent or other gas-generating impurities into the deposit during plating. Gas generation on heating expands the deposit (Fig. 45-3) and causes decrease of density, hardness, and strength as noted in previous sections. The expansivity specimen from panel No. 339, after final heating, was distorted, brittle, and friable.

The pyrophosphate and cyanide deposits, which had low expansivities, underwent small permanent con-

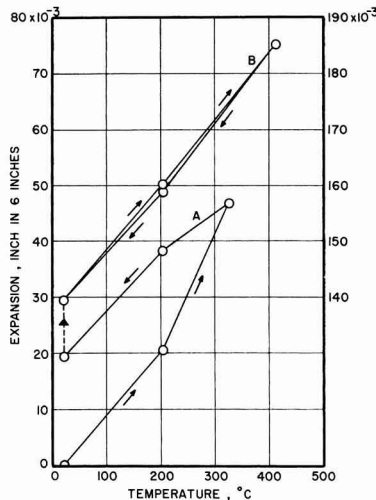


Fig. 58. Thermal expansion of a copper deposit from sulfate bath Cu₂-H₃ containing 3.5 g/l triisopropanolamine, 30°C, 5 A/dm². Curve A shows first heating and cooling cycle—use scale on left. Curve B shows third cycle after specimen was annealed at 550°C for 1 hr—use scale on right. Permanent expansion of 0.12 in. occurred between heatings represented by curves A and B. Specimen length, 6 in.

tractions. The contraction and the low expansivity are undoubtedly related. The pyrophosphate deposit on second heating had nearly normal expansivity. Expansion curves for these deposits are shown in Fig. 56 and 57. They show the small hysteresis effect associated with the slightly smaller expansivity always noted on the cooling cycle. The effect is larger for the CN-8 deposit (Fig. 57) than for the pyrophosphate deposit (Fig. 56).

3. Qualitative tests of thermal expansion.—The results of the qualitative tests described above in Section VIII-E-1 are tabulated in Table XXIX. The amine deposit undergoes significant permanent expansion, but only about 1/15 that of the TIPA deposit (Table XXVIII). The proprietary bright sulfate deposit undergoes about 50% more permanent elongation than the TIPA deposit and is quite brittle after heating. The deposit from the sulfate bath containing 0.1 g/l gelatin is the only other deposit that underwent marked permanent expansion. It was very brittle, but this was also its condition before heating. None of the deposits in Table XXIX showed distortion of shape except the amine deposit, which was severely blistered.

It is probable that the deposits in Table XXIX that undergo only a small permanent expansion have thermal expansivities very close to the value for the deposit in Table XXVIII, line 26.

F. Structure of Deposits

1. Optical micrographs.—Structure in relation to various parameters has already been illustrated with many optical micrographs in preceding figures. In this section we restrict the consideration of optically determined structure to comparisons between typical deposits from various types of baths (Fig. 59).

In Fig. 59-1 and 59-2, deposits from non-addition agent sulfate and fluoborate baths are compared. The concentration of copper was the same in each bath, and operating conditions (bath temperature, current density, and cellulose filter) were the same for each deposit. The finer, more fibrous structure of the deposit from the fluoborate bath must, therefore, be ascribed to some unique effect of the fluoborate anion. The finer

Table XXIX. Effect of heating on dimensions and ductility of a variety of copper deposits
Deposits held 15 min at 500°C

Line No., Table I	Panel No.	Bath symbol	Operating conditions		Addition agent		Increase in length ^a % = $\frac{(l_{500.25} - l_{25})}{l_{25}} \times 100$	Ductility ^d After heating No. of bends
			Bath temp, °C	C.D., A/dm ²	Name	Conc., g/l		
150	329	Amine	55	2	None		0.16 ^b	<1
79	306	Cu2-H3	30	4	None	PR, 5-2 sec	0.00	3
77	226	—	22	4	Prop. A ^c	—	3.6	<1
43	5-4	Cu2-H3	30	2	Dextrin	0.02	0.06	3
44	5-6	Cu2-H3	30	2	Dextrose	0.05	0.04	2
45	219	Cu2-H3	30	2	EA + M ^c	0.3, 2.0	0.01	2
15	65	Cu2-H1	30	2	Gelatin	0.003	0.05	2
46	81	Cu2-H3	30	2	Gelatin	0.01	0.02	3
47	83	Cu2-H3	30	2	Gelatin	0.1	1.2	0
48	5-5	Cu2-H3	30	2	Glycerol	1.0	0.03	4
49	5-2	Cu2-H3	30	2	Glycine	0.1	0.09	4
50	214	Cu2-H3	30	2	LA ^c	0.05	0.00	4
54	91	Cu2-H3	30	2	NDS ^c	1.8	0.04	3
52	160	Cu2-H3	30	2	β -NQ ^c	0.1	0.14	2
59	71	Cu2-H3	30	2	PSA ^c	1.0	0.03	3-4
64	166	Cu2-H3	30	2	SeO ₂	10-4 Se	0.06	3
68	5-1	Cu2-H3	30	2	Sorbitol	0.1	0.00	3
70	88	Cu2-H3	30	2	TU ^c	0.015	0.4	<1

^a Nominal length of specimens: 6 in. $l_{500.25}$ is length at 25°C, after cooling from 500°C. l_{25} is initial length at 25°C.

^b Blisters formed during heating of the deposit from the amine bath.

^c Prop. A = proprietary addition agent containing a sulfonate and an azo dye; EA + M = ethyl alcohol plus molasses; LA = lactic acid; NDS = 1,5-naphthalenedisulfonic acid; β -NQ = β -naphthoquinoline; PSA = phenolsulfonic acid; TU = thiourea.

^d A qualitative check of physical damage caused by heating. Specimens were bent onto themselves and creased with pliers, opened, and repeated.

structure is associated with slightly better mechanical properties than those of the sulfate deposit.

The pyrophosphate deposit, Fig. 59-3 and 59-4, appears to have a fine random structure. However, this conclusion is in conflict with the magnitudes of the properties of this deposit, with its behavior on annealing (already discussed in Section VIII-B-5-d), and with the results of x-ray diffraction examination presented in the next section.

The deposit from the high-efficiency cyanide bath, the structure of which is shown in Fig. 59-5, is similar to that from the pyrophosphate bath and involves similar contradictions. It appears to have a fine random grain, in conflict with its properties and with the x-ray data. An explanation for these anomalies is suggested in the next section following the presentation of the x-ray data. Similar contradictory data on grain size, as determined optically and by x-ray, have been noted by Read.¹⁹

The deposit from the amine bath, shown in Fig. 59-6, appears to have a very fine, random structure with no resolved crystals. The properties of this deposit, such as fairly high strength, low ductility, and high hardness, summarized in Section VIII-H, confirm the reality of its fine structure.

2. X-ray diffraction.—*a. Back-reflection patterns.*—Back-reflection patterns were obtained from both the final and starting faces of the six deposits listed in Table XXX to obtain information on grain size. Ilford CX film was used to enhance resolution. Specimens were used as plated; i.e., the faces were not polished. Specimens were positioned normal to the beam, with 6 cm between specimen and film. Filtered radiation from an iron target was used, collimated to a beam diameter of 1 mm.

Grain size is estimated from the degree of resolution of spots in the back-reflection patterns (Fig. 60). However, accurate values of grain size cannot be determined by this method unless the following conditions are met: (a) specimens must be free of internal stress; (b) grain orientation should be random; (c) grain size should be uniform. While some as-plated electrodeposits approach these criteria, most fail in one or more of them. Furthermore, grain size estimated by the x-ray method and by optical methods under ASTM standards is not comparable because a twin is not regarded as a new grain in optical determinations, but does give rise to a new x-ray spot. Because of these factors, the grain sizes given in Table XXX

can be regarded only as qualitative and as showing relative fineness of grain for the various deposits.

In Fig. 60, the diffraction index of the outer ring is 311 ($K\alpha$), middle ring 222 ($K\alpha$), and inner ring 400 ($K\beta$). The absence of the resolution of the $K\alpha$ doublets may be due to internal stress or to very small grain size.

Following are interpretations of the patterns shown in Fig. 60:

1—Panel No. 323 (line 26), a soft-type deposit from a sulfate bath. Figure 60-1-F shows the pattern for side F, the final plated surface. It shows blurring to very large spots, indicating a wide range of grain size. Figure 60-1-B shows the pattern for side B, next to the basis metal. It contains continuous rings with doublets resolved, indicating very small grain size and low stress.

2—Panel No. 337 (line 76), a hard, strong deposit from a sulfate bath containing triisopropanolamine. Figures 60-2-F and 60-2-B show the patterns for sides F and B, respectively. The rings are continuous, with doublets unresolved, indicating a uniform fine grain throughout the deposit.

3—Panel No. 343 (line 91), a soft-type deposit from a fluoroborate bath. Figure 60-3-F shows the pattern for side F. The 222 and 400 lines are absent, indicating texture. The 311 line contains 2 large spots and a very faint continuous line, indicating a mixture of fine and large grains. The rings for Fig. 60-3-B, with no resolution of spots and poor resolution of doublets, indicate a very fine structure of the fluoroborate deposit in the basal zone. These x-ray results for panels No. 323, 337, and 345 confirm the grain sizes seen in the optical micrographs, Fig. 59-7, 59-8, and 59-2, respectively.

4—Panel No. 320 (line 95), a deposit from a pyrophosphate bath. Figures 60-4-F and 4-B show the patterns for the final and starting surfaces of the deposit, respectively. Both show large isolated spots with some faint blurring, indicating large grains intermixed with some fine grains. The indicated grain size in the basal zone is not quite as large as in the final plated zone. The absence of the 222 reflection indicates that the deposit is textured.

The x-ray evidence in the preceding paragraph, physical property data, and behavior on annealing (Section VIII-B) indicate that the pyrophosphate deposit has a large grain size. However, contradictory evidence was found by optical examination (Fig. 59-3 and 59-4). Since evidence for a relatively large grain

¹⁹ H. J. Read, Pennsylvania State University, University Park, Pennsylvania, Private communication.

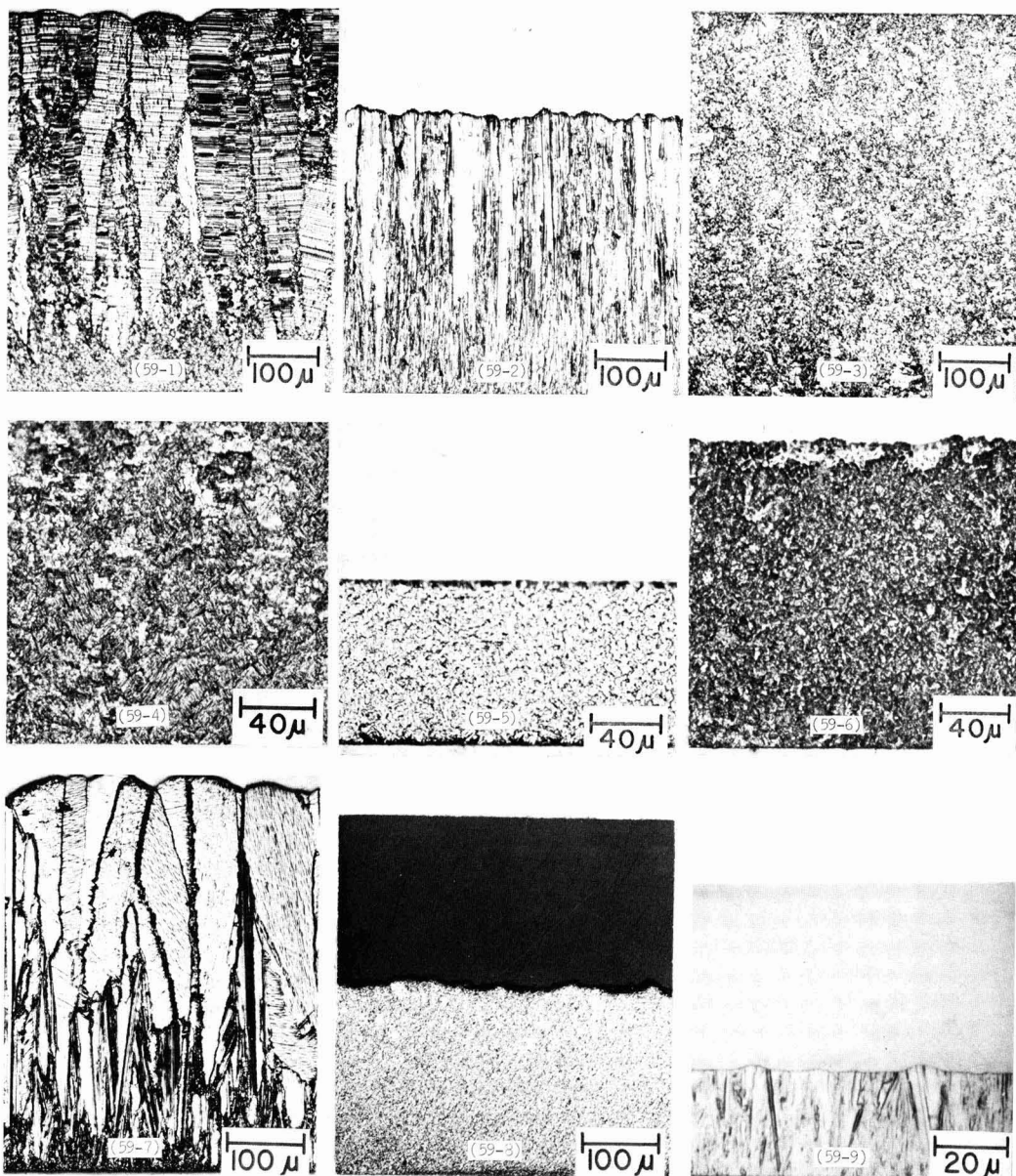


Fig. 59. Comparison of structure of deposits of copper from all types of baths: (59-1) Cu2-H3, 30°C, 8 A/dm²; (59-2) F-1, 30°C, 8 A/dm²; (59-3) and (59-4) pyrophosphate, 50°C, 2 A/dm²; (59-5) CN-8, 80°C, 6 A/dm²; (59-6) amine bath, 55°C, 4 A/dm²; (59-7) Cu2-H2, 30°C, 2 A/dm²; (59-8) Cu2-H3 containing 2 g/l triisopropanolamine, 30°C, 5 A/dm²; (59-9) CN-1, 40°C, 1 A/dm².

size is preponderant, we conclude that the optical structure is misleading. We suggest the following two theories to account for the apparent discrepancy: (a) A columnar structure such as seen in Fig. 47-4 and 47-5 after annealing may be present in the as-plated deposit, but the etching technique used for preparing the photomicrograph specimen was inadequate to reveal it. (b) The fine structure seen in Fig. 59-3 and 59-4 represents an end-view of crystals whose main axes lie in the plane of the deposit. The pyrophosphate photomicrographs would thus be analogous to a view normal to the surface of, e.g., the fluoborate deposit, Fig. 59-2. This theory would require that the grains in the pyrophosphate deposit grow in a directional parallel to, or nearly parallel to, the plane of

the deposit. This could occur by a mechanism in which shallow crystal steps are located with their faces nearly normal to the plane of the deposit, with growth occurring by build-up on these faces (38). We favor this theory, as it is also in accord with the semibrightness of the pyrophosphate deposits.

5—Panel No. 128 (line 101), a deposit from a strike-type cyanide bath, CN-1. The diffraction lines, Fig. 60-5-F and 5-B, which are continuous, indicate fine grain size on both the final plated side and in the basal zone of the deposit. The photomicrograph (Fig. 59-9) and the electron micrographs (Fig. 36) show columnar grains, of the order of 1 μm in diameter, in agreement with what the x-ray sees in a view normal to the plane of the deposit.

Table XXX. Structural features of copper deposits determined from x-ray diffraction and optical micrographs and their relationships to properties and impurities

Line No., Table I	Panel No.	Bath symbol	Addition agent	Bath temp., °C	Current density, A/dm ²	Panel ^a	Type of surface	Crystal ^b size (estimated), μm	Preferential orientation ^c of diffraction plane parallel to surface					Photomicrograph structure	Tensile ^d strength, psi	Hardness KHN, kg/mm ²	Elec. resistivity 25°C, ohm-cm	Total impurities, w/o
									(111)	(200)	(220)	(311)						
26	323	Cu ²⁺ -H ₂	None	30	2	F	Matte	1 to 60	0.06	0.06	10.9	0.2		Large-grained columnar. Fine in basal zone.	55	1.73 $\times 10^{-6}$	0.0035	
76	337	Cu ²⁺ -H ₃	TIPA	30	5	F	Matte	<1	0.5	0.5	1.8	0.9		Fine, columnar texture or grain resolution.	144	1.89	0.022	
91	343, 345	F-1	3.5 g/l	30	8	F	Matte	1 to 50	1.3	0.4	1.3	0.9		Fibrous columnar. Finer than line 26. Fine in basal zone.	81	1.73	0.0041	
95	320	Pyrophosphate	None	50	2	B	Semibright	<100	0.08	0.5	3.8	0.6		Very fine, lamellae, visible at 380 \times .	83	1.75	0.003-4	
101	128	CN-1	None	40	1	F	Matte	1 to 40	0.5	0.6	2.0	0.7		Very fine columnar grains.	162	1.79	0.01	
138	268	CN-8	None	80	6	B	Semibright	1 to 25	1.3	1.2	0.8	1.0		Similar to line 95.	98	1.76	0.0053	

^a F, x-ray beam directed at final plated surface; B, beam directed at starting surface, i.e., the surface that was adjacent to the basis metal.

^b Estimated values of crystal size are qualitative.

^c The magnitude of the number for a given plane indicates the ratio of the intensity of diffraction by that plane to the intensity that would occur if orientation were random. If the orientation were random, the number would be unity for all planes. Kilogram per square millimeter (kg/mm²).

^d Values from Table XXXI. For panel 337, sulfur was estimated by analogy with 323. For panel 320, phosphorus was estimated by analogy with 323. For panel 128, impurity content is assumed to be similar to that of panel 145 (line 110 in Table XXXI), which was made under similar conditions.

6—Panel No. 268 (line 138), a deposit from a high-efficiency cyanide bath, CN-8, containing no addition agent, made without periodic current reversal. Individual spots in the back-reflection patterns are resolved, although smaller than those in the patterns of the large-grained deposits. There is no significant difference between the final plated side and the basal side (Fig. 60-6-F and 6-B). An intermediate grain size is indicated, as shown in Table XXX.

The optical micrograph for this deposit, Fig. 59-5, shows a very fine grain. Thus, for this deposit we have the same contradictions as for the pyrophosphate deposit, and the discussion above in paragraph 4 applies.

b. *Texture analysis.*—A preferred orientation, or fiber texture, of crystals in electrodeposits has been noted and studied by many authors. The results of these studies of copper deposits were reviewed briefly in the first paper of this series (3). Most deposits from sulfate baths have been reported to contain a predominance of crystals oriented with the (110) plane in the plane of the deposit. Quantitative measurement of the angular distribution of the degree of preferred orientation of the (110) plane about the normal to the surface of a copper deposit was made by Ogburn and Newton (39). Under certain conditions, (100) and (111) textures occur in deposits from sulfate baths (40-42). According to the results of a recent publication (43), a shift of orientation from (110) to (113) to (210) planes parallel to the plane of the deposit occurs with increase in current density. The (113) and (210) orientations were obtained at current densities in the range of 60-200 A/dm² with violent agitation. In the upper part of the range the deposits were arboreal and very weak. Most nickel deposits have a (100) texture (2).

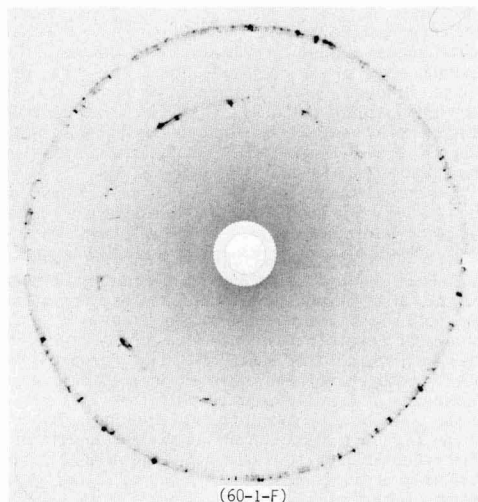
The present measurements were made with a diffractometer, using a cobalt target. The radiation was monochromated with the (111) plane of a lithium fluoride crystal at the receiving detector. The front and back surface of each specimen was step-scanned over the diffraction peaks indicated, at 0.05 deg 2 θ steps, with a counting period at each step of 100 sec. Background was subtracted and area integrated by the Simpson 1/3 rule. A number representing the relative intensity of the diffraction peak from the planes listed in Table XXX to its expected intensity was then calculated. This number, given in Table XXX, is the ratio of the intensity of diffraction by a given plane to the intensity that would occur if orientation were random. If orientation were random, the number would be unity for all planes.

Since the 220 diffraction peak is the second order of the (110) plane, the results in Table XXX show a fairly strong preferred orientation of the (110) plane in the plane of the deposit for panel No. 323, the non-addition agent sulfate deposit, and still stronger identical orientation in the fluoroborate deposit. The basal zone of both of these deposits shows a small preferred orientation of the same plane. The strike-type deposit from the cyanide bath, which shows a columnar grain orientation, shows a small degree of preferred orientation, also of the (110) plane.

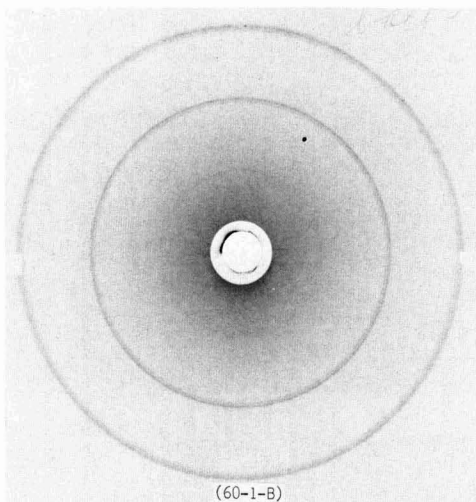
Orientation in the deposit from the sulfate bath containing triisopropanolamine is nearly random, with just a hint of preferred (110) orientation.

The deposits from the pyrophosphate and high-efficiency cyanide baths depart from the above pattern in that the former shows a high degree of preferred orientation with the (111) plane in the plane of the deposit, and the latter the (200) plane, equivalent to the (100) plane, in the plane of the deposit. The latter is unusual in that the orientation is strong in the basal zone but has become random at the final surface.

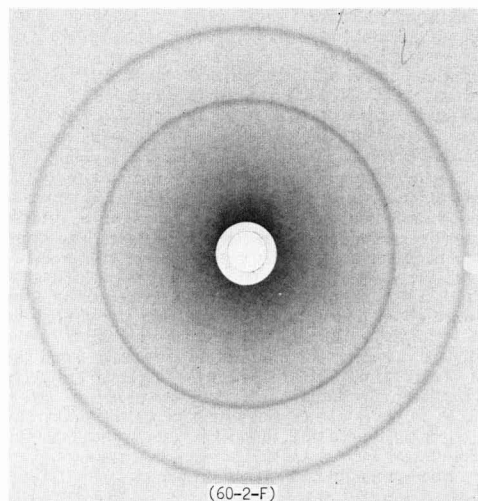
It was noted that the intensity of diffraction from the oriented plane in the final plated surface of specimens No. 323, 320, and especially 345, approached that from a single crystal. It should be noted that the method used did not give a complete survey of all



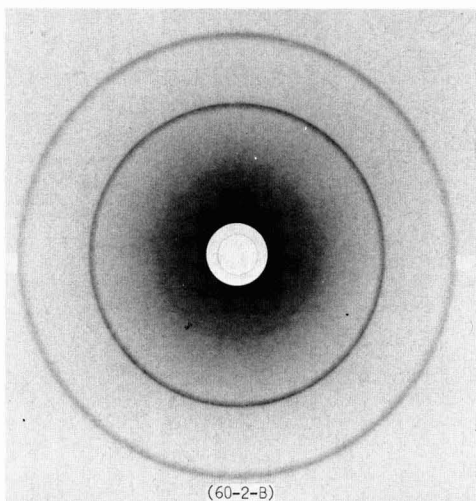
(60-1-F)



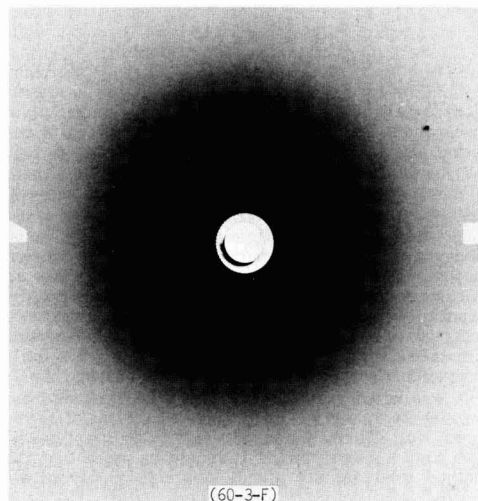
(60-1-B)



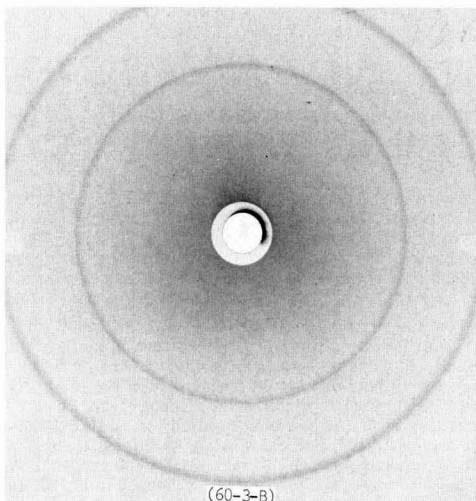
(60-2-F)



(60-2-B)



(60-3-F)



(60-3-B)

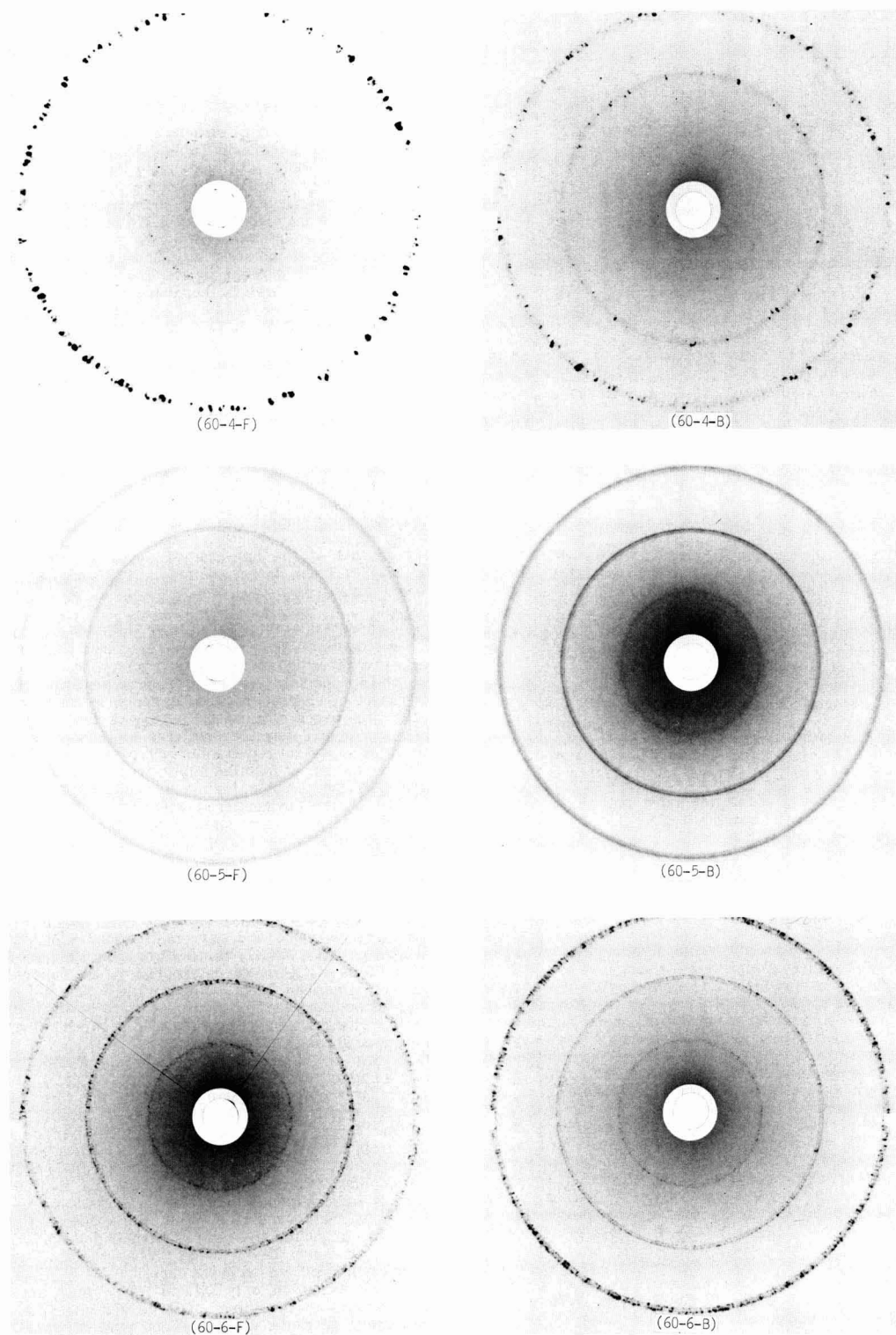


Fig. 60. Back-reflection x-ray patterns of copper deposits. F and B represent patterns with the beam directed at the final plated surface and the starting surface, respectively. (60-1-F and B) Cu₂-H₂, 30°C, 2 A/dm²; (60-2-F and B) Cu₂-H₃ plus 3.5 g/l triisopropanolamine, 30°C, 5 A/dm²; (60-3-F and B) fluoborate F-1, 30°C, 8 A/dm²; (60-4-F and B) pyrophosphate, 50°C, 2 A/dm²; (60-5-F and B) cyanide CN-1, 40°C, 1 A/dm²; (60-6-F and B) cyanide CN-8, 80°C, 6 A/dm².

Table XXXI. Nonmetallic impurities in copper electrodeposits

Line No., Table I	Panel No.	Bath symbol	Addition agent Name	Conc., g/l	Other variable	Bath temp., °C	C.D., A/dm ²	Oxygen	Hydrogen	Ratio, O/H	Content of impurity, % by weight			
											Nitrogen	Carbon	Boron	Sulfur
26	323	Cu2-H2				30	2	0.00038	<0.0001	>4	0.0010	0.0005		0.0011
42	297					60	20	0.00054 ^a	0.0003	40		0.0015 ^b		0.0039
46	81	Cu2-H3	Gelatin	0.01		30	2	0.00038	0.0003					
47	83					30	2	0.0021 ^a	0.0015	14	0.0021			
66	172		SeO ₂	0.001 Se		30	2	0.0350	0.0040	8.8	0.0530 ^b			
67	173		TIPA ^c	3.5		30	2	0.0050	0.0006	8.3	0.0094	0.0062		0.00006
91	345	F-1				30	8	0.0008	<0.0001	>8	0.0017		<0.0001	
95	320	Pyrophosphate				50	2	0.00053 ^a	<0.0001	>7	0.0015			
110	145					60	2	0.00058	<0.0001	>33	0.0055			
127	193	CN-5				80	4	0.0033 ^a	<0.0001	>13	0.0036	0.0005		
138	269	CN-8				80	6	0.0013 ^a	<0.0001	>10	0.0021			
141	281	CN-8			PR, 15-5 sec	80	6	0.0010	<0.0001			0.0022 ^b		
147	303	CN-9	Prop. B ^c			80	6	0.00051 ^a	<0.0001					0.0011

^a and ^b Values designated ^a and ^b were determined at the laboratories of American Metal Climax, Inc., and E. I. du Pont de Nemours & Co., Inc., respectively. All other determinations were made at NBS.

^c TIPA: triisopropanolamine; Prop. B: proprietary brightener, selenium type.

possible preferentially oriented planes. For example, the (211) plane was not examined.

We are indebted to C. J. Bechtoldt of the NBS Metallurgy Division, Lattice Defects and Microstructure Section, for the x-ray measurements and for interpretation of the results.

3. Correlations among structure, properties, and impurities.—The deposits in Table XXX fall into two distinct groups, those with medium to large grain size (non-addition agent sulfate, fluoborate, pyrophosphate, and high-efficiency cyanide), and those with fine grain (sulfate-TIPA, and cyanide, CN-1). The deposits in the coarse-grained group have low to medium tensile strength, hardness, and resistivity, and a small content of impurities. The deposits in the fine-grained group have high tensile strength, hardness, resistivity, and impurity content.

As discussed by Brenner (2) and others, the primary factor that determines properties of electrodeposits is impurity content. A high content of impurities interferes with crystal growth, causing fine grain and associated high values of properties. Impurity content in turn is determined primarily by type of bath and by the kind and concentration of addition agent used. Variations in operating conditions of baths, in the normal range, have minor effects in comparison with type of bath and addition agent. This theory is confirmed for copper by the results summarized in Table XXX. Thus, the total impurity content of the four large-grained deposits is in the range of 0.003-0.005%, whereas that of the fine-grained deposits (lines 76 and 101) is much larger, namely, 0.022 and 0.01%, respectively.

G. Composition and Impurity Content of Deposits

1. Introduction.—It is generally recognized that impurities in deposits may significantly affect their structure and properties. About 20 papers dealing with this aspect of electrodeposited copper were reviewed in the first paper of this series (3). In the present work we have determined metallic and nonmetallic impurities in several representative types of deposits.

Determinations of metallic impurities in both anodes and deposits were made, mainly to monitor the effectiveness of our purification procedures. The results of these determinations, already presented in Table V, were discussed in Section II-A.

In this section we consider nonmetallic impurities in several typical kinds of deposits.

2. Results of determinations of nonmetallic impurities in copper deposits.—*a. Hydrogen and oxygen.*—Content of hydrogen and oxygen in various deposits is shown in Table XXXI. Values of oxygen designated "a" in Table XXXI were determined in the laboratories of American Metal Climax, Inc.²⁰ The other values of both oxygen and hydrogen were determined at NBS.²⁰ Reasonable agreement is seen between values determined at the two laboratories.

The ratio of O/H in nickel and chromium deposits has been found to be close to 8 on the average, indicating that they enter these metals in the form of adsorbed water or hydrated salts (1,2). Ratios of O/H for copper deposits calculated from our data range from 4 to 40, with 5 out of the 10 values equal or close to 8 (Table XXXI). One might conclude that in a significant proportion of deposits the hydrate theory is indicated, but that in several kinds of deposits other factors must be acting. For example, the high value of 40 for the sample from panel No. 297 (line 42) is shown below to be probably caused by the inclusion of sulfate ion in the deposit.

With one exception, only 1/10 to 1/2 as much oxygen is present in the three soft-type deposits (non-addition agent sulfate, fluoborate, and pyrophosphate) as in the addition agent and cyanide deposits.

²⁰ Determinations at American Metal Climax, Inc., were made by courtesy of G. C. Van Tilburg. Oxygen, hydrogen, and nitrogen were determined by J. T. Sterling of the Analytical Chemistry Division, NBS, by a vacuum fusion method.

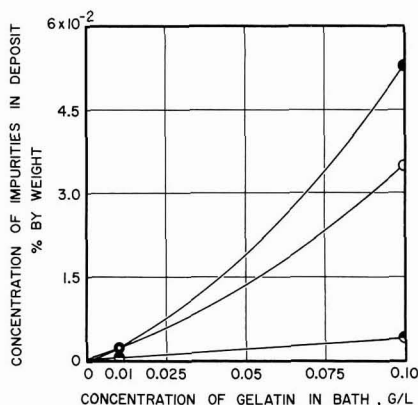


Fig. 61. Relationship between concentration of gelatin in a sulfate bath and concentration of impurities in deposits from the baths. Bath: Cu₂-H₃, 30°C, 2 A/dm². ○—oxygen; ●—nitrogen or carbon; ●—hydrogen.

One would expect the concentrations of oxygen and hydrogen in deposits from acid-type copper baths to be lower than in deposits from nearly neutral nickel baths. This is the relationship that occurs. On the average, we found the content of oxygen and hydrogen in copper deposits to be less than 1/10 of that reported in nickel deposits (2).

The effect of concentration of an addition agent in the bath on concentration of impurities in the deposit is seen in Fig. 61. The concentration in the deposit increases more rapidly than that in the bath. This relationship implies that part of the impurities in the deposit may be entrapped by a mechanism other than adsorption, because, as is well known, the amount of a material adsorbed on a surface increases less rapidly than its concentration in the contacting fluid.

b. Nitrogen.—The possibility exists that nitrogen will enter deposits from sulfate baths that contain a nitrogen compound as an addition agent (gelatin, TIPA) and from pyrophosphate and cyanide baths, both of which contain nitrogen compounds. Nitrogen was found in these deposits in reasonable relative concentrations (Table XXXI). It is surprising that nitrogen was found in the deposits from the non-addition agent sulfate bath or from the fluoride bath. The source of the small amounts in the latter deposits could be accidental, e.g., contamination of the surface of the samples that were analyzed, although precautions were taken to minimize surface contamination.

c. Carbon.—The relatively high content of carbon²¹ in the gelatin and TIPA deposits is to be expected, due to adsorption of these carbon-containing addition agents (Table XXXI).

The amount of carbon in the cyanide deposits is small, indicating that the amount of cyanide ion adsorbed by the deposit is small. If the carbon in the cyanide deposits does enter *via* adsorption of CN ion, the ratio C/N might be expected to be close to 12/14 = 0.86. Since the deposits in lines 138 and 141 are similar, it is valid to use the concentration of carbon in one and nitrogen in the other to obtain C/N, which is seen to equal 1.05. This is close enough to 0.86 to indicate that carbon and nitrogen do enter the deposit as CN ion. On the other hand, the ratio for the deposit from bath CN-5 (line 127) is about 7, a large deviation. Not much weight can be given to this speculation, based on only two determinations.

d. Boron and fluorine in deposits from the fluoborate bath.—The very low concentrations of boron²² and

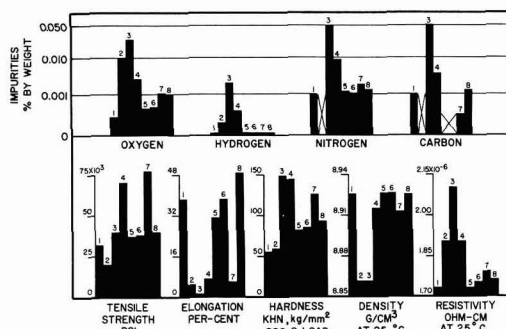


Fig. 62. Correlations between impurities in deposits and properties of deposits for various types of baths: 1—sulfate bath Cu₂-H₂, 30°C, 2 A/dm²; 2—sulfate bath Cu₂-H₃, 60°C, 20 A/dm²; 3—sulfate bath Cu₂-H₃ containing 0.1 g/l gelatin, 30°C, 2 A/dm²; 4—sulfate bath Cu₂-H₃ containing 3.5 g/l triisopropanolamine, 30°C, 5 A/dm²; 5—fluoborate bath F-1, 30°C, 8 A/dm²; 6—pyrophosphate bath, 50°C, 2 A/dm²; 7—cyanide bath CN-5, 80°C, 4 A/dm²; 8—cyanide bath CN-8, 80°C, 6 A/dm². Note pseudo-logarithmic impurity scale. Metric conversion: one pound per square inch (psi) = 0.000704 kilogram per square millimeter (kg/mm²).

fluorine²² in the deposits from the fluoborate bath indicate that there is very little inclusion of fluoborate ion in the deposits (Table XXXI).

e. Selenium in deposits from baths containing selenium compounds as addition agents.—Selenium²³ is present in the deposits from the sulfate bath containing SeO₂ and in the deposit from the high-efficiency cyanide bath containing the proprietary selenium-type brightener (Table XXXI). Evidently very small concentrations of selenium in copper deposits produce marked effects on structure and properties. (Sections III-A-4-e, III-B-3-e, III-F-2-e, VII-B-3-g, VII-C-2-f, VII-G-1, and Fig. 20 and 34).

f. Sulfur in deposits from sulfate baths.—The low concentration of sulfur²⁴ in the deposit from the non-addition agent sulfate bath (Table XXXI, line 26) indicates very little inclusion of sulfate ion in normal deposits. The high current density deposit (line 42) contains more than three times as much, which correlates with the high value of the ratio, O/H, for this deposit.

3. Correlations between concentrations of impurities and properties of deposits.—Correlations between impurity content and properties for eight representative types of deposit are shown in the bar graphs in Fig. 62, from which one can visualize the interrelationships. While some variations from regular correlations will be noted, there are, in general, fairly close correlations between, on the one hand, concentrations of the various impurities, and, on the other hand, between these impurities and the various properties. It should be noted that the correlations with impurities are inverse in the case of elongation and density. Close study of this figure will reveal many details regarding correlations that we leave to the reader to ferret out. Relationships between total impurity content, structure, and properties were discussed above (Table XXX, section VIII-F-3).

H. Summary of Properties and General Correlations

In this section we present a general analysis and correlation of all properties for all as-plated deposits.

²¹ Boron was determined by quantitative spectrography by Virginia C. Stewart and fluorine by a wet method by J. R. Baldwin, both of the staff of the Analytical Chemistry Division, NBS.

²² Selenium was determined by neutron activation analysis by D. A. Becker of the Analytical Chemistry Division, NBS.

²³ Sulfur was determined by combustion by J. R. Baldwin of the Analytical Chemistry Division, NBS.

²⁴ Determinations of carbon were made in the laboratories of E. I. du Pont de Nemours and Company, Inc., by courtesy of O. B. Mathre. Carbon was also determined, by combustion, by J. R. Baldwin of the Analytical Chemistry Division, NBS.

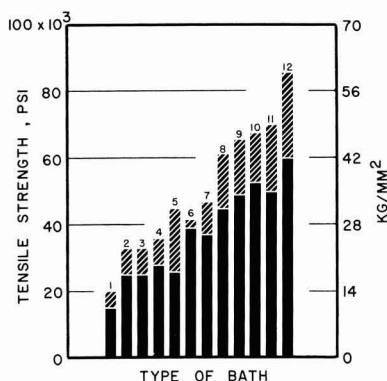


Fig. 63. Ranges and comparative magnitudes of tensile strength of copper deposits from various types of baths: 1—Sulfate baths: plus thiourea (0.005 g/l) and spangled deposits. 2—Sulfate baths, no addition agent, all conditions. 3—Sulfate bath plus addition agents with small effect on strength: dextrin, ethyl alcohol and molasses, glycerol, glycine, lactic acid, 1,5-naphthalenedisulfonic acid, sorbitol, thiourea (0.015 g/l). 4—Fluoborate baths, all conditions. 5—Cyanide baths that yield deposits with lower strengths than those from low-concentration baths: CN-7, CN-8, CN-9. 6—Pyrophosphate bath, all conditions. 7—Sulfate baths plus addition agents or other conditions that cause a moderate increase in strength: gelatin, β -naphthoquinoline, phenolsulfonic acid, selenium dioxide, thiourea plus 1,5-naphthalenedisulfonic acid, thin deposits (2 mils), periodic current reversal (PR). 8—Cyanide bath, sodium ion Rochelle salt type, CN-6. 9—Cyanide baths, all low-concentration types, CN-1 through CN-5, all conditions. 10—Amine bath. 11—Sulfate baths plus addition agents or other conditions that cause a large increase in strength: proprietary A, selenium dioxide (thin deposits, 2 mils), triisopropanolamine. 12—Cyanide baths plus addition agents or other conditions that cause a large increase in strength: CN-8 plus PR, CN-8 containing KCNS plus PR, CN-9 plus PR.

1. *Correlations between tensile strength and types of deposits.*—In Fig. 63, values of tensile strength are plotted for all deposits that we studied. The data are shown for groups of deposits, classified in part on the basis of bath and in part on magnitude of tensile strength, arranged with increasing strength from left to right on the graph. The limits of the shaded zones at the tops of the bars represent minimum and maximum values of tensile strength for the group. The limits plotted for each group are based mainly on the average deviation from the mean within the group. However, if several deposits within the group had values appreciably lower or higher than the limits defined by the average deviation, the range plotted was enlarged to take account of these deviant deposits. The plotted values are thus somewhat subjective, but in our judgment best represent the group. This procedure was followed for determining the plotted values of upper and lower limits for Fig. 63-65 and 67-70, inclusive.

Figures 63 to 70 were prepared primarily to serve as a convenient visual reference summary, and are therefore discussed only briefly. For example, it is seen in Fig. 63 that the over-all range of strength varies by a factor of four, with spangled sulfate deposits the weakest and PR cyanide deposits the strongest. Changes of tensile strength due to large-effect variables, such as type of bath or addition agents, are readily seen. However, changes in strength due to small-effect variables, such as current density, are not revealed. For the latter type of information, the reader must refer to the appropriate preceding section.

2. *Correlations between the yield strength-tensile strength ratio and types of deposits.*—The ratio, yield strength/tensile strength, is very low (about 25%) for soft-type deposits, considerably lower than that of an-

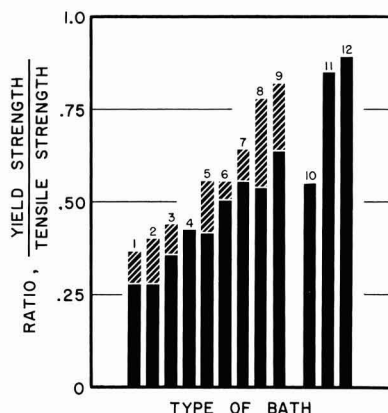


Fig. 64. Ranges and comparative magnitudes of the yield ratio of copper deposits from various types of baths: 1—Sulfate baths, non-addition agent, all conditions. 2—Sulfate baths plus addition agents that cause minor change in yield ratio: lactic acid, β -naphthoquinoline, 1,5-naphthalenedisulfonic acid, phenolsulfonic acid, selenium dioxide, thiourea (0.005 g/l), thiourea plus 1,5-naphthalenedisulfonic acid. 3—Fluoborate baths, all conditions. 4—Cyanide bath, CN-9. 5—Sulfate baths plus addition agents or other conditions that cause a moderate increase in yield ratio: ethyl alcohol plus molasses, thiourea (0.015 g/l), triisopropanolamine, periodic current reversal (PR), thin deposits (2 mils) from bath containing 1,5-naphthalenedisulfonic acid. 6—Pyrophosphate bath, all conditions. 7—Cyanide bath, CN-8 plus PR. 8—Sulfate baths plus addition agents or other conditions that cause a large increase in yield ratio: gelatin, proprietary A, thin deposits (2 mils) from a bath containing selenium dioxide. 9—Amine bath. 10—Commercial wrought copper, annealed. 11—Commercial wrought copper, half hard (21% reduction). 12—Commercial wrought copper, extra hard (50% reduction).

nealed wrought copper (55%). The ratio increases progressively with strength, approaching that of cold-worked wrought copper for the strongest electrodeposits.

3. *Correlations between elongation and types of deposits.*—Figure 65 discloses a general inverse relationship between elongation and type of bath, as compared with Fig. 63 for tensile strength. Thus, the deposits from the amine bath, among the highest in tensile strength, are the most brittle, and the soft-type sulfate deposits, next to weakest, are third from most ductile. The deposits from the pyrophosphate and high-efficiency cyanide baths, with the highest ductilities, are somewhat more ductile than would be predicted from their position in Fig. 63. This could be the result of the crystal orientation hypothesized in Section VIII-F-2-a.

4. *Correlations between modulus of elasticity, tensile strength, and types of deposits.*—A general correlation between tensile strength and modulus is seen in Fig. 66. However, the higher range of modulus, 16 and 17 x 10⁶ psi, embraces a rather large range of tensile strength (40,000-86,000 psi). Modulus values for wrought copper are seen to be located in the mid-range of the correlation band. Correlations between modulus and type of deposit are similar to those between tensile strength and type of deposit, although the fluoborate and sulfate-TIPA deposits deviate conspicuously from the predominant pattern, having abnormally low moduli.

5. *Correlations between hardness and types of deposits.*—The type-grouping for hardness, Fig. 67, is closely parallel to that for tensile strength, Fig. 63.

6. *Correlations between internal stress and types of deposits.*—Examination of the groupings in Fig. 68 shows many deviations from the group order that

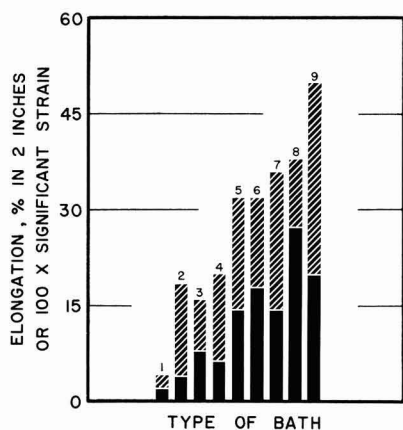


Fig. 65. Ranges and comparative magnitudes of elongation of copper deposits from various types of baths: 1—Amine bath. 2—Sulfate baths plus addition agents or other conditions that cause significant lowering of ductility: dextrin, ethyl alcohol plus molasses, glycerol, glycine, lactic acid, β -naphthoquinoline, sorbitol, thiourea (0.005 and 0.015 g/l), triisopropanolamine, proprietary A, non-addition agent thin deposits (2 mils), thin deposits (2 mils) from baths containing 1,5-naphthalenedisulfonic acid or selenium dioxide, spangled deposits. 3—Cyanide baths, all low-concentration types, CN-1 through CN-5, all conditions. 4—Cyanide baths, high concentration types that yield deposits with ductility nearly the same as those from low concentration baths: CN-8 containing KCNS plus periodic current reversal (PR), CN-9. 5—Fluoborate baths, all conditions. 6—Sulfate baths plus addition agents or other conditions that cause minor effect on ductility: gelatin (0.003 g/l), 1,5-naphthalenedisulfonic acid, phenolsulfonic acid, selenium dioxide, thiourea plus naphthalene disulfonic acid, PR. 7—Sulfate baths, no addition agent, all conditions. 8—Pyrophosphate bath, all conditions. 9—Cyanide baths that yield deposits that are significantly more ductile than those from low-concentration baths: CN-6, CN-7, CN-8, CN-8 plus PR, CN-9 plus PR.

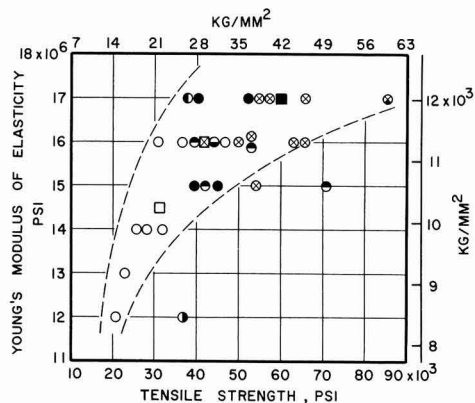


Fig. 66. Relationship between tensile strength and modulus of elasticity of copper deposits from various types of baths: ○—non-addition agent sulfate baths; ●—sulfate baths containing gelatin; ●—sulfate bath containing selenium dioxide; ●—sulfate bath containing triisopropanolamine; ○—fluoborate bath; ●—pyrophosphate bath; ⊗—cyanide baths, CN-1 through CN-5; ⊗—CN-8 containing KCNS plus periodic current reversal (PR); □—commercial wrought copper, annealed; ⊗—commercial wrought copper, half hard (21% reduction); ■—commercial wrought copper, extra hard (50% reduction).

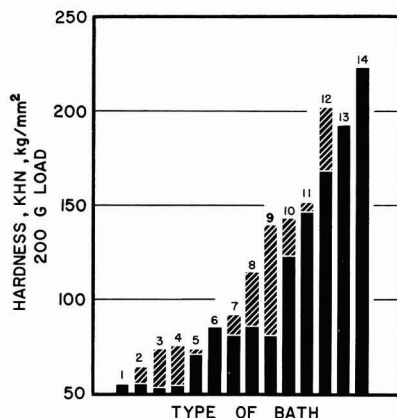


Fig. 67. Ranges and comparative magnitudes of hardness of copper deposits from various types of baths: 1—Sulfate bath, Cu₂H₃, 30°C, 2 A/dm², severe exposure to cellulose. 2—Sulfate baths plus addition agents that have minor effect on hardness: dextrin, ethyl alcohol plus molasses, glycerol, sorbitol. 3—Sulfate baths, no addition agent, all conditions. 4—Fluoborate baths, all conditions. 5—Cyanide bath, CN-9. 6—Sulfate bath, spangled deposit. 7—Pyrophosphate bath, all conditions. 8—Cyanide baths, CN-7 and CN-8, all conditions. 9—Sulfate baths plus addition agents: includes all addition agents in Table XIII except those in "2" above. 10—Cyanide baths, CN-1 through CN-6, all conditions. 11—Cyanide baths: CN-8 plus periodic current reversal (PR); CN-8 plus KCNS plus PR, cycle 15 sec cathodic, 5 sec anodic. 12—Amine bath. 13—Cyanide bath, CN-8 plus KCNS plus PR, cycle 30 sec cathodic, 10 sec anodic. 14—Cyanide bath, CN-9 plus PR.

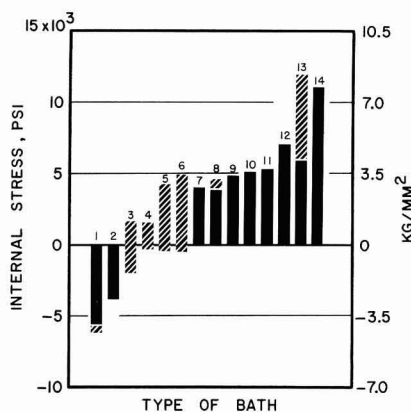


Fig. 68. Ranges and comparative magnitudes of internal stress in copper deposits from various types of baths. Negative stress is compressive. 1—Amine bath. 2—Sulfate bath containing 0.1 g/l gelatin. 3—Pyrophosphate bath, all conditions. 4—Fluoborate baths, all conditions. 5—Sulfate baths, no addition agent, all conditions. 6—Sulfate baths plus all addition agents in Table XIII except gelatin (0.1 g/l), β -naphthoquinoline, triisopropanolamine (30°, 5 A/dm²). 7—Sulfate bath plus periodic current reversal (PR). 8—Cyanide baths: CN-8, CN-8 plus PR. 9—Cyanide bath, CN-6. 10—Cyanide bath, CN-8 plus 2 g/l KCNS plus PR. 11—Sulfate bath plus β -naphthoquinoline. 12—Sulfate bath plus triisopropanolamine (30°, 5 A/dm²). 13—Cyanide baths: CN-1 through CN-5, CN-7, all conditions. 14—Cyanide bath, CN-9.

exists in the other graphs in this set (Fig. 63-70). This individuality of internal stress, or lack of consistent relationships with other properties, has been previously noted.

7. Correlations between density and types of deposits.—Except for the low values of density seen in

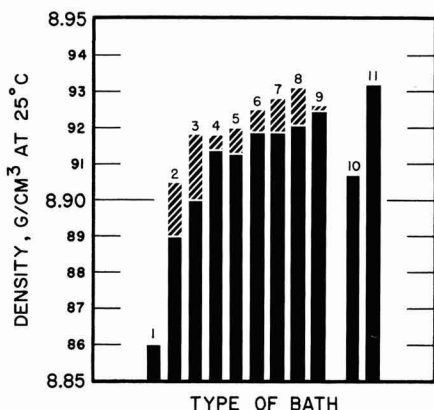


Fig. 69. Ranges and comparative magnitudes of density of copper deposits from various types of baths: 1—Sulfate baths plus addition agents or other conditions that cause a large decrease of density: gelatin, 0.1 g/l; Cu₂H₃, 60°C, 20 A/dm² (high current density). 2—Amine bath. 3—Cyanide baths: CN-1 through CN-5, all conditions. 4—Sulfate baths plus addition agents that have slight lowering effect on density: gelatin, 0.003 g/l; triisopropanolamine, 30°, 5 A/dm²; proprietary brightener A. 5—Cyanide baths: CN-6 and CN-7, all conditions; CN-8 plus KCNS plus periodic current reversal (PR). 6—Cyanide baths: CN-8, CN-9. 7—Sulfate baths, no addition agent, all conditions. 8—Sulfate baths plus addition agents or other conditions that have no significant effect on density: ethyl alcohol plus molasses, lactic acid, 1,5-naphthalenedisulfonic acid, β -naphthoquinoline, phenolsulfonic acid, selenium dioxide, thiourea, thiourea plus naphthalenedisulfonic acid, triisopropanolamine, 30°, 2 A/dm²; periodic current reversal; spangling. 9—Fluoborate and pyrophosphate baths, all conditions. 10—Commercial sheet, half hard (21% reduction). 11—Single crystal.

the first two groups of Fig. 69, all deposits have rather high density, with only small differences between groups. Nevertheless, the lower density of cyanide deposits and the reduction of the density of sulfate deposits due to "active" addition agents is apparent.

8. *Correlations between electrical resistivity and types of deposits.*—Type groupings for electrical resistivity, Fig. 70, are quite parallel to those for tensile strength and hardness (Fig. 63 and 67, respectively).

9. *General correlations among properties and types of deposits.*—Some of the properties of the main types of deposits are represented in Fig. 71. In the first group, the seven types of deposits are arranged in increasing order of tensile strength. The same order, type 1 to 7 serially, is maintained in the representations of the other properties, so that deviations from regular correlations will be apparent. There is general parallelism between tensile strength, hardness, and resistivity, and to some extent internal stress, and inverse correlation of these properties with elongation and density.

The higher than "normal" elongation of the deposits from the high-efficiency cyanide bath and pyrophosphate bath is apparent, as is the inverse relationship between ductility and tensile strength of the deposits from the amine bath and from sulfate baths containing high-effect addition agents. The average hardness of the latter group of deposits is lower than normal. This is the only significant deviation from a regular hardness pattern.

We have remarked several times that internal stress is the most unique property in that it is least correlated with other properties. While this is true, Fig. 71 does show several regular correlations. Abnormally low stress of the pyrophosphate and amine baths is the main deviation from normal correlation.

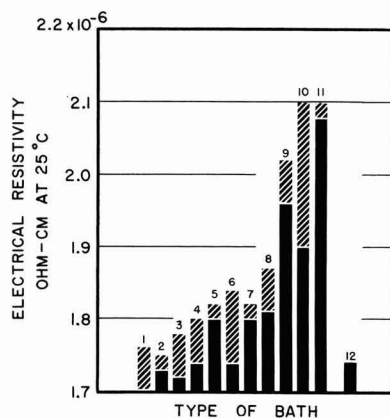


Fig. 70. Ranges and comparative magnitudes of electrical resistivity of copper deposits from various types of baths: 1—Sulfate baths, no addition agent, all conditions. 2—Fluoborate and pyrophosphate baths, all conditions. 3—Sulfate baths containing addition agents that have minor effect on resistivity: ethyl alcohol plus molasses, β -naphthoquinoline, gelatin (0.003 and 0.01 g/l), lactic acid, naphthalenedisulfonic acid, phenolsulfonic acid, selenium dioxide, thiourea, thiourea plus naphthalene disulfonic acid, triisopropanolamine (30°C, 2 A/dm²), periodic current reversal (PR). 4—Cyanide baths: CN-7 and CN-8, all conditions; CN-8 plus PR. 5—Sulfate baths plus factors that have medium effect on resistivity: thin deposits (2 mils); proprietary brightener A. 6—Cyanide baths: CN-1 through CN-5, all conditions. 7—Cyanide bath: CN-9 (proprietary B). 8—Cyanide baths: thin deposits (0.25 mil) from CN-1 through CN-3; CN-6, all conditions. 9—Cyanide baths: CN-8 plus KCNS plus PR; CN-9 (proprietary B) plus PR. 10—Sulfate baths plus addition agents or other factors that have large effect on resistivity: Cu₂H₃, 60°, 20 A/dm² (high current density); gelatin (0.1 g/l); triisopropanolamine plus high current density (5 A/dm²); spangling. 11—Amine bath. 12—Commercial wrought copper: annealed electrolytic tough pitch.

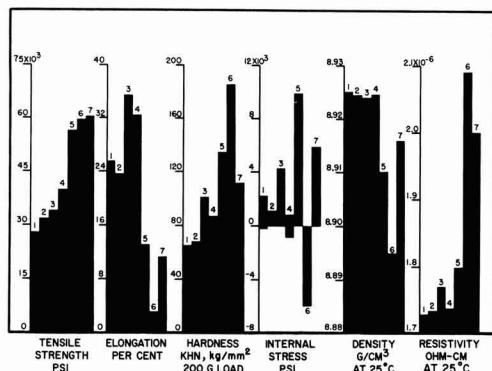


Fig. 71. General correlations among properties of copper deposits from various types of baths: 1—Sulfate baths, all non-addition agent deposits. 2—Fluoborate baths, all conditions. 3—Cyanide bath, CN-8, all conditions except no addition agent nor periodic current reversal (PR). 4—Pyrophosphate bath, all conditions. 5—Cyanide baths, CN-1 through CN-5, all conditions. 6—Amine bath. 7—Sulfate baths plus large effect addition agents. Notes: Elongation is in per cent in 2 in. except for column "5" which is 100X significant strain. Negative values of internal stress represent compressive stress. Metric conversion: one pound per square inch (psi) = 0.000704 kilogram per square millimeter (kg/mm²).

Considering density, correlation is regular except for the same reversed positions between the deposits from the amine bath and the sulfate bath containing high-effect addition agents, also noted for elongation

and hardness, and repeated again for electrical resistivity. The low value of resistivity of the pyrophosphate deposit is also apparent. The consistent deviation of the properties of the pyrophosphate deposits from the normal, in general in favorable directions, is the most apparent phenomenon shown in these comparisons. It is quite likely that it is associated with a unique structure, as hypothesized in Section VIII-F-2-a.

IX. Acknowledgments

The authors acknowledge the assistance of the following for help with experimental work: J. F. Berkeley and G. I. Reid of the Electrolysis and Metal Deposition Section, NBS, for preparation of metallographic specimens, measurements of expansivity, and preparation of photomicrographs, and T. R. Shives of the Metallurgy Division, NBS, for measurements of hardness. The assistance of many other members of the staff of NBS has been acknowledged at appropriate points in the text.

We also acknowledge the valuable help and advice given by the following: C. H. Sample, District Supervisor, Project 21; R. A. Ehrhardt and A. M. Max, previous and present chairman of the Project 21 committee; and members W. Blum, A. Brenner, S. Lyman, O. B. Mathre, C. W. Ostrander, H. J. Read, D. A. Swalheim, G. C. Van Tilburg, M. L. Whitehurst, and C. I. Whitman.

We gratefully acknowledge the donation of anodes by American Metal Climax, Inc.

Financial support for the project was supplied jointly by the American Electroplaters' Society, Inc., through the Research Board, and by the International Copper Research Association, Inc., the Copper Development Association, and the National Bureau of Standards.

X. Appendix

A. Procedures Used for Preparation of Electron Micrographs (Fig. 36)²⁵

Mechanically polished cross sections were electropolished in a commercial electropolishing unit with a proprietary polishing solution containing H_3PO_4 , 250 ml; distilled water, 500 ml; ethanol, 250 ml; propanol, 50 ml; urea, 5g; proprietary constituent, 2 ml. Conditions were: time, 5 sec; temperature, 25°C; current, 0.6A. Contact to one specimen was made with a solder spot at the base of the mount and to another with silver paint. No significant difference in structure was seen due to the brief heating during soldering. After electropolishing, chemical etching was done in the etch mixture: NH_4OH , 30 ml; H_2O_2 -3%, 30 ml; H_2O , 30 ml; 5 sec, 25°C.

Replicas were made with cellulose acetate tape. The negative replicas were rotary shadowed at an angle of 25° with palladium and backed with carbon at an angle of 90°.

B. Development of Fatigue Relationships

1. Calculation of σ_e in Table XXVI.—The fatigue specimen is represented in Fig. 72 with exaggerated thickness and curvature and with the U-bend at the top replaced with an equivalent rigid bar so that the rotational moments may be visualized. The lower end of the right-hand strip is rigidly fixed. The vertical force, P , causes bending as shown. We consider the bending of only one arm, recognizing that the same forces are present in both. Thus, the force, P , may be thought of as divided in two equal parts, $P/2$, each part causing the bending of one arm. Therefore, the moment causing rotation about O and corresponding bending about O' is

$$\frac{P}{2} \cdot a = M \quad [1]$$

M , the moment about O' , is also equal to the integral

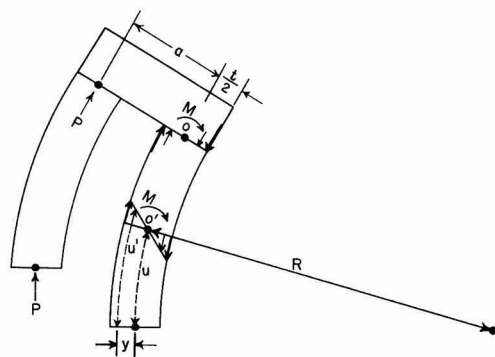


Fig. 72. Stresses and moments in a flexed fatigue specimen

over the cross section of the specimen of the product of the fiber stresses (represented by the small arrows) and their respective moment arms. It is thus expressed as

$$M = \int \sigma y dA \quad [2]$$

where σ is the fiber stress at distance y from the neutral plane of the strip and dA is an element of area in a normal plane. By definition

$$\sigma = E\delta \quad [3]$$

where E is Young's modulus of elasticity and δ is strain. From Fig. 72, $\delta = (u' - u)/u$. Substituting in [3]

$$\sigma = E \left[\frac{u' - u}{u} \right] \quad [4]$$

Again from Fig. 72

$$\frac{R}{R + y} = \frac{u}{u'} \quad [5]$$

from which

$$u' = u + \frac{yu}{R} \quad [6]$$

Substituting u' from [6] in [4]

$$\sigma = \frac{Ey}{R} \quad [7]$$

Substituting for σ from [7] in [2]

$$M = \frac{E}{R} \int y^2 dA = \frac{EI}{R} \quad [8]$$

where $I = \int y^2 dA$, the geometrical moment of inertia around O' .

For a rectangular beam of width b and thickness t , $dA = bdy$; hence

$$I = b \int y^2 dy = 2b \left[\frac{y^3}{3} \right]_0^{t/2} = \frac{bt^3}{12} \quad [9]$$

Equation [7] gives the actual stress in any given plane at distance y from the neutral plane. The distance y to the outer plane is $t/2$. Therefore the surface stress is given by

$$\sigma = \frac{E}{R} \cdot \frac{t}{2} \quad [10]$$

From Eq. [8], $E/R = M/I$. Substituting this in [10]

$$\sigma = \frac{M}{I} \cdot \frac{t}{2} \quad [11]$$

Substituting the value of M from [1] and the value of I from [9] in Eq. [11] gives

$$\sigma = \frac{Pa}{2} \cdot \frac{12}{bt^3} \cdot \frac{t}{2} = \frac{3Pa}{bt^2} \quad [12]$$

Equation [12] gives surface stress, and is the relation

²⁵ Electron micrographs were made by D. B. Ballard, NBS Metallurgy Division, Lattice Defects and Microstructure Section, who also supplied the data on procedures used.

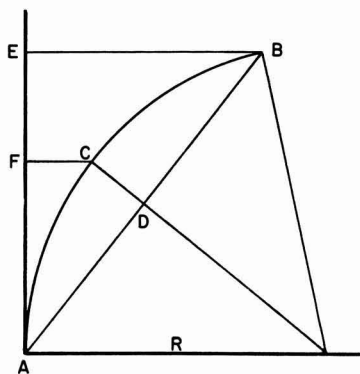


Fig. 73. Relationship between radius of curvature and deflection of an arc.

used for calculating σ_c in Table XXVI. P is obtained from the machine calibration, a is 0.30 in. for our specimens, b is 0.50 in., and t is the measured thickness of the specimen.

2. *Calculations of σ_m in Table XXVI.*—The arc ACB in Fig. 73 represents an edge view of a short segment of one arm of a flexed fatigue specimen. C is the longitudinal center, i.e., the point of minimum width. Index marks were placed on the edge of the specimen at C and at points A and B , with AC and CB each equal to $1/8$ in. The variation in width of the specimen over the span AB is small, so that the curvature is nearly uniform. The specimen was statically flexed and clamped in the flexed position in a jig. The distances EB , FC , AE , and AF were then measured with a micrometer microscope to an accuracy of 0.1 mil. Their values were then plotted on large paper on a magnified scale of 100X. From the plot, CD and AD were measured. The following right triangle relationship is apparent from Fig. 73

$$(R - \overline{CD})^2 + \overline{AD}^2 = R^2 \quad [13]$$

Expanding [13] and solving for R gives

$$R = \frac{\overline{CD}^2 + \overline{AD}^2}{2\overline{CD}} \quad [14]$$

From Eq. [10] in the preceding Section X-B-1

$$\sigma = \frac{E}{R} \cdot \frac{t}{2} \quad [10]$$

Substituting in [10] the value of R from [14]

$$\sigma = \frac{Et}{2} \left[\frac{2\overline{CD}}{\overline{CD}^2 + \overline{AD}^2} \right] \quad [15]$$

This is the value of σ designated as σ_m in Table XXVI. The values of E (modulus) used in [15] were determined by us or estimated from values for similar deposits. CD and AD were determined from the direct measurements and graphical evaluation just described.

REFERENCES

34. G. Földes, *Sheet Metal Ind.*, **34**, 749 (1957).
35. R. P. Reed and R. P. Mikesell, "Low Temperature Mechanical Properties of Copper and Selected Copper Alloys," *Nat. Bur. Std. (U.S.) Monograph*, **101**, (1967), Supt. of Documents, U.S. Govt. Printing Office, Washington, D.C. 20402.
36. P. Hidnert and W. Souder, *Nat. Bur. Std. (U.S.) Circ.*, No. 486 (1950).
37. P. Hidnert and H. S. Krider, *J. Res. Nat. Bur. Std.*, **39**, 419 (1947).
38. J. O'M. Bockris and B. E. Conway, "Modern Aspects of Electrochemistry—No. 3," p. 293, Butterworths, Washington, D. C. (1964).
39. F. Ogburn and C. Newton, *This Journal*, **110**, 1148 (1963).
40. H. Leidheiser and A. T. Gwathmey, *Trans. Electrochem. Soc.*, **91**, 95 (1947).
41. S. Okada and S. Magari, *This Journal*, **102**, 580 (1955).
42. S. C. Barnes, *ibid.*, **111**, 296 (1964).
43. L. Krushev, V. Pangarova, and N. Pangarov, *Plating*, **55**, 841 (1968).

Abstracts of "Recent News" Papers

Presented at the Electronics Division Sessions, Atlantic City, New Jersey, October 4-8, 1970

232 RNP

Vacancy Cluster Formation in Dislocation-Free Floating Zone Silicon Crystals

A. J. R. de Kock, Philips Research Laboratories.

During growth of dislocation-free silicon crystals with the floating zone technique, vacancy clusters are formed. These defects can be detected by, e.g., preferential etching or copper decoration in combination with x-ray topography and infrared microscopy. A model describing the vacancy clustering process, in which vacancy-oxygen complex formation plays an essential part, is discussed. From this model, two methods for the prevention of vacancy clustering can be obtained, both based on the elimination of vacancy-oxygen complex formation during growth.

233 RNP

The Growth of Dislocation-Free Floating Zone Silicon Crystals Without Vacancy Clusters

A. J. R. de Kock, Philips Research Laboratories.

Conditions are described under which dislocation-free floating zone silicon crystals were grown without formation of vacancy clusters. These conditions are based on our model describing the vacancy clustering process. Small amounts of impurities, which interact with oxygen, were added to the growing crystals. In combination with adjusted growth conditions, the formation of vacancy nucleation sites (vacancy-oxygen complexes) was prevented. In these crystals, no vacancy clusters could be detected.

234 RNP

Growth of Stacking Faults in (100) Epitaxial Silicon during Steam Oxidation: Effect of HF

C. M. Drum and W. Van Gelder, Bell Telephone Laboratories, Inc.

When (100) epitaxial silicon or (100) heat-treated bulk silicon is exposed to HF and then oxidized in steam or in wet oxygen, stacking faults are formed. This does not occur on wafers with (111) surfaces. The faults are revealed by etching or by electron microscopy. Since these defects can adversely affect device performance, it is important to have processes which keep the silicon lattice free from these faults. Such processes include (a) dry oxygen oxidation, (b) dry oxygen-steam-dry oxygen oxidation, and (c) etching of the epitaxial surface followed by HF and steam oxidation.

235 RNP

Donor Diffusivities in Silicon Free from Surface Effects

R. N. Ghoshtagore, Westinghouse Research Laboratories.

P-32 has been used to show the extrinsic effects associated with the normal diffusion process in silicon. Consequently, P, As, Sb, and Bi have been diffused into (111) silicon from doped epitaxially deposited source layers in hydrogen atmosphere. The diffusion coefficients obtained between 1130° and 1405°C show values uniformly much lower than those available in the literature. These

data are analyzed to indicate the most probable diffusion mechanism in silicon.

236 RNP

Reduced Dislocation Densities in Liquid Phase Epitaxy Layers by Intermittent Growth

R. H. Saul, Bell Telephone Laboratories.

GAP liquid phase epitaxy (LPE) layers, grown using an interrupted cooling rate to induce intermittent growth, exhibit an abrupt reduction in dislocation density, ρ , which coincides with the interface between growth increments. Constant cooling rates interrupted by partial melt-back (heating) of the LPE layer or isothermal annealing are both effective in reducing ρ , typically by factors of 3-6. Successive reductions in ρ could be achieved by employing several interruptions in cooling rate. These results are discussed in terms of proposed mechanisms for dislocation elimination in crystals.

237 RNP

Evaluation of a New Polish for GaAs Using a Peroxide-Alkaline Solution

J. C. Dymant and G. A. Rozgonyi, Bell Telephone Laboratories.

The effectiveness of H₂O₂-NH₄OH or peroxide-alkaline (PA) as a new polishing solution for GaAs* has been compared with a standard bromine-methanol (BM) solution and also a Syton-bromine-methanol (SBM) solution. We have compared the surface roughness, orientation dependence, polishing rates, and residual surface damage as determined by x-ray topography. The PA and BM solutions are superior to the SBM in terms of residual surface damage; however, the PA solution has better aging properties and will also polish the (111) Ga-face. Finally, PA polished substrates have yielded diffused junction lasers with threshold current densities comparable to the best BM values.

* This solution was first used by A. J. Sayko of these laboratories.

238 RNP

Effects of Crystalline Defects on Arsenic-Emitter Transistors

M. L. Joshi, T. H. Yeh, J. J. Chang, M. Vora, A. S. Oberai, and H. N. Ghosh, IBM Components Division.

It is well known that the high concentration phosphorus diffusion in the emitter regions of the NPN transistors introduces defects such as dislocations and precipitations in those regions. In addition, there is always the emitter-push effect, i.e., the enhanced movement of the base-collector junction under an emitter, if one uses phosphorus to form the emitters. Because of the emitter-push effect, the doping profile in the base region tends to spread out and cause the reduction in the integrated base dopant. For the high-speed devices, one needs the combination of narrow base-width and certain integrated base dopant. This combination, up to now, is very difficult to achieve, if one uses phosphorus to form the emitters. But we found it can be done by using arsenic instead of phosphorus, and NPN transistors with extreme high current gain, β , and cut-off frequency, f_t , have been made. Advantages of using arsenic to form the emitters plus its impurity distribution under various conditions of time, temperature, and source concentration are presented and discussed.

239 RNP

Thin High-Quality Silicon Layers on Insulating Substrates

George Wallis, P. R. Mallory & Co., Inc.

A new procedure is described by which silicon-on-insulator structures suitable for MOS and bipolar IC's are obtained. The silicon layers, 1-20 μ thick, have the electrical properties of bulk crystals. The layers are joined to substrates of Pyrex or 4-5 μ thick thermal oxide on single-crystal silicon. Joining is accomplished by a new method which utilizes high electrostatic fields to form strong bonds at relatively low temperatures without the use of adhesives.

240 RNP

Potential Distributions on Diffused Silicon Surfaces

R. E. Gegenwarth, IBM Components Division.

Potential distributions have been measured on the surface of diffused silicon wafers to test the accuracy of previously published three-dimensional models and to determine the range of applicability of a two-dimensional model. Boron-diffused samples having junction depths ranging from 0.38 μ to 11.47 μ were measured. The normalized potential distributions of all samples were essentially equal and showed that the potential distributions in the vicinity of a current contact could be described very well by a two-dimensional model. Whereas the potential distribution decreased rapidly in the vicinity of a finite area contact on a semi-infinite or thick layer, it did not do so in the case of thin layers. It is therefore necessary to consider the effect of sample geometry on surface resistivity measurements and spreading resistance profiling.

241 RNP

Resistivity and Lifetime of N-Type Silicon Affected by Gold Diffusion, Platinum Diffusion, and Electron Radiation

C. K. Chu, D. K. Schroder, and P. E. Felice, Westinghouse Electric Corp.

In the fabrication of high power, fast switching silicon devices, gold diffusion, platinum diffusion, and high energy electron irradiation were used to achieve a reduction of lifetime. P-NP₁ devices were diffused at

Abstracts of "Recent News Papers" 405C-407C

Electronics Division Award	408C
Section News	408C
News Item	408C
ECS Summer Fellowship Award	410C
ECS Battery Technology Symposium ..	410C
New Products	410C
From Publishers	410C
Book Reviews	411C
ECS Membership Statistics	411C
Positions Wanted	412C
Instruction to Authors	413C-414C
Call For Papers	415C-418C



LITHIUM BATTERY ANODES IN ORGANIC ELECTROLYTES

New Technology for High Energy Density Batteries

If you're working with lithium metal, Foote can furnish your complete requirements—from ingots to finished anodes. Our continuing development program on new forms of lithium for use in high energy density batteries now makes it possible to offer these options:

Expanded Screen can be filled with lithium metal and low melting lithium alloys, increasing thicknesses by only one mil, thus maintaining dimensional tolerances.

Porous Metal Composites: Sintered compacts can be filled with lithium.

Bimetallic Strips: Stainless, nickel, copper and many other metals in various thicknesses can be coated on one or both sides.

Anodes can be produced by various methods to customer specification.

Casings and Wire Connections can be furnished for any of the above anodes.



Let's talk. **Foote Mineral Company**,
Dept. 111, Route 100, Exton, Pa. 19341.
Phone: 215-363-6500.

865° ± 2°C for varying times or irradiated with 2 MeV electrons at a dose of 10¹⁴ to 10¹⁵ electrons/cm². The samples were evaluated by measuring the resistance (spreading resistance technique) and the lifetime (open-circuit voltage decay) before and after the above treatments. All three processes reduce the lifetime effectively. While the resistivity of the N-bulk is increased for gold diffused samples, there is no appreciable resistivity change due to platinum diffusion or electron irradiation. Experimental procedures and quantitative results are discussed in this paper.

242 RNP

Effects of Low Energy Electron Beam Bombardment on Semiconductor Properties

J. R. Fiebigler and R. S. Muller, University of California, Berkeley, Calif.

Investigations of semiconductor and integrated-circuit properties using the scanning electron microscope (SEM) have become very widespread. Experiments using the SEM have been regarded generally as non-destructive because the requisite voltages and beam-current densities for most studies can be shown to produce negligible heating in the structures. We describe here a systematic study of the effects on fundamental semiconductor parameters of SEM measurements. Specifically, a theoretical and experimental study of the effects of bombardment of germanium and silicon by 10-30 keV electron beams on the basic semiconductor properties mobility, μ , diffusion constant, D , and lifetime, τ , has been completed.

243 RNP

Conductor Defects in Multilayer LSI Structures

M. A. Schuster, D. S. Herman, J. Grossman, and H. G. Oehler

Mechanisms which account for ohmic contact, isolation, and interconnection failures in multilayer structures, and process design criteria, for achieving their control are described. Substrate/aluminum₁ contacts must minimize interfacial and substrate alloying as well as contact resistance. Aluminum₁ grain growth and via-pattern photoengraving parameters interact to control (aluminum)₁-SiO₂-(aluminum)₁ isolation. Continuity of upper level interconnections is dependent on shaping the profile (edge geometry, height, and surface planarity) of the underlying metal stripes and their dielectric over-coat.

244 RNP

Electromigration Behavior in Alloy Concentration Gradient Regions of Thin Aluminum Films

J. J. Gniewek, IBM Components Division.

The effect of alloying elements on electromigration in thin aluminum films was investigated by observing the migration behavior in alloy concentration gradient regions produced by selected area diffusion. The special test structure consisted of long pure aluminum stripes containing small alloy regions. The resulting series connection of pure and alloy aluminum was powered at 10⁶ A/cm² for various times and temperatures. Any effect of the alloy constituent is evidenced by an atom flux divergence at the diffusion site. Examples of beneficial and degrading constituents are shown by the results for copper and beryllium additions. Detailed microprobe and scanning electron microscopy results are presented for the copper specimens.

245 RNP

Mobile Ion Transfer to SiO₂ from Ethanol

S. I. Raider and R. Flitsch, IBM Components Division.

Hofstein reported ionic drift in thermally grown SiO₂ as a result of contamination with tritiated ethanol. He related the observed ionic drift to protonic conduction.

The effect of contamination of an SiO_2 surface with ethanol with respect to subsequent ionic drift is re-examined. The ionic drift results obtained are in disagreement with those previously reported by Hofstein. The differences are attributed to the purity of the ethanol samples.

246 RNP

Transient Electron Injection into SiO_2 from Metal Electrodes

E. H. Nicollian and C. N. Berglund, Bell Telephone Laboratories.

By driving an MOS capacitor with a large amplitude a-c field exceeding about 2 mV/cm, d-c electron currents as high as 100 μA have been injected into thick ($>500\text{\AA}$) SiO_2 layers from the metal electrode. The magnitude of this injected current depends on the perimeter of the gate electrode rather than its area. The explanation of the electrode injection is that the electric field existing in the oxide within a short distance of the electrode edge can be much higher than the average electric field under the electrode. Experimental evidence supporting the model is described.

247 RNP

An Analysis of Impurity Distribution in Homoepitaxial n on n^+ Films of GaAs which Contain High Resistivity Regions

J. V. DiLorenzo, R. B. Marcus, and R. Lewis, Bell Telephone Laboratories.

The occurrence of a high resistivity region (i layer) at the interface of n -type GaAs films on n^+ GaAs substrates has been a recurring problem in the halide synthesis transport growth of these films for microwave devices. Although consistent success has been achieved in the elimination of an i layer by deposition of an n^+ epitaxial film substrate prior to the growth of the active n film, the nature and cause of the i layer has remained unknown.

248 RNP

Heteroepitaxial GaAs on Al_2O_3 , III. The Formation and Electrical Properties of Zn- and Cd-Doped Films

H. M. Manasevit and A. C. Thorsen, Autonetics Division, Rockwell Corp.

An all metal-organic-hydride chemical vapor deposition process has been used to produce p -type GaAs films on sapphire. Dimethylcadmium (DMCd) and diethylzinc (DEZ) have been combined with trimethyl-gallium-arsine to produce films with maximum net acceptor carrier concentrations of about 2×10^{17} and $8 \times 10^{16} \text{ cm}^{-3}$ respectively. These upper limits on doping level are found to be an exponential function of temperature and can be related to the vapor pressure of the respective elements. Nearly bulk electrical properties have been achieved in Zn-doped films as thin as 1μ and in thick ($>10 \mu\text{m}$) Cd-doped films.

249 RNP

Plasma Resonance on P-Type Gallium Arsenide

J. W. Philbrick, C. A. Pillus, and C. P. Schneider, IBM Components Division.

The variation of the position of the infrared reflectivity minimum with carrier concentration from our Hall Effect and reflectivity measurements, from unpublished data of other workers, and from selected data from the literature was determined. The calibration curve for the determination of concentration is

$$\text{Lambda} = 1.796 \times 10^{11} N^{-0.5000}$$

where: Lambda is the wavelength position of the reflectivity minimum in microns, and N is the concentration in cm^{-3} . The equation is valid for concentrations from 3.5×10^{16} to 1.2×10^{20} . Concentrations determined from this equation agree with those determined from Hall measurements to $\pm 12.64\%$ (1 std dev).

250 RNP

The Precipitation of Ga_2O_3 in GaP

M. Kowalchik, A. S. Jordan, and M. H. Read, Bell Telephone Laboratories.

Needlelike precipitates (up to 60 μm long) of β - Ga_2O_3 have been observed in O-doped GaP crystals grown between 1050°-1035°C by liquid-phase epitaxy under nearly isothermal conditions in sealed ampoules. The amount of this precipitated second phase in GaP drastically increases with increasing Ga_2O_3 additions to the melt between 0.01 and 0.35 m/o. The precipitates can be eliminated by either adding less than 0.01 m/o Ga_2O_3 to the melt or by imposing a temperature gradient over the ampoule.

251 RNP

Electroluminescence Characteristics and Efficiency of GaAs Si Diodes

I. Ladany, RCA Laboratories.

The need for devices to pump visible light-emitting phosphors has led to a study of the peak wavelength, spectral half-width, and efficiency of liquid phase epitaxial GaAs:Si diodes as a function of silicon concentration in the melt. The peak of the emission spectrum could be shifted from about 9200 to 10,000 \AA by varying the silicon concentration. For all wavelengths investigated, uncoated diodes with 6% efficiency could be made, with some going as high as 10%. External, room temperature, d-c efficiencies up to 32% were measured on diodes provided with high-index glass domes. The spectral half-width was found to increase with silicon concentration, and was especially large for growth on the 111B plane. The internal absorption loss was found to be significant for all peak wavelengths. These findings are discussed in the light of current models of recombination processes in heavily doped semiconductors.

252 RNP

Defect Scattering in Epitaxial PbTe Thin Films

T. S. Jayadevaiah and R. E. Kirby, University of Wisconsin, Milwaukee, Wis.

Mobility studies have been made on single-crystal (100) PbTe thin films grown on NaCl substrates. The defect scattering mobility is determined by subtracting the lattice and surface scattering mobilities from the experimental effective mobility. The T^{-1} dependence of the defect scattering in films of 2000-10,000 \AA thickness indicates dislocation scattering as opposed to the usual model of boundary-limited scattering in lead chalcogenide films. Electron microscopic studies support this result. The mobility increases with thickness because the films improve structurally with a consequent decrease in defect scattering decreases, and the contribution of surface scattering is insignificant to this effect.

253 RNP

Stress Effects and Interjunction Dislocations Formed during Phosphorus Diffusion into Silicon

E. D. Jungbluth, General Telephone & Electronics Laboratories, and P. C. Parekh, Sylvania Electric Products, Inc.

Planar phosphorus-type diffusions into silicon create a variety of dislocations both inside and outside the diffused-junction volumes. Four types of dislocations due to diffusion stresses are discussed. These include a high concentration of dislocation arrays within less than a micrometer of the surface, emitter-edge-type loops at junction boundaries, and two sets of linear arrays penetrating at least five times deeper than the junction and extending laterally between junctions into the nondiffused matrix. Stress effects as a function of depth are analyzed by x-ray diffraction topography. Evidence for dislocation motion and image force effects due to stress discontinuities are presented. Conditions necessary to promote dislocation generation in the nondiffused zones of both (111) and (001) surfaces are described.

Silicon and Germanium for your

▲ Research

▲ Engineering

▲ Development

▲ Radiation Detector

▲ Other Special

▲ Device Needs

Your responsive source for high quality ingots, slices, and polished wafers of silicon and germanium.

box 2047, midland, michigan 48640 (517) 631-1771

high performance technology inc.

semiconductor material center

First Annual Electronics Division Award



Forrest A. Trumbore

Dr. Forrest A. Trumbore of the Bell Telephone Laboratories received the first annual Electronics Division Award of The Electrochemical Society at the Spring Meeting in Los Angeles. The award was presented by Society president Mr. N. Corey Cahoon to Dr. Trumbore for his pioneering work in the

fields of solute incorporation in semi-conducting solid solutions and the role of impurities in pn junction luminescence. The award is granted annually to a member of the Society upon some recent technical achievement in, or outstanding contribution to, Electronic Science.

Dr. Trumbore received his B.S. degree in chemistry from Dickinson College in 1946 and his Ph.D. in Physical Chemistry from the University of Pittsburgh in 1950. He is the author or co-author of about forty publications and patents in the fields of crystal growth, luminescence and phase equilibria with primary emphasis on semiconductors, particularly on gallium phosphide in recent years. Dr. Trumbore joined Bell Laboratories in 1952. He is a member of The Electrochemical Society, the American Physical Society, and the American Association for the Advancement of Science. He has served as a Semiconductor Division Editor for the JOURNAL. He is an honorary member of Sigma Xi, Phi Lambda Upsilon, and Phi Beta Kappa.

F. M. Becket Memorial Award

The Electrochemical Society will offer the F. M. Becket Memorial Award to a qualified graduate student for the summer of 1971. This Award commemorates F. M. Becket, a man of great research and administrative ability and a former President of the Society, whose accomplishments in science and industry were outstanding. The stipend valued at \$1500 provides a grant-in-aid toward a summer's (at least two months) research and study overseas in the laboratory of a recognized research institute or institution of higher learning, selected from the approved list maintained by the F. M. Becket Memorial Award Committee.

The objectives of this Award are to stimulate and encourage education and participation in the fields of electrochemical science and industry concerned with specialty materials and processes as follows:

- Materials** such as refractory metals and compounds, intermetallics, graphite, fused salts, and rare earth metals;
- Equipment** for the utilization of electrical energy in materials synthesis;
- Processes** using arcs, vacua, plasmas, and electron and ion beams; and
- High temperature kinetics and thermodynamics phenomena** such as melting, vaporization, reactions, sintering, diffusion or oxidation occurring at high temperatures, high pressures, or vacua involving high temperature materials.

To be eligible for the Award, the entrant must qualify in one of the two following categories. He must be either

- a graduating senior of demonstrated ability, regularly enrolled in any recognized college, university, or institute of technology in continental United States or Canada, who intends to seek an advanced degree, or
- a graduate student, similarly enrolled, who is seeking an advanced degree. No limitations of sex, race, nationality, or religion are to be imposed by the Award Committee in determining the recipient of the Award.

The Award shall be presented on the basis of the following material:

- A complete transcript of the student's academic record.
- Two copies of a letter, over the signature of the head of the College or Department in which the student is enrolled, describing briefly his academic work, his campus activities, and presenting an estimate of his abilities.
- Two copies of a letter, over the student's signature, containing a brief biographical sketch, a detailed description of the nature and extent of his academic work, particularly as it may relate to the field of the Award, and an outline of his plans for the future. The student shall indicate, from the list provided by the Award Committee, his choice of a place of residence under the Award.

Application forms are available from the Executive Secretary, Mr. Ernest G. Enck, The Electrochemical Society, Inc., 30 East 42nd Street, New York, N. Y. 10017. Deadline for receipt of completed applications will be February 1, 1971; and the Award winner will be announced on April 1, 1971.

SECTION NEWS

Chicago Section

The Chicago section will hold the following meetings at the Chicago Engineering Club during 1970-1971:

November 12, 1970—"Zinc-Air Cells," Arthur Fleischer, Orange, N. J.

December 10, 1970—"The Influence of Reaction Product Properties on Corrosion Processes," M. J. Pryor, Olin Corporation, New Haven, Conn.

January 14, 1971—"Electronic Materials—Present and Future," N. B. Hannay, Executive Director of Research Materials Division, Bell Telephone Labs, Murray Hill, N. J.

February 11, 1971—"New Movements in Patent Law," Phil Hill, Patent and Licensing Department, Standard Oil of Indiana.

March 11, 1971—"Electrochemistry of Fused Salts," H. Laitinen, University of Illinois, Urbana, Ill.

April 9, 1971—"Electrochemistry as a Valuable Tool in Organic Synthesis," R. A. Benkeser, Purdue University, W. Lafayette, Ill.

A social hour and dinner will precede each meeting.

Metropolitan New York Section

The Metropolitan New York Section held its first meeting of the 1970-71 schedule at Stonehall Inn, 6 Stone Street, New York City, on September 23, 1970. A small group braved the heat and disregarded the daylong harping by news media on an imminent power failure in the city. They were rewarded by Ralph J. Brodd's interesting, excellent, and straightforward presentation, "Current Distribution In and On Porous Electrodes." Dr. Brodd set the stage by his application of Shepherd's work on the representation of battery capacities, to the current distribution over the apparent electrode area and showed how practical deductions may be derived by defining applicable thermodynamic, kinetic, and structural conditions. The application of the principles was illustrated for the porous "flow-through" electrode using oxygen dissolved in solution as the reactant (active material or depolarizer).

Palmer Langdon
Secretary-Treasurer

NEWS ITEM

Electrodeposition Process Licensed

General Technologies Corporation, a subsidiary of Cities Service Company, has acquired an exclusive license for Union Carbide Corporation's patented electrodeposition process for refractory metals.



Web specialists

We are proud of the broad acceptance of our polyamide separator/adsorber webs, a basic ingredient of most closed cell secondary alkaline batteries produced throughout the free world.

But there is more to our product line:

By employing virtually all known non-woven manufacturing techniques . . . and then some we produce other separators for primary and secondary batteries and fuel cells. Our separators are specifically designed for resistance to acid, alkaline or non-aqueous electrolyte—even for heat sterilized systems; they are adsorbent, have controlled porosity, can be heat sealed and gauged down to 1 mil if necessary.

If we don't already have what you need we'll develop it—just for you!

Pellon®
CORPORATION
Industrial Division

Webs to meet the exacting requirements of today's industry.
221 Jackson St., Lowell, Mass. 01852
617-454-0461 © Pellon Corp. 1970

plenum
PUBLISHING CORPORATION

ADVANCES IN CORROSION SCIENCE AND TECHNOLOGY*

VOLUME 1

Edited by **M. G. Fontana** and **R. W. Staehle**, Corrosion Center, Department of Metallurgical Engineering, Ohio State University, Columbus, Ohio
For the first time a new series on corrosion science and technology will attempt to offer solutions to complex technological corrosion problems by applying analytical techniques which have served physical metallurgy, fundamental chemistry, measurement science, and continuum theory.

CONTENTS: D. de G. Jones and H. G. Masterson, Techniques for the measurement of electrode processes at temperatures above 100 degrees C • R. M. Latanision and A. R. C. Westwood, Surface and environment-sensitive mechanical behavior • Giordano TrabANELLI and Vittorio Carassiti, Mechanism and phenomenology of organic inhibitors • Sakae Tajima, Anodic oxidation of aluminum.

374 PAGES
SBN 306-39501-0

SEPTEMBER 1970

\$22.50

HETEROGENEOUS KINETICS AT ELEVATED TEMPERATURES

Edited by **G. R. Belton** and **W. L. Worrell**, School of Metallurgy and Materials Science, University of Pennsylvania, Philadelphia, Pa.

This book emphasizes the latest experimental techniques, as well as the most recent research findings. The papers contained in the book form an up-to-date and authoritative report on current knowledge of the kinetics of interfacial reactions between the gaseous phase and a condensed phase or between gaseous phases. The papers also discuss in detail microscopic and macroscopic transport phenomena that have a direct bearing on the investigation and interpretation of high temperature interfacial reactions.

Proceedings of an International Conference in Metallurgy and Materials Science held at the University of Pennsylvania, September 8-10, 1969

532 PAGES
SBN 306-30500-3

AUGUST 1970

\$27.50

SILICON CARBIDE

Structure, Properties, and Uses

Edited by **I. N. Frantsevich**, Institute of Materials Science, Academy of Sciences of the Ukrainian SSR

Translated from Russian by **Simon Lyse**

Detailed presentation of such topics as: equilibria in systems containing silicon carbide, crystal structure and optical and electrophysical properties, physical and chemical bases for preparing materials from polycrystalline silicon carbide, the behavior of these materials in various media, and methods of preparing and doping silicon carbide single crystals for semiconductor use.

276 PAGES
SBN 306-10838-0

MAY 1970

\$35.00

PROTECTIVE COATINGS ON METALS*

VOLUME 2

Edited by **G. V. Samsonov**, Laboratory of Metallurgy of Rare Metals and Refractory Compounds, Institute of Cermet and Special Alloys, Academy of Sciences of the Ukrainian SSR, Kiev

Translated from Russian by **Z. S. Michalewicz**

Reports on many new theoretical and practical aspects of research for obtaining materials with different surface and bulk properties by means of surface impregnation. In view of the scarcity and high cost of such metals as nickel and molybdenum, the techniques described in this volume offer industry the opportunity for substantial economies.

212 PAGES
SBN 306-18322-6

APRIL 1970

\$27.50

* Place your continuation order today for books in this series. It will ensure the delivery of new volumes immediately upon publication; you will be billed later. This arrangement is solely for your convenience and may be cancelled by you at any time.

consultants bureau/plenum press

Divisions of Plenum Publishing Corporation
227 W. 17th ST., NEW YORK, NEW YORK 10011

(News Item Continued)

Three \$1000 Electrochemical Society Summer Fellowships to be Awarded

The Electrochemical Society will offer three fellowships for qualified graduate students for the summer of 1971. Each fellowship will have a stipend of \$1000 and its purpose is to assist a student to continue his graduate work during the summer months in a field of interest to The Electrochemical Society. These fellowships are to be known as The Edward Weston Fellowship, The Colin Garfield Fink Fellowship, and the ECS Summer Fellowship Award.

Candidates qualifications: "The award shall be made without regard to sex, citizenship, or race, or financial need. It shall be made to a graduate student pursuing work between the degree of B.S. and Ph.D. in a college or university in the United States or Canada, and who has received a nine-month grant preceding the summer period and who will continue his studies after the summer period. A previous holder of the award is eligible for reappointment."

Qualified graduate students are invited to apply for these fellowships. Ap-

plicants should complete an application form and supply:

1. A brief statement of educational objectives.
2. A brief statement of the thesis research problem, including objectives, work already accomplished, and work planned for the summer of 1971.
3. A transcript of undergraduate and graduate academic work.
4. Two letters of recommendation, one of which should be from his research adviser.

Application forms are available from the Chairman of the Fellowship Awards Subcommittee, to whom completed applications and letters of recommendation should be sent: Professor David M. Mohilner, Department of Chemistry, Colorado State University, Fort Collins, Colo. 80521.

Deadline for receipt of completed applications will be March 2, 1971, and award winners will be announced on May 1, 1971.

The licensing agreement grants General Technologies all rights to process patents and technical know-how as well as production deposition cells developed exclusively for the process by Union Carbide. General Technologies will make the process available under the trade name "Metalating."

"Metalating" services will initially offer deposition of tantalum metal coatings. Processing cells are now in operation and General Technologies is accepting materials for tantalum plating.

NEW PRODUCTS

Battery-Powered Semiconductor Lasers—Bell Laboratories scientists have devised a new laser, smaller than a grain of sand, that can be powered by ordinary dry cell batteries. It will emit a beam of near-visible infrared light. The new laser, designed by Izuo Hayashi and Morton Panish with the aid of their co-workers P. W. Foy and S. Sumski, is a semiconductor device that operates continuously at normal room temperature (75-80°F).

The new semiconductor laser is a double heterostructure diode composed of four layers of gallium aluminum arsenide alternating with gallium arsenide. These layers are doped with tin, silicon, zinc, and germanium. They are grown by a technique known as liquid phase epitaxy.

New Nickel-Cadmium Batteries—A new complete product line of industrial nickel-cadmium batteries has been announced by Exide Power Systems Division of ESB Incorporated, Philadelphia.

Operating within a temperature range of -60°F and 140°F the Exide nickel-cadmium batteries feature a choice of three plate types including a double-positive steel pocket plate. Three cell ranges, low rate, medium rate, and high rate are listed. Exide offers the 169 new cell types in either plastic or steel cell containers.

For further information please contact: O. D. Dean, Vice President, Electro-Mechanical and Alkaline Products, Exide Power Systems Division, ESB Incorporated, Rising Sun & Adams Avenues, Philadelphia, Pa. 19120.

FROM PUBLISHERS

"Sputtering," Defense Documentation Center, Alexandria, Va., April 1970. Order DDC bibliography AD-703 900, 158 pages; \$3.00.

"Activation Analysis: A Bibliography," edited by G. J. Lutz, R. J. Boreni, R. S. Macdock, and W. W. Meinke, National Bureau of Standards, December 1969. Order SD Cat. No. C13.46:467; or NBS TN-467, 264 pages; \$8.50 per set of 2 volumes, sold in sets only.

6TH ADVANCES IN BATTERY TECHNOLOGY SYMPOSIUM

Sponsored by the Southern California-Nevada Section of The Electrochemical Society, December 4, 1970, Union Oil Auditorium, 461 South Boyleston Street, Los Angeles, California, at 9 A.M.

INVITED SPEAKERS AND TOPICS INCLUDE:

- Galen Frysinger (Electric Storage Battery, Inc.) Batteries for the 70's
- David Feder (Bell Telephone), Bell Systems Lead Acid Battery Design
- Jose Giner (Tyco Laboratories, Inc.), Rechargeable Oxygen Electrode
- Argonne National Labs, Electrode Structures for Molten Salt Batteries
- George Hoffman (McDonnell Douglas Astronautics Co.), The All-Electric Bus
- T. Katan (Lockheed Missiles & Space Co.), Structure and Performance of Oxygen Electrodes
- C. J. Menard (Gould Inc.), Nickel Plaque Substrates for Cadmium Electrodes
- F. G. Will (General Electric Co.), Morphology and Capacity of a Cadmium Electrode: Studies on a Simulated Pore

A Registration Fee of \$10 includes the published proceedings of the meeting. Those desiring to pre-register may send checks payable to Southern California-Nevada Section ECS to E. L. Littauer, Co-chairman, Lockheed Aircraft Service Company, Box 33, Ontario, California 91764.

"Bibliography on the High Temperature Chemistry and Physics of Materials," J. J. Diamond, editor, April 1970. Order SD Cat. No. C13.10:315-5; or NBS-SP 315-5,* 18 pages; \$7.50.

"Electrolytic Conductance and the Conductances of the Halogen Acids in Water," by W. J. Hamer and H. J. DeWane, May 1970. Order SD Cat. No. C13.48:33; or NSRDS-NBS 33,* 37 pages; \$5.00.

* Order from the Superintendent of Documents, U.S. Government Printing Office, Washington, D.C. 20402; or the Clearinghouse for Federal Scientific and Technical Information, Springfield, Va. 22151.

BOOK REVIEWS

"Clean Surfaces: Their Preparation and Characterization for Interfacial Studies" edited by G. Goldfinger. Published by Marcel Dekker, Inc., New York, 1970. pp. xix and 385; \$18.75.

This is another symposium volume with the addition that the papers given in April 1968 were subsequently revised and amplified. Some key words and phrases from the chapter headings are polyethylene, monodisperse latexes, blood, ellipsometry, ultrahigh vacuum, scanning electron microscope, alkali halides, chemisorption, supersaturated colloidal states, electrochemical spreading of liquids, aqueous, leached glass, mineral, finite lattices, oxide and organic contaminants. Thus the attempt to bring together all kinds of surface chemists and their disciplines appears to have succeeded.

The general appearance of the book is good, most of the photographic reproductions being quite clear. It is unfortunate that no subject index is included—this severely limits usage for casual reference.

K. E. Johnson
University of Saskatchewan
Chemistry Department

"Characterization of Semiconductor Materials," Texas Instruments Electronics Series, by Philip F. Kane and Graydon B. Larrabee. Published by McGraw-Hill Book Co., New York, 1970. 351 pages; \$18.50.

This book is a first of its kind in an area thus far carefully ignored by authors of technical books in solid state physics and technology. The only objection one might have is that the list of references on the second chapter, entitled "Semiconductor Principles," is somewhat thin.

The third chapter entitled "Bulk-material Characterization," one of the highlights of the book, discusses most of the common elements of semiconductor technology in terms of their histories, sources, and purity analysis.

The remaining seven chapters consider the evaluation of bulk grown, epitaxially grown, and diffused semiconductor material in practically all of the known and accepted ways. In general the balance in the descriptions of the many various techniques appears to

ECS Membership Statistics

The following three tables give a breakdown of membership as of October 1, 1970. In Table I it should be noted that the totals appearing in the right-hand column are not the sum of the figures in that line since members belong to more than one Division. The totals listed are the total membership in each section.

Table I. ECS Membership By Sections and Divisions

Section	Division											
	Battery	Corrosion	Dielectrics & Insulation	Electro-deposition	Electronics	Electro-Organic	Electrothermics & Metallurgy	Industrial Electrolytic	Theoretical Electrochemistry	No Division	Total as of 10/1/69	Total as of 10/1/70
Chicago	52	33	13	35	43	17	12	15	30	6	178	182
Cleveland	52	26	3	31	35	14	22	27	47	7	176	166
Detroit	44	40	9	61	22	16	11	6	51	4	147	140
Midland	3	4	1	2	10	3	6	11	4		42	34
New York												
Metropolitan	151	89	49	123	262	47	67	53	118	21	706	665
Niagara Falls	15	15	14	20	35	7	25	33	20	11	133	122
Pacific N.W.	11	10	3	12	6	5	5	13	20	1	57	50
Philadelphia	57	31	13	41	64	11	21	21	46	12	231	217
Pittsburgh	13	43	12	34	59	8	37	26	40	3	183	177
San Francisco	20	23	23	23	116	6	18	11	36	2	192	213
National Capital Area	48	28	12	27	39	8	16	6	42	1	163	152
Ontario-Quebec	15	29	15	26	37	1	41	30	37		145	148
Boston	38	39	15	35	121	11	29	6	52	5	270	261
S. Calif.-Nevada	64	44	16	58	132	20	37	27	75	4	269	288
Columbus	16	22	7	15	22	4	19	6	19	1	87	80
Indianapolis	7	10	9	8	23	4	9	3	13		68	56
North Texas	13	9	13	17	93	7	11	4	12	3	149	132
South Texas	4	10	1	2	12	3	2	7	11	3	38	41
Non-Section	186	169	69	170	256	73	116	124	227	83	855	936
TOTAL as of October 1, 1969	837	678	262	758	1387	259	525	452	918	168	4089	
TOTAL as of October 1, 1970	809	674	297	740	1387	265	504	429	900	167		4060

Table II. ECS Membership By Grade

	Total as of 10/1/69	Total as of 10/1/70
Active	3658	3606
Life	23	25
Emeritus	98	100
Honorary	7	7
Associate	29	32
Student	156	165
Representatives of Patron and Sustaining Members	118	125
Total	4089	4060
Delinquent	173	231
Total	4262	4291

Table III. ECS Patron and Sustaining Membership

	Total as of 10/1/69	Total as of 10/1/70
Patron Member Companies	7	7
Sustaining Member Companies	119	122

Puzzle Me This*

Solution to puzzle shown on page 380C



Only 2 marbles can be transferred out of the first cup. The contents of the 2 cups will then be one of the following:

	FIRST CUP			SECOND CUP		
	Color A	Color B	Color C	Color A	Color B	Color C
1st Possibility	3	3	1	3*	3*	5
2nd Possibility	3	2	2	3	4	4

To assure at least 2 of each color in the first cup, at least 7 marbles must be transferred back, because the first 6 might be the 3 Color A and the 3 Color B marbles represented by the starred 3's in the first possibility shown above. Therefore, there will be 4 marbles remaining in the second cup.



STACKPOLE

GRAPHANODES®
Your best answer, also.

PURIFIED SALTS AND SALT MIXTURES FOR ELECTROCHEMICAL AND FUSED SALT CHEMISTRY



**ANDERSON PHYSICS
LABORATORIES, INC.**

Box 2680 Station A

Champaign, Illinois

Telephone 1 (217) 356-1347

be satisfactory, but there are a few glaring distortions. For example, the inclusion of Hall measurement data sheets on pages 94, 95, and 96 is probably excessive detail, while the short section on the differential capacitance technique overlooks all of the recent developments using automatic profiling machines. On the whole, this book is a timely and worthwhile contribution. Its greatest value will be as a reference book, and it should be found readily accessible in all semiconductor characterization laboratories.

Stephen Knight
Bell Telephone Laboratories,
Murray Hill, N. J.

POSITIONS WANTED

Please address replies to the box number shown, c/o The Electrochemical Society, Inc., 30 East 42 St., New York, N.Y. 10017.

Positions Wanted

Society members of any class may, at no cost and for the purposes of professional employment, place not more than three identical insertions per calendar year, not to exceed 8 lines each. Count 43 characters per line, including box number, which the Society will assign.

Electrochemist—Ph.D.—Six years' basic and applied research in electrodeposition, high energy density batteries, corrosion, and electroanalytical techniques. Publications. Seeks R & D or teaching position. Reply Box C-39.

Physical-Inorganic Chemist—Ph.D. 1957. Diverse experience in product and process R & D. Extractive metallurgy, refractory metals. Special and electronic materials, pigments, chlor-alkali. Seeks responsible R & D or technical staff position. Reply Box C-40.

ADVERTISER'S INDEX

Anderson Physics Laboratories	412C
Foote Mineral Company	406C
Great Lakes Carbon Corp., Graphite Products Division	Cover 2
High Performance Technology	407C
The Kendall Company	375C
Pellon Corp. Industrial Division	409C
Plenum Publishing Corp.	409C
Stackpole Carbon Corp.	380C, 412C
Veeco Instruments Inc.	379C

ATTENTION, MEMBERS AND SUBSCRIBERS

Whenever you write to The Electrochemical Society about your membership or subscription, please include your Magazine address label to ensure prompt service.

ATTACH LABEL HERE

Change of Address

To change your address, place magazine address label here. Print your NEW address below. If you have any question about your subscription or membership, place your magazine label here and clip this form to your letter.

Mail to the Circulation
Department, The Electro-
chemical Society, Inc., 30
East 42 St., New York,
N. Y. 10017.

name

address

city

state

zip code



INSTRUCTIONS TO AUTHORS OF PAPERS
 (Revised 4/1/69)

Statements of Editorial Content

JOURNAL OF THE ELECTROCHEMICAL SOCIETY is the official journal of the Society and contains four sections totaling some 2500 editorial pages annually:

Electrochemical Science

the fundamental research section serves the interdisciplinary needs of chemistry, physics, biology, and medicine, as they pertain to electrochemistry and to electrochemical phenomena. Its editorial interests include research work in such areas as batteries, fuel cells, corrosion, electrothermics and metallurgy, electrodeposition, electro-organic reactions and phenomena, and allied work of a theoretical electrochemical nature. Written for the research scientist in industry, government, the independent laboratory, and the university, it contains contributed Papers, Notes, and Brief Communications describing current basic research of original character.

Solid State Science

the fundamental research section serves the interdisciplinary interests of chemistry, physics, electronics, biology, and medicine, as they pertain to solid state electrochemistry and to solid state electrochemical phenomena. Its editorial interests include such areas as dielectrics and insulation, electrothermics and metallurgy, semiconductors, luminescence, and related solid state investigations. Written for the research scientist in industry, government, the independent laboratory, and the university, it contains contributed Papers, Notes, and Brief Communications describing current basic research of original character.

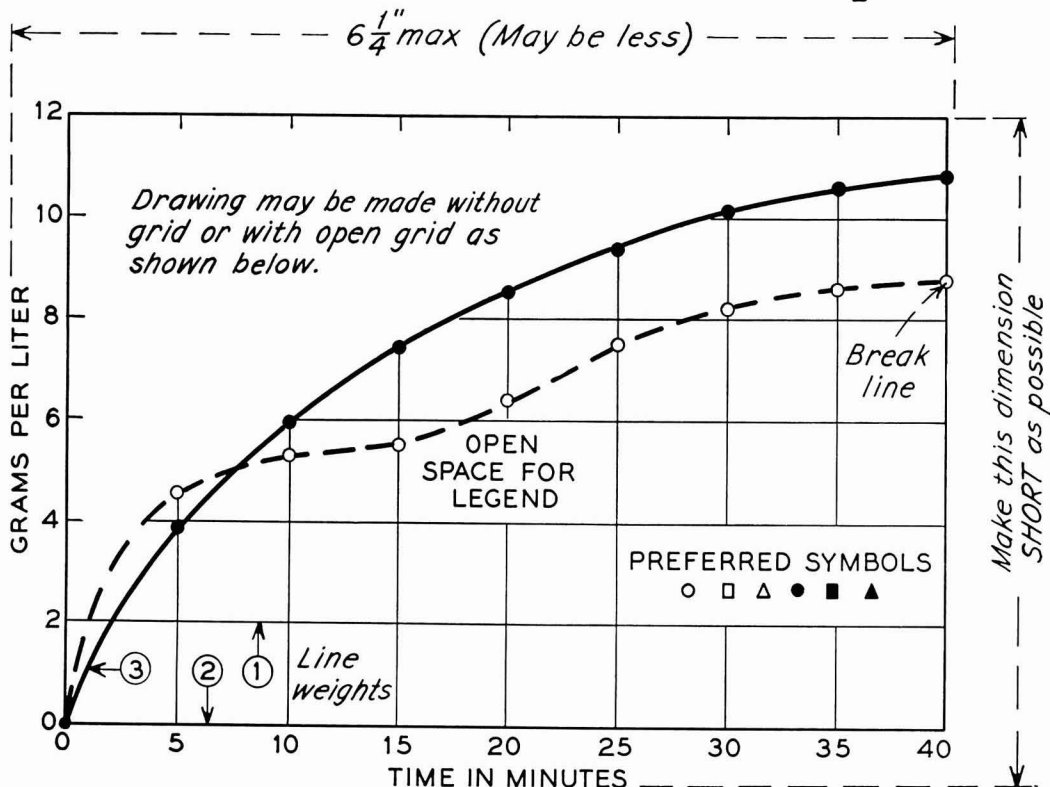
Electrochemical Technology

those responsible for research and development of electrochemical processes, and in design and production of products and systems which rely on electrochemical phenomena for their function. It is written for the researcher, engineer, designer, and scientist concerned with such products and processes as: batteries, fuel cells, corrosion, dielectrics and insulation, electrodeposition, electrothermics and metallurgy, semiconductors, luminescence, and related solid state investigations. Written for the research scientist in industry, government, the independent laboratory, and the university, it contains contributed Papers, Notes, and Brief Communications describing current application of electrochemistry and electrochemical phenomena to products and systems. Its editorial interest is current progress in the application of electrochemistry and electrochemical phenomena to new and improved processes for the preparation of materials and devices and to the solution of manufacturing and processing problems.

Electrochemical Society Reviews and News

is the section serving the interdisciplinary interests of chemistry, physics, electronics, metallurgy, biology, medicine, and engineering, as they pertain to electrochemistry and to electrochemical phenomena. Written for the scientist and engineer in industry, government, the independent laboratory, and the university, it publishes invited and contributed reviews of current research in such areas as batteries, fuel cells, corrosion and reaction mechanisms, electrothermics and metallurgy, semiconductors, luminescence, and related solid state investigations. The normal review should not exceed 20 manuscript pages and furnish a current and critical analysis with citation only of truly pertinent references. Also included is the Electrochemical Society News Section, keeping the readers apprised of Society activities, news of its 19 sections and 9 divisions, book reviews, symposium plans, personals, etc.

SAMPLE CURVE DRAWING FOR REDUCTION TO $\frac{1}{2}$ SIZE



GENERAL

Manuscripts must be submitted in triplicate to expedite review. They should be typewritten, double-spaced, on one side, with 2½–4 cm (1½ in.) margins.

Titles should be brief, followed by the author's name and professional connection. Text should be as brief as is consistent with clarity and should omit introductory or explanatory material which may be regarded as familiar to specialists in the particular field. Proprietary and trade names should be generally avoided; if used with discretion, they should be capitalized to protect the owners' rights. Authors are encouraged to suggest qualified reviewers for their manuscripts; the Editor reserves the right to final choice. It is helpful if the author tells which ECS Division would be most interested in his paper.

Present Society policy permits manuscript review in several weeks. Manuscripts returned to the author for revision should be resubmitted promptly to allow publication in five months or less from date of original receipt.

TYPES OF ARTICLES

Fundamental Papers describe original research of basic nature and must have adequate scientific depth. **Applied Technical Papers** may deal with any practical aspect of the fields of interest to the Society, e.g., plant design or operation, production and control methods, economics. Articles of wide diversity of interest are acceptable, but subjects primarily covered in other specialized journals (e.g., analytical or nuclear chemistry) are not considered appropriate. **Review Papers** furnish a current and critical analysis of the subject with only pertinent references cited. Each paper should begin with an **Abstract** which should state the scope of the paper and summarize fully its results and contents. Suitable headings and subheadings should be included, but sections should not be numbered. Articles in recent issues should be consulted for current style.

Notes are used for reporting briefer research, developmental work, process technology, new or improved devices, materials, techniques, or processes which do not involve more extensive basic scientific study. No abstract is required. **Brief Communications** are used only to report new information of scientific or technological importance which warrants rapid dissemination. They need not necessarily reflect a complete research project; interim reports are acceptable. Length should be a nominal 700 words, with up to two illustrations. No abstract is required. Publishing time is normally less than three months.

EQUATIONS

Mathematical Equations should be written on a single line if possible, and parentheses, brackets, the solidus ($/$), negative exponents, etc., may be used freely for this purpose. Authors are urged to consult Chapter VI of the "Style Manual" of the American Institute of Physics (available for \$1.00 at American Institute of Physics, 335 East 45 Street, New York, N. Y. 10017) and to follow the patterns described there.

SYMBOLS

Authors are encouraged to use symbols extensively. These should be defined in a list at the end of the paper, with units given. For example:

a, b, \dots = empirical constants of Brown equation

f_1 = fugacity of pure i th component, atm

D_e = volume diffusion coefficient, cm²/sec

KEY WORDS

Authors are responsible for supplying a list of key words, to facilitate information retrieval. Generic terms generally are to be avoided. Key words acceptable to **Chemical Abstracts** are also generally acceptable in Society publications. List key words in the margin of the first page of the manuscript.

ABBREVIATIONS AND UNITS

The AIP "Style Manual" referred to here gives a suitable list of common **Abbreviations**. Units usually will be abbreviated without periods throughout the text, as sec, min, hr, cm, mm, etc. **Metric Units** should be used throughout, unless English units are clearly more appropriate in the area of discussion.

POTENTIAL SIGNS

Electrode Potentials: Authors are urged to state and make use of the polarity of test electrodes with respect to the reference electrode used, i.e., Zn is normally negative, Cu normally positive with respect to the standard hydrogen electrode. The sign for the emf of a cell should conform to the free energy change of the chemical reaction as written or implied, in accordance with the definition $\Delta G = -nFE$. These suggestions agree with the IUPAC conventions adopted in 1953.

REFERENCES

Literature References should be listed on a separate sheet at the end of the paper in the order in which they are cited in the text. Authors' initials must be given, and the style and abbreviations adopted by **Chemical Abstracts** should be used. Any recent issue of Society Journals may be consulted. Literature cited should be readily available; consequently personal communications, Department of Defense (DOD), and Office of Technical Services (OTS) citations should be minimized. When references are not readily accessible, **Chemical Abstracts** citation numbers must be supplied.

PUBLICATION CHARGE

A charge of \$40 per printed page is made for publication of technical material in Society journals. A 10% reduction is allowed if at least one author of an article is an ECS member or an employee of a Patron or Sustaining Member firm. However, acceptance of a manuscript is in no way dependent on such payment, and the charge may be waived in individual cases.

ILLUSTRATIONS

Photographs should be used sparingly, must be glossy prints, and should be mailed with protection against folding. **Micrographs** should have a labeled length unit drawn or pasted on the picture. On both, label "top" where any uncertainty might arise. **Captions** for figures (including photographs) must be included on a separate sheet. Figure numbers must not appear in the body of the figure; they will be removed if they do. **Numerical Data** should not be duplicated in tables and figures.

Drawings and Graphs ordinarily will be reduced to 8.3 cm (3¼ in.) column width, and after such reduction should have lettering no less than 0.15 cm high. Lettering must be of letter-guide quality. India ink on tracing cloth or paper is preferred, but India ink on coordinate paper with blue ruling is acceptable. Line weight 2 is used for borders and zero lines. When several curves are shown, each may be numbered and described in the caption. Lettering shown is approximately ⅓ in. in plotting current or potential as ordinate, increasing negative values should go down. The following information conforms to suggestions of the United States of America Standards Institute (USA Report Y14.1-1959).

Call for Papers

139th National Meeting

Washington, D.C., May 9-14, 1971

Divisions which have scheduled sessions are listed on overleaf, along with symposium topics.

1. Symposium Papers.

Authors desiring to contribute papers to a symposium listed on overleaf should check first with the symposium chairman to ascertain appropriateness of the topic.

2. General Session Papers.

Each of the several Society Divisions which meet in Washington, D. C., can plan a general session. If your paper does not fit readily into a planned symposium, you should specify "General Session."

3. To Submit a Meeting Paper.

Each author who submits a paper for presentation at a Society National Meeting must do three things:

A—Submit one original 75-word abstract of paper to be delivered, use the form printed on the overleaf or a facsimile. This abstract is required for consideration for scheduling at the meeting. **Deadline for receipt of 75-word abstract is December 1, 1970.**

B—Submit original and one copy of an Extended Abstract of the paper. **Deadline for receipt of Extended Abstract is January 1, 1971.** See (5) below for details.

C—Determine whether the meeting paper is to be submitted to the Society Journal for publication. See (6) below for details.

Send all material to The Electrochemical Society, Inc., 30 East 42nd Street, New York, N. Y. 10017.

Unless the 75-word and required Extended Abstracts are received by stated deadlines, the papers will not be considered for inclusion in the program.

4. Meeting Paper Acceptance.

Notification of acceptance for meeting presentation, along with scheduled time, will be mailed to authors with general instructions no earlier than two months before the meeting. Those authors who require more prompt notification are requested to submit with their abstracts a self-addressed postal card with full author-title listing on the reverse.

5. Extended Abstract Book Publication.

Division programs will be the subject of an Extended Abstracts volume in a manner prescribed by the Society Board of Directors. The volume is published by photo-offset directly from typewritten copy submitted by the author. Therefore, special care should be given to the following instructions to insure legibility.

A—Abstracts are to be from 500 to 1000 words in length (maximum two pages, single spaced) and are to contain to whatever extent practical all significant experimental data to be presented during oral delivery.

B—Please send original and one copy of the abstract typed single spaced. Use white bond paper, size 8½ x 11 inches, with 1¼ inch margins on all sides. Typing guide forms are available from symposium session chairman and from National Headquarters. Submit all copy in black ink. No handwritten corrections, please.

C—Title of paper should be in capital letters. Author(s) name and affiliation should be typed immediately below the title.

diately below. It is not necessary in the heading or body to designate paper as "Extended Abstract" or to quote the divisional symposium involved.

D—If figures, tables, or drawings are used total space for these cannot exceed one page. Submit only the important illustrations and avoid use of halftones. Lettering and symbols should be no smaller than ⅛ inch in size. Type captions no wider than figure dimensions, placing figure caption at bottom of figure and table title at top of table.

E—Mail to The Electrochemical Society, Inc., 30 East 42nd Street, New York, N. Y. 10017, unfolded.

Abstracts exceeding the stipulated length will be returned to author for condensation and retyping.

6. Manuscript Publication in a Society Journal.

All meeting papers upon presentation become the property of The Electrochemical Society, Inc. However, presentation incurs no obligation to publish. If publication in Journal is desired, papers should be submitted as promptly as possible in full manuscript form in order to be considered. If publication elsewhere after presentation is desired, written permission from Society Headquarters is required.

Washington, D. C., Meeting Symposia Plans—Spring 1971

May 9-14, 1971

Dielectrics and Insulation Division Symposia Plans

The Dielectrics and Insulation Division has planned Symposia on Electronic Applications of Ceramic Materials and Deposited Thin Film Dielectric Materials and Processes, as well as a Joint Symposium with the Electronics Division on Plastics for Environmental Protection and Encapsulation of Electronic Devices for the Spring Meeting in Washington, D. C., May 9-14, 1971.

Electronic Applications of Ceramic Materials

This Symposium will cover the general field of electronic ceramic materials. Specific topics to be included will be insulators or substrates for thick and thin film applications and electro-optic materials. A number of invited papers will be presented and contributed papers are also being solicited. For further information contact R. E. Mistler, Western Electric Engineering Research Center, P. O. Box 900, Princeton, N. J. 08540.

Deposited Thin Film Dielectric Materials and Processes

A Symposium on Deposited Thin Film Dielectric Materials and Processes is scheduled for the Spring 1971 Meeting of the Society.

There will be a number of invited papers; contributed papers are also being actively solicited. Subject matter for this symposium includes:

a. Studies on the electrical and mechanical properties of deposited thin film dielectrics.

b. New techniques for the deposition or control of thin film dielectrics.

c. Properties and applications of thin film dielectrics.

Comments and suggestions are welcome and should be directed to the Chairman of the Symposium, F. Vratny, and Co-Chairmen W. R. Sinclair and R. J. Strain, Bell Telephone Laboratories, Inc., Mountain Avenue, Murray Hill, N. J. 07974.

Dielectrics and Insulation and Electronics Divisions Joint Symposium Plans

Plastics for Environmental Protection and Encapsulation of Electronic Devices

The purpose of this Joint Symposium of the Dielectrics and Insulation and the Electronics Divisions is to present and discuss the various means to protect and encapsulate electronic devices and circuits by means of plastics and polymeric materials.

Topics of interest are the packaging requirements and device interactions (electrical mechanical, thermal, and chemical) as well as material types and properties. This includes techniques, equipment, testing, evaluation, repair, and long range reliability.

In particular we encourage papers on the theoretical and explanatory aspects of the behavior of plastics on electronic

a.) For receipt no later than December 1, 1970, submit a 75-word abstract of the paper to be delivered, on the form overleaf. b.) For receipt no later than January 1, 1971, submit two copies of

devices. All types of devices, both passive and active, including discrete semiconductors, integrated circuits, and hybrids will be considered. Suggestions and questions for the Dielectrics and Insulation Division should be directed to the Symposium Co-Chairman, A. Pfahnl, Bell Telephone Laboratories, 555 Union Blvd., Allentown, Pa. 18103. Suggestions and questions for the Electronics Division should be directed to the Symposium Co-Chairman, Ralph Olberg, Fairchild Research and Development Lab, Materials and Processes Department, 4001 Miranda Avenue, Palo Alto, Cal. 94304

Electronics Division Symposium Plans

In addition to the Joint Symposium with the Dielectrics and Insulation Division on Plastics for Environmental Protection and Encapsulation of Electronic Devices and the Joint Symposium with the Electrothermics and Metallurgy Division on New Techniques for Materials Characterization, the Electronics Division has planned a Symposium on Infrared Excited Visible Luminescence. There will also be Semiconductor General Sessions and Luminescence General Sessions.

Infrared Excited Visible Luminescence

The areas of interest for this Symposium will include the preparation, characterization, optical properties, energy transfer and luminescent properties of materials exhibiting luminescence from incoherent multiphoton excitation, as well as discussion of any properties of interest to their use in optoelectronic displays. Papers may range from theoretical investigations to device applications. For further information please contact Symposium Chairman Dr. Ralph Hewes, Lighting Research Laboratory, General Electric Company, Nela Park, Cleveland, Ohio 44112.

Semiconductor General Sessions

Original papers relating to the following areas are being solicited for the Semiconductor General Sessions.

1. Semiconductor Materials Preparation: synthesis, purification, crystal growth, shaping, epitaxy, heteroepitaxy, and thin film deposition.
2. Semiconductor Materials Evaluation: measurements of physical, chemical electrical, and optical properties.
3. Semiconductor Materials Processing for Devices and Integrated Circuits: diffusion, epitaxy, ion implantation, and effects of processing on materials properties.
4. Characterization of Semiconductor

an extended abstract, 500-1000 words.

Send all material to The Electrochemical Society, Inc., 30 East 42nd Street, New York, N. Y. 10017. See details on preceding page.

Materials for Specific Device and Integrated Circuit Application.

5. Dielectric Films Used on Semiconductor Devices and Integrated Circuits: grown films, deposited films, control of film properties, defects, patterning, MIS effects, breakdown phenomena in dielectric films, thin film capacitors, amorphous film switches, and dielectric isolation.

6. Metal Films Used on Semiconductor Devices and Integrated Circuits: film properties, silicon contact effects, deposition techniques and control, film defects related to substrate topology, electromigration, intermetallic formation, multilayer metallization, and burnout.

7. Resistive Films Used on Semiconductor Devices and Integrated Circuits: deposition techniques, control of film properties, and contact effects.

8. Reliability: physics of failure related to the materials and processes utilized in the fabrication of semiconductor components, and accelerated reliability testing.

9. Radiation Effects Pertinent to the Materials Systems Utilized in Semiconductor Devices and Integrated Circuits.

10. Packaging: materials and technologies important to the encapsulation of semiconductor components, and testing methods and results.

Suggestions and questions should be directed to the Chairman, I. A. Lesk, Motorola Semiconductor Products Division, 5005 East McDowell Road, Phoenix, Ariz. 85008.

Luminescence General Sessions

General sessions on luminescence and laser materials are being organized by the Luminescence Section of the Electronics Division for the Spring 1971 meeting in Washington, D. C. The areas of interest will include such topics as materials and phosphor synthesis, optical and luminescent properties of rare earth and non-rare earth activated phosphors, laser materials and properties, energy transfer, cathodoluminescence and phosphor screen applications.

Papers are being solicited from those workers active in research and development in these areas. The papers may range from theoretical investigations to device applications. While 25 minutes is the usual time allotted for presentation and discussion of scheduled papers, authors desiring more or less time should indicate this when submitting their short abstract. Questions concerning the program should be addressed to the Program Chairman, Frank C. Palilla, General Tele-

phone & Electronics Laboratories, 208-20 Willets Point Blvd., Bayside, N.Y. 11360.

There will also be a Recent News Papers Session. Triplicate copies of the 75-word abstract should be sent to Mr. Palilla at the above address. The submission deadline is April 1, 1971. Authors requiring more or less than the standard 15 minutes should so indicate.

Electronics and Electrothermics and Metallurgy Divisions Joint Symposium Plans New Techniques for Materials Characterization

The Electronics Division is jointly sponsoring this Symposium with the Electrothermics & Metallurgy Division to be held during the Spring Meeting, Washington, D. C. May 9-14, 1971.

This Symposium will cover new techniques for surface and bulk characterization of materials of interest to The Electrochemical Society. Suitable topics include: scanning electron microscopy, electron microprobe analysis, auger electron analysis, field ion microscopy, and high resolution electron microscopy.

Invited papers will predominate but appropriate contributed papers are also welcome. The Symposium Chairman is Victor A. Phillips, General Electric Research & Development Center, P. O. Box 8, Schenectady, N. Y. 12301.

Electro-Organic Division Symposia Plans

The Electro-Organic Division will sponsor a Symposium on New Directions in Organic Electrochemistry and will hold General Sessions at the Washington, D. C., Meeting, May 9-14, 1971. In addition, this Division is cosponsoring a Symposium on Electrochemistry and Biological Processes with the Theoretical Division.

New Directions in Organic Electrochemistry

This Symposium will be organized by Prof. Ralph N. Adams, Dept. of Chemistry, University of Kansas, Lawrence, Kansas, and Dr. Thomas B. Reddy, Stamford Research Laboratories, American Cyanamid Co., 1937 W. Main St., Stamford, Conn. 06904. The object of the Symposium will be to explore new trends in organic electrochemistry. A round table discussion of important new areas in this field will be conducted. Potential contributors may contact Prof. Adams.

General Sessions

The Electro-Organic Division will also hold General Sessions and papers are needed for inclusion in such sessions. For information please contact Dr. Thomas B. Reddy, American Cyanamid Co., 1937 W. Main St., Stamford, Conn. 06904.

Electro-Organic and Theoretical Divisions Joint Symposium Plans

Electrochemistry and Biological Processes

The Electro-Organic and Theoretical Divisions are scheduling a Joint Sym-

posium on Electrochemistry and Biological Processes for the Spring Meeting to be held in Washington, D. C., May 9-14, 1971. There will be approximately sixteen invited and contributed papers. The topics for discussion will be:

1. Electrochemistry of Biologically Significant Compounds
2. Charge Transfer in Membranes
3. Biological Electrodes

For further information, please contact, Dr. H. P. Silverman, Manager, Biosciences and Electrochemistry Dept., Systems Group of TRW, Inc., One Space Park, R1/2094, Redondo Beach, Cal. 90278.

Electrothermics and Metallurgy Division Symposia Plans

The Electrothermics and Metallurgy Division program for the Spring 1971 Washington, D. C., Meeting will include two Symposia, Chemical Reactions in Gaseous Discharges and Directional Solidification of Eutectics, as well as General Sessions. In addition the Division is cosponsoring a Symposium on New Techniques for Materials Characterization with the Electronics Division.

Directional Solidification of Eutectics

Recent developments in the application of controlled solidification of eutectic systems have identified the possibility of utilizing this technique to produce new materials for high temperature, high strength, as well as optical, electronic and magnetic applications. This Symposium will document the latest developments pertinent to directional solidification of eutectic systems including: theories of controlled eutectic freezing, crystallography and microstructure of eutectic alloys prepared by controlled solidification, as well as, utilization of modern chemical and analytical techniques pertinent to this area. Additional information can be obtained by contacting the Vice Chairman of the Electrothermics and Metallurgy Division, Dr. Joan B. Berkowitz, Arthur D. Little, Inc., 15 Acorn Park, Cambridge, Mass. 02140.

Authors wishing to submit papers for this Symposium should submit the normal 75-word and extended abstract by the appropriate date directly to Society Headquarters.

Chemical Reactions in Gaseous Discharges

The purpose of this Symposium is to discuss homogeneous gas phase reactions occurring in electric discharges and the engineering aspects of reactor design and scale-up. Papers pertinent to economic investigations or systems which possess commercialization feasibility would be particularly welcome. In addition the Symposium will cover research in the area of film deposition from species produced in the gas phase, including sputtering of material from target to a substrate. Specific topics of greatest interest include:

1. Discussions of the basic mechanisms of discharge reactions and

the relationship between the production of atomic and free radical intermediates and the electrical parameters controlling the discharge.

2. Proposals for reactor design and scale-up and evaluation of the economics of applying electric discharge chemistry.

3. Discussions of thin film deposition by the use of discharge devices, exclusive of transport of matter from electrodes.

4. Interpretation of material transfer processes occurring during sputtering glow discharge environments.

Authors wishing to participate in this Symposium should submit the normal 75-word and extended abstract directly to Society Headquarters by the appropriate dates. Additional information pertinent to this Symposium can be obtained by contacting Professor Alexis T. Bell, Department of Chemical Engineering, University of California, Berkeley, Cal. 94720, or Dr. Eric Kay, IBM Research Laboratories, Monterey and Cottle Roads, San Jose, Cal. 95114.

General Sessions

In addition to the Symposia on Chemical Reactions in Gaseous Discharges, Directional Solidification of Eutectics, and the Joint Symposium on New Techniques for Materials Characterization, General Sessions will be scheduled if sufficient papers pertinent to the interest of the Division are submitted. Suggestions and questions should be directed to Dr. Stanley T. Wlodek, Chairman E&M Division, c/o Stellite Division, Cabot Corporation, 1020 West Park Avenue, Kokomo, Ind. 46901.

Industrial Electrolytic Division Symposium Plans

Anodes for the Electrolytic Industries

This Symposium will cover metal, graphite and other nonconsumable anodes for the aqueous electrolytic industries. Papers are solicited covering anode materials, design, preparation, production, economics, mechanisms and operating characteristics in use. Suggestions and inquiries should be directed to the Chairman; Dr. W. C. Gardiner, Crawford and Russell, Inc., Stamford, Conn. 06904; or to the Co-Chairman, Dr. P. A. Danna, Olin Corporation, Research Center, 275 Winchester Avenue, New Haven, Conn. 06504.

Theoretical Electrochemistry Division

General Session

The Theoretical Electrochemistry Division will hold a General Session at the Spring 1971 Meeting to be held in Washington, D. C., May 9-14, 1971. Included in the program will be a panel discussion on the topic "Are Universities Meeting the Current Employment Needs in Electrochemistry"? For further information contact the session chairman, Dr. Christie G. Enke, Dept. of Chemistry, Michigan State University, East Lansing, Mich. 48823.

75-Word Abstract Form

WASHINGTON, D.C. MEETING

MAY 9-14, 1971

The Electrochemical Society, Inc.,
30 East 42 St., New York, N. Y. 10017

ABSTRACT NO.
(do not write in this space)

.....
(Title of paper)
.....

.....
(Authors) (Underline name of author presenting paper)
.....

.....
(Business Affiliation)
.....

.....
(Address)
.....

.....
(Tel. No.)
.....

.....
ECS Division
.....

.....
and Symposium
.....

Papers presented before a national technical meeting become the property of the Society and may not be published elsewhere without written permission of the Society. Papers presented at national technical meetings must be authored by a member or sponsored by an active member.

.....
Insert name of Society member author or sponsor
.....

(Type abstract in this area—double spaced.)

For Office Use

75-word Abstract sent to:

Date Extended Abstract rec'd:

Do you require any audiovisual equipment?

- ☐ 3¼ x 4 in. slide projector
☐ 35 mm (2 x 2 in.) slide projector
☐ other (specify)

Is a full length paper on this work to be submitted for Society Journal publication?

☐ Yes ☐ No

THE ELECTROCHEMICAL SOCIETY PATRON MEMBERS

Aluminum Co. of Canada, Ltd., Montreal, Que., Canada

The International Nickel Co., Inc., New York, N. Y.

Dow Chemical Co.

Inorganic Chemicals Dept., Midland, Mich.

Olin Corporation

Chemicals Div., Research Dept.,
New Haven, Conn.

General Electric Co.

Battery Business Section, Gainesville, Fla.

Chemical Laboratory, Knolls Atomic Power Laboratory,
Schenectady, N. Y.

Electronic Capacitor & Battery Dept., Irmo, S. C.

Lamp Div., Cleveland, Ohio

Materials & Process Laboratory, Large Steam
Turbine-Generator Dept., Schenectady, N.Y.

Nucleonics Laboratory, Pleasanton, Calif.

Research and Development Center,

Physical Chemistry Laboratory,

Solid State Physics Laboratory,
Schenectady, N.Y.

Union Carbide Corp.

Divisions:

Carbon Products Div., New York, N. Y.

Consumer Products Div., New York, N. Y.

Westinghouse Electric Corp.

Electronic Tube Div., Elmira, N. Y.

Lamp Div., Bloomfield, N. J.

Molecular Electronics Div., Elkridge, Md.

Research Laboratories, Pittsburgh, Pa.

Semiconductor Div., Youngwood, Pa.

THE ELECTROCHEMICAL SOCIETY SUSTAINING MEMBERS

Airco Spear Electrodes and Anodes,
St. Marys, Pa.

Allen-Bradley Co.,
Milwaukee, Wis.

Allied Chemical Corp.,
Industrial Chemicals Division,
Solvay, N. Y.

Aluminum Co. of America,
New Kensington, Pa.

American Cyanamid Co.,
Stamford Research Laboratories,
Stamford, Conn.

American Gas & Chemicals, Inc.,
New York, N. Y.

American Metal Climax, Inc.,
New York, N. Y.

American Potash & Chemical Corp.,
Los Angeles, Calif.

American Smelting and Refining Co.,
South Plainfield, N. J.

American Zinc Co.,
St. Louis, Mo.

The M. Ames Chemical Works, Inc.,
Glens Falls, N. Y.

Ampex Corp.,
Redwood City, Calif.

Applied Electrochemistry Inc.
Mountain View, California

Beckman Instruments, Inc.,
Fullerton, Calif.

Bell Telephone Laboratories, Inc.,
Murray Hill, N. J. (2 memberships)

Bethlehem Steel Corp.,
Bethlehem, Pa. (2 memberships)

Boeing Co.,
Seattle, Wash.

Burndy Corp.,
Norwalk, Conn.

Canadian Industries Ltd.,
Montreal, Que., Canada

Carborundum Co.,
Niagara Falls, N. Y.

Chrysler Corp.,
Detroit, Mich.

Clevite Corp.,
Burgess Battery Div.,
Freeport, Ill. (2 memberships)

Cominco Ltd.,
Trail, B. C., Canada

Dargo Technical Research Ltd.
London N.W.9, England

The Detroit Edison Co.,
Detroit, Mich.

Diamond Shamrock Corp.,
Painesville, Ohio

E. I. du Pont de Nemours & Co., Inc.,
Wilmington, Del.

Eagle-Picher Industries, Inc.,
Electronics Div.,
Joplin, Mo.

Eastman Kodak Co.,
Rochester, N. Y.

Electrode Corporation
Chardon, Ohio

Eltra Corp.,
Prestolite Div., Toledo, Ohio
C&D Batteries, Conshohocken, Pa.

Engelhard Industries, Inc.,
Newark, N. J.

The Eppley Laboratory, Inc.,
Newport, R. I.

ESB Inc.,
Philadelphia, Pa. (2 memberships)

Esso Research and Engineering Co.,
Engineering Technology Div.,
Florham Park, N. J.

Exmet Corp.,
Bridgeport, Conn.

SUSTAINING MEMBERS (CONTINUED)

Fairchild Semiconductor Corp.,
Palo Alto, Calif.

Falconbridge Nickel Mines Ltd.,
Thornhill, Ont., Canada

FMC Corp.,
Inorganic Chemicals Div.,
Buffalo, N. Y.
Inorganic Chemicals Div.,
South Charleston, W. Va.

Foote Mineral Co.,
Exton, Pa.

Ford Motor Co.,
Dearborn, Mich.

General Motors Corp.,
AC Electronics Div., Milwaukee, Wis.
Allison Div., Indianapolis, Ind.
Delco-Remy Div., Anderson, Ind.
Research Laboratories Div., Warren,
Mich.

**General Telephone & Electronics Labora-
tories, Inc.,** Bayside, N. Y.

Globe-Union, Inc.,
Milwaukee, Wis.

B. F. Goodrich Chemical Co.,
Cleveland, Ohio

Gould-National Batteries, Inc.,
Minneapolis, Minn.

Great Lakes Carbon Corp.,
New York, N. Y.

Harshaw Chemical Co.,
Cleveland, Ohio (2 memberships)

Hill Cross Co., Inc.,
West New York, N. J.

Honam Electric Industrial Co.,
Kwangju City, Korea

Honeywell, Inc.,
Minneapolis, Minn.

Hooker Chemical Corp.,
Niagara Falls, N. Y. (2 memberships)

HP Associates,
Palo Alto, Calif.

**Hughes Research Laboratories, Div. of
Hughes Aircraft Co.,** Malibu, Calif.

International Business Machines Corp.,
New York, N. Y.

International Minerals & Chemical Corp.,
Skokie, Ill.

IRC, Division of TRW, Inc.,
Philadelphia, Pa.

Jones & Laughlin Steel Corp.,
Pittsburgh, Pa.

K. W. Battery Co.,
Skokie, Ill.

Kaiser Aluminum & Chemical Corp.,
Div. of Metallurgical Research,
Spokane, Wash.

Kawecki Chemical Co.,
Boyetown, Pa.

Kennecott Copper Corp.,
New York, N. Y.

**Leesona Moos Laboratories, Div. of Lee-
sona Corp.,** Great Neck, N. Y.

Arthur D. Little, Inc.,
Cambridge, Mass.

Lockheed Aircraft Corp.,
Missiles & Space Div.,
Sunnyvale, Calif.

Mobil Oil Corp.,
Dallas, Texas

Molybdenum Corporation of America,
New York, N. Y.

Monsanto Chemical Co.,
St. Louis, Mo.

Motorola Inc.,
Phoenix, Ariz.

M&T Chemicals Inc.,
Detroit, Mich.

Nalco Chemical Co.,
Chicago, Ill.

National Cash Register Co.,
Dayton, Ohio

National Lead Co.,
New York, N. Y.

National Steel Corp.,
Weirton, W. Va.

Nortec Electronics Corp.,
Santa Clara, Calif.

North American Rockwell Corp.,
El Segundo, Calif.

Northern Electric Co.,
Montreal, Que., Canada

Norton Research Corp.,
Cambridge, Mass.

Nova Devices, Inc.,
New York, N. Y.

Owens-Illinois Glass Co.,
Toledo, Ohio

Park Electrochemical Corp.,
Great Neck, N. Y.

Pennwalt Corp.,
Philadelphia, Pa.

Phelps Dodge Refining Corp.,
Maspeth, N. Y.

Philips Laboratories, Inc.,
Briarcliff Manor, N. Y.

PPG Industries, Inc.,
Chemical Div.,
Pittsburgh, Pa.

Radio Corp. of America,
Electronic Components and Devices,
Lancaster, Pa.

Republic Foil Inc.,
Danbury, Conn.

Reynolds Metals Co.,
Richmond, Va.

Shawinigan Chemicals Ltd.,
Montreal, Que., Canada

Sonotone Batteries,
Marathon Battery Co.,
Cold Spring, N. Y.

Sprague Electric Co.,
North Adams, Mass.

Stackpole Carbon Co.,
St. Marys, Pa.

The Standard Oil Company of Ohio,
Cleveland, Ohio

Stauffer Chemical Co.,
Dobbs Ferry, N. Y.

Syncro Corp.,
Oxford, Mich.

Teletype Corp.,
Skokie, Ill.

Texas Instruments Inc.,
Dallas, Texas

3 M Company
St. Paul, Minn.

Titanium Metals Corp. of America,
Henderson, Nev.

Tyco Laboratories, Inc.,
Waltham, Mass.

Udylite Corp.,
Detroit, Mich. (4 memberships)

United States Steel Corp.,
Pittsburgh, Pa.

Varian Associates,
Palo Alto, Calif.

Western Electric Co., Inc.,
Chicago, Ill.

Wyandotte Chemicals Corp.,
Wyandotte, Mich.

Yardney Electric Corp.,
New York, N. Y.

Zenith Radio Corp.,
Chicago, Ill.